ISSN 2095-8137
CN 53-1229/Q
Volume 46 Issue 1
18 January 2025

ZR

Zoological Research



CODEN: DOYADI
www.zoores.ac.cn

KUNMING INSTITUTE OF ZOOLOGY, CAS
CHINA ZOOLOGICAL SOCIETY
Science Press

ZOOLOGICAL RESEARCH

Volume 46, Issue 1 18 January 2025

CONTENTS

The golden era of scientific publishing in China ····· *Yong-Gang Yao*, *Yong-Tang Zheng* (1)

Palmitoylation-mediated NLRP3 inflammasome activation in teleosts highlights evolutionary divergence in immune regulation ····· *Li Nie*, *Xiang-Yu Wu*, *Zi-Yue Zhao*, *Chen-Jie Fei*, *Ting-Fang Zhu*, *Jian-Zhong Shao*, *Jiong Chen* (3)

Enhanced risk assessment framework integrating distribution dynamics, genetically inferred populations, and morphological traits of *Diploderma* lizards ····· *Qi Xiao*, *Xiu-Dong Shi*, *Lin Shi*, *Zhong-Yi Yao*, *You-Hua Chen*, *Wei-Zhao Yang*, *Zi-Yan Liao*, *Yin Qi* (15)

Both 20S and 19S proteasome components are essential for meiosis in male mice ····· *Ting-Ting Han*, *Li-Ying Wang*, *Qiu-Xing Zhou*, *Wei Wei*, *Yan-Jie Ma*, *Ying-Hong Chen*, *Wei Li*, *Zhen-Yu Ju*, *Chao Liu* (27)

Novel mouse model of Alzheimer's disease exhibits pathology through synergistic interactions among amyloid-β, tau, and reactive astrogliosis ····· *Young-Eun Han*, *Sunhwa Lim*, *Seung Eun Lee*, *Min-Ho Nam*, *Soo-Jin Oh* (41)

Ribosome profiling and single-cell RNA sequencing identify the unfolded protein response as a key regulator of pigeon lactation ····· *Jing Liu*, *San-Feng Liu*, *Hui-Rong Mao*, *Hong-Xia Jiang*, *Shui-Bing Liu*, *Xiao-Fei Xu*, *Jin-Tao Wu*, *Xun Liu*, *Wen-Tao Zhang*, *Xiao-Long Hu*, *Biao Chen* (54)

Transposable elements shape the landscape of heterozygous structural variation in a bird genome ··· *Bo-Ping Li*, *Na Kang*, *Zao-Xu Xu*, *Hao-Ran Luo*, *Shi-Yu Fan*, *Xiao-Han Ao*, *Xing Li*, *Ya-Peng Han*, *Xiao-Bin Ou*, *Luo-Hao Xu* (75)

DNA2 knockout aggravates cerebral ischemia/reperfusion injury by reducing postsynaptic Homer1a ····· *Ting Ma*, *Yu-Meng Li*, *Peng-Yu Ren*, *Shi-Quan Wang*, *Xiang-Long Liu*, *Wen-Bo Lv*, *Wu-Gang Hou*, *Wen-Qiang Zuo*, *Wei-Qiang Lin*, *Jian Sima*, *An-Qi Geng* (87)

Identification of novel rodent and shrew orthohepeviruses sheds light on hepatitis E virus evolution ····· *Fu-Li Li*, *Bo Wang*, *Pei-Yu Han*, *Bei Li*, *Hao-Rui Si*, *Yan Zhu*, *Hong-Min Yin*, *Li-Dong Zong*, *Yi Tang*, *Zheng-Li Shi*, *Ben Hu*, *Xing-Lou Yang*, *Yun-Zhi Zhang* (103)

Transcription coactivator YAP1 promotes CCND1/CDK6 expression, stimulating cell proliferation in cloned cattle placentas ····· *Shan-Shan Wu*, *Xiao-Yu Zhao*, *Lei Yang*, *Chao Hai*, *Di Wu*, *Xue-Fei Liu*, *Li-Shuang Song*, *Chun-Ling Bai*, *Guang-Hua Su*, *Guang-Peng Li* (122)

Reciprocal translocation experiments reveal gut microbiome plasticity and host specificity in a Qinghai-Xizang Plateau lizard ····· *Wei Yu*, *Jing Yang*, *Li-Wei Teng*, *Xiao-Long Zhao*, *Ze-Yu Zhu*, *Shuang Cui*, *Wei-Guo Du*, *Zhen-Sheng Liu*, *Zhi-Gao Zeng* (139)

sRNA113 regulates *Pseudomonas plecoglossicida* motility to affect immune response against infection in pearl gentian grouper ····· *Li He*, *Mei-Qin Mao*, *Ling-Min Zhao*, *Qi Li*, *Hui Ge*, *Jiao-Nan Zhang*, *Jiao-Lin Zhang*, *Qing-Pi Yan* (152)

Deciphering the toxic effects of polystyrene nanoparticles on erythropoiesis at single-cell resolution ····· *Eun Jung Kwon*, *Hyeon Mi Sung*, *Hansong Lee*, *Soyul Ahn*, *Yejin Kim*, *Chae Rin Lee*, *Kihun Kim*, *Kyungjae Myung*, *Won Kyu Kim*, *Dokyoung Kim*, *Sanghwa Jeong*, *Chang-Kyu Oh*, *Yun Hak Kim* (165)

Multi-omics analysis and experimental verification reveal testicular fatty acid metabolism disorder in non-obstructive azoospermia ····· *Zhou Li*, *Yi-Jian Xiang*, *Zhi-Chuan Zou*, *Yu-Ming Feng*, *Hui Wang*, *Wei-Qing Chen*, *Xie Ge*, *Jin-Zhao Ma*, *Jun Jing*, *Bing Yao* (177)

Cross-species single-cell transcriptomics reveals neuronal similarities and heterogeneity in amniote pallium ····· *Fu-Bao-Qian Huang*, *Kuo Liao*, *Yu-Nong Sun*, *Zi-Hao Li*, *Yan-Ru Zhang*, *Ping-Fang Liao*, *Si-Yuan Jiang*, *Zhi-Yong Zhu*, *Duo-Yuan Chen*, *Ying Lei*, *Shi-Ping Liu*, *You-Ning Lin*, *Zhen-Kun Zhuang* (193)

Intranasal iron administration induces iron deposition, immunoactivation, and cell-specific vulnerability in the olfactory bulb of C57BL/6 mice ····· *Xiao-Qing Mi*, *Bao-Chen Liu*, *Le Qu*, *Yu Yuan*, *Hui Li*, *Ao-Yang Xu*, *Yu-Lin Zhang*, *Jun-Xia Xie*, *Ning Song* (209)

Elevated CXCL1 triggers dopaminergic neuronal loss in the substantia nigra of C57BL/6J mice: Evaluation of a novel Parkinsonian mouse model ····· *Xi-Zhen Ma*, *Guo-Rui Jia*, *Meng-Yu Li*, *Sheng-Han Zhang*, *Zhao-Xin Wang*, *Ning Song*, *Ying-Juan Liu*, *Jun-Xia Xie* (225)

Functional evolution of thyrotropin-releasing hormone neuropeptides: Insights from an echinoderm ····· *Yingqiu Zheng*, *Huachen Liu*, *Xin Dang*, *Juan Diego Gaitán-Espitia*, *Muyan Chen* (236)

Advances and applications of genome-edited animal models for severe combined immunodeficiency ····· *Xiao Zheng*, *Chun-Hui Huang*, *Sen Yan*, *Ming-Deng Rong* (249)

Cover image: The golden pheasant (*Chrysolophus pictus*). Photo by Hua Ding. **Design**: Li-Bin Wu

Inside back cover design: Li-Bin Wu

Yao & Zheng. *Zool. Res.* 2025, 46(1): 1−2
https://doi.org/10.24272/j.issn.2095-8137.2024.465
https://cstr.cn/32248.14.zr.2024.465

ZR | Zoological Research

Editorial Open Access

The golden era of scientific publishing in China

In Chinese culture, the dragon symbolizes faith, strength, courage, and an air of mystery. In 2024, guided by this auspicious emblem and supported by authors, readers, reviewers, and editorial board members, *Zoological Research* (*ZR*) has successfully completed its annual publishing objectives, achieved significant progress, and secured continued national funding support through its selection for China's Science and Technology Journal Excellence Action Plan (phase II). As we enter the year of the snake, a symbol of wisdom, renewal, transformation, and growth, we take this opportunity to reflect on past achievements and express our sincere appreciation to all contributors.

ZR demonstrated a steady increase in academic influence in 2024. According to the latest Journal Citation Report, its impact factor reached 4.0 (Q1), ranking 4th out of 180 SCI journals in the Zoology category, while also ranking 2nd in the same category based on the Journal Citation Indicator. Additionally, the *ZR* Scopus CiteScore reached 7.6, placing it 14th and within the top 4% of 490 journals in the Animal Science and Zoology section. The estimated impact factor, based on citations of *ZR* papers published in 2022–2023, has already surpassed 4.2, further solidifying its leading position in the field of Zoology as we move into 2025.

In 2024, *ZR* continued to focus on publishing high-impact research within its core topics, showcasing many interesting and impactful studies. For example, several papers on large animal models were published, highlighting their critical role in studies on human disease pathogenesis and therapeutic development (Li & Lai, 2024), as well as the application and advancement of cynomolgus monkeys, rhesus macaques, pigs, and rabbits, emphasizing their essential role in neurodegenerative disease research (Han et al., 2024; Pan et al., 2024). Another notable contribution was the comprehensive review by Yao et al. (2024b), which detailed the progress and challenges of utilizing tree shrew models, which offer unique advantages as alternatives to non-human primates in biomedical research. To spotlight research efforts by Chinese scientists, Hu & Zheng (2024) curated a special column focusing on the mechanisms of pain and the neurobiological basis of addiction and anesthesia. *ZR* also published several groundbreaking reports and reviews on Alzheimer's disease, offering novel perspectives on its underlying mechanisms and contributing to the fight against this devastating neurodegenerative condition (Cao & Zhang, 2024; Wang et al., 2024c).

Many studies published in 2024 have already attracted considerable attention and citations, despite their recent release. Among the most highly cited works, many featured advanced multi-omics analyses and microbiota research. For instance, Liu et al. (2024) conducted a sophisticated multi-omics analysis that identified the antiviral potential of alpha-linolenic acid in mitigating fish iridovirus infections, a study that has already been cited multiple times. Wang et al. (2024a) explored microbiota-host interactions through a comprehensive analysis of the gut microbiome and post-translational modifications. Zhao et al. (2024) identified a novel microbiota-gut-brain axis, revealing how chronic sleep deprivation induces cognitive deficits through NLRP3-mediated autophagy dysfunction and tau hyperphosphorylation.

Although listing all highly cited studies is beyond the scope of this editorial, these accomplishments reflect the high quality of recent publications and the rigorous editorial standards of the journal. Despite various challenges, such as the misclassification of letters as articles in the Web of Science database, which artificially lowered the impact factor of *ZR* (Zhang et al., 2024), the journal has maintained a strong performance. Looking ahead to 2025, the journal remains committed to delivering an exceptional publishing experience, with increasing numbers of authors choosing *ZR* as the preferred platform for high-impact publications.

The inaugural issue of *Zoological Research*: *Diversity and Conservation* (*ZRDC*) was also proudly released on 3 March 2024, coinciding with World Wildlife Day. As a sister journal to *ZR*, *ZRDC* is a quarterly, open-access, multidisciplinary international journal that aims to address globally significant questions in biodiversity and conservation science. The mission of *ZRDC*, as articulated in the editorial for its inaugural issue, is "*to publish major advances in theoretical and technical animal diversity research*, *resolve universally significant and cutting-edge scientific questions*, *and contribute to the harmonious coexistence of humans and nature and the synergistic development of society and the environment*, *with the hope that all countries on Earth will move towards a successful and ecologically sustainable future*" (Yao et al., 2024a). The inaugural issue of *ZRDC* featured several notable studies, including important research on mammals (Li et al., 2024b), birds (Wu et al., 2024), and amphibians (Wang et al., 2024b) of the Gaoligong Mountains in China, as well as a comprehensive review of the achievements and challenges of primate conservation in China (Li et al., 2024a). A special issue further explored the profound effects of habitat fragmentation on biodiversity (Ferreira et al., 2024; Palmeirim et al., 2024; Si et al., 2024). These high-quality publications exemplify our determination and confidence in establishing *ZRDC* as a leading journal in biodiversity and conservation in the near future.

ZR and *ZRDC* warmly invite proposals for organizing special issues/columns addressing both foundational and emerging scientific questions. Active researchers interested in

This is an open-access article distributed under the terms of the Creative Commons Attribution Non-Commercial License (http://creativecommons.org/licenses/by-nc/4.0/), which permits unrestricted non-commercial use, distribution, and reproduction in any medium, provided the original work is properly cited.

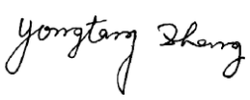
Copyright ©2025 Editorial Office of Zoological Research, Kunming Institute of Zoology, Chinese Academy of Sciences

contributing as guest editors, or those wishing to join the editorial boards of either journal, are encouraged to contact the editorial offices of *ZR* or *ZRDC*. Working together to advance innovative and impactful scientific research remains a priority, and we look forward to fostering meaningful collaborations that contribute to the continued success of *ZR* and *ZRDC*.

In closing, we extend our sincere gratitude for your steadfast, generous, and enduring support throughout a productive 2024. We look forward to your valuable contributions to both *ZR* and *ZRDC* in 2025, and we wish you all a very happy, prosperous, and vibrant year of the snake.



Yong-Gang Yao, Editor-in-Chief
Kunming Institute of Zoology, *Chinese Academy of Sciences*, *Kunming*, *Yunnan* 650223, *China*



Yong-Tang Zheng, Executive Editor-in-Chief
Kunming Institute of Zoology, Chinese Academy of Sciences, Kunming, Yunnan 650223, *China*

REFERENCES

Cao J, Zhang YW. 2024. Targeting synaptic pathology in Alzheimer's disease. *Zoological Research*, **45**(4): 875–876.

Ferreira JVA, Somavilla A, Benchimol M, et al. 2024. Environmental determinants of social wasp diversity and assemblage structure in an Amazonian archipelagic landscape. *Zoological Research: Diversity and Conservation*, **1**(2): 121–129.

Han BF, Liang WE, Li XJ, et al. 2024. Large animal models for Huntington's disease research. *Zoological Research*, **45**(2): 275–283.

Hu J, Zheng P. 2024. The neuroscience of pain, addiction, and anesthesia. *Zoological Research*, **45**(3): 709–710.

Li BG, Zhang H, Li M, et al. 2024a. Achievements and challenges of primate conservation in China. *Zoological Research: Diversity and Conservation*, **1**(1): 66–74.

Li Q, Li XY, Hu WQ, et al. 2024b. Mammals of Gaoligong Mountain in China: diversity, distribution, and conservation. *Zoological Research: Diversity and Conservation*, **1**(1): 3–19.

Li XJ, Lai LX. 2024. A booming field of large animal model research. *Zoological Research*, **45**(2): 311–313.

Liu L, Zhang Y, Yuan MD, et al. 2024. Integrated multi-omics analysis reveals liver metabolic reprogramming by fish iridovirus and antiviral function of alpha-linolenic acid. *Zoological Research*, **45**(3): 520–534.

Palmeirim AF, Benchimol M, Storck-Tonon D, et al. 2024. Biodiversity responses to insular fragmentation in Amazonia: two decades of research in the Balbina Hydroelectric Reservoir. *Zoological Research: Diversity and Conservation*, **1**(2): 106–116.

Pan MT, Zhang H, Li XJ, et al. 2024. Genetically modified non-human primate models for research on neurodegenerative diseases. *Zoological Research*, **45**(2): 263–274.

Si XF, Jin TH, Li WD, et al. 2024. TIL20: a review of island biogeography and habitat fragmentation studies on subtropical reservoir islands of Thousand Island Lake, China. *Zoological Research: Diversity and Conservation*, **1**(2): 89–105.

Wang HY, Liu LX, Chen XY, et al. 2024a. Comprehensive analysis of the gut microbiome and post-translational modifications elucidates the route involved in microbiota-host interactions. *Zoological Research*, **45**(1): 95–107.

Wang K, Yu ZB, Wu YH, et al. 2024b. Herpetofauna diversity of the Gaoligong Mountain in China: checklist, zoogeography, and conservation. *Zoological Research: Diversity and Conservation*, **1**(3): 169–179.

Wang Q, Zhu BT, Lei P. 2024c. Animal models of Alzheimer's disease: Current strategies and new directions. *Zoological Research*, **45**(6): 1385–1407.

Wu F, Gao JY, Yan D, et al. 2024. Bird species composition and conservation challenges in the Gaoligong Mountains, one of the most diverse bird areas in the world. *Zoological Research: Diversity and Conservation*, **1**(1): 20–50.

Yao YG, Jiang XL, Li SQ. 2024a. Why we need a new journal in diversity and conservation. *Zoological Research: Diversity and Conservation*, **1**(1): 1–2.

Yao YG, Lu L, Ni RJ, et al. 2024b. Study of tree shrew biology and models: A booming and prosperous field for biomedical research. *Zoological Research*, **45**(4): 877–909.

Zhang XP, Jiang XL, Yao YG. 2024. Impact of letters to the editor and publications in 2023. *Zoological Research*, **45**(1): 136–137.

Zhao N, Chen X, Chen QG, et al. 2024. NLRP3-mediated autophagy dysfunction links gut microbiota dysbiosis to tau pathology in chronic sleep deprivation. *Zoological Research*, **45**(4): 857–874.

Nie et al. *Zool. Res.* 2025, 46(1): 3−14
https://doi.org/10.24272/j.issn.2095-8137.2024.409
https://cstr.cn/32248.14.zr.2024.409

ZR | Zoological Research

Article Open Access

Palmitoylation-mediated NLRP3 inflammasome activation in teleosts highlights evolutionary divergence in immune regulation

Li Nie[1,2,3,#,*], Xiang-Yu Wu[1,2,3,#], Zi-Yue Zhao[1,2,3], Chen-Jie Fei[1,2,3], Ting-Fang Zhu[1,2,3], Jian-Zhong Shao[4,*], Jiong Chen[1,2,3,*]

[1] *State Key Laboratory for Managing Biotic and Chemical Threats to the Quality and Safety of Agro-Products*, *School of Marine Sciences*, *Ningbo University*, *Ningbo*, *Zhejiang* 315211, *China*

[2] *Laboratory of Biochemistry and Molecular Biology*, *School of Marine Sciences*, *Ningbo University*, *Ningbo*, *Zhejiang* 315211, *China*

[3] *Key Laboratory of Aquaculture Biotechnology of Ministry of Education*, *Ningbo University*, *Ningbo*, *Zhejiang* 315211, *China*

[4] *College of Life Sciences*, *Key Laboratory for Cell and Gene Engineering of Zhejiang Province*, *Zhejiang University*, *Hangzhou*, *Zhejiang* 310058, *China*

ABSTRACT

NLRP3 inflammasome activation is pivotal for cytokine secretion and pyroptosis in response to diverse stimuli, playing a crucial role in innate immunity. While extensively studied in mammals, the regulatory mechanisms governing NLRP3 activation in non-mammalian vertebrates remain largely unexplored. Teleosts, as basal vertebrates, represent an ideal model for exploring the evolutionary trajectory of inflammasome regulation. In this study, ABE assays, confocal microscopy, and biochemical analyses were applied to systematically characterize the mechanisms underlying NLRP3 inflammasome in teleosts, using large yellow croakers (*Larimichthys crocea*, *Lc*) and zebrafish (*Danio rerio*, *Dr*) as representative models. Our findings revealed a previously unrecognized palmitoylation-dependent regulatory mechanism essential for teleost NLRP3 activation. Specifically, zDHHC18-mediated palmitoylation at a teleost-specific cysteine residue (C946 in *Lc*NLRP3, C1037 in *Dr*NLRP3) was required for the translocation of NLRP3 to the dispersed trans-Golgi network, facilitating its subsequent recruitment to the microtubule-organizing center. This membrane trafficking was crucial for inflammasome assembly and downstream inflammatory responses. These findings provide new insights into the distinct regulatory mechanisms of NLRP3 activation in teleosts, highlighting an evolutionary divergence that contributes to innate immunity adaptation in early vertebrates.

Keywords: NLRP3; Palmitoylation; zDHHC18; Teleost; Inflammasome activation

This is an open-access article distributed under the terms of the Creative Commons Attribution Non-Commercial License (http://creativecommons.org/licenses/by-nc/4.0/), which permits unrestricted non-commercial use, distribution, and reproduction in any medium, provided the original work is properly cited.

Copyright ©2025 Editorial Office of Zoological Research, Kunming Institute of Zoology, Chinese Academy of Sciences

INTRODUCTION

The inflammasome serves as a critical molecular hub for initiating inflammatory responses by activating inflammatory caspases and driving cytokine maturation (Martinon et al., 2002). Among the various inflammasomes identified to date, the NLRP3 inflammasome is the most extensively studied due to its broad involvement in diverse biological processes and its involvement in the pathogenesis of numerous diseases (Holbrook et al., 2021; Mangan et al., 2018; Sharma & Kanneganti, 2021; Tan et al., 2013). The canonical NLRP3 inflammasome is a multi-protein complex composed of the sensor molecule NACHT-, leucine-rich repeat (LRR)- and pyrin domain (PYD)-containing protein 3 (NLRP3), the adaptor protein apoptosis associated speck-like protein containing a CARD (ASC), and the effector protein pro-Caspase-1 (He et al., 2016a). Upon activation, Caspase-1 cleaves the cytokine precursors pro-IL-1β and pro-IL-18 into their mature forms, driving robust inflammatory responses. Concurrently, Caspase-1 cleaves and activates gasdermin D (GSDMD), releasing its N-terminal domain to form plasma membrane-spanning pores, thereby inducing pyroptosis, a lytic and highly inflammatory form of programmed cell death (Franchi et al., 2009; Shi et al., 2015).

Despite its well-established role in innate immunity, our understanding of the regulatory mechanisms governing NLRP3 inflammasome activation is primarily limited to mammalian species, leaving significant gaps in our

Received: 14 November 2024; Accepted: 09 December 2024; Online: 10 December 2024

Foundation items: This work was supported by the National Natural Science Foundation of China (32473194), Natural Science Foundation of Zhejiang Province (LY23C190002), Natural Science Foundation of Ningbo City (202003N4011), and One Health Interdisciplinary Research Project of Ningbo University (HZ202201)

[#]Authors contributed equally to this work

*Corresponding authors, E-mail: nieli@nbu.edu.cn; shaojz@zju.edu.cn; chenjiong@nbu.edu.cn

understanding of its function and evolutionary development in non-mammalian vertebrates. The components, membrane translocation, assembly, and regulation of the NLRP3 inflammasome in non-mammalian vertebrates remain largely unexplored, although the innate immune network in lower vertebrates is considerably more complex than in mammals. Teleosts, positioned at the intersection of innate and adaptive immunity (Boehm & Swann, 2014), provide an ideal model for studying the evolutionary regulation of the NLRP3 inflammasome.

Recent studies underscore the suitability of teleosts for inflammasome research. Key inflammasome components, including NLRP3, ASC, Caspase-1, and GSDME — the sole gasdermin family member associated with pyroptosis in teleosts—have been identified in teleosts in recent years. For instance, in Japanese flounder, NLRP3 inflammasome activation has been shown to play a vital role in restricting *Edwardsiella piscicida* colonization through the maturation of IL-1β, a crucial step in mounting effective host immune responses against bacterial infections (Chen et al., 2020). Similarly, zebrafish studies have demonstrated that the NLRP3 inflammasome coordinates ASC-dependent IL-1β maturation and GSDME-mediated pyroptosis, highlighting its pivotal role in inflammation and cell death (Li et al., 2020b). Unique inflammatory regulatory mechanisms have also been discovered in turbot, where *Sm*Caspase, an inflammatory caspase, mediates both canonical and non-canonical inflammasome pathways. *Sm*Caspase possesses the ability to recognize cytosolic lipopolysaccharides (LPS) via its N-terminal CARD domain, driving pyroptosis and antibacterial defenses (Chen et al., 2021). Moreover, *Sm*Caspase interacts with *Sm*NLRP3-*Sm*ASC to form the NLRP3 inflammasome complex, further emphasizing its multifunctionality in teleost immune responses. Comparative studies on *Salmo salar* and *Tetraodon* have also provided insights into the role of the NLRP3 inflammasome in immune regulation and its evolutionary conservation with mammals (Acevedo et al., 2023). Notably, fish inflammasomes can function independently of caspase-1 for IL-1β processing, as observed in seabream macrophages, indicating the presence of alternative cytokine maturation pathways (Angosto et al., 2012). Furthermore, two distinct models of NLRP3 inflammasome assembly have emerged in teleosts, distinguished by the domain architecture of their Caspase-1 homologs: one involving PYD-containing Caspase-1, as seen in zebrafish, and the other involving CARD-containing Caspase-1, which resembles the mammalian homolog and is found in most teleost species (Chuphal et al., 2022; Li et al., 2020b).

In this study, the large yellow croaker (*Larimichthys crocea*, *Lc*), an economically important marine species endemic to China, was used as a representative CARD-containing Caspase-1 inflammasome model with a well-sequenced genome. Large yellow croakers are highly susceptible to environmental stress and pathogen-induced diseases (Ao et al., 2015; Chen et al., 2019; Kon et al., 2021; Wu et al., 2014), particularly systemic infections caused by *Pseudomonas plecoglossicida*, which result in severe tissue necrosis, systemic damage, and high mortality rates. Such infections trigger robust inflammatory responses, characterized by elevated pro-inflammatory cytokine expression (Tang et al., 2020; Yuan et al., 2022). This pathogen exhibits sophisticated immune evasion strategies, including inhibition of phagocytosis and manipulation of immune signaling pathways (Sun et al., 2019; Tao et al., 2020; Wu et al., 2022), making it an ideal candidate for studying inflammasome-mediated immune mechanisms. Additionally, the zebrafish (*Danio rerio*, *Dr*) was used as a representative PYD-containing Caspase-1 inflammasome model for comparative study. Together, these two teleost species facilitated a systematic investigation into the palmitoylation-mediated activation of the NLRP3 inflammasome in teleosts. Our findings revealed a previously unrecognized palmitoylation-dependent mechanism for NLRP3 activation, with palmitoylation sites and palmitoyl transferase pathways distinct from that described in mammals. Specifically, a teleost-specific cysteine residue (C946 in *Lc*NLRP3, C1037 in *Dr*NLRP3) was identified as the site of palmitoylation by zDHHC18, a modification essential for NLRP3 translocation to the dispersed trans-Golgi network (dTGN) and subsequent localization to the microtubule-organizing center (MTOC). This membrane trafficking event is critical for inflammasome assembly and subsequent initiation of immune responses. This species-specific palmitoylation event highlights a unique regulatory adaptation in teleosts, suggesting a co-evolution of palmitoyl transferases and palmitoylation mechanisms in teleosts, enabling fine-tuned immune responses adapted to their specific environmental challenges.

MATERIALS AND METHODS

Fish and ethics statements

Large yellow croakers (100±20 g) were purchased from a maricultural farm in Xiangshan County, Ningbo, China, and were maintained at 25°C in a flow-through seawater system. Fish were acclimated to this environment for at least two weeks prior to use in experiments. All experiments involving animals were approved by the Ningbo University Institutional Animal Care and Use Committee (approval No. 12838) and were carried out in compliance with the National Institutes of Health's Guide for the Care and Use of Laboratory Animals.

Antibodies

Antibodies and compounds used in this study included: anti-TOMM20 (1:200, #sc-17764, Santa Cruz Biotechnology, USA), anti-Calnexin (1:100, #sc-23954, Santa Cruz Biotechnology, USA), anti-γ-tubulin (1:500, #T6557, Sigma Aldrich, USA), anti-TGN46 (1:100, #sc-166594, Santa Cruz Biotechnology, USA), anti-ninein (1:100, #sc-376420, Santa Cruz Biotechnology, USA), goat anti-mouse IgG2b Cross-adsorbed secondary antibody, Alexa Fluor™ 555 (1:500, #A-21147, Thermo Fisher Scientific, USA), goat anti-rabbit IgG (H+L) cross-adsorbed secondary antibody, Alexa Fluor™ 488 (1:500, #A-11008, Thermo Fisher Scientific, USA), goat anti-rabbit IgG, horseradish-peroxidase (HRP) conjugated secondary antibody (1:3000, #M21002, Abmart, China), goat anti-mouse IgG, HRP conjugated secondary antibody (1:3000, #M21001, Abmart, China), mouse anti-HA (1:3000, #M20003, Abmart, China), rabbit anti-HA (1:3000, #TT0050, Abmart, China), rabbit anti-FLAG tag (1:3000, #TT0053, Abmart, China), mouse anti-FLAG tag (1:3000, #M20008, Abmart, China), mouse anti-Myc (1:3000, #M20002, Abmart, China), anti-β-tubulin (1:2000, #M20005, Abmart, China), anti-GAPDH (1:2000, M20006, Abmart, China), anti-FLAG® M2 affinity gel (#A2220, Sigma-Aldrich, USA), monoclonal anti-HA-agarose (#A2095, Sigma-Aldrich, USA).

Plasmids

Various plasmids, including pcDNA3-*Lc*NLRP3-Flag, pcDNA3-*Lc*NLRP3-HA, pcDNA3-*Lc*Pro-Caspase-1-Flag, pcDNA3-*Lc*Pro-Caspase-1-HA, pcDNA3-*Lc*Pro-Caspase-1-Myc, pcDNA3-*Lc*ASC-HA, pcDNA3-*Lc*ASC-Myc, pcDNA3-*Lc*GSDME-HA, and pcDNA3-*Lc*GSDME-Flag, were generated in this study. The 22 pcDNA3-*Lc*ZDHHCs-HA plasmids were previously constructed by our lab (Dai et al., 2024). Primer sequences used in this study are provided in Supplementary Table S1.

Cell culture and bacteria

HEK293T cells were cultured in Dulbecco's Modified Eagle Medium (DMEM, #11966025, Gibco, Thermo Fisher Scientific, USA) supplemented with 10% (v/v) fetal bovine serum (FBS, #26140079, Thermo Fisher Scientific, USA) and 1% penicillin/streptomycin (#15140148, Thermo Fisher Scientific, USA). The HEK293T cells were originally obtained from the Cell Bank of the Shanghai Institute of Biochemistry and Cell Biology (https://www.cellbank.org.cn/) and cultured at 37°C with 5% CO_2.

Large yellow croaker primary head kidney monocytes/macrophages (*Lc*MO/MΦs) were isolated and cultured as described in previous research, with minor modifications (Li et al., 2020a). Briefly, fish were immersed in near-freezing water for 30 min to mitigate pain or stress and after a lethal blow to the head, head kidneys were aseptically removed and homogenized using a sterile syringe plunger through a 100 μm nylon cell strainer (#352360, Corning, USA) in RPMI1640 medium (#11875093, Thermo Fisher Scientific, USA). Cell suspensions (1 mL) were layered on 4 mL of Ficoll (45-001-751, Thermo Fisher Scientific, USA), followed by centrifugation at 400 ×*g* for 30 min at room temperature. The buffy coat layer was then collected, and cells were twice washed in RPMI1640 medium. Isolated cells were seeded in 6-well plates and grown at 24°C and 5% CO_2 in complete RPMI1640 medium supplemented with 5% fish serum, 5% FBS, and 1% penicillin/streptomycin. After overnight incubation, non-adherent cells were removed prior to experiments.

Gram-negative *P. plecoglossicida* strains were a kind gift from Professor Yan's Lab (Huang et al., 2018). Briefly, the bacteria were grown at 18°C with shaking in nutrient broth medium (#12795084, Thermo Fisher Scientific, USA). Cells were harvested at the logarithmic growth phase by centrifugation at 5 000 ×*g* for 15 min at room temperature and washed with sterile phosphate-buffered saline (PBS) prior to usage.

Antibody preparation

Rabbit polyclonal antibodies against *Lc*pro-Caspase-1 p10 (anti-*Lc*pro-Caspase-1) were generated. Briefly, a 15 amino acid sequence "CEGLPFRNIRQMPTK" within the p10 subunit of *Lc*pro-Caspase-1 was synthesized and conjugated to keyhole limpet hemocyanin (KLH) proteins, with further immunization, serum collection, antibody purification, and validation performed by the GenScript Biotech Corporation (China).

***Lc*NLRP3 inflammasome activation and immunoblotting**

To examine endogenous *Lc*NLRP3 inflammasome activation, *Lc*MO/MΦs (1×10^6 cells) were primed with lipopolysaccharide (LPS; #L7895, Sigma Aldrich, USA) at a concentration of 10 μg/mL for 8 h, followed by nigericin (#N7143, Sigma Aldrich, USA; 40 μmol/L) or adenosine triphosphate (ATP, A7699, Sigma Aldrich, USA; 5 mmol/L) activation for 1 h and 5 h, respectively. Alternatively, *Lc*MO/MΦs (1×10^6 cells) were infected with *P. plecoglossicida* at a multiplicity of infection (MOI) of 10 for the indicated time points.

To examine exogenous *Lc*NLRP3 inflammasome activation, key components and downstream effectors, including *Lc*NLRP3, *Lc*ASC, *Lc*pro-Caspase-1, and/or *Lc*GSDME were cloned into respective constructs, which were cotransfected (1 μg/10^6 cells) into HEK293T cells using Lipofectamine 3000 (#L3000015, Thermo Fisher Scientific, USA) for 24 h. The transfected cells were subsequently trypsinized, reseeded, subjected to various stimulation groups for further analysis.

To investigate the impact of palmitoylation on *Lc*NLRP3 inflammasome activation, cells were treated with palmitoylation activators and inhibitors, including palmitic acid (#P5585, Sigma Aldrich, USA; 200 μmol/L), 2-bromohexadecanoic acid (2-BP; #21604, Sigma Aldrich, USA; 100 μmol/L), and palmostatin B (Palm B; #508738, Sigma Aldrich, USA; 5 μmol/L). These treatments were applied during the priming stage for 12 hours and maintained throughout the assays.

Immunoblotting was further performed to detect cleavage products of *Lc*pro-Caspase-1 and *Lc*GSDME. Briefly, cells were lysed in pre-chilled RIPA lysis buffer (#89901, Thermo Fisher Scientific, USA) supplemented with a protease inhibitor cocktail (#A32965, Thermo Fisher Scientific, USA). After 30 min of lysis on ice, lysates were mixed with 4×Laemmli buffer (#1610747, Bio-Rad, USA) and denatured at 100°C for 12 min, followed by centrifugation for 30 s at 13 000 ×*g* at room temperature. Denatured samples were then resolved using sodium dodecyl-sulfate polyacrylamide gel electrophoresis (SDS-PAGE) and transferred to nitrocellulose membranes (#GE10600007, Sigma Aldrich, USA). The membranes were then incubated for 1 h in 5% skim milk and probed using respective primary antibodies at 4°C. After overnight incubation, membranes were incubated at room temperature in respective HRP-conjugated secondary antibodies for 1 h. Immunoreactive bands were detected using an ECL western blotting substrate (#32106, Thermo Fisher Scientific, USA; #WBKLS0500, Millipore, USA), followed by exposure to X-ray films.

Cellular transfection and co-immunoprecipitation

HEK293T cells were used to reconstitute the LcNLRP3 inflammasome due to their high transfection efficiency and lack of endogenous NLRP3 inflammasome components, making them an ideal "bioreactor" for studying inflammasome components and interactions from other species, as demonstrated in many studies (He et al., 2016b; Li et al., 2020b; Shi et al., 2016). HEK293T cells (1×10^6 cells) were cotransfected with the following plasmid combinations: Flag-*Lc*NLRP3 (2 μg) and HA-*Lc*NLRP3 (2 μg); Flag-*Lc*NLRP3 (2 μg) and HA-*Lc*ASC (2 μg); HA-*Lc*pro-Caspase-1 (2 μg) and Myc-*Lc*ASC (3 μg); Flag-*Lc*NLRP3 (2 μg), Myc-*Lc*ASC (3 μg), and HA-*Lc*pro-Caspase-1 (2 μg); HA-*Lc*NLRP3 (2 μg) and Flag-*Lc*NLRP3-C946A (2 μg; cysteine 946 mutated to alanine); and HA-*Lc*ASC (2 μg) and Flag-*Lc*NLRP3-C946A (2 μg). Briefly, the specified amounts of plasmids were transfected into HEK293T cells using Lipofectamine 3000 (#L3000015, Thermo Fisher Scientific, USA). After 48 h, the cells were lysed in pre-chilled RIPA lysis buffer supplemented with a protease inhibitor cocktail. The lysates were incubated

on ice for 30 min, then centrifuged at 13 000 ×*g* for 5 min at 4°C. The resulting supernatants were incubated overnight at 4°C under gentle rotation with anti-FLAG M2 affinity gel (#A2220, Sigma Aldrich, USA) or anti-HA (#2095, Sigma Aldrich, USA) agarose beads. The agarose beads were subsequently washed five times with wash buffer (10 mmol/L Tris-HCl (pH 7.5), 10 mmol/L KCl, 1.5 mmol/L $MgCl_2$, 500 mmol/L NaCl, 0.1% Tween 20) prior to SDS-PAGE and western blot analyses as detailed above using respective antibodies.

To identify potential palmitoyl transferases interacting with *Lc*NLRP3, HEK293T cells were cotransfected with Flag-*Lc*NLRP3 (2 μg) and HA-zDHHC plasmids (2 μg) using Lipofectamine 3000. After 48 h, the cells were lysed, co-immunoprecipitated, and immunoblotted as described above.

Acyl-biotin exchange (ABE) assay

The ABE assay was performed to analyze the palmitoylation status of *Lc*NLRP3, following previously described protocols (Balasubramanian et al., 2024). In brief, HEK293T cells were transfected with the Flag-*Lc*NLRP3 (3 μg) or Flag-*Dr*NLRP3 (3 μg) constructs or their respective mutants, or cotransfected with Flag-*Lc*NLRP3 (3 μg) and HA-*Lc*ZDHHC5/9/17/18 (2 μg), using Lipofectamine 3000. After 48 h, cells were sonicated for 30 s (2 s intervals, 20 kHz) in PBS supplemented with protease inhibitor cocktail. Sonicated samples were centrifuged at 13 000 ×*g* for 5 min at 4°C and the resulting supernatants were assayed to determine total protein (#5000002, Bio-Rad, USA). Collected supernatants (3 mg of protein) were then incubated with blocking buffer (250 mmol/L HEPES pH 7.4, 1 mmol/L EDTA, 2.5% SDS, 20 mmol/L methyl methanethiosulfonate (MMTS; #208795, Sigma Aldrich, USA)) at 50°C for 40 min with constant shaking to block free thiols and were precipitated three times with chloroform/methanol/water (v/v 1:4:3) to remove the remaining MMTS. Samples were then equally divided into two parts and incubated with HAM buffer (0.7 mol/L hydroxylamine (#55460, Sigma Aldrich, USA), 1 mmol/L BiotinHPDP (#16459, Cayman Chemical, USA), 0.2% Triton X-100, 0.1% protease inhibitor cocktail) or a negative control (50 mmol/L HEPES, 1 mmol/L biotin-HPDP, 0.2% Triton X-100, 0.1% protease inhibitor cocktail) at room temperature for 1 h. The samples were precipitated again, resolved, and diluted with dilution buffer (20 mmol/L HEPES pH 7.4, 100 mmol/L NaCl, 1 mmol/L EDTA, 0.5% Triton X-100, 0.1% protease inhibitor cocktail) to reach an SDS concentration compatible with avidin capture, then incubated with 30 μL of streptavidin beads (#20347, Thermo Fisher Scientific, USA) with shaking at 4°C for 1 h. The beads were washed three times with wash buffer (20 mmol/L HEPES pH 7.4, 600 mmol/L NaCl, 1 mmol/L EDTA, 0.5% Triton X-100, 0.1% protease inhibitor cocktail), followed by a final wash with dilution buffer. The beads were then mixed with 2×Laemmli buffer (#1610737EDU, Bio-Rad, USA) and denatured at 95°C for 10 min prior to SDS-PAGE and western blot analyses using indicated antibodies, as detailed above.

Immunofluorescence and live cell microscopy

For immunofluorescence microscopy, HEK293T cells were transfected or cotransfected with following plasmid combinations: Flag-*Lc*NLRP3 (1 μg); Flag-*Lc*ASC (1 μg); Flag-*Lc*NLRP3-C946A (1 μg); HA-*Lc*zDHHC18 (1 μg); Flag-*Lc*NLRP3 (1 μg) and HA-*Lc*NLRP3 (1 μg); Myc-*Lc*ASC (1.5 μg) and Flag-*Lc*pro-Caspase-1 (1 μg); HA-*Lc*ASC(1 μg) and Flag-*Lc*NLRP3-C946A (1 μg); and Flag-*Lc*NLRP3 (1 μg) and HA-*Lc*zDHHC18 (1 μg) for 24 h, then seeded at a density of 2×10^5 cells/mL on coverslips. In some experiments, cells were pre-treated with PA (200 μmol/L) or 2-BP (100 μmol/L) during transfection. After 24 h of cultivation on coverslips, the cells were stimulated with nigericin (40 μmol/L) for 1 h or directly fixed with 4% paraformaldehyde in sterile PBS at room temperature for 15 min. The cells were then permeabilized with 0.25% Triton X-100 (for GTU and Ninein) or 0.5% saponin (for TGN46, TOMM20, Calnexin and Flag-, HA- and Myc-tagged proteins) for an additional 15 min before incubation in PBS containing 5% BSA for 1 h at room temperature. After blocking, the cells were labeled with respective primary and secondary antibodies, with the nuclei then visualized by 4',6-diamidino-2-phenylindole (DAPI) staining (#62248, Thermo Fisher Scientific, USA).

For live cell imaging, HEK293T and *Lc*MO/MΦ cell models were used to observe pyroptosis. Briefly, HEK293T cells (1×10^6) were transfected or cotransfected with the following plasmid combinations: HA-*Lc*GSDME (2 μg); HA-*Lc*GSDME (2 μg) and Flag-*Lc*NLRP3 (2 μg); HA-*Lc*GSDME (2 μg) and Flag-*Lc*pro-Caspase-1 (2 μg); HA-*Lc*GSDME (2 μg) and HA-*Lc*ASC (2 μg); and HA-*Lc*GSDME (2 μg), Flag-*Lc*NLRP3 (2 μg)/Flag-*Lc*NLRP3-C946A (2 μg), Flag-*Lc*pro-Caspase-1 (2 μg), and HA-*Lc*ASC (2 μg). After 48 h of transfection, the cells were incubated in culturing medium containing 20 nmol/L SYTOX Green (#S7020, Thermo Fisher Scientific, USA) for 4 h before nigericin (40 μmol/L) stimulation for an additional 1 h at 37°C. *Lc*MO/MΦ cells (1×10^6) were cultured in medium containing 20 nmol/L SYTOX Green for 4 h, then stimulated with *P. plecoglossicida* (MOI=10) or primed with LPS (10 μg/mL) for 8 h followed by ATP (5 mmol/L) or nigericin (40 μmol/L) activation for indicated time points at 26°C. All culture dishes for live cell imaging were placed into a microscope stage chamber supplemented with 5% CO_2 and heated to 37°C or 26°C.

All images were collected and analyzed using a Zeiss LSM 880 confocal microscope (Carl Zeiss AG, Germany) and ZEN Blue software (Carl Zeiss AG, Germany), respectively.

Lactate dehydrogenase (LDH) assay

LDH release was measured in cell culture supernatants immediately after the experiments using the CytoTox96® Non-Radioactive Cytotoxicity Assay (#G1780, Promega, USA), following the manufacturer's instructions. Results were normalized to a lysis control, with background values from blank medium subtracted.

siRNA interference

To knockdown *zDHHC18* expression in *Lc*MO/MΦs, *Lc*MO/MΦ cells were transfected with 1 μg of *zDHHC18* siRNAs using Lipofectamine™ RNAiMAX (#13778150, Thermo Fisher Scientific, USA), according to the manufacturers' instructions. After 48 h of transfection, the cells were collected, followed by total RNA isolation and reverse transcription-quantitative real-time polymerase chain reaction (RT-qPCR). The siRNA sequences used included: Scramble control, 5'-ACGGTGTACTGCGGATCTAACCA-3'; *LcZDHHC18* siRNA #1, 5'-GTTTCTTCTACACCTTCAT-3'; *LcZDHHC18* siRNA #2, 5'-CCAGAGCTTTCAACAAGCT-3'; and *LcZDHHC18* siRNA #3, 5'-CGTGATATGTTTCTTCTCA-3'.

Model building and structure representation

The tertiary structures of *Lc*ZDHHC18 and *Dr*ZDHHC18 were

analyzed and modeled using SWISS-MODEL (https://swissmodel.expasy.org/interactive). To explore the structural characteristics of oligomerized *Lc*NLRP3, the six-fold double-ring cage structure of mouse NLRP3 (PDB ID: 7LFH) was used as a template in SWISS-MODEL. The *Lc*NLRP3 protein sequence was applied to generate homology models of oligomerized *Lc*NLRP3.

Quantification and statistical analysis

Data are presented as mean±standard deviation (SD). Statistical analyses were performed using GraphPad Prism v.8. Differences among multiple groups were analyzed using one-way analysis of variance (ANOVA), followed by Tukey's multiple comparison tests, while differences between two groups were assessed using Student's *t*-tests. Statistical significance was denoted as *: $P<0.05$ and **: $P<0.01$.

RESULTS

NLRP3 palmitoylation is required for inflammasome activation in teleosts

To investigate the regulatory mechanisms of NLRP3 inflammasome activation in teleosts, we characterized the assembly and function of the large yellow croaker NLRP3 (*Lc*NLRP3) inflammasome, building upon prior studies of the zebrafish NLRP3 (*Dr*NLRP3) (Li et al., 2020b). Structural analyses suggested that, similar to its mammalian counterpart, *Lc*NLRP3 oligomerized to a cage-like configuration (Andreeva et al., 2021) (Supplementary Figure S1A, B) and interacted with the adaptor molecule *Lc*ASC (Supplementary Figure S1C), which subsequently recruited *Lc*pro-Caspase-1 to assemble the *Lc*NLRP3 inflammasome (Supplementary Figure S1D). Notably, the presence of *Lc*ASC was required for the interaction between *Lc*NLRP3 and *Lc*pro-Caspase-1 (Supplementary Figure S1E, F). Additionally, the presence of all three components and stimulation with nigericin (a common NLRP3 activator) were required for the *Lc*NLRP3 inflammasome to induce *Lc*pro-caspase-1 cleavage, resulting in the formation of the p10 band (Figure 1A; Supplementary Figure S1G). Correspondingly, cleavage of the downstream effector *Lc*GSDME was observed, along with induction of pyroptosis and release of lactate dehydrogenase (LDH). These effects were only observed in cells co-expressing *Lc*NLRP3, *Lc*ASC, and *Lc*pro-Caspase-1 and subjected to nigericin stimulation (Figure 1B, C; Supplementary Figure S1H). *In vivo* analyses further confirmed that stimulation with classical NLRP3 activators (LPS priming followed by nigericin or ATP) or infection with *P. plecoglossicida* induced robust *Lc*NLRP3 inflammasome formation and subsequent *Lc*pro-Caspase-1 cleavage, generating the p10 fragment (Figure 1D; Supplementary Figure 1I) and ultimately leading to pyroptosis in head kidney-derived *Lc*MO/MΦs (Supplementary Figure S1J).

The dynamic membrane trafficking of mammalian NLRP3, involving the TGN, mitochondria, and endoplasmic reticulum (ER), has been extensively documented in the context of inflammasome activation (Arumugam et al., 2022; Chen & Chen, 2018; Zhou et al., 2020). However, the role of membrane translocation in teleost NLRP3 inflammasome activation and the precise site of inflammasome assembly remain unexplored. Our results showed that, under resting conditions, *Lc*NLRP3 exhibited a diffuse cytoplasm distribution without specific localization to the dTGN, mitochondria, or ER membranes (Supplementary Figure S1K). Upon nigericin stimulation, *Lc*NLRP3 translocated primarily to the dTGN membrane, with no significant association with mitochondria or ER membranes (Figure 1E). Additionally, *Lc*NLRP3 inflammasome assembly occurred at the MTOC, as evidenced by the formation of *Lc*NLRP3-ASC specks and the colocalization of *Lc*NLRP3, *Lc*ASC, and *Lc*Caspase-1 with the MTOC marker GTU (Figure 1F, G). These observations indicate that teleost NLRP3 inflammasome activation also requires TGN-mediated translocation of *Lc*NLRP3 to the MTOC, where inflammasome assembly occurs.

Palmitoylation, a lipid modification known to mediate protein membrane targeting (Bijlmakers & Marsh, 2003; Rocks et al., 2010), was investigated as a potential regulator of teleost NLRP3 activation, based on prior evidence suggesting the involvement of zebrafish *Dr*NLRP3 in palmitoylation-mediated activation (Nie et al., 2024). In the present study, ABE assays confirmed that *Lc*NLRP3 also undergoes palmitoylation (Drisdel et al., 2006) (Supplementary Figure S2A). Notably, *Lc*NLRP3 palmitoylation levels were significantly increased following palmitate acid (PA) treatment and almost abolished in the presence of 2-BP, a palmitoyl transferase inhibitor (Figure 2A, B).

To assess the functional relevance of *Lc*NLRP3 palmitoylation, its impact on inflammasome assembly and activation was evaluated. Results showed that palmitoylation inhibition with 2-BP suppressed *Lc*NLRP3 oligomerization and reduced interactions with *Lc*ASC during inflammasome assembly (Figure 2C, D). Colocalization of *Lc*NLRP3 with the MTOC marker ninein and the formation of *Lc*NLRP3-ASC specks were substantially impaired in the presence of 2-BP, while PA treatment significantly enhanced these interactions (Figure 2E, F). These observations were consistent with functional assays: PA treatment significantly increased pyroptosis levels and LDH release, whereas 2-BP treatment led to a marked decrease in these pyroptotic responses (Figure 2G; Supplementary Figure S2B, C). Cleavage of *Lc*pro-Caspase-1 was enhanced by PA or Palm B, an acyl-protein thioesterase inhibitor, while 2-BP treatment resulted in dose-dependent inhibition (Figure 2H, I). Similar effects were observed for *Lc*GSDME cleavage and corresponding changes in LDH secretion (Figure 2J, K). Furthermore, the induced expression levels of inflammasome-related genes, including *LcNLRP3*, *LcASC*, and *LcCaspase-1*, were unaffected by 2-BP treatment (Supplementary Figure S2D), indicating that the observed decrease in downstream effector cleavage with palmitoylation inhibition was attributable to impaired inflammasome assembly rather than altered mRNA levels.

Teleost NLRP3s are palmitoylated at unique residues distinct from mammalian counterparts

Recent studies have identified several palmitoylation sites in mammalian NLRP3, each playing distinct regulatory roles in its activation and function (Hu et al., 2024; Nie et al, 2024; Wang et al, 2023; Yu et al, 2024; Zheng et al, 2023). However, key residues implicated in palmitoylation, such as C130 and C958 in human and mouse NLRP3, are absent in teleost NLRP3 (Supplementary Figure S2E), indicating potential evolutionary divergence. Therefore, teleost NLRP3 was screened for possible palmitoylation sites based on predictions by GPS-Palm (http://gpspalm.biocuckoo.cn/download.php). A unique cysteine residue (C946 in *Lc*NLRP3 and C1037 in *Dr*NLRP3) was identified, which exhibited the

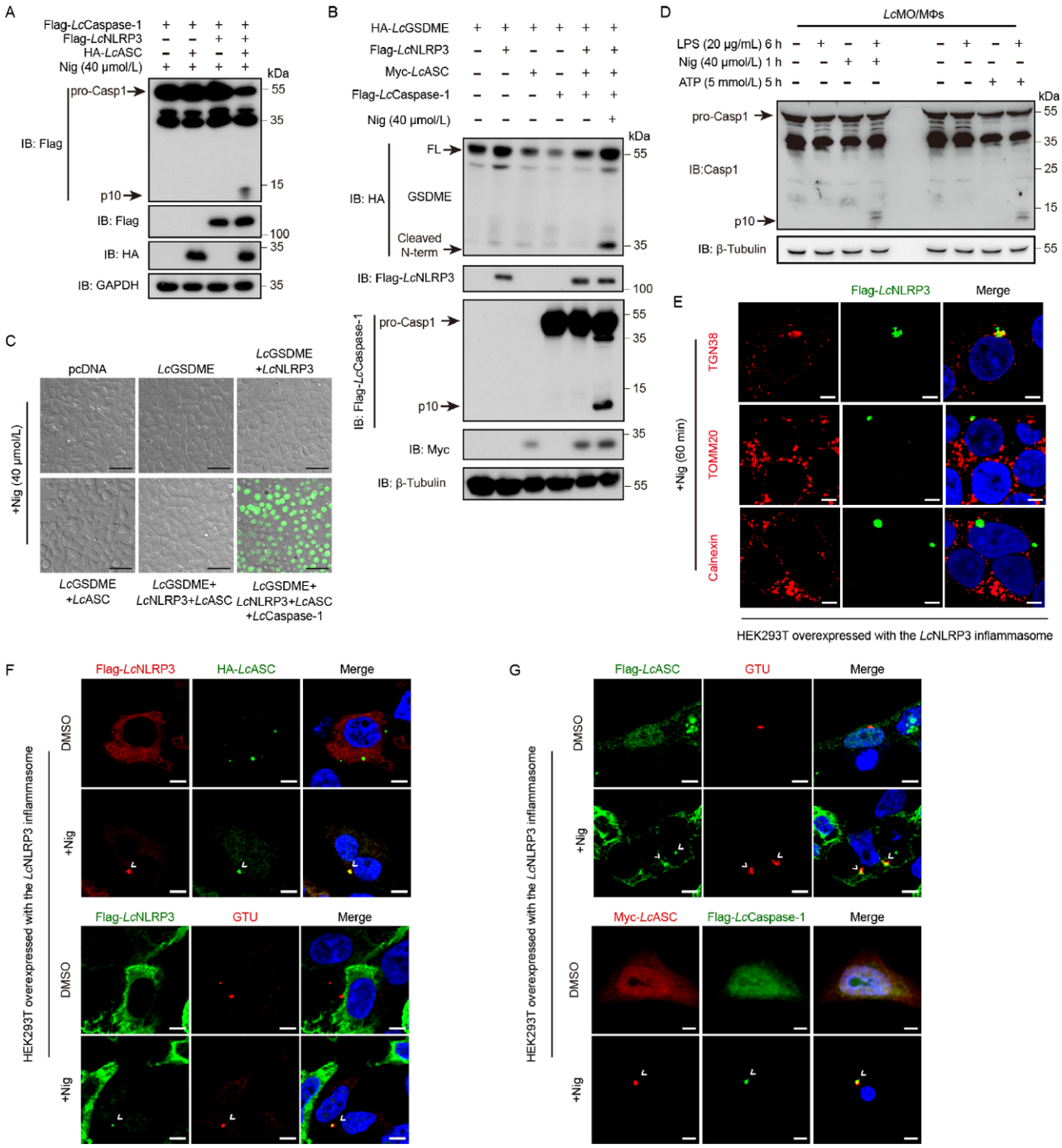


Figure 1 Components and activation of large yellow croaker NLRP3 inflammasome

A: Caspase-1 processing (p10) in nigericin (40 μmol/L)-stimulated HEK293T cells overexpressing Flag-*Lc*Caspase-1, with or without other inflammasome components, Flag-*Lc*NLRP3, and/or HA-*Lc*ASC. B: Gasdermin E (cleaved N-term) processing in HEK293T cells overexpressing HA-*Lc*GSDME, with or without Flag-*Lc*NLRP3, Myc-*Lc*ASC, and/or Flag-*Lc*Caspase-1, stimulated with nigericin (40 μmol/L) or not. C: Live cell imaging of pyroptosis in nigericin (40 μmol/L)-stimulated HEK293T cells overexpressing HA-*Lc*GSDME, with or without other inflammasome components, using SYTOX Green for nucleic acid staining. Scale bars: 50 μm. D: Caspase-1 processing (p10) upon NLRP3 inflammasome activation in isolated large yellow croaker head kidney *Lc*MO/MΦs primed with LPS and stimulated with nigericin or ATP for 60 min. E: Immunofluorescence images showing colocalization of *Lc*NLRP3 with TGN38 (trans-Golgi network marker), TOMM20 (mitochondria marker), and calnexin (ER marker) in HEK293T cells overexpressing *Lc*NLRP3 inflammasome components and stimulated with nigericin. Scale bars: 5 μm. F: Immunofluorescence images showing formation of *Lc*NLRP3-ASC puncta and colocalization of NLRP3 puncta with MTOC marker GTU in HEK293T cells overexpressing *Lc*NLRP3 inflammasome components, with or without nigericin stimulation. Scale bars: 5 μm. G: Immunofluorescence images showing colocalization of ASC puncta with MTOC marker GTU and colocalization of *Lc*ASC and *Lc*Caspase-1 in HEK293T cells overexpressing *Lc*NLRP3 inflammasome components, with or without nigericin stimulation. Scale bars: 5 μm. All immunofluorescence images are representative of three independent experiments. Blue indicates nuclear staining by DAPI. Arrowheads indicate puncta.

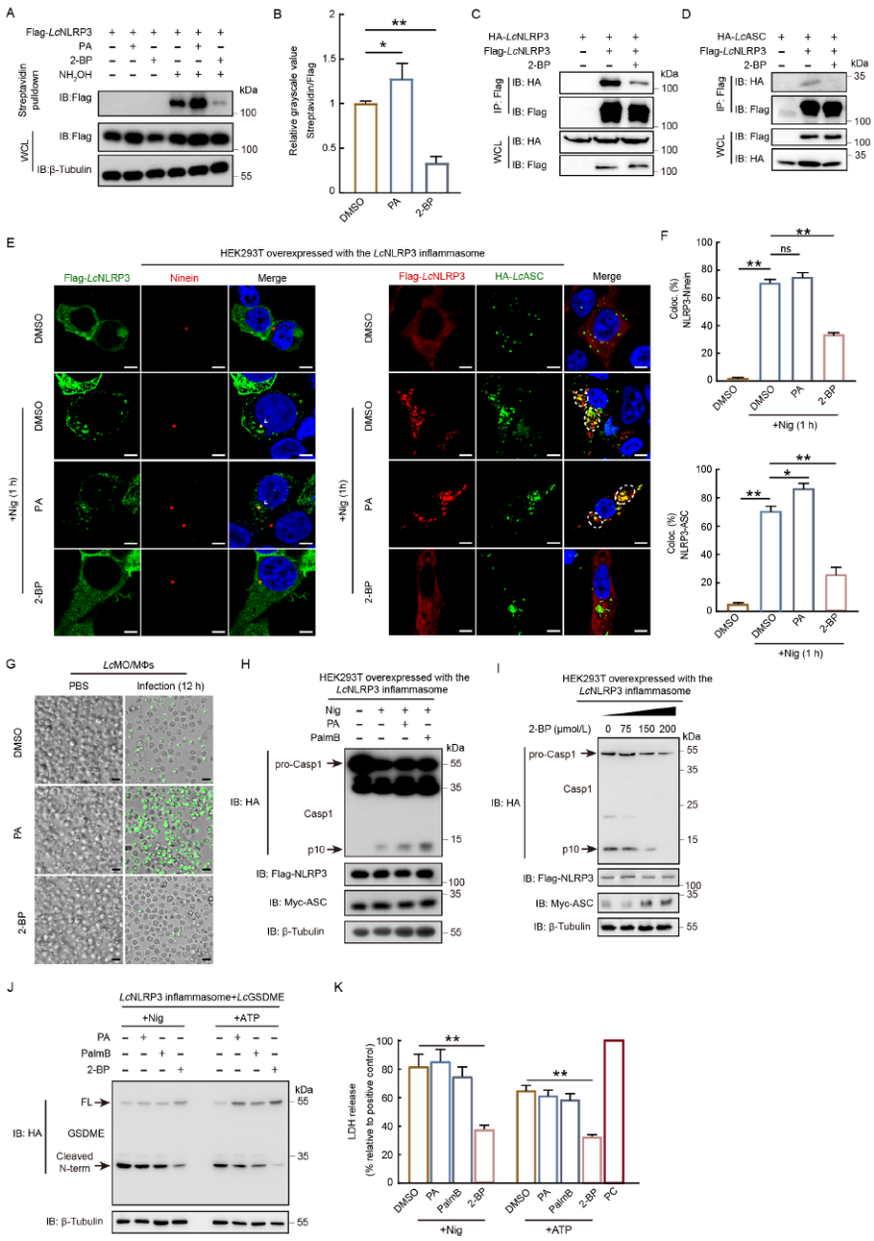


Figure 2 Palmitoylation of teleost NLRP3 is required for inflammasome activation

A: ABE assay of palmitoylation levels of Flag-*Lc*NLRP3 expressed in HEK293T cells treated with PA (200 μmol/L) or 2-BP (100 μmol/L), with or without hydroxylamine. B: Semi-quantitative analysis of relative grayscale values of immunoblot bands from (A) to evaluate S-palmitoylation levels of *Lc*NLRP3 in each group. Mean±SD, n=3. *: P<0.05; **: P<0.01. Data were analyzed using an unpaired two-tailed Student's t-test. C: Immunoblotting of whole-cell lysate (WCL) and anti-Flag IPs derived from HEK293T cells transfected with HA-*Lc*NLRP3 and Flag-*Lc*NLRP3, with or without 2-BP (100 μmol/L), to examine *Lc*NLRP3 oligomerization. D: Immunoblotting of WCL and anti-Flag IPs derived from HEK293T cells transfected with HA-*Lc*ASC and Flag-*Lc*NLRP3, with or without 2-BP (100 μmol/L), to examine interactions between *Lc*NLRP3 and *Lc*ASC. E: Immunofluorescence images showing colocalization of *Lc*NLRP3 puncta with MTOC marker ninein or formation of *Lc*NLRP3-ASC puncta in HEK293T cells overexpressing *Lc*NLRP3 inflammasome components, with or without nigericin stimulation, in the presence of PA (200 μmol/L) or 2-BP (100 μmol/L). Blue indicates nuclear staining by DAPI. Arrowheads indicate puncta; dashed circles indicate colocalization areas. Scale bars: 5 μm. F: Quantification of percentage of cells exhibiting *Lc*NLRP3-ninein or *Lc*NLRP3-ASC colocalization in (E). Mean±SD, n=3 fields, *: P<0.05; **: P<0.01; ns: Not significant. Data were analyzed using an unpaired two-tailed Student's t-test. G: Live cell imaging of pyroptosis in *Lc*MO/MΦs infected with *P. plecoglossicida* for 12 h, using SYTOX Green nucleic acid staining, in the presence of PA (200 μmol/L) or 2-BP (100 μmol/L). Scale bars: 50 μm. H: Caspase-1 processing (p10) in HEK293T cells overexpressing *Lc*NLRP3 inflammasome components, with or without nigericin (40 μmol/L) stimulation, in the presence of PA (200 μmol/L) or Palm-B (5 μmol/L). I: Caspase-1 processing (p10) in nigericin (40 μmol/L)-stimulated HEK293T cells overexpressing *Lc*NLRP3 inflammasome components, treated with increasing concentrations of 2-BP. J: Gasdermin E (cleaved N-term) processing in nigericin or ATP-stimulated HEK293T cells overexpressing *Lc*NLRP3 inflammasome components and *Lc*GSDME, in the presence of PA (200 μmol/L), Palm-B (5 μmol/L), or 2-BP (100 μmol/L). K: Relative LDH release levels in nigericin or ATP-stimulated HEK293T cells overexpressing *Lc*NLRP3 inflammasome components and *Lc*GSDME. Mean±SD, n=3, **: P<0.01. Data were analyzed using an unpaired two-tailed Student's t-test.

highest probability of palmitoylation (Supplementary Figure S2E), suggesting an adaptive modification distinct from mammalian counterparts.

Palmitoylation at this site was further investigated, alongside corresponding palmitoylation sites identified in mammalian NLRP3 (C837/844 in human NLRP3, corresponding to C778/785 in *Lc*NLRP3 and C867/874 in *Dr*NLRP3). Mutation of C946 or C1037 to alanine (C946A/C1037A) significantly reduced palmitoylation levels, while mutations at C778/785 or C867/874 had no detectable effect (Figure 3A–D). Structural modeling indicated that C946 residue was located in the LRR domain of *Lc*NLRP3, with a palmitic acid chain at this site likely enhancing the "face to face" interactions between monomers during oligomerization, predominantly associated with membranes (Andreeva et al., 2021) (Supplementary Figures S1B, S2F). Consistently, the interaction between *Lc*NLRP3 monomers was substantially weakened in the C946A mutant compared to the wild-type (WT) *Lc*NLRP3 (Figure 3E). Moreover, mutation of C946 inhibited the interaction between *Lc*NLRP3 and *Lc*ASC, indicating failed inflammasome assembly (Figure 3F).

To further assess the physiological significance of this teleost-specific palmitoylation site, the role of C946 was assessed in NLRP3 inflammasome activation using the large yellow croaker homolog as a model. Overexpression of either WT *Lc*NLRP3 or the C946A mutant, along with *Lc*ASC, in HEK293T cells revealed that C946 mutation substantially decreased the colocalization of *Lc*NLRP3 with the MTOC marker ninein and disrupted the formation of NLRP3-ASC puncta at the MTOC (Figure 3G). In line with these findings, cleavage of *Lc*pro-Caspase-1 and *Lc*GSDME, as well as pyroptosis and LDH secretion, were significantly diminished in cells reconstituted with the C946A mutant (Figure 3H–K).

Palmitoylation regulates teleost NLRP3 membrane translocation

Palmitoylation, a crucial post-translational protein modification, facilitates protein targeting to subcellular membranes (Rocks et al., 2010). Our results demonstrated that teleost NLRP3, similar to its mammalian counterparts, localized to the dTGN membrane during activation and subsequently translocated to the MTOC for inflammasome assembly and downstream inflammatory events. Notably, none of the known palmitoylation sites in mammalian NLRP3 were conserved or palmitoylated in teleost NLRP3 (Figure 3B, D; Supplementary Figure S2E). Therefore, we further investigated whether the identified teleost-specific palmitoylation site regulates NLRP3 trafficking to the dTGN and its subsequent translocation to the MTOC.

Detailed analysis of *Lc*NLRP3 membrane trafficking during inflammasome activation (Figures 1E–G, 2E) and the conservation of this palmitoylation event across teleost species (Supplementary Figure S2E) highlighted the significance of the C946 residue in *Lc*NLRP3. Inhibition of palmitoylation by 2-BP significantly impaired dTGN localization of *Lc*NLRP3 (Figure 3L). Consistently, mutation of the palmitoylated C946 residue prevented *Lc*NLRP3 translocation to the dTGN membrane, with no detectable localization on mitochondria or ER membranes (Figure 3M). Collectively, these findings suggest that palmitoylation at this unique teleost residue is critical for the proper localization of teleost NLRP3 on dTGN vesicles, thus enabling dTGN-mediated transportation of teleost NLRP3 to the MTOC, where inflammasome assembly occurs.

zDHHC18 serves as the primary palmitoyl transferase mediating teleost NLRP3 palmitoylation

Palmitoylation is mediated by a family of palmitoyl transferases, known as aspartate-histidine-histidine-cysteine (DHHC) enzymes (Lemonidis et al., 2015). Based on 22 recently identified zDHHCs in large yellow croaker (Dai et al., 2024), immunoprecipitation experiments in HEK293T cells were conducted on teleost NLRP3-interacting proteins, using *Lc*NLRP3 as a model. Results revealed interactions between *Lc*NLRP3 and four zDHHC enzymes, including *Lc*zDHHC5, *Lc*zDHHC9, *Lc*zDHHC17 and *Lc*zDHHC18 (Supplementary Figure S3A). However, only ectopic overexpression of *Lc*zDHHC18 significantly increased *Lc*NLRP3 palmitoylation levels, establishing it as the primary palmitoyl transferase for this modification (Figure 4A).

The interaction between *Lc*zDHHC18 and *Dr*NLRP3 was further validated, given the high conservation of zDHHC18 across teleost species (Supplementary Figure S3B). Results demonstrated that *Dr*NLRP3 indeed interacted with *Lc*zDHHC18, and overexpression of *Lc*zDHHC18 increased *Dr*NLRP3 palmitoylation levels (Supplementary Figure S3C; Figure 4B). Confocal microscopy confirmed colocalization of *Lc*zDHHC18 and *Lc*NLRP3 upon nigericin stimulation (Figure 4C). These results indicate that zDHHC18 is the primary palmitoyl transferase mediating NLRP3 palmitoylation in teleosts, in contrast to the diverse zDHHC enzymes reported for mammalian NLRP3 palmitoylation.

To determine the physiological relevance of zDHHC18 in regulating teleost NLRP3 inflammasome activation, its role in *Lc*pro-Caspase-1 cleavage during *Lc*NLRP3 inflammasome activation was assessed. Overexpression of *Lc*zDHHC18, but not *Lc*ZDHHC5, *Lc*ZDHHC9, or *Lc*ZDHHC17, significantly promoted *Lc*pro-Caspase-1 cleavage in an exogenous reconstitution model (Figure 4D). To further examine its endogenous role, *Lc*zDHHC18 expression was silenced in *Lc*MO/MΦs (Supplementary Figure S3D), followed by activation of the *Lc*NLRP3 inflammasome using LPS+nigericin/ATP stimulation or *P. plecoglossicida* infection. Knockdown of *Lc*zDHHC18 significantly inhibited *Lc*pro-Caspase-1 cleavage in both activation models, mirroring the results observed in the reconstituted system (Figure 4E, F). Consistent with these observations, cell pyroptosis and LDH secretion were significantly reduced upon *Lc*zDHHC18 knockdown (Figures 4G–J). Collectively, these results establish zDHHC18 as the primary physiological palmitoyl transferase responsible for mediating teleost NLRP3 palmitoylation and its downstream functional activity, including inflammasome assembly and activation.

DISCUSSION

This study elucidated a novel mechanism of palmitoylation-mediated activation of the NLRP3 inflammasome in teleosts, using large yellow croaker and zebrafish as representative models. The components and membrane trafficking events of the teleost NLRP3 inflammasome were systematically characterized, highlighting the critical role of species-adapted palmitoylation in governing teleost NLRP3 inflammasome activation.

Recent mammalian studies have demonstrated the importance of palmitoylation in regulating NLRP3 inflammasome activation, either by promoting or inhibiting its

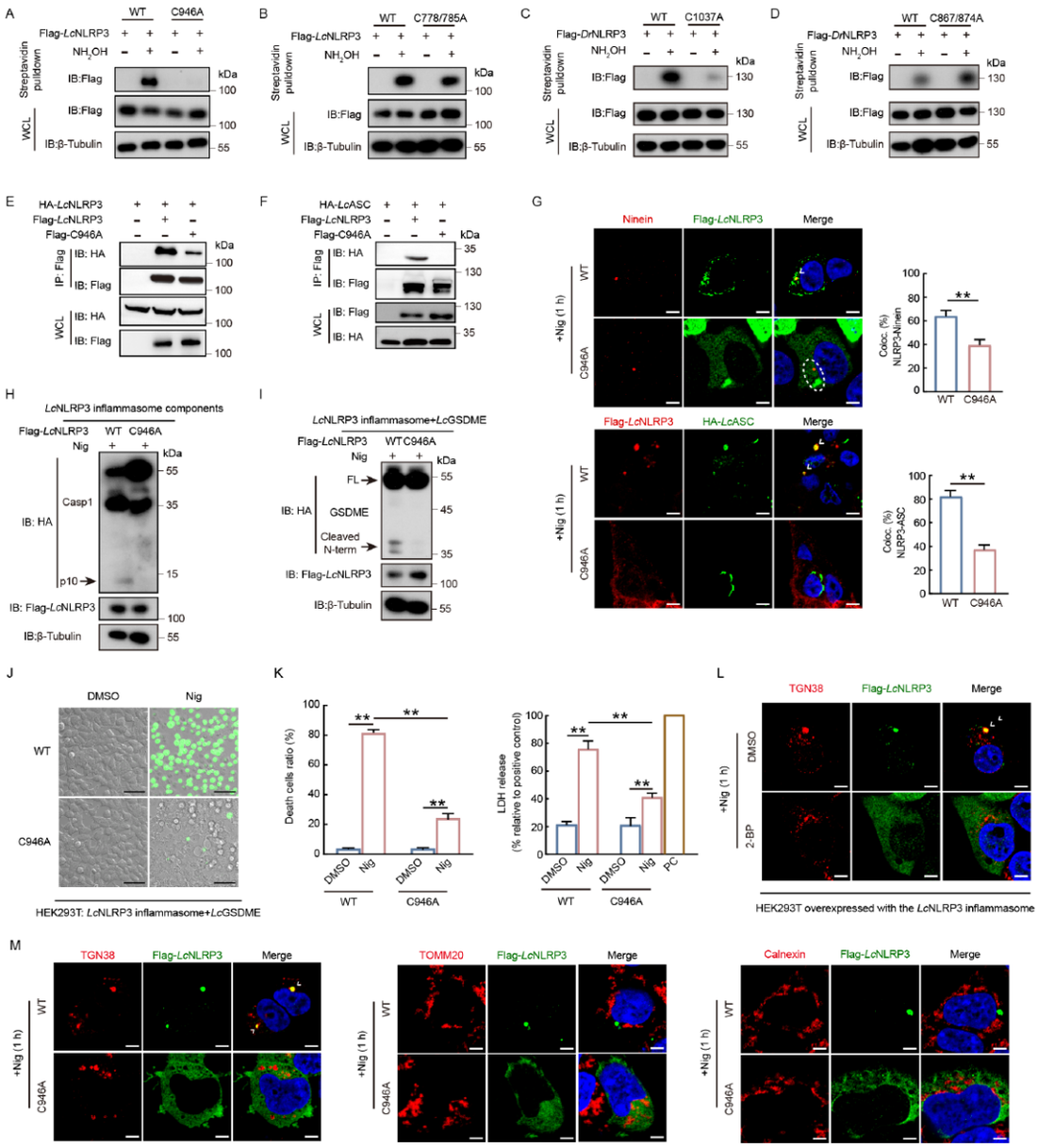


Figure 3 Palmitoylation of teleost NLRP3 at a unique residue facilitates membrane translocation

A, B: ABE assay of palmitoylation levels of Flag-*Lc*NLRP3, C946A, or C778/785A mutants overexpressed in HEK293T cells, with or without hydroxylamine. C, D: ABE assay of palmitoylation levels of Flag-*Dr*NLRP3, C1037A, or C867/874A mutants overexpressed in HEK293T cells, with or without hydroxylamine. E: Immunoblotting of WCL and anti-Flag IPs derived from HEK293T cells transfected with HA-*Lc*NLRP3 and either wild-type (WT) Flag-*Lc*NLRP3 or Flag-*Lc*NLRP3 C946A mutant to examine *Lc*NLRP3 oligomerization. F: Immunoblotting of WCL and anti-Flag IPs derived from HEK293T cells transfected with HA-*Lc*ASC and either WT Flag-*Lc*NLRP3 or Flag-*Lc*NLRP3 C946A mutant to examine interactions between *Lc*NLRP3 and *Lc*ASC. G: Immunofluorescence images showing colocalization of *Lc*NLRP3 puncta with MTOC marker ninein or formation of *Lc*NLRP3-ASC puncta in HEK293T cells overexpressing WT *Lc*NLRP3 or C946A mutant, and other inflammasome components, stimulated with nigericin. Cells exhibiting *Lc*NLRP3-ninein or *Lc*NLRP3-ASC colocalization in each group were quantified. Mean±SD, *n*=3 fields, **: *P*<0.01. Data were analyzed using an unpaired two-tailed Student's *t*-test. H: Caspase-1 processing (p10) in HEK293T cells overexpressing WT *Lc*NLRP3 or C946A mutant, along with other inflammasome components, stimulated with nigericin for inflammasome activation. I: Gasdermin E (cleaved N-term) processing in nigericin (40 μmol/L)-stimulated HEK293T cells overexpressing WT *Lc*NLRP3 or C946A mutant with other inflammasome components. J: Live cell imaging of pyroptosis in nigericin (40 μmol/L)-stimulated HEK293T cells overexpressing WT *Lc*NLRP3 or C946A mutant, along with other inflammasome components and HA-*Lc*GSDME, using SYTOX Green nucleic acid staining. Scale bars: 50 μm. K: Quantification of percentage of cells showing positive SYTOX Green signals and relative levels of LDH release in (I). Mean±SD, *n*=3, **: *P*<0.01. Data were analyzed using an unpaired two-tailed Student's *t*-test. L: Immunofluorescence images showing colocalization of *Lc*NLRP3 with trans-Golgi network marker TGN38 in nigericin (40 μmol/L)-stimulated HEK293T cells overexpressing *Lc*NLRP3 inflammasome components, with or without 2-BP (100 μmol/L). Scale bars: 5 μm. M: Immunofluorescence images showing colocalization of *Lc*NLRP3 with TGN38 (trans-Golgi network marker), TOMM20 (mitochondria marker), and calnexin (ER marker) in nigericin-stimulated HEK293T cells overexpressing WT *Lc*NLRP3 or C946A mutant with other inflammasome components. Scale bars: 5 μm. All immunofluorescence images are representative of three independent experiments. Blue indicates nuclear staining by DAPI; arrowheads indicate puncta.

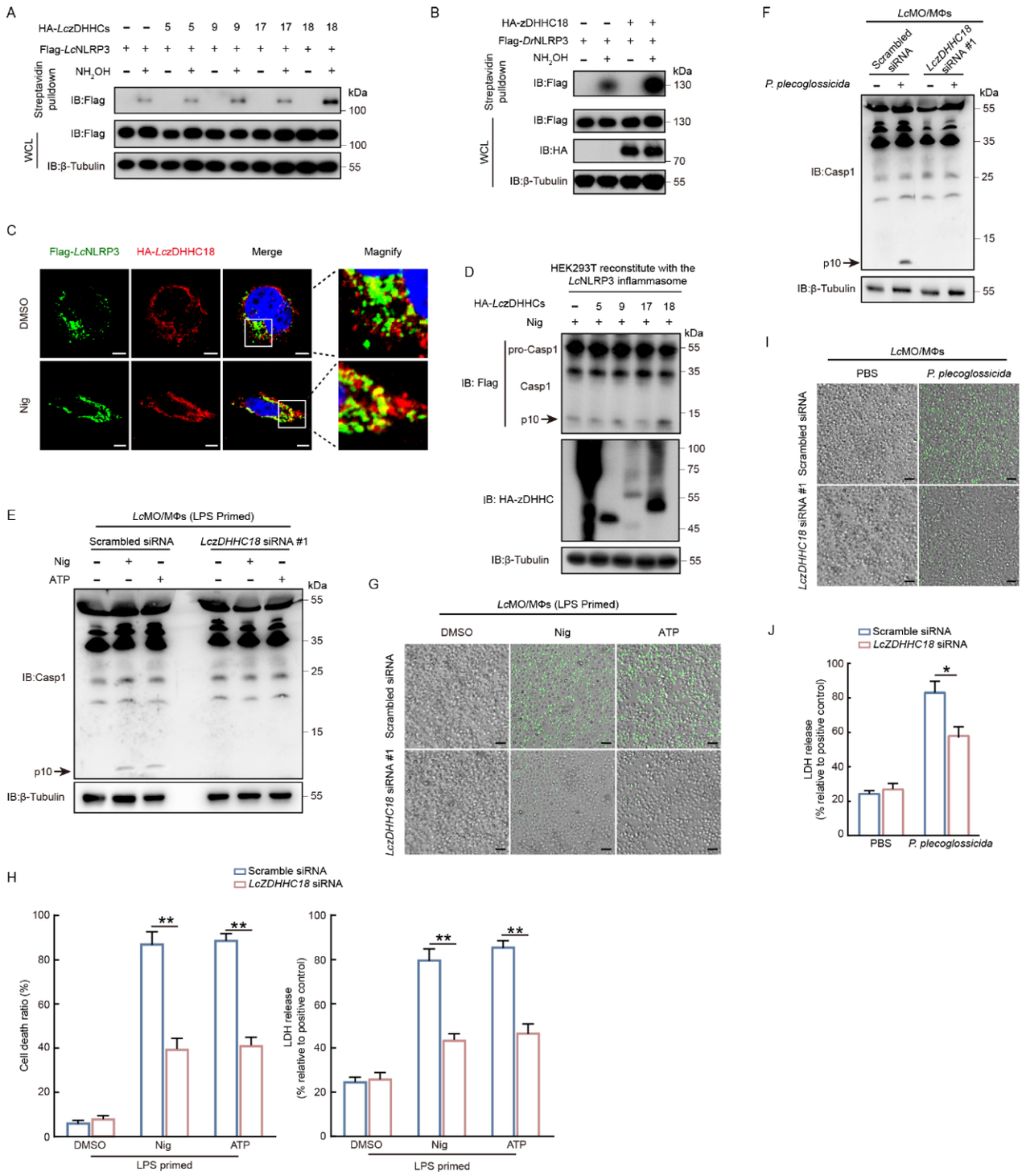


Figure 4 zDHHC18 serves as the primary palmitoyl transferase mediating teleost NLRP3 palmitoylation

A: ABE assay of palmitoylation levels of Flag-*Lc*NLRP3 in HEK293T cells overexpressing Flag-*Lc*NLRP3 alone, or with HA-*Lcz*DHHC5/9/17/18, with or without hydroxylamine. B: ABE assay of palmitoylation levels of Flag-*Dr*NLRP3 in HEK293T cells overexpressing Flag-*Dr*NLRP3 alone or with HA-*Lcz*DHHC18, with or without hydroxylamine. C: Immunofluorescence images showing colocalization of *Lc*NLRP3 and *Lcz*DHHC18 in overexpressed HEK293T cells, with or without nigericin stimulation. Blue indicates nuclear staining by DAPI. Scale bars: 5 μm. D: Caspase-1 processing (p10) in nigericin (40 μmol/L)-stimulated HEK293T cells overexpressing *Lc*NLRP3 inflammasome components, with or without HA-*Lcz*DHHC5/9/17/18. E, F: Caspase-1 processing (p10) upon NLRP3 inflammasome activation in *Lc*MO/MΦs transfected with scrambled siRNA or zDHHC18 siRNA. Cells were primed with LPS and stimulated with nigericin or ATP for 60 min (E) or infected with *P. plecoglossicida* (F) for inflammasome activation. G: Live cell imaging of pyroptosis of cells from (E) using SYTOX Green nucleic acid staining. Scale bars: 50 μm. H: Quantification of percentage of cells showing positive SYTOX Green signals and levels of LDH release in (E). Mean±SD, n=3, **: P<0.01. Data were analyzed using an unpaired two-tailed Student's t-test. I: Live cell imaging of pyroptosis of cells from (F) using SYTOX Green nucleic acid staining. Scale bars: 50 μm. J: LDH release levels in cells in (F). Mean±SD, n=3, *: P<0.05. Data were analyzed using an unpaired two-tailed Student's t-test. All immunofluorescence images are representative of three independent experiments.

function (Nie et al., 2024; Wang et al., 2023; Yu et al., 2024; Zheng et al., 2023). However, the palmitoylated residues identified in mammals are absent or not palmitoylated in teleost NLRP3 (Figure 3A–D; Supplementary Figure S2E), indicating an evolutionary adaptation specific to these species. Investigating whether palmitoylation-dependent regulatory mechanisms also exist in lower vertebrates and understanding the underlying mechanisms could offer valuable insights into the evolutionary origins and diversification of this critical innate immune platform.

C946 of *Lc*NLRP3 was identified as a conserved teleost-specific palmitoylation site through GPS-Palm predictions (Supplementary Figure S2E). Mutation of this residue to alanine abolished palmitoylation, prevented *Lc*NLRP3 localization to the dTGN and MTOC, and disrupted its interaction with *Lc*ASC at the MTOC, impairing inflammasome assembly (Figure 3A, E–M). Structural modeling suggested that palmitoylation at C946 may enhance interactions between *Lc*NLRP3 monomers, facilitating the formation of the oligomerized 'cage' structure necessary for membrane association (Supplementary Figure S2F). Similarly, the corresponding cysteine 1037 (C1037) residue in *Dr*NLRP3 also exhibited a significant reduction in palmitoylation levels when mutated, indicating that this palmitoylation event represents a teleost-specific evolutionary adaptation.

*Lc*zDHHC18 was further identified as the primary palmitoyl transferase responsible for palmitoylating *Lc*NLRP3 at C946 and *Dr*NLRP3 at C1037 (Figure 4A, B; Supplementary Figure S3A–C), differing from those mediating NLRP3 palmitoylation in mammals. Overexpression of zDHHC18 enhanced *Lc*NLRP3 and *Dr*NLRP3 palmitoylation and promoted inflammasome activation, while knockdown hindered inflammasome assembly, *Lc*pro-Caspase-1 cleavage, and cell pyroptosis (Figure 4; Supplementary Figure S3D). This teleost-specific adaptation of palmitoylation residues and transferases likely reflects evolutionary flexibility of immune regulatory mechanisms to the unique environmental challenges faced by teleosts in aquatic environments, such as fluctuating temperatures, oxygen availability, and pH levels (Blewett et al., 2022). Such challenges demand a finely tuned immune system capable of rapid and adaptive responses to diverse pathogens, such as bacteria, viruses, and parasites. Palmitoylation-mediated regulation may offer teleosts a mechanism to balance robust immune activation with the need to mitigate excessive inflammation during environmental stressors like hypoxia.

Elucidating the molecular mechanisms underpinning inflammasome activation in teleosts could lead to new strategies for managing immune-related diseases in aquaculture, where the rapid onset of immune responses is often critical for preventing large-scale outbreaks. Understanding palmitoylation-dependent regulation could inform the development of targeted vaccines or immune modulators tailored to specific teleost species, thereby improving disease resistance and overall aquaculture sustainability.

In conclusion, this study uncovered a novel palmitoylation-dependent mechanism for NLRP3 inflammasome activation in teleosts, involving a unique palmitoylation site and a distinct palmitoyl transferase. These findings advance our understanding of the molecular regulation of innate immunity and highlight the evolutionary diversity of immune mechanisms across vertebrates, thereby contributing to a cross-species understanding of the molecular basis underlying the origin and evolution of innate immunity.

SUPPLEMENTARY DATA

Supplementary data to this article can be found online.

COMPETING INTERESTS

The authors declare that they have no competing interests.

AUTHORS' CONTRIBUTIONS

Conceptualization: L.N., J.Z.S., J.C.; Methodology: L.N., C.J.F.; Investigation: L.N., X.Y.W., Z.Y.Z., C.J.F., T.F.Z.; Visualization: L.N., X.Y.W., Z.Y.Z., C.J.F., T.F.Z.; Funding acquisition: L.N., J.C.; Project administration: L.N., J.Z.S., J.C.; Supervision: L.N., J.Z.S., J.C.; Writing – original draft: L.N.; Writing – review & editing: L.N., C.J.F., J.Z.S., J.C. All authors read and approved the final version of the manuscript.

REFERENCES

Acevedo W, Morán-Figueroa R, Vargas-Chacoff L, et al. 2023. Revealing the *Salmo salar* NLRP3 inflammasome: insights from structural modeling and transcriptome analysis. *International Journal of Molecular Sciences*, **24**(19): 14556.

Andreeva L, David L, Rawson S, et al. 2021. NLRP3 cages revealed by full-length mouse NLRP3 structure control pathway activation. *Cell*, **184**(26): 6299–6312. e22.

Angosto D, López-Castejón G, López-Muñoz A, et al. 2012. Evolution of inflammasome functions in vertebrates: inflammasome and caspase-1 trigger fish macrophage cell death but are dispensable for the processing of IL-1β. *Innate Immunity*, **18**(6): 815–824.

Ao JQ, Mu YN, Xiang LX, et al. 2015. Genome sequencing of the perciform fish *Larimichthys crocea* provides insights into molecular and genetic mechanisms of stress adaptation. *PLoS Genetics*, **11**(4): e1005118.

Arumugam S, Qin YQ, Liang ZW, et al. 2022. GSK3β mediates the spatiotemporal dynamics of NLRP3 inflammasome activation. *Cell Death & Differentiation*, **29**(10): 2060–2069.

Balasubramanian A, Hsu AY, Ghimire L, et al. 2024. The palmitoylation of gasdermin D directs its membrane translocation and pore formation during pyroptosis. *Science Immunology*, **9**(94): eadn1452.

Bijlmakers MJ, Marsh M. 2003. The on–off story of protein palmitoylation. *Trends in Cell Biology*, **13**(1): 32–42.

Blewett TA, Binning SA, Weinrauch AM, et al. 2022. Physiological and behavioural strategies of aquatic animals living in fluctuating environments. *Journal of Experimental Biology*, **225**(9): jeb242503.

Boehm T, Swann JB. 2014. Origin and evolution of adaptive immunity. *Annual Review of Animal Biosciences*, **2**(1): 259–283.

Chen BH, Zhou ZX, Ke QZ, et al. 2019. The sequencing and *de novo* assembly of the *Larimichthys crocea* genome using PacBio and Hi-C technologies. *Scientific Data*, **6**(1): 188.

Chen H, Ding SF, Tan JC, et al. 2020. Characterization of the Japanese flounder NLRP3 inflammasome in restricting *Edwardsiella piscicida* colonization *in vivo*. *Fish & Shellfish Immunology*, **103**: 169–180.

Chen JQ, Chen ZJ. 2018. PtdIns4P on dispersed *trans*-Golgi network mediates NLRP3 inflammasome activation. *Nature*, **564**(7734): 71–76.

Chen SW, Jin P, Chen H, et al. 2021. Dual function of a turbot inflammatory caspase in mediating both canonical and non-canonical inflammasome activation. *Developmental & Comparative Immunology*, **121**: 104078.

Chuphal B, Rai U, Roy B. 2022. Teleost NOD-like receptors and their downstream signaling pathways: a brief review. *Fish and Shellfish Immunology Reports*, **3**: 100056.

Dai T, Zhao ZY, Zhu TF, et al. 2024. The anti-inflammatory role of zDHHC23 through the promotion of macrophage M2 polarization and macrophage necroptosis in large yellow croaker (*Larimichthys crocea*).

Frontiers in Immunology, **15**: 1401626.
Drisdel RC, Alexander JK, Sayeed A, et al. 2006. Assays of protein palmitoylation. *Methods*, **40**(2): 127–134.
Franchi L, Eigenbrod T, Muñoz-Planillo R, et al. 2009. The inflammasome: a caspase-1-activation platform that regulates immune responses and disease pathogenesis. *Nature Immunology*, **10**(3): 241–247.
He Y, Hara H, Núñez G. 2016a. Mechanism and regulation of NLRP3 inflammasome activation. *Trends in Biochemical Sciences*, **41**(12): 1012–1021.
He Y, Zeng MY, Yang DH, et al. 2016b. NEK7 is an essential mediator of NLRP3 activation downstream of potassium efflux. *Nature*, **530**(7590): 354–357.
Holbrook JA, Jarosz-Griffiths HH, Caseley E, et al. 2021. Neurodegenerative disease and the NLRP3 inflammasome. *Frontiers in Pharmacology*, **12**: 643254.
Hu DW, Li YT, Wang XY, et al. 2024. Palmitoylation of NLRP3 modulates inflammasome activation and inflammatory bowel disease development. *The Journal of Immunology*, **213**(4): 481–493.
Huang L, Zhao L, Su Y, et al. 2018. Genome sequence of *Pseudomonas plecoglossicida* strain NZBD9. *Genome Announcements*, **6**(4): e01412–17.
Kon T, Pei LY, Ichikawa R, et al. 2021. Whole-genome resequencing of large yellow croaker (*Larimichthys crocea*) reveals the population structure and signatures of environmental adaptation. *Scientific Reports*, **11**(1): 11235.
Lemonidis K, Werno MW, Greaves J, et al. 2015. The zDHHC family of S-acyltransferases. *Biochemical Society Transactions*, **43**(2): 217–221.
Li CH, Chen J, Nie L, et al. 2020a. MOSPD2 is a receptor mediating the LEAP-2 effect on monocytes/macrophages in a teleost, *Boleophthalmus pectinirostris*. *Zoological Research*, **41**(6): 644–655.
Li JY, Wang YY, Shao T, et al. 2020b. The zebrafish NLRP3 inflammasome has functional roles in ASC-dependent interleukin-1β maturation and gasdermin E-mediated pyroptosis. *Journal of Biological Chemistry*, **295**(4): 1120–1141.
Mangan MSJ, Olhava EJ, Roush WR, et al. 2018. Targeting the NLRP3 inflammasome in inflammatory diseases. *Nature Reviews Drug Discovery*, **17**(8): 588–606.
Martinon F, Burns K, Tschopp J. 2002. The inflammasome: a molecular platform triggering activation of inflammatory caspases and processing of proIL-beta. *Molecular Cell*, **10**(2): 417–426.
Nie L, Fei CJ, Fan YZ, et al. 2024. Consecutive palmitoylation and phosphorylation orchestrates NLRP3 membrane trafficking and inflammasome activation. *Molecular Cell*, **84**(17): 3336–3353. e7.
Rocks O, Gerauer M, Vartak N, et al. 2010. The palmitoylation machinery is a spatially organizing system for peripheral membrane proteins. *Cell*, **141**(3): 458–471.
Sharma BR, Kanneganti TD. 2021. NLRP3 inflammasome in cancer and metabolic diseases. *Nature Immunology*, **22**(5): 550–559.
Shi HX, Murray A, Beutler B, 2016. Reconstruction of the mouse inflammasome system in HEK293T cells. *Bio-protocol*, **6**(21): e1986.
Shi JJ, Zhao Y, Wang K, et al. 2015. Cleavage of GSDMD by inflammatory caspases determines pyroptotic cell death. *Nature*, **526**(7575): 660–665.
Sun YJ, Nie P, Zhao LM, et al. 2019. Dual RNA-Seq unveils the role of the *Pseudomonas plecoglossicida fliA* gene in pathogen-host interaction with *Larimichthys crocea*. *Microorganisms*, **7**(10): 443.
Tan MS, Yu JT, Jiang T, et al. 2013. The NLRP3 inflammasome in Alzheimer's disease. *Molecular Neurobiology*, **48**(3): 875–882.
Tang Y, Xin G, Zhao LM, et al. 2020. Novel insights into host-pathogen interactions of large yellow croakers (*Larimichthys crocea*) and pathogenic bacterium *Pseudomonas plecoglossicida* using time-resolved dual RNA-seq of infected spleens. *Zoological Research*, **41**(3): 314–327.
Tao Z, Xu Y, Zhou SM, et al. 2020. Acquisition of a type VI secretion system is critical for *Pseudomonas plecoglossicida* induced granulomas in fish internal organs. *Aquaculture*, **516**: 734629.
Wang LQ, Cai J, Zhao X, et al. 2023. Palmitoylation prevents sustained inflammation by limiting NLRP3 inflammasome activation through chaperone-mediated autophagy. *Molecular Cell*, **83**(2): 281–297. e10.
Wu CW, Zhang D, Kan MY, et al. 2014. The draft genome of the large yellow croaker reveals well-developed innate immunity. *Nature Communications*, **5**(1): 5227.
Wu XY, Xiong JB, Fei CJ, et al. 2022. Prior exposure to ciprofloxacin disrupts intestinal homeostasis and predisposes ayu (*Plecoglossus altivelis*) to subsequent *Pseudomonas plecoglossicida*-induced infection. *Zoological Research*, **43**(4): 648–665.
Yu T, Hou D, Zhao JQ, et al. 2024. NLRP3 Cys126 palmitoylation by ZDHHC7 promotes inflammasome activation. *Cell Reports*, **43**(4): 114070.
Yuan B, Zhao LM, Zhuang ZX, et al. 2022. Transcriptomic and metabolomic insights into the role of the *flgK* gene in the pathogenicity of *Pseudomonas plecoglossicida* to orange-spotted grouper (*Epinephelus coioides*). *Zoological Research*, **43**(6): 952–965.
Zheng SH, Que XY, Wang SX, et al. 2023. ZDHHC5-mediated NLRP3 palmitoylation promotes NLRP3-NEK7 interaction and inflammasome activation. *Molecular Cell*, **83**(24): 4570–4585. e7.
Zhou Y, Tong ZZ, Jiang SH, et al. 2020. The roles of *Endoplasmic Reticulum* in NLRP3 inflammasome activation. *Cells*, **9**(5): 1219.

Xiao et al. *Zool. Res.* 2025, 46(1): 15−26
https://doi.org/10.24272/j.issn.2095-8137.2024.287
https://cstr.cn/32248.14.zr.2024.287

ZR | Zoological Research

Article Open Access

Enhanced risk assessment framework integrating distribution dynamics, genetically inferred populations, and morphological traits of *Diploderma* lizards

Qi Xiao[1,2,#], Xiu-Dong Shi[1,#], Lin Shi[1], Zhong-Yi Yao[1], You-Hua Chen[1], Wei-Zhao Yang[1], Zi-Yan Liao[1,*], Yin Qi[1,3,*]

[1] *Chengdu Institute of Biology*, *Chinese Academy of Sciences*, *Chengdu*, *Sichuan* 610299, *China*

[2] *University of Chinese Academy of Sciences*, *Beijing* 101408, *China*

[3] *Mangkang Ecological Station*, *Xizang Ecological Safety Monitor Network*, *Changdu*, *Xizang* 854500, *China*

ABSTRACT

Assessing the threat status of species in response to global change is critical for biodiversity monitoring and conservation efforts. However, current frameworks, even the IUCN Red List, often neglect critical factors such as genetic diversity and the impacts of climate and land-use changes, hindering effective conservation planning. To address these limitations, we developed an enhanced extinction risk assessment framework using *Diploderma* lizards as a model. This framework incorporates long-term field surveys, environmental data, and land-use information to predict distributional changes for 10 recently described *Diploderma* species on the Qinghai-Xizang Plateau, which hold ecological significance but remain underassessed in conservation assessment. By integrating the distribution data and genetically inferred effective population sizes (*Ne*), we conducted scenario analyses and used a rank-sum approach to calculate Risk ranking scores (RRS) for each species. This approach revealed significant discrepancies with the IUCN Red List assessments. Notably, *D. yangi* and *D. qilin* were identified as facing the highest extinction risk. Furthermore, *D. vela*, *D. batangense*, *D. flaviceps*, *D. dymondi*, *D. yulongense*, and *D. laeviventre*, currently classified as “Least Concern”, were found to warrant reclassification as “Vulnerable” due to considerable threat from projected range contractions. Exploring the relationship between morphology and RRS revealed that traits such as snout-vent length and relative tail length could serve as potential predictors of extinction risk, offering preliminary metrics for assessing species vulnerability when comprehensive data are unavailable. This study enhances the precision of extinction risk assessment frameworks and demonstrates their capacity to refine and update risk assessments, especially for lesser-known taxa.

Keywords: Lizard; Extinction Risk Assessment; IUCN Red List; Conservation Status; Effective Population Size; Morphological Traits

INTRODUCTION

Assessing the threat status of species involves systematically categorizing taxa based on extinction risk, which is critical for biodiversity monitoring and conservation planning (Bachman et al., 2019). The International Union for Conservation of Nature (IUCN) Red List of Threatened Species is widely recognized as a leading framework for evaluating extinction risk (Brooks et al., 2019), applying five quantitative criteria regarding species distribution, population size, structure, and trends (Supplementary Table S1). These criteria include reduction in population size (Criterion A), restricted geographic range (Criterion B), and very small or declining populations (Criterion D). The Red List serves as an essential tool for guiding biodiversity conservation, informing sustainable development, and shaping policy decisions (Anderson, 2023; Betts et al., 2020; Le Breton et al., 2019; Williams et al., 2021).

However, the IUCN Red List has faced criticism for not adequately incorporating threats from climate change and land-use modifications (Dakhil et al., 2021; Peng et al., 2023). This gap can result in underestimations of extinction risk for various taxa, including plants, mammals, birds, reptiles, and amphibians (Li et al., 2024; Mi et al., 2023; Peng et al., 2023; Santini et al., 2019). In addition, severe data limitations and insufficient research pose significant challenges in maintaining accurate and up-to-date assessments. Currently, only a small

This is an open-access article distributed under the terms of the Creative Commons Attribution Non-Commercial License (http://creativecommons.org/licenses/by-nc/4.0/), which permits unrestricted non-commercial use, distribution, and reproduction in any medium, provided the original work is properly cited.

Copyright ©2025 Editorial Office of Zoological Research, Kunming Institute of Zoology, Chinese Academy of Sciences

Received: 04 September 2024; Accepted: 16 December 2024; Online: 18 December 2024

Foundation items: This work was supported by the Second Tibetan Plateau Scientific Expedition and Research Program (STEP, 2019QZKK0402), Science and Technology Plan Project of Xizang Autonomous Region to Y.Q. (XZ202201ZY0030G), National Natural Science Foundation of China (32201424 to Z.Y.L. and 31872233 to Y.Q.)

[#]Authors contributed equally to this work

*Corresponding authors, E-mail: liaozy@cib.ac.cn; qiyin@cib.ac.cn

proportion of known species have been assessed as threatened and prioritized for conservation action (Cazalis et al., 2022), and many remain classified as “Data Deficient” (DD), even within otherwise thoroughly assessed groups (Borgelt et al., 2022; Cazalis et al., 2022). Studies indicate that DD species are more likely to face vulnerability compared to data-sufficient (DS) species (Borgelt et al., 2022; Roberts et al., 2016). An improved framework is urgently needed to address these deficiencies by integrating both current and future threats, such as climate and land-use changes, into assessments of species distribution ranges and population sizes, with a particular focus on DD species.

The geographic distribution of a species constitutes a fundamental unit of biodiversity conservation (Hamilton et al., 2022; Jetz et al., 2019). For most species, understanding and characterizing geographic ranges, along with their changes over time, is fundamental to assessing extinction risk, forming the basis of the IUCN Red List of Threatened Species (Cazalis et al., 2022; IUCN, 2024). To quantify distributional ranges, the IUCN applies two key measures: extent of occurrence (EOO) and area of occupancy (AOO). EOO represents the geographical range of a species, calculated as the area within the minimum convex polygon encompassing all known, observed, or inferred locations of occurrence (Anderson, 2023; IUCN, 2024). Complementarily, AOO denotes the area actually occupied by a species, typically estimated by mapping known or projected distribution points onto a 2 km×2 km grid and counting the number of occupied cells (IUCN, 2024). These metrics are not only vital for well-documented species in the IUCN Red List but are also integral to evaluating regional endemic, rare, keystone, and flagship species, highlighting their critical role in extinction risk assessments (Braby et al., 2018; Chakona et al., 2022; Dong et al., 2023; Gaston & Fuller, 2009; Marcer et al., 2013).

Climate and land-use changes are driving a profound global redistribution of life (Pecl et al., 2017), reshaping ecosystems and threatening biodiversity. These shifts in distribution represent some of the most significant threats to species survival (Root et al., 2003; Yu et al., 2022). Species distribution models (SDMs) have become indispensable tools for predicting variations in spatial distribution under scenarios of climate and land-use change and informing conservation strategies (Hamann & Aitken, 2013; Liang et al., 2024). Outputs from SDMs, particularly those focused on climate-based scenarios, play a crucial role in informing extinction risk assessments, providing quantitative data relevant to “population reduction” under Criterion A or “continuing decline” under Criterion B or C2, which pertain to EOO, AOO, and small population sizes (IUCN, 2024). However, despite the projected acceleration of climate change, the incorporation of climate projections into IUCN Red List assessments of population trends remains a considerable challenge and is limited to a minority of species (Mancini et al., 2024).

Genetic parameters are increasingly recognized as essential components of conservation assessments, especially when ecological and demographic data alone prove insufficient for accurately evaluating extinction risk (Garner et al., 2020; Hoban et al., 2020). Among these, long-term effective population size (*Ne*) represents a fundamental metric, reflecting the size of an idealized population experiencing genetic drift at a rate equivalent to the actual population (Wright, 1931). Traditionally, conservation genetics has applied *Ne* thresholds of 50 and 500 to assess short- and long-term population viability. The post-2020 framework of the Convention on Biological Diversity (CBD) recently designated *Ne* values exceeding 500 as a critical benchmark for gauging a population’s ability to maintain genetic diversity and mitigate extinction risk (Hoban et al., 2020; Mastretta-Yanes et al., 2024).

Lizards in the genus *Diploderma* provide an ideal model for evaluating the efficacy of enhanced risk assessment frameworks. As ectothermic animals, lizards rely heavily on environmental temperatures and habitat for thermoregulation, making them particularly vulnerable to the impacts of climate and land-use changes. This vulnerability is compounded in *Diploderma*, which is the most species-rich lizard genus in China, comprising 47 recognized species, 41 of which are endemic to the region (Cai et al., 2024). The recent surge in *Diploderma* species discoveries has highlighted significant knowledge gaps in their life history, distribution, and habitat. As such, a high proportion of these species are classified as DD, complicating conservation efforts and limiting their prioritization (Wang et al., 2021, 2024). Additionally, nearly 70% of *Diploderma* species are concentrated in the Hengduan Mountains and nearby regions, where many are confined to narrow valleys. These habitats have been severely impacted by human infrastructure (e.g., hydropower projects and roads), leading to habitat degradation, frequent roadkill incidents, and the destruction of limestone environments (Shi et al., 2023; Wang et al., 2021, 2022). In recognition of their vulnerability, seven species were designated as nationally protected in 2021, underscoring the urgency of developing comprehensive and accurate risk assessments.

Given the urgent need to assess the conservation status of DD species, recent studies have combined IUCN threat assessments with additional data to predict extinction risks. Functional traits such as morphology, life history, demographics, and range size are frequently employed in extinction risk analyses (Senior et al., 2021). Extensive research has demonstrated strong correlations between these traits and threat status across diverse taxa (Chichorro et al., 2019). Among these, morphological traits offer distinct advantages for extinction risk assessment, as they are closely associated with factors influencing population dynamics and habitat specialization (Miles, 2020). Importantly, morphological traits can often be quantified from museum and historical collections, providing valuable insights even in the absence of contemporary ecological or demographic information. Therefore, exploring the relationship between morphological traits and extinction risk is essential for advancing extinction risk assessment frameworks.

This study presents an enhanced risk assessment framework using *Diploderma* species as a model system. By integrating long-term field survey data with environmental and land cover datasets, we simulated the AOO for 10 *Diploderma* species and predicted changes in their AOO under three future climate and land-use scenarios (SSP126, SSP370, and SSP585). Population genetic data obtained from field sampling were used to estimate the *Ne* for each species. This study aimed to: (1) develop an enhanced framework for assessing extinction risk and conservation priorities that integrates projections of future climate and land-use changes as well as genetically inferred *Ne*, addressing key limitations of the IUCN Red List methodology; (2) apply this framework to *Diploderma* species, addressing critical gaps in conservation knowledge for this ecologically significant but understudied

genus; and (3) establish a preliminary method for assessing extinction risk in DD species by correlating morphological traits with distribution dynamics, habitat area, and genetically inferred *N*e. Overall, this integrative approach highlights significant shortcomings in existing IUCN assessments and provides a foundation for the development of more targeted conservation strategies for *Diploderma* species and lesser-known taxa in regions that may serve as future climate refuges.

MATERIALS AND METHODS

Ethics statement

All applicable international, national, and/or institutional guidelines for the care and use of animals were strictly followed. All relevant procedures involving animal experiments presented in this study were compliant with the ethical regulations regarding animal research and conducted under the approval of the Chengdu Institute of Biology, Chinese Academy of Sciences (Approval No.: CIBDWLL2022004).

Studied species

Ten recently described *Diploderma* species from the Qinghai-Xizang Plateau were selected to evaluate the effectiveness of the enhanced risk assessment framework (Figure 1A). These species are distributed across the Nujiang, Lancang Jiang, Jinsha Jiang, Yalong Jiang, and Dadu river valleys (details in Supplementary Table S2).

Prediction of distribution range using ensemble of small models

The geographic ranges of each species were quantified using EOO and AOO. EOO was defined as the area within a minimum convex polygon (MCP) for each *Diploderma* species constructed in ArcGIS based on known distribution records (Shi et al., 2023). The coordinates of distribution records were primarily obtained from field surveys conducted between 2020 and 2023, supplemented with data from published literature (Flower et al., 2013; Thomas et al., 2012; Wang et al., 2016, 2019). Specific information and sources are shown in Supplementary Table S3. After removing duplicate records and those lacking precise geographic information, 249 species occurrences were retained, comprising 19 for *D. aorun*, 14 for *D. batangense*, 28 for *D. drukdaypo*, 14 for *D. dymondi*, 12 for *D. flaviceps*, 26 for *D. laeviventre*, 13 for *D. qilin*, 39 for *D. vela*, 28 for *D. yangi*, and 56 for *D. yulongense*. However, given the limited number of occurrences for these species (Guisan et al., 2017), a rare species modeling strategy, ensemble of small models (ESM) (Liao et al., 2022), was employed. As dispersal assumptions are critical for *in situ* conservation (Thuiller et al., 2019), AOO was calculated within the empirical distribution range. To achieve this, the distribution ranges predicted by the ensemble model were intersected with the EOOs in ArcGIS, and the area of the intersection was used to estimate the AOO. The total number of grid cells within the intersected area was then used to quantify the AOO for each species.

To predict species distribution, 19 bioclimatic variables, net primary productivity (NPP), and growing season length (GSL) were utilized, sourced from the CHELSA V2 (CMIP6) dataset for both the current period (1981–2010) and future projections (2071–2100) (http://chelsa-climate.org/). The ecological relevance of these variables is provided in Supplementary Table S4. Prior to modeling, 21 variables were pre-screened to avoid multicollinearity issues (Villemant et al., 2011) using a variance inflation factor (VIF) threshold of less than 5, implemented with the *vifstep* function in the R package “usdm” (Naimi, 2014).

Species distribution shifts were predicted under three climate change scenarios outlined in the Intergovernmental Panel on Climate Change (IPCC) Sixth Assessment Report: SSP126 (low-emission scenario), SSP370 (medium-to-high emission scenario), and SSP585 (high-emission scenario) (Kissling et al., 2010). To account for uncertainties in climate projections, data from five Earth system models were incorporated, including GFDL-ESM4, IPSL-CM6A-LR, MPI-ESM1-2-HR, MRI-ESM2-0, and UKESM1-0-LL. The ESM approach was applied to predict the distribution ranges of *Diploderma* species under current and future climate conditions. Four algorithms were selected for their ability to balance computational efficiency and predictive accuracy, including regression tree (CTA), artificial neural network (ANN), generalized boosted regression model (GBM), and generalized additive model (GAM). Model parameters were adjusted using the best-fitting ESM approach, based on observed distribution records and 10 000 randomly sampled pseudo-absence points within the study region (Breiner et al., 2018).

The Somers’ D score was employed to evaluate model performance, with 75% of the sampling data randomly selected for model training and the remaining 25% used for testing. Bivariate models yielding a Somers’ D score below zero were assigned a value of zero and excluded from the final ensemble of the ESM. Model accuracy was evaluated using two metrics: the area under the receiver operating characteristic curve (AUC) and the true skill statistic (TSS). The receiver operating characteristic (ROC) curve connects all possible threshold points, plotting the false positive rate as the abscissa and the true positive rate as the ordinate (Phillips et al., 2006). The AUC value represents the area of the ROC curve enclosed by abscissas, serving as a threshold-independent measure of model performance (Phillips et al., 2006). AUC values range from 0 to 1, with values closer to 1 indicating better predictive accuracy. Models with an AUC below 0.7 are generally considered to have poor predictive accuracy, while those with an AUC above 0.8 are considered to have good predictive accuracy (Peterson et al., 2011; Zank et al., 2014). TSS, calculated as the sum of sensitivity and specificity minus one, measures the proportion of correctly predicted validation points (Chu et al., 2017). TSS values closer to 1 indicate higher predictive accuracy of the model, with values exceeding 0.5 generally regarded as acceptable for predictive purposes.

The potential distribution area for each species was estimated based on binary predictions, and changes in distribution size were quantified under current and future periods. Outputs from the five Earth system models were arithmetically weighted. To generate binary distribution maps, the maximum training sensitivity plus specificity (MTSS) threshold was applied, converting continuous habitat suitability into suitable (1) and not suitable (0). Changes in distribution areas were analyzed by calculating the portions of habitat expected to decrease, increase, or remain the same under each future climate scenario. Crucially, the predicted distributions were refined based on extensive field sampling data and expert knowledge of the actual distribution ranges of the 10 species (Shi et al., 2023). This refinement involved

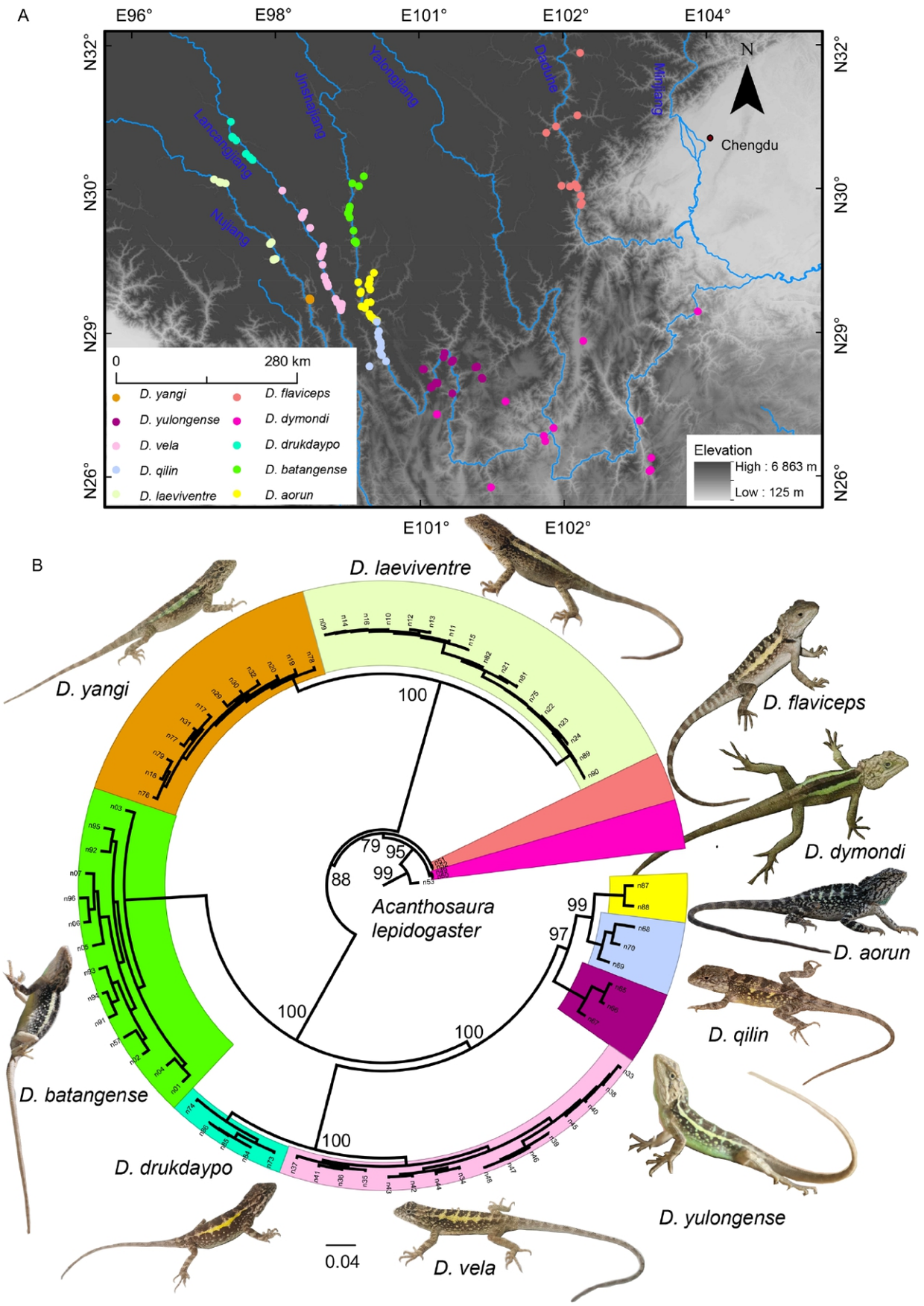


Figure 1 Distribution of sampling sites and phylogenetic relationships of *Diploderma* species

A: Distribution of sampling sites for *Diploderma* species. B: Phylogenetic tree of 10 *Diploderma* species analyzed in this study. *D. qilin*, photo by Kai Wang; *D.aorun* and *D. flaviceps*, photos by Ya-Yong Wu; *D. batangense*, *D. yulongense* and *D. dymondi*, photos by Xiu-Dong Shi; *D. drukdaypo*, *D. laeviventre*, *D. vela* and *D. yangi*, photos by Lin Shi.

constraining the modeled distributions to ecological niches currently occupied by the species, thus limiting predictions to the basins and major branch streams where these species have been observed.

Genetic analyses and effective population size estimation

To analyze genetic diversity and estimate *N*e for each species, 2–16 toe-clipping tissue samples were collected. Detailed locality information is provided in Supplementary Table S5. Genomic DNA was extracted using a MolPure Cell/Tissue DNA Kit (Yeasen, China), double-digest restriction site-associated DNA (ddRAD) sequencing was performed to generate individual genotypes. The RAD library was prepared following standard protocols (Peterson et al., 2012), with some modifications (Yang et al., 2018), and sequencing was carried out using the Illumina NovaSeq platform (Novogene, China). Given the absence of a robust reference genome, the RAD data were demultiplexed and analyzed using the "denovo_map.pl" pipeline in STACKS (v.2.64; Catchen et al., 2011; Rochette et al., 2019) to identify genetic variants under the Marukilow model (Maruki & Lynch, 2017). Genome-wide nucleotide diversity (θ_π) was calculated using vcftools (v.0.1.16) with a sliding window of 10 kbp (Danecek et al., 2011). *N*e was estimated under the simplifying assumption of mutation-drift equilibrium using

$$Ne = \theta_\pi / 4\mu \tag{1}$$

where μ represents the mutation rate. As specific mutation rates for *Diploderma* species are unavailable, the mean mutation rate for reptiles, derived from available genomic data (1.17×10^{-8} per site per generation, 95% confidence interval of the mean=5.34×10^{-9} to 1.80×10^{-8}), was used (Bergeron et al., 2023). *N*e values of 50 and 500, long recognized as the minimum thresholds for avoiding inbreeding decline in the short term and maintaining evolutionary potential over the long term, respectively, were applied in this study (Jamieson & Allendorf, 2012). These thresholds play an important role in the development and implementation of the IUCN Red List categorization system for threatened species (Frankham et al., 2014), particularly as genetic data become more accessible and affordable.

Risk assessment

Building on the dynamics of species distributions and genetically inferred population sizes, we developed an enhanced extinction risk assessment framework, encompassing five scenarios.

For scenario 1 (S1), the RRS for each species was derived by integrating EOO, AOO, and *N*e (Figure 2). The EOO, AOO, and estimated *N*e values of each species were first ranked in descending order, with ranks summed to determine the relative threat status of each species. Lower cumulative scores indicated a lower extinction risk to the species.

For scenario 2 (S2), both current climatic and habitat suitability were considered. Climatically suitable areas that do not align with the habitat preferences of the species were excluded (Figure 2). To achieve this, the global land cover projection dataset, which maintains a consistent 1-km spatial resolution and includes 20 land types projected for the 2015 to 2100 period at five-year intervals, was employed. These projections incorporate the latest IPCC scenarios that account for interactions between socioeconomic factors and climate change (Chen et al., 2022). Within the AOO, land-use classification of each grid cell was identified, designating croplands and urban areas as unsuitable habitats, and needleleaf and deciduous forests and grasslands as suitable habitats (Supplementary Table S6). Suitable habitat areas were then ranked in descending order and combined with the rankings of EOO, AOO, and *N*e to compute the updated RRS. Lower RRS values corresponded to reduced risk to the species.

For scenario 3 (S3), both current and future climatically suitable areas were considered. The AOO was calculated for each climate scenario across five Earth system models (Figure 2). The differences in AOO between the current climate and future projections were averaged across the models for each scenario (SSP126, SSP370, and SSP585) (Eq.1). The average rates of AOO loss under the three climate scenarios were ranked from smallest to largest, with these ranks added to those obtained from Scenario 1 to derive an updated RRS for each species.

$$AOO_{(\text{Loss of future climate scenario})} = \left(\sum\left(AOO_{(\text{Current})} - AOO_{(\text{Future})}/AOO_{(\text{Current})}\right)100\right)\%/5 \tag{2}$$

For scenario 4 (S4), habitat loss within suitable areas was considered under land-use change scenarios based on the RRS calculated in S2 (Figure 2). Specifically, habitat loss rates were averaged across the different Earth system models for each climate scenario (similar to Equation 2). For each species, the average habitat loss rates under each climate scenario were ranked from smallest to largest (values ranging from 1 to 10).

For scenario 5 (S5), the cumulative extinction risk was determined by summing all RRS values from the preceding four scenarios (S1 to S4) (Figure 2). This comprehensive score was calculated by aggregating the rank summaries of non-overlapping assessment criteria across all scenarios. Species were then ranked from smallest to largest values, with smaller scores indicating a lower risk for the species.

Testing the relationships between morphological characters and risk status

To facilitate the initial assessment of some DD species, the influence of morphological traits on extinction risk was evaluated. Eight functionally relevant characteristics were measured for each species, including competition-related snout-vent length (SVL), head length (HL), and head width (HW); movement-related tail length (TL), forelimb length (FLL), and hind limb length (HLL); and sensory-related diameter of the eye (DE) and snout-eye distance (SED). To enable meaningful multi-species comparisons, all measurements were exclusively taken from males, using either field-collected live individuals or specimens. A vernier caliper (Pr'sKit) with an accuracy of 0.01 mm was employed for all measurements, and at least five male individuals were sampled per species to ensure reliability.

To account for the influence of phylogenetic relationships on morphological differentiation, a phylogenetic tree was constructed for related lizard species based on simplified genomes, with *Acanthosaura lepidogaster* designated as the outgroup (Figure 1B). Variant data from RAD sequencing were concatenated, and the maximum-likelihood (ML) phylogeny was inferred under a GTR+ASC model with 1 000 bootstrap replicates using IQ-TREE (Nguyen et al., 2015).

To explore the correlation between morphological traits and relative extinction risk, phylogenetic generalized least-squares (PGLS) regression was used. Prior to formal analysis,

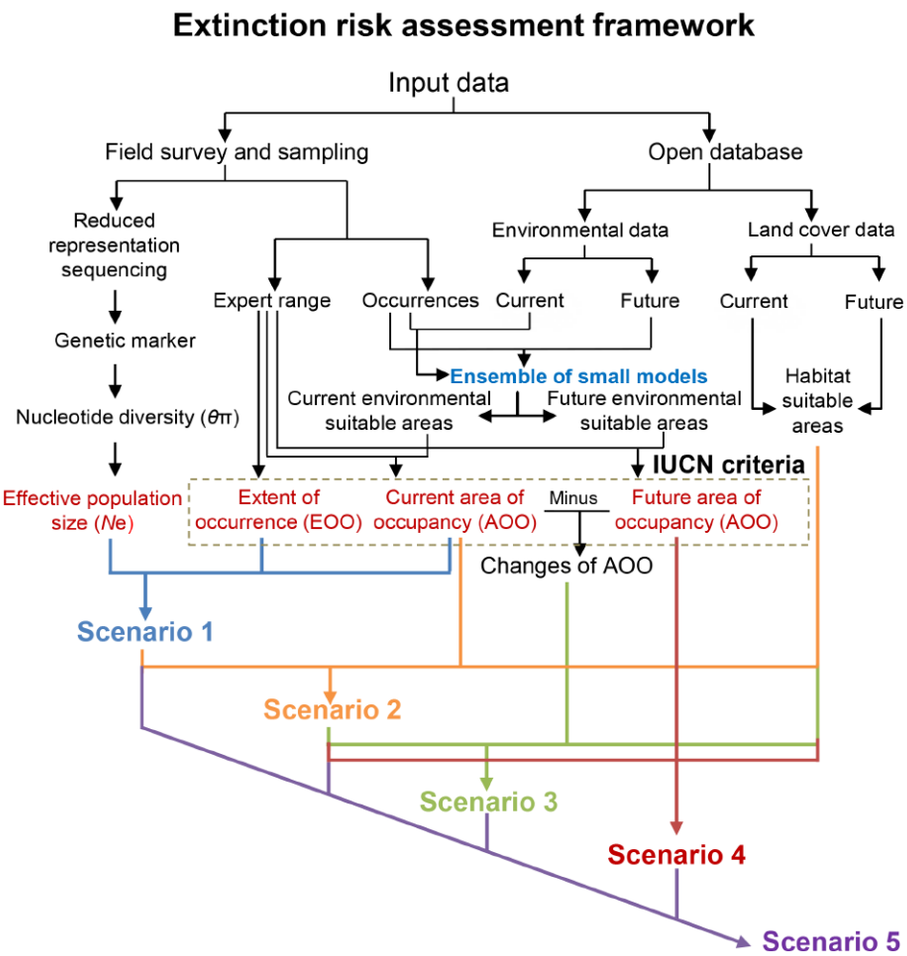


Figure 2 Risk assessment framework

The framework is divided into multiple sections to evaluate risks associated with changes in species distribution under climate and land-use change scenarios.

morphological measurements for all species were standardized by SVL. The PGLS model was constructed with morphological traits as independent variables and RRS as the dependent variable, using the "caper" R package (Orme et al., 2023). The phylogenetic signal strength was assessed using lambda (λ), where values range from 0 (indicating trait evolution independent of phylogeny; weak phylogenetic signal) to 1 (indicating trait divergence comparable with Brownian motion; strong phylogenetic signal).

RESULTS

EOO and AOO of *Diploderma* species

Field surveys combined with literature data revealed significant variability in the geographic ranges of *Diploderma* species. Among the study taxa, *D. dymondi* exhibited the largest EOO, while *D. yangi* occupied the smallest range. Notable overlaps in distribution were observed between *D. qilin* and *D. aorun*, as well as between *D. vela* and *D. drukdaypo*. In contrast, *D. flaviceps* demonstrated a more isolated distribution range, with its northernmost limit located farther from other species (Supplementary Figure S1). By integrating empirical distribution data with predictions from the ensemble of small models, the estimated average AOO for each species was calculated. Results showed considerable variation across taxa: *D. aorun* had an average AOO of 553 km², *D. batangense* 399 km², *D. drukdaypo* 504 km², *D. dymondi* 737 km², *D. flaviceps* 312 km², *D. laeviventre* 477 km², *D. qilin* 346 km², *D. vela* 1 068 km², *D. yangi* 27 km², and *D. yulongense* 387 km² (Supplementary Figures S2–S11).

Dynamics of AOO under future climate and land-use change scenarios

Projected changes in the AOO under different climate scenarios reveal substantial variations in habitat loss across *Diploderma* species. Under the low-emission SSP126 scenario, *D. qilin* and *D. yulongense* experienced the highest AOO losses, at 73.47%±34.65% and 73.28%±32.67%, respectively, with corresponding losses of potentially suitable habitats of 70.76%±34.15% and 70.15%±32.59%. In contrast, *D. vela* showed the least impact, with AOO loss of only 12.38%±24.33%. Under the SSP370 scenario, the AOO loss for most species exhibited a substantial increase compared to the SSP126 scenario. For instance, the AOO loss of *D. flaviceps* increased dramatically from 48.27%±42.43% under SSP126 to 73.59%±47.66% under SSP370. Notably, *D. dymondi* was the only species to show a slight decrease in AOO loss, from 44.94%±61.47% under SSP126 to 42.31%±66.31% under SSP370. While *D. qilin* and *D. yulongense* continued to experience the highest losses, reaching 99.60%±0.01% and 97.16%±0.04%, respectively, *D. vela* showed a sharp increase in AOO loss, rising to 67.55%±30.49%. The high-emission SSP585 scenario demonstrated the most severe impact, with considerable loss of AOO and potentially suitable habitats across all species.

The empirical distribution ranges of *D. yangi* and *D. qilin* were completely eradicated. Most other species faced AOO reductions exceeding 90%, including *D. aorun*, *D. drukdaypo*, *D. dymondi*, *D. flaviceps*, *D. laeviventre*, *D. vela*, and *D. yulongense*. Even *D. batangense*, which exhibited the least loss, experienced a significant reduction of 79.45%±29.78%. These extensive losses in AOO predominantly resulted from reductions in potentially suitable habitats, as unsuitable habitats constituted a negligible proportion under most climate change scenarios. For example, suitable habitat loss for *D. yangi* was 50.40%±36.63% under SSP126 but 89.60%±20.80% under SSP370 (Figure 3).

Risk assessment based on IUCN Red List criteria

Using the IUCN Red List criteria B1 and B2, EOO and AOO were analyzed to determine the conservation status of the 10 *Diploderma* species. According to the IUCN thresholds, a species is classified as "Critically Endangered" (CR), "Endangered" (EN), and "Vulnerable" (VU) based on EOO values of 100, 5 000, and 20 000 km², respectively, with corresponding thresholds for AOO of 10, 500, and 2 000 km², respectively. As shown in Figure 4, *D. yangi* met the criteria for EN under both EOO and AOO, indicating its position as the species facing the highest risk of extinction. Among the three species currently lacking formal IUCN Red List assessments, *D. aorun*, *D. drukdaypo*, and *D. qilin* fell within the VU category based on their EOO and AOO measurements. In addition, species previously assessed by the IUCN as 'Least Concern' (LC), including *D. vela*, *D. batangense*, and *D. laeviventre*, were found to meet the criteria for VU, warranting a reclassification to reflect their heightened vulnerability.

Risk assessment based on multi-scenario risk ranking scores

In most scenarios, *D. yangi* consistently exhibited the highest RRS, driven by significant losses in suitable habitats (S2), projected future distribution under climate change (S3), and future habitat changes (S4). Similarly, *D. qilin* ranked among the most at-risk species, with relatively high RRS values, ranking 10th in S5 and S3, 9th in S2 and S4, and 8th in S1 (Supplementary Table S7). Despite having relatively large EOO and AOO values, *D. qilin* is expected to lose nearly all its distribution range and habitat under future climate change scenarios, resulting in elevated extinction risk. In contrast, *D.*

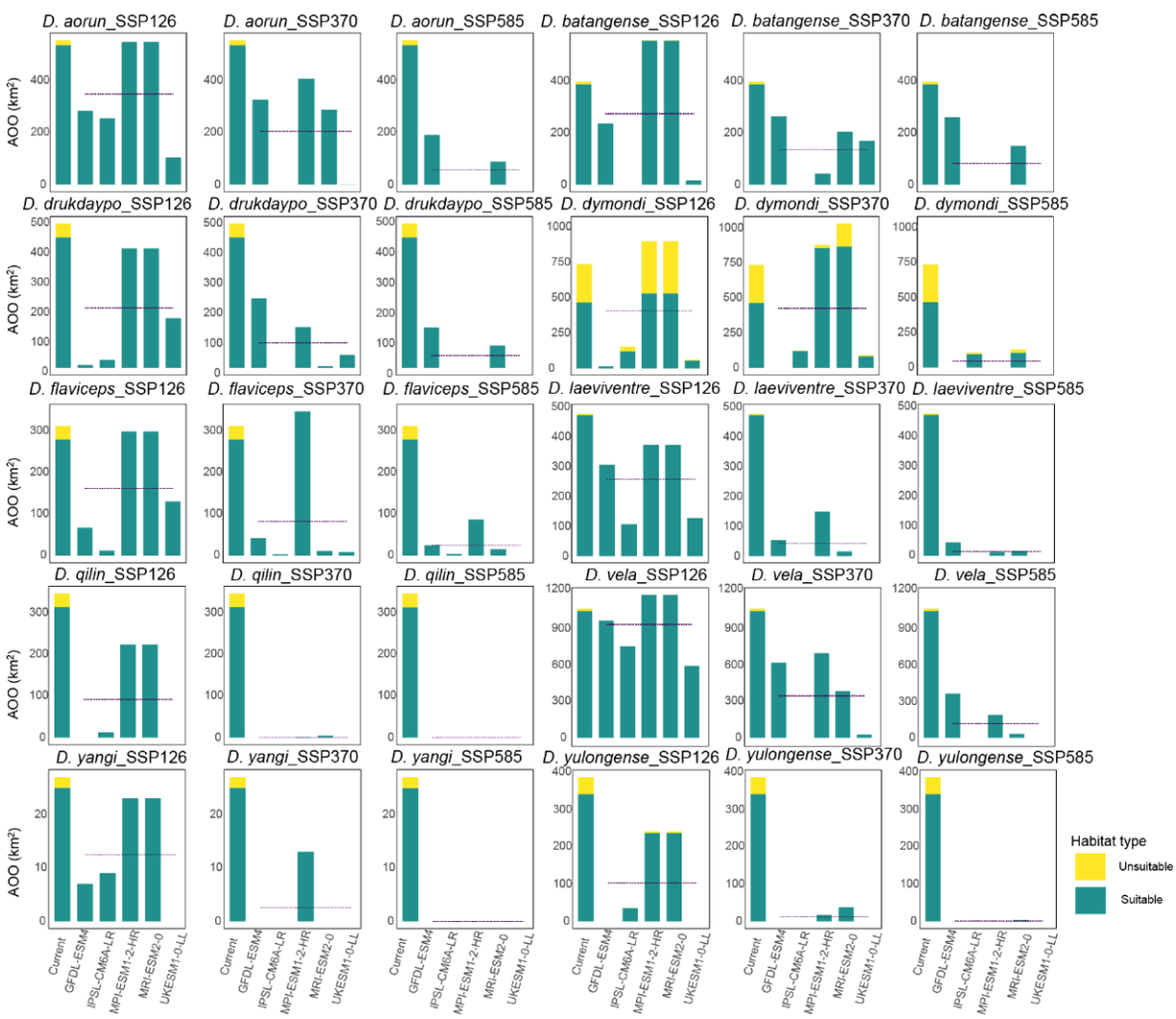


Figure 3 Area of occupancy (AOO) and potentially suitable/unsuitable habitats of *Diploderma* species under different climate and land-use change scenarios

SSP126, SSP370 and SSP585 represent future climate data under different emission scenarios. GFDL-ESM4, IPSL-CM6A-LR, MPI-ESM1-2HR, MRI-ESM2-0, UKESM1-0-LL represent different Earth system models.

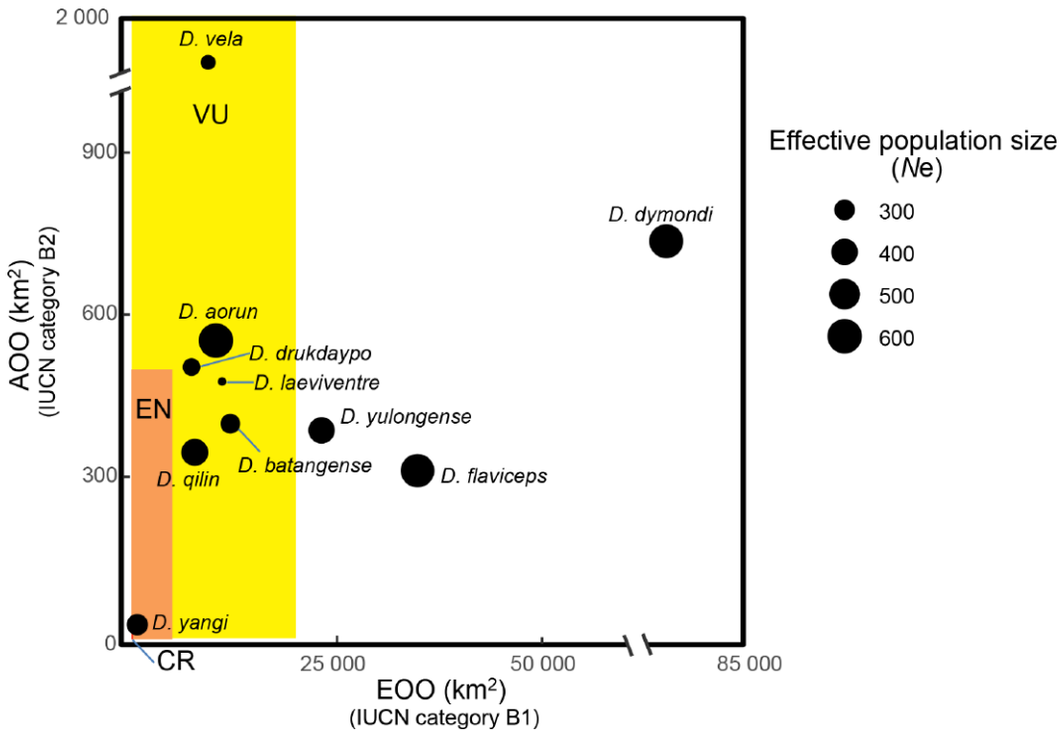


Figure 4 Assessment of current species threat status using IUCN criteria B1 and B2

Species were assessed based on extent of occurrence (EOO) and area of occupancy (AOO). For EOO, species with an EOO<100 km^2 were classified as Critically Endangered (CR), those with an EOO<5 000 km^2 were classified as Endangered (EN), and those with an EOO<20 000 km^2 were classified as Vulnerable (VU). For AOO: species with an AOO<10 km^2 were classified as CR, those with an AOO<500 km^2 were classified as EN, and those with an AOO<2 000 km^2 were classified as VU. Circle size represents effective population size (*Ne*), with larger circles indicating greater population sizes.

aorun and *D. dymondi* demonstrated lower extinction risks, achieving the lowest RRS ranking across three scenarios (S1, S2, and S3) and two scenarios (S4 and S5), respectively (Figure 5). Although *D. flaviceps* does not appear to be a threatened species based solely on EOO and AOO metrics, its risk rankings increased to 9th when potentially suitable habitats (S2) were considered. Its vulnerability further increased to 5th when habitat loss under future climate and land-use scenarios (S3 and S4) was accounted for. When all factors were combined (S5), *D. flaviceps* ranked at a moderate threat level, placing 5th overall.

Relationships between morphological characters and risk ranking scores

PGLS analysis revealed significant correlations between morphological traits and RRS across scenarios. SVL showed a strong association with the RRS of S1 and S2 (Figure 6), while relative diameter of the eye (RDE) was positively correlated with the RRS of S2. Notably, relative tail length (RTL) and relative head width (RHW) exhibited significant correlations across all five evaluation scenarios, although in opposite directions (Figure 6). These findings highlight the potential predictive value of specific morphological traits in extinction risk assessments.

DISCUSSION

Accurate, comprehensive, and predictive assessments of endangered species are essential for advancing biodiversity conservation efforts. In this study, an enhanced risk assessment framework was developed, integrating distribution dynamics, genetically inferred *Ne*, and morphological traits. By incorporating multiple climatic scenarios, land-use patterns, and species occurrence data, this framework enabled the construction of robust species distribution models to predict future changes in climatically suitable areas and potentially suitable habitat availability for 10 *Diploderma* species, which served as a model system for testing the effectiveness of the proposed framework. Compared to existing IUCN assessment approaches, this framework offers several key advantages: First, it explicitly accounts for the dynamic impacts of climate change and land-use modifications on species distributions, enabling more accurate risk evaluations. Second, it integrates multiple climate and land-use change scenarios, incorporating uncertainties to produce more robust predictions. Third, the inclusion of *Ne* as a metric provides insights into extinction risk from a genetic diversity perspective, addressing a critical gap in existing assessment systems.

Enhanced framework provided more accurate evaluations

The application of this enhanced risk assessment framework highlighted significant shortcomings in existing IUCN evaluations, particularly in underestimating the extinction risk of *Diploderma* species. One critical limitation of the IUCN Red List is its omission of genetic diversity patterns, which are essential for assessing long-term survival of species. Genetic diversity plays a pivotal role in species adaptability, with the post-2020 framework of the CBD prioritizing its preservation to prevent genetic erosion and safeguard the adaptive potential of both wild and domesticated populations (Laikre et al., 2020). Our framework integrates a *Ne* value greater than 500 as a critical indicator, aligning with this goal (Hoban et al., 2020). *Ne* reflects both the rate of random genetic drift and inbreeding levels, with smaller *Ne* values leading to increased

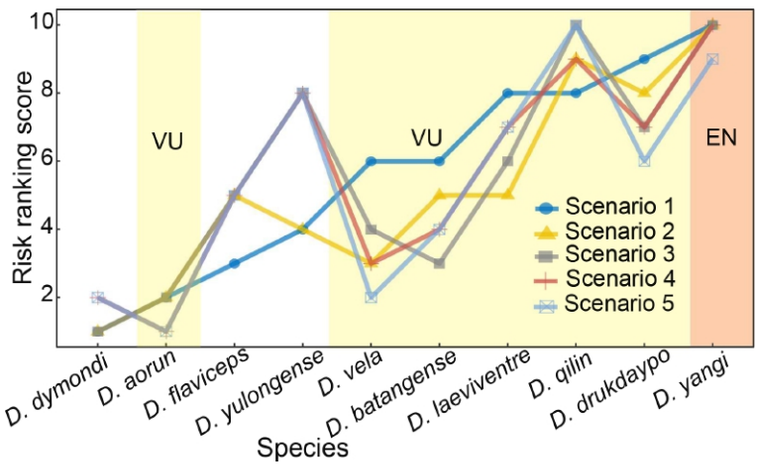


Figure 5 Risk ranking scores for 10 *Diploderma* species under different risk assessment scenarios

VU: Vulnerable; EN: Endangered.

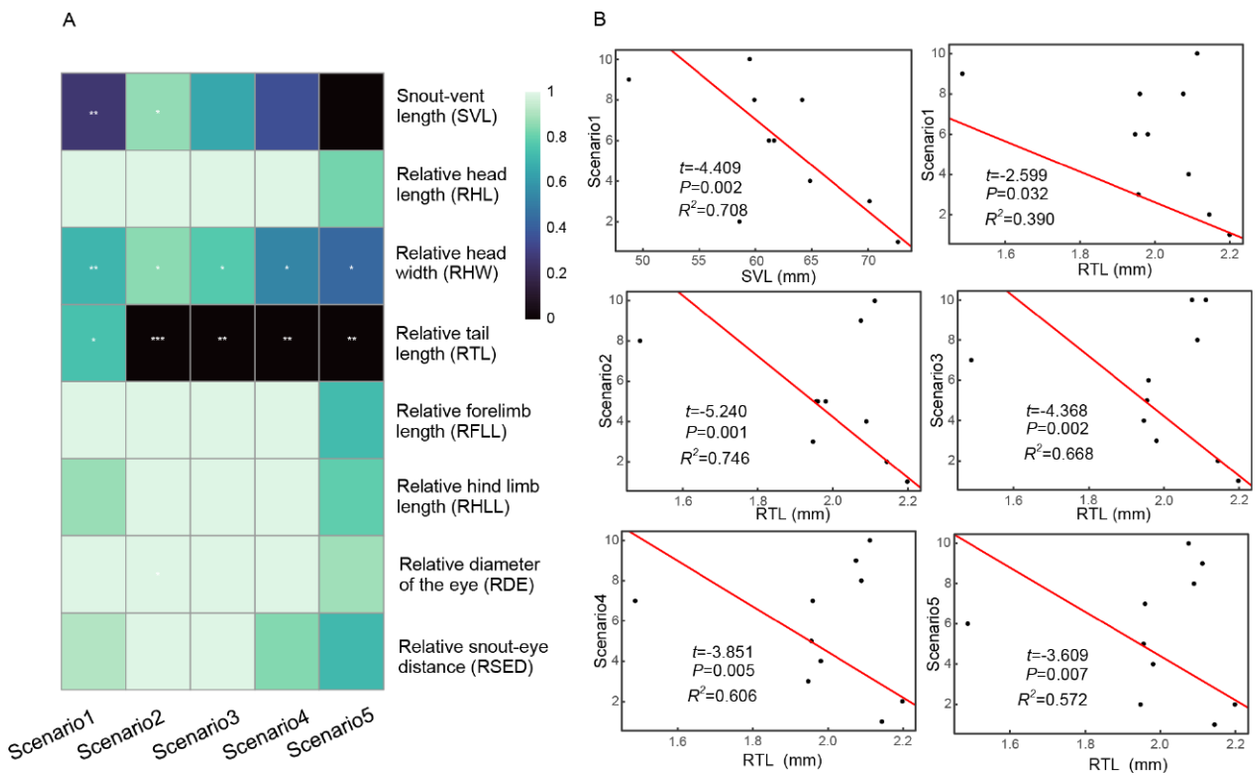


Figure 6 Correlations between morphological traits and risk ranking scores of each species

A: Lambda value of phylogenetic generalized least-squares (PGLS) analysis of traits and assessment indicators. Symbols indicating statistical significance, ns: Not significant; *: $P>0.05$; **: $P\leq0.01$; ***: $P\leq0.001$; ****: $P\leq0.0001$. B: Correlations between morphological traits and risk ranking scores of each species.

inbreeding, reduced fitness, decreased population size, and increased susceptibility to extinction (Ren et al., 2022; Willi et al., 2022). According to the widely used 50/500 rule, none of the *Diploderma* species faces immediate threat of inbreeding depression, with all *Ne* above 50. However, *D. vela*, *D. batangense*, *D. drukdaypo*, *D. laeviventre*, *D. yulongense*, *D. yangi*, and *D. qilin* had *Ne* values below 500, suggesting insufficient genetic diversity for adapting to future environmental changes (Ryman et al., 2019). When evaluated against the more recent 100/1 000 minimum *Ne* threshold, all studied species fell below the recommended levels, highlighting the need for long-term conservation planning (Frankham et al., 2014; Hoban et al., 2024).

Additionally, the proposed framework also revealed that the endangered status of *Diploderma* species has been underestimated due to inadequate consideration of habitat loss under future climate and land-use changes. SDM and land-use change projections indicated alarming habitat reductions. For example, under the high-emission SSP585 scenario, the estimated AOO losses for *D. batangense* and *D. laeviventre* were 79.45%±8.86% and 96.93%±0.15%, respectively. Similarly, despite its low current distribution range and *Ne* ranking, *D. flaviceps* faces significant loss of habitat under future climate conditions, posing a significant threat to its survival. The extensive loss of habitat predicted under climate change scenarios emphasizes the urgent need

for greater conservation attention and strategic planning to protect these species.

Enhanced framework highlighted higher risk for DD species underestimated by the IUCN

This study explored risk assessment for species lacking sufficient data from existing IUCN assessments. Species such as *D. drukdaypo*, *D. aorun*, *D. qilin*, and *D. yangi* are not recorded in the IUCN Red List, resembling DD taxa whose conservation needs are often overlooked. The absence of registration or critical ecological data for species can substantially influence conservation efforts. Research suggests that DD species face a higher extinction risk than many evaluated species, with 56% of unevaluated taxa in the IUCN Red List potentially at risk, suggesting potential biases in current conservation priorities (Borgelt et al., 2022). Based on our framework, *D. aorun*, *D. drukdaypo*, and *D. qilin* met the criteria for classification as VU, while the recently described *D. yangi* should be classified as EN. *Diploderma yangi* is restricted to the upper Salween River Valley in Zayu County in the Xizang Autonomous Region of China, extending to the Xizang-Yunnan border region. This species, identified as having the smallest surveyed distribution range, exhibited the highest relative threat level based on multi-scenario assessments (S2 to S5). Nevertheless, compared to other species, its limited distribution range makes it more susceptible to habitat destruction and environmental changes, underscoring the importance of habitat preservation, particularly shrub protection, within the Salween River basin.

These findings emphasize the conservation significance of many DD species that are at risk of extinction but remain unclassified as EN by the IUCN (de Oliveira Caetano et al., 2022). Enhanced and precise evaluations of unregistered or DD species are vital for refining conservation priorities and ensuring their inclusion in sustainable development goals and biodiversity preservation.

Enhanced framework identified morphological traits as preliminary risk indicators

The latest IUCN Red List has assessed the threat status of 10 254 reptile species, identifying 14.55% as DD. Addressing the conservation needs of these DD (including unassessed) species is critical, as their unknown status poses challenges to biodiversity preservation. To bridge this gap, studies have increasingly utilized key functional trait data to preliminarily predict extinction risk. Large body size is often associated with a higher extinction risk, as it is associated with ecological characteristics that heighten vulnerability, including low population densities, extensive home ranges, and slower recovery from rapid environmental disturbances (Reed & Shine, 2002; Zhong et al., 2022). Large lizards, for example, are particularly susceptible to predation by invasive species, further increasing their extinction risk (Tingley et al., 2013). However, within the genus *Diploderma*, a contrasting pattern emerged. Notably, SVL showed a negative correlation with endangered status, likely due to its positive relationship with species distribution range (R^2=0.493), with a smaller SVL associated with a reduced EOO, a critical predictor of extinction risk in the assessment framework. Limited range size has been consistently identified as a major predictor of extinction risk in birds, certain terrestrial mammals, and reptiles, showing a strong negative correlation with extinction risk (Ripple et al., 2017). In addition to SVL, other morphological traits such as RTL and RHW emerged as proxy indicators for extinction risk in the genus *Diploderma*. These traits may influence sensory abilities or locomotion capabilities, enabling species to navigate environmental disturbances. Although their precise roles remain unclear, further research is needed to explore the potential connections between these traits and species vulnerability.

In summary, this study proposes a new risk assessment framework based on AOO, EOO, *N*e, suitable habitat area, and projected changes in AOO due to future climate scenarios. Furthermore, this study proposes an automated assessment framework that incorporates morphological traits to predict extinction risk as an initial step prior to more detailed evaluations. This dynamic framework represents a significant advancement in assessing the risk of DD species, particularly in global biodiversity hotspots, ultimately bridging the assessment gaps for lesser-known taxa and offering a promising tool for global conservation efforts and effective prioritization of species at risk.

DATA AVAILABILITY

All sequences data generated in this study have been deposited in the NCBI (BioProjectID PRJNA1195238), Genome Sequence Archive (GSA) database with accession number CRA020990, National Genomics Data Center (NGDC) with accession number PRJCA029744, and Science Data Bank database (DOI: 10.57760/sciencedb.j00139.00148.

SUPPLEMENTARY DATA

Supplementary data to this article can be found online.

COMPETING INTERESTS

The authors declare that they have no competing interests.

AUTHORS' CONTRIBUTIONS

Q.X.: Conceptualization, Methodology, Software, Visualization, Writing – original draft, Writing – review & editing. X.D.S.: Visualization, Data curation, Resources, Writing – review & editing. L.S.: DNA extraction and Sequencing data analysis. Z.Y.Y.: Distribution records data curation. Y.H.C.: Writing – review & editing. W.Z.Y.: Methodology, Data curation, Resources. Z.Y.L.: Conceptualization, Methodology, Software, Supervision, Writing – original draft, Writing – review & editing, Validation. Y.Q.: Conceptualization, Supervision, Writing – review & editing, Validation. All authors read and approved the final version of the manuscript.

ACKNOWLEDGMENTS

The authors would like to thank Dr. Na Wu (Chengdu Institute of Biology, Chinese Academy of Sciences) for assistance with mapping.

REFERENCES

Anderson RP. 2023. Integrating habitat-masked range maps with quantifications of prevalence to estimate area of occupancy in IUCN assessments. *Conservation Biology*, **37**(1): e14019.

Bachman SP, Field R, Reader T, et al. 2019. Progress, challenges and opportunities for Red Listing. *Biological Conservation*, **234**: 45–55.

Bergeron LA, Besenbacher S, Zheng J, et al. 2023. Evolution of the germline mutation rate across vertebrates. *Nature*, **615**(7951): 285–291.

Betts J, Young RP, Hilton-Taylor C, et al. 2020. A framework for evaluating the impact of the IUCN Red List of threatened species. *Conservation Biology*, **34**(3): 632–643.

Borgelt J, Dorber M, Høiberg MA, et al. 2022. More than half of data deficient species predicted to be threatened by extinction. *Communications Biology*, **5**(1): 679.

Braby MF. 2018. Threatened species conservation of invertebrates in Australia: an overview. *Austral Entomology*, **57**(2): 173–181.

Breiner FT, Nobis MP, Bergamini A, et al. 2018. Optimizing ensembles of small models for predicting the distribution of species with few occurrences. *Methods in Ecology and Evolution*, **9**(4): 802–808.

Brooks TM, Pimm SL, Akçakaya HR, et al. 2019. Measuring terrestrial area of habitat (AOH) and its utility for the IUCN Red List. *Trends in Ecology & Evolution*, **34**(11): 977–986.

Cai B, Liu FJ, Liang D, et al. 2024. A new species of *Diploderma* (Squamata, Agamidae) from the valley of Dadu River in Sichuan Province, with a redescription of topotypes of *D. splendidum* from Hubei Province, China. *Animals*, **14**(9): 1344.

Catchen JM, Amores A, Hohenlohe P, et al. 2011. *Stacks*: building and genotyping loci *de novo* from short-read sequences. *G3 Genes*| *Genomes*| *Genetics*, **1**(3): 171–182.

Cazalis V, Di Marco M, Butchart SHM, et al. 2022. Bridging the research-implementation gap in IUCN Red List assessments. *Trends in Ecology & Evolution*, **37**(4): 359–370.

Chakona A, Jordaan MS, Raimondo DC, et al. 2022. Diversity, distribution and extinction risk of native freshwater fishes of South Africa. *Journal of Fish Biology*, **100**(4): 1044–1061.

Chen GZ, Li X, Liu XP. 2022. Global land projection based on plant functional types with a 1-km resolution under socio-climatic scenarios. *Scientific Data*, **9**(1): 125.

Chichorro F, Juslén A, Cardoso P. 2019. A review of the relation between species traits and extinction risk. *Biological Conservation*, **237**: 220–229.

Chu JM, Li YF, Zhang L, et al. 2017. Potential distribution range and conservation strategies for the endangered species *Amygdalus pedunculata*. *Biodiversity Science*, **25**(8): 799–806.

Dakhil MA, Halmy MWA, Liao ZY, et al. 2021. Potential risks to endemic conifer montane forests under climate change: Integrative approach for conservation prioritization in Southwestern China. *Landscape Ecology*, **36**(11): 3137–3151.

Danecek P, Auton A, Abecasis G, et al. 2011. The variant call format and VCFtools. *Bioinformatics*, **27**(15): 2156–2158.

de Oliveira Caetano GH, Chapple DG, Grenyer R, et al. 2022. Automated assessment reveals that the extinction risk of reptiles is widely underestimated across space and phylogeny. *PLoS Biology*, **20**(5): e3001544.

Dong H, Zhang NN, Shen SM, et al. 2023. Effects of climate change on the spatial distribution of the threatened species *Rhododendron purdomii* in Qinling-Daba mountains of Central China: implications for conservation. *Sustainability*, **15**(4): 3181.

Flower A, Murdock TQ, Taylor SW, et al. 2013. Using an ensemble of downscaled climate model projections to assess impacts of climate change on the potential distribution of spruce and Douglas-fir forests in British Columbia. *Environmental Science & Policy*, **26**: 63–74.

Frankham R, Bradshaw CJA, Brook BW. 2014. Genetics in conservation management: revised recommendations for the 50/500 rules, Red List criteria and population viability analyses. *Biological Conservation*, **170**: 56–63.

Garner BA, Hoban S, Luikart G. 2020. IUCN Red List and the value of integrating genetics. *Conservation Genetics*, **21**(5): 795–801.

Gaston KJ, Fuller RA. 2009. The sizes of species' geographic ranges. *Journal of Applied Ecology*, **46**(1): 1–9.

Guisan A, Thuiller W, Zimmermann NE, et al. 2017. Habitat Suitability and Distribution Models: with Applications in R. Cambridge: Cambridge University Press.

Hamann A, Aitken SN. 2013. Conservation planning under climate change: accounting for adaptive potential and migration capacity in species distribution models. *Diversity and Distributions*, **19**(3): 268–280.

Hamilton H, Smyth RL, Young BE, et al. 2022. Increasing taxonomic diversity and spatial resolution clarifies opportunities for protecting US imperiled species. *Ecological Applications*, **32**(3): e2534.

Hoban S, Bruford M, Jackson JDU, et al. 2020. Genetic diversity targets and indicators in the CBD post-2020 global biodiversity framework must be improved. *Biological Conservation*, **248**: 108654.

Hoban S, da Silva JM, Hughes A, et al. 2024. Too simple, too complex, or just right? Advantages, challenges, and guidance for indicators of genetic diversity. *BioScience*, **74**(4): 269–280.

IUCN. 2024. IUCN red list of threatened species. https://www.iucnredlist.org/en.

Jamieson IG, Allendorf FW. 2012. How does the 50/500 rule apply to MVPs?. *Trends in Ecology & Evolution*, **27**(10): 578–584.

Jetz W, McGeoch MA, Guralnick R, et al. 2019. Essential biodiversity variables for mapping and monitoring species populations. *Nature Ecology & Evolution*, **3**(4): 539–551.

Kissling WD, Field R, Korntheuer H, et al. 2010. Woody plants and the prediction of climate-change impacts on bird diversity. *Philosophical Transactions of the Royal Society B: Biological Sciences*, **365**(1549): 2035–2045.

Laikre L, Hoban S, Bruford MW, et al. 2020. Post-2020 goals overlook genetic diversity. *Science*, **367**(6482): 1083–1085.

Le Breton TD, Zimmer HC, Gallagher RV, et al. 2019. Using IUCN criteria to perform rapid assessments of at-risk taxa. *Biodiversity and Conservation*, **28**(4): 863–883.

Li Q, Shao WJ, Jiang Y, et al. 2024. Assessing reptile conservation status under global climate change. *Biology*, **13**(6): 436.

Liang J, Wang WT, Cai Q, et al. 2024. Prioritizing conservation efforts based on future habitat availability and accessibility under climate change. *Conservation Biology*, **38**(3): e14204.

Liao ZY, Chen YH, Pan KW, et al. 2022. Current climate overrides past climate change in explaining multi-site beta diversity of Lauraceae species in China. *Forest Ecosystems*, **9**: 100018.

Mancini G, Santini L, Cazalis V, et al. 2024. A standard approach for including climate change responses in IUCN Red List assessments. *Conservation Biology*, **38**(3): e14227.

Marcer A, Sáez L, Molowny-Horas R, et al. 2013. Using species distribution modelling to disentangle realised versus potential distributions for rare species conservation. *Biological Conservation*, **166**: 221–230.

Maruki T, Lynch M. 2017. Genotype calling from population-genomic sequencing data. *G3 Genes*| *Genomes*| *Genetics*, **7**(5): 1393–1404.

Mastretta-Yanes A, da Silva JM, Grueber CE, et al. 2024. Multinational evaluation of genetic diversity indicators for the Kunming-Montreal global biodiversity framework. *Ecology Letters*, **27**(7): e14461.

Mi CR, Ma L, Yang MY, et al. 2023. Global protected areas as refuges for amphibians and reptiles under climate change. *Nature Communications*, **14**(1): 1389.

Miles DB. 2020. Can morphology predict the conservation status of Iguanian Lizards?. *Integrative and Comparative Biology*, **60**(2): 535–548.

Naimi B, Hamm NAS, Groen TA, et al. 2014. Where is positional uncertainty a problem for species distribution modelling?. *Ecography*, **37**(2): 191–203.

Nguyen LT, Schmidt HA, Von Haeseler A, et al. 2015. IQ-TREE: a fast and effective stochastic algorithm for estimating maximum-likelihood phylogenies. *Molecular Biology and Evolution*, **32**(1): 268–274.

Orme D, Freckleton R, Thomas G, et al. 2023. Caper: comparative analyses of phylogenetics and evolution in R (version 1.0. 3). https://cran.r-project.org/web/packages/caper.

Pecl GT, Araújo MB, Bell JD, et al. 2017. Biodiversity redistribution under climate change: impacts on ecosystems and human well-being. *Science*, **355**(6332): eaai9214.

Peng SJ, Shrestha N, Luo Y, et al. 2023. Incorporating global change reveals extinction risk beyond the current Red List. *Current Biology*, **33**(17): 3669–3678. e4.

Peterson AT, Soberón J, Pearson RG, et al. 2011. Ecological Niches and Geographic Distributions (MPB-49). Princeton: Princeton University Press.

Peterson BK, Weber JN, Kay EH, et al. 2012. Double digest RADseq: an inexpensive method for de novo SNP discovery and genotyping in model and non-model Species. *PLoS One*, **7**(5): e37135.

Phillips SJ, Anderson RP, Schapire RE. 2006. Maximum entropy modeling of species geographic distributions. *Ecological Modelling*, **190**(3–4): 231–259.

Reed RN, Shine R. 2002. Lying in wait for extinction: ecological correlates of conservation status among Australian elapid snakes. *Conservation Biology*, **16**(2): 451–461.

Ren JL, Yan CC, Peng ZL, et al. 2022. Sichuan hot-spring snakes imperiled: reason, situation, and protection. *Zoological Research*, **43**(1): 95–97.

Ripple WJ, Wolf C, Newsome TM, et al. 2017. Extinction risk is most acute for the world's largest and smallest vertebrates. *Proceedings of the National Academy of Sciences of the United States of America*, **114**(40): 10678–10683.

Roberts DL, Taylor L, Joppa LN. 2016. Threatened or data deficient: assessing the conservation status of poorly known species. *Diversity and Distributions*, **22**(5): 558–565.

Rochette NC, Rivera-Colón AG, Catchen JM. 2019. Stacks 2: analytical methods for paired-end sequencing improve RADseq-based population genomics. *Molecular Ecology*, **28**(21): 4737–4754.

Root TL, Price JT, Hall KR, et al. 2003. Fingerprints of global warming on wild animals and plants. *Nature*, **421**(6918): 57–60.

Ryman N, Laikre L, Hössjer O. 2019. Do estimates of contemporary effective population size tell us what we want to know?. *Molecular Ecology*, **28**(8): 1904–1918.

Santini L, Butchart SHM, Rondinini C, et al. 2019. Applying habitat and population-density models to land-cover time series to inform IUCN Red List assessments. *Conservation Biology*, **33**(5): 1084–1093.

Senior AF, Böhm M, Johnstone CP, et al. 2021. Correlates of extinction risk in Australian squamate reptiles. *Journal of Biogeography*, **48**(9): 2144–2152.

Shi L, Shi XD, Cao YN, et al. 2023. Response of distribution range against climate change and habitat preference of four national protected *Diploderma* species in Tibetan Plateau. *Asian Herpetological Research*, **14**(4): 319–330.

Thomas CD, Gillingham PK, Bradbury RB, et al. 2012. Protected areas facilitate species' range expansions. *Proceedings of the National Academy of Sciences of the United States of America*, **109**(35): 14063–14068.

Thuiller W, Guéguen M, Renaud J, et al. 2019. Uncertainty in ensembles of global biodiversity scenarios. *Nature Communications*, **10**(1): 1446.

Tingley R, Hitchmough RA, Chapple DG. 2013. Life-history traits and extrinsic threats determine extinction risk in New Zealand lizards. *Biological Conservation*, **165**: 62–68.

Villemant C, Barbet-Massin M, Perrard A, et al. 2011. Predicting the invasion risk by the alien bee-hawking yellow-legged hornet *Vespa velutina nigrithorax* across Europe and other continents with niche models. *Biological Conservation*, **144**(9): 2142–2150.

Wang K, Gao W, Wu YY, et al. 2024. Current status and future perspectives on the research of the genus *Diploderma* (Reptilia: Agamidae). *Chinese Journal of Zoology*, **59**(1): 129–131.

Wang K, Jiang K, Ren J, et al. 2019. A new species of dwarf *Japalura sensu* lato (Reptilia: Squamata: Agamidae) from the upper Mekong River in eastern Tibet, China, with notes on morphological variation, distribution, and conservation of two congeners along the same river. *Zootaxa*, **4544**(4): 505–522

Wang K, Jiang K, Zou DH, et al. 2016. Two new species of *Japalura* (Squamata: Agamidae) from the Hengduan Mountain Range, China. *Zoological Research*, **37**(1): 41–56.

Wang K, Ren JL, Wu JW, et al. 2021. Systematic revision of mountain dragons (Reptilia: Agamidae: *Diploderma*) in China, with descriptions of six new species and discussion on their conservation. *Journal of Zoological Systematics and Evolutionary Research*, **59**(1): 222–263.

Wang K, Zhang YP, Li XQ. 2022. A new species of *Diploderma* (Reptilia: Squamata: Agamidae) from the upper Salween River in eastern Tibet, China. *Zootaxa*, **5099**(2): 201–220.

Willi Y, Kristensen TN, Sgrò CM, et al. 2022. Conservation genetics as a management tool: the five best-supported paradigms to assist the management of threatened species. *Proceedings of the National Academy of Sciences of the United States of America*, **119**(1): e2105076119.

Williams BA, Watson JEM, Butchart SHM, et al. 2021. A robust goal is needed for species in the post-2020 global biodiversity framework. *Conservation Letters*, **14**(3): e12778.

Wright S. 1931. Evolution in Mendelian populations. *Genetics*, **16**(2): 97–159.

Yang WZ, While GM, Laakkonen H, et al. 2018. Genomic evidence for asymmetric introgression by sexual selection in the common wall lizard. *Molecular Ecology*, **27**(21): 4213–4224.

Yu Y, He G, Li DY, et al. 2022. Climate change challenge, extinction risk, and successful conservation experiences for a threatened primate species in China: golden snub-nosed monkey (*Rhinopithecus roxellana*). *Zoological Research*, **43**(6): 940–944.

Zank C, Becker FG, Abadie M, et al. 2014. Climate change and the distribution of neotropical red-bellied toads (*Melanophryniscus*, Anura, Amphibia): how to prioritize species and populations?. *PLoS One*, **9**(4): e94625.

Zhong YX, Chen CW, Wang YP. 2022. Biological and extrinsic correlates of extinction risk in Chinese lizards. *Current Zoology*, **68**(3): 285–293.

Han et al. *Zool. Res.* 2025, 46(1): 27−40
https://doi.org/10.24272/j.issn.2095-8137.2024.281
https://cstr.cn/32248.14.zr.2024.281

ZR | Zoological Research

Article Open Access

Both 20S and 19S proteasome components are essential for meiosis in male mice

Ting-Ting Han[1,#], Li-Ying Wang[2,#], Qiu-Xing Zhou[2], Wei Wei[2], Yan-Jie Ma[2], Ying-Hong Chen[2], Wei Li[2,*], Zhen-Yu Ju[1,*], Chao Liu[2,*]

[1] *Key Laboratory of Regenerative Medicine of Ministry of Education*, *Institute of Aging and Regenerative Medicine*, *Department of Developmental & Regenerative Medicine*, *College of Life Science and Technology*, *Jinan University*, *Guangzhou*, *Guangdong* 510632, *China*

[2] *Guangzhou Women and Children's Medical Center*, *Guangzhou Medical University*, *Guangzhou*, *Guangdong* 510623, *China*

ABSTRACT

The proteasome, an evolutionarily conserved proteolytic complex comprising the 20S core particle and 19S regulatory particles, performs both shared and distinct functions across various tissues and organs. Spermatogenesis, a highly complex developmental process, relies on proteasome activity at multiple stages to regulate protein turnover. In this study, we selected the 20S subunit PSMA1 and 19S regulatory subunit PSMD2 to investigate the potential functions of the proteasome in spermatogenesis. Using *Psma1-EGFP* and *Psmd2-mCherry* knock-in mouse models, we confirmed the expression of both subunits in all spermatogenic cell types, with pronounced presence in early germ cell development. To further clarify their functional significance, we specifically knocked out *Psma1* and *Psmd2* in germ cells. Deletion of either PSMA1 or PSMD2 led to disrupted spermatogenesis, characterized by the complete absence of sperm in the epididymis. Subsequent analysis indicated that loss of these proteasome components impaired meiotic initiation. *Psma1* and *Psmd2* knockout germ cells showed accumulation of DMRT1, a key regulator of mitosis-to-meiosis transition, leading to a reduction in STRA8 levels and consequent disruption of meiosis initiation. This study sheds light on the molecular mechanisms that govern meiotic initiation and identifies potential genes associated with male infertility.

Keywords: Proteasome; PSMA1; PSMD2; Meiotic initiation; Spermatogenesis

INTRODUCTION

The proteasome is a highly organized proteolytic complex responsible for the degradation of ubiquitinated proteins, playing a pivotal role in nearly all cellular processes by eliminating misfolded, oxidized, and unnecessary proteins (Jung & Grune, 2012). Structurally, the proteasome is composed of a catalytic 20S core particle (CP) and one or two 19S regulatory particles (RPs), which together form the 26S proteasome complex. The 20S CP is comprised of 28 subunits arranged into four stacked rings—two outer α rings and two inner β rings. The α rings facilitate substrate recognition and entry into the proteolytic chamber, while the β rings house the catalytic sites responsible for proteolysis (Groll et al., 2000; Jung & Grune, 2012; Li et al., 2010). The 19S RPs, consisting of 19 components, associate with the 20S CP to function as proteasome gatekeepers, identifying and processing specific proteins for degradation (Tanaka & Kasahara, 1998; Tanaka, 2009; Xiong et al., 2022). Proteasome dysfunction or misregulation can severely disrupt cellular homeostasis, and targeted manipulation of proteasome activity has emerged as a promising strategy in therapeutic development and bioengineering (Coux et al., 2020).

Proteasome composition varies across tissues, aligning with the specialized functional requirements of each cell type. In immune cells, the immunoproteasome generates antigenic peptides with higher efficiency than the constitutive proteasome, which is essential for adaptive immunity (Tanaka & Kasahara, 1998). In thymic cortical epithelial cells, the "thymoproteasome" facilitates the positive selection of thymocytes, a crucial step in T cell development (Murata et al., 2007). In male germ cells, the conventional α4 subunit is substituted with the homolog α4s, an essential modification for proper meiotic exit (Uechi et al., 2014). Alongside the common 19S RP (PA700), other RPs have been identified, including PA28 in immune cells and PA200 in male germ cells (Jung &

This is an open-access article distributed under the terms of the Creative Commons Attribution Non-Commercial License (http://creativecommons.org/licenses/by-nc/4.0/), which permits unrestricted non-commercial use, distribution, and reproduction in any medium, provided the original work is properly cited.

Copyright ©2025 Editorial Office of Zoological Research, Kunming Institute of Zoology, Chinese Academy of Sciences

Received: 29 August 2024; Accepted: 23 October 2024; Online: 24 October 2024

Foundation items: This work was supported by the National Science Fund for Distinguished Young Scholars (81925015), Science and Technology Project of Guangzhou (2023A03J0886, 2023A03J0871), and National Natural Science Foundation of China (82030039, 32400709)

[#]Authors contributed equally to this work

*Corresponding authors, E-mail: leways@lzu.edu.cn; zhenyuju2016@jnu.edu.cn; liuchao@gwcmc.org

Grune, 2012; Khor et al., 2006; Preckel et al., 1999). The range of tissue-specific variations highlights the role of the proteasome in coordinating both constitutive and specialized functions across diverse biological processes.

In mammals, spermatogenesis proceeds through a series of orchestrated stages, including renewal and differentiation of spermatogonia, meiosis, and spermiogenesis (Oatley & Brinster, 2012). During the initial phase, spermatogonia undergo multiple rounds of mitosis before transitioning to meiosis, a shift regulated by retinoic acid through the meiotic initiation factor STRA8. Additionally, the RBM46/YTHDC2/MEIOC complex serves as the principal post-transcriptional regulator in mammals, selectively targeting and degrading mitotic transcripts to ensure successful progression of germ cells into meiosis (Abby et al., 2016; Liu et al., 2021; Qian et al., 2022; Wojtas et al., 2017). However, STRA8 and its associated proteins alone are insufficient to fully initiate meiosis, as additional meiotic suppressors have also been identified as key regulators in this process. For example, in fetal testes, CYP26B1 and NANOS2 act as inhibitors to prevent premature meiotic entry (Lin et al., 2008; Suzuki & Saga, 2008; Suzuki et al., 2010). Another critical mammalian regular, Doublesex and Mab-3 Related Transcription factor 1 (DMRT1), suppresses meiosis by specifically blocking the transcriptional induction of *Stra8* (Matson et al., 2010). Notably, several E3 ligases are reported to down-regulate these meiotic suppressors, for example, the E3 ligase SCFβ-TrCP targets DMRT1 for ubiquitination, a process essential for mitosis-to-meiosis transition in male germ cells. While these findings underscore the importance of ubiquitination in the early stages of spermatogenesis (Sun et al., 2023; Živković et al., 2022), the functional roles of the proteasome in this regulatory process remain largely unknown.

To elucidate the role of the proteasome in spermatogenesis, we focused on the 20S CP component PSMA1 and 19S RP component PSMD2, both of which show high expression during the early stages of spermatogenesis. PSMA1 has been linked to repetitive fertilization failure in patients following intracytoplasmic sperm injection (ICSI) (Torra-Massana et al., 2021). In contrast, PSMD2, one of the three non-ATPase subunits within the 19S base subunit and a ubiquitin-like protein (UBL), has not been previously studied in the context of spermatogenesis. We first generated *Psma1-GFP* and *Psmd2-mCherry* knock-in mice to examine their expression patterns during spermatogenesis. Our findings indicated that although PSMA1 and PSMD2 were present throughout spermatogenesis, their functions appeared to be concentrated on the early stages. To further clarify the roles of the 20S CP and 19S RP in spermatogenesis, we generated germ cell-specific *Psma1* and *Psmd2* knockout mice. Results showed that depletion of either of these two components led to complete infertility in male mice, characterized by massive germ cell arrest at meiotic initiation. This meiotic blockade in *Psma1* and *Psmd2* knockout mice was associated with impaired degradation of the meiosis inhibitory protein DMRT1. These findings highlight the essential role of the proteasome in facilitating meiosis entry during spermatogenesis.

MATERIALS AND METHODS

Animals

Psma1-EGFP and *Psmd2-mCherry* knock-in mice were generated using the CRISPR/Cas9 system (Cyagen Biosciences, China), based on the following design strategy. The *Psma1* gene (NCBI reference sequence: NM_011965.2), located on mouse chromosome 7 and containing 10 exons, was modified by replacing the TAA stop codon with "3×EAAAK-EGFP". The genotyping primers were: *Psma1-EGFP* Forward 1 (F1): 5'-CAGCAGTGAAACATAAGAAAGGCT-3', *Psma1-EGFP* Reverse 1 (R1): 5'-ACTTGACACAATAGGTGGTGAAAC-3', *Psma1-EGFP* F2: 5'-TATATCATGGCCGACAAGCAGAAG-3', and *Psma1-EGFP* R2: 5'-TACCCTTTCAAAGAAAATGCACCCC-3'. For *Psmd2-mCherry* mice, the *Psmd2* gene (NCBI reference sequence: NM_134101.2), located on mouse chromosome 16 and containing 21 exons, was modified by substituting the TGA stop codon in exon 21 with "3×EAAAK-mCherry". The genotyping primers were: *Psmd2-mCherry* F1: 5'-CTCCCGTTTCTGGAATCTGTACT-3', *Psmd2-mCherry* R1: 5'-GTGTTAGGCTGAACAGTGCTTCC-3', *Psmd2-mCherry* F2: 5'-ACTTCATTATTTTCATCCCACAGGC-3', and *Psmd2-mCherry* R2: 5'-GCCGTACATGAACTGAGGGG-3'. The *Stra8-GFPCre* knock-in mouse line was kindly gifted by Dr. Ming-Han Tong (Chinese Academy of Sciences Center for Excellence in Molecular Cell Science) (Lin et al., 2017), and the *Stra8-Cre* knock-in mouse line was kindly gifted by Dr. Fei Gao (Chinese Academy of Sciences, Institute of Zoology). The *Psma1*$^{Flox/Flox}$ and *Psmd2*$^{Flox/Flox}$ mice were also generated using the CRISPR/Cas9 system (Cyagen Biosciences, China). Briefly, loxP sequences were inserted into the flanking regions of exons 5 to 7 of the *Psma1* gene and into the flanking regions of exons 4 to 8 of the *Psmd2* gene. The genotyping primers were: *Psma1*$^{Flox/Flox}$ F1: 5'-CATCTAGTCAACATTTGATGAGGGC-3', *Psma1*$^{Flox/Flox}$ R1: 5'-TCATGTCACATCTGATGACCAAGT-3', *Psma1*$^{Flox/Flox}$ F2: 5'-TCTGTCTAAGGAGCTTTGCTAGAG-3', *Psma1*$^{Flox/Flox}$ R2: 5'-TCAGGACTTCATTTCCTTTGCAGT-3', *Psmd2*$^{Flox/Flox}$ F1: 5'-TTCCCTGGAACTGGAGTTAGGCT-3', *Psmd2*$^{Flox/Flox}$ R1: 5'-TTGGCCTCAACATTCTAGACCCA-3', *Psmd2*$^{Flox/Flox}$ F2: 5'-TTAAAGTTGGAGACTGGGCTAGCA-3', and *Psmd2*$^{Flox/Flox}$ R2: 5'-TACTCGCCTCTGCCTCTGCCAAGT-3'. Finally, the *Psma1*$^{Flox/Flox}$ and *Psmd2*$^{Flox/Flox}$ male mice were mated with *Stra8-Cre* transgenic females to produce germ cell-specific *Psma1* and *Psmd2* knockout models.

Ethics statement

All animal experiments were conducted following the ethical standards of animal welfare, strictly adhering to the regulations of the Research Ethics Committee of Guangzhou Women and Children's Medical Center (Animal Ethics Number: RSDW202301255).

Antibodies

The following antibodies were used for immunoblotting and immunofluorescence (IF): rabbit anti-PSMA1 (1175-1-AP, Proteintech, China), rabbit anti-PSMD2 (bs7260, Bio-World, USA), rabbit anti-PSMA8 (14022-1-AP, Proteintech, China), rabbit anti-PSME4 (18799-1-AP, Proteintech, China), rabbit anti-mCherry (43590, CST, USA), rabbit anti-GFP (generated by Dia-An Biotechnology, China; 1:100 for IF), rabbit anti-tubulin (10094-1-AP, Proteintech, China), mouse anti-GAPDH (10494-1-AP, Proteintech, China), mouse anti-DDX4 (ab27591, Abcam, UK), mouse anti-PLZF (sc-28319, Santa Cruz Biotechnology, Norway), rabbit anti-SOX9 (AB5535, Millipore, USA), rabbit anti-γH2AX (AP0687, ABclonal, China), guinea pig anti-SYCP3 (generated by Dia-An Biotechnology, Wuhan, China; 1:1 000 for IF), rabbit anti-STRA8 (Ab49405,

Abcam, UK), rabbit anti-Ki67 (Ab15580-100ug, Abcam, UK), goat anti-c-KIT (AF1356, R&D, USA), mouse anti-DMRT1 (sc-377167, Santa Cruz Biotechnology, Norway), rabbit anti-DMRT1 (28149-1-AP, Proteintech, China), rabbit anti-cleaved caspase-3 (9661S, CST, USA), PNA-488 (L21409, Thermo Fisher, USA), and PNA-594 (L32459, Thermo Fisher, USA).

Tissue collection and histological analysis

Mouse testes and cauda epididymis were dissected after euthanasia and fixed with Bouin's fixative (HT10132, Sigma, USA) or 4% paraformaldehyde (PFA, P1110, Solarbio, China) for 24 h. The testes were then dehydrated with graded ethanol, embedded in paraffin, sliced into 5 μm sections, and placed on glass slides for further processing. After deparaffinization, the tissue sections were stained with hematoxylin and eosin (H&E) (G1140, G1110, Solarbio, China) and periodic acid-Schiff (PAS, G1280, Solarbio, China) for histological analysis.

Epididymal sperm count

The cauda epididymis was isolated immediately after euthanasia. Sperm were released from the cauda epididymis, incubated in phosphate-buffered saline (PBS) for 15 min at 37℃, and counted using a hemocytometer.

Immunoblotting

Testis proteins were extracted in RIPA lysis buffer (R0010, Solarbio, China) supplemented with 1 mmol/L phenylmethylsulfonyl fluoride (PMSF, 0754, Amresco, USA) and protease inhibitor cocktail (PIC, 04693132001, Roche Diagnostics, Switzerland), as previously reported (Liu et al., 2023). After homogenizing the testis tissue and performing ultrasonication, samples were incubated on ice for 30 min, then centrifuged at 12 000 *g* for 15 min at 4℃. The supernatants of the extracts were collected in fresh tubes for immunoblotting. Protein samples were separated by electrophoresis and electrotransferred to a nitrocellulose membrane. After incubation with primary and secondary antibodies, the membranes were scanned using Alliance Q9 Advanced Auto (UVITEC, UK).

Immunofluorescence

After deparaffinization, the tissue sections were washed three times with PBS (5 min each) and permeated with 0.1% TritonX-100 (T8200, Solarbio, China) for 15 min. The tissue sections were then washed three times with PBS and blocked with 5% bovine serum albumin (BSA, A4737, Sigma, USA) in PBS for 1 h. The tissue sections were subsequently incubated with primary antibodies diluted with 1% BSA at 4°C overnight, washed with PBS, and incubated with secondary antibodies diluted with PBS for 1 h at 37°C. The tissue sections were washed with PBS, stained with DAPI (D9542, Sigma, USA) diluted with PBS for 10 min, washed with PBS for 10 min, and mounted on slides with Fluoromount-G medium (S2100, Solarbio, China). TUNEL assays were carried out using an *In Situ* Cell Death Detection Kit (Roche Diagnostics, 11684795910, Switzerland) according to the manufacturer's instructions. Immunofluorescence images were taken using an SP8 microscope (Leica, Germany).

mRNA levels of proteasome subunits

The mRNA levels of proteasome subunits in the mouse reproductive system were retrieved using the Gameteomics database (http://gametesomics.cn/#/) (Li et al., 2024). In brief, each target gene was searched on the website, and expression levels in mouse sperm were recorded. The data collected were then plotted using GraphPad Prism v.8.0.

Reverse transcription-quantitative real-time polymerase chain reaction (RT-qPCR) analysis

Total RNA was isolated from testes using a FastPure Cell/Tissue Total RNA Isolation Kit V2 (RC112-01, Vazyme, China). Subsequently, RNA was reverse transcribed into cDNA using PrimeScript RT Master Mix (RR036A, Takara, Japan) according to the manufacturer's instructions. qPCR was then performed using Universal SYBR qPCR Master Mix (Q711-02, Vazyme, China) on the QuantStudio 6 Real-Time PCR Detection System (Thermo Fisher, USA).

Separation of germ cells

Separation of germ cells was performed using a modified STA-PUT method, as previously described (Bryant et al., 2013). During sedimentation, 20 μmol/L MG132 (HY-13259, MCE, USA) was added to the gradient buffer for 3 h of treatment.

Statistical analysis

All data are presented as means±standard error of the mean (SEM). Statistical significance between group means was determined using Student's *t*-tests with paired two-tailed distribution. Results were considered significant at $P<0.05$ (*), 0.01 (**), and 0.001 (***).

RESULTS

PSMA1 and PSMD2 are highly expressed during spermatogenesis in mice

To elucidate the role of the proteasome in spermatogenesis, we characterized the expression profiles of various proteasome components at different stages of spermatogenic development. We first analyzed the mRNA levels of proteasome subunits, including both constitutive and testis-specific proteasome components, such as PSMA8 and PA200, within the mouse reproductive system using the Gameteomics database (Li et al., 2024). The 20S and 19S subunits of the classical proteasome, including PSMA1 and PSMD2, showed higher expression than PSMA8 and PA200 in spermatogonia and early spermatocytes (Supplementary Figure S1A). We further assessed the expression of the 20S component PSMA1 and 19S component PSMD2 at the protein level to validate the dynamics of these proteasomes across the male reproductive system. Analyses revealed consistent expression levels of both PSMA1 and PSMD2 from postnatal day 7 (P7) to adulthood (Supplementary Figure S1B), highlighting their stable presence throughout testis maturation. In contrast, PSMA8 and PSME4 (PA200) expression levels were barely detectable during the first two weeks of life but exhibited a notable upsurge subsequently (Supplementary Figure S1B). This expression pattern corresponds with the developmental timeline of mouse testes, where germ cells progress through a maturation cycle, culminating in the appearance of pachytene spermatocytes by P14 (Bellvé et al., 1977), consistent with previous research (Zhang et al., 2019).

Subsequently, to detect PSMA1 localization in the mouse testis, we first generated *Psma1-EGFP* transgenic mice using the CRISPR/Cas9 system (Figure 1A), then conducted PCR analysis and comprehensive Sanger sequencing to verify accurate insertion of the EGFP sequence (Figure 1B). We extracted and analyzed proteins from various tissues of the

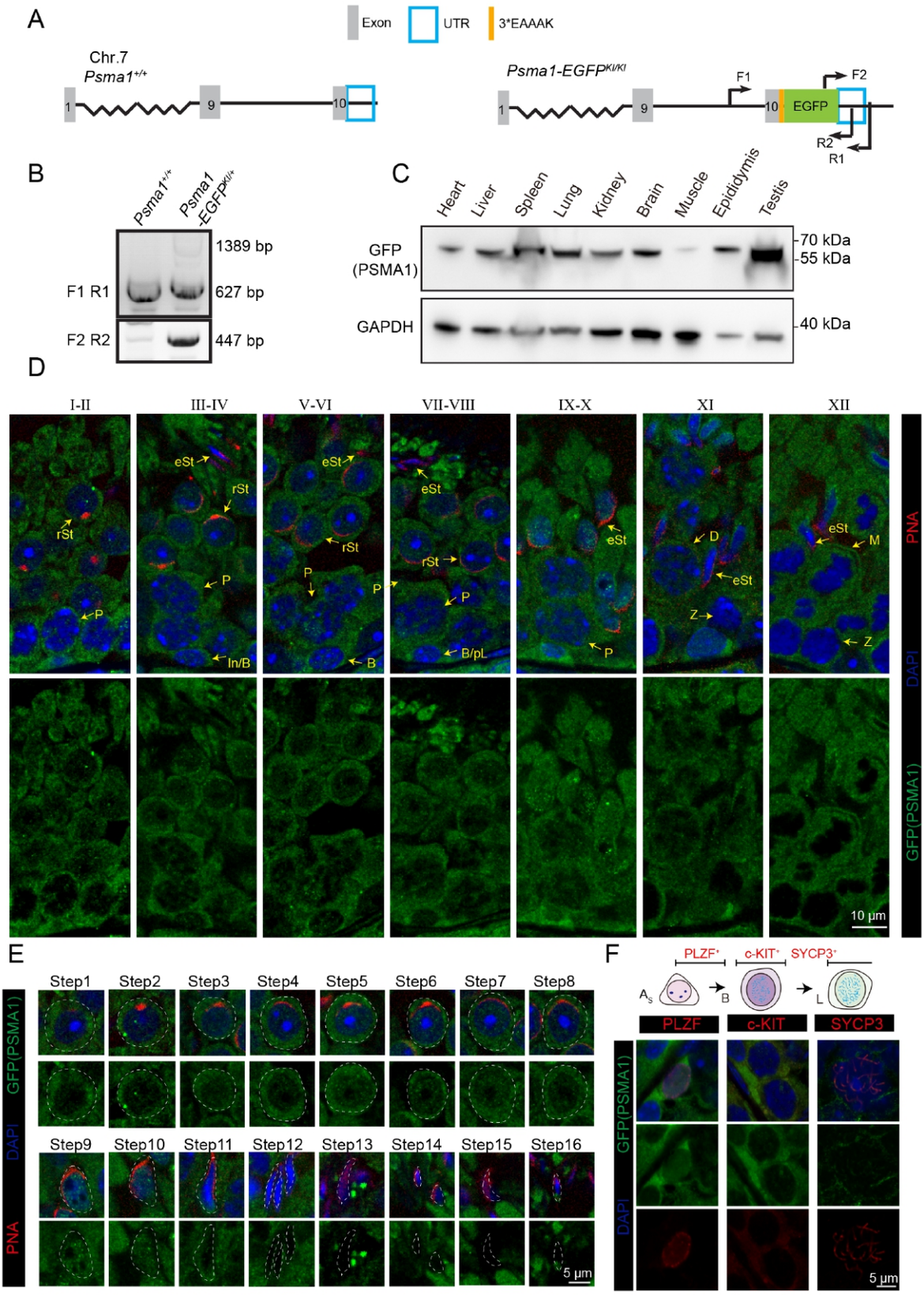


Figure 1 Expression of PSMA1 during spermatogenesis in mice

A: Schematic of construction of *Psma1-EGFP* mice. B: Genotyping of *Psma1-EGFP* mice. C: Expression of PSMA1-EGFP protein in various tissues of adult *Psma1-EGFP* mice, with GAPDH as the loading control. D: Immunofluorescence co-staining for GFP (PSMA1, green) and PNA (red) in *Psma1-EGFP* mouse testis sections. A, A-type spermatogonia; In, Intermediate spermatogonia; B, B-type spermatogonia; pL, Preleptotene spermatocyte; L, Leptotene spermatocyte; Z, Zygotene spermatocyte; P, Pachytene spermatocyte; D, Diplotene spermatocyte; M, Meiotic spermatocyte; rSt, Round spermatid; eSt, Elongating spermatid. E: GFP (green) and PNA (red) staining of spermatids at different steps in *Psma1-EGFP* mice. F: Co-staining of GFP (green) with marker proteins PLZF (red) or SYCP3 (red) in *Psma1-EGFP* mouse testis sections.

Psma1-EGFP transgenic mice. Analysis revealed that the PSMA1-EGFP fusion protein was ubiquitously expressed in all tissues examined, with notably higher levels in the testis, suggesting a potentially increased proteasome requirement during spermatogenesis (Figure 1C).

We further examined PSMA1 localization across different stages of germ cell development. PSMA1 exhibited low nuclear presence in spermatogonia, was strongly localized in spermatocyte nuclei, and was absent in the heads of elongated spermatids (Figure 1D, E). To gain further insights into the expression dynamics of PSMA1 during early spermatogenesis, we performed immunostaining with PLZF and SYCP3, markers for spermatogonia and spermatocytes, respectively (Buaas et al., 2004; Takeo & Hawley, 2012), on testicular sections from *Psma1-EGFP* mice. Results showed that EGFP signals extended from spermatogonia to pachytene spermatocytes, suggesting that PSMA1 plays a role in spermatogenesis in mice (Figure 1F).

To characterize PSMD2 expression during spermatogenesis, we generated *Psmd2-mCherry* transgenic mice via the CRISPR/Cas9 system (Figure 2A) and confirmed successful integration through genomic PCR (Figure 2B). Analysis of PSMD2-mCherry across various tissues showed widespread expression, with pronounced levels in the testes (Figure 2C). To further elucidate the expression profile of PSMD2 during spermatogenesis, lectin peanut agglutinin (PNA) staining was performed to delineate specific stages of spermatogenesis in *Psmd2-mCherry* mouse testes. PSMD2-mCherry was detected in spermatogonia, spermatocytes, and round spermatids (Figure 2D). Further examination of spermatid differentiation indicated that PSMD2-mCherry was present in round spermatids but absent in elongated spermatids (Figure 2E). Using specific germ cell markers, we confirmed precise localization of PSMD2 in spermatogonia and early spermatocytes (Figure 2F). Collectively, these results confirm that both 20S and 19S proteasome components are likely involved in all stages of spermatogenesis.

Both 20S and 19S proteasome components are required for spermatogenesis

To explore the roles of the 20S and 19S components in male fertility and spermatogenesis, we generated germ cell-specific knockout alleles of *Psma1* and *Psmd2* (Figure 3A, C). *Psma1*$^{Flox/Flox}$ (*Psma1*$^{F/F}$) mice, in which exons 5–7 are flanked by loxP sites, were crossed with *Stra8-Cre* transgenic mice, where Cre recombinase expression is driven by the *Stra8* promoter and initiates in A type spermatogonia (Figure 3A, B) (Sadate-Ngatchou et al., 2008). Similarly, *Psmd2*$^{Flox/Flox}$ (*Psmd2*$^{F/F}$) mice, with loxP sites flanking exons 4–8, were crossed with *Stra8-GFPCre* mice (Figure 3C, D). Hereafter, the germ cell-specific knockout mice for *Psma1* or *Psmd2* will be referred to as *Psma1 cKO* or *Psmd2 cKO* mice, respectively.

To assess *Psma1* knockout efficiency, total protein was extracted from the *Psma1*$^{F/F}$ and *Psma1 cKO* mouse testes for immunoblotting with the PSMA1 antibody. Results showed a marked reduction in PSMA1 protein levels in *Psma1 cKO* testes compared to *Psma1*$^{F/F}$ testes, with residual PSMA1 protein signals in *Psma1 cKO* testes likely reflecting non-germ cell expression within the testes (Figure 3E). At 2 months of age, *Psma1 cKO* males exhibited significantly smaller testes compared to *Psma1*$^{F/F}$ males (Figure 3F), with both absolute testis weight and the testis-to-body weight ratio showing marked reductions (Figure 3G, H). Analysis of spermatozoa retrieved from the cauda epididymis demonstrated a substantial decline in sperm count in *Psma1 cKO* mice relative to *Psma1*$^{F/F}$ mice (Figure 3I). Histological examination with H&E staining showed severe disruption of seminiferous tubule structure in *Psma1 cKO* mice, with extensive cellular loss and absence of mature sperm in the epididymis (Figure 3J). These findings underscore the essential role of the 20S proteasome in spermatogenesis.

Similarly, PSMD2 protein expression was significantly reduced in the testes of *Psmd2 cKO* mice compared to *Psmd2*$^{F/F}$ mice (Figure 3K), accompanied by significantly smaller and lighter testes (Figure 3L–N). Additionally, a substantial decrease in total spermatozoa number was observed in the cauda epididymis of *Psmd2 cKO* mice (Figure 3O). Histological analysis with H&E staining revealed disrupted architecture in the seminiferous tubules of *Psmd2 cKO* mice, with pronounced vacuolation of the seminiferous epithelium. Furthermore, spermatocytes and spermatids were completely absent from the central regions of the seminiferous tubules in *Psmd2 cKO* mice, and no spermatozoa were detected in the cauda epididymis (Figure 3P). These findings reveal that the knockout of either the 20S or 19S proteasome component profoundly impairs spermatogenesis.

Proteasome depletion of 20S or 19S components leads to absence of meiotic cells during spermatogenesis

To determine the stages of spermatogenesis impacted by *Psma1* or *Psmd2* knockout, PAS-hematoxylin staining was performed on testis sections from *Psma1 cKO* and *Psmd2 cKO* mice. Analysis revealed a striking absence of cells across all stages of testicular development in both *Psma1 cKO* and *Psmd2 cKO* mice, with only a vestige of spermatogonia persisting (Figure 4A, B). Immunostaining for the germ cell marker DDX4 showed sparse and disorganized germ cell clusters restricted to the basement of seminiferous tubules in *Psma1 cKO* and *Psmd2 cKO* mice at 2 months of age (Figure 4C, D). To further identify the remaining germ cell populations in *Psma1 cKO* and *Psmd2 cKO* mouse testes, co-staining with PLZF (marker of undifferentiated spermatogonia) (Buaas et al., 2004) and SOX9 (marker of Sertoli cells) was performed (Kent et al., 1996). Quantitative analysis showed that PLZF$^+$ and SOX9$^+$ cell populations were comparable between *Psma1*$^{F/F}$ and *Psma1 cKO* mice, as well as between *Psmd2*$^{F/F}$ and *Psmd2 cKO* mice (Figure 4E–J). However, SYCP3 staining, marking prophase I spermatocytes (Page & Hawley, 2004), revealed a complete absence of SYCP3$^+$ germ cells in *Psma1 cKO* and *Psmd2 cKO* mice (Figure 4I–J). These results indicate that loss of PSMA1 or PSMD2 causes severe defects in spermatogenesis, with an absence of spermatocytes.

Depletion of PSMA1 or PSMD2 disrupts meiotic initiation

The absence of spermatocytes in the seminiferous tubules of 2-month-old *Psma1 cKO* and *Psmd2 cKO* mice suggested a defect in the mitosis-to-meiosis transition. The first wave of spermatogenesis progresses synchronously (Griswold, 2016), with spermatogonia exiting mitosis at P10, followed by the appearance of leptotene and zygotene spermatocytes at P12 and pachytene spermatocytes at P14 (Ahmed & De Rooij, 2009; Bellvé et al., 1977; Roosen-Runge, 1962). To determine the stages of spermatogenesis affected by *Psma1* or *Psmd2* knockout, we examined testicular morphology at P10, P12,

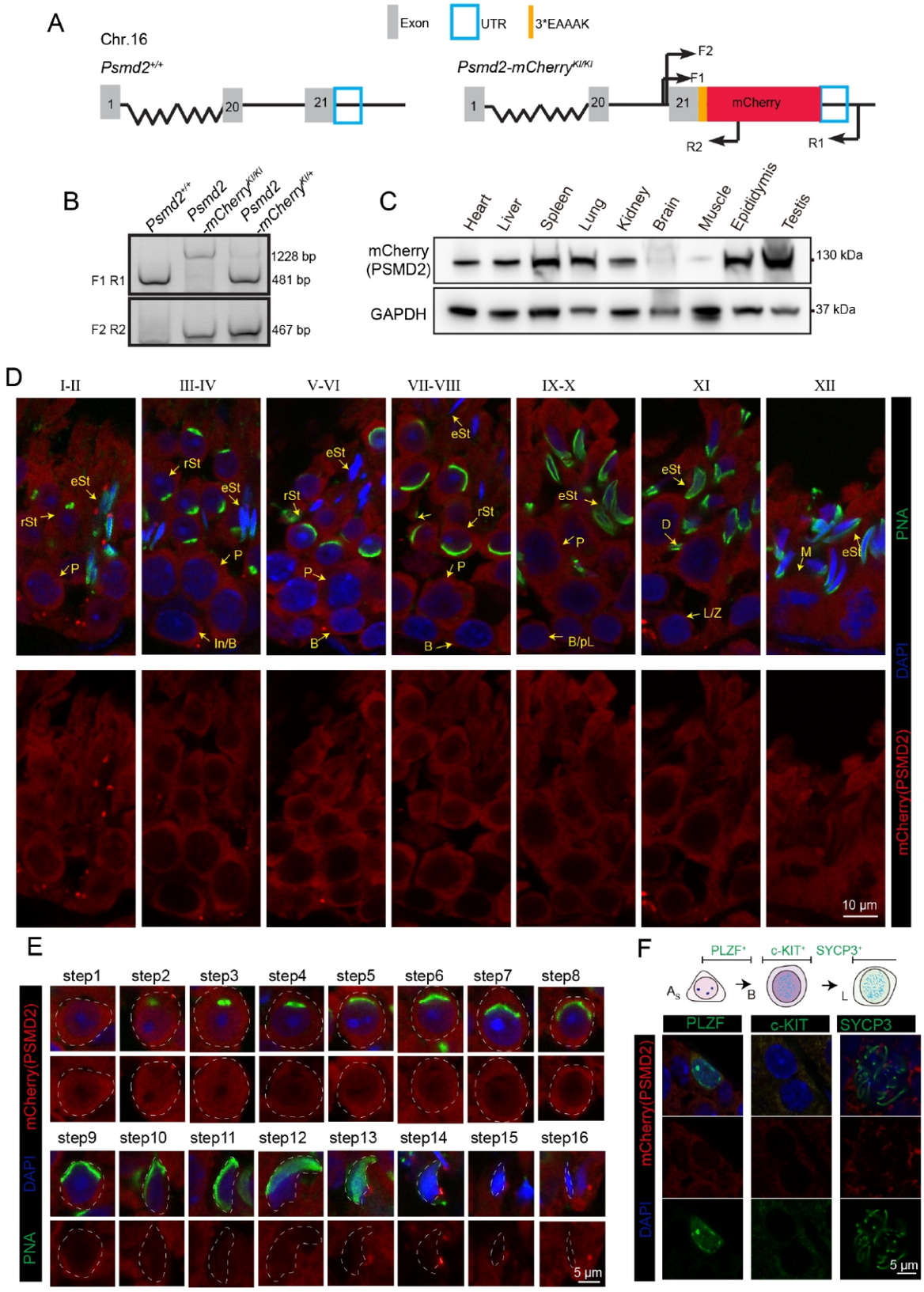


Figure 2 PSMD2 expression during spermatogenesis

A: Schematic of construction of *Psmd2-mCherry* mice. B: Genotyping of *Psmd2-mCherry* mice. C: Expression of PSMD2-mCherry protein in various tissues of adult *Psmd2-mCherry* mice, with GAPDH as the loading control. D: Immunofluorescence co-staining for mCherry (PSMD2, red) and PNA (green) in *Psmd2-mCherry* mouse testis sections. A, A-type spermatogonia; In, Intermediate spermatogonia; B, B-type spermatogonia; pL, Preleptotene spermatocyte; L, Leptotene spermatocyte; Z, Zygotene spermatocyte; P, Pachytene spermatocyte; D, Diplotene spermatocyte; M, Meiotic spermatocyte; rSt, Round spermatid; eSt, Elongating spermatid. E: mCherry (red) and PNA (green) staining of spermatids at different steps in *Psmd2-mCherry* mice. F: Co-staining of mCherry (red) with PLZF (green) or SYCP3 (green) in *Psmd2-mCherry* mouse testis sections.

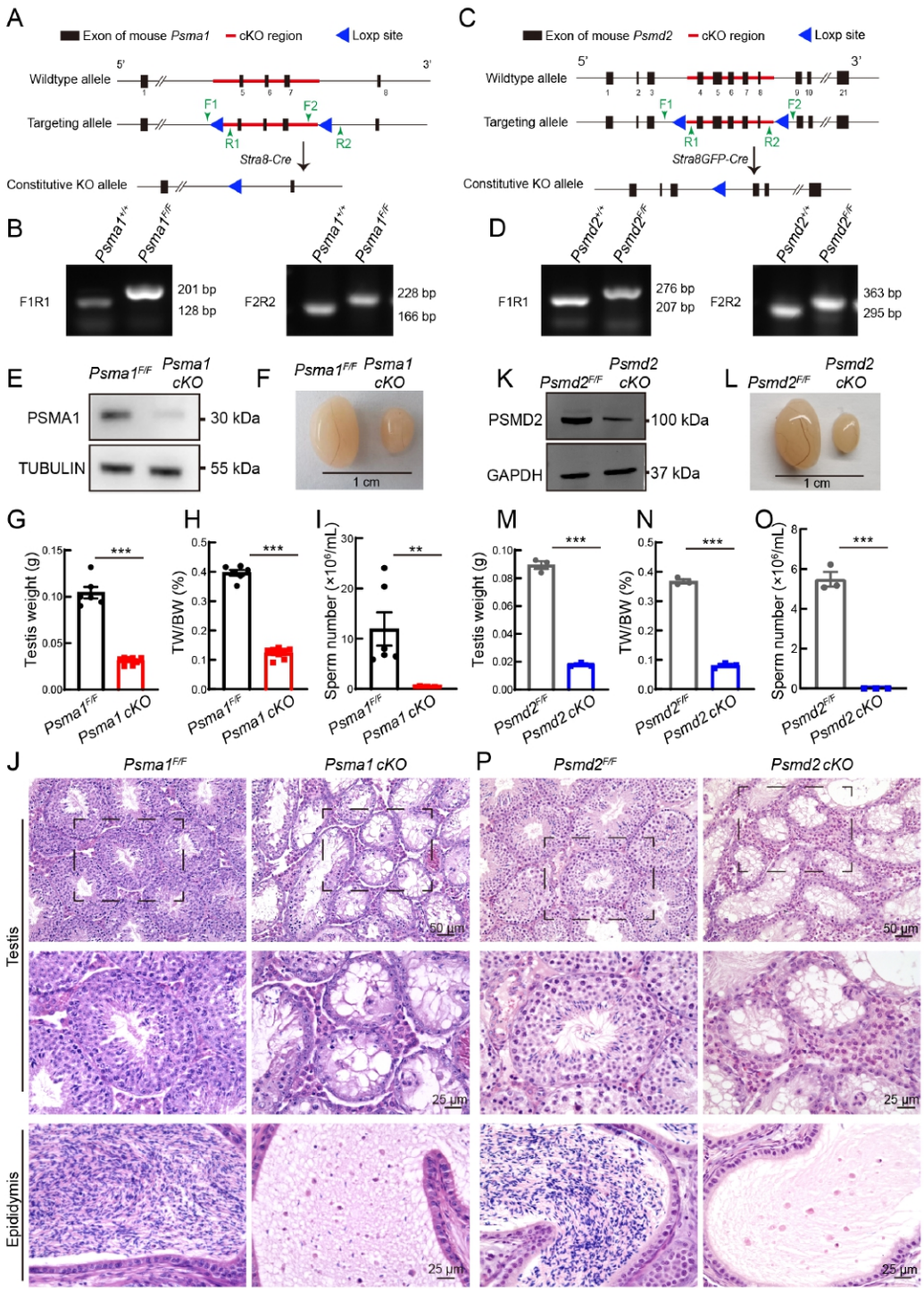


Figure 3 Depletion of 20S and 19S proteasome components in germ cells impairs spermatogenesis in adult male mice

A: Schematic of construction of germ cell-specific knockout *Psma1* mice. B: Genotyping of *Psma1*$^{F/F}$ mice. C: Schematic of construction of germ cell-specific knockout *Psmd2* mice. D: Genotyping of *Psmd2*$^{F/F}$ mice. E: Immunoblotting of PSMA1 in *Psma1*$^{F/F}$ and *Psma1 cKO* testes. TUBULIN was used as the loading control. F: Testes were smaller in *Psma1 cKO* mice compared to *Psma1*$^{F/F}$ mice. G, H: *Psma1*$^{F/F}$ and *Psma1 cKO* mouse testis weight (G) and testis-to-body weight ratio (TW/BW) (H) (*n*=6 independent experiments). I: Sperm counts from cauda epididymis were significantly lower in *Psma1 cKO* mice compared to *Psma1*$^{F/F}$ mice (*n*=6 independent experiments). J: Histological analysis of seminiferous tubules and cauda epididymis of *Psma1*$^{F/F}$ and *Psma1 cKO* mice by hematoxylin and eosin staining. K: Immunoblotting of PSMD2 was performed in *Psmd2*$^{F/F}$ and *Psmd2 cKO* testes. TUBULIN was used as the loading control. L: Testes were smaller in *Psmd2 cKO* mice than in *Psmd2*$^{F/F}$ mice. M, N: *Psmd2*$^{F/F}$ and *Psmd2 cKO* mouse testis weight (M) and testis-to-body weight ratio (N) (*n*=3 independent experiments). O: Sperm counts from cauda epididymis were significantly lower in *Psmd2 cKO* mice compared to *Psmd2*$^{F/F}$ mice (*n*=3 independent experiments). P: Histological analysis of seminiferous tubules and cauda epididymis of *Psmd2*$^{F/F}$ and *Psmd2 cKO* mice by hematoxylin and eosin staining. Black dots represent *Psma1*$^{F/F}$ mice, red dots represent *Psma1 cKO* mice, gray dots represent *Psmd2*$^{F/F}$ mice, and blue dots represent *Psmd2 cKO* mice. Data are mean±SEM, **: *P*<0.01; ***: *P*<0.001.

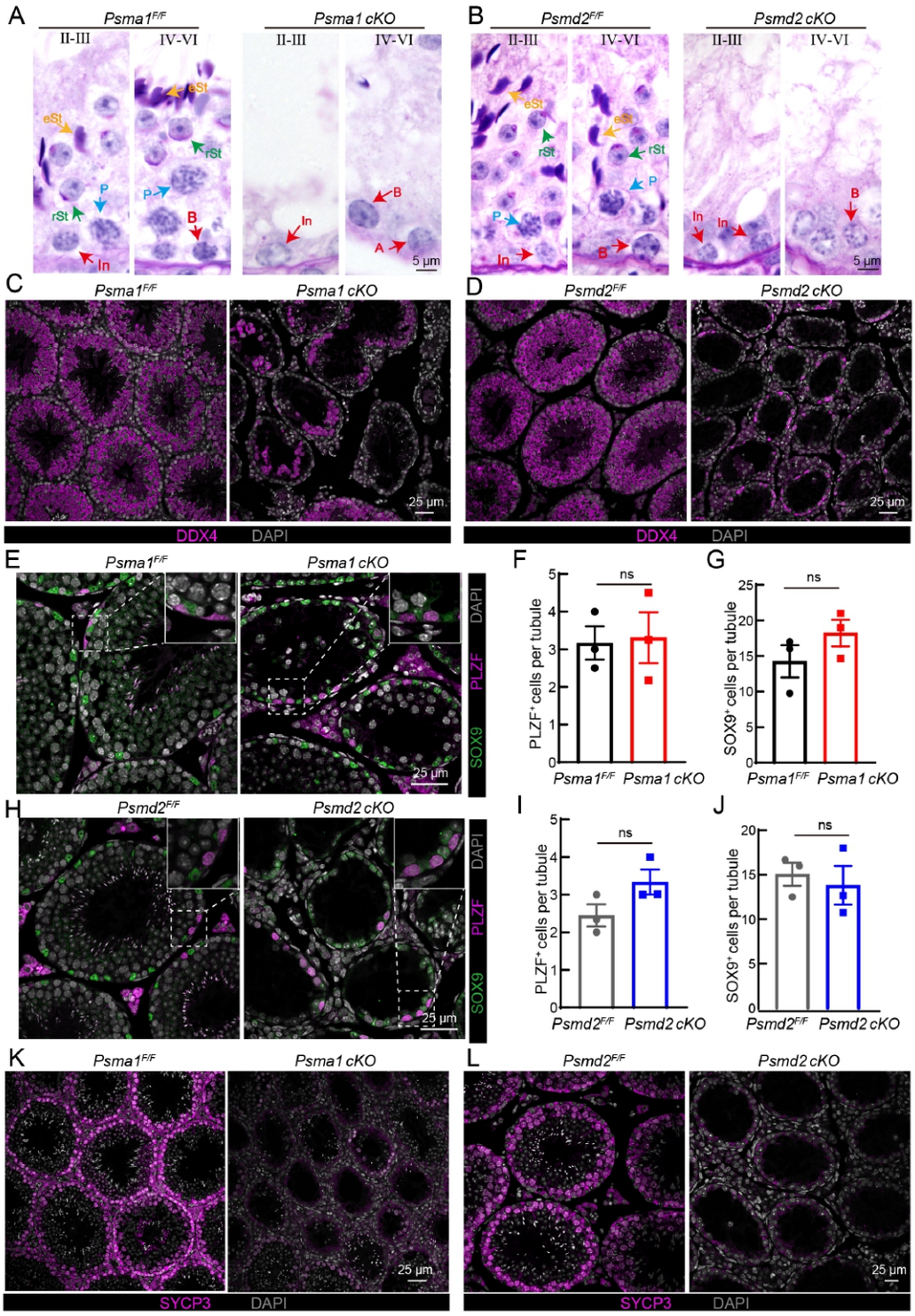


Figure 4 Loss of meiotic cells in *Psma1 cKO* and *Psmd2 cKO* testes

A, B: PAS-hematoxylin staining of seminiferous tubules in *Psma1*$^{F/F}$ and *Psma1 cKO* mice (A) and in *Psmd2*$^{F/F}$ and *Psmd2 cKO* mice (B). A, A-type spermatogonia; In, Intermediate spermatogonia; B, B-type spermatogonia; P, Pachytene spermatocyte; rSt, Round spermatid; eSt, Elongating spermatid. C, D: Immunofluorescence staining for DDX4 (magenta) in 2-month-old *Psma1*$^{F/F}$ and *Psma1 cKO* testes (C) and *Psmd2*$^{F/F}$ and *Psmd2 cKO* testes (D). E, H: Co-staining for PLZF (magenta) and SOX9 (green) in 2-month-old *Psma1*$^{F/F}$ and *Psma1 cKO* testes (E) and *Psmd2*$^{F/F}$ and *Psmd2 cKO* testes (H). F: Count of PLZF-positive cells in seminiferous tubules of 2-month-old *Psma1*$^{F/F}$ and *Psma1 cKO* testes (*n*=3 independent experiments). G: Count of SOX9-positive cells in seminiferous tubules of 2-month-old *Psma1*$^{F/F}$ and *Psma1 cKO* testes (*n*=3 independent experiments). I: Count of PLZF-positive cells in seminiferous tubules of 2-month-old *Psmd2*$^{F/F}$ and *Psmd2 cKO* testes (*n*=3 independent experiments). J: Count of SOX9-positive cells in seminiferous tubules of 2-month-old mouse *Psmd2*$^{F/F}$ and *Psmd2 cKO* testes (*n*=3 independent experiments). K, L: Immunofluorescence staining of SYCP3 (magenta) in 2-month-old *Psma1*$^{F/F}$, *Psma1 Cko* (K), *Psmd2*$^{F/F}$, and *Psmd2 cKO* (L) testes. Black dots represent *Psma1*$^{F/F}$ mice, red dots represent *Psma1 cKO* mice, gray dots represent *Psmd2*$^{F/F}$ mice, and blue dots represent *Psmd2 cKO* mice. Data are mean±SEM, ns: Not significant.

and P14. Results showed that testicular size in *Psma1 cKO* mice remained relatively unchanged at P10 but exhibited a reduction at P12 compared to the controls (Supplementary Figure S2A, B). Similarly, *Psmd2 cKO* mice showed no testicular size reduction at P10 but a pronounced decrease from P12 to P14 (Supplementary Figure S2C, D). Histological H&E staining of testicular sections from P10, P12, and P14 revealed the presence of type A spermatogonia (A), intermediate spermatogonia (In), and type B spermatogonia (B) in both control and cKO testes. At P12, some germ cells in control testes had entered meiosis, developing into leptotene and zygotene spermatocytes, with pachytene spermatocytes becoming apparent at P14. In contrast, spermatocytes were conspicuously scarce in the seminiferous tubules of *Psma1 cKO* and *Psmd2 cKO* mice at P12 and P14 (Supplementary Figure S2E, F). These observations suggest that the loss of the 20S or 19S proteasome components critically disrupts the initiation of meiosis during spermatogenesis.

Spermatogonia undergo multiple rounds of proliferation and differentiation to form spermatocytes with the capacity for meiosis (Song & Wilkinson, 2014). To assess whether spermatogonia were affected in *Psma1 cKO* and *Psmd2 cKO* mice, we analyzed undifferentiated and differentiated spermatogonia markers (PLZF and c-KIT, respectively) in P10 testes. Immunostaining analysis revealed that the numbers of PLZF-positive and c-KIT-positive cells in *Psma1 cKO* and *Psmd2 cKO* mice were comparable to those in control mice (Figure 5A–H), suggesting normal development of spermatogonia in these knockout models.

We further investigated proliferative activity in germ cells by analyzing the proliferation marker Ki67 alongside DDX4. A slight reduction in $Ki67^{+}DDX4^{+}$ cells was detected in both P10 and P12 testes (Supplementary Figure S3A–D). Co-staining of Ki67 and PLZF in P10 *Psma1 cKO* and *Psmd2 cKO* testes showed no significant difference in the number of $Ki67^{+}PLZF^{+}$ spermatogonia compared to the controls (Supplementary Figure S3E–G). Considering that Ki67 expression may also be present in spermatocytes (Traut et al., 2002), we performed Ki67 and SYCP3 co-staining in P10 testes and found that some $SYCP3^{+}$ cells also expressed Ki67 (Supplementary Figure S3I, J). Given the marked reduction of $SYCP3^{+}$ cells in *Psma1* and *Psmd2 cKO* testes (Figure 4I, J), the observed decrease in $Ki67^{+}$ germ cells may be attributable to meiotic initiation defects in *Psma1* and *Psmd2 cKO* mice.

To further explore meiotic progression, we performed co-staining for SYCP3 and γH2AX, a marker of double-strand DNA breaks (DSBs), in P10 and P12 testes. Immunofluorescence analysis indicated a significant reduction in γH2AX-positive germ cells, with approximately 60% observed in *Psma1 cKO* and 40% in *Psmd2 cKO* P10 testes compared to controls. By P12, SYCP3-positive cells were nearly undetectable in the seminiferous tubules of both *Psma1 cKO* and *Psmd2 cKO* mice (Figure 5I–L).

Further histological examination of P10 *Psma1 cKO* and *Psmd2 cKO* testes using H&E staining revealed degenerated cells with condensed nuclei, suggestive of apoptosis (Supplementary Figure S4A, B). To confirm these findings, we employed cleaved-caspase 3 immunofluorescence on testes from $Psma1^{F/F}$, *Psma1 cKO*, $Psmd2^{F/F}$, and *Psmd2 cKO* mice at P10. Results indicated a substantial increase in apoptotic cells in both *Psma1* and *Psmd2 cKO* testes relative to the controls (Supplementary Figure S4C–F). Additionally, TUNEL staining at P10 and P12 corroborated the elevated apoptosis levels in *Psma1* and *Psmd2 cKO* testes compared to control groups (Supplementary Figure S4G, H). Given that spermatogonia development appeared normal in *Psma1 cKO* and *Psmd2 cKO* mice, this increase in degenerated cells may be due to defects in meiotic initiation. In summary, knockout of either *Psma1* or *Psmd2* impairs the normal initiation of meiosis, highlighting the essential roles of these proteasome components in meiotic entry.

Psma1 and _Psmd2_ knockout leads to abnormal expression of meiotic initiation factors

The mitosis-to-meiosis transition during spermatogenesis is orchestrated by a series of tightly regulated changes in proteins and transcription factor expression (Kimble, 2011; Qian et al., 2022; Sun et al., 2022; Zhang & Zarkower, 2017). DMRT1, a key regulator in this transition, is expressed in mitotic spermatogonia, where it suppresses the expression of STRA8, thereby blocking premature meiotic initiation (Ishiguro, 2023; Zhang & Zarkower, 2017). DMRT1 has been thoroughly demonstrated to be ubiquitinated by the SCFβ-TrCP E3 ligase complex, subsequently identified and degraded by the proteasome (Lei et al., 2007; Matson et al., 2010; Nakagawa et al., 2017; Zarkower, 2013; Zhang et al., 2016; Zhang & Zarkower, 2017), which enables the transition from mitosis to meiosis by removing its inhibitory effect on meiotic entry. As proteasomes are responsible for the degradation of ubiquitin-conjugated substrates (Sadowski et al., 2012), to investigate the impact of proteasomal disruption on this process, DMRT1 expression was analyzed in the testes of *Psma1 cKO* and *Psmd2 cKO* mice.

We initially investigated DMRT1 expression in the testes of P8 mice using western blotting and immunofluorescence co-staining with the spermatogonial marker PLZF. In *Psma1 cKO* mice, DMRT1 expression levels in P8 testes were comparable to those in wild-type controls (Supplementary Figure S5A–C). Although PSMA1 protein levels were reduced in P8 testes, this reduction was not statistically significant, likely due to insufficient time for complete PSMA1 degradation following CRE expression. Consequently, no differences in DMRT1 and STRA8 protein levels were observed between $Psma1^{F/F}$ and *Psma1 cKO* mice at this stage (Supplementary Figure S5A–C). By P10, however, immunofluorescence staining revealed a marked increase in DMRT1 signals in *Psma1 cKO* testes compared to the controls (Figure 6A). This accumulation of DMRT1 likely inhibited meiotic initiation by suppressing *Stra8* expression, as indicated by the significant reduction in STRA8 signals in P10 *Psma1 cKO* testes (Figure 6B). Protein quantification corroborated both the accumulation of DMRT1 and decrease in STRA8 (Figure 6C, D). To confirm that this accumulation resulted from impaired protein degradation rather than increased transcription, RT-qPCR analysis was performed and showed no significant changes in DMRT1 transcription in *Psma1 cKO* P10 testes (Figure 6E), indicating that DMRT1 accumulation stemmed from abnormal protein degradation. Parallel analyses in $Psmd2^{F/F}$ and *Psmd2 cKO* mice yielded consistent results, with no differences in DMRT1 and STRA8 expression at P8 (Supplementary Figure S5D–F) but notable DMRT1 accumulation and decreased STRA8 expression in P10 *Psmd2 cKO* testes (Figure 6F–I). Furthermore, RT-qPCR analysis indicated that there were no significant changes in transcription levels of DMRT1 in *Psmd2 cKO* P10 testes (Figure 6E). Thus, depletion of PSMA1 and PSMD2 led to DMRT1 accumulation and the near absence of STRA8 in the testes at a critical developmental stage. Additionally, *in vitro*

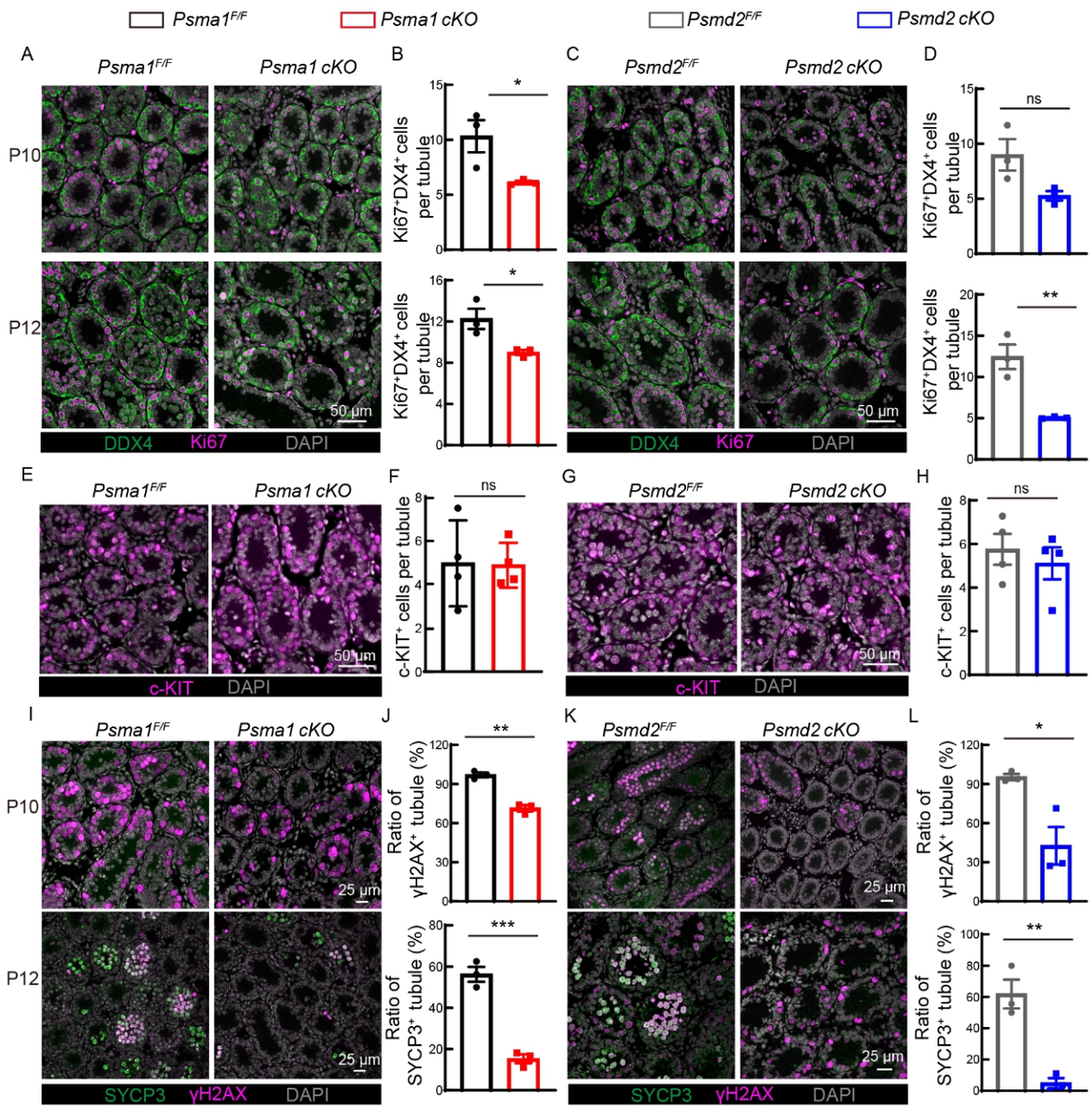


Figure 5 *Psma1* or *Psmd2* knockout leads to defects in meiotic initiation

A, C: Immunofluorescence staining for PLZF (magenta) in *Psma1*$^{F/F}$ and *Psma1 cKO* testes (A) and *Psmd2*$^{F/F}$ and *Psmd2 cKO* testes (C) at P10. B, D: PLZF-positive cells per tubule cross-section of *Psma1*$^{F/F}$ and *Psma1 cKO* testes (B) and *Psmd2*$^{F/F}$ and *Psmd2 cKO* testes (D) (*n*=3 independent experiments). E, G: Immunofluorescence staining for c-KIT (magenta) in *Psma1*$^{F/F}$ and *Psma1 cKO* testes (E) and *Psmd2*$^{F/F}$ and *Psmd2 cKO* testes (G) at P10. F, H: c-KIT-positive cells per tubule cross-section of *Psma1*$^{F/F}$ and *Psma1 cKO* testes (F) and *Psmd2*$^{F/F}$ and *Psmd2 cKO* testes (H) (*n*=5 independent experiments). I, K: Co-immunofluorescence staining for SYCP3 (green) and γH2AX (magenta) in *Psma1*$^{F/F}$ and *Psma1 cKO* testes (I) and *Psmd2*$^{F/F}$ and *Psmd2 cKO* testes (K) at P10 and P12. J: Ratio of γH2AX$^+$ tubule cross-sections in *Psma1*$^{F/F}$ and *Psma1 cKO* testes at P10 (above). Ratio of SYCP3$^+$ tubule cross-sections in *Psma1*$^{F/F}$ and *Psma1 cKO* testes at P12 (bottom) (*n*=3 independent experiments). L: Ratio of γH2AX$^+$ tubule cross-sections in *Psmd2*$^{F/F}$ and *Psmd2 cKO* testes at P10 (above). Ratio of SYCP3$^+$ tubule cross-sections in *Psmd2*$^{F/F}$ and *Psmd2 cKO* testes at P12 (bottom). Black dots represent *Psma1*$^{F/F}$ mice, red dots represent *Psma1 cKO* mice, gray dots represent *Psmd2*$^{F/F}$ mice, and blue dots represent *Psmd2 cKO* mice. Data are mean±SEM, ns: Not significant, *: P<0.05; **: P<0.01; ***: P<0.001.

inhibition of proteasome activity with 20 μmol/L MG132 led to DMRT1 accumulation in germ cells (Figure 6K–L), supporting a link between proteasome dysfunction and increased DMRT1 levels.

In summary, these findings highlight the essential role of the proteasome in regulating key factors that govern the transition into meiosis during spermatogenesis. Disruption of proteasome components, such as PSMA1 and PSMD2, results in the accumulation of DMRT1 and significant inhibition of STRA8 expression, ultimately impairing meiotic initiation.

DISCUSSION

In male germ cells, the stability of proteins is rigorously regulated by the ubiquitin proteasome system (UPS)

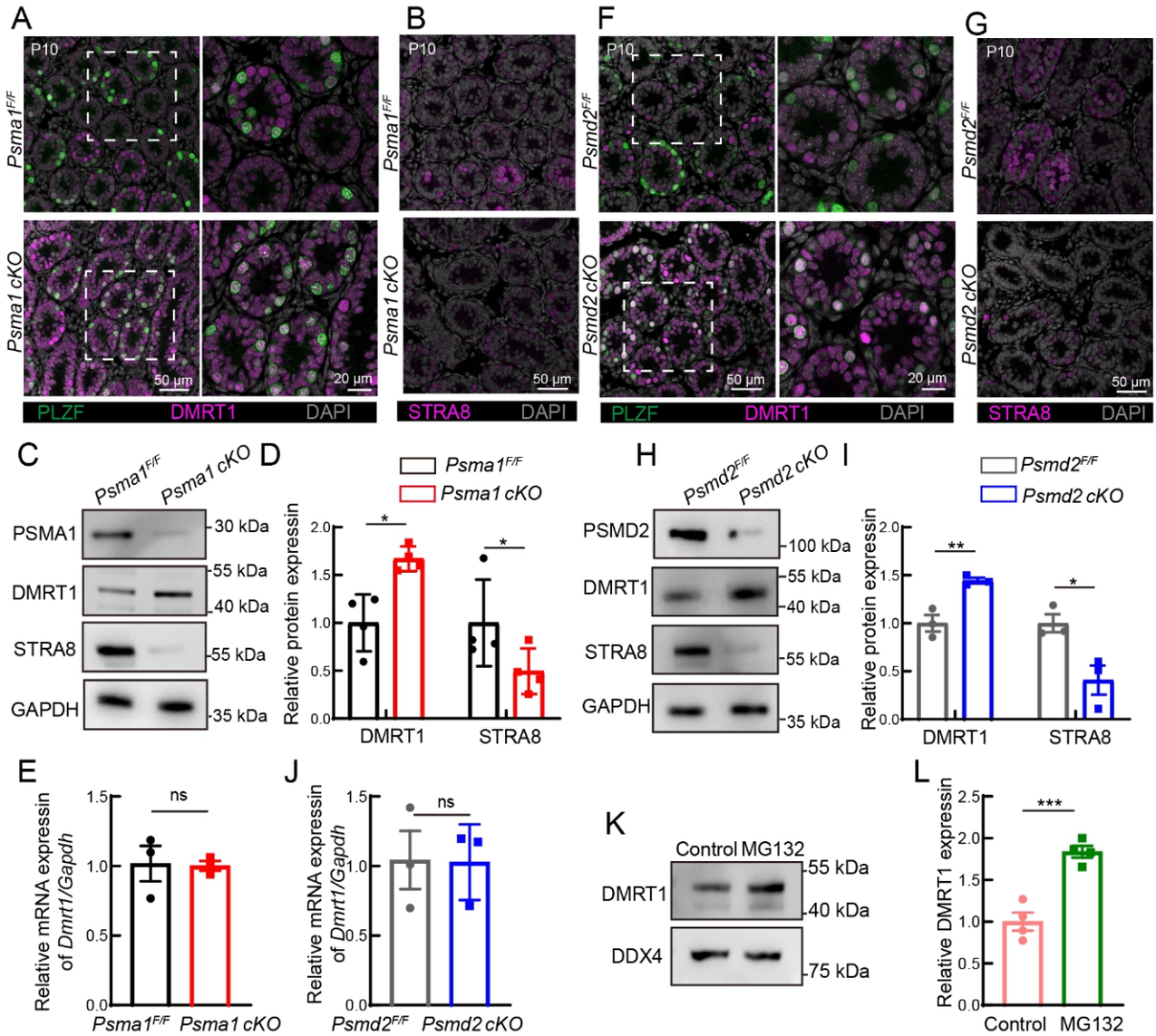


Figure 6 Knockout of *Psma1* or *Psmd2* in germ cells leads to DMRT1 accumulation

A: Immunofluorescence staining for DMRT1 (magenta) and PLZF (green) in *Psma1*$^{F/F}$ and *Psma1 cKO* testes at P10. B: Immunofluorescence staining for STRA8 (magenta) in *Psma1*$^{F/F}$ and *Psma1 cKO* testes at P10. C: Immunoblotting of PSMA1, DMRT1, and STRA8 in P10 *Psma1*$^{F/F}$ and *Psma1 cKO* testes. D: Quantification of STRA8 and DMRT1 protein levels in (C) (n=4 independent experiments). E: mRNA levels of DMRT1 in *Psma1*$^{F/F}$ and *Psma1 cKO* testes at P10 (n=3 independent experiments). F: Immunofluorescence staining for DMRT1 (magenta) and PLZF (green) in *Psmd2*$^{F/F}$ and *Psmd2 cKO* testes at P10. G: Immunofluorescence staining for STRA8 (magenta) in *Psmd2*$^{F/F}$ and *Psmd2 cKO* testes at P10. H: Immunoblotting of PSMD2, DMRT1, and STRA8 in P10 *Psmd2*$^{F/F}$ and *Psmd2 cKO* testes. I: Quantification of STRA8 and DMRT1 protein levels in (H) (n=3 independent experiments). J: mRNA levels of DMRT1 in *Psmd2*$^{F/F}$ and *Psmd2 cKO* testes at P10 (n=3 independent experiments). K: Immunoblotting of DMRT1 in P8–P10 testis germ cells treated with MG132. L: Quantification of DMRT1/GAPDH protein levels in (K) (n=3 independent experiments). Black dots represent *Psma1*$^{F/F}$ mice, red dots represent *Psma1 cKO* mice, gray dots represent *Psmd2*$^{F/F}$ mice, and blue dots represent *Psmd2 cKO* mice. Data are mean±SEM, ns: Not significant, *: P<0.05; **: P<0.01; ***: P<0.001.

(Anderson et al., 2008; Lu et al., 2010; Suzuki & Saga, 2008; Wang et al., 2006), which includes the ubiquitination and subsequent degradation and deubiquitination of substrates for recycling (Abi Habib et al., 2022). During spermatogenesis, the proteasome can degrade both ubiquitin-conjugated and non-conjugated substrates (Sadowski et al., 2012). Previous mass spectrometry analyses have illuminated the complexity of proteasome composition in developing male germ cells, revealing dynamic changes in proteasome structure throughout spermatogenesis, such as the increase in 20S proteasomes in mature sperm, replacement of α4 by α4s in spermatocytes, and assembly of PA200-20S proteasomes in spermatocytes and spermatid cells. Moreover, in the testes, the 19S RP primarily associates with PSMA8, while PA200 exhibits higher or similar affinity for PSMA7 (Živković et al., 2022). These findings demonstrate that different proteasome species contribute to protein homeostasis, functioning either concurrently or at specific stages of spermatogenesis (Li et al., 2010; Živković et al., 2022).

Testis-specific proteasome isoforms are essential for successful spermatogenesis. PSMA8, for example, plays a crucial role in DNA repair and meiotic division during spermatogenesis in mice, with its knockout leading to arrest at the meiotic M phase in spermatocytes (Gómez-H et al., 2019;

Zhang et al., 2019, 2021). PA200 is implicated in later spermiogenesis processes, such as histone replacement and mitochondrial sheath formation (Khor et al., 2006; Qian et al., 2013; Sato et al., 2023). In contrast, approximately 98% of CPs in spermatogonia and preleptotene spermatocytes consist of the classical 20S complex (Živković et al., 2022), suggesting a potential role of this proteasome type in early meiosis. Our findings indicated that the classical 20S and 19S proteasomes were predominant in early spermatogonia and preleptotene spermatocytes, suggesting that 26S proteasomes are primarily responsible for protein hydrolysis during early spermatogenesis. Depletion of PSMA1 and PSMD2 components led to the loss of spermatocytes, resulting in male infertility in mice. To address the specific developmental stage impacted by *Psma1* and *Psmd2* knockout in germ cells, we analyzed testicular morphology and seminiferous tubule structure in young mice. At P10, a critical period when germ cells are preparing for meiosis, there were no observable differences in testicular morphology between knockout and control mice. However, at P12, there was a marked reduction in spermatocyte signals in both *Psma1 cKO* and *Psmd2 cKO* mice, indicating a blockade of meiosis onset. Furthermore, the reduction in proliferative signals in germ cells at P10 and P12 in both knockout models suggests that different proteasome components may have additional, currently unidentified functions in spermatogenesis. PSMA1 and PSMD2, integral components of the 20S and 19S proteasome complexes, are reported to function independently in various cellular contexts. The 20S proteasome is more efficient at degrading proteins with disordered internal regions (Asher et al., 2006; Liu et al., 2003) and proteins damaged by oxidative stress (Abi Habib et al., 2020). In contrast, 19S has demonstrated functions outside its association with the proteasome core (Farrell et al., 2024; Sun et al., 2023). Additionally, proteasomes associated with RPs such as PA28αβ, PA28γ, and PA200 are capable of adenosine triphosphate (ATP)- and ubiquitin-independent protein degradation (Pickering & Davies, 2012). Consequently, the 19S and 20S proteasome complexes may have distinct functions during spermatogenesis. Moreover, the use of *Stra8-cre* transgenic mice, where Cre recombinase expression is driven by the *Stra8* promoter and activated in A type spermatogonia, may introduce slight phenotypic differences between *Psma1 cKO* and *Psmd2 cKO* mice.

Previous studies have demonstrated that DMRT1 is crucial for inhibiting meiosis-related protein expression in spermatogonia, thereby preventing premature meiotic entry (Nakagawa et al., 2017). The initiation of meiosis necessitates the targeted degradation of DMRT1, achieved via its ubiquitination by the SCFβ-TrCP complex. Disruption of *SCFβ-TrCP* prevents DMRT1 degradation, leading to its accumulation and impairing mitosis-to-meiosis transition (Nakagawa et al., 2017; Zhang et al., 2016). Furthermore, DMRT1 inhibits *Stra8* activation through direct transcriptional repression and general inhibition of retinoic acid (RA)-dependent transcriptional activity (Matson et al., 2010). Using *Psma1 cKO* and *Psmd2 cKO* mice, we observed an accumulation of DMRT1 protein in germ cells at P10, which subsequently reduced STRA8 expression compared to controls. This finding is consistent with the known inhibitory role of DMRT1 on STRA8 expression. However, at P8, levels of both DMRT1 and STRA8 remained unchanged. Immunoblotting analysis at this stage revealed that PSMA1 and PSMD2 proteins were still detectable in *Psma1 cKO* and *Psmd2 cKO* testes, suggesting that these proteasome components may exhibit long half-lives. The residual proteasome activity in P8 *Psma1 cKO* and *Psmd2 cKO* testes may be sufficient to mediate DMRT1 degradation.

Based on our findings and existing research, we propose a mechanism by which the proteasome modulates DMRT1 stability during spermatogenesis. As spermatogonia transition from mitosis to meiosis, the ubiquitin ligase SCFβ-TrCP catalyzes the ubiquitination of DMRT1. This post-translational modification targets DMRT1 for recognition by the 19S RP of the proteasome, including subunits such as PSMD2. Following binding, ATP hydrolysis facilitates the removal of polyubiquitin chains and subsequent unfolding of DMRT1, which is then translocated into the 20S CP for proteolytic degradation. The degradation of DMRT1 alleviates its inhibitory effect on *Stra8*, a gene essential for meiotic initiation, leading to the up-regulation of STRA8 expression and progression into meiosis. The successful transition of germ cells from mitosis to meiosis is critical for mammalian reproduction, involving a finely tuned network of proteins. Additionally, other meiosis-inhibitory proteins may also undergo proteasomal degradation in conjunction with DMRT1 as meiosis initiates, suggesting a broader regulatory role for the proteasome in this critical developmental transition. Hence, whether additional meiosis-inhibitory proteins require degradation during the mitosis-to-meiosis transition remains to be explored.

SUPPLEMENTARY DATA

Supplementary data to this article can be found online.

COMPETING INTERESTS

The authors declare that they have no competing interests.

AUTHORS' CONTRIBUTIONS

T.T.H. and L.Y.W.: conceptualization, investigation, data curation, validation, project administration, methodology, formal analysis, and writing-original draft. Y.J.M.: writing-original draft. Q.X.Z., W.W., and Y.H.C.: investigation, methodology, and formal analysis. W.L., C.L., and Z.Y.J.: conceptualization, resources, supervision, funding acquisition, writing—original draft, review, and editing. All authors read and approved the final version of the manuscript.

REFERENCES

Abby E, Tourpin S, Ribeiro J, et al. 2016. Implementation of meiosis prophase I programme requires a conserved retinoid-independent stabilizer of meiotic transcripts. *Nature Communications*, **7**: 10324.

Abi Habib J, De Plaen E, Stroobant V, et al. 2020. Efficiency of the four proteasome subtypes to degrade ubiquitinated or oxidized proteins. *Scientific Reports*, **10**(1): 15765.

Abi Habib J, Lesenfants J, Vigneron N, et al. 2022. Functional differences between proteasome subtypes. *Cells*, **11**(3): 421.

Ahmed EA, De Rooij DG. 2009. Staging of mouse seminiferous tubule cross-sections. *Methods in Molecular Biology*, **558**: 263–277.

Anderson EL, Baltus AE, Roepers-Gajadien HL, et al. 2008. Stra8 and its inducer, retinoic acid, regulate meiotic initiation in both spermatogenesis and oogenesis in mice. *Proceedings of the National Academy of Sciences of the United States of America*, **105**(39): 14976–14980.

Asher G, Reuven N, Shaul Y. 2006. 20S proteasomes and protein degradation "by default". *BioEssays*, **28**(8): 844–849.

Bellvé AR, Cavicchia JC, Millette CF, et al. 1977. Spermatogenic cells of the prepuberal mouse. Isolation and morphological characterization. *The Journal of Cell Biology*, **74**(1): 68–85.

Bryant JM, Meyer-Ficca ML, Dang VM, et al. 2013. Separation of spermatogenic cell types using STA-PUT velocity sedimentation. *Journal of Visualized Experiments*, (80): 50648.

Buaas FW, Kirsh AL, Sharma M, et al. 2004. Plzf is required in adult male germ cells for stem cell self-renewal. *Nature Genetics*, **36**(6): 647–652.

Coux O, Zieba BA, Meiners S. 2020. The proteasome system in health and disease. *Advances in Experimental Medicine and Biology*, **1233**: 55–100.

Farrell K, Auerbach A, Musaus M, et al. 2024. Phosphorylation of RPT6 controls its ability to bind DNA and regulate gene expression in the hippocampus of male rats during memory formation. *Journal of Neuroscience*, **44**(4): e1453232023.

Gómez-H L, Felipe-Medina N, Condezo YB, et al. 2019. The PSMA8 subunit of the spermatoproteasome is essential for proper meiotic exit and mouse fertility. *PLoS Genetics*, **15**(8): e1008316.

Griswold MD. 2016. Spermatogenesis: the commitment to meiosis. *Physiological Reviews*, **96**(1): 1–17.

Groll M, Bajorek M, Köhler A, et al. 2000. A gated channel into the proteasome core particle. *Nature Structural Biology*, **7**(11): 1062–1067.

Ishiguro KI. 2023. Mechanism of initiation of meiosis in mouse germ cells. *Current Topics in Developmental Biology*, **151**: 1–26.

Jung T, Grune T. 2012. Structure of the proteasome. *Progress in Molecular Biology and Translational Science*, **109**: 1–39.

Kent J, Wheatley SC, Andrews JE, et al. 1996. A male-specific role for SOX9 in vertebrate sex determination. *Development*, **122**(9): 2813–2822.

Khor B, Bredemeyer AL, Huang CY, et al. 2006. Proteasome activator PA200 is required for normal spermatogenesis. *Molecular and Cellular Biology*, **26**(8): 2999–3007.

Kimble J. 2011. Molecular regulation of the mitosis/meiosis decision in multicellular organisms. *Cold Spring Harbor Perspectives in Biology*, **3**(8): a002683.

Lei N, Hornbaker KI, Rice DA, et al. 2007. Sex-specific differences in mouse DMRT1 expression are both cell type- and stage-dependent during gonad development. *Biology of Reproduction*, **77**(3): 466–475.

Li DY, Li H, Wang T, et al. 2010. Structural basis for the assembly and gate closure mechanisms of the Mycobacterium tuberculosis 20S proteasome. *The EMBO Journal*, **29**(12): 2037–2047.

Li YF, Li QY, Wu L, et al. 2024. SperMD: the expression atlas of sperm maturation. *BMC Bioinformatics*, **25**(1): 29.

Lin YF, Gill ME, Koubova J, et al. 2008. Germ cell-intrinsic and -extrinsic factors govern meiotic initiation in mouse embryos. *Science*, **322**(5908): 1685–1687.

Lin Z, Hsu PJ, Xing XD, et al. 2017. Mettl3-/Mettl14-mediated mRNA N^6-methyladenosine modulates murine spermatogenesis. *Cell Research*, **27**(10): 1216–1230.

Liu C, Wang LY, Li YN, et al. 2023. RNase H1 facilitates recombinase recruitment by degrading DNA-RNA hybrids during meiosis. *Nucleic Acids Research*, **51**(14): 7357–7375.

Liu CW, Corboy MJ, Demartino GN, et al. 2003. Endoproteolytic activity of the proteasome. *Science*, **299**(5605): 408–411.

Liu R, Kasowitz SD, Homolka D, et al. 2021. YTHDC2 is essential for pachytene progression and prevents aberrant microtubule-driven telomere clustering in male meiosis. *Cell Reports*, **37**(11): 110110.

Lu LY, Wu JX, Ye L, et al. 2010. RNF8-dependent histone modifications regulate nucleosome removal during spermatogenesis. *Developmental Cell*, **18**(3): 371–384.

Matson CK, Murphy MW, Griswold MD, et al. 2010. The mammalian doublesex homolog DMRT1 is a transcriptional gatekeeper that controls the mitosis versus meiosis decision in male germ cells. *Developmental Cell*, **19**(4): 612–624.

Murata S, Sasaki K, Kishimoto T, et al. 2007. Regulation of CD8+ T cell development by thymus-specific proteasomes. *Science*, **316**(5829): 1349–1353.

Nakagawa T, Zhang T, Kushi R, et al. 2017. Regulation of mitosis-meiosis transition by the ubiquitin ligase β-TrCP in male germ cells. *Development*, **144**(22): 4137–4147.

Oatley JM, Brinster RL. 2012. The germline stem cell niche unit in mammalian testes. *Physiological Reviews*, **92**(2): 577–595.

Page SL, Hawley RS. 2004. The genetics and molecular biology of the synaptonemal complex. *Annual Review of Cell and Developmental Biology*, **20**: 525–558.

Pickering AM, Davies KJA. 2012. Differential roles of proteasome and immunoproteasome regulators Pa28αβ, Pa28γ and Pa200 in the degradation of oxidized proteins. *Archives of Biochemistry and Biophysics*, **523**(2): 181–190.

Preckel T, Fung-Leung WP, Cai Z, et al. 1999. Impaired immunoproteasome assembly and immune responses in PA28-/- mice. *Science*, **286**(5447): 2162–2165.

Qian BM, Li Y, Yan RY, et al. 2022. RNA binding protein RBM46 regulates mitotic-to-meiotic transition in spermatogenesis. *Science Advances*, **8**(34): eabq2945.

Qian MX, Pang Y, Liu CH, et al. 2013. Acetylation-mediated proteasomal degradation of core histones during DNA repair and spermatogenesis. *Cell*, **153**(5): 1012–1024.

Roosen-Runge EC. 1962. The process of spermatogenesis in mammals. *Biological Reviews*, **37**(3): 343–376.

Sadate-Ngatchou PI, Payne CJ, Dearth AT, et al. 2008. Cre recombinase activity specific to postnatal, premeiotic male germ cells in transgenic mice. *Genesis*, **46**(12): 738–742.

Sadowski M, Suryadinata R, Tan AR, et al. 2012. Protein monoubiquitination and polyubiquitination generate structural diversity to control distinct biological processes. *IUBMB Life*, **64**(2): 136–142.

Sato B, Kim J, Morohoshi K, et al. 2023. Proteasome-associated proteins, PA200 and ECPAS, are essential for murine spermatogenesis. *Biomolecules*, **13**(4): 586.

Song HW, Wilkinson MF. 2014. Transcriptional control of spermatogonial maintenance and differentiation. *Seminars in Cell & Developmental Biology*, **30**: 14–26.

Sun C, Desch K, Nassim-Assir B, et al. 2023. An abundance of free regulatory (19*S*) proteasome particles regulates neuronal synapses. *Science*, **380**(6647): eadf2018.

Sun SF, Jiang YM, Zhang QL, et al. 2022. Znhit1 controls meiotic initiation in male germ cells by coordinating with Stra8 to activate meiotic gene expression. *Developmental Cell*, **57**(7): 901–913. e4.

Suzuki A, Saga Y. 2008. Nanos2 suppresses meiosis and promotes male germ cell differentiation. *Genes & Development*, **22**(4): 430–435.

Suzuki H, Saba R, Sada A, et al. 2010. The Nanos3–3'UTR is required for germ cell specific NANOS3 expression in mouse embryos. *PLoS One*, **5**(2): e9300.

Takeo S, Hawley RS. 2012. Rumors of its disassembly have been greatly exaggerated: the secret life of the synaptonemal complex at the centromeres. *PLoS Genetics*, **8**(6): e1002807.

Tanaka K. 2009. The proteasome: overview of structure and functions. *Proceedings of the Japan Academy. Series B, Physical and Biological Sciences*, **85**(1): 12–36.

Tanaka K, Kasahara M. 1998. The MHC class I ligand-generating system: roles of immunoproteasomes and the interferon-4gMY-inducible proteasome activator PA28. *Immunological Reviews*, **163**(1): 161–176.

Torra-Massana M, Jodar M, Barragán M, et al. 2021. Altered mitochondrial function in spermatozoa from patients with repetitive fertilization failure after ICSI revealed by proteomics. *Andrology*, **9**(4): 1192–1204.

Traut W, Endl E, Scholzen T, et al. 2002. The temporal and spatial distribution of the proliferation associated Ki-67 protein during female and

male meiosis. *Chromosoma*, **111**(3): 156–164.
Uechi H, Hamazaki J, Murata S. 2014. Characterization of the testis-specific proteasome subunit α4s in mammals. *Journal of Biological Chemistry*, **289**(18): 12365–12374.
Wang XL, Ye YH, Lencer W, et al. 2006. The viral E3 ubiquitin ligase mK3 uses the Derlin/p97 endoplasmic reticulum-associated degradation pathway to mediate down-regulation of major histocompatibility complex class I proteins. *Journal of Biological Chemistry*, **281**(13): 8636–8644.
Wojtas MN, Pandey RR, Mendel M, et al. 2017. Regulation of m^6A Transcripts by the 3'→5' RNA Helicase YTHDC2 is essential for a successful meiotic program in the mammalian germline. *Molecular Cell*, **68**(2): 374–387. e12.
Xiong Y, Yu C, Zhang QT. 2022. Ubiquitin-proteasome system-regulated protein degradation in spermatogenesis. *Cells*, **11**(6): 1058.
Zarkower D. 2013. DMRT genes in vertebrate gametogenesis. *Current Topics in Developmental Biology*, **102**: 327–356.
Zhang QT, Ji SY, Busayavalasa K, et al. 2019. Meiosis I progression in spermatogenesis requires a type of testis-specific 20S core proteasome. *Nature Communications*, **10**(1): 3387.
Zhang T, Oatley J, Bardwell VJ, et al. 2016. DMRT1 is required for mouse spermatogonial stem cell maintenance and replenishment. *PLoS Genetics*, **12**(9): e1006293.
Zhang T, Zarkower D. 2017. DMRT proteins and coordination of mammalian spermatogenesis. *Stem Cell Research*, **24**: 195–202.
Zhang ZH, Jiang TX, Chen LB, et al. 2021. Proteasome subunit α4s is essential for formation of spermatoproteasomes and histone degradation during meiotic DNA repair in spermatocytes. *Journal of Biological Chemistry*, **296**: 100130.
Živković D, Sanchez Dafun A, Menneteau T, et al. 2022. Proteasome complexes experience profound structural and functional rearrangements throughout mammalian spermatogenesis. *Proceedings of the National Academy of Sciences of the United States of America*, **119**(15): e2116826119.

Han et al. *Zool. Res.* 2025, 46(1): 41−53
https://doi.org/10.24272/j.issn.2095-8137.2024.257
https://cstr.cn/32248.14.zr.2024.257

ZR | Zoological Research

Article Open Access

Novel mouse model of Alzheimer's disease exhibits pathology through synergistic interactions among amyloid-β, tau, and reactive astrogliosis

Young-Eun Han[1,#], Sunhwa Lim[1,#], Seung Eun Lee[2], Min-Ho Nam[1], Soo-Jin Oh[1,*]

[1] *Brain Science Institute*, *Korea Institute of Science and Technology (KIST)*, *Seoul* 02792, *Republic of Korea*

[2] *Research Animal Resources Center*, *Korea Institute of Science and Technology (KIST)*, *Seoul* 02792, *Republic of Korea*

ABSTRACT

Alzheimer's disease (AD) is a progressive neurodegenerative disorder characterized by cognitive impairment and distinct neuropathological features, including amyloid-β plaques, neurofibrillary tangles, and reactive astrogliosis. Developing effective diagnostic, preventative, and therapeutic strategies for AD necessitates the establishment of animal models that accurately recapitulate the pathophysiological processes of the disease. Existing transgenic mouse models have significantly contributed to understanding AD pathology but often fail to replicate the complexity of human AD. Additionally, these models are limited in their ability to elucidate the interplay among amyloid-β plaques, neurofibrillary tangles, and reactive astrogliosis due to the absence of spatially and temporally specific genetic manipulation. In this study, we introduce a novel AD mouse model (APP/PS1-TauP301L-Adeno mice) designed to rapidly induce pathological symptoms and enhance understanding of AD mechanisms. Neurofibrillary tangles and severe reactive astrogliosis were induced by injecting AAV_{DJ}-EF1a-hTauP301L-EGFP and Adeno-GFAP-GFP viruses into the hippocampi of 5-month-old APP/PS1 mice. Three months post-injection, these mice exhibited pronounced astrogliosis, substantial amyloid-β plaque accumulation, extensive neurofibrillary tangles, accelerated neuronal loss, elevated astrocytic GABA levels, and significant spatial memory deficits. Notably, these pathological features were less severe in AAV-TauP301L-expressing APP/PS1 mice without augmented reactive astrogliosis. These findings indicate an exacerbating role of severe reactive astrogliosis in amyloid-β plaque and neurofibrillary tangle-associated pathology. The APP/PS1-TauP301L-Adeno mouse model provides a valuable tool for advancing therapeutic research aimed at mitigating the progression of AD.

Keywords: Alzheimer's disease mouse model; Neurofibrillary tangles; Amyloid-β plaques; Reactive astrogliosis; Alzheimer's disease pathology

INTRODUCTION

Alzheimer's disease (AD) is a neurodegenerative disorder and the primary cause of dementia, characterized by progressive cognitive decline, neuronal loss, and hippocampal atrophy. The pathological features of AD include extracellular amyloid-β (Aβ) plaques and intracellular neurofibrillary tangles (NFTs), composed of Aβ peptide and hyperphosphorylated tau (p-tau) protein, respectively (Querfurth & Laferla, 2010). Mutations in genes associated with the amyloid precursor protein (APP) processing pathway, particularly in familial AD, accelerate amyloid pathology through increased Aβ42 aggregation, leading to neuronal degeneration and memory deficits (Selkoe & Kopan, 2003). Additionally, tau, encoded by the microtubule-associated protein tau (*MAPT*) gene, dissociates from microtubules, undergoes hyperphosphorylation, and forms pathological tau, driving neuronal cell death and cognitive deficits (Di et al., 2016).

In addition to Aβ plaques and NFTs, growing evidence suggests that reactive astrogliosis severity is also associated with AD progression (Chun et al., 2020; Ingelsson et al., 2004). In the AD brain, astrocytes proximal to Aβ plaques or NFTs undergo morphological, molecular, and functional alterations that drive reactive astrogliosis. Key characteristics of reactive astrocytes include the up-regulation of intermediate filaments, such as glial fibrillary acidic protein (GFAP) and

This is an open-access article distributed under the terms of the Creative Commons Attribution Non-Commercial License (http://creativecommons.org/licenses/by-nc/4.0/), which permits unrestricted non-commercial use, distribution, and reproduction in any medium, provided the original work is properly cited.

Copyright ©2025 Editorial Office of Zoological Research, Kunming Institute of Zoology, Chinese Academy of Sciences

Received: 06 August 2024; Accepted: 11 November 2024; Online: 12 November 2024

Foundation items: This study was supported by the National Research Foundation of Korea (NRF) funded by the Ministry of Science, ICT & Future Planning (2022R1A2C2006229, 2022R1A6A3A01086868), Korea Dementia Research Project through the Korea Dementia Research Center (KDRC) funded by the Ministry of Health & Welfare and Ministry of Science and ICT, Republic of Korea (RS-2024-00345328), and KIST Institutional Grant (2E32851)

[#]Authors contributed equally to this work

*Corresponding author, E-mail: osj@kist.re.kr

vimentin, as well as the development of hypertrophic processes (Bardehle et al., 2013; Jiwaji et al., 2022; Jo et al., 2014; Kato et al., 1998; Simpson et al., 2010; Yamada et al., 1992). In addition to morphological changes, reactive astrocytes also exhibit molecular dysregulation, including aberrant GABA synthesis and release, which suppress neuronal activity and contribute to memory deficits in AD (Chun et al., 2020; Jo et al., 2014; Nam et al., 2023). Brain insults, including injury, inflammation, and infection, can trigger widespread astrocyte reactivity. Notably, intracerebral injection of high-titer adenovirus, such as Adeno-GFAP-GFP, into the hippocampus of APP/PS1 mice has been shown to induce severe neuroinflammation and reactive astrogliosis, exacerbating neurodegeneration and cognitive deficits (Chun et al., 2020; Nam et al., 2020; Woo et al., 2017). Compared to adeno-associated virus (AAV), adenovirus elicits a stronger inflammatory response (Shirley et al., 2020) and is suitable for inducing reactive astrocytes through astrocyte-specific infection. Additionally, adenovirus-induced reactive astrogliosis has been shown to exacerbate pathology in Parkinson's disease models (An et al., 2021), suggesting that reactive astrogliosis may represent a common pathological mechanism in various neurodegenerative diseases. Based on these findings, we propose that the artificial induction of reactive astrogliosis, in conjunction with Aβ plaques and p-tau pathology, may exacerbate the pathological features of AD, providing a valuable and efficient mouse model for AD research.

Effective animal models that reflect the progressive neuropathology and cognitive decline of AD are essential for expanding our understanding of its molecular pathology and developing therapeutic approaches. While widely utilized transgenic mouse models, including APP/PS1, 5xFAD, and 3xTg, have provided valuable insights into AD, they fail to replicate key AD features. For example, APP/PS1 and 5xFAD mouse models do not exhibit neuronal loss or NFTs even after one year (Jackson et al., 2016). Similarly, 3xTg mouse models show limited accumulation of Aβ plaques and NFTs even after two years, and their pathology remains less severe than what is typically observed in human AD (Drummond & Wisniewski, 2017). Moreover, these models lack the temporal and spatial precision necessary to understand the complex interplay among Aβ plaques, NFTs, and reactive astrogliosis. These limitations highlight the need for virus-based AD mouse models capable of inducing pathology with spatial and temporal specificity.

To address these limitations, we developed a novel AD mouse model (APP/PS1-TauP301L-Adeno mice). The model was established by injecting AAV_{DJ}-EF1α-hP301L-EGFP (AAV-TauP301L) and Adeno-GFAP-GFP viruses into the hippocampus of APP/PS1 mice. This approach generated a comprehensive AD phenotype marked by severe reactive astrogliosis, extensive NFT formation, exacerbated Aβ plaque deposition, and substantial neurodegeneration, closely mirroring human AD pathology. Collectively, these pathological markers contributed to pronounced hippocampus-dependent memory impairments. Using this model, we demonstrated that the induction of reactive astrogliosis via Adeno-GFAP-GFP infection, in the presence of toxic molecules such as Aβ and p-Tau, markedly amplified the aggregation of Aβ plaques and NFTs, ultimately exacerbating pathological symptoms of AD, such as neuronal loss and memory deficits. The APP/PS1-TauP301L-Adeno model thus provides a robust platform for investigating the interrelationship between key AD pathologies and should serve as a valuable tool for developing and testing novel therapeutic strategies in AD.

MATERIALS AND METHODS

Animals

Five-month-old hemizygous APPswe/PSEN1dE9 (APP/PS1) mice on a C57BL/6;C3H genetic background (Jackson Laboratory, #004462, USA) were used to assess the effects of increased tau pathology and activation on Aβ. Age-matched non-transgenic littermates were used as wild-type (WT) controls. Both male and female transgenic and WT mice were included in the study. Mice were maintained on a 12-h light-dark cycle with free access to food and water. All animal care and handling procedures were performed under the Institutional Animal Care and Use Committee (IACUC) guidelines of the Korea Institute of Science and Technology (KIST) (Approval number: KIST-IACUC-2019-051).

Viral vector design and production

All AAV and adenoviral vector plasmids were generated by the KIST Virus Facility. For AAV-based TauP301L expression, the TauP301L sequence from pRK5-EGFP-TauP301L (Addgene, #46908, USA) was inserted into the AAV-EF1α-EGFP vector backbone (Addgene, #60058, USA) at the KpnI and NcoI restriction sites using infusion cloning (Clontech, #639649, USA). The control vector, AAV-EF1α-EGFP (Addgene, #60058, USA), was similarly prepared. The resulting viral vectors were pseudotyped, with the transgene of interest flanked by inverted terminal repeats of the AAV2 and packaged in AAV-DJ capsids. The AAV-DJ capsids were engineered using DNA family shuffling technology, creating a hybrid capsid from eight standard AAV serotypes. Recombinant AAV (rAAV) vector production required four plasmids: AAV-DJ-serotype, AAV vector transfer plasmid, plasmid encoding rep and serotype-specific cap, and plasmid encoding adenoviral helper sequences. All vectors were purified via iodixanol gradients by the KIST Virus Facility. To induce reactive astrogliosis, we utilized an adenoviral vector (Adeno-GFAP-GFP) driven by the gfaABC1D promoter, a truncated version of the human GFAP promoter optimized for high astrocyte specificity (Lee et al., 2008). The AAV_{DJ}-EF1α-EGFP and AAD_{DJ}-EF1α-hTauP301L-EGFP titers were 1.26×10^{13} GC/mL, while the Adeno-GFAP-GFP titer was 2.25×10^{11} GC/mL.

Stereotaxic surgery

To achieve neuronal expression of human P301L-mutant tau, 5-month-old APP/PS1 transgenic mice and their littermate controls were anesthetized via isoflurane and secured in a stereotaxic frame (David Kopf Instruments, USA). After craniotomy, a 0.5 mm bore hole was drilled on each side of the skull using a drill handpiece (Komet Dental, Germany). Viral suspensions were microinjected using a 33-gauge blunt needle connected to a 25 μL Hamilton syringe and an automated microsyringe pump (kdScientific, USA). AAV_{DJ}-EF1α-EGFP (Control), AAV_{DJ}-EF1α-hTauP301L-EGFP (TauP301L), or Adeno-GFAP-GFP (adenovirus) was bilaterally injected into the CA1 region and dentate gyrus (DG) of the hippocampus based on the following coordinates: AP=−1.96, ML=±1.5, and DV=−1.7 for the DG; AP=−1.96, ML=±1.5, and DV=−1.2 for the CA1 to the dura surface. The

AAV-control, AAV-TauP301L, and Adeno-GFAP-GFP viruses were diluted 1:1 and a total volume of 1.5 μL was injected into each region at a rate of 0.2 μL/min. For co-injections of AAV-TauP301L and Adeno-GFAP-GFP, equal volumes of each virus (0.75 μL) were mixed and diluted with 0.5 μL of sterilized saline, with a total volume of 2.0 μL injected into each region at a rate of 0.2 μL/min. Before withdrawal, the needle was kept in position for an additional 5 min to prevent leakage of the infused solution. The injection site was then sutured, and the mice were maintained on a heating pad until fully recovered before being returned to their home cages.

Behavioral analyses

To assess cognitive and memory changes at the behavioral level, APP/PS1 transgenic mice (5 months old) and non-transgenic WT littermates (5 months old), with or without TauP301L and adenovirus injections, were assessed at 3 months post-injection. Behavioral tests were conducted sequentially, including the open field test, novel object recognition test, Y-maze test, and passive avoidance test. Before testing, all mice were extensively handled and habituated to an empty testing apparatus for 10 min daily over six consecutive days. Mice were also habituated to the testing room for 30 min before each test. Sex ratios of mice were balanced across experimental groups to minimize variability.

Open field test: Locomotor activity and anxiety-related behaviors were evaluated using the open field test. Testing was performed in an open field arena measuring 40 cm×40 cm. Testing commenced at least 24 h after the final habituation session. Mice remained in their home cages until testing and were transported to the arena immediately prior to the test. Mice were individually placed in the center of the arena and allowed to explore freely for 30 min. The total distance traveled, as well as the time and distance spent in the center versus the perimeter, were recorded using Noldus tracking software (EthoVision XT, 8.5, USA).

Novel object recognition (NOR) test: Recognition memory was evaluated using the NOR test. To prevent navigation-related behaviors from interfering with object interaction, each mouse underwent a 30 min open field training session 24 h before the test. During the familiarization phase, each mouse was placed in a 40 cm×40 cm arena containing two identical objects fixed on stationary bases positioned on opposite sides. The mice were allowed to explore the objects for 30 min before being returned to their home cages (familiarization phase). After 1 h, one of the familiar objects was replaced with a novel object, each mouse was reintroduced to the arena and allowed to explore both the familiar and novel objects for 15 min (testing phase). All experiments were videotaped, and the time spent oriented towards the objects was manually scored using the EthoVision manual scoring system. Interaction with an object was defined as the time spent exploring it within a distance of 1.5 times the size of the object during the observation period. The discrimination ratio was defined as the time spent investigating the novel object divided by the time spent investigating both the novel and familiar objects (total time of exploratory behavior). The arena and all objects were cleaned with 70% ethanol between trials to eliminate olfactory cues.

Y-maze: To evaluate short-term spatial recognition working memory, mice were placed at the end of the B arm of a Y-maze and allowed to explore freely for 8 min. The Y-maze consisted of three arms, each 40 cm long, 4 cm wide, and 16 cm high, arranged at 120° angles. The maze, constructed from gray polyvinyl plastic, included posters on the walls to serve as spatial cues. After the exploration phase, each mouse was returned to its home cage for a 30 min interval. The maze was cleaned with 70% ethanol and dried before each trial to eliminate olfactory cues. During the test, overhead video recording was used to monitor behavior. Spatial working memory performance was assessed based on the proportion of alternations, defined as the number of arm entries in which the mouse selected a different arm from the previous two consecutive entries, relative to the total number of arm entries.

Passive avoidance test: The passive avoidance test was performed to measure long-term memory using a two-compartment apparatus consisting of light and dark chambers connected by a sliding door. During the acquisition trial on the first day, each mouse was placed in the light chamber and allowed to explore for 60 s, with the door separating the two spaces raised. When the mouse placed its paws in the dark chamber, the door was closed to prevent the mouse from returning to the light side and a 0.4 mA electrical shock was delivered through the metal grid for 2 s. Following the shock, the mouse was removed from the apparatus and returned to its home cage. The following day, retention was assessed by placing the mouse back into the light chamber. The sliding door was opened, and the latency to enter the dark chamber was recorded. No electrical stimulation was applied during the retention trial. The cut-off time for both the acquisition and retention trials was set to 600 s.

Immunohistochemical analysis

Mice were anesthetized with 2% avertin (20 μg/g, intraperitoneally) (Sigma-Aldrich, #T48402, USA) 13 weeks after virus injection. The anesthetized mice were transcardially perfused with phosphate-buffered saline (PBS, pH 7.4) and 4% paraformaldehyde in PBS. After perfusion, tissues were immediately removed and post-fixed for 12 h in the same fixative, followed by dehydration in 30% sucrose until they sank. Brains were coronally sectioned on a freezing microtome (Thermo Scientific, USA) at 30 μm thickness.

The blocking of non-specific binding sites was performed by incubating the sections in 0.1 mol/L PBS containing 0.3% Triton X-100 (Sigma, #T8787, USA), 2% goat serum (Abcam, ab7481, USA), and 2% donkey serum (Genetex, GTX27475, USA) for 2 h at room temperature (RT). Primary antibodies were prepared in blocking buffer and applied overnight at 4°C. After washing three times (5 min each) in 0.1 mol/L PBS, the brain slices were incubated in appropriate secondary antibodies (Jackson Laboratory) for 1.5 h at RT. The sections were again washed three times in 0.1 mol/L PBS and mounted in fluorescent mounting medium (Agilent Dako, S3023, USA). A series of fluorescent images were taken using an A1 Nikon confocal microscope. Z stack projections were made from serial images in 3 μm steps. Any alterations in brightness or contrast were equally applied to the entire image set. IMARIS software (Bitplane, UK) was used to view the three-dimensional (3D) reconstruction of all z-stacks.

Brain sections were stained with chicken anti-GFAP (1:500, MERCK, ab5541, USA), mouse anti-phosphorylated tau AT8 (pSer202 and pThr205; 1:200, Thermo Fisher Scientific, MN1020, USA), rabbit anti-phosphorylated human tau S199 (pSer199; Abcam, ab81268, USA), rabbit anti-neurofibrillary tangle (1:200, MERCK, ab1518, USA), rabbit anti-beta amyloid (1:500, Abcam, ab2539, USA), and guinea pig anti-

NeuN (MERCK, ABN90P, USA).

For NFT staining, sections were incubated with 3% hydrogen peroxide (H_2O_2) in PBS for 10 min at RT, then washed three times in PBS for 15 min. Non-specific binding sites were blocked by incubating the sections in 3% normal goat serum (Life Technologies, NC2459021, USA) and 3% Triton X-100 in PBS for 1 h at RT. The sections were then incubated overnight at 4℃ with primary antibodies against NFT (1:400, MERCK, ab1518, USA). After three washes in PBS, a biotinylated goat anti-rabbit (Vector Laboratories, BP-1000-1.5, USA) secondary antibody diluted 1/200 in PBS was applied for 2 h at RT. Following the manufacturer's instructions, a Vectastain ABC Elite Kit (Vector Laboratories, PK6101, USA) was used for peroxidase detection. Sections were washed and developed with 3,3'-diaminobenzidine (DAB, Sigma Aldrich, USA) plus H_2O_2 in Tris-buffered saline (TBS). The DAB-stained sections were mounted on microscopic slides, air-dried, and coverslipped. Images were obtained using an Olympus IX50 microscope with a 2× or 4× objective. Quantitative analyses were performed using ImageJ software to measure mean optical density.

Thioflavin-S staining

For thioflavin-S staining, frozen brain sections were incubated in 1 mmol/L thioflavin-S (Sigma Aldrich, USA) 50% ethanol for 8 min at RT, then washed twice in 80% ethanol for 5 min and twice in PBS for 10 min. Images were taken using an Olympus IX50 microscope (Japan) with a green fluorescence protein (GFP) filter set. The region of interest (ROI) (mm^2) in the cortex was measured using ImageJ software (NIH, USA). Counting was performed using a low-magnification objective lens (×2) and images were quantified as the number of plaques in the cortex. Data quantification was conducted via surface rendering of Aβ plaques using IMARIS (Bitplane, UK).

Image quantification

Quantitative analysis of confocal microscopic images was performed using IMARIS software. The ROI was determined as the 3D structure of the GFP-positive region using a "surface object" generated using a 0.312 μm diameter. Smaller, adjacent neurons were separated into multiple objects using the "split touching objects" function with an estimated 6 μm diameter. Thus, large puncta were potentially separated into several individual neurons. Average intensity of the pixels of different wavelengths (405 nm, 594 nm, and 647 nm) was measured by masking them with a GFP-positive cell. At least four mice per group were sacrificed after behavioral experiments, and 2–3 slices per mouse were stained and analyzed for quantification. Sholl analysis was performed using maximal projection images of GFAP signals. The Neuroanatomy Sholl analysis plugin in ImageJ was used to automatically generate consecutive concentric circles at 10 μm intervals, centered on the DAPI-stained nucleus and extending to the furthest reach of the astrocytic process. Subsequently, the sum of all intercepts of GFAP processes in each circle was quantified.

Monoamine oxidase-B (MAO-B) activity assay

Mice were anesthetized with avertin (tribromoethanol) via intraperitoneal injection and transcardially perfused with saline. Brain tissue was removed from six mouse groups. Different regions, including the hippocampus and cortex, were dissected separately under cold conditions. Fresh tissues from each mouse were homogenized in lysis buffer (250 mmol/L sucrose, 2 mmol/L HEPES (pH 7.4), 0.1 mmol/L EGTA), and centrifuged at 570 ×*g* for 10 min at 4°C to remove large debris. The supernatants were collected and centrifuged at 14 290 ×*g* for 10 min at 4°C to obtain a mitochondrial-rich fraction. The pellet was resuspended in PBS, and MAO-B activity was measured using 20 μg in each well. MAO-B enzymatic activity was measured using an Amplex Red Monoamine Oxidase Assay Kit (ThermoFisher Scientific. #A12214, USA), following the manufacturer's instructions. MAO-B was reacted at 37°C for 30 min with or without adding selegiline, a MAO-B inhibitor, then reacted with benzylamine, a MAO-B substrate. H_2O_2 production resulting from MAO-B activity was assessed using the colorimetric change of the Amplex Red reagent after 2 h of enzymatic reaction. The color change was quantified by measuring absorbance at 570 nm using an Infinite M200 PRO microplate reader (TECAN, Switzerland).

Statistical analysis

Results were presented as mean±standard error of the mean (SEM). All data were analyzed statistically using Prism v.9.0 (GraphPad Software, USA). Statistical significance was determined by either one-way or two-way analysis of variance (ANOVA), as reported in each figure legend. One-way ANOVA with Tukey's multiple comparison test was conducted to compare multiple groups. Two-way ANOVA followed by Bonferroni's multiple comparison test was used to assess changes under different conditions across multiple groups. Differences were considered significant at *: $P<0.05$, **: $P<0.01$, ***: $P<0.001$, ****: $P<0.0001$ (ns, not significant). All raw data are shown as dot plots on each graph. The corresponding figure legend or graph describes the number of animals used. Experimental groups were balanced regarding animal age, sex, and weight.

RESULTS

Rapid accumulation of p-tau and NFTs in APP/PS1-TauP301L-Adeno AD mice

We investigated the progression of AD pathology in APP/PS1 mice when mutant tau overexpression and reactive astrogliosis were concurrently induced. To induce tau pathology, human mutant tau was overexpressed by injecting AAV_{DJ}-EF1α-hP301L-EGFP (AAV-TauP301L) into the DG and CA1 of the hippocampus of 5-month-old APP/PS1 mice. Immunostaining confirmed elevated levels of p-tau and NFTs upon AAV-TauP301L overexpression in both APP/PS1 mice and age-matched WT littermates. p-Tau levels were significantly increased in WT and APP/PS1 mice injected with AAV-TauP301L compared to mice injected with control virus (AAV_{DJ}-EF1α-EGFP) (Supplementary Figure S1A, B). The accumulation of p-tau was further increased when mutant tau was overexpressed in APP/PS1 mice (Figure 1A, C). In addition to p-tau, NFTs also significantly accumulated in AAV-TauP301L-injected APP/PS1 mice (Supplementary Figure S1A, C), indicating that Aβ synergistically mediates tau phosphorylation and NFT accumulation, in line with previous findings (Gomes et al., 2019). Furthermore, after induction of mutant tau in APP/PS1 mice, a concomitant increase in GFAP intensity was observed compared to APP/PS1 mice injected with the control virus (Figure 1A, B), suggesting that the accumulation of Aβ plaques and p-tau aggravates reactive astrogliosis.

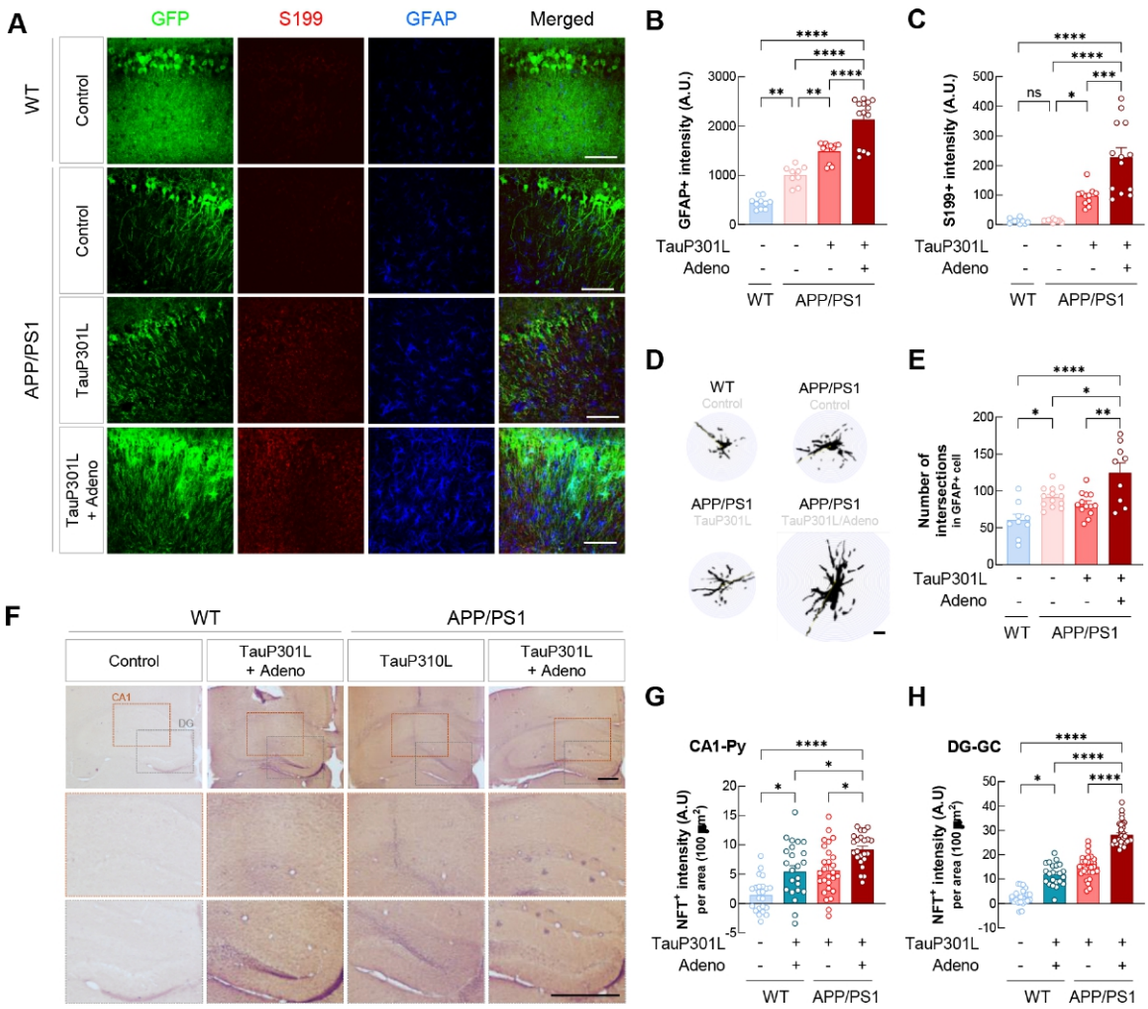


Figure 1 TauP301L overexpression and adenovirus-induced reactive astrogliosis in the hippocampus of APP/PS1 mice induces phosphorylated tau, reactive astrogliosis, and NFTs

A: Representative immunohistochemical images of S199 (p-tau, red) and GFAP (astrocyte, blue) in 8-month-old WT-Control, APP/PS1-Control, APP/PS1-TauP301L, and APP/PS1-TauP301L-Adeno mice. Scale bars: 40 μm. B, C: Bar graph showing mean intensity of GFAP (B) and S199 (C). Each bar represents mean±SEM. Sample sizes: WT-control (*n*=10), APP/PS1-Control (*n*=9), APP/PS1-TauP301L (*n*=11), APP/PS1-TauP301L-Adeno (*n*=14), *n*: number of slices, collected from 3–4 mice per group. Mean±SEM values: (B) WT-control=439.354±36.525, APP/PS1-Control=1 007.23±69.796, APP/PS1-TauP301L=1 489.587±61.307, APP/PS1-TauP301L-Adeno=2 137.64±123.507. (C) WT-control=11.963±2.66, APP/PS1-Control=13.645±1.712, APP/PS1-TauP301L=96.347±9.63, and APP/PS1-TauP301L-Adeno=227.446±32.95. D: Representative Sholl analysis images of GFAP-positive astrocytes in WT-Control, APP/PS1-Control, APP/PS1-TauP301L, and APP/PS1-TauP301L-Adeno mice. Circles centered around soma are separated by radial intervals of 10 μm. Scale bars: 50 μm. E: Bar graph showing number of intersections in GFAP-positive cells. Each bar represents mean±SEM. Sample sizes: WT-control (*n*=9), APP/PS1-Control (*n*=13), APP/PS1-TauP301L (*n*=13), APP/PS1-TauP301L-Adeno (*n*=9), *n*: GFAP-positive cells collected from 3–4 mice per group. Mean±SEM values: WT-control=60.333±7.878, APP/PS1-Control=91.538±3.847, APP/PS1-TauP301L=82.069±4.423, and APP/PS1-TauP301L-Adeno=124.666±13.497. F: Representative photomicrographs of NFTs stained using ABC/DAB in APP/PS1-TauP301L-Adeno brain sections. Scale bars: 500 μm. G, H: Bar graph showing quantification of NFT-positive intensity per area (100 μm^2) in CA1 and DG of hippocampus. Each bar represents mean±SEM. (G, CA1 pyramidal layer). Sample sizes: WT-Control (*n*=23), WT-TauP301L/Adeno (*n*=24), APP/PS1-TauP301L (*n*=27), and APP/PS1-TauP301L-Adeno (*n*=23). (H, DG granule cell layer) Sample sizes: WT-Control (*n*=22), WT-TauP301L/Adeno (*n*=22), APP/PS1-TauP301L (*n*=31), and APP/PS1-TauP301L-Adeno (*n*=33). Each dot represents an individual area measurement, with data collected from 3–6 mice per group. Mean±SEM values: (G, CA1 pyramidal layer) WT-Control=1.459±0.588, WT-TauP301L/Adeno=5.382±1.043, APP/PS1-TauP301L=5.647±0.804, APP/PS1-TauP301L-Adeno=9.199±0.576, (H, DG granule cell layer) WT-Control=2.604±0.662, WT-TauP301L/Adeno=11.88±0.964, APP/PS1-TauP301L=15.006±0.825, and APP/PS1-TauP301L-Adeno=28.19±0.832. Statistical analysis was conducted using one-way ANOVA with Tukey's *post-hoc* test, ns: Not significant; *: P<0.05; **: P<0.01; ***: P<0.001; ****: P<0.0001.

To further explore the impact of severe reactive astrogliosis, we co-injected Adeno-GFAP-GFP with AAV-TauP301L into the hippocampal DG and CA1 in APP/PS1 mice. Remarkably, this co-injection resulted in a marked enhancement of GFAP intensity compared to AAV-TauP301L injection alone (Figure 1A, B). In addition, astrocyte morphological changes, including increased branching and ramification, were significantly increased in APP/PS1-TauP301L-Adeno mice (Figure 1D, E). These findings indicate that Aβ plaques initiate astrocyte reactivity, which is subsequently enhanced by overexpression of AAV-TauP301L in APP/PS1 mice. Furthermore, the accumulation of Aβ plaques and p-tau, in

conjunction with adenovirus-induced reactive astrogliosis, profoundly intensifies the severity of astrocyte reactivity.

To investigate whether adenovirus-induced reactive astrogliosis with mutant tau overexpression exacerbates p-tau and NFT accumulation in APP/PS1 mice, p-tau and NFT immunostaining was performed after simultaneous injection of AAV-TauP301L and Adeno-GFAP-GFP into the hippocampal DG and CA1 regions of APP/PS1 mice. The accumulation of p-tau and NFTs notably increased when Adeno-GFAP-GFP was injected along with AAV-TauP301L in APP/PS1 mice (Figure 1A, C, F–H). These results suggest that severe reactive astrogliosis exacerbates tau pathology in the presence of mutant tau in APP/PS1 mice. Interestingly, NFT accumulation levels in WT mice co-injected with AAV-TauP301L and Adeno-GFAP-GFP were comparable to those observed in APP/PS1 mice injected with AAV-TauP301L alone, implying that Adeno-GFAP-GFP-induced reactive astrogliosis mimics the effects of Aβ plaque-induced reactive astrogliosis. Collectively, these findings suggest that interplay between Adeno-GFAP-GFP-induced severe reactive astrogliosis, AAV-TauP301L-induced p-tau expression, and Aβ pathology contributes to accelerated reactive gliosis and NFT accumulation in the hippocampus of APP/PS1 mice.

Overexpression of AAV-TauP301L and Adeno-GFAP-GFP enhances Aβ plaque accumulation in APP/PS1 mice

We next investigated the impact of mutant tau overexpression and adenovirus-induced reactive astrogliosis on Aβ plaque accumulation in APP/PS1 mice. Reactive astrocytes are known to exacerbate the pathological features of AD, contributing to glial activation, tauopathy, neuronal death, brain atrophy, cognitive impairment, and eventual death via H_2O_2 production (Chun et al., 2020). Based on these observations, we hypothesized that severe reactive astrocytes driven by Aβ plaques, mutant tau overexpression, and adenovirus-induced reactivity would further enhance Aβ plaque accumulation. Immunostaining for Aβ plaques in APP/PS1-TauP301L-Adeno mice exhibited significantly larger plaques in the hippocampus compared to controls (Figure 2A, B). This suggests that the combination of mutant tau overexpression and adenovirus-induced astrocyte reactivity amplifies reactive gliosis and NFT formation, subsequently accelerating Aβ plaque accumulation.

To further validate our hypothesis, thioflavin-S staining was used to assess Aβ deposition in the adjacent cortical regions. A progressive increase in Aβ deposition was observed in the somatosensory S1 cortex and piriform cortex of mice, with severity ranking as APP/PS1-Control, APP/PS1-TauP301L, and APP/PS1-TauP301L-Adeno, and WT mice (no deposition) (Figure 2C). The number of thioflavin-S-positive plaques in the somatosensory S1 cortex and piriform cortex of APP/PS1-TauP301L-Adeno mice significantly exceeded those in APP/PS1-Control and APP/PS1-TauP301L mice, indicating that adenovirus-induced reactive astrogliosis, coupled with mutant tau overexpression, accelerates Aβ accumulation (Figure 2D, E). APP/PS1-TauP301L mice also displayed significantly more Aβ plaques than APP/PS1-Control mice, supporting the notion that overexpression of mutant tau amplifies reactive astrogliosis (Figure 1A, B), further exacerbating Aβ plaque deposition. These findings imply that the induction of tau pathology and reactive astrogliosis is pivotal in accelerating Aβ deposition in APP/PS1-TauP301L-Adeno mice.

Abundant astrocytic GABA and increased MAO-B activity in APP/PS1-TauP301L-Adeno mice

Aberrant astrocytic GABA has been implicated in inhibiting neuronal activity and contributing to learning and memory impairments in AD (Jo et al., 2014). To evaluate astrocytic GABA levels in APP/PS1-TauP301L-Adeno mice, co-immunostaining of GABA and GFAP was performed on hippocampal slices. Astrocytes in APP/PS1-control mice exhibited a trend toward increased GABA immunoreactivity compared to age-matched WT mice. Furthermore, GFAP-positive astrocytes in APP/PS1-TauP301L and APP/PS1-TauP301L-Adeno mice displayed more robust GABA immunoreactivity compared to both APP/PS1-control and WT mice (Figure 3A, B).

MAO-B, a key enzyme involved in astrocytic GABA production, is up-regulated in post-mortem AD brain tissue and AD mouse models (Adolfsson et al., 1980; Jo et al., 2014). To assess the potential increase in MAO-B activity in the APP/PS1-TauP301L-Adeno AD mouse model, a fluorometric assay was performed on mitochondrial-rich fractions isolated from hippocampal tissue homogenates (Figure 3C). A substantial increase in MAO-B enzyme activity was observed in the hippocampus of APP/PS1 mice compared to WT mice (Figure 3D). Notably, MAO-B enzyme activity was significantly increased in APP/PS1-TauP301L and APP/PS1-TauP301L-Adeno mice compared to WT mice (Figure 3D). Treatment with selegiline, a selective and irreversible MAO-B inhibitor, significantly attenuated MAO-B activity across experimental groups (Figure 3D). These results suggest that mutant tau overexpression and adenovirus-induced reactive astrogliosis in the hippocampus of APP/PS1 mice can increase MAO-B activity, leading to the production and release of astrocytic GABA.

Acceleration of neuronal degeneration in the CA1 region of APP/PS1-TauP301L-Adeno mice

The formation of Aβ plaques and NFTs leads to neuronal loss (Knowles et al., 1999; Malek-Ahmadi et al., 2016). We hypothesized that neuronal loss would be exacerbated in APP/PS1 mice after the induction of mutant tau and adenovirus-induced reactive astrogliosis into the hippocampus. To test this, immunostaining with the neuronal marker NeuN was performed. Interestingly, a substantial reduction of NeuN signaling was observed in the CA1 pyramidal layer of APP/PS1-TauP301L-Adeno mice. In contrast, NeuN staining in age-matched WT, APP/PS1, and APP/PS1-TauP301L-Adeno mice remained intact (Figure 4A). Quantitative analysis confirmed a marked decrease in the number of NeuN-positive cells in the CA1 pyramidal layer of APP/PS1-TauP301L-Adeno mice (Figure 4B). These results indicate that neurodegeneration occurred within 3 months of AAV-TauP301L and Adeno-GFAP-GFP injections into the 5-month-old APP/PS1 mice. This finding suggests that APP/PS1-TauP301L-Adeno mice show an earlier onset of neuronal loss compared to the timeline reported in previous research, which identified neuronal loss in APP/PS1 mice at 17 months of age (Rupp et al., 2011).

Overexpression of P301L human mutant tau and severe reactive astrogliosis exacerbates hippocampus-dependent memory impairment in APP/PS1 mice

The impact of mutant tau overexpression and adenovirus-induced reactive astrogliosis on locomotor activity, anxiety, and hippocampus-dependent memory in APP/PS1 mice was

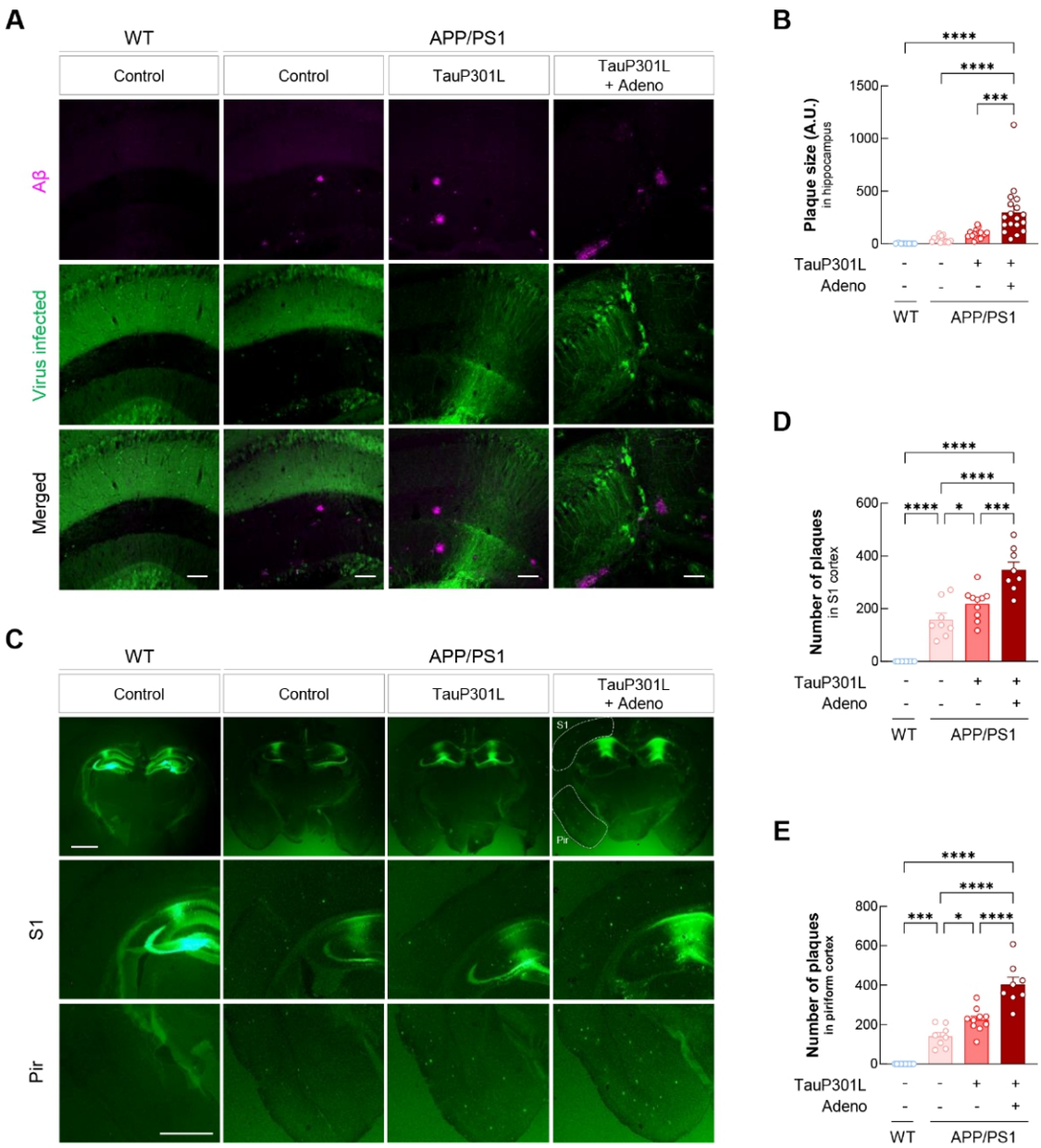


Figure 2 TauP301L overexpression and adenovirus-induced reactive astrogliosis in the hippocampus of APP/PS1 mice induces robust amyloid pathologies

A: Representative immunofluorescence images of Aβ (magenta) staining in hippocampal CA1 from WT-Control, APP/PS1-Control, APP/PS1-TauP301L, and APP/PS1-TauP301L-Adeno mice. Scale bars: 40 μm. B: Bar graph showing quantification of Aβ plaque size in the hippocampus. Each bar represents mean±SEM. Sample sizes: WT-control (*n*=8), APP/PS1-Control (*n*=13), APP/PS1-TauP301L (*n*=17), APP/PS1-TauP301L-Adeno (*n*=18), *n*: number of slices, collected from three mice per group. Mean±SEM values: WT-control=1.924±1.329, APP/PS1-Control=40.663±8.291, APP/PS1-TauP301L=91.938±10.201, and APP/PS1-TauP301L-Adeno=299.923±57.433. C: Representative images showing Aβ plaques stained with thioflavin-S (thio-S). S1 indicates S1 somatosensory cortex, Pir indicates piriform cortex. Scale bars: 1 mm. D, E: Bar graph showing quantification of number of Aβ plaques in the S1 somatosensory cortex (D) and piriform cortex (E). Each bar represents mean±SEM. Sample sizes: (D, E) WT-control (*n*=10), APP/PS1-Control (*n*=8), APP/PS1-TauP301L (*n*=10), APP/PS1-TauP301L-Adeno (*n*=8), with data collected from three mice per group. Mean±SEM values: (D) WT-control=0, APP/PS1-Control=158.038±24.752, APP/PS1-TauP301L=217.972±18.255, APP/PS1-TauP301L-Adeno=347.858±29.539. (E) WT-control=0, APP/PS1-Control=140.775±19.422, APP/PS1-TauP301L=224.287±18.873, APP/PS1-TauP301L-Adeno=402.746±37.664. Statistical analysis was conducted using one-way ANOVA with Tukey's *post-hoc* test, *: $P<0.05$; ***: $P<0.001$; ****: $P<0.0001$.

systematically evaluated. Locomotor activity and anxiety levels were assessed using the open field test (Supplementary Figure S2A). Total distance traveled revealed increased locomotor activity in both APP/PS1-TauP301L and APP/PS1-TauP301L-Adeno mice, consistent with previous findings (Jul et al., 2016; Wang et al., 2022) (Supplementary Figure S2B). However, neither the distance traveled nor time spent in the center zone differed significantly between groups, suggesting that anxiety levels were unaltered by mutant tau overexpression or additional reactive astrogliosis induction (Supplementary Figure S2C, D).

Hippocampus-dependent memory and cognitive

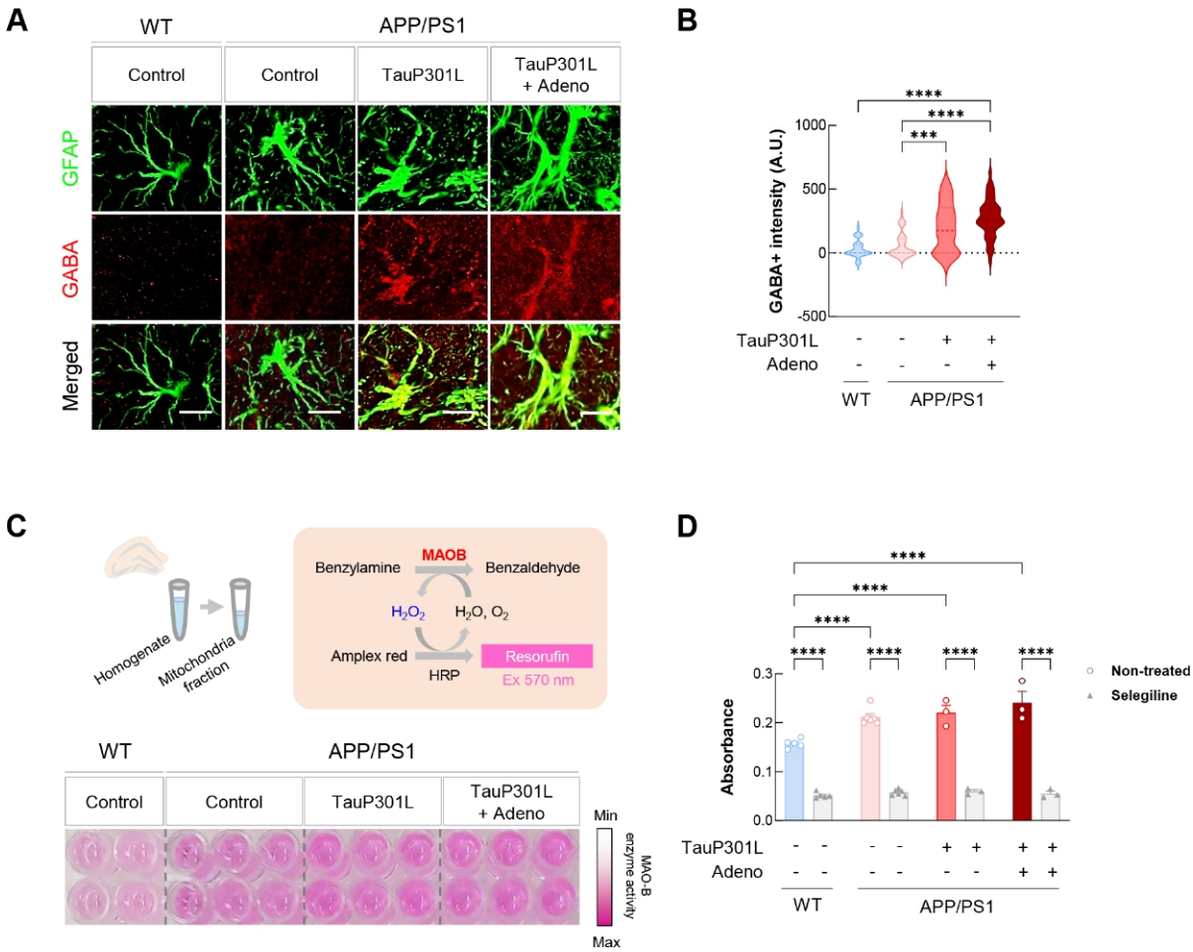


Figure 3 TauP301L overexpression and adenovirus-induced reactive astrogliosis in the hippocampus of APP/PS1 mice increases astrocytic GABA and MAO-B enzyme activity

A: Representative confocal images of astrocytes (GFAP, green) and GABA (red) in the molecular layer of CA3 from 8-month-old WT-Control, APP/PS1-Control, APP/PS1-TauP301L, and APP/PS1-TauP301L-Adeno mice. Scale bars: 5 μm. B: Violin plots showing GABA intensity in GFAP-positive astrocytes, representing the distribution of data within each group. Dashed lines indicate median, dotted lines represent quartiles. Sample sizes: WT-Control (*n*=28), APP/PS1-Control (*n*=38), APP/PS1-TauP301L (*n*=31), APP/PS1-TauP301L/Adeno (*n*=41), with GFAP-positive cells collected from four mice per group. Mean±SEM values: WT-Control=31.931±13.091, APP/PS1-Control=61.623±15.829, APP/PS1-TauP301L=200.939±33.855, and APP/PS1-TauP301L-Adeno=274.775±23.761. C: Schematic of MAO-B enzyme activity assay in the hippocampus (Top). Representative images of color change after 20 min of MAO-B reaction (Bottom, *n*=2 for 8-month-old WT-Control; *n*=3 for other groups). D: Bar graph showing MAO-B enzyme activity measured by absorbance at 570 nm in hippocampal tissue. Each bar represents mean absorbance±SEM, with sample sizes: WT-Control (*n*=5), APP/PS1-Control (*n*=6), APP/PS1-TauP301L (*n*=3), and APP/PS1-TauP301L-Adeno (*n*=3). One hippocampal tissue sample from one hemisphere was examined per mouse. Mean absorbance±SEM values: non-treated WT-control=0.157±0.004, selegiline-treated WT-control=0.052±0.003; non-treated APP/PS1-Control=0.211±0.007, selegiline-treated APP/PS1-Control=0.058±0.003; on-treated APP/PS1-TauP301L=0.22±0.015, selegiline-treated APP/PS1-TauP301L=0.06±0.004; non-treated APP/PS1-TauP301L-Adeno=0.24±0.023, and selegiline-treated APP/PS1-TauP301L-Adeno=0.24±0.023. Statistical analysis was conducted using one-way ANOVA with Tukey's *post-hoc* test, ***: *P*<0.001; ****: *P*<0.0001.

impairments in 8-month-old APP/PS1-TauP301L-Adeno mice were further investigated using the NOR task, Y-maze test, and passive avoidance test (Figure 5A, D, G). During the NOR familiarization phase, all groups exhibited no preference for any specific object. In the testing session, WT, APP/PS1, WT-TauP301L/Adeno, and APP/PS1-TauP301L mice demonstrated a preference for the novel object, while APP/PS1-TauP301L-Adeno mice failed to exhibit this preference, indicating impaired recognition memory (Figure 5B, C).

Spatial working memory was assessed using the Y-maze test, which records sequences of arm entries to analyze the percentage of spontaneous alternations (Figure 5D). APP/PS1-TauP301L-Adeno mice exhibited a significant reduction in spontaneous alternations compared to age-matched WT and APP/PS1-TauP301L mice, highlighting deficits in spatial working memory (Figure 5E, F). These results suggest that adenovirus-induced reactive astrogliosis, together with mutant tau overexpression, not only accelerates pathological features of AD, such as NFT and Aβ plaque accumulation, severe reactive astrocytes, neuronal loss, and elevation of astrocytic GABA levels, but also contributes to hippocampus-dependent memory impairment.

To further corroborate these findings, cognitive dysfunction and memory performance were evaluated using the passive avoidance test (Figure 5G). During the acquisition phase, no significant differences were observed in the time taken to enter the dark chamber across groups, indicating similar

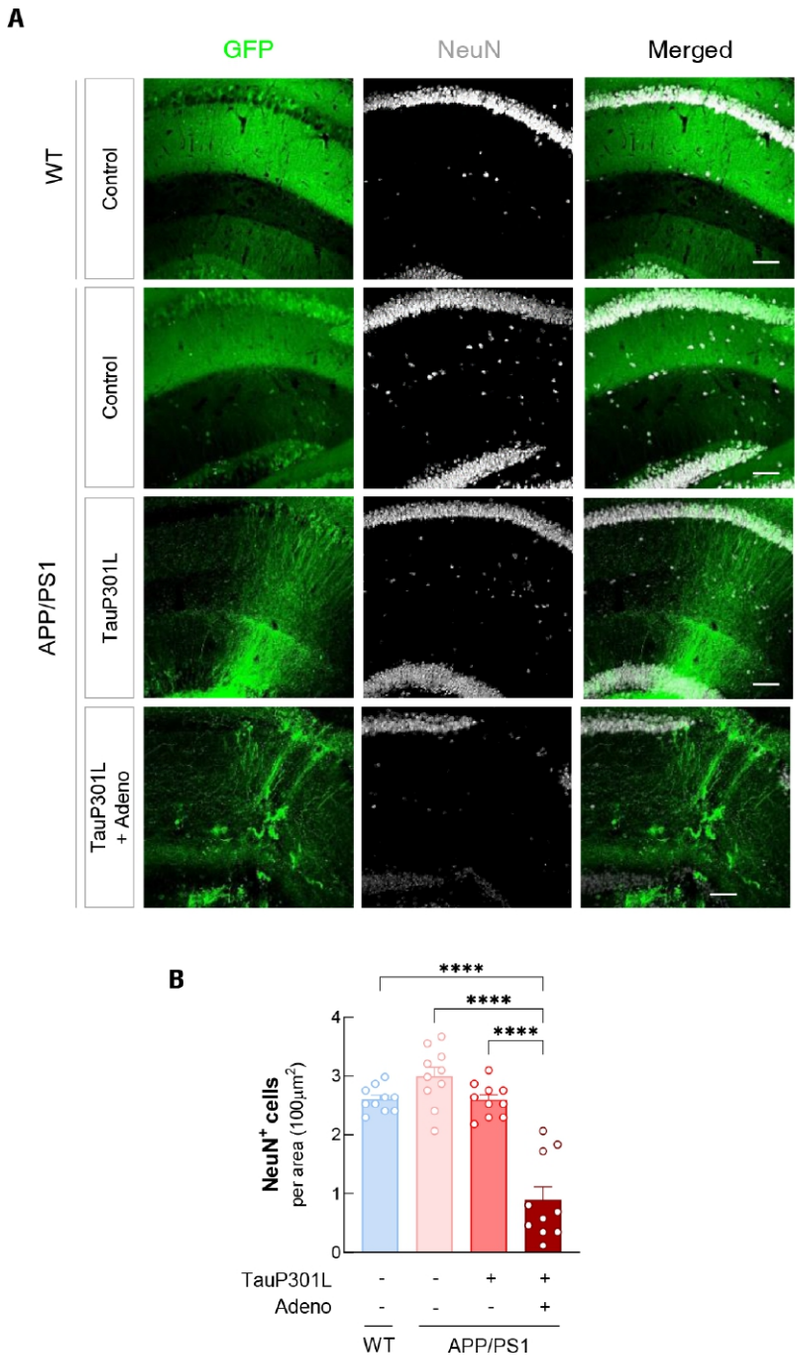


Figure 4 TauP301L overexpression and adenovirus-induced reactive astrogliosis in the hippocampus of APP/PS1 mice accelerates neurodegeneration

A: Representative confocal images of NeuN (neuron, white) in the CA1 pyramidal layer of 8-month-old WT-Control, APP/PS1-Control, APP/PS1-TauP301L, and APP/PS1-TauP301L-Adeno mice. Scale bars: 40 μm. B: Bar graph showing number of NeuN-positive cells per area (100 μm^2). Each bar represents mean±SEM. Sample sizes for all groups: n=10, with each dot representing the average count from three area per slice. Ten slices were analyzed from 3–4 mice per group. Mean±SEM values: WT-Control=2.605±0.069, APP/PS1-Control=2.995±0.157, APP/PS1-TauP301L=2.593±0.091, and APP/PS1-TauP301L-Adeno=0.895±0.226). Statistical analysis was conducted using one-way ANOVA with Tukey's *post-hoc* test, ****: P<0.0001.

baseline anxiety levels. During the retention phase conducted 24 h post-electrical shock, the APP/PS1-TauP301L-Adeno mice displayed a significantly shorter latency to enter the dark chamber compared to WT mice (Figure 5H), indicating that the simultaneous induction of mutant tau and adenovirus-induced reactive astrogliosis in APP/PS1 mice exacerbates impairment of hippocampus-dependent memory, consistent with the NOR and Y-maze results.

Taken together, these findings establish APP/PS1-TauP301L-Adeno mice as a robust animal model of AD, in which augmented reactive astrogliosis by Adeno-GFAP-GFP infection in the presence of toxic molecules such as Aβ and p-Tau further amplifies the aggregation of Aβ plaques and NFTs, ultimately exacerbating pathological symptoms of AD, such as neuronal loss and memory deficits (Figure 6). This model offers a valuable tool for investigating the mechanistic

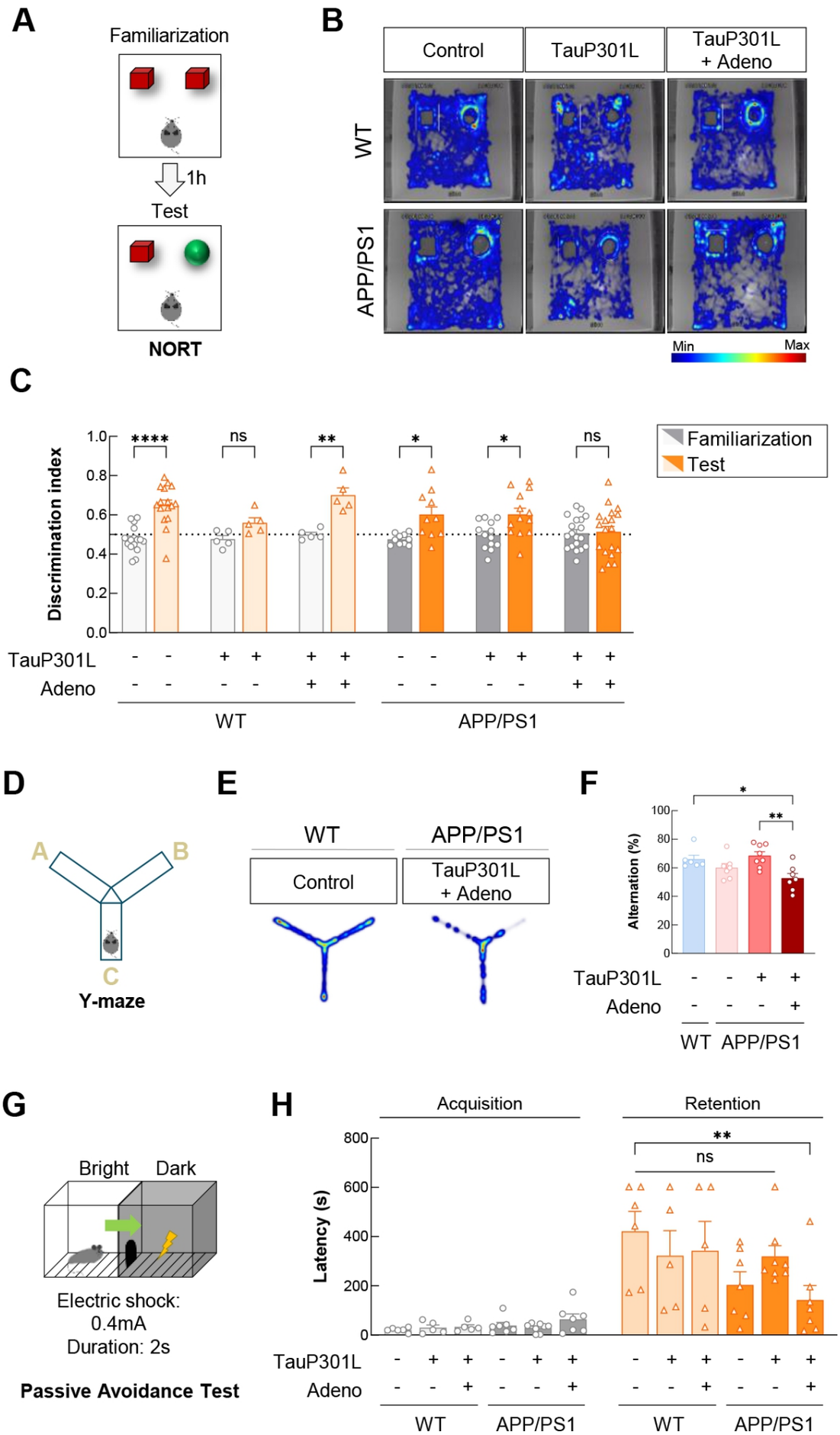

A
Familiarization
1h
Test
NORT
B
Control
TauP301L
TauP301L + Adeno
WT
APP/PS1
Min
Max
C
Discrimination index
1.0
0.8
0.6
0.4
0.2
0.0
****
ns
**
*
*
ns
Familiarization
Test
TauP301L
Adeno
WT
APP/PS1
D
A
B
C
Y-maze
E
WT
APP/PS1
Control
TauP301L + Adeno
F
Alternation (%)
100
80
60
40
20
0
*
**
TauP301L
Adeno
WT
APP/PS1
G
Bright
Dark
Electric shock:
0.4mA
Duration: 2s
Passive Avoidance Test
H
Acquisition
Retention
Latency (s)
800
600
400
200
0
**
ns
TauP301L
Adeno
WT
APP/PS1
WT
APP/PS1

Figure 5 TauP301L overexpression and adenovirus-induced reactive astrogliosis in the hippocampus of APP/PS1 mice impairs hippocampus-dependent memory

A, B: Schematic of novel object recognition (NOR) test (A) and representative heatmap image in NOR square chamber (gray) during test session (B). C: Bar graph showing discrimination index, calculated as: Discrimination index=exploration time in novel object/total exploration time (novel+familiar). Each bar represents mean±SEM, with sample sizes (number of mice): WT-Control (n=16), WT-TauP301L (n=5), WT-TauP301L/Adeno (n=5), APP/PS1-Control (n=10), APP/PS1-TauP301L (n=13), and APP/PS1-TauP301L-Adeno (n=19). Statistical analysis was conducted using two-way ANOVA with Bonferroni test, ns: Not significant; *: P<0.05; **: P<0.01; ****: P<0.0001. Mean±SEM values: (Familiarization) WT-Control=0.475±0.016, WT-TauP301L=0.475±0.019, WT-TauP301L/Adeno=0.499±0.012, APP/PS1-Control=0.476±0.009, APP/PS1-TauP301L=0.497±0.019 and APP/PS1-TauP301L-Adeno=0.507±0.019. (Test) WT-Control=0.65±0.026, WT-TauP301L=0.56±0.025, WT-TauP301L/Adeno=0.7±0.037, APP/PS1-Control=0.602±0.039, APP/PS1-TauP301L=0.603±0.031, and APP/PS1-TauP301L-Adeno=0.513±0.028. D, E: Schematic of Y-maze (D) and representative heatmap of tracks (E) in Y-maze spontaneous alternation test. F: Bar graph showing average percentage of triad alternations relative to total arm entries. Each bar represents mean±SEM, with sample sizes (number of mice): WT-Control (n=6), APP/PS1-Control (n=7), APP/PS1-TauP301L (n=8), and APP/PS1-TauP301L-Adeno (n=7). Statistical analysis was conducted using one-way ANOVA with Tukey's *post-hoc* test, *: P<0.05; **: P<0.01. Mean±SEM values: WT-Control=65.855±2.892, APP/PS1-Control=59.946±2.999, APP/PS1-TauP301L=68.399±2.794, and APP/PS1-TauP301L-Adeno=52.629±3.402. G: Schematic of passive avoidance test (PAT). H: Bar graph showing time for latency to enter dark chamber. Each bar represents mean±SEM, with sample sizes (number of mice): WT-Control (n=6), WT-TauP301L (n=5), WT-TauP301L-Adeno (n=5), APP/PS1-Control (n=7), APP/PS1-TauP301L (n=8), and APP/PS1-TauP301L-Adeno (n=7). Statistical analysis was conducted using two-way ANOVA with Bonferroni test, ns: Not significant; **: P<0.01. Mean±SEM values: (Acquisition) WT-Control=20.75±3.748, WT-TauP301L=29.8±10.918, WT-TauP301L-Adeno=32.9±8.532, APP/PS1-Control=38.214±12.636, APP/PS1-TauP301L=29.188±6.408, APP/PS1-TauP301L-Adeno=63.886±21.87. (Retention) WT-Control=421.85±80.612, WT-TauP301L=322.5±101.528, WT-TauP301L-Adeno=342.4±119.582, APP/PS1-Control=203.614±53.403, APP/PS1-TauP301L=319.55±43.637, and APP/PS1-TauP301L-Adeno=142.471±58.3.

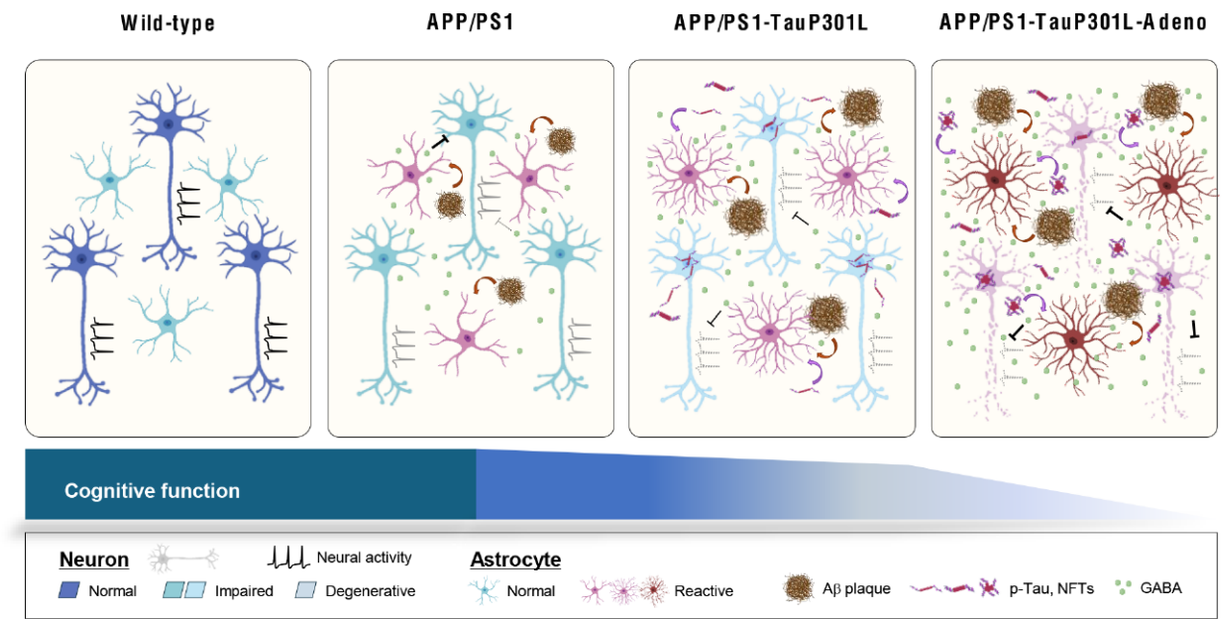


Figure 6 Summary of APP/PS1-TauP301L-Adeno mouse model

Summary figure illustrates progression of pathological features in both APP/PS1-TauP301L and APP/PS1-TauP301L-Adeno mice. At 8 months of age, 3 months post-injection, APP/PS1-TauP301L mice exhibited increased reactive astrogliosis and accumulation of Aβ plaque in the hippocampus compared to APP/PS1-control mice, but did not display any significant impairment of hippocampus-dependent cognitive function. In contrast, APP/PS1-TauP301L-Adeno mice showed exacerbated reactive astrogliosis and further accumulation of Aβ plaques, as well as NFT development, further exacerbating hippocampus-dependent cognitive impairment.

interplay between reactive astrogliosis, tau pathology, and Aβ deposition in AD progression.

DISCUSSION

As a highly prevalent neurodegenerative disorder, AD is characterized by cognitive decline, neuronal loss, and hippocampal atrophy, with key pathological features such as Aβ plaques, p-tau, and NFTs. Inflammatory responses, such as microglial activation and reactive astrogliosis, are also integral components of AD pathology (Bloom, 2014; Kinney et al., 2018). Current treatment options provide limited symptomatic relief and fail to modify the underlying disease progression, highlighting the need for a deeper understanding of disease mechanisms and the development of early-stage therapeutic strategies before irreversible pathological changes occur.

Reliable animal models that accurately recapitulate AD pathophysiology are critical for advancing preventive, diagnostic, and therapeutic approaches. Among these, APP/PS1 mice, which harbor familial AD-associated mutations in the *APP* and *PS1* genes, are widely used in AD research (Chen & Zhang, 2022; Wang et al., 2024). This model exhibits hallmark features of AD, including reactive astrocytes and

activated microglia surrounding Aβ deposits as early as 2 months of age (Radde et al., 2006) and mild memory impairment from 5 months of age (Zhu et al., 2017). Astrocytes are known to respond to Aβ, with reactive astrogliosis histologically detectable before plaque formation (Heneka et al., 2005; Pike et al., 1994), suggesting that reactive astrogliosis may serve as an early indicator of neurological disorders.

Several studies have demonstrated that aberrant tonic GABA released from reactive astrocytes activates extrasynaptic $GABA_A$ receptors on neighboring neurons, leading to impaired neuronal activity and memory deficits (Chun et al., 2020; Jo et al., 2014). These findings highlight a pivotal role for reactive astrogliosis in early AD pathology, with synaptic dysfunction occurring before overt neurodegeneration. Notably, neuronal death is not observed in APP/PS1 mice until approximately 12 months of age (Matousek et al., 2012), with modest neuronal loss becoming apparent only by 17 months (Rupp et al., 2011). These observations suggest that memory deficits in AD are initially driven by synaptic impairments mediated by reactive astrogliosis, rather than by direct neuronal loss.

The 6xTg mouse model, generated by crossbreeding 5xFAD mice with TauP301L-expressing mice, has recently been introduced as a potential model for AD. This model exhibits rapid onset of pathology, with Aβ deposits appearing at 2 months of age, NFTs developing by 4 months of age, and cognitive impairment detectable as early as 2 months of age (Kang et al., 2021). Despite the rapid onset of histological pathology and cognitive decline in 6xTg mice, establishing causal relationships among amyloid pathology, tau pathology, and reactive astrogliosis remains challenging.

To address these limitations, we developed the APP/PS1-TauP301L-Adeno mouse model, designed to investigate the individual effects of Aβ plaques, mutant tau, and reactive astrogliosis on AD progression in a spatially and temporally specific manner (Figure 6). This optimized model demonstrated intensified Aβ deposition (Figure 2), increased NFT formation (Figure 1), and severe reactive astrogliosis (Figure 1) at 8 months of age, 3 months after the introduction of both mutant tau overexpression and adenovirus-induced reactive astrogliosis into the hippocampus of APP/PS1 mice. These pathological changes were associated with accelerated neuronal loss (Figure 4) and significant memory deficits (Figure 5).

In contrast, APP/PS1 mice with mutant tau overexpression alone, without adenovirus-induced reactive astrogliosis, exhibited only minor pathological changes. Although slight but significant increases in astrogliosis, p-tau, and Aβ plaque accumulation were observed compared to APP/PS1-Control mice, these mice showed no substantial neurodegeneration or memory impairment (Figures 4, 5). These results highlight the critical role of adenovirus-induced reactive astrogliosis in exacerbating the neurodegenerative and cognitive deficits associated with Aβ plaques and p-tau. In addition to the various pathological phenotypes and symptoms identified in our novel animal model, further research is needed to validate additional pathological features of AD, such as synapse loss and microglial activation.

Interestingly, reactive astrocytes play a paradoxical role in neurodegenerative diseases. On the one hand, astrocytes initiate detoxification pathways, such as the autophagy-to-urea pathway, to clear toxic molecules including Aβ oligomers and diphtheria toxin (Chun et al., 2020; Ju et al., 2022; Kim et al., 2024). However, in AD mouse models, Aβ accumulation disrupts astrocytic autophagy, which exacerbates Aβ plaque accumulation (Kim et al., 2024). The addition of tau pathology in APP/PS1 mice, such as NFT formation, may further disrupt astrocytic autophagy, thereby accelerating Aβ plaque accumulation (Figure 2). Although the autophagy-to-urea cycle is generally beneficial, its downstream product, putrescine, is metabolized into GABA via the MAO-B activity, a process with detrimental implications (Ju et al., 2022). Astrocytic GABA impairs CA1 pyramidal neuronal activity and contributes to memory deficits in APP/PS1 mice (Jo et al., 2014; Park et al., 2019). In addition to GABA production, severe astrocytic reactivity leads to neurodegeneration and brain atrophy through MAO-B and its by-product, H_2O_2 (Chun et al., 2020). Given these findings, future studies are needed to investigate the involvement of H_2O_2 in neurodegeneration and memory deficits in APP/PS1-TauP301L-Adeno mice.

Our animal model, in line with previous studies, primarily focuses on early-onset familial AD associated with mutations in APP, PS1, and TauP301L (Chen & Zhang, 2022; Wang et al., 2024). However, the majority of AD cases involve late-onset sporadic AD, which is not linked to specific genetic mutations. The absence of a clear genetic marker for sporadic AD presents a significant challenge in developing appropriate animal models (Chen & Zhang, 2022). Emerging evidence suggests that mitochondrial dysfunction, oxidative stress, and neuroinflammation in reactive astrocytes (Chun et al., 2020; Ju et al., 2022; Kim et al., 2024) may precede the abundant accumulation of Aβ plaques or Tau pathology (Krstic & Knuesel, 2013; Zlokovic, 2011). These early disruptions may play a critical role in the pathogenesis of late-onset sporadic AD. Thus, we propose that reactive astrocytes induced by Adeno-GFAP-GFP may also serve as a valuable strategy for sporadic AD research.

In conclusion, this study introduces APP/PS1-TauP301L-Adeno mice as a promising and novel AD mouse model. By leveraging spatial and temporal-specific genetic manipulation of tau pathology and reactive astrogliosis through the injection of AAV-TauP301L and Adeno-GFAP-GFP into the hippocampus of APP/PS1 mice, this model recapitulates key pathological hallmarks of AD. Notably, these mice exhibit a marked increase in Aβ plaques and tau pathology, manifesting significantly earlier than in established APP/PS1 mice. This time-efficient model provides a promising framework for studying AD progression and exploring therapeutic interventions, with potential applicability to both familial and sporadic forms of the disease.

SUPPLEMENTARY DATA

Supplementary data to this article can be found online.

COMPETING INTERESTS

The authors declare that they have no competing interests.

AUTHORS' CONTRIBUTIONS

S.J.O. and M.H.N. conceived and designed the project. Y.E.H. and S.L. performed the behavioral and molecular experiments, immunohistochemical analysis, and statistical analyses, and wrote the manuscript. S.E.L. designed the viral vector and produced all types of virus we used. M.H.N. provided technical support and conceptual advice. S.J.O. supervised the project. All authors read and approved the final version of the manuscript.

REFERENCES

Adolfsson R, Gottfries CG, Oreland L, et al. 1980. Increased activity of brain and platelet monoamine oxidase in dementia of Alzheimer type. *Life Sciences*, **27**(12): 1029–1034.

An H, Lee H, Yang S, et al. 2021. Adenovirus-induced reactive astrogliosis exacerbates the pathology of Parkinson's disease. *Experimental Neurobiology*, **30**(3): 222–231.

Bardehle S, Krüger M, Buggenthin F, et al. 2013. Live imaging of astrocyte responses to acute injury reveals selective juxtavascular proliferation. *Nature Neuroscience*, **16**(5): 580–586.

Bloom GS. 2014. Amyloid-β and Tau: the trigger and bullet in Alzheimer disease pathogenesis. *JAMA Neurology*, **71**(4): 505–508.

Chen ZY, Zhang Y. 2022. Animal models of Alzheimer's disease: applications, evaluation, and perspectives. *Zoological Research*, **43**(6): 1026–1040.

Chun H, Im H, Kang YJ, et al. 2020. Severe reactive astrocytes precipitate pathological hallmarks of Alzheimer's disease via $H_2O_2^-$ production. *Nature Neuroscience*, **23**(12): 1555–1566.

Di J, Cohen LS, Corbo CP, et al. 2016. Abnormal tau induces cognitive impairment through two different mechanisms: synaptic dysfunction and neuronal loss. *Scientific Reports*, **6**: 20833.

Drummond E, Wisniewski T. 2017. Alzheimer's disease: experimental models and reality. *Acta Neuropathologica*, **133**(2): 155–175.

Gomes LA, Hipp SA, Rijal Upadhaya A, et al. 2019. Aβ-induced acceleration of Alzheimer-related τ-pathology spreading and its association with prion protein. *Acta Neuropathologica*, **138**(6): 913–941.

Heneka MT, Sastre M, Dumitrescu-Ozimek L, et al. 2005. Focal glial activation coincides with increased BACE1 activation and precedes amyloid plaque deposition in APP[V717I] transgenic mice. *Journal of Neuroinflammation*, **2**: 22.

Ingelsson M, Fukumoto H, Newell KL, et al. 2004. Early Aβaccumulation and progressive synaptic loss, gliosis, and tangle formation in AD brain. *Neurology*, **62**(6): 925–931.

Jackson RJ, Rudinskiy N, Herrmann AG, et al. 2016. Human tau increases amyloid βplaque size but not amyloid β-mediated synapse loss in a novel mouse model of Alzheimer's disease. *European Journal of Neuroscience*, **44**(12): 3056–3066.

Jiwaji Z, Tiwari SS, Avilés-Reyes RX, et al. 2022. Reactive astrocytes acquire neuroprotective as well as deleterious signatures in response to Tau and Ass pathology. *Nature Communications*, **13**(1): 135.

Jo S, Yarishkin O, Hwang YJ, et al. 2014. GABA from reactive astrocytes impairs memory in mouse models of Alzheimer's disease. *Nature Medicine*, **20**(8): 886–896.

Ju YH, Bhalla M, Hyeon SJ, et al. 2022. Astrocytic urea cycle detoxifies Aβ-derived ammonia while impairing memory in Alzheimer's disease. *Cell Metabolism*, **34**(8): 1104–1120. e8.

Jul P, Volbracht C, de Jong IEM, et al. 2016. Hyperactivity with agitative-like behavior in a mouse tauopathy model. *Journal of Alzheimer's Disease*, **49**(3): 783–795.

Kang S, Kim J, Chang KA. 2021. Spatial memory deficiency early in 6xTg Alzheimer's disease mouse model. *Scientific Reports*, **11**(1): 1334.

Kato S, Gondo T, Hoshii Y, et al. 1998. Confocal observation of senile plaques in Alzheimer's disease: senile plaque morphology and relationship between senile plaques and astrocytes. *Pathology International*, **48**(5): 332–340.

Kim S, Chun H, Kim Y, et al. 2024. Astrocytic autophagy plasticity modulates Aβ clearance and cognitive function in Alzheimer's disease. *Molecular Neurodegeneration*, **19**(1): 55.

Kinney JW, Bemiller SM, Murtishaw AS, et al. 2018. Inflammation as a central mechanism in Alzheimer's disease. *Alzheimer's & Dementia*: *Translational Research & Clinical Interventions*, **4**: 575–590.

Knowles RB, Wyart C, Buldyrev SV, et al. 1999. Plaque-induced neurite abnormalities: implications for disruption of neural networks in Alzheimer's disease. *Proceedings of the National Academy of Sciences of the United States of America*, **96**(9): 5274–5279.

Krstic D, Knuesel I. 2013. Deciphering the mechanism underlying late-onset Alzheimer disease. *Nature Reviews Neurology*, **9**(1): 25–34.

Lee Y, Messing A, Su M, et al. 2008. *GFAP* promoter elements required for region-specific and astrocyte-specific expression. *Glia*, **56**(5): 481–493.

Malek-Ahmadi M, Perez SE, Chen KW, et al. 2016. Neuritic and diffuse plaque associations with memory in non-cognitively impaired elderly. *Journal of Alzheimer's Disease*, **53**(4): 1641–1652.

Matousek SB, Ghosh S, Shaftel SS, et al. 2012. Chronic IL-1β-mediated neuroinflammation mitigates amyloid pathology in a mouse model of Alzheimer's disease without inducing overt neurodegeneration. *Journal of Neuroimmune Pharmacology*, **7**(1): 156–164.

Nam MH, Cho J, Kwon DH, et al. 2020. Excessive astrocytic GABA causes cortical hypometabolism and impedes functional recovery after subcortical stroke. *Cell Reports*, **32**(3): 107975.

Nam MH, Ko HY, Kim D, et al. 2023. Visualizing reactive astrocyte-neuron interaction in Alzheimer's disease using ^{11}C-acetate and ^{18}F-FDG. *Brain*, **146**(7): 2957–2974.

Park JH, Ju YH, Choi JW, et al. 2019. Newly developed reversible MAO-B inhibitor circumvents the shortcomings of irreversible inhibitors in Alzheimer's disease. *Science Advances*, **5**(3): eaav0316.

Pike CJ, Cummings BJ, Monzavi R, et al. 1994. β-amyloid-induced changes in cultured astrocytes parallel reactive astrocytosis associated with senile plaques in Alzheimer's disease. *Neuroscience*, **63**(2): 517–531.

Querfurth HW, Laferla FM. 2010. Alzheimer's disease. *New England Journal of Medicine*, **362**(4): 329–344.

Radde R, Bolmont T, Kaeser SA, et al. 2006. Aβ42-driven cerebral amyloidosis in transgenic mice reveals early and robust pathology. *EMBO Reports*, **7**(9): 940–946.

Rupp NJ, Wegenast-Braun BM, Radde R, et al. 2011. Early onset amyloid lesions lead to severe neuritic abnormalities and local, but not global neuron loss in APPPS1 transgenic mice. *Neurobiology of Aging*, **32**(12): 2324.e1–6.

Selkoe D, Kopan R. 2003. Notch and presenilin: regulated intramembrane proteolysis links development and degeneration. *Annual Review of Neuroscience*, **26**: 565–597.

Shirley JL, De Jong YP, Terhorst C, et al. 2020. Immune responses to viral gene therapy vectors. *Molecular Therapy*, **28**(3): 709–722.

Simpson JE, Ince PG, Lace G, et al. 2010. Astrocyte phenotype in relation to Alzheimer-type pathology in the ageing brain. *Neurobiology of Aging*, **31**(4): 578–590.

Wang Q, Zhu BT, Lei P. 2024. Animal models of Alzheimer's disease: Current strategies and new directions. *Zoological Research*, **45**(6): 1385–1407.

Wang TQ, Chen Y, Zou Y, et al. 2022. Locomotor hyperactivity in the early-stage Alzheimer's disease-like pathology of APP/PS1 mice: associated with impaired polarization of astrocyte aquaporin 4. *Aging and Disease*, **13**(5): 1504–1522.

Woo J, Im SK, Chun H, et al. 2017. Functional characterization of resting and adenovirus-induced reactive astrocytes in three-dimensional culture. *Experimental Neurobiology*, **26**(3): 158–167.

Yamada T, Kawamata T, Walker DG, et al. 1992. Vimentin immunoreactivity in normal and pathological human brain tissue. *Acta Neuropathologica*, **84**(2): 157–162.

Zhu SH, Wang JH, Zhang YB, et al. 2017. The role of neuroinflammation and amyloid in cognitive impairment in an APP/PS1 transgenic mouse model of Alzheimer's disease. *CNS Neuroscience & Therapeutics*, **23**(4): 310–320.

Zlokovic BV. 2011. Neurovascular pathways to neurodegeneration in Alzheimer's disease and other disorders. *Nature Reviews Neuroscience*, **12**(12): 723–738.

Liu et al. *Zool. Res.* 2025, 46(1): 54−74
https://doi.org/10.24272/j.issn.2095-8137.2024.336
https://cstr.cn/32248.14.zr.2024.336

ZR | Zoological Research

Article Open Access

Ribosome profiling and single-cell RNA sequencing identify the unfolded protein response as a key regulator of pigeon lactation

Jing Liu[2,#], San-Feng Liu[2,3,#], Hui-Rong Mao[2,3,#], Hong-Xia Jiang[2,3], Shui-Bing Liu[2,3], Xiao-Fei Xu[4], Jin-Tao Wu[2,3], Xun Liu[2,3], Wen-Tao Zhang[2,3], Xiao-Long Hu[2,3], Biao Chen[1,2,3,*]

[1] *National Key Laboratory for Swine Genetic Improvement and Germplasm Innovation*, *Ministry of Science and Technology of China*, *Jiangxi Agricultural University*, *Nanchang*, *Jiangxi* 330045, *China*

[2] *College of Animal Science and Technology*, *Jiangxi Agricultural University*, *Nanchang*, *Jiangxi* 330045, *China*

[3] *Poultry Institute*, *Jiangxi Agricultural University*, *Nanchang*, *Jiangxi* 330045, *China*

[4] *Zhongshan Shiqi Pigeon Breeding Limited Company*, *Zhongshan*, *Guangdong* 528400, *China*

ABSTRACT

Pigeons and certain other avian species produce a milk-like secretion in their crop sacs to nourish offspring, yet the detailed processes involved are not fully elucidated. This study investigated the crop sacs of 225-day-old unpaired non-lactating male pigeons (MN) and males initiating lactation on the first day after incubation (ML). Using RNA sequencing, ribosome profiling, and single-cell transcriptome sequencing (scRNA-seq), we identified a significant up-regulation of genes associated with ribosome assembly and protein synthesis in ML compared to MN. Results from scRNA-seq analysis identified 12 distinct cell types and 22 clusters, with secretory epithelial cells (SECs) exhibiting marked expression of plasma cell markers, including *IGLL1* and *MZB1*. RNA fluorescence *in situ* hybridization (RNA FISH) and IgY quantification confirmed the critical role of SECs in producing endogenous IgY during lactation. We propose that fibroblast-derived BAFF signals activate SECs, mimicking B cell transformation and enhancing protein production through the unfolded protein response (UPR). These findings shed light on the cellular dynamics of pigeon milk production and contribute to a broader understanding of avian biology.

Keywords: Pigeon; Crop lactation; Secretory epithelial cells; Single-cell RNA sequencing; Ribosome profiling; Signaling pathway

INTRODUCTION

Lactation, a critical process for offspring survival, has been extensively explored across various species (Capuco & Akers, 2009; Dai et al., 2022). Mammalian lactation and nursing behaviors support neonatal growth, immune defense, and the establishment of mother-offspring bonds (Fewtrell et al., 2020). While lactation is exceptionally rare in birds, certain species, such as pigeons (*Columbidae*), produce crop milk, a nutrient-rich substance essential for chick development (Horseman & Buntin, 1995). Similar to mammalian milk, crop milk is rich in proteins, lipids, and immunoglobulins, providing both nutritional support and immunological protection to offspring (Gillespie et al., 2012). Notably, both male and female pigeons can produce this secretion, a unique adaptation that has garnered considerable scientific interest (Wang et al., 2023c). Despite these intriguing features, the mechanisms governing pigeon crop milk production remain poorly understood, particularly in light of China's recent reclassification of pigeons as poultry (https://www.gov.cn/xinwen/2020-05/29/content_5515954.htm), which has driven expansion in the pigeon meat industry.

Crop milk in pigeons is synthesized and secreted by epithelial cells lining the crop sac, a process regulated through cell division, protein and lipid biosynthesis, and holocrine secretion (Horseman & Buntin, 1995). This complex mechanism involves precise coordination of genetic, cellular, and physiological pathways. The IRS1/Akt/TOR signaling pathway has been implicated in the regulation of protein synthesis during domestic pigeon lactation (Hu et al., 2016). Recent studies have identified regulatory roles for long non-coding RNAs (lncRNAs), messenger RNA (mRNAs), and circular RNAs (circRNAs) in this process, providing insights into the underlying molecular mechanisms (Ma et al., 2020,

This is an open-access article distributed under the terms of the Creative Commons Attribution Non-Commercial License (http://creativecommons.org/licenses/by-nc/4.0/), which permits unrestricted non-commercial use, distribution, and reproduction in any medium, provided the original work is properly cited.

Copyright ©2025 Editorial Office of Zoological Research, Kunming Institute of Zoology, Chinese Academy of Sciences

Received: 30 September 2024; Accepted: 22 November 2024; Online: 23 November 2024

Foundation items: This work was supported by the Department of Agriculture and Rural Affairs of Jiangxi Province, China (JXARS-09), and Science and Technology Program of Guangdong Province, China (2020B1212060060)

[#]Authors contributed equally to this work

*Corresponding author, E-mail: chenbiao@jxau.edu.cn

2022). Transcriptome analyses have also revealed important roles for genes involved in cornification and triglyceride synthesis, which are essential for milk production (Gillespie et al., 2013). Furthermore, Wang et al. (2023c) identified various lactation-associated genes involved in lipid and protein metabolism and demonstrated the impact of promoter-enhancer reorganization on the occurrence of rapid morphological and functional changes in the pigeon crop during lactation. However, key questions remain and the secretion and regulatory mechanisms underlying pigeon crop lactation have yet to be determined. It is also unclear whether immunoglobulins are synthesized directly by epithelial cells in the crop sac or derived from lymphoid tissues and transported via the bloodstream, similar to mammalian systems (Liao et al., 2024).

Single-cell RNA sequencing (scRNA-seq) is a powerful technique for delineating cellular populations and elucidating biological processes at the single-cell level (Cao et al., 2019; Li et al., 2024; Mantri et al., 2021). High-throughput ribosome sequencing (Ribo-seq), which captures mRNA fragments bound to active ribosomes, facilitates precise measurement of translational activity and protein synthesis rates (Ferguson et al., 2023; Ingolia et al., 2009). To explore the mechanisms underlying pigeon milk secretion, this study investigated the heterogeneity of the crop sac at single-cell resolution. Ribo-seq was applied to assess RNA translation efficiency, while integrated RNA-seq was employed for in-depth analysis of the biological processes involved in protein and fat synthesis within crop sac epithelial cells. Our findings revealed that secretory epithelial cells (SECs) synthesize pigeon milk and immunoglobulins via the unfolded protein response (UPR) pathway, offering a robust framework for understanding avian crop sac secretion mechanisms and physiological processes relevant to poultry incubation.

MATERIALS AND METHODS

Ethical statement

All animal experiments conducted in this study received approval from the Animal Ethics Committee of Jiangxi Agricultural University (approval number [2018]30). All animals were handled in accordance with humane treatment protocols.

Animal experiments

A total of 200 pigeons (100 males and 100 females) were procured from Zhongshan Shiqi Pigeon Breeding Ltd. Co. (China). The pigeons were separated by sex and reared in the reserve breeder room of the same farm, following standardized feeding protocols. At 180 days of age, 50 male and female reserve breeders were paired, while the remaining 50 male and 50 female pigeons were maintained unpaired. The paired breeders laid and incubated their eggs through natural incubation. On the day the first chick hatched (225 days), 10 paired male breeders were selected as the pigeon milk group (male-lactating group, ML) and 10 unpaired male breeders were selected as the control group (male-non-lactating group, MN). Following sacrifice, tissue samples were collected, including the left and right lobes of the crop, crop sac contents, brain, cerebellum, hypothalamus, pituitary, liver, and spleen. Crop sac tissues used for scRNA-seq were washed in phosphate-buffered saline (PBS) (Thermo Fisher, USA) and subsequently incubated in a Type I collagenase solution (Thermo Fisher, USA) to generate single-cell suspensions. Samples for histological examination were fixed in 4% paraformaldehyde (Servicebio, China), while those intended for long-term storage were rapidly frozen in liquid nitrogen and preserved at –80°C.

Histological observation

Fixed tissue samples were dehydrated in ethanol (Servicebio, China) solutions (75%, 85%, 95% I, 95% II, 100% I, 100% II) for 60 min per step, cleared in xylene I and II (Servicebio, China) for 45 min each, infiltrated in paraffin I, II, and III (Servicebio, China) for 50–60 min each, embedded in paraffin, and sectioned. The sections were deparaffinized by baking and sequentially immersed in xylene I and II (10 min each), anhydrous ethanol I and II (Servicebio, China) (3 min each), 95% alcohol (3 min), 80% alcohol (3 min), and pure water (Servicebio, China) (2 min). Staining involved hematoxylin (Servicebio) (3–5 min), rinsing, differentiation with 1% hydrochloric acid alcohol (Servicebio, China), bluing, rinsing, eosin staining (Servicebio, China) (3–5 min), and rinsing.

Stained sections were rapidly dehydrated using 80% ethanol, 95% ethanol, and anhydrous ethanol (I and II) (Servicebio, China), then mounted with a super clean advanced medium. Images were taken using a Nikon TS2R-FL fluorescence inverted microscope (China).

Transcriptome RNA-seq and data analysis

RNA was extracted from three samples each from the ML and MN groups using Trizol reagent (Thermo Fisher, USA), as per the provided manual. RNA quality was assessed through agarose gel electrophoresis, Agilent 2100 Bioanalyzer (Agilent, USA), and a Nanodrop spectrophotometer. Samples passing quality control were used for RNA library construction, with mRNA purified, fragmented, converted to cDNA, and ligated with adapters. After purification and amplification, the library underwent quality control before being sequenced using PE150 on the Illumina NovaSeq 6000 platform (Genedenovo, China), following the company's guidelines.

Quality control was performed using Fastp to filter low-quality data, resulting in clean reads suitable for downstream analysis (Chen et al., 2018). Sequence alignment was conducted using Hisat2, mapping the clean reads to the pigeon reference genome (https://www.ncbi.nlm.nih.gov/datasets/genome/GCA_000337935.2/) (Kim et al., 2015). The transcriptome was reconstructed using StringTie (Pertea et al., 2015), and gene expression levels were quantified using RSEM (RNA-Seq by Expectation Maximization) (Li & Dewey, 2011), with expression levels represented as fragments per kilobase of transcript per million mapped reads (FPKM). Principal component analysis (PCA) analysis and Pearson correlation analysis were conducted in R to assess sample relationships. Differential gene analysis was conducted using the R package edgeR with a filter threshold of false discovery rate (FDR)<0.05 and $|\log_2 FC|>1$(Robinson et al., 2010). Gene Ontology (GO) and Kyoto Encyclopedia of Genes and Genomes (KEGG) enrichment analysis of differentially expressed genes (DEGs) was conducted using the Omicsmart online tool (https://www.omicsmart.com/). Gene set enrichment analysis (GSEA) and MSigDB were used to identify differentially expressed pathways between two groups. Gene ranking was performed using the Signal2Noise method and enrichment scores (ES), *P*-values, and FDR values were calculated using default parameters.

Ribosome profile sequencing

Ribosome profiling was performed following previously

established methods (Wang et al., 2023a). Briefly, tissue lysates from three samples each of the ML group and MN groups were prepared. Tissues were lysed in lysis buffer, transferred to new microtubes, mixed by pipetting, and incubated on ice for 10 min. The resulting lysates were triturated 10 times using a 26-G needle, then subjected to centrifugation at 20 000 ×*g* for 10 min at 4°C, with the resulting supernatant collected. To generate ribosome footprints (RFs), 10 μL of RNase I (New England Biolabs (NEB), USA) and 6 μL of DNase I (NEB, USA) were added to 400 μL of lysate. The mixture was incubated for 45 min at room temperature with gentle mixing on a Nutator mixer. Nuclease activity was halted with 10 μL of SUPERase·In RNase inhibitor (Ambion, USA). Size exclusion columns (Illustra MicroSpin S-400 HR Columns; GE Healthcare; cat. no. 27-5140-01, USA) were equilibrated with 3 mL of polysome buffer via gravity flow, then centrifuged at 600 ×*g* for 4 min at room temperature. Following this, 100 μL of the digested RFs was introduced to the column and centrifuged again at 600 ×*g* for 2 min at room temperature. The eluted RFs were treated with 10 μL of a 10% (wt/vol) sodium dodecyl sulfate (SDS) solution, and RFs longer than 17 nucleotides were isolated using an RNA Clean and Concentrator-25 Kit (Zymo Research, #R1017, China). Short antisense DNA probes (50–80 bases) complementary to rRNA sequences were added to the RF solution, followed by the addition of RNase H (NEB, USA) and DNase I to degrade rRNA and residual DNA probes. The RFs underwent further purification using magnetic beads (Vazyme, China).

Ribo-seq libraries were prepared using the NEBNext® Multiple Small RNA Library Prep Set for Illumina® (cat. no. E7300S, E7300L, USA). Adapters were ligated to both ends of the RFs, followed by reverse transcription polymerase chain reaction (RT-PCR). The resulting PCR products (140–160 bp) were enriched to generate a cDNA library, which was subsequently sequenced on the Illumina HiSeq™ X10 platform (USA) by Genedenovo (China).

Raw reads were processed for quality control using Fastp to generate clean reads (Chen et al., 2018). Reads were mapped to the rRNA, GenBank, and Rfam databases using Bowtie2 (Pertea et al., 2015) to remove sequences corresponding to rRNAs, tRNAs, snRNAs, snoRNAs, and miRNAs. The remaining reads were aligned to the pigeon genome (https://www.ncbi.nlm.nih.gov/datasets/genome/GCA_000337935.2/) using STAR with the 2-pass setting enabled (Dobin et al., 2013). The RFs were subsequently classified according to genomic features, including the 5' untranslated region (UTR), coding sequence (CDS), 3'UTR, and intronic regions, determined by the 5' end position of the alignment. Three-nucleotide periodicity was then analyzed and visualized using the riboWaltz R package (Lauria et al., 2018). RFs of specific lengths were allocated to frames 1, 2, or 3 according to their 5' end positions within protein-coding genes, and the frame distribution proportions were computed for all protein-coding genes. Global single codon pauses were analyzed using PausePred (https://pausepred.ucc.ie/). Read counts for coding regions were calculated using RSEM (Li & Dewey, 2011), and expression levels were normalized to FPKM. Differentially translated genes (DTGs) between MN and ML were identified using edgeR. Genes with a fold change≥2 and FDR<0.05 were considered significant DTGs (Robinson et al., 2010). GO, KEGG, and GSEA enrichment analyses were performed following previously described methods (https://www.omicsmart.com/).

Combined translatomic and transcriptomic analysis

To investigate the relationship between gene expression and translation levels, Pearson correlation analysis was performed, with results visualized using a scatter plot. Based on changes at the transcriptional and translational levels, genes were classified into five groups: transcription (significantly different only at the transcriptional level); translation (significantly different only at the translational level); homodirection (significantly different at both levels with consistent trends); opposite (significantly different at both levels with opposite trends); and unchanged (not significantly different at either levels). Genes from these groups were subjected to GO and KEGG pathway enrichment analyses. Translation efficiency (TE), defined as the ratio of translating mRNAs to total mRNAs for a given gene, was calculated and compared between samples and groups using the following formula:

$$TE = \frac{FPKM \text{ in Ribo-seq}}{FPKM \text{ in RNA-seq}} \quad (1)$$

Differential translation efficiency between groups was analyzed using RiboDiff (Zhong et al., 2017), identifying genes with a fold change≥2 and FDR<0.05. These significant genes, classified as differential translation efficiency genes (DTEGs), were subsequently subjected to GO and KEGG pathway enrichment analyses.

Quantitative real-time polymerase chain reaction (qPCR) validation

For qPCR validation, the cDNA library was prepared as per the manufacturer's specification. Reverse transcription was performed using a Monad MonScript™ All-in-One Kit with DNase (Biopro, China), and qPCR for candidate genes was performed using 2×T5 Fast qPCR Mix (Tsingke, China) kit. Quantitative primers for candidate genes were designed using NCBI Blast and synthesized by Hunan Tsingke Biotech (China). Primer details are provided in Supplementary Table S1. The qPCR results are presented as mean±standard error of the mean (SEM), and differences between MN and ML were analyzed using Student's *t*-test.

Preparation of single-cell suspension, library construction, and sequencing

Crop sac tissues from each group were digested with 0.1 mg/ml Type I collagenase (Thermo Fisher, USA) at 37°C for 30 min with gentle shaking. Digestion was halted using Dulbecco's Modified Eagle Medium/Nutrient Mixture F-12 (DMEM/F12, Gibco, USA) with 15% fetal bovine serum (Gibco, USA). Cells were then collected by centrifugation at 1 300 r/min (centrifugal radius: 12 cm) for 5 min at 4°C, filtered through a 40-micron strainer, and resuspended in PBS with 1% bovine serum albumin (BSA) (Thermo Fisher, USA). A single-cell suspension was mixed with 0.4% trypan blue dye at a 9:1 ratio, and cell counting was performed using a Countess® II Automated Cell Counter (Thermo Fisher, USA) to ensure a live cell ratio of ≥90%. The cell concentration was adjusted to at least 1 000 cells/μL. Gel beads with barcodes were combined with the cell suspension and enzymes, then encapsulated in oil surfactant droplets using a microfluidic system to form Gel Bead-In-Emulsions (GEMs). The GEMs were collected, and gel beads were dissolved to release barcoded sequences, reverse transcribe cDNA fragments, and label samples. After breaking the gel beads and oil droplets, PCR amplification was performed using cDNA as a template.

The products from all GEMs were then combined to create a standard sequencing library. The cDNA was fragmented into 200–300 bp segments, and sequencing adapter P5 and primer R1 were added. The sequencing library was amplified by PCR and sequenced using the PE150 paired-end mode on the Illumina NovaSeq 6000 platform (Genedenovo, China).

scRNA-seq data analysis

Quality control, genome alignment, and gene quantification: Raw BCL files were converted to FASTQ format, aligned, and quantified using 10× Genomics Cell Ranger (v.3.1.0). Low-quality barcodes and Unique Molecular Identifiers (UMIs) were filtered out, and the remaining reads were mapped to the pigeon reference genome (https://www.ncbi.nlm.nih.gov/datasets/genome/GCA_000337935.2/). Only reads uniquely mapped to the transcriptome and overlapping an exon by at least 50% were counted. Cell Ranger employed STAR for aligning Read2 sequences from Illumina data to the pigeon reference genome. Using GTF annotation, reads were categorized as exonic, intronic, or intergenic. Exonic reads were subsequently re-aligned to annotated transcripts, during which barcodes and UMIs were filtered and corrected, ensuring cell barcodes exactly matched known sequences. UMIs with "N" or with a base quality score below 10 were removed. For each gene, UMIs with one mismatch to a higher count UMI (with the same barcode and gene ID) were corrected to the higher count UMI. Only reads with valid barcodes and UMIs were counted. For each barcode, UMIs per gene ID were deduplicated, and the unique UMIs were counted to determine gene expression in each cell.

Effective cell filtering: Effective cell filtering was initiated by sorting barcodes by UMI counts in descending order, selecting the top N barcodes, where N represents the expected cell count. The 99th percentile UMI count among these barcodes was defined as m. Barcodes with UMI counts below 10% of m were discarded, leaving the filtered set of effective cells. EmptyDrops was employed in Cell Ranger to identify effective barcodes with low RNA content (Lun et al., 2019). Barcodes with very low UMI counts were used to model empty GEMs, creating a background for comparison. A gene expression model for non-empty GEMs was constructed using the Good-Turing smoothing algorithm. Barcodes deemed ineffective were compared against the background model, and those significantly differing from this model were retained as effective cells.

Cell clustering analysis: Once Cell Ranger completed gene expression identification, the resulting expression matrix was processed using Seurat (v.2) for further analysis (Butler et al., 2018). Although Cell Ranger applied automatic filtering, additional filtering was conducted before subpopulation classification. This involved removing multi-cells based on their rate and excluding abnormal cells based on gene count, UMI count, and mitochondrial gene ratio. DoubletFinder was used to calculate the probability (pANN) of a GEM containing multiple cells (McGinnis et al., 2019). The multi-cell rate for each sample was then determined based on the effective cell count provided by 10× (post-Cell Ranger filtering). Multi-cells are subsequently filtered out based on the following criteria: (1) number of genes per cell (200–3 800), (2) total UMIs per cell (under 24 000), and (3) mitochondrial gene expression (under 25%). High-quality cells passing these thresholds were normalized using log normalization. Data merging and batch effect correction were performed using Harmony (Korsunsky et al., 2019). Cells were clustered using PCA in Seurat, with each principal component representing a set of genes with similar expression patterns. A graph-based clustering method was used, beginning with the calculation of Euclidean distance between cells based on principal components. A shared-nearest neighbor (SNN) graph was constructed from these distances and divided into quasi-groups using the local Jaccard distance. The Louvain algorithm was then applied to group the cells into clusters (Rotta & Noack, 2011). High-dimensional data were reduced to two dimensions using uniform manifold approximation and projection (UMAP), enabling visualization of cells with similar expression patterns (Becht et al., 2019). Cell types were annotated using SingleR, which compared expression patterns of the clustered cells to reference cells.

Analysis of up-regulated genes in subgroups: Differential gene expression analysis across cell subgroups was conducted using Seurat's rank-sum test. Up-regulated genes were selected based on the following criteria: $\log_2$FC≥0.36 (fold change≥1.28), P≤0.01, and expression detected in more than 25% of cells within the target subgroup. Protein-protein interaction (PPI) analysis for the identified genes was performed using STRING (v.12.0, https://string-db.org), and interaction networks were visualized using Cytoscape (v.3.7.1).

Differential expression analysis: Differential gene significance was evaluated using Seurat and the Model-based Analysis of Single-Cell Transcriptomics (MAST), with P-values adjusted for multiple testing. Genes were selected based on the following criteria: absolute $\log_2$FC≥1, adjusted P≤0.05, and gene expression in at least 10% of target cells (Finak et al., 2015).

Enrichment analysis: Up-regulated and DEGs from the subgroups were mapped to GO terms or KEGG pathways. Enrichment was assessed using a hypergeometric test to identify significantly enriched GO terms or KEGG pathways relative to the background gene set. Gene set variation analysis (GSVA) was performed using eight MsigDB datasets to analyze gene expression patterns across clusters. Genes in each sample were ranked by their expression levels, and the analysis evaluated whether a gene set ranked higher or lower among all genes. Enrichment scores (ES) were computed to quantify the degree of enrichment for each gene set in each sample.

Pseudotime analysis: Pseudotime analysis was performed using Monocle2 to process the cell gene expression matrix and reduce the data to two dimensions (Trapnell et al., 2014). Cells were then organized into a tree-like differentiation trajectory consisting of branches and nodes. The cell group in the earliest differentiation state, identified by the smallest pseudotime value, was used as a reference to calculate pseudotime values for all cells. In this study, the MN group cell subgroup was designated as the starting point of differentiation. Different branch cell sets were then selected for subsequent up-regulated gene and enrichment analyses.

Cell communication analysis: Intercellular communication among cell types in the pigeon crop was analyzed with CellChat (v.1.0.5), using ligand-receptor interactions to visualize communication networks between cell subgroups. Analyses included cell interaction analysis, ligand-receptor analysis, signal pathway level communication analysis, pathway-related ligand-receptor pair analysis, and inter-group cell communication strength difference analysis. Results were

visualized to provide a comprehensive overview of cell-cell communication dynamics.

Weighted gene co-expression analysis (WGCNA): WGCNA was conducted in accordance with established methodologies with minor modifications (Morabito et al., 2021). Expression data from 22 datasets, representing fibroblasts, epithelial cells, and SECs from the ML and MN groups were used as input. Co-expression networks were constructed using the WGCNA package (v.1.47) in R. Following gene filtering, gene expression values were imported into WGCNA to construct co-expression modules using the automatic network construction function, blockwiseModules, with default settings, except for the soft-thresholding power, which was set to 9. Module eigengenes were calculated to identify biologically significant modules by computing their correlation coefficients with cell clusters. Intramodular connectivity and module membership (MM) for each gene were determined using the WGCNA R package, identifying hub genes with high connectivity and potential critical functions. Correlation analyses were conducted using module eigengenes. Subsequently, the hub genes were subjected to GO and KEGG pathway analyses, as well as PPI network visualization.

RNA fluorescence *in situ* hybridization (RNA FISH)

Briefly, tissues were removed, rinsed with PBS (Servicebio, China), and fixed in an *in situ* hybridization solution (Servicebio, China) for over 12 h. After fixation, tissues were placed in 15% sucrose for 8 h, then in 30% sucrose overnight. Frozen sections were prepared, air-dried, fixed in 4% paraformaldehyde (Servicebio, China) for 10 min, and washed in PBS. After cooling, sections were digested with protease K (Servicebio, China) and subsequently washed with pure water and PBS. Pre-hybridization was performed by incubating the sections with a pre-hybridization solution (Servicebio, China) at 40°C for 1 h. Hybridization was conducted by adding a hybridization solution (Servicebio, China) containing a *KRT13* probe and incubating overnight. The sections were washed with buffer, gently dried, and treated with a preheated branch probe hybridization solution (Servicebio, China). The sections were then incubated in a wet box at 40°C for 45 min for hybridization, followed by rinsing with preheated washing buffer (Servicebio, China) at 40°C. The hybridization process was repeated using an *IGLL1* probe. A 4',6-diamidino-2-phenylindole (DAPI) solution (Servicebio, China) was added to the sections and incubated in the dark for 8 min. After rinsing, an anti-fluorescence quenching tablet (Servicebio, China) was added, and the sections were imaged using a Nikon upright fluorescence microscope. Details of the probes used are provided in Supplementary Table S1.

Frozen section immunofluorescent

Frozen sections were baked at 37°C for 10–20 min, then fixed in a solution (Servicebio, China) for 30 min. The sections were washed three times in PBS on a shaking table. Antigen retrieval was performed carefully, after which the sections were allowed to cool naturally before being washed again in PBS on a shaking table. After slightly drying, a circle was drawn around the tissue with a tissue pen, and BSA (Servicebio, China) was applied to block non-specific binding. Primary antibody was not applied, but the sections were incubated with secondary antibody (Chicken IgY, 1:250, RS2301, Immunoway, China) at room temperature for 50 min in the dark. The sections were then washed in PBS, followed by the addition of DAPI for further incubation in the dark for 10 min. Tissue autofluorescence was quenched by washing the sections in PBS, followed by the application of Quenching agent B (Servicebio, China) for 5 min and rinsing in water for 10 min. The sections were sealed with anti-fluorescence quenching tablets and images were acquired using the following settings: DAPI (excitation 330–380 nm, emission 420 nm), IgY (excitation 465–495 nm, emission 515–555 nm).

RESULTS

Histological observations

This study utilized transcriptome sequencing, translatome sequencing, and scRNA-seq to analyze variations in cellular composition, as well as transcriptional and translational differences in crop sacs between lactating and non-lactating (never mated) male pigeons (Figure 1A). In 225-day-old non-lactating pigeons, the crop sac exhibited a thin structure with sparse vascularization and minimal fat distribution on its surface (Figure 1B). In contrast, the crop sac of lactating male pigeons of the same age demonstrated increased thickness, with a well-developed vascular network and clusters of fat prominently distributed on the surface (Figure 1C). Histological analysis using hematoxylin and eosin (H&E) staining emphasized these differences. Notably, the crop sac of the non-lactating pigeons consisted of a smooth muscle layer, a basal layer, an epithelial layer, and a mucous membrane within the epithelial layer (Figure 1D). The epithelial layer, resembling intestinal villi, showed only a limited number of vesicular cells (Figure 1D). In contrast, the lactating male crop sac exhibited discernible smooth muscle, basal, and epithelial layers, along with cross-sectional blood vessels visible on the outer surface (Figure 1D). Notably, the epithelial layer exhibited a significant increase in thickness, with capillaries arranged in a tree-like configuration. A pronounced increase in vesicular cell numbers was observed, alongside a substantial emergence of vacuolated anuclear cells along the inner edge of the epithelial layer (Figure 1D). These histological findings highlight significant morphological differences between lactating and non-lactating crop sacs, establishing a crucial foundation for subsequent multi-omics analyses.

Changes in transcriptome of pigeon crop sac during first lactation

To investigate changes in gene expression in the pigeon crop sac during lactation, transcriptome sequencing was performed. Analysis revealed high-quality sequencing data and robust reproducibility across all three biological replicates (Figure 2A; Supplementary Table S2), with a genome alignment rate of over 80% (Figure 2B; Supplementary Table S3). Validation using qPCR for genes *CP35*, *DGAT2*, *PRDX1*, *BDH1*, *Plac8*, *GLUL*, *PTGDS*, and *GSTT1* demonstrated strong concordance between the sequencing data and qPCR results (Supplementary Figure S1A). A total of 12 457 genes were detected across all samples (Figure 2C). In the MN group, the top five expressed genes were *S100a9*, *KRT13*, *EEF1A*, *CP37*, and *FTH*, whereas in the ML group, the top five genes were *KRT13*, *CP35*, *KRT5*, *CP37*, and *FTH* (Supplementary Table S2). Differential expression analysis, applying FDR<0.05 and absolute $\log_2$(FC)>1, identified 1 153 significantly up-regulated genes and 2 354 significantly down-regulated genes (Figure 2D; Supplementary Table S4). Enrichment analyses revealed that DEGs were notably

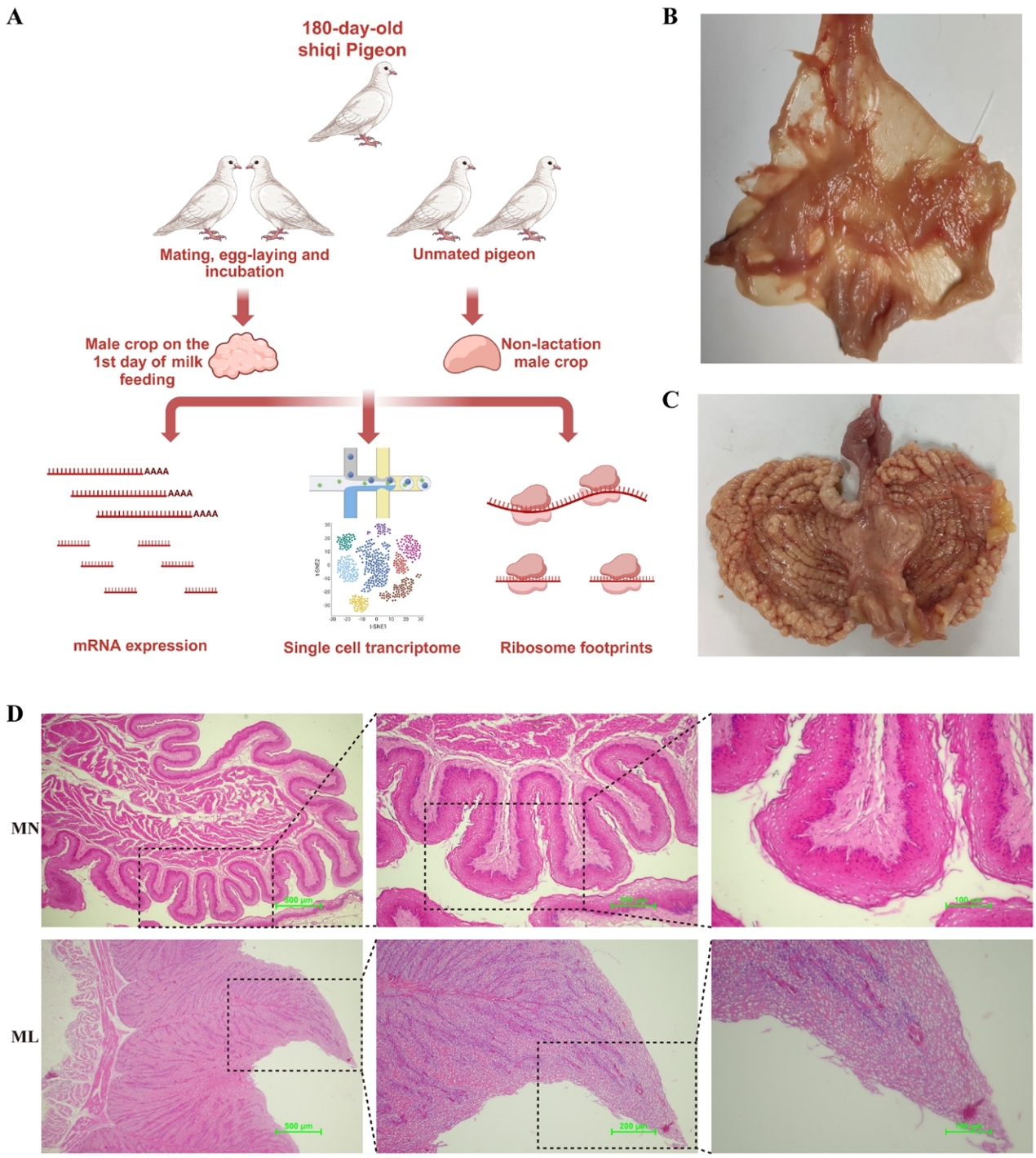


Figure 1 Morphological differences between lactating and non-lactating male pigeon crops

A: Schematic of the approach used in this study; illustrations created with BioRender.com. B: Phenotypic characteristics of crop sacs from 225-day-old unpaired MN pigeons. C: Phenotypic characteristics of crop sacs from 225-day-old ML pigeons that began lactating on the first day post-incubation. D: Hematoxylin and eosin (H&E)-stained sections of crop sacs from MN and ML groups, presented at various magnifications. ML: Male-lactating group. MN: Male-non-lactating group.

enriched in GO Biological Process (BP) terms associated with tissue development, microtubule formation, and cell migration, as well as KEGG pathways related to protein and lipid metabolism, signal transduction, and the cell cycle (Figure 2E; Supplementary Figure S1B and Tables S5, S6). Additionally, GSEA indicated that the expressed genes were primarily enriched in GO terms related to ribosome assembly, gene expression, and protein metabolism (Figure 2F; Supplementary Table S7), and KEGG pathways associated with ribosome biogenesis, cell proliferation, and oxidative phosphorylation (Figure 2G; Supplementary Table S8). Collectively, these findings demonstrate profound transcriptomic changes in the crop sac of male pigeons transitioning from a non-lactating to a lactating state.

Changes in RNA translation levels and efficiency during pigeon crop lactation

To investigate the differences in mRNA translation between

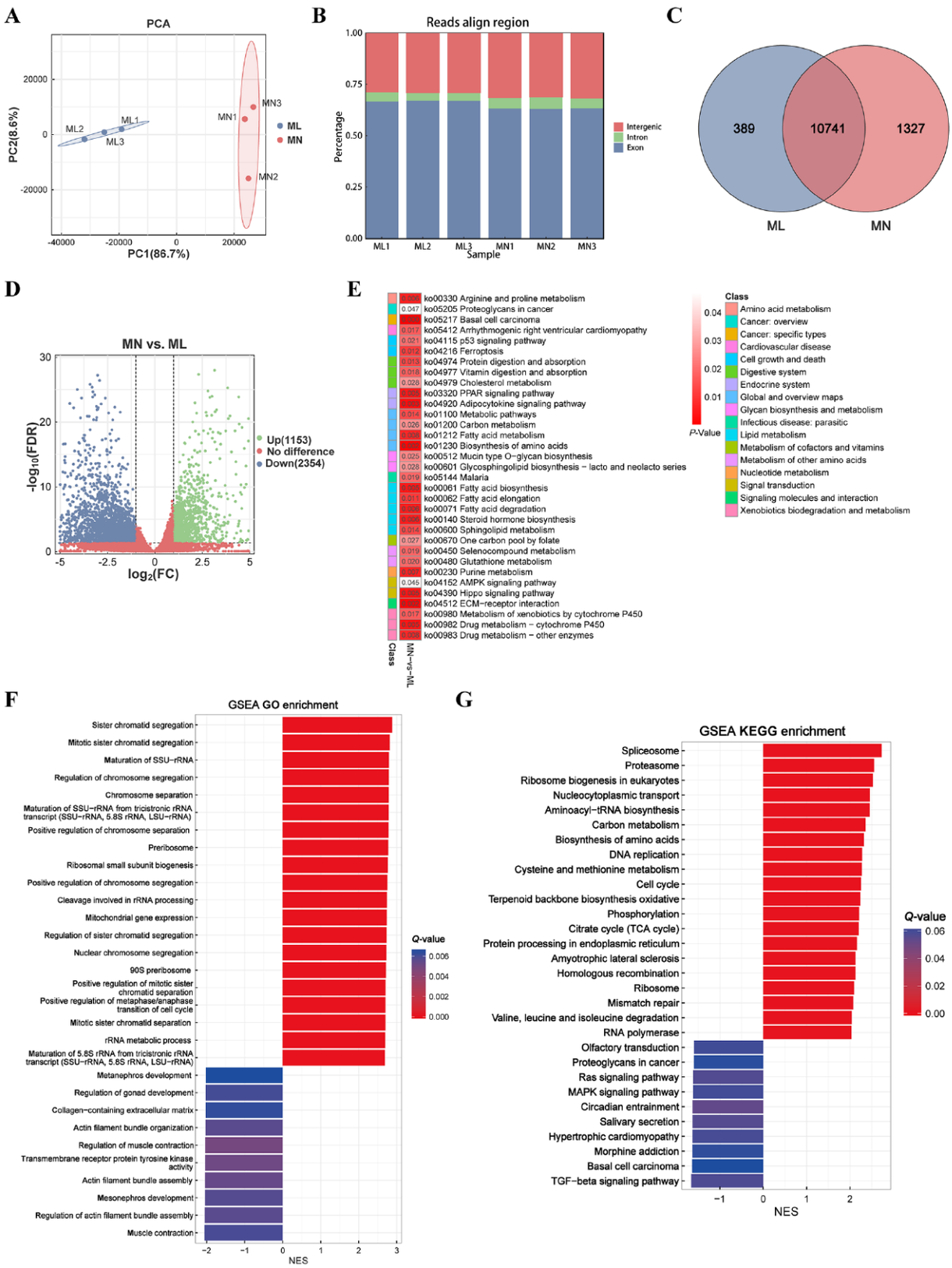


Figure 2 Comparative transcriptomic analysis between male lactating (ML) and non-lactating (MN) crop sacs

A: Principal component analysis (PCA) plot illustrating gene expression across all six samples, with MN group in red and ML group in blue. B: Mapping ratio of clean reads obtained from RNA-seq. C: Venn diagram displaying shared and unique genes identified in both MN and ML groups. D: Volcano plot depicting differential mRNA expression between MN and ML groups. E: Kyoto Encyclopedia of Genes and Genomes (KEGG) enrichment analysis of differentially expressed genes (DEGs) between MN and ML groups. F, G: Gene set enrichment analysis (GSEA) of Gene Ontology (GO) and KEGG pathways for genes expressed in both groups, highlighting top 20 GO terms or KEGG pathways with the highest normalized enrichment score (NES) and smallest *Q*-values, as well as top 10 terms or pathways with the lowest NES and smallest *Q*-values.

non-lactating and lactating male pigeons, ribosome profiling sequencing was performed. Analysis of RF lengths revealed an average fragment size of approximately 28 bp (Supplementary Figure S2 and Table S9). PCA of RF reads demonstrated strong reproducibility among the three MN group replicates. Although the ML replicates exhibited slight variability, the two groups were distinctly segregated, highlighting the impact of lactation on translational processes (Figure 3A). Genome alignment of RFs revealed distinct distribution patterns across gene regions. The majority of RFs were localized within the CDS region, with smaller proportions in introns, 5'UTR, and 3'UTR (Figure 3B). Notably, the ML group displayed a higher proportion of RFs in the CDS region, indicating increased active translation, whereas the MN group exhibited a greater proportion of RFs in intronic regions (Figure 3B). Normalization of RF counts to FPKM identified 1 576 up-regulated genes and 2 599 down-regulated genes, indicating a profound effect of lactation on RNA translation (Figure 3C; Supplementary Table S10). Enrichment analysis showed that these DTGs were significantly enriched in GO-BP terms related to cell adhesion, RNA translation, cell proliferation, and key signaling pathways such as ribosome assembly, protein metabolism, and lipid metabolism (Figure 3D, E; Supplementary Tables S11, S12).

Integrated analysis of mRNA expression (RNA-seq) and translation (Ribo-seq) data revealed strong correlations between mRNA levels and ribosome occupancy, with Pearson correlation coefficients of 0.68 for the MN group and 0.72 for the ML group (Figure 3F, G). Among the identified genes, 2 398 exhibited significant alterations at both the transcriptional and translational levels, while 797 showed significant changes solely at the transcriptional level and 1 776 displayed significant changes solely at the translational level. Notably, no genes displayed contradictory transcriptional and translational trends, underscoring the concordance between these regulatory layers (Figure 3H; Supplementary Table S13). Translation efficiency, defined as the ratio of ribosome occupancy to mRNA abundance, was also computed across samples. Comparative analysis between ML groups identified 101 genes with significantly higher translation efficiency in the ML group, including genes associated with ribosome function and transcription initiation (Figure 3I; Supplementary Table S14). Conversely, 30 genes exhibited significantly higher translation efficiency in the MN group (Figure 3I; Supplementary Table S14). These genes were primarily enriched in GO-BP terms and KEGG pathways related to cellular translation, membrane proteins, and ribosome assembly (Figure 3J; Supplementary Tables S15, S16). The combined RNA-seq and Ribo-seq analyses suggested that the lactation process in pigeon crops involves multiple biological processes, including ribosome assembly, gene transcription, RNA translation, protein processing and modification, amino acid metabolism, oxidative phosphorylation, and organ formation. Despite these insights, the specific biological mechanisms underlying epithelial proliferation, protein synthesis (including immunoglobulins), and lipid production warrant further investigation.

Cell composition in lactating and normal pigeon crop sac

To investigate the cellular heterogeneity of the pigeon crop sac and epithelial modifications associated with lactation, scRNA-seq was performed on ML and MN samples. After library construction, data processing, and filtering using Cell Ranger, a total of 8 305 cells from ML1, 8 715 cells from ML3, 5 000 cells from MN2, and 6 315 cells from MN3 were successfully captured and profiled (Supplementary Table S17). On average, each cell exhibited 3 882 UMIs and expressed approximately 1 210.5 genes, with a mean detection rate of 17 841.25 genes per sample (Supplementary Table S17). UMAP analysis identified 22 distinct cell clusters from the transcriptomic data, designated as clusters 0–21 (Figure 4A). Heatmap visualization of the top five highly expressed genes in each cluster demonstrated clear transcriptional distinctions, confirming separation of the clusters (Figure 4B). Comparative analysis of cell proportions across clusters revealed notable changes in clusters 0, 1, 2, 3, 5, and 6, indicating substantial differences in cell proportions between the ML and MN groups during lactation (Figure 4C; Supplementary Table S18). The 22 clusters were subsequently classified into 12 distinct cell types based on highly expressed genes in each subgroup, corroborated by existing literature (Figure 4D). Notably, clusters 0, 6, 11, and 18 showed significant overexpression of *COL6A3*, *COL1A2*, *PLOD2*, and *GPX3*, characteristic of fibroblasts (Costea et al., 2013; Nie et al., 2014; Zou et al., 2008). Clusters 2 and 9 exhibited pronounced overexpression of *EPCAM*, *EZR*, *Elf3*, *KRT5*, and *KRT13*, characteristic of epithelial cells (McDonald et al., 2020; Zhang et al., 2021). Cluster 3 demonstrated significant overexpression of *CD3D*, *CD3E*, *CD2*, and *RGS1*, characteristic of T lymphocytes (Zheng et al., 2020). Clusters 4 and 10 were identified as macrophages based on the expression of *CD74*, *CSF1R*, *CD83*, *LY86*, and *IFI30* (Sehgal et al., 2018). Clusters 5 and 19 were identified as erythrocytes based on the expression of *HBB* and *HBAA*. Additionally, based on their marker genes, clusters 12, 14, 15, 20, and 21 were categorized as dendritic cells (*IL1B*, *CXCL8*, *NFKBIA*, and *GPX1*), mastocytes (*KIT* and *HDC*) (Cheng et al., 2021), endothelial cells (*CDH5*, *PECAM1*, and *PODXL*) (Mantri et al., 2021), platelets (*RGS18*, *ITGA2*, and *ITGA2B*), and smooth muscle cells (*MYH11*, *MYL9*, *TAGLN*, *DES*, and *RGS5*), respectively. Clusters 1, 7, 8, 13, and 16 overexpressed plasma cell marker genes *Jchain*, *IGLL1*, *MZB1*, and *XBP1* (Biton et al., 2018; Domínguez Conde et al., 2022; Wu et al., 2022). Cluster 17 could not be definitively categorized due to the absence of clear marker gene expression and was designated as “unknown”. Violin plots further illustrated the expression of marker genes associated with each cell type across the various clusters (Figure 4E–O).

Identification and characterization of SECs

Clusters 1, 7, 8, 13, and 16 displayed significant overexpression of plasma cell marker genes, including *Jchain*, *IGLL1*, *MZB1*, and *XBP1*. However, H&E-stained sections from both the ML and MN groups revealed a notable absence of typical plasma cell structures (Figure 1D). Furthermore, cell clustering analysis indicated a lack of epithelial cells in the ML group, contradicting the findings from tissue sections (Supplementary Figure S3A, B). Based on these observations, we hypothesized that the cells in these five clusters are not bona fide plasma cells but instead represent plasmacyte-like cells.

To further elucidate the nature of these clusters, three-dimensional UMAP analysis was performed to examine their positional relationships with other clusters. Results indicated that cluster 2, identified as epithelial cells, was connected to cluster 1 via cluster 13 (Figure 5A), suggesting that clusters 1,

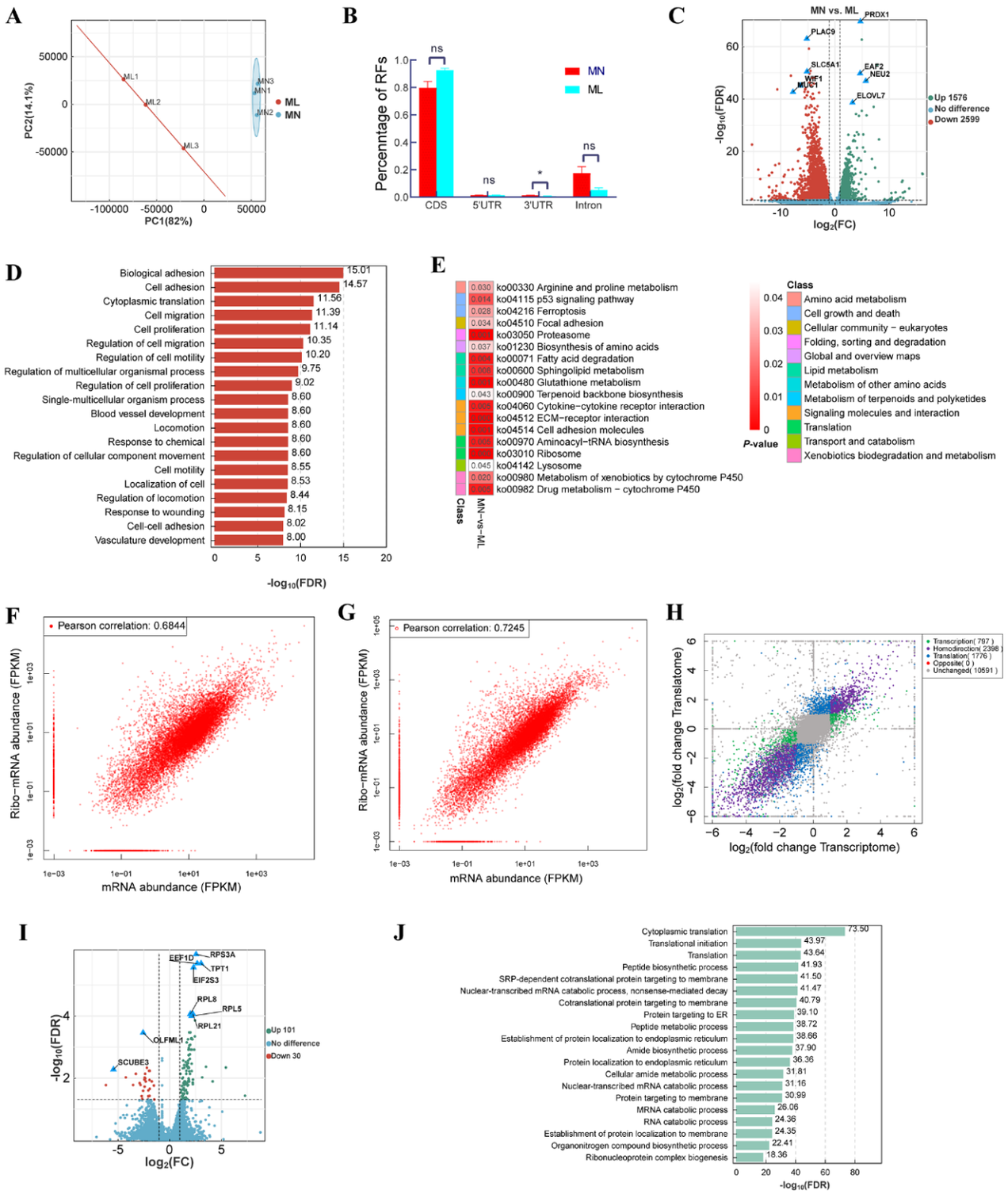


Figure 3 Translational alterations during pigeon crop lactation

A: PCA plot of ribosome footprints (RFs) across all six samples, with MN group in blue and ML group in red. B: Statistical distribution of RFs among different gene regions. C: Differential analysis of gene expression at the translational level between MN and ML groups. D, E: GO Biological Process (BP) (D) and KEGG (E) enrichment analyses of differentially translated genes (DTGs) between MN and ML groups. F, G: Pearson correlation coefficients between genes derived from RNA-seq and Ribo-seq data in MN and ML groups, respectively. H: Scatter plot of fold changes at both transcriptional and translational levels in MN vs. ML comparison, categorizing all genes into five groups. I: Differential analysis of translation efficiency. J: GO-BP enrichment analysis of genes with differential translation efficiency, presenting top 20 biological process terms. ML: Male-lactating group. MN: Male-non-lactating group. ns indicates not significant; * indicates P<0.05.

7, 8, 13, and 16 may either originate from epithelial cells or share similar gene expression profiles. This hypothesis was corroborated by RNA FISH experiments, which confirmed that the epithelial cell marker gene *KRT13* and plasma cell marker gene *IGLL1* were predominantly expressed within the epithelial layer of both MN and ML samples (Figure 5B).

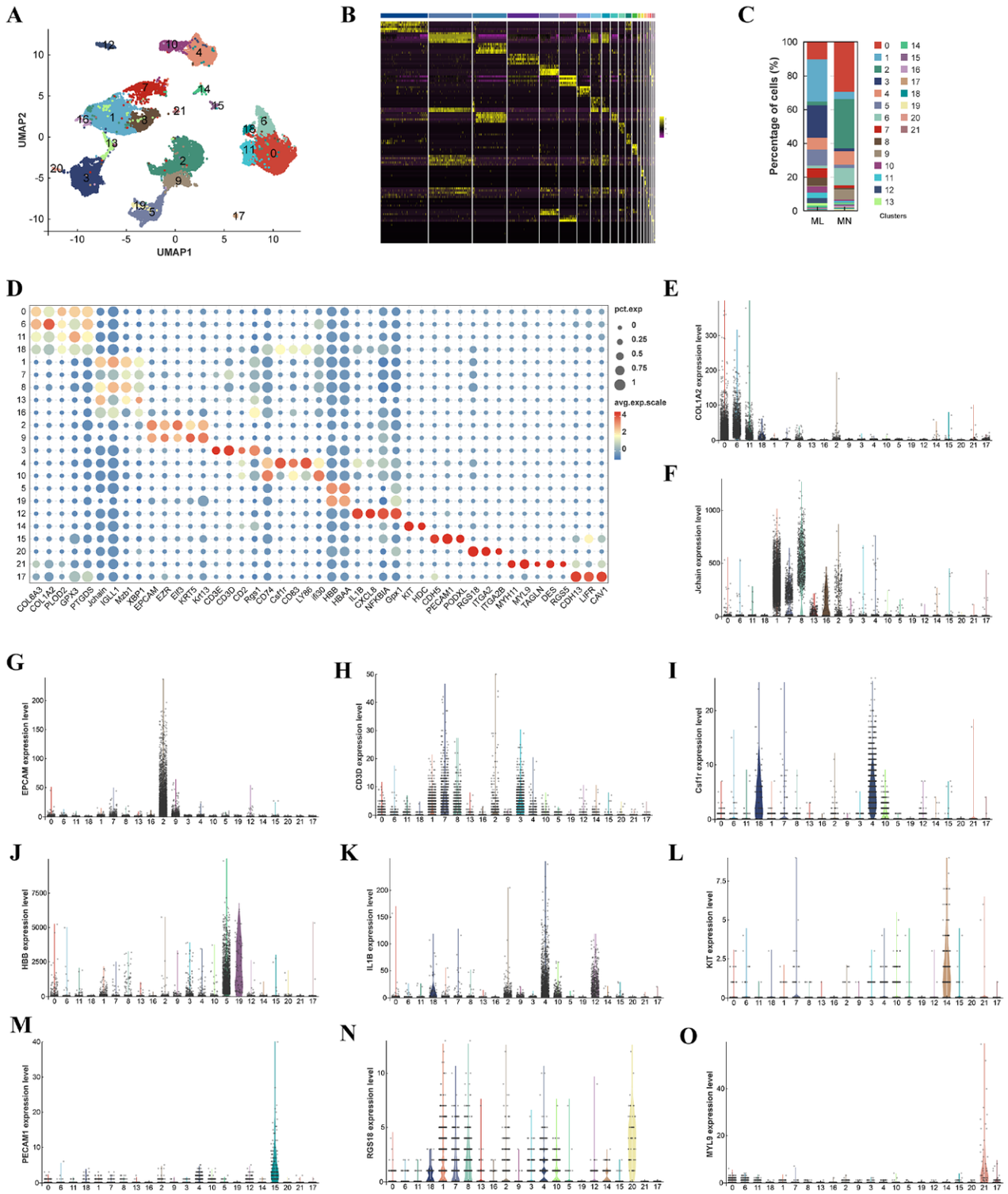


Figure 4 Cellular heterogeneity in male pigeon crop

A: Dimensionality reduction of cells from pigeon crop sacs using uniform manifold approximation and projection (UMAP). B: Heatmap showing top five highly expressed genes in each cluster, with each column representing a cluster and each row corresponding to a gene; yellow indicates maximum expression, purple indicates no expression. C: Proportion of cells in each cluster relative to total cell count in MN and ML groups, respectively. D: Dot plot of single-cell RNA-seq (scRNA-seq) data indicating marker gene expression patterns in each cluster. Pct.exp (percentage expression) indicates the expression proportion of a gene within cell subpopulations. Avg.exp.scale (average expression scale) represents the normalized average expression value of a gene within cell subpopulations. E–O: Violin plots of marker genes across 11 cell types, with the marker gene for cluster 17 omitted. ML: Male-lactating group. MN: Male-non-lactating group.

To investigate the presence of immunoglobulins in the pigeon crop, immunofluorescence staining using a secondary antibody specific to chicken IgY was performed. Results showed a substantial IgY presence within the epithelial layer

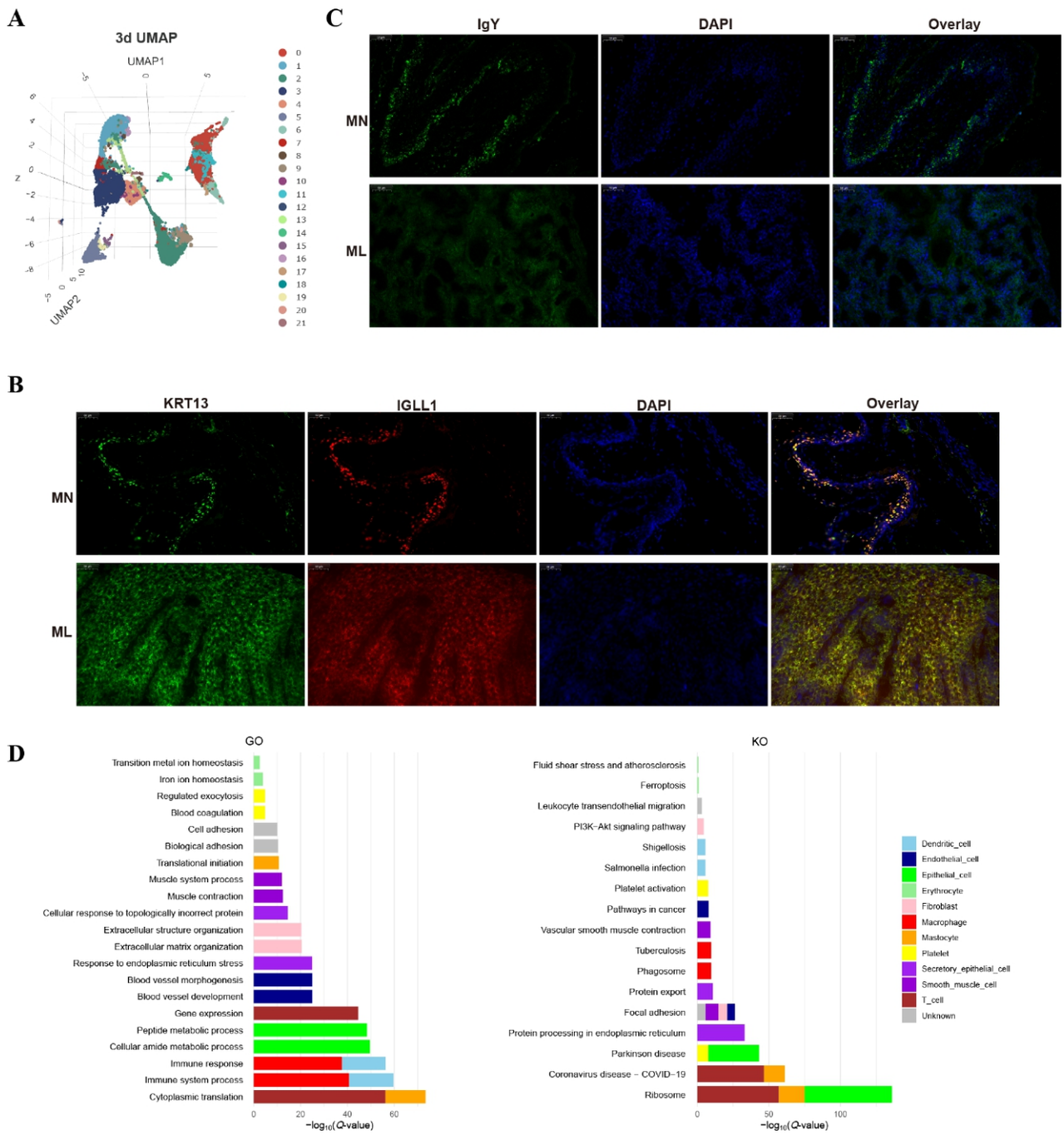


Figure 5 Identification of secretory epithelial cells (SECs)

A: Three-dimensional uniform manifold approximation and projection (UMAP) analysis of pigeon crop cells, with cluster 13 (light green) linked to both SECs (cluster 1, light blue) and epithelial cells (cluster 2, dark green). B: RNA FISH results of expression locations of *KRT13* (green) and *IGLL1* (red) in crop tissue from both MN and ML groups. Scale bar: 50 μm. C: Immunofluorescence staining of IgY (green) in crop tissue sections for both groups. Scale bar: 50 μm. D: Enrichment analysis of up-regulated genes in each cell type, showing top two terms or pathways for each. ML: Male-lactating group. MN: Male-non-lactating group.

of the ML group crop sacs, with additional signals also observed in the basal layer and mucosa of the MN group (Figure 5C). These findings suggest that the plasmacyte-like cells identified in these clusters are a specialized type of SECs. Moreover, the significant expression of genes associated with immunoglobulin synthesis in the pigeon crop indicates active production of immunoglobulins.

Following the identification of SEC subgroups, GO and KEGG enrichment analyses were conducted on up-regulated genes across all 12 subgroups. Epithelial cells exhibited enrichment in pathways associated with amino acid metabolism and ribosomal functions (Figure 5D). In contrast, up-regulated genes in SECs were primarily enriched in biological processes such as the cellular response to misfolded proteins and protein export, reflecting their secretory role (Figure 5D). Immune cells, including macrophages, T cells, dendritic cells, and mast cells, were enriched in immune response pathways (Figure 5D). For fibroblasts, up-regulated genes were associated with extracellular matrix organization, while endothelial cells showed significant enrichment in

angiogenesis-related pathways (Figure 5D).

Heterogeneity of SECs in pigeon crop sac

The pigeon crop sac, which primarily functions as a storage and softening site for ingested food (van Dijk et al., 2008), also plays critical roles in immune defense and secretion through its epithelial cells (Classen et al., 2016). Despite its importance, the diversity and specialization of epithelial cells in the crop sac remains largely unexplored. To elucidate the functional heterogeneity of epithelial cells and SECs, GO and KEGG enrichment analyses were conducted on up-regulated genes within each cluster.

Enrichment analysis revealed distinct functional roles for the epithelial cell clusters. In cluster 2, up-regulated genes were predominantly associated with biological processes related to translation, amide metabolism, peptide generation, lipid synthesis, and fat metabolism. These genes were also linked to pathways involved in the ribosome, oxidative phosphorylation, and tricarboxylic acid cycle (Figure 6A, B; Supplementary Figure S4A and Tables S19, S20). Cluster 9 showed significant enrichment in processes related to translation, peptide synthesis, and membrane protein synthesis, along with pathways involved in ribosome, oxidative phosphorylation, and proteasome (Figure 6A; Supplementary Figure S4B and Tables S21, S22). Notably, cluster 2 also exhibited significant enrichment in pathways linked to exocytosis (Figure 6B). GSVA indicated a high degree of similarity between clusters 2 and 9, particularly in pathways related to adipogenesis and fatty acid metabolism (Figure 6C; Supplementary Table S23). Furthermore, expression levels of lipid biosynthesis-associated genes, such as *FABP5*, *ELOVL6*, and *PPARγ*, were significantly up-regulated in cluster 2 compared to other clusters (Figure 6D, E; Supplementary Figure S4C). This finding suggests that basal epithelial cells facilitate lipid synthesis, transferring synthesized lipids via exocytosis to SECs, which subsequently secrete these lipids into the crop sac as part of pigeon milk.

Up-regulated genes in the SEC clusters displayed distinct functional profiles. Cluster 1 showed strong enrichment in biological processes associated with endoplasmic reticulum stress, UPR, protein processing in the endoplasmic reticulum, and protein export pathways (Figure 6F; Supplementary Figure S4D and Tables S24, S25). Cluster 7 was predominantly enriched in ribosome production, gene transcription, and translation, as well as ribosome, spliceosome, and proteasome pathways (Figure 6F; Supplementary Figure S4E and Tables S26, S27). Cluster 8 exhibited functional enrichment in endoplasmic reticulum stress, protein N-glycosylation, and pathways related to protein processing in the endoplasmic reticulum and N-glycan biosynthesis (Figure 6F; Supplementary Figure S4F and Tables S28, S29). Cluster 13 appeared as a transitional group, connecting epithelial cells and SECs in UMAP analysis, with up-regulated genes associated with endoplasmic reticulum stress, RNA processing, and protein processing/export pathways (Figure 6F; Supplementary Figure S4G and Tables S30, S31). Cluster 16 genes were enriched in membrane protein, RNA degradation, and ribosome pathways (Figure 6F; Supplementary Figure S4H and Tables S32, S33). GSVA highlighted functional similarities between clusters 1 and 8, as well as between clusters 13 and 16. Cluster 7, however, showed unique enrichment in hallmark pathways such as UPR, mTORC1 signaling, E2F targets, and G2M checkpoint (Figure 6C; Supplementary Table S23).

Comparative analysis of epithelial and SEC clusters between the MN and ML groups revealed that SEC marker genes, such as *MZB1*, *TNFRSF17*, and *XBP1*, were highly up-regulated in several clusters in the ML group but down-regulated in cluster 16 (Figure 6G; Supplementary Table S34). Using the STRING database, interactions among up-regulated genes in cluster 1 and DEGs between the MN and ML groups were visualized. Results indicated multiple interactions among UPR-related genes, with *XBP1* as a central node (Figure 6H), highlighting the importance of the UPR in driving adaptive proliferation of the epithelial layer, as well as extensive protein and lipid synthesis for pigeon milk secretion.

To further explore the developmental relationships of SECs, pseudotime analysis using Monocle 2 was conducted, providing insights into cellular differentiation processes (Trapnell et al., 2014). Results partitioned clusters 1, 7, 8, 13, and 16 into seven distinct states (Figure 7A, B). State 1 predominantly comprised cells from the MN group, while state 7 was primarily composed of cells from the ML group (Figure 7B, C). In the two predominant SEC subgroups, cluster 1 cells were uniformly distributed across all states, whereas cluster 7 cells were primarily confined to states 1 and 7 (Supplementary Figure S5A). State 4, exclusively composed of ML cells, exhibited distinct differentiation branches compared to states 2 and 6. Hence, state 1 was designated as the pre-branch, with states 4 and 7 representing divergent differentiation pathways.

Pseudotime analysis identified five gene clusters based on expression patterns along differentiation trajectories. Genes in cluster 1, including *JAK1*, *STAT1*, *CD44*, and *TLR3*, were enriched in multiple immune-related pathways (Figure 7G, H; Supplementary Table S35) and showed higher expression in the state 1-3-5-6-7 branch relative to the state 1-3-4 branch (Figure 7D; Supplementary Figure S5B). Cluster 2 genes, such as *MZB1*, *TNFRSF17*, and *XBP1*, were enriched in the cellular UPR process (Figure 7D–G; Supplementary Figure S5C and Table S36). Genes in cluster 3, such as *CCND2*, *CCNI*, and *G2E3*, were significantly enriched in pathways related to the cell cycle and cellular proliferation (Figure 7D, G; Supplementary Figure S5D–F and Table S37). Notably, genes in cluster 1 were significantly enriched in the primary immunodeficiency pathway (Figure 7H, I; Supplementary Table S38), a key process in B-cell differentiation and antibody production.

These findings emphasize the critical role of SECs in cellular secretion and immunoglobulin synthesis, which involve signaling pathways and biological processes analogous to those governing B-cell maturation and antibody secretion. These results also suggest lactation-related adaptations in the pigeon crop sac contribute to enhanced immune function, further underscoring the multifunctional nature of this specialized tissue.

Cell communication analysis targeting SECs

The coordinated functionality of complex organs depends on effective signal transduction and collaboration among diverse cell populations. To investigate the genetic mechanisms underlying lactation in the pigeon crop sac, CellChat was used to analyze intercellular communication networks. Ligand-receptor pairs were predicted and quantified across cell clusters based on transcriptomic data from both the ML and MN groups (Figure 8A, B; Supplementary Tables S39, S40).

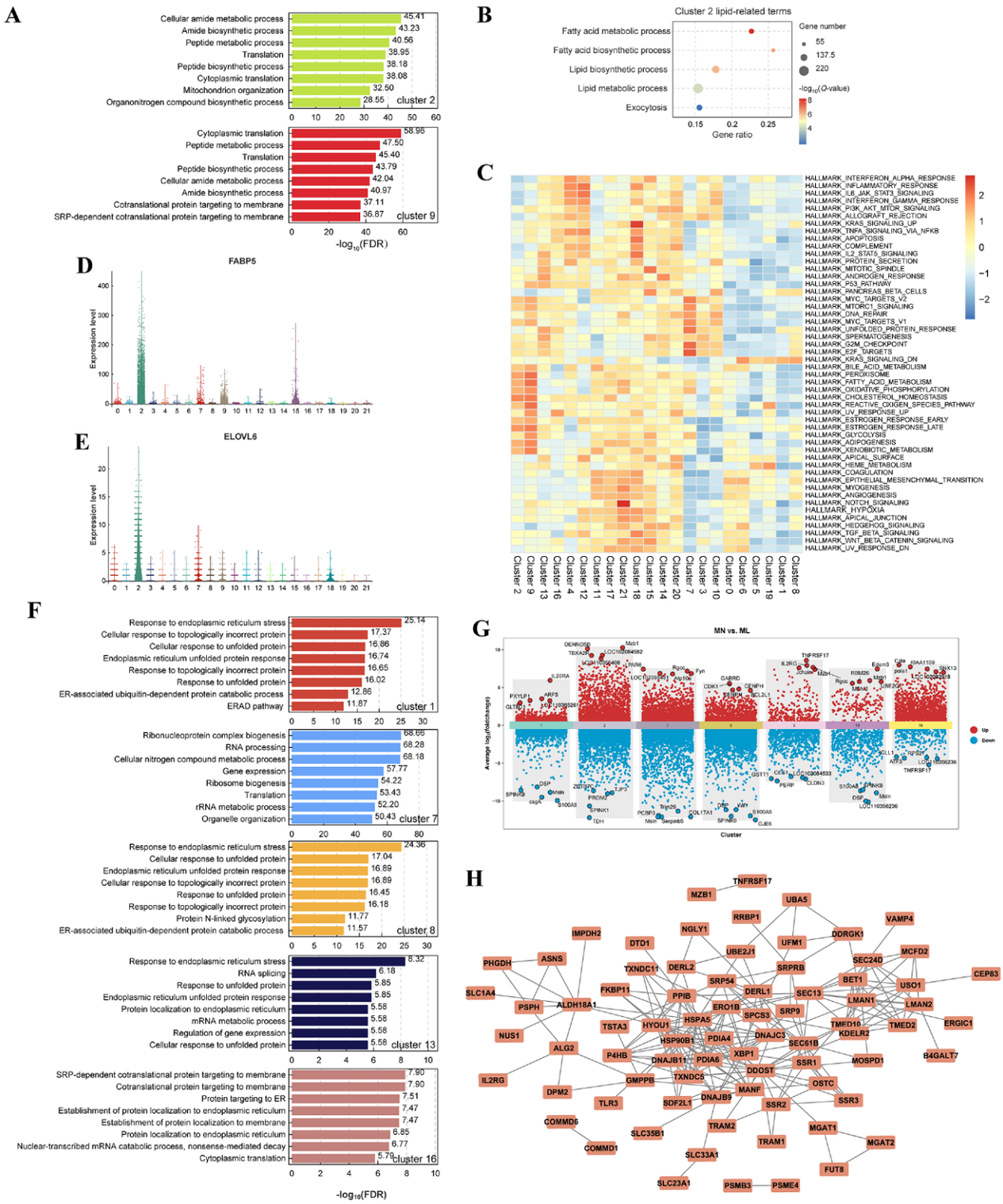


Figure 6 Functional annotation of genes in epithelial cells and SECs

A: GO enrichment analysis of up-regulated genes in clusters 2 and 9, respectively, showing eight biological process terms with smallest false discovery rate (FDR). B: Lipid metabolism-related biological processes enriched in up-regulated genes in cluster 2. C: Gene set variation analysis (GSVA) of up-regulated genes across all clusters, focusing on hallmark gene sets. D, E: Violin plots of *FABP5* and *ELOVL6* expression in all 22 clusters. F: GO enrichment analysis of up-regulated genes in each SEC cluster, exhibiting eight biological process terms with the smallest FDR values. G: Differential analysis of gene expression between epithelial cells and SECs in MN and ML groups. H: Protein-protein interaction network of intersecting genes up-regulated in cluster 1 and significantly up-regulated in MN vs. ML within this cluster. ML: Male-lactating group. MN: Male-non-lactating group.

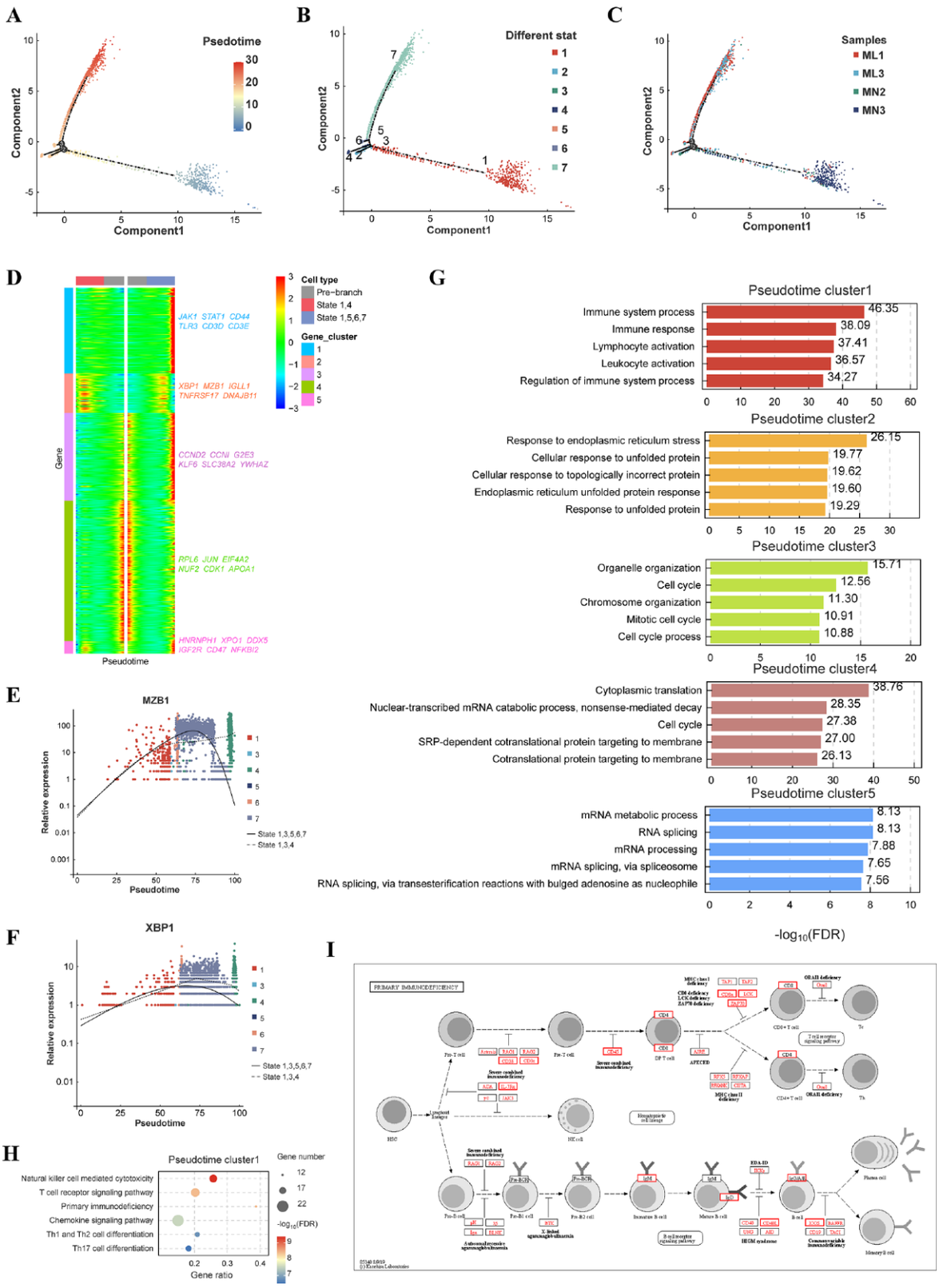


Figure 7 Pseudotime reconstruction of SEC differentiation trajectory

A: Differentiation trajectories of SECs constructed using Monocle 2. B: Single-cell trajectory reconstruction within SECs, revealing seven distinct states. C: Composite differentiation trajectory of SECs across various samples. D: Heatmap showing dynamic changes in DEGs across different branches of SEC differentiation trajectory. E, F: Expression dynamics of *MZB1* and *XBP1* along pseudotime trajectory of SECs, comparing states 1, 3, and 4 with states 1, 3, 5, 6, and 7; dashed line represents state 1, 3, 4 branch, while solid line represents state 1, 3, 5, 6, 7 branch. G: GO enrichment analysis of genes within each gene cluster, showing top five biological process terms. H: KEGG enrichment analysis of genes in gene cluster 1, highlighting top five signaling pathways. I: Significant enrichment of genes within gene cluster 1 in the primary immunodeficiency pathway. ML: Male-lactating group. MN: Male-non-lactating group.

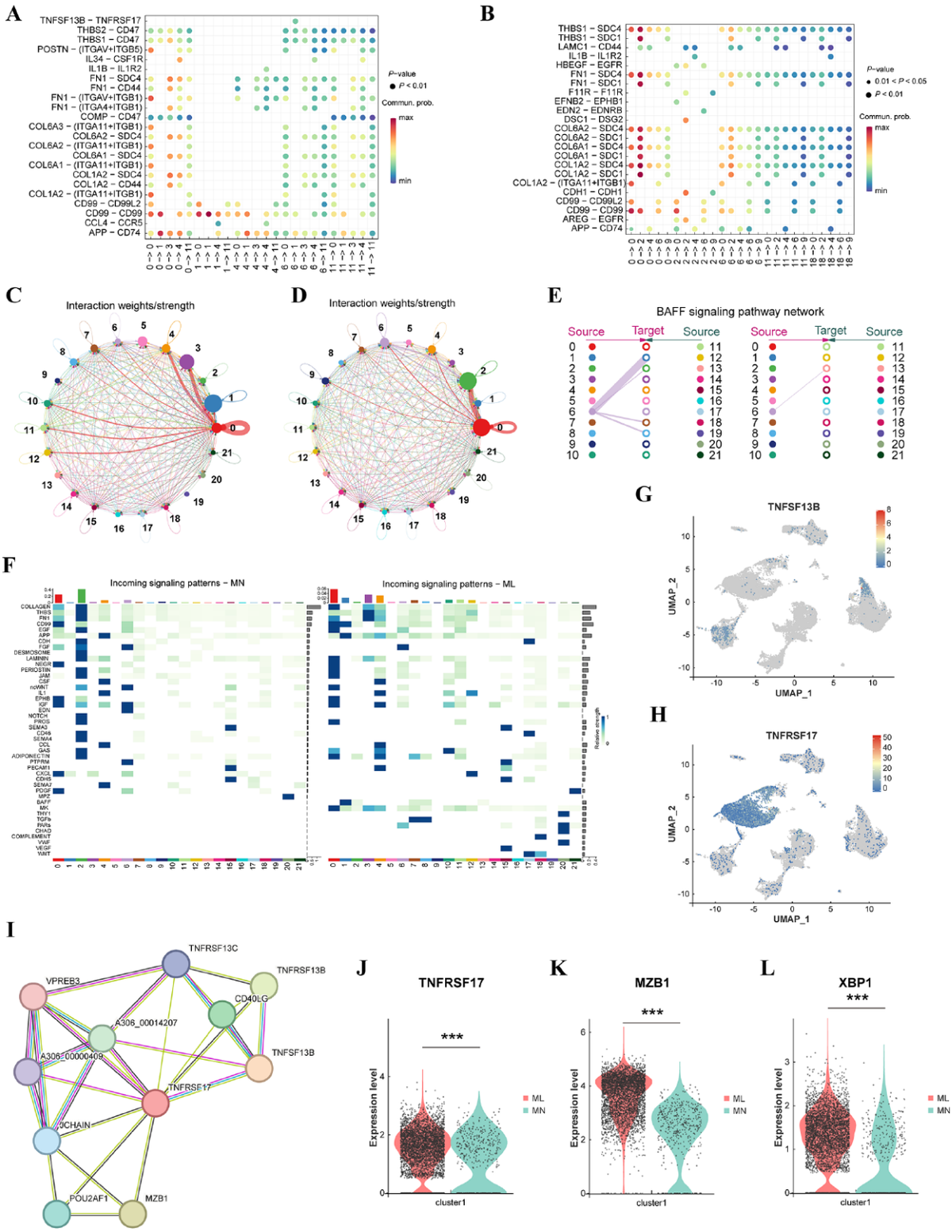


Figure 8 Examination of signaling interactions among various cellular subgroups in the pigeon crop sacs

A, B: Ligand-receptor pairs displayed across all 22 clusters in the ML (A) and MN (B) groups, with top five ligands and receptors highlighted based on communication probability. Commun. prob. represents communication probability. C, D: Circular plots demonstrating cell communication probabilities among clusters in MN (C) and ML (D) groups; circle size corresponds to number of ligand-receptor pairs, edge width indicates communication probability. E: Hierarchical plot illustrating intercellular communication network specific to the BAFF signaling pathway, with edge width representing communication probability. F: Heatmap depicting incoming signals in MN versus ML groups. G, H: Expression patterns of *TNFSF13B* and *TNFRSF17* across different cell types, visualized on the UMAP plot. I: Interaction network of *TNFRSF17* based on data from the STRING database. J–L: Differential expression analysis of *TNFRSF17* (J), *MZB1* (K), and *XBP1* (L) in cluster 1, comparing MN and ML groups. ML: Male-lactating group. MN: Male-non-lactating group. *** indicates P<0.001.

Analysis revealed intricate cellular interactions, as reflected by the number of ligand-receptor pairs and their associated communication probabilities, highlighting an extensive signaling network within the crop sac (Figure 8C, D). Our analysis focused on ligand-receptor interactions and signaling pathways involving SECs as receptors. Among the identified pathways, the B-cell activating factor (BAFF), crucial for mediating B cell survival and differentiation, was transmitted by fibroblast cluster 6 and received by epithelial cell clusters 1, 2, 7, 8, and 13, with cluster 1 exhibiting the highest communication probability (Figure 8E). Furthermore, SECs were found to receive signals primarily via the TNFSF13B-TNFRSF17 interaction (Figure 8A). Comparative analysis of communication pathways revealed that the relative strength of incoming BAFF signals was significantly higher in cluster 1 of the ML group compared to the MN group, suggesting enhanced signaling activity during lactation (Figure 8F).

Expression analysis demonstrated that the receptor *TNFRSF17* was predominantly expressed in SECs, while *TNFSF13B* was primarily found in fibroblasts and T cells (Figure 8G, H). PPI network analysis indicated direct interactions between *TNFRSF17* and *TNFSF13B*, as well as co-expression of *TNFRSF17* with marker genes such as *Jchain*, *MZB1*, and *POU2AF1* (Figure 8I). Within SEC cluster 1, *TNFRSF17*, *MZB1*, and co-expressed transcription factor *XBP1* were significantly up-regulated in the ML group compared to the MN group, suggesting their critical roles in epithelial proliferation and protein synthesis within the pigeon crop (Figure 8J–L). Based on these findings, we hypothesize that fibroblasts stimulate SECs to undergo B cell-like proliferation and maturation via the BAFF signaling pathway, thereby activating the UPR pathway and leading to substantial protein synthesis and secretion of pigeon milk.

WGCNA of epithelial cells, SECs, and fibroblasts

To further identify key genes involved in pigeon milk secretion by SECs, WGCNA was conducted on the gene expression profiles of epithelial cells, SECs, and fibroblasts from both the MN and ML groups. After filtering genes, subsequent analyses and visualizations were performed using a power value of 9, enabling the construction of co-expression modules with high connectivity (Supplementary Figure S6A). Based on the gene expression patterns, nine distinct modules were identified, designated as black, blue, grey, brown, darkgrey, darkorange, greenyellow, lightcyan, and midnightblue, each comprising co-expressed genes with similar expression patterns (Figure 9A). The number of co-expressed genes within various modules is provided in Supplementary Figure S6B.

Analysis of sample-specific expression patterns revealed module-specific associations with particular cell clusters. In the ML group, the darkgrey module exhibited elevated eigenvalues in clusters 1, 2, 7, 8, and 13 (Figure 9B). The darkorange module showed relatively high eigenvalues in fibroblast clusters (0, 6, 11, 18) across both groups (Figure 9B). Notably, the greenyellow module displayed markedly elevated eigenvalues in cluster 13 of the ML group (Figure 9B). Correlation analysis revealed strong interconnections between the darkgrey, greenyellow, and midnightblue modules (Supplementary Figure S6C). These three modules were significantly expressed within the SEC cluster, further indicating their relevance.

Functional enrichment analysis revealed that the 138 genes within the darkgrey module were significantly associated with biological processes and pathways pertinent to UPR, protein modification, and protein transport (Figure 9C). Specifically, genes within this module were enriched in processes such as endoplasmic reticulum stress responses, N-linked glycosylation, protein localization to the endoplasmic reticulum, protein processing within the endoplasmic reticulum, protein export, and N-glycan biosynthesis (Figure 9C; Supplementary Figure S6D and Tables S41, S42). The darkgrey module included genes associated with the UPR pathway, such as *XBP1*, members of the SEC gene family (*SEC13*, *SEC11C*, *SEC22A*, *SEC11A*, *SEC61A1*, *SEC61B*, and *SEC61G*), *DNAJB11*, and *DNAJC3*, as well as key genes associated with immunoglobulin secretion, such as *Jchain*, *MZB1*, *IGLL1*, *TNFRSF17*, and *IGHV3-23* (Figure 9D). The WGCNA results provide compelling evidence supporting the critical role of the UPR pathway, along with the genes *XBP1*, *MZB1*, and *TNFRSF17*, in the secretion of proteins and immunoglobulins by SECs in the pigeon crop, facilitating the synthesis of pigeon milk.

DISCUSSION

The pigeon meat industry represents a significant segment of the poultry sector in China (Chang et al., 2023). A unique feature of squab development is their dependence on parental feeding during the early stages of hatching, which prolongs the breeding cycle and presents challenges to industrial expansion (Wang et al., 2023b). Investigating the mechanisms underlying lactation in the pigeon crop sac offers a valuable opportunity to compare avian and mammalian reproductive strategies, elucidate the composition of pigeon milk, and facilitate the development of artificial alternatives to meet industry demands. In this study, an integrative multi-omics approach combining RNA-seq, Ribo-seq, and scRNA-seq was employed to compare the transcriptomic, translatomic, and cellular changes in the crop sacs of lactating and non-lactating male pigeons. To reduce interference from smooth muscle cells during scRNA-seq and enhance the resolution of epithelial cell profiling, breeding pigeons in their first laying stage were selected as experimental subjects. Consistent with previous research, transcriptomic analyses identified that DEGs were enriched in pathways related to protein and lipid synthesis, as well as broader metabolic pathways. However, the aforementioned omics approaches alone were insufficient to delineate the specific biological processes driving the structural and functional adaptations in the epithelial layer during lactation. The use of scRNA-seq provided single-cell resolution insights into tissue dynamics, identifying SECs with plasma cell-like characteristics and revealing that pigeon crop milk secretion is primarily driven by *XBP1* activation and the UPR pathway.

The crop, an expandable storage structure located at the anterior end of the avian digestive tract, is mainly composed of epithelial cells along with various immune cells (Fu et al., 2023; Kierończyk et al., 2016; Wang et al., 2023c). Single-cell transcriptome analysis confirmed that the pigeon crop consisted primarily of epithelial cells, fibroblasts, endothelial cells, smooth muscle cells, and various immune-related cells, including T cells, macrophages, dendritic cells, and mast cells. Clusters 1, 7, 8, 13, and 16 displayed elevated expression of immunoglobulin-secreting plasma cell marker genes, including *Jchain*, *IGLL1*, *IGHV3-23*, *MZB1*, and *XBP1* (Biton et al., 2018; Domínguez Conde et al., 2022; Wu et al., 2022). Despite the absence of typical plasma cell morphology in

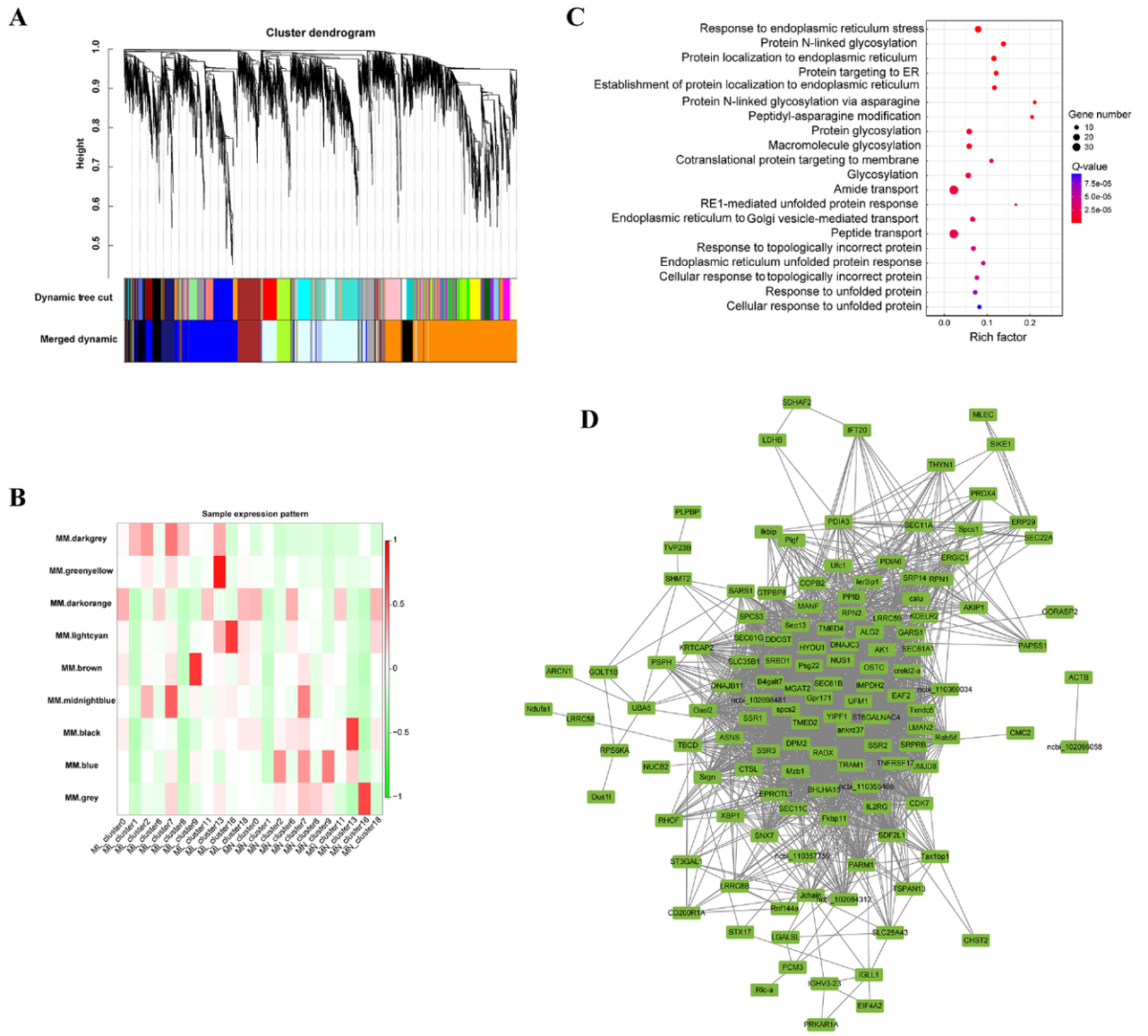


Figure 9 Weighted gene co-expression network analysis (WGCNA) of epithelial cells, SECs, and fibroblasts from male pigeon crop sacs

A: Hierarchical clustering dendrogram identifying nine gene co-expression modules. B: Heatmap showing expression patterns across clusters; x-axis represents cell clusters in SECs, epithelial cells, and fibroblasts, y-axis represents modules with module eigenvalues plotted. C: GO enrichment analysis of genes in the darkgrey module, presenting top 20 biological process terms. D: Protein-protein interaction network revealing potential interactions among genes in darkgrey module. ML: Male-lactating group. MN: Male-non-lactating group.

H&E-stained sections, we hypothesized that these cells represent plasmacytoid cells. *In situ* hybridization targeting *KRT13* and *IGLL1* confirmed robust expression in the epithelial layer, supporting the hypothesis that these plasmacytoid cells are proliferating SECs characterized by significant protein and lipid accumulation. Furthermore, immunofluorescence assays detected abundant IgY within the proliferating epithelial layer, aligning with the high expression of *IGLL1*, *Jchain*, *MZB1*, and *IGHV-23* in SECs, further establishing their role as key contributors to pigeon milk production.

The origin of immunoglobulins in mammalian milk—whether derived from systemic circulation or synthesized *de novo* within mammary glands—has been a subject of long-standing scientific inquiry (Korhonen et al., 2000; Stelwagen et al., 2009). Recent evidence suggests that mammary epithelial cells are capable of producing substantial quantities of immunoglobulins (Liao et al., 2024). Similarly, tumoral tissues have been shown to synthesize immunoglobulins while mediating their N-glycan modifications (Drake et al., 2017; Lan et al., 2016). However, the source of immunoglobulins in pigeon milk remains unresolved. It is unclear whether these immunoglobulins are synthesized by parental immune organs and transported to the milk via the bloodstream or are directly produced within the pigeon crop sac (Shao et al., 2021). Previous studies have suggested that immunoglobulins may be secreted into the crop through blood transport, contributing to the innate immunity of squabs (Engberg et al., 1992; Ismail et al., 2013).

Our findings demonstrated that SECs in the epithelial layer of the pigeon crop exhibited high expression of genes involved in immunoglobulin synthesis (*IGLL1*, *Jchain*, *IGHV-23*, *MZB1*, *XBP1*, and *TNFRSF17*), alongside a significant presence of IgY. Analysis indicated that these up-regulated genes and DEGs in the SECs were notably enriched in GO-BP terms related to protein N-terminal glycosylation, a critical step in the

functional maturation of immunoglobulins. While the possibility of immunoglobulins being transported to pigeon milk via the bloodstream cannot be entirely discounted, our results strongly suggest that a considerable proportion of immunoglobulins are synthesized by the SECs within the crop sac.

Lactation is a complex physiological process requiring the coordination of hormonal, metabolic, neural, and circadian signaling pathways (Hannan et al., 2023). This intricate interplay of hormones and tissues governs the initiation, maintenance, and regulation of milk production (Hannan et al., 2023). Among the key hormonal regulators, prolactin plays a pivotal role by binding to receptors on mammary gland cells and activating the JAK2/STAT5 signaling pathway to regulate the expression of milk protein genes (Chen et al., 2024). Growth hormone, insulin, and leptin further contribute to this tightly regulated physiological process (Hannan et al., 2023). Additionally, adipose tissue serves as a critical endocrine organ, secreting adipokines that function as hormones and cytokines, essential for energy metabolism (McNamara & Huber, 2018). The transcription factor XBP1 is integral to lactation, influencing mammary gland development, UPR, endoplasmic reticulum formation, and hormonal signaling (Sharmin et al., 2021). It also plays a crucial role in gene expression, cell growth, and differentiation, all of which are vital for optimal mammary gland function (Hasegawa et al., 2015). Evidence from murine studies has shown that *XBP1* deletion in mice disrupts the increase in endoplasmic reticulum abundance and complexity in mammary epithelial cells during lactation (Davis et al., 2016). Furthermore, spliced *XBP1* and other UPR markers, such as *ATF4* and *CHOP*, show significant postnatal increases in mammary gland tissue (Yonekura et al., 2018). Our study provides compelling evidence of the central role of *XBP1* and UPR in lactation-specific adaptations within the pigeon crop sac. Notably, our scRNA-seq results indicated that up-regulated genes in SEC clusters 1, 7, 8, and 13 were significantly enriched in UPR-related processes, while clusters 1, 7, 8, 13, and 16 showed marked enrichment in protein processing in the endoplasmic reticulum. Furthermore, *XBP1* expression was significantly elevated in both epithelial cells and SECs in the ML group compared to the MN group, underscoring the importance of *XBP1* and the UPR pathway in pigeon crop lactation.

Plasma cells, differentiated from B cells, are essential for mounting an immune response through their production and secretion of immunoglobulins (Pioli, 2019). This differentiation and subsequent immunoglobulin secretion are tightly regulated processes influenced by several factors, notably the BAFF signaling pathway (Daridon et al., 2008; Smulski & Eibel, 2018). BAFF, a critical cytokine, promotes B cell maturation, survival, and differentiation into plasma cells, thereby supporting robust immunoglobulin production and the regulation of humoral immunity (Smulski & Eibel, 2018). BAFF (TNFSF13B) exerts its effects by binding to specific receptors, including BAFF-R, TACI, and BCMA (TNFRSF17), thereby activating downstream signaling pathways that support B cell functionality (Eslami et al., 2024). Dysregulation of this pathway has been linked to various immune-related disorders (Saidoune et al., 2021). In this study, fibroblasts were shown to interact with epithelial cells and SECs via the TNFSF13B-TNFRSF17 ligand-receptor pair within the BAFF signaling pathway, with a notable amplification in BAFF signaling observed in the ML group. We propose that the incubation behavior of pigeons may stimulate SEC proliferation through the BAFF signaling pathway, enhancing *XBP1* expression and activating the UPR. This activation likely drives large-scale synthesis of proteins and immunoglobulins, essential for pigeon milk production.

This study recognizes several limitations and highlights potential avenues for future research. Firstly, our research did not explore cellular heterogeneity between male and female pigeons nor identify commonalities and differences in their lactation processes. Such comparative analysis could provide valuable insights into sex-specific regulatory pathways. Secondly, our study was limited to examining the crop of male pigeons on the first day of lactation, without examining samples across different stages of the lactation period. Thirdly, epithelial cells with vanishing nuclei, likely undergoing holocrine secretion, were observed but may have been excluded from scRNA-seq analysis due to their near-apoptotic state and active mitochondrial expression. Even single-cell nuclear transcriptomics may fail to detect these cells. Therefore, sampling proliferative crops prior to the onset of pigeon milk production may allow for the identification of these cells at earlier stages of nuclear disappearance. Fourthly, the role of androgens—key hormones known to regulate *XBP1* and the UPR (Stelloo et al., 2020)—in male pigeon lactation remains unclear. Further studies are needed to determine whether androgens are primarily responsible for lactation in male pigeons, providing a basis for comparison with mammalian systems. Fifthly, the stimuli prompting male pigeons to exhibit incubation behavior, thereby triggering crop milk production, remain unclear. Identifying these triggers could reveal novel behavioral and hormonal mechanisms unique to avian species. Lastly, characterizing the types and concentrations of immunoglobulins in pigeon crop milk is an important direction for future research, as it could aid in the artificial formulation of crop milk to reduce breeding cycles in the pigeon industry. This study thus opens new directions for further research in this field.

CONCLUSIONS

This study revealed the complex cellular structure of the pigeon crop, identifying key cell types and signaling pathways involved in the synthesis of proteins, lipids, and immunoglobulins. SECs emerged as critical contributors to this process, employing the *XBP1* and UPR pathways for biomolecule production. Our study also elucidated the mechanisms underlying lipid production in these cells via exocytosis and endocytosis, highlighting the intricacies of crop lactation. Fibroblasts were shown to significantly contribute to the growth and protein synthesis of SECs via the BAFF signaling pathway, indicating important intercellular interactions (Figure 10). These findings enhance our understanding of the cellular and molecular mechanisms underpinning crop lactation in male pigeons and establish a foundation for future studies on similar processes in other avian species. This research contributes to a greater comprehension of avian biology and its significance for evolutionary and physiological research.

DATA AVAILABILITY

The raw sequencing data presented in this study were deposited in the Genome Sequence Archive within the National Genomics Data Center, part of the China National Center for Bioinformation/Beijing Institute of Genomics, Chinese Academy of Sciences. The datasets, including the

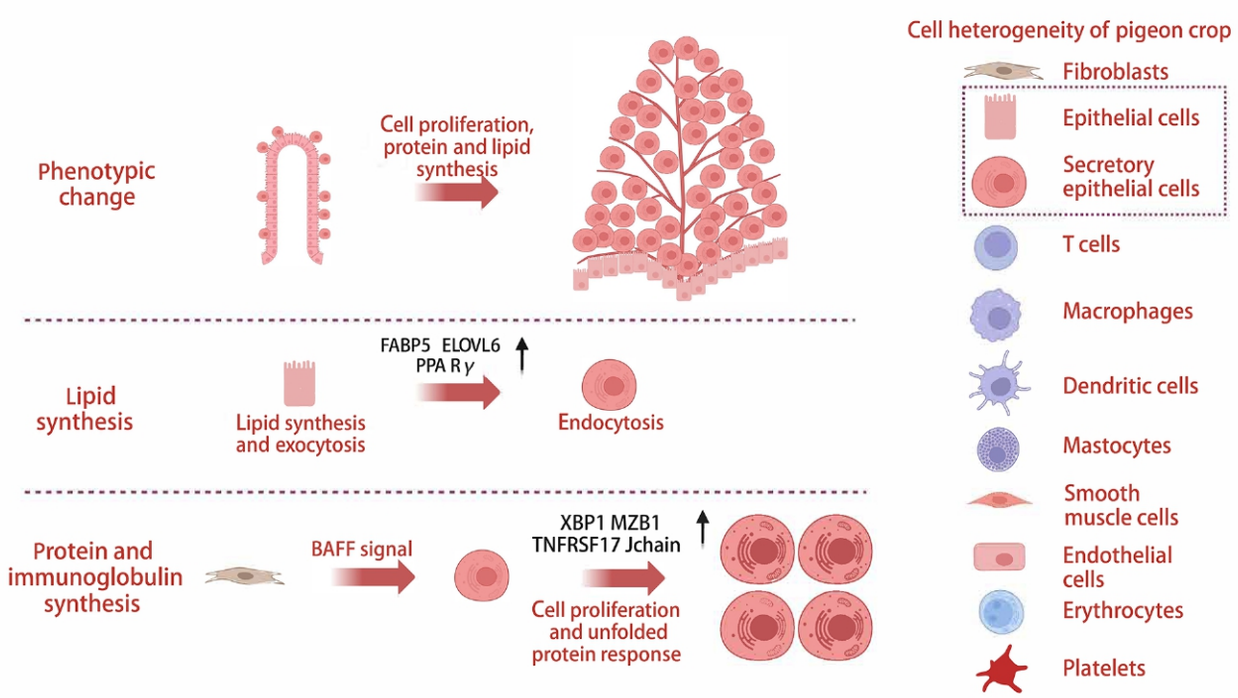


Figure 10 Schematic summarizing key findings of the study

RNA-seq (GSA: CRA018073), ribosome profiling (GSA: CRA018075), and single-cell RNA sequencing (GSA: CRA018097) data, are publicly accessible at https://ngdc.cncb.ac.cn/gsa. The aforementioned sequencing data can also be found in the Science Data Bank (https://www.scidb.cn/c/zoores, doi: 10.57760/sciencedb.j00139.00133) and the National Center for Biotechnology Information (NCBI) Sequence Read Archive (SRA) (https://submit.ncbi.nlm.nih.gov/subs/sra/), with the following accession numbers: RNA-seq (PRJNA1201361), Ribo-seq (PRJNA1201554), and scRNA-seq (PRJNA1202839).

SUPPLEMENTARY DATA

Supplementary data to this article can be found online.

COMPETING INTERESTS

The authors declare that they have no competing interests.

AUTHORS' CONTRIBUTIONS

J.L.: Conceptualization, Formal analysis, Investigation, Visualization, Methodology; S.FL.: Conceptualization, Funding acquisition, Project administration, Writing - review and editing; H.R.M.: Project administration, Writing - review and editing; H.X.J.: Software, Formal analysis, Investigation, Provided material support, Visualization, Methodology; S.B.L.: Software, Formal analysis, Investigation, Provided material support, Visualization, Methodology; X.F.X.: Provided material support, Methodology; J.T.W.: Software, Formal analysis, Investigation, Provided material support, Visualization, Methodology; X.L.: Software, Formal analysis, Investigation, Provided material support, Visualization, Methodology; W.T.Z.: Software, Formal analysis, Investigation, Provided material support, Visualization, Methodology; X.L.H.: Formal analysis, Methodology, Writing - review and editing; B.C.: Conceptualization, Software, Data curation, Formal analysis, Supervision, Funding acquisition, Investigation, Visualization, Methodology, Writing - original draft, Project administration, Writing - review and editing. All authors read and approved the final version of the manuscript.

ACKNOWLEDGMENTS

We sincerely thank Dr. Qing Zhang, Dr. Xiao-Xiao Zou, and Dr. Yu Ye from the National Key Laboratory for Swine Genetic Improvement and Germplasm Innovation, Ministry of Science and Technology of China, for their invaluable insights on data analysis. We also appreciate the support from Guangzhou Genedenovo Biotechnology Co., Ltd. for their assistance with sequencing and bioinformatics analysis. Finally, we acknowledge ChatGPT for contributions to spelling and grammar checks, as well as linguistic enhancement.

REFERENCES

Becht E, McInnes L, Healy J, et al. 2019. Dimensionality reduction for visualizing single-cell data using UMAP. *Nature Biotechnology*, **37**(1): 38–44.

Biton M, Haber AL, Rogel N, et al. 2018. T helper cell cytokines modulate intestinal stem cell renewal and differentiation. *Cell*, **175**(5): 1307–1320. E22.

Butler A, Hoffman P, Smibert P, et al. 2018. Integrating single-cell transcriptomic data across different conditions, technologies, and species. *Nature Biotechnology*, **36**(5): 411–420.

Cao JY, Spielmann M, Qiu XJ, et al. 2019. The single-cell transcriptional landscape of mammalian organogenesis. *Nature*, **566**(7745): 496–502.

Capuco AV, Akers RM. 2009. The origin and evolution of lactation. *Journal of Biology*, **8**(4): 37.

Chang LL, Tang QP, Zhang R, et al. 2023. Evaluation of meat quality of local pigeon varieties in China. *Animals*, **13**(8): 1291.

Chen S, Long M, Li XY, et al. 2024. *Codonopsis lanceolata* polysaccharide ameliorates high-fat diet induced-postpartum hypogalactia via stimulating prolactin receptor-mediated Jak2/Stat5 signaling. *International Journal of Biological Macromolecules*, **259**: 129114.

Chen SF, Zhou YQ, Chen YR, et al. 2018. fastp: an ultra-fast all-in-one FASTQ preprocessor. *Bioinformatics*, **34**(17): i884–i890.

Cheng SJ, Li ZY, Gao RR, et al. 2021. A pan-cancer single-cell transcriptional atlas of tumor infiltrating myeloid cells. *Cell*, **184**(3): 792–809. E23.

Classen HL, Apajalahti J, Svihus B, et al. 2016. The role of the crop in poultry production. *World's Poultry Science Journal*, **72**(3): 459–472.

Costea DE, Hills A, Osman AH, et al. 2013. Identification of two distinct

carcinoma-associated fibroblast subtypes with differential tumor-promoting abilities in oral squamous cell carcinoma. *Cancer Research*, **73**(13): 3888–3901.

Dai WT, White R, Liu JX, et al. 2022. Organelles coordinate milk production and secretion during lactation: insights into mammary pathologies. *Progress in Lipid Research*, **86**: 101159.

Daridon C, Youinou P, Pers JO. 2008. BAFF, APRIL, TWE-PRIL: who's who?. *Autoimmunity Reviews*, **7**(4): 267–271.

Davis KR, Giesy SL, Long QM, et al. 2016. XBP1 regulates the biosynthetic capacity of the mammary gland during lactation by controlling epithelial expansion and endoplasmic reticulum formation. *Endocrinology*, **157**(1): 417–428.

Dobin A, Davis CA, Schlesinger F, et al. 2013. STAR: ultrafast universal RNA-seq aligner. *Bioinformatics*, **29**(1): 15–21.

Domínguez Conde C, Xu C, Jarvis LB, et al. 2022. Cross-tissue immune cell analysis reveals tissue-specific features in humans. *Science*, **376**(6594): eabl5197.

Drake RR, Powers TW, Jones EE, et al. 2017. MALDI mass spectrometry imaging of *N*-linked glycans in cancer tissues. *Advances in Cancer Research*, **134**: 85–116

Engberg RM, Kaspers B, Schranner I, et al. 1992. Quantification of the immunoglobulin classes IgG and IgA in the young and adult pigeon (*Columba livia*). *Avian Pathology*, **21**(3): 409–420.

Eslami M, Schuepbach-Mallepell S, Diana D, et al. 2024. Unique and redundant roles of mouse BCMA, TACI, BAFF, APRIL, and IL-6 in supporting antibody-producing cells in different tissues. *Proceedings of the National Academy of Sciences of the United States of America*, **121**(29): e2404309121.

Ferguson L, Upton HE, Pimentel SC, et al. 2023. Streamlined and sensitive mono- and di-ribosome profiling in yeast and human cells. *Nature Methods*, **20**(11): 1704–1715.

Fewtrell MS, Mohd Shukri NH, Wells JCK. 2020. 'Optimising' breastfeeding: what can we learn from evolutionary, comparative and anthropological aspects of lactation?. *BMC Medicine*, **18**(1): 4.

Finak G, McDavid A, Yajima M, et al. 2015. MAST: a flexible statistical framework for assessing transcriptional changes and characterizing heterogeneity in single-cell RNA sequencing data. *Genome Biology*, **16**: 278.

Fu YT, Song Y, Jiang DL, et al. 2023. Comprehensive transcriptomic and metabolomic analysis revealed the functional differences in pigeon lactation between male and female during the reproductive cycle. *Animals*, **14**(1): 75.

Gillespie MJ, Crowley TM, Haring VR, et al. 2013. Transcriptome analysis of pigeon milk production – role of cornification and triglyceride synthesis genes. *BMC Genomics*, **14**: 169.

Gillespie MJ, Stanley D, Chen HL, et al. 2012. Functional similarities between pigeon 'milk' and mammalian milk: induction of immune gene expression and modification of the microbiota. *PLoS One*, **7**(10): e48363.

Hannan FM, Elajnaf T, Vandenberg LN, et al. 2023. Hormonal regulation of mammary gland development and lactation. *Nature Reviews Endocrinology*, **19**(1): 46–61.

Hasegawa D, Calvo V, Avivar-Valderas A, et al. 2015. Epithelial Xbp1 is required for cellular proliferation and differentiation during mammary gland development. *Molecular and Cellular Biology*, **35**(9): 1543–1556.

Horseman ND, Buntin JD. 1995. Regulation of pigeon cropmilk secretion and parental behaviors by prolactin. *Annual Review of Nutrition*, **15**: 213–238.

Hu XC, Gao CQ, Wang XH, et al. 2016. Crop milk protein is synthesised following activation of the IRS1/Akt/TOR signalling pathway in the domestic pigeon (*Columba livia*). *British Poultry Science*, **57**(6): 855–862.

Ingolia NT, Ghaemmaghami S, Newman JRS, et al. 2009. Genome-wide analysis in vivo of translation with nucleotide resolution using ribosome profiling. *Science*, **324**(5924): 218–223.

Ismail A, Jacquin L, Haussy C, et al. 2013. Food availability and maternal immunization affect transfer and persistence of maternal antibodies in nestling pigeons. *PLoS One*, **8**(11): e79942.

Kierończyk B, Rawski M, Długosz J, et al. 2016. Avian crop function – a review. *Annals of Animal Science*, **16**(3): 653–678.

Kim D, Langmead B, Salzberg SL. 2015. HISAT: a fast spliced aligner with low memory requirements. *Nature Methods*, **12**(4): 357–360.

Korhonen H, Marnila P, Gill HS. 2000. Milk immunoglobulins and complement factors. *British Journal of Nutrition*, **84**(S1): 75–80.

Korsunsky I, Millard N, Fan J, et al. 2019. Fast, sensitive and accurate integration of single-cell data with Harmony. *Nature Methods*, **16**(12): 1289–1296.

Lan Y, Hao C, Zeng X, et al. 2016. Serum glycoprotein-derived N- and O-linked glycans as cancer biomarkers. *American Journal of Cancer Research*, **6**(11): 2390–2415

Lauria F, Tebaldi T, Bernabò P, et al. 2018. riboWaltz: optimization of ribosome P-site positioning in ribosome profiling data. *PLoS Computational Biology*, **14**(8): e1006169.

Li B, Dewey CN. 2011. RSEM: accurate transcript quantification from RNA-Seq data with or without a reference genome. *BMC Bioinformatics*, **12**: 323.

Li JB, Zhang XA, Wang XQ, et al. 2024. Single-nucleus transcriptional and chromatin accessible profiles reveal critical cell types and molecular architecture underlying chicken sex determination. *Journal of Advanced Research*, doi: 10.1016/j.jare.2024.05.007.

Liao QY, Jiang DY, Zhang S, et al. 2024. Expression and function of mammary epithelial cell-derived immunoglobulins. *In*: Qiu XY, Huang J, Xu XJ. Non B Cell-Derived Immunoglobulins: The Structure, Characteristics and the Implication on Clinical Medicine. Singapore: Springer, 169–177.

Lun ATL, Riesenfeld S, Andrews T, et al. 2019. EmptyDrops: distinguishing cells from empty droplets in droplet-based single-cell RNA sequencing data. *Genome Biology*, **20**(1): 63.

Ma H, Bian SX, Li YL, et al. 2022. Analyses of circRNAs profiles of the lactating and nonlactating crops in pigeon (*Columba livia*). *Poultry Science*, **102**(3): 102464.

Ma H, Ni AX, Ge PZ, et al. 2020. Analysis of long non-coding RNAs and mRNAs associated with lactation in the crop of pigeons (*Columba livia*). *Genes*, **11**(2): 201.

Mantri M, Scuderi GJ, Abedini-Nassab R, et al. 2021. Spatiotemporal single-cell RNA sequencing of developing chicken hearts identifies interplay between cellular differentiation and morphogenesis. *Nature Communications*, **12**(1): 1771.

McDonald D, Wu Y, Dailamy A, et al. 2020. Defining the teratoma as a model for multi-lineage human development. *Cell*, **183**(5): 1402–1419. E18.

McGinnis CS, Murrow LM, Gartner ZJ. 2019. DoubletFinder: doublet detection in single-cell RNA sequencing data using artificial nearest neighbors. *Cell Systems*, **8**(4): 329–337. E4.

McNamara JP, Huber K. 2018. Metabolic and endocrine role of adipose tissue during lactation. *Annual Review of Animal Biosciences*, **6**(1): 177–195.

Morabito S, Miyoshi E, Michael N, et al. 2021. Single-nucleus chromatin accessibility and transcriptomic characterization of Alzheimer's disease. *Nature Genetics*, **53**(8): 1143–1155.

Nie LH, Lyros O, Medda R, et al. 2014. Endothelial-mesenchymal transition in normal human esophageal endothelial cells cocultured with esophageal adenocarcinoma cells: role of IL-1β and TGF-β2. *American Journal of Physiology - Cell Physiology*, **307**(9): C859–C877.

Pertea M, Pertea GM, Antonescu CM, et al. 2015. StringTie enables improved reconstruction of a transcriptome from RNA-seq reads. *Nature Biotechnology*, **33**(3): 290–295.

Pioli PD. 2019. Plasma cells, the next generation: beyond antibody

secretion. *Frontiers in Immunology*, **10**: 2768.

Robinson MD, McCarthy DJ, Smyth GK. 2010. edgeR: a Bioconductor package for differential expression analysis of digital gene expression data. *Bioinformatics*, **26**(1): 139–140.

Rotta R, Noack A. 2011. Multilevel local search algorithms for modularity clustering. *Journal of Experimental Algorithmics (JEA)*, **16**: 2.3.

Saidoune F, Even G, Lamri Y, et al. 2021. Effects of BAFF neutralization on atherosclerosis associated with systemic lupus erythematosus. *Arthritis & Rheumatology*, **73**(2): 255–264.

Sehgal A, Donaldson DS, Pridans C, et al. 2018. The role of CSF1R-dependent macrophages in control of the intestinal stem-cell niche. *Nature Communications*, **9**(1): 1272.

Shao YX, Ma WH, Ji F, et al. 2021. Exploration of proteomics analysis of crop milk in pigeons (*Columba livia*) during the lactation period. *ACS Omega*, **6**(42): 27726–27736.

Sharmin MM, Hayashi S, Miyaji M, et al. 2021. Insulin-like growth factor-1 induces IRE1-XBP1–dependent endoplasmic reticulum biogenesis in bovine mammary epithelial cells. *Journal of Dairy Science*, **104**(11): 12094–12104.

Smulski CR, Eibel H. 2018. BAFF and BAFF-receptor in B cell selection and survival. *Frontiers in Immunology*, **9**: 2285.

Stelloo S, Linder S, Nevedomskaya E, et al. 2020. Androgen modulation of XBP1 is functionally driving part of the AR transcriptional program. *Endocrine-Related Cancer*, **27**(2): 67–79.

Stelwagen K, Carpenter E, Haigh B, et al. 2009. Immune components of bovine colostrum and milk. *Journal of Animal Science*, **87**(13 Suppl): 3–9.

Trapnell C, Cacchiarelli D, Grimsby J, et al. 2014. The dynamics and regulators of cell fate decisions are revealed by pseudotemporal ordering of single cells. *Nature Biotechnology*, **32**(4): 381–386.

van Dijk A, Veldhuizen EJA, Haagsman HP. 2008. Avian defensins. *Veterinary Immunology and Immunopathology*, **124**(1-2): 1–18.

Wang LN, Zhu LF, Liang C, et al. 2023a. Targeting N6-methyladenosine reader YTHDF1 with siRNA boosts antitumor immunity in NASH-HCC by inhibiting EZH2-IL-6 axis. *Journal of Hepatology*, **79**(5): 1185–1200.

Wang LX, Zhu JG, Xie P, et al. 2023b. Pigeon during the breeding cycle: behaviors, composition and formation of crop milk, and physiological adaptation. *Life*, **13**(9): 1866.

Wang YJ, Wang X, Luo Y, et al. 2023c. Spatio-temporal transcriptome dynamics coordinate rapid transition of core crop functions in 'lactating' pigeon. *PLoS Genetics*, **19**(6): e1010746.

Wu YC, Yang SX, Ma JQ, et al. 2022. Spatiotemporal immune landscape of colorectal cancer liver metastasis at single-cell level. *Cancer Discovery*, **12**(1): 134–153.

Yonekura S, Tsuchiya M, Tokutake Y, et al. 2018. The unfolded protein response is involved in both differentiation and apoptosis of bovine mammary epithelial cells. *Journal of Dairy Science*, **101**(4): 3568–3578.

Zhang M, Hu SF, Min M, et al. 2021. Dissecting transcriptional heterogeneity in primary gastric adenocarcinoma by single cell RNA sequencing. *Gut*, **70**(3): 464–475.

Zheng YX, Chen ZY, Han YC, et al. 2020. Immune suppressive landscape in the human esophageal squamous cell carcinoma microenvironment. *Nature Communications*, **11**(1): 6268.

Zhong Y, Karaletsos T, Drewe P, et al. 2017. RiboDiff: detecting changes of mRNA translation efficiency from ribosome footprints. *Bioinformatics*, **33**(1): 139–141.

Zou YQ, Zhang RZ, Sabatelli P, et al. 2008. Muscle interstitial fibroblasts are the main source of collagen VI synthesis in skeletal muscle: implications for congenital muscular dystrophy types Ullrich and Bethlem. *Journal of Neuropathology & Experimental Neurology*, **67**(2): 144–154.

Li et al. *Zool. Res.* 2025, 46(1): 75−86
https://doi.org/10.24272/j.issn.2095-8137.2024.237
https://cstr.cn/32248.14.zr.2024.237

ZR | Zoological Research

Article Open Access

Transposable elements shape the landscape of heterozygous structural variation in a bird genome

Bo-Ping Li[1,2,3,#,*], Na Kang[2,#], Zao-Xu Xu[1,#], Hao-Ran Luo[2,4], Shi-Yu Fan[2], Xiao-Han Ao[2], Xing Li[2], Ya-Peng Han[1], Xiao-Bin Ou[1,*], Luo-Hao Xu[2,*]

[1] *Gansu Key Laboratory of Protection and Utilization for Biological Resources and Ecological Restoration in Longdong*, *Longdong University*, *Qingyang*, *Gansu* 745000, *China*

[2] *Integrative Science Center of Germplasm Creation in Western China (Chongqing) Science City*, *MOE Key Laboratory of Freshwater Fish Reproduction and Development*, *School of Life Sciences*, *Southwest University*, *Chongqing* 400715, *China*

[3] *College of Medicine*, *Longdong University*, *Qingyang*, *Gansu* 745000, *China*

[4] *Key Laboratory of Ministry of Education for the Coastal and Wetland Ecosystems*, *College of the Environment and Ecology*, *Xiamen University*, *Xiamen*, *Fujian* 361102, *China*

ABSTRACT

Avian genomes exhibit compact organization and remarkable chromosomal stability. However, the extent and mechanisms by which structural variation in avian genomes differ from those in other vertebrate lineages are poorly explored. This study generated a diploid genome assembly for the golden pheasant (*Chrysolophus pictus*), a species distinguished by the vibrant plumage of males. Each haploid genome assembly included complete chromosomal models, incorporating all microchromosomes. Analysis revealed extensive tandem amplification of immune-related genes across the smallest microchromosomes (dot chromosomes), with an average copy number of 54. Structural variation between the haploid genomes was primarily shaped by large insertions and deletions (indels), with minimal contributions from inversions or duplications. Approximately 28% of these large indels were associated with recent insertions of transposable elements, despite their typically low activity in bird genomes. Evidence for significant effects of transposable elements on gene expression was minimal. Evolutionary strata on the sex chromosomes were identified, along with a drastic rearrangement of the W chromosome. These analyses of the high-quality diploid genome of the golden pheasant provide valuable insights into the evolutionary patterns of structural variation in avian genomes.

Keywords: Golden pheasant; Structural variation; Transposable elements; Chromosome evolution

This is an open-access article distributed under the terms of the Creative Commons Attribution Non-Commercial License (http://creativecommons.org/licenses/by-nc/4.0/), which permits unrestricted non-commercial use, distribution, and reproduction in any medium, provided the original work is properly cited.

Copyright ©2025 Editorial Office of Zoological Research, Kunming Institute of Zoology, Chinese Academy of Sciences

INTRODUCTION

Aves, among the most species-rich vertebrate lineages, occupy nearly every global habitat (Armstrong et al., 2020). Avian genomes are characterized by distinct features, including a relatively small size compared to other vertebrates (Zhang et al., 2014), typically about 1.1 Gb, a feature attributed to a reduced abundance of repetitive sequences (Kapusta & Suh, 2017). Another hallmark of avian genomes is their highly conserved synteny, with very few intra- and interchromosomal rearrangements observed across divergent lineages (O'connor et al., 2024). Despite these evolutionary constraints, rapid evolutionary changes occur in regions associated with traits such as feather pigmentation, beak morphology, and ecological adaptations (Feng et al., 2020). Notably, the genetic variations underlying such traits are frequently located in non-coding regions, highlighting their potential role in avian evolution (Seki et al., 2017; Yusuf et al., 2020).

Although avian genomes have been the focus of large-scale genomic analyses, most available genome assemblies have relied on short-read sequencing technologies (Bravo et al., 2021; Stiller et al., 2024), which can inherently limit resolution. Key genomic regions, including the smallest microchromosomes (dot chromosomes), have historically been absent from assemblies until recent advancements enabled their successful reconstruction (Huang et al., 2023; Luo et al., 2023). Other complex genomic regions, including the major histocompatibility complex (MHC) (Zhu et al., 2023), segmental duplicates (Wang et al., 2024), subtelomeric

Received: 02 November 2024; Accepted: 26 November 2024; Online: 27 November 2024

Foundation items: This work was supported by the Foundation of Gansu Key Laboratory of Protection and Utilization for Biological Resources and Ecological Restoration in Longdong (LDSWZY202103) and Natural Science Foundation of Gansu Province (22JR5RM210) to B.P.L., and Gansu Ziwuling Ecosystem Observation and Research Station (20JR10RA658)

[#]Authors contributed equally to this work

*Corresponding authors, E-mail: bopingli0616@126.com; xbou@zju.edu.cn; luohaox@gmail.com

regions (Li et al., 2022), and sex chromosomes (Benham et al., 2024; Xu et al., 2024a), remain underexplored, further emphasizing the need for comprehensive analyses to elucidate avian genomic architecture.

Comparisons between *de novo* genome assemblies are thought to provide more accurate structural variation (SV) callings than read-mapping-based approaches. However, such comparisons require haplotype-resolved genome assemblies, which remain scarce for many taxa. Previous studies using diploid genome assemblies have revealed significant diversity in SVs between haploid genomes in mammals and plants (Sun et al., 2020; Yang et al., 2021). For instance, 11 663 SVs larger than 50 bp have been identified between the haploid genomes of a primate species, including a large 304 kb inversion (Yang et al., 2021). Despite advances in genomic sequencing, very few bird genome assemblies have been resolved to the haplotype level with chromosome-scale phasing. Emerging technologies, such as the integration of High-fidelity (HiFi) and Hi-C sequencing, enable scalable diploid genome assembly (Cheng et al., 2024) and have been applied to species such as turkeys (Barros et al., 2023) and chukars (Zhou et al., 2024). However, in-depth analyses of SVs in bird diploid genomes remain limited. Recent graph-based pangenome studies of 30 chicken genomes have demonstrated the effectiveness of haplotype-resolved genome assemblies for accurate SV calling in avian species.

The golden pheasant (*Chrysolophus pictus*), known for its beautiful plumage in males, has been introduced to various countries since the 18th century and shares its family, Phasianidae, with domesticated chicken (Xu et al., 2024b). Subject to extensive artificial breeding, this species offers a unique model for genomic exploration. Using a combination of Illumina short reads, Nanopore ultra-long reads, PacBio HiFi reads, and Hi-C mapping, coupled with a trio-binning assembly strategy (Koren et al., 2018), we generated near-complete diploid genome assemblies for the golden pheasant, resolving both haploid genomes to the chromosome level. Analyses revealed frequent tandem amplifications of immune-related genes on dot chromosomes. Additionally, intra- and interchromosomal segmental duplications (SDs) were characterized, alongside a landscape of SVs primarily shaped by transposable element (TE) insertions. These findings provide valuable insights into the structural dynamics of avian genomes and highlight the golden pheasant as a genomic model for investigating evolutionary processes.

MATERIALS AND METHODS

Sample collection

An F1 female golden pheasant and her parents were obtained from a local farm in Qingyang, Gansu Province, China, and raised at the Longdong College Agricultural Science and Technology Park under an artificial breeding program. The F1 chick, which died of natural causes, was immediately dissected. Muscle tissue was collected for long-read sequencing, while various tissues were preserved for RNA sequencing (RNA-seq) (Supplementary Table S1). Blood samples (1 mL) were collected from each parent for short-read sequencing. All research protocols were approved by the Institutional Animal Care and Use Committee (IACUC) of Southwest University (Approval No. IACUC-20241031-06).

HiFi sequencing

HiFi sequencing was performed on the F1 female golden pheasant following the protocols provided with the SMRTbell® Prep Kit 3.0 (Pacific Biosciences, USA). DNA quality was assessed using the Femto Pulse system (Agilent Technologies, USA) and DNA shearing and cleanup were conducted using Megaruptor 3 (Diagenode, Belgium). The preparation process included DNA repair, A-tailing, adapter ligation, and cleanup steps, followed by nuclease treatment and library size selection. Sequencing was performed on the PacBio Revio system (Pacific Biosciences, USA), with high-precision HiFi reads generated using CCS software (https://github.com/PacificBiosciences/ccs) with default parameters (minimum pass number=3, minimum RQ=0.99), achieving read quality exceeding Q20.

Ultralong Nanopore sequencing

An ultralong-read sequencing library was constructed using the SQK-LSK114 Kit (Oxford Nanopore Technologies, UK) for the same F1 female golden pheasant, with sequencing performed on a PromethION instrument (Oxford Nanopore Technologies, UK). DNA preparation involved dilution, end-repair, and purification. Specifically, after thawing and centrifuging (20°C, 10 s, 500 ×*g*) the DNA reference (DCS), 1 μg of genomic DNA was diluted to 47 μg with nuclease-free water. The reaction mixture, prepared in a polymerase chain reaction (PCR) tube, consisted of the DNA sample, ligation buffer, fast T4 DNA ligase, and adapter. Each component was gently mixed after addition, followed by gentle centrifugation and incubation at 20°C and 65°C for 5 min each. AMPure XP beads were resuspended and added to the reaction mixture, which was incubated at room temperature for 5 min. The beads were washed twice with 70% ethanol and resuspended in 61 μg of nuclease-free water. The eluate was transferred to a new tube for Qubit quantification (Thermo Fisher Scientific, USA). Ligation adapters and T4 DNA ligase were added to complete the adapter ligation, finalizing the preparation for sequencing.

Hi-C sequencing

Genomic DNA was extracted from the spleen of the F1 female golden pheasant to construct Hi-C libraries, sequenced on the Illumina MGI-2000 platform (MGI, China). Approximately 2 g of tissue was cut into strips and fixed with 2% formaldehyde in NIB buffer at 4°C under vacuum. Samples were subsequently washed, frozen, ground, and filtered. Nuclei were lysed with 0.1% sodium dodecyl-sulfate (SDS) at 65°C, and DNA was digested with DPN II at 37°C. Biotinylated nucleotides were used to label restriction ends, followed by blunt-end ligation at 16°C overnight. Crosslinks were reversed using proteinase K and DNA was purified using a QIAamp DNA Mini Kit (Qiagen, Germany). The purified DNA was then sheared to approximately 400 bp for sequencing.

RNA-seq

Total RNA was extracted from the heart, glandular stomach, kidney, gizzard, liver, bone, and muscle tissues. RNA quality was checked using 1% agarose gels, Qubit® RNA Assay Kit with a Qubit® 2.0 Fluorometer (Life Technologies, USA), and RNA Nano 6000 Assay Kit on the Bioanalyzer 2100 system (Agilent Technologies, USA).

RNA library preparation was performed with 1 μg of input RNA and the TruSeq RNA Library Preparation Kit (Illumina, USA). mRNA was purified from total RNA using poly-T magnetic beads. First-strand cDNA synthesis was carried out with random hexamer primers and M-MuLV reverse transcriptase, followed by second-strand synthesis with DNA

polymerase I and RNase H. Overhangs were converted to blunt ends, and Illumina adapters were ligated after adenylating the 3' ends. cDNA fragments of 150–200 bp were purified using the AMPure XP system, followed by PCR amplification with Phusion High-Fidelity DNA Polymerase and indexed primers. The libraries were purified again and assessed for quality on an Agilent Bioanalyzer 2100 (Agilent Technologies, USA). The libraries were then clustered using the cBot system and sequenced on the Illumina NovaSeq platform (Illumina, USA), generating 150 bp paired-end reads.

Short-read sequencing

Genomic DNA from parental blood samples was extracted using the cetyltrimethylammonium bromide (CTAB) method. Library preparation was performed with the MGIEasy Universal DNA Library Preparation Kit v.1.0 (MGI, China). Genomic DNA (1 μg) was fragmented to an average size of 200–400 bp using a Covaris instrument, and fragments were screened using MGIEasy DNA Clean beads (MGI, China). The selected fragments were subjected to end-repair, adenylation, and adapter ligation, followed by PCR amplification and purification with the same beads. The double-stranded PCR products were heat denatured and circularized to obtain single-stranded circular DNA (ssCir DNA) using MGIEasy circulation software. Final library quality was verified and sequenced using the DNBSEQ-T7RS platform (MGI, China).

Genome assembly and assessment

A high-quality diploid genome assembly for the golden pheasant was constructed using a trio-binning strategy, combining short-read sequencing data from the two parents and long-read sequencing data from the F1 individual. Assembly was performed with Hifiasm (v.0.19.3) in trio mode (Cheng et al., 2021) under default parameters, generating two sets of contig-level haploid genomes. Hi-C data facilitated scaffolding of the contigs using the Juicer (v.1.5) pipeline (Durand et al., 2016b). Visualization of Hi-C heatmaps using Juicebox (v.1.11.08) (Durand et al., 2016a) enabled manual adjustment of contig order and orientation. Genome assembly completeness was assessed using Benchmarking Universal Single-Copy Orthologs (BUSCO v.5.5.0) (Di Tommaso et al., 2017) with the aves_odb10 lineage (*n*=8 338) in genome mode.

Genome annotation

Repetitive sequences were annotated by constructing a custom repeat library with RepeatModeler (v.2.0.3) (Flynn et al., 2020) and Satellite Repeat Finder (SRF) (Zhang et al., 2023). The resulting library was combined with the chicken repeat library (Peona et al., 2021) and used to mask repeat sequences with RepeatMasker (v.4.1.2-p1). After soft-masking the repeats, the gene models were annotated based on homologous proteins, *de novo* prediction, and RNA-seq data. RNA-seq data from seven tissues (Supplementary Table S1) were assembled into transcripts using Trinity (v.2.8.5) (Grabherr et al., 2011). Gene predictions incorporated evidence from assembled transcripts and homologous proteins through MAKER (v.2.31.10) (Campbell et al., 2014; Grabherr et al., 2011). Transcripts were further assembled using a genome-guided approach with the HISAT2 (v.2.2.1)-StringTie (v.2.2.1) pipeline (Kim et al., 2015; Sirén et al., 2014). Gene model training was performed with Augustus (v.3.5.0) (Stanke et al., 2008) through the BUSCO (v.5.5.0) pipeline (Di Tommaso et al., 2017), with gene models predicted using the trained profile. The predicted gene models and aligned transcripts were integrated by EvidenceModeler (EVM, v.1.1.1) (Haas et al., 2008), and gene models were polished using the PASA pipeline (v.2.4.1) (Haas et al., 2008) with the transcripts generated by Trinity. Chromosome 16 was manually annotated using IGV-GSAman (Haas et al., 2008) based on RNA-seq transcript data.

Hi-C chromatin interaction

The BWA-MEM algorithm (v.0.7.17-r1188) was used to align Hi-C reads with the parameters "-A 1 -B 4 -E 50 -L 0 -t 16". The hicBuildMatrix function from HiCExplorer (v.3.6) was applied with the parameters "-binSize 100000, –inputBufferSize 400000, –restrictionSequence GATC", producing a Hi-C matrix file as output. This matrix was then normalized using hicCorrectMatrix with default parameters to account for the number of restriction sites per bin and biases related to open chromatin. The resulting h5 file was converted into ginteractions format using hicConvertFormat and subsequently used to calculate chromosomal interaction frequencies with custom Perl scripts (https://github.com/lurebgi/chicken-T2T/blob/main/Hi-C_analysese).

DNA methylation

Nanopore reads were aligned against the reference genome using minimap2 (v.2.26) (Li and Alkan, 2021) with the "map-ont" setting. Nanopolish (v.0.13.2) (Loman et al., 2015) was used to detect 5-methylcytosine bases in a CpG context. Methylation frequencies at individual sites were calculated using the script "calculate_methylation_frequency" from the Nanopolish package. Methylation data were further summarized in 500 bp windows to provide an overview of methylation patterns.

Gene expression

RNA-seq datasets used for expression analysis are shown in Supplementary Table S1. The HISAT2-StringTie pipeline (Kim et al., 2015; Sirén et al., 2014) was employed to map raw RNA-seq reads and calculate transcripts per million (TPM) values. For each gene, the mean expression level across tissues was determined to provide a comprehensive view of gene expression patterns.

Phylogenetic analysis

Phylogenetic trees were constructed using the longest protein sequences from the mallard (*Anas platyrhynchos*, GCA_015476345.1), chicken (*Gallus gallus*, GCA_024206055.2), common pheasant (*Phasianus colchicus*) (He et al., 2021), Swinhoe's pheasant (*Lophura swinhoii*, GCA_030408155.1), wild turkey (*Meleagris gallopavo*, GCA_000146605.4), Lady Amherst's pheasant (*Chrysolophus amherstiae*) (Garg et al., 2024), and golden pheasant (this study) (Bian et al., 2024). Single-copy orthologous genes among these species were identified using OrthoFinder (v.2.5.5) (Emms & Kelly, 2019) (Supplementary Table S2). Protein sequences within each orthologous group were aligned using MUSCLE (v.5.1.linux64) (Edgar, 2004), and the alignments were further filtered with the strict model in trimAl (v.1.4.rev15) (Capella-Gutiérrez et al., 2009). The aligned sequences of all orthologous groups for each species were concatenated to construct a species tree using IQ-TREE (v.2.1.2) (Nguyen et al., 2015). Divergence time estimations were determined using the approximate likelihood calculation method in PAML-MCMCTREE (PAML v.4.9j). Initial branch

lengths were estimated with PAMLCodeML, using gradient and Hessian information for the ultrametric tree, which was taken as input for MCMCTREE analysis (Nguyen et al., 2015). Markov chain Monte Carlo (MCMC) chains were run for 20 million steps to estimate divergence times. Fossil records of Galloanserae (66–86.8 million years (Ma)) were used for calibration (Clarke et al., 2005), along with TimeTree5 divergence estimates for chicken and turkey (26.02–31.55 Ma) (Li et al., 2015; Stein et al., 2015).

Single nucleotide polymorphism (SNP) heterozygosity rate analysis

Short reads were mapped to the CPswu2 reference genome using BWA (v.0.7.17) (Li & Durbin, 2009) with default parameters. BAM files were sorted, and duplicate reads were filtered using SAMtools (v.1.18) (Li & Durbin, 2009; Li et al., 2009) and Picard (v.1.56) (http://broadinstitute.github.io/picard). SNPs were called using the HaplotypeCaller and GenotypeGVCFs commands in the Genome Analysis ToolKit (v.3.8), then filtered using the VariantFiltration command with the following criteria: "DP<1.0/3.0; DP>3 || QD<2.0 || FS>60.0 || SOR>3.0 || MQ<40 || MQRankSum<-12.5 || ReadPosRankSum<-8.0". Finally, all SNPs were exported in variant call format (VCF) files (Liu et al., 2022). The SNP heterozygosity rate was calculated by dividing the number of heterozygous SNPs by the total number of genome bases (Wu et al., 2023).

Demographic history

The historical effective population size (*Ne*) of the golden pheasant and Lady Amherst's pheasant was estimated using the Pairwise Sequentially Markovian Coalescent model (PSMC, v0.6.5) (Liu & Hansen, 2016). Parameters were set to "-N30 -t15 -r5 -p '4+25*2+4+6'". The mutation of the golden pheasant was assumed to be 4.02e-9, with a generation time of 2 years based on Xu et al. (2024b).

Synteny analysis

Gffread (v.0.12.7) (Pertea & Pertea, 2020) was used to extract the protein sequences of each chromosome from the GGswu1 (Huang et al., 2023) and CPswu2 genomes. Synteny analysis was conducted using MCScan within the JCVI package (Tang et al., 2008). Macrosynteny for all chromosomes was visualized with "Jcvi.graphics.karyotype", while microsynteny, including analyses of chromosome 16 and chrW, was visualized using "jcvi.graphics.synteny".

Tandem amplification analysis

Dot chromosome annotation was performed using Miniprot (v.0.12-r237) and Augustus (v.3.5.0), identifying extensive tandem amplification of immune-related genes, including *WC1.1, CHIR* (Ig-like receptor) and *VH1* (heavy chain variable region of immunoglobulins). Gffread (v.0.12.7) and Seqkit (v.2.8.0) were used to extract the protein sequence of each gene, which were verified through BLAST on the National Center for Biotechnology Information (NCBI) database. MUSCLE (v.5.1.linux64), trimAl (v.1.4.rev15) and IQ-TREE (v.2.1.2) were used to build the phylogenetic trees (see Phylogenetic analysis). Additional tandem duplications were identified for other genes, such as *ANXA4* (annexin A4) and OR (olfactory receptor), which were analyzed using the same approach.

Segmental duplications

Segmental duplications (SDs) were identified with SDquest (v.0.1) (Pu et al., 2018) after masking repeats. Criteria for SD detection included sequence identity greater than 90% and lengths exceeding 2 kb. The identified SDs were further classified as interchromosomal or intrachromosomal. In total, 32 unique SDs were found in the golden pheasant, all present as single copies in chicken. For example, on chromosome 15, a segmental duplication involving *P2RX6* and nearby genes was detected in the golden pheasant. Hisat2 (v.2.2.1) was used to map the RNA-seq data of various tissues from the golden pheasant and chicken to the genome and Integrative Genomics Viewer (IGV) (Robinson et al., 2017) was used for visualization (Supplementary Figure S1).

SV identification and analysis

SVs were identified using nucmer (v.4.0.0) to align the two haploid genomes with parameters -b 500 to extend alignment clusters by 500 bp, followed by delta-filtering with stringent criteria (-1 -i 90 -l 200) to exclude alignments with <90% similarity or lengths <200 bp. SVs were identified using Assemblytics (v.1.2.1) (Nattestad & Schatz, 2016) and SyRi (v.1.6.4) (Goel et al., 2019), and results were merged for downstream analyses. HiFi read alignments were manually inspected in IGV to validate SV boundaries. RepeatMasker (v.4.1.2-p1) was used to perform genome-wide transposon analysis and parseRM.pl was used to analyze insertion time with the parameters "-p -l 50,1 -m 0.0019 -v" (Zhang et al., 2014). After extracting large indel intervals, the intersect and closest functions in bedtools (v.2.30.0) were applied to search for long terminal repeats (LTRs) and analyze the distance to the nearest exon. Expression analysis of SNPs proximal to large indels across the two haplotypes was conducted using the Genome Analysis ToolKit (v.3.8) and RNA-seq data from various tissues. VCF files were compared and analyzed (please refer to SNP heterozygous rate analysis).

Sex chromosome evolution

Evolutionary strata on the Z and W chromosomes were identified by first masking repetitive elements, followed by alignment of Z and W chromosomes using lastz (v.1.04.03) with parameters ("--step=19 --hspthresh=2 200 --inner=2 000 --ydrop=3 400 --gappedthresh=10 000") (Huang et al., 2022). Sequence similarity between the Z and W chromosomes was calculated using the pslScore script from the UCSC Genome Browser (https://genome.ucsc.edu/). Alignments with sequence similarity below 60% were excluded to reduce false positives, while those exceeding 90% were removed to account for potential unmasked repeats. Sequence similarity between the Z and W chromosomes was summarized over 100 kb non-sliding windows along the Z chromosomes.

RESULTS

Diploid genome assembly with complete chromosome models

A female chick from a golden pheasant trio family was sampled for haplotype-resolved diploid genome assembly. Sequencing generated 55.1 Gb of Nanopore, 64.7 Gb of HiFi, and 93.4 Gb of Hi-C sequencing reads for the F1 chick (Supplementary Table S1), along with 28.9 Gb and 36.5 Gb of short reads from the female and male parents, respectively. Genome assembly using Hifiasm in trio mode produced two phased haploid genomes, designated CPswu1 (maternal) and CPswu2 (paternal). Both haploid genomes exhibited high completeness, with total sequence lengths of 1.00 Gb and

1.06 Gb, respectively (Supplementary Table S3), comparable to the previous GCA_003413605.1 assembly (1.02 Gb) (Gao et al., 2018). CPswu1 contained 227 contigs with a N50 size of 33.0 Mb, while CPswu2 contained 198 contigs with a N50 size of 37.8 Mb, significantly improving on 38.2 kb in GCA_003413605.1. Hi-C data further anchored these contigs into chromosome models for both haplotypes. As expected, CPswu1 included a W chromosome, while CPswu2 included a Z chromosome. The assemblies revealed 41 chromosome models for each haploid genome (40 autosomes and one sex chromosome) (Supplementary Figure S2), consistent with the known karyotype of the golden pheasant. Autosomal models were categorized into 11 macrochromosomes, 19 microchromosomes, and 10 dot chromosomes based on size and epigenetic features (Figures 1A, 2A). BUSCO scores of 97.0% and 96.9% confirmed the high completeness of CPswu1 and CPswu2, respectively (Supplementary Figure S3). Repeat content was comparable between the two haploid genomes (15.1% vs. 14.5%, Supplementary Table S4). Long interspersed nuclear elements (LINEs) were dominant among TEs (Jae Lee et al., 2021), accounting for 6.96% and 7.43% of the genomes, respectively (Supplementary Figure S4) (Jin et al., 2022). CPswu1 and CPswu2 contained 18 and 19 chromosome models with no gaps, respectively, while 114 and 99 gaps were scattered across the genomes, predominantly in subtelomeric regions of macrochromosomes and on dot chromosomes (Supplementary Table S5).

Phylogenetic analysis was conducted using 3 192 single-copy orthologous genes from seven avian species (Supplementary Tables S1, S6) (Zhao et al., 2021), including six Galliformes species (chicken, golden pheasant, Swinhoe's pheasant, common pheasant, Lady Amherst's pheasant, and wild turkey) and one outgroup species (mallard). Results estimated that the golden pheasant diverged from other Galliformes species approximately 7.98 Ma (Figure 1B).

The golden pheasant, which is not considered threatened and can be artificially bred, exhibited an estimated heterozygosity rate of 0.53%, higher than that of most Galliformes species investigated (Figure 1C). Historical effective population size estimates revealed larger population sizes for the golden pheasant compared to its close relative, Lady Amherst's pheasant, over much of their evolutionary history (Figure 1D).

Restoration of acrocentric morphology of macrochromosomes

In the absence of CENP-A ChIP-seq data, centromeres in CPswu1 were located by identifying homologous centromeric regions in the chicken genome. Despite the overall high synteny between chicken and golden pheasant chromosomes, frequent telomeric inversions were observed in macrochromosomes (Figure 2B). For instance, telomeric inversions in chr7 and chr8 involved the entire short arm, relocating centromeres to the chromosome ends in the golden pheasant. Additionally, a macrochromosome fission event in chr2 was identified, consistent with findings from previous

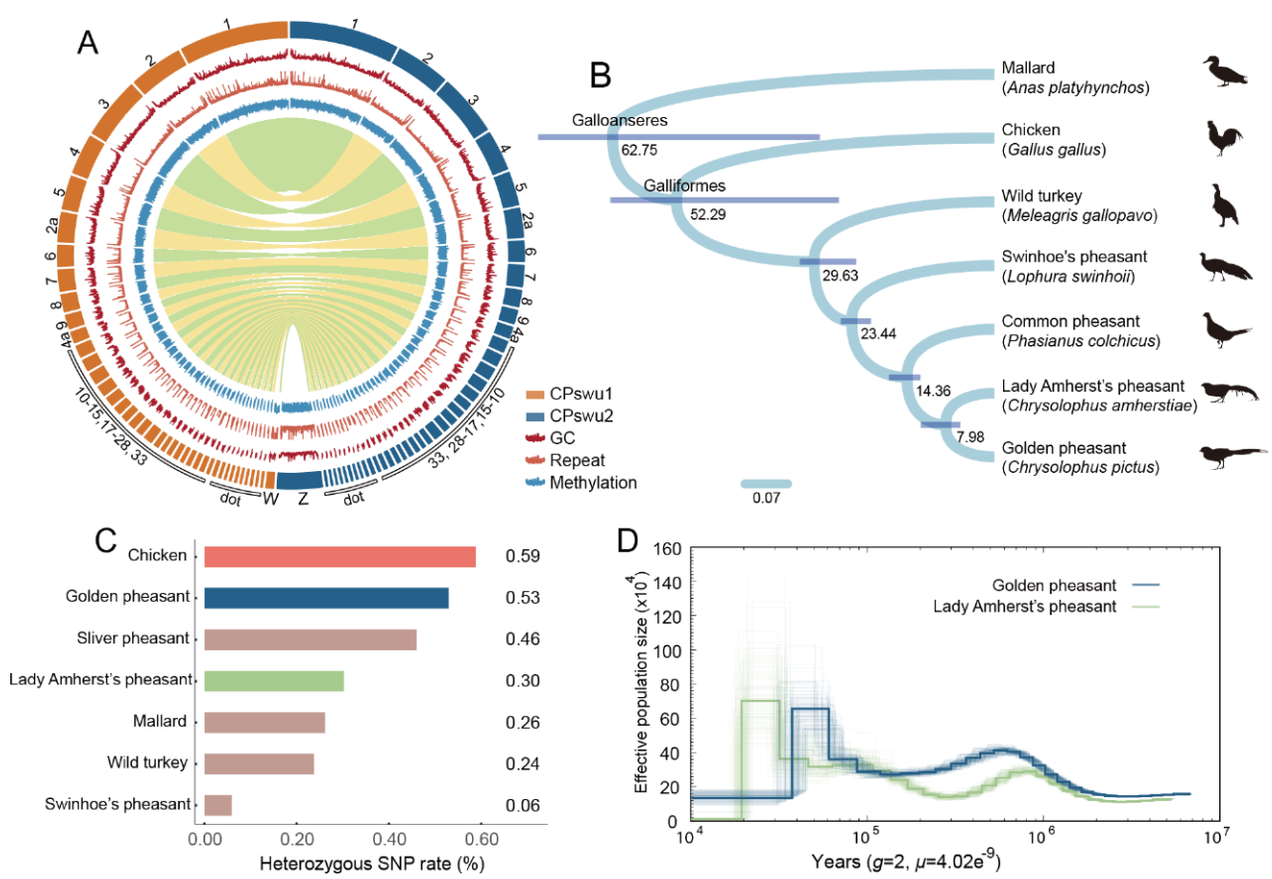


Figure 1 High-quality chromosome assembly and genomic features of golden pheasant

A: Circles show distribution of GC, repeat, and methylation content in CPswu1 and CPswu2 genomes. Synteny between two haplotypes is shown in the center. B: Phylogenetic tree was inferred with single-copy orthologs. Galloanserae fossil records (66–86.8 Ma) and divergence time for chicken and turkey (26.02–31.44 Ma) were used for calibration. C: Golden pheasant showed relatively high heterozygosity among seven Galloanserae genomes. D: Golden pheasant showed a higher effective population size than Lady Amherst's pheasant.

comparative cytogenetic analyses. Interestingly, the split sites coincided with chicken centromeres, resulting in two acrocentric chromosomes (Figure 2B).

To assess the potential impact of altered chromosome morphology on 3D genome organization in the nucleus, interchromosomal chromatin interactions were analyzed using Hi-C data. No interchromosomal interactions involving centromeres were detected; however, frequent interactions among macrochromosome telomeres were identified (Figure 2A). Moreover, while expected frequent interactions among microchromosomes were observed (Liu et al., 2021), intensive interactions between macrochromosome euchromatin and microchromosomes were also detected (Figure 2A; Supplementary Figure S5). These findings suggest that macrochromosome euchromatin may position closer to the nuclear interior (Figure 2C) and potentially contribute to the regulation of microchromosome gene expression.

Tandem amplification of immune genes

The duplication of immune-related genes was analyzed with a focus on chr16, one of the most complex bird chromosomes, known for harboring many immune-related genes including the MHC region (Kulski et al., 2019). The assembled sizes of chr16 in the golden pheasant were 4.61 Mb (CPswu1) and 4.64 Mb (CPswu2), similar to that of the chicken (4.93 Mb). The euchromatic regions of chr16 exhibited high synteny between the two species, except for two inversions near the MHC-Y region (Figure 3A).

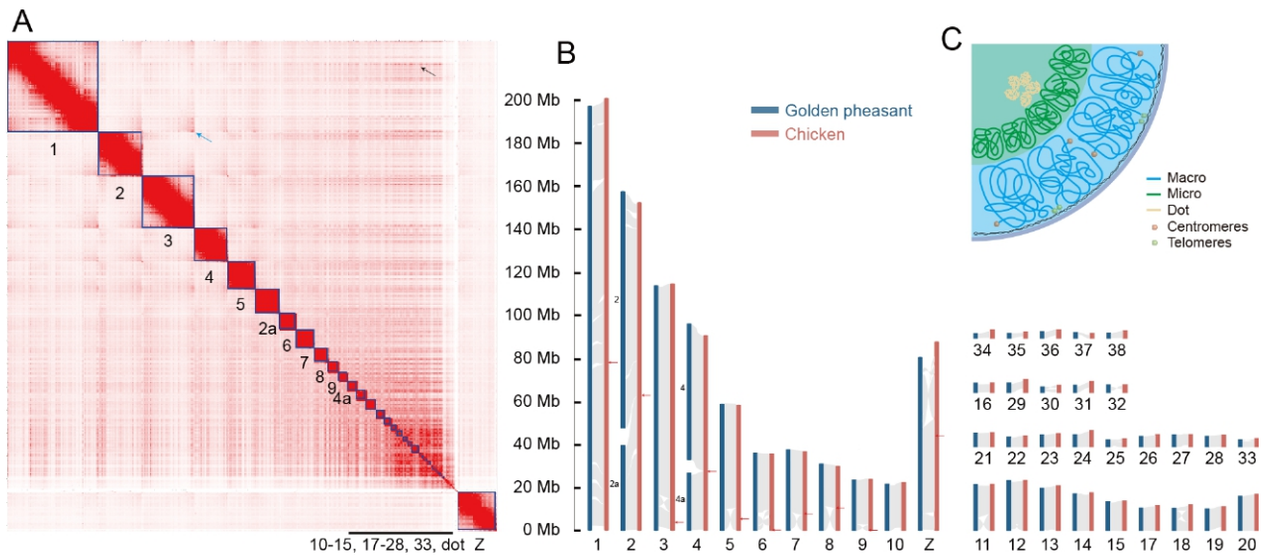


Figure 2 Acrocentric chromosome morphology

A: Hic interaction map showing frequent interactions between macrochromosome telomeric regions (blue arrow) and between macrochromosome euchromatin and microchromosomes (black arrow). B: Conserved chromosomal synteny between chicken and golden pheasant inferred by MCScan. Red arrow indicates chicken centromeres. C: Proposed chromosome positioning in the nucleus.

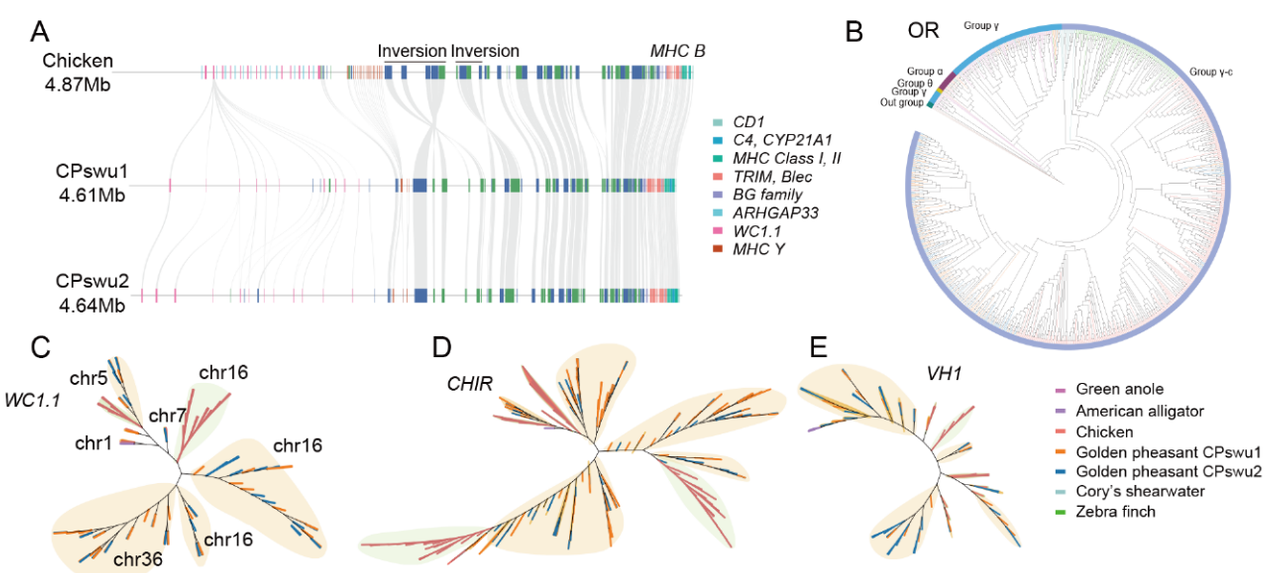


Figure 3 Amplification of immune-related genes on dot chromosomes

A: Microsynteny visualization of chr16 between chicken and diploid golden pheasant genomes. B: Phylogenetic tree for amplified genes of olfactory receptor (OR) re-rooted with adenosine receptor A2b from GenBank. C–E: Phylogenetic trees for amplified genes *WC1.1* (C), *CHIR* (immunoglobulin-like receptor) (D), and *VH1* (immunoglobulin heavy chain variable) (E) re-rooted with American alligator orthologs.

Manual annotation revealed 137 protein-coding genes in chicken chr16, and 111 and 110 genes in CPswu1 and CPswu2, respectively. Although the euchromatic regions of chr16 shared similar gene content between the chicken and golden pheasant (Supplementary Table S7), the heterochromatic regions displayed notable differences (Figure 3A). In the heterochromatic part of chr16, 10 and 12 copies of the *WC1.1* gene were identified in CPswu1 and CPswu2, respectively (Figure 3A), compared to 13 copies in the chicken chr16. Phylogenetic analysis suggested independent amplification of *WC1.1* in the two species (Figure 3C). Furthermore, golden pheasants exhibited further amplification of *WC1.1* on chr36, another dot chromosome, an event absent in chicken (Figure 3C).

Beyond chr16, amplification of other immune-related genes was detected on dot chromosomes. *CHIR* (Ig-like receptor) and *VH1* (heavy chain variable region of immunoglobulins) were amplified on chr31 and chr34, respectively. On chr31, 96 copies of *CHIR* were annotated in the chicken, compared to 136 copies in CPswu1 and 80 copies in CPswu2. Phylogenetic analysis indicated that *CHIR* likely underwent three duplication events before divergence of the chicken and golden pheasant (Figure 3D), followed by species-specific amplifications, resembling the scenario for *WC1.1*. Similarly, the *VH1* gene was duplicated multiple times in the Phasianidae ancestor but experienced more extensive amplification in the golden pheasant compared to the chicken (Figure 3E).

Amplification of other genes

In addition to immune-related genes, several other amplified genes were identified (Supplementary Tables S8, S9), including annexin A4 (*ANXA4*) (Supplementary Figure S6) and the olfactory receptor (OR) gene family (Figure 3B). *ANXA4*, which encodes a protein that potentially interacts with adenosine triphosphate (ATP) and is normally expressed almost exclusively in epithelial cells, was recurrently amplified on four different dot chromosomes in the golden pheasant: chr16, chr30, chr36, and chr37, with 15, five, 15, and five copies, respectively. This amplification was absent in chicken. The OR gene family exhibited significant amplification on chr29 in both chickens and golden pheasants (Supplementary Table S9).

Segmental duplications contribute to gene copy number variation

A total of 155 intrachromosomal SDs (Figure 4A) and 87 interchromosomal SDs (Figure 4B) with alignment identities higher than 90% and lengths larger than 2 kb were identified (Supplementary Tables S10, S11). Among these, 34.7% exhibited sequence identities exceeding 97% between pairs (Figure 4C), suggesting recent duplication events. Gene duplications were associated with 32 (or 13.3%) of the identified SDs (Supplementary Table S12). For instance, *P2RX6* and its nearby genes were duplicated due to a ~15 kb SD (Figure 4D). This duplication was present in both haploid genomes and validated through long-read mapping

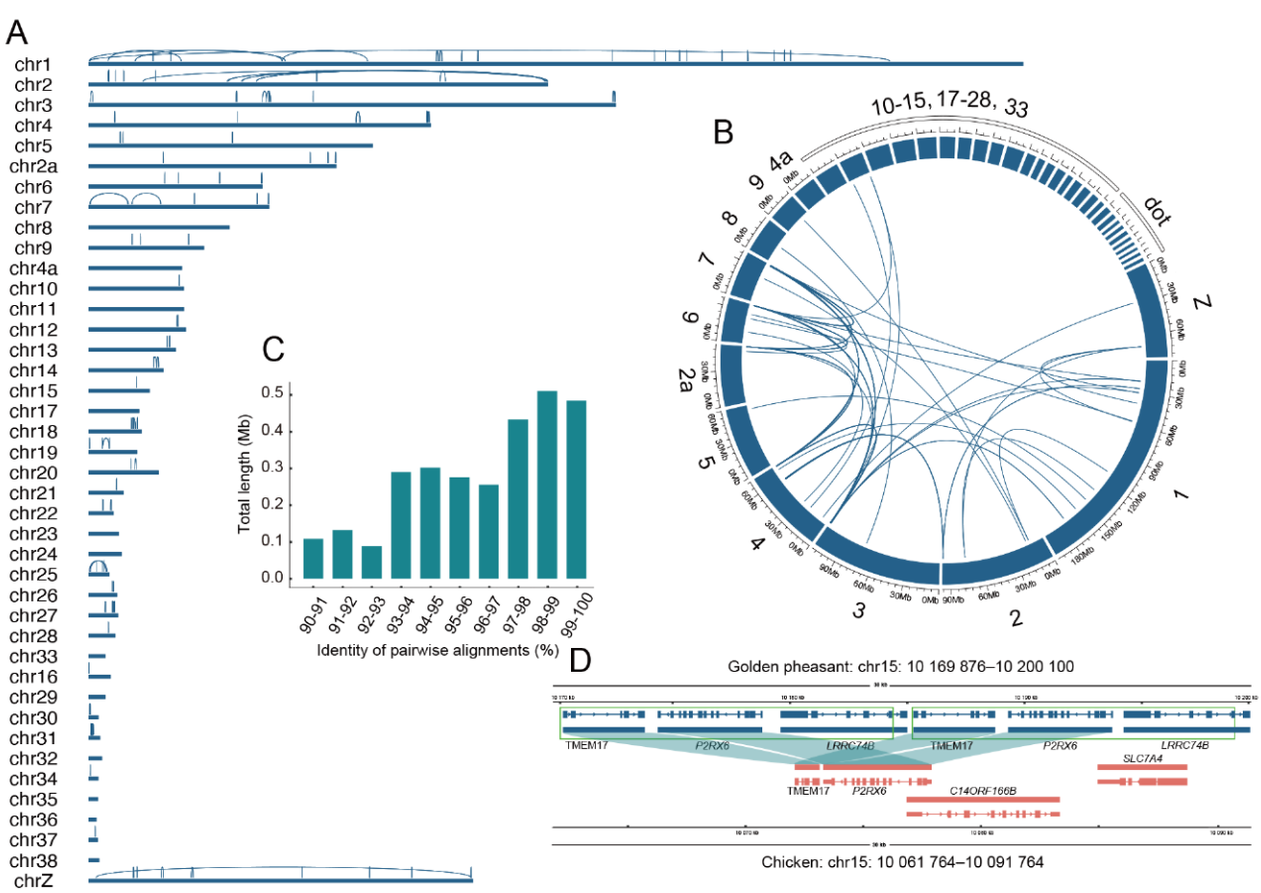


Figure 4 Segmental duplication (SD) landscape

A, B: Intrachromosomal (A) and interchromosomal (B) SDs are shown. C: Histogram for total lengths of SDs of varying identities. D: Example of SD involving *P2RX6*, *TMEM17*, and *LRRC14B*, with single copies in chicken but two copies in golden pheasant.

(Supplementary Figure S6). The expression patterns of the duplicated *P2RX6* remained consistent with those of the original copy (Supplementary Figure S6), a trend observed for most duplicated genes (Supplementary Table S13).

Frequent large indels driven by recent TE insertions

The diploid genome assembly enabled the identification of SVs between the two haplotypes of the golden pheasant genome. A total of 11 432 SVs were detected, comprising 9 576 large indels (>50 bp), 1 747 copy-number variants, 64 translocations, eight inversions, and 37 inverted translocations (Figure 5A; Supplementary Table S14). Large indels (83.8%) represented the majority of SVs, while inversions (0.1%) were rare. A disproportionate number of SVs were observed in the heterochromatin of dot chromosomes (Supplementary Figure S7), possibly due to the low recombination rates in these regions.

Over 91.4% of the large indels were shorter than 1 kb, with a notable enrichment of indels around 7 kb in length (Figure 5B). Indels measuring 5–8 kb accounted for 15.8% of the total indel length (Figure 5C). These larger indels were predominantly associated with TEs, particularly LTRs. The large LTRs linked to these indels ranged from 5–10 kb in size (Figure 5C), consistent with full-length LTRs. Supporting this, the insertion times of indel-associated LTRs were more recent than the genome-wide average, with multiple waves occurring in the last 30 Ma (Figure 5D; Supplementary Table S15).

To evaluate the functional impact of large indels, their distance to gene bodies was analyzed. Large indels were found to occur further away from gene bodies than expected, with lower proportions located within gene bodies or their flanking regions (Figure 5E). Furthermore, few genes near large indels exhibited biased allele expression, suggesting minimal disruption to gene regulation (Supplementary Figure S8).

Structurally rearranged W chromosome with conserved gene expression

The assembled W chromosome of the golden pheasant was 12.9 Mb in size, comparable to the 14.2 Mb chicken W chromosome. Similar to the chicken W assembly, the golden pheasant W assembly contained 14 gaps, suggesting that the sequence remains incomplete. Repetitive sequences accounted for 87.45% of the golden pheasant W chromosome, with ERVK being the dominant TE family in both species (Figure 6E). Annotation identified 29 non-redundant W-linked genes in the golden pheasant, 28 of which have homologs in the chicken (Figure 6A; Supplementary Table S16). The chicken W chromosome contained only two additional genes (Figure 6D), highlighting the high conservation of W chromosome gene content between the two species. However, the chromosomal locations of these conserved genes were not collinear, likely due to frequent inversions.

Gene expression analysis revealed no significant differences in W-linked gene expression between the two birds. Consistent with earlier findings (Xu et al., 2019), W-linked genes in both species were widely expressed across tissues, with most exhibiting high expression levels (Figure 6B). Remarkably, the expression patterns of W-linked genes remained highly conserved, despite ~50 Ma of divergence and differences in sexual dimorphism between the two species. Finally, an analysis of sex chromosome evolutionary strata due to recombination suppression (Figure 6C) indicated that the two birds share a common history of sex chromosome degeneration, reflected in the similar number and length of these strata.

DISCUSSION

The SV landscape in avian genomes remains poorly understood, largely due to the limited availability of haplotype-

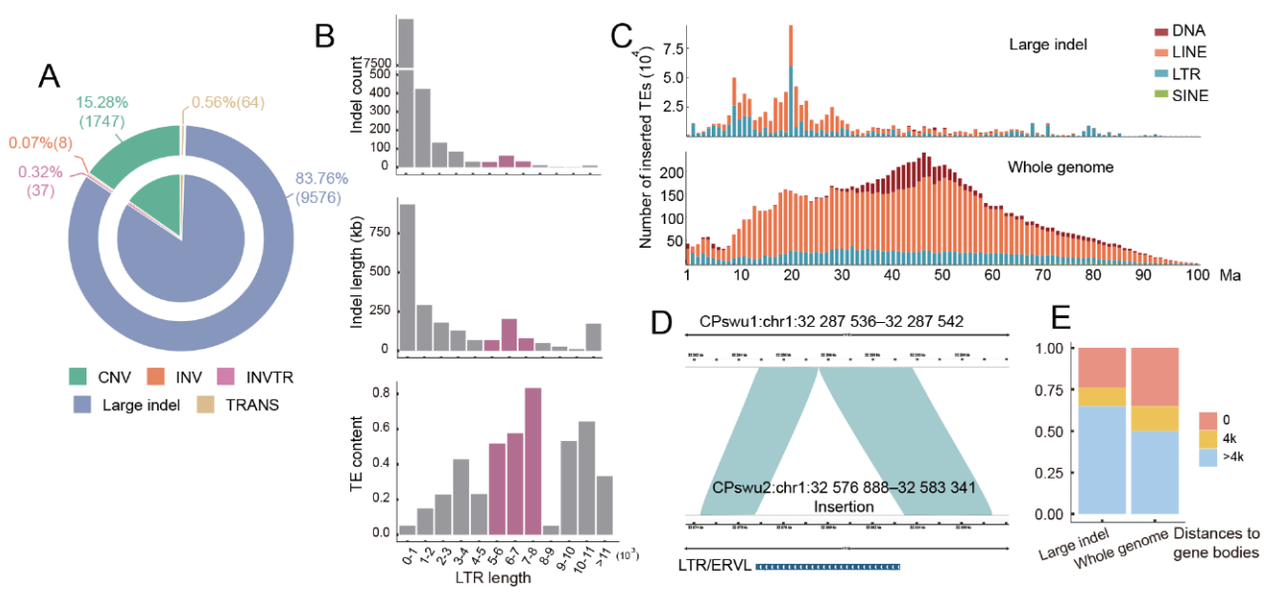


Figure 5 Frequent large indels caused by recent TE insertions

A: Proportion and number of each SV type, including copy number variants (CNV), single nucleotide variant (SNVs), inversions (INVs), translocations (TRANS), and inverted translocations (INVTRs). B: Number and total length of large indels, and TE content over different lengths of LTRs. Results showed enrichment of large LTRs in the 5–8 kb range, with those LTRs exhibiting higher TE content. C: More recent TE insertions in large indel regions relative to whole-genome background. D: Example of a large indel involving a full-length LTR in chr1. E: Large indels tended to be distant from gene bodies or gene-flanking regions. X-axis refers to distance from gene bodies.

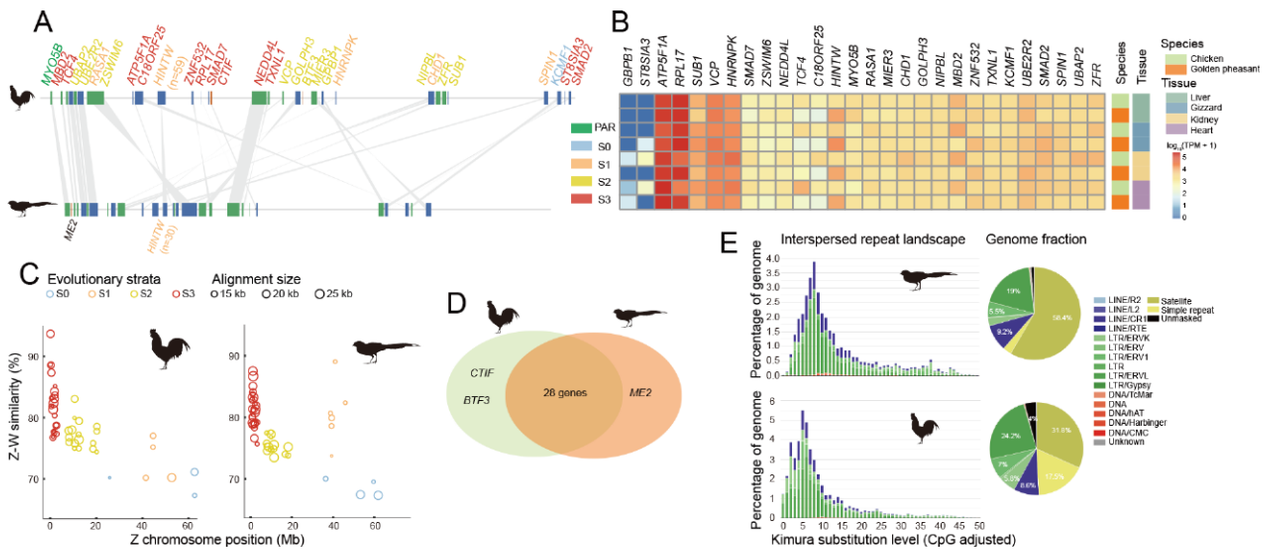


Figure 6 Evolutionary history of golden pheasant sex chromosomes

A: Gene order of W chromosome was extensively rearranged. B: Gene expression profile of the W-linked genes was conserved between both birds. C: Sequence divergence of Z and W chromosomes revealed a pattern of evolutionary strata with shared evolutionary history between the two species. X-axis shows the position of the Z chromosome, Y-axis shows the sequence similarity of Z and W. D: A large proportion of W-linked genes were shared by both birds. E: Divergence of TEs on W chromosomes of chicken and golden pheasant.

resolved genome assemblies or long-read-based pangenomes (Fang & Edwards, 2024). By employing a trio-binning approach, this study assembled a near-complete diploid genome of the golden pheasant, achieving telomere-to-telomere completeness for nearly half of its chromosomes. This level of resolution is unprecedented for avian genome assemblies, where small microchromosomes (dot chromosomes) are frequently missing (Ko et al., 2022). While all dot chromosomes were identified in both haploid assemblies, they retained more assembly gaps and higher SV frequencies than other chromosomes, suggesting that their genetic diversity may be underappreciated. The challenges associated with sequencing dot chromosomes are likely attributed to their repetitive nature and high GC-rich regions (Huang et al., 2023). To bridge the remaining gaps, additional Oxford Nanopore Technology (ONT) sequencing is needed, as GA-rich simple repeats are difficult to sequence using HiFi sequencing technology.

Unlike the metacentric or submetacentric macrochromosomes in chickens, formed due to fusions of ancestral acrocentric chordate chromosomes, most golden pheasant chromosomes exhibited acrocentric morphology, including many macrochromosomes that appear to have reverted to an acrocentric state, except for two large macrochromosomes retaining their original structure. Chromosome synteny analysis identified the centromeric breakpoints of inversions and fissions responsible for the formation of acrocentric chromosomes in the golden pheasant. These chromosomal rearrangements likely contributed to alterations in 3D chromatin architecture, as evidenced by the observed telomeric clustering (Bista et al., 2024) near the nuclear periphery (Figure 2C).

The golden pheasant genome revealed a striking depletion of inversions but a comparable number of copy number variations to mammalian genomes and an unexpectedly high prevalence of large indels (Supplementary Table S14). Avian genomes are typically characterized by smaller sizes, lower TE accumulation, and stronger evolutionary constraints (Zhang et al., 2014). The prevalence of extensive heterozygous large indels driven by recent TE insertions suggests that avian genomes may lack strong selective pressure for purging TEs, indicating that TE insertion polymorphism may be more common than previously thought. While most TE insertions were located in the intergenic region (68.4%), a considerable proportion also occurred in the introns (26.6%), with a smaller proportion found in the exons (5.0%), suggesting that some TE insertions may have important functional implications. Comprehensive pangenome analyses are essential for characterizing the dynamics of TE insertion polymorphisms (He et al., 2024) and determining whether TEs have been co-opted or exapted for regulatory functions, a question requiring future expression and epigenetic studies (Capy, 2021).

Our study identified a surprisingly high number of duplicated genes, primarily immune-related, on dot chromosomes —a genomic feature often overlooked in previous research. Chicken chr16, one such dot chromosome, is well known for containing MHC genes (He et al., 2021; O'connor et al., 2019). Duplication of MHC and other immune-related genes is an important source of genetic diversity, enabling a rapid and robust response to a wide range of pathogens (Conrad & Antonarakis, 2007). The relatively frequent TE activity observed on dot chromosomes raises the intriguing possibility that TEs may have contributed to immune gene duplications, warranting further investigation (Gozashti et al., 2024). Our findings provide new opportunities to deepen our understanding of genetic variation in avian immune genes and their responses to avian pathogens.

The W chromosome remains one of the most complex and evolutionarily dynamic regions of bird genomes (Peona et al., 2020; Peona et al., 2021; Xu et al., 2019; Xu & Zhou, 2020). Due to its highly repetitive and heterochromatic nature, a complete sequence assembly has yet to be achieved, consistent with other degenerated W chromosomes in birds (Huang et al., 2022; Wang et al., 2021). Previous studies have revealed extensive rearrangements in the W chromosome between chickens and songbirds (Peona et al., 2021), which diverged over 66 Ma. Remarkably, our findings demonstrated

that this pattern of rapid chromosomal reorganization persisted even between closely related species, suggesting that the W chromosome in birds evolved rapidly in terms of chromosomal organization, although its sequence evolution appears to have progressed more slowly compared to autosomes (Zhou et al., 2014). In the golden pheasant, we found that gene content and expression patterns of the W chromosome were almost identical to those of the chicken, despite extensive rearrangements in gene order and significant species divergence. Thus, our analysis suggests that the gene repertoire of the Galliformes W chromosome was likely shaped by ancient W chromosome decay, with minimal gene losses or gains following species divergence, and that gene synteny is not required to maintain the conserved gene expression patterns.

CONCLUSIONS

Using a trio-binning approach, we successfully assembled a near-complete diploid genome for the golden pheasant, achieving unprecedented resolution in genome completeness and quality. The high-quality assemblies enabled comprehensive analyses of SVs, segmental duplications, gene amplifications, and sex chromosomes. Our findings highlighted the critical role of TEs in driving heterozygous SVs in bird genomes, corroborating their functional significance in shaping avian genome architecture (Kapusta & Suh, 2017). Chromosomal rearrangements, including inversions and fissions, were shown to influence chromosome morphology and 3D chromosome configuration. However, these structural changes appear to have limited regulatory impact on the expression of W-linked genes. This study highlights the utility of trio-binning and similar approaches for exploring genome diversity and evolution in non-model organisms.

DATA AVAILABILITY

All sequencing data were deposited in the NCBI database under BioProjectID PRJNA857339 and the Genome Sequence Archive (Chen et al., 2021) at the National Genomics Data Center (CNCB-NGDC Members and Partners, 2022), China National Center for Bioinformation / Beijing Institute of Genomics, Chinese Academy of Sciences (GSA: CRA021136). A full list of accession IDs is available in Supplementary Table S1. The genome assembly data were deposited at the Science Data Bank (https://doi.org/10.57760/sciencedb.18296) and NCBI under BioProject ID PRJNA1048143 and PRJNA1048144.

SUPPLEMENTARY DATA

Supplementary data to this article can be found online.

COMPETING INTERESTS

The authors declare that they have no competing interests.

AUTHORS' CONTRIBUTIONS

L.H.X. and X.B.O. conceived and designed the project. B.P.L. and Y.P.H. collected experimental samples. N.K., Z.X.X., H.R.L., S.Y.F., X.H.A., and X.L. performed data analysis. L.H.X. and N.K. wrote the manuscript. B.P.L., X.B.O., and Z.X.X. participated in revising the manuscript. All authors read and approved the final version of the manuscript.

REFERENCES

Armstrong J, Hickey G, Diekhans M, et al. 2020. Progressive cactus is a multiple-genome aligner for the thousand-genome era. *Nature*, **587**(7833): 246–251.

Barros CP, Derks MFL, Mohr J, et al. 2023. A new haplotype-resolved turkey genome to enable turkey genetics and genomics research. *GigaScience*, **12**: giad051.

Benham PM, Cicero C, Escalona M, et al. 2024. Remarkably high repeat content in the genomes of sparrows: the importance of genome assembly completeness for transposable element discovery. *Genome Biology and Evolution*, **16**(4): evae067.

Bian C, Li R H, Ruan Z Q, et al. 2024. Chromosome-level genome assembly of the glass catfish (*Kryptopterus vitreolus*) reveals molecular clues to its transparent phenotype. *Zoological Research*, **45**(5): 1027–1036.

Bista B, González-Rodelas L, Álvarez-González L, et al. 2024. De novo genome assemblies of two cryptodiran turtles with ZZ/ZW and XX/XY sex chromosomes provide insights into patterns of genome reshuffling and uncover novel 3D genome folding in amniotes. *Genome Research*, **34**(10): 1553–1569.

Bravo GA, Schmitt CJ, Edwards SV. 2021. What have we learned from the first 500 avian genomes? *Annual Review of Ecology, Evolution, and Systematics*, **52**: 611–639.

Campbell MS, Holt C, Moore B, et al. 2014. Genome annotation and curation using MAKER and MAKER‐P. *Current Protocols in Bioinformatics*, **48**: 4–11.

Capella-Gutiérrez S, Silla-Martínez JM, Gabaldón T. 2009. trimAl: a tool for automated alignment trimming in large-scale phylogenetic analyses. *Bioinformatics*, **25**(15): 1972–1973.

Capy P. 2021. *Taming, domestication* and *exaptation*: trajectories of transposable elements in genomes. *Cells*, **10**(12): 3590.

Chen TT, Chen X, Zhang SS, et al. 2021. The genome sequence archive family: toward explosive data growth and diverse data types. *Genomics, Proteomics & Bioinformatics*, **19**(4): 578–583.

Cheng HY, Asri M, Lucas J, et al. 2024. Scalable telomere-to-telomere assembly for diploid and polyploid genomes with double graph. *Nature Methods*, **21**(6): 967–970.

Cheng HY, Concepcion GT, Feng XW, et al. 2021. Haplotype-resolved de novo assembly using phased assembly graphs with hifiasm. *Nature Methods*, **18**(2): 170–175.

Clarke JA, Tambussi CP, Noriega JI, et al. 2005. Definitive fossil evidence for the extant avian radiation in the cretaceous. *Nature*, **433**(7023): 305–308.

CNCB-NGDC Members and Partners. 2022. Database resources of the national genomics data center, china national center for bioinformation in 2022. *Nucleic Acids Research*, **50**(D1): D27–D38.

Conrad B, Antonarakis SE. 2007. Gene duplication: a drive for phenotypic diversity and cause of human disease. *Annual Review of Genomics and Human Genetics*, **8**: 17–35.

Di Tommaso P, Chatzou M, Floden EW, et al. 2017. Nextflow enables reproducible computational workflows. *Nature Biotechnology*, **35**(4): 316–319.

Durand NC, Robinson JT, Shamim MS, et al. 2016a. Juicebox provides a visualization system for Hi-C contact maps with unlimited zoom. *Cell Systems*, **3**(1): 99–101.

Durand NC, Shamim MS, Machol I, et al. 2016b. Juicer provides a one-click system for analyzing loop-resolution Hi-C experiments. *Cell Systems*, **3**(1): 95–98.

Edgar RC. 2004. MUSCLE: multiple sequence alignment with high accuracy and high throughput. *Nucleic Acids Research*, **32**(5): 1792–1797.

Emms DM, Kelly S. 2019. OrthoFinder: phylogenetic orthology inference for comparative genomics. *Genome Biology*, **20**(1): 238.

Fang B, Edwards SV. 2024. Fitness consequences of structural variation inferred from a House Finch pangenome. *Proceedings of the National Academy of Sciences of the United States of America*, **121**(47): e2409943121.

Feng SH, Stiller J, Deng Y, et al. 2020. Dense sampling of bird diversity

increases power of comparative genomics. *Nature*, **587**(7833): 252–257.

Flynn JM, Hubley R, Goubert C, et al. 2020. RepeatModeler2 for automated genomic discovery of transposable element families. *Proceedings of the National Academy of Sciences of the United States of America*, **117**(17): 9451–9457.

Gao GQ, Xu M, Bai CL, et al. 2018. Comparative genomics and transcriptomics of *Chrysolophus* provide insights into the evolution of complex plumage coloration. *GigaScience*, **7**(10): giy113.

Garg KM, Dovih P, Chattopadhyay B. 2024. Hybrid *de novo* genome assembly of the sexually dimorphic Lady Amherst's pheasant. *DNA Research*, **31**(1): dsae001.

Goel M, Sun HQ, Jiao WB, et al. 2019. SyRI: finding genomic rearrangements and local sequence differences from whole-genome assemblies. *Genome Biology*, **20**(1): 277.

Gozashti L, Hartl DL, Corbett-Detig R. 2024. Universal signatures of transposable element compartmentalization across eukaryotic genes. *Nature*, **620**(7973): 123–130.

Grabherr MG, Haas BJ, Yassour M, et al. 2011. Full-length transcriptome assembly from RNA-Seq data without a reference genome. *Nature Biotechnology*, **29**(7): 644–652.

Haas BJ, Salzberg SL, Zhu W, et al. 2008. Automated eukaryotic gene structure annotation using EVidenceModeler and the program to assemble spliced alignments. *Genome Biology*, **9**(1): R7.

He K, Minias P, Dunn PO, et al. 2021. Long-read genome assemblies reveal extraordinary variation in the number and structure of MHC loci in birds. *Genome Biology and Evolution*, **13**(2): evaa270.

He X, Qi ZY, Liu ZP, et al. 2024. Pangenome analysis reveals transposon-driven genome evolution in cotton. *BMC Biology*, **22**(1): 92.

Huang Z, De O. Furo I, Liu J, et al. 2022. Recurrent chromosome reshuffling and the evolution of neo-sex chromosomes in parrots. *Nature Communications*, **13**(1): 944.

Huang Z, Xu ZX, Bai H, et al. 2023. Evolutionary analysis of a complete chicken genome. *Proceedings of the National Academy of Sciences of the United States of America*, **120**(8): e2216641120.

Jae Lee S, Kim JH, Jo E, et al. 2021. Chromosomal assembly of the Antarctic toothfish (*Dissostichus mawsoni*) genome using third-generation DNA sequencing and Hi-C technology. *Zoological Research*, **42**(1): 124–129.

Jin W, Cao XJ, Ma XY, et al. 2022. Chromosome-level genome assembly of the freshwater snail *Bellamya purificata* (Caenogastropoda). *Zoological Research*, **43**(4): 683–686.

Kapusta A, Suh A. 2017. Evolution of bird genomes—a transposon's‐eye view. *Annals of the New York Academy of Sciences*, **1389**(1): 164–185.

Kim D, Langmead B, Salzberg SL. 2015. HISAT: a fast spliced aligner with low memory requirements. *Nature Methods*, **12**(4): 357–360.

Ko BJ, Lee C, Kim J, et al. 2022. Widespread false gene gains caused by duplication errors in genome assemblies. *Genome Biology*, **23**(1): 205.

Koren S, Rhie A, Walenz BP, et al. 2018. *De novo* assembly of haplotype-resolved genomes with trio binning. *Nature Biotechnology*, **36**(12): 1174–1182.

Kulski JK, Shiina T, Dijkstra JM. 2019. Genomic diversity of the major histocompatibility complex in health and disease. *Cells*, **8**(10): 1270.

Li H. 2021. New strategies to improve minimap2 alignment accuracy. *Bioinformatics*, **37**(23): 4572–4574.

Li H, Durbin R. 2009. Fast and accurate short read alignment with Burrows–Wheeler transform. *Bioinformatics*, **25**(14): 1754–1760.

Li H, Handsaker B, Wysoker A, et al. 2009. The sequence alignment/map format and SAMtools. *Bioinformatics*, **25**(16): 2078–2079.

Li M, Sun CJ, Xu NY, et al. 2022. De novo assembly of 20 chicken genomes reveals the undetectable phenomenon for thousands of core genes on microchromosomes and subtelomeric regions. *Molecular Biology and Evolution*, **39**(4): msac066.

Li XJ, Huang Y, Lei FM. 2015. Comparative mitochondrial genomics and phylogenetic relationships of the *Crossoptilon* species (Phasianidae, Galliformes). *BMC Genomics*, **16**(1): 42.

Liu BJ, Zhang K, Zhang SF, et al. 2022. Chromosome-level genome assembly of the dotted gizzard shad (*Konosirus punctatus*) provides insights into its adaptive evolution. *Zoological Research*, **43**(2): 217–220.

Liu J, Wang ZJ, Li J, et al. 2021. A new emu genome illuminates the evolution of genome configuration and nuclear architecture of avian chromosomes. *Genome Research*, **31**(3): 497–511.

Liu SL, Hansen MM. 2017. PSMC (pairwise sequentially Markovian coalescent) analysis of RAD (restriction site associated DNA) sequencing data. *Molecular Ecology Resources*, **17**(4): 631–641.

Loman NJ, Quick J, Simpson JT. 2015. A complete bacterial genome assembled *de novo* using only nanopore sequencing data. *Nature Methods*, **12**(8): 733–735.

Luo HR, Jiang XR, Li BP, et al. 2023. A high-quality genome assembly highlights the evolutionary history of the great bustard (*Otis tarda*, Otidiformes). *Communications Biology*, **6**(1): 746.

Nattestad M, Schatz MC. 2016. Assemblytics: a web analytics tool for the detection of variants from an assembly. *Bioinformatics*, **32**(19): 3021–3023.

Nguyen LT, Schmidt HA, Von Haeseler A, et al. 2015. IQ-TREE: a fast and effective stochastic algorithm for estimating maximum-likelihood phylogenies. *Molecular Biology and Evolution*, **32**(1): 268–274.

O'Connor EA, Westerdahl H, Burri R, et al. 2019. Avian MHC evolution in the era of genomics: phase 1.0. *Cells*, **8**(10): 1152.

O'Connor RE, Kretschmer R, Romanov MN, et al. 2024. A bird's-eye view of chromosomic evolution in the class aves. *Cells*, **13**(4): 310.

Peona V, Blom MPK, Xu LH, et al. 2020. Identifying the causes and consequences of assembly gaps using a multiplatform genome assembly of a bird‐of‐paradise. *Molecular Ecology Resources*, **21**(1): 263–286.

Peona V, Palacios-Gimenez OM, Blommaert J, et al. 2021. The avian W chromosome is a refugium for endogenous retroviruses with likely effects on female-biased mutational load and genetic incompatibilities. *Philosophical Transactions of the Royal Society B: Biological Sciences*, **376**(1833): 20200186.

Pertea G, Pertea M. 2020. GFF utilities: GffRead and GffCompare. *F1000Research*, **9**: 304.

Pu LR, Lin Y, Pevzner PA. 2018. Detection and analysis of ancient segmental duplications in mammalian genomes. *Genome Research*, **28**(6): 901–909.

Robinson JT, Thorvaldsdóttir H, Wenger AM, et al. 2017. Variant review with the integrative genomics viewer. *Cancer Research*, **77**(21): e31–e34.

Seki R, Li C, Fang Q, et al. 2017. Functional roles of Aves class-specific *cis*-regulatory elements on macroevolution of bird-specific features. *Nature Communications*, **8**(1): 14229.

Sirén J, Välimäki N, Mäkinen V. 2014. Indexing graphs for path queries with applications in genome research. *IEEE/ACM Transactions on Computational Biology and Bioinformatics*, **11**(2): 375–388.

Stanke M, Diekhans M, Baertsch R, et al. 2008. Using native and syntenically mapped cDNA alignments to improve *de novo* gene finding. *Bioinformatics*, **24**(5): 637–644.

Stein RW, Brown JW, Mooers AØ. 2015. A molecular genetic time scale demonstrates cretaceous origins and multiple diversification rate shifts within the order Galliformes (Aves). *Molecular Phylogenetics and Evolution*, **92**: 155–164.

Stiller J, Feng SH, Chowdhury AA, et al. 2024. Complexity of avian evolution revealed by family-level genomes. *Nature*, **629**(8013): 851–860.

Sun XP, Jiao C, Schwaninger H, et al. 2020. Phased diploid genome assemblies and pan-genomes provide insights into the genetic history of apple domestication. *Nature Genetics*, **52**(12): 1423–1432.

Tang HB, Bowers JE, Wang XY, et al. 2008. Synteny and collinearity in plant genomes. *Science*, **320**(5875): 486–488.

Wang SN, Shen Y, Lin ZC, et al. 2024. New genes driven by segmental duplications share a testis‐specific expression pattern in the chromosome‐level genome assembly of tree sparrow. *Integrative Zoology*, **19**(5): 1004–1008.

Wang ZJ, Chen GJ, Zhang GJ, et al. 2021. Dynamic evolution of transposable elements, demographic history, and gene content of paleognathous birds. *Zoological Research*, **42**(1): 51–61.

Wu XL, Mu DP, Yang QS, et al. 2023. Comparative genomics of widespread and narrow-range white-bellied rats in the *Niviventer niviventer* species complex sheds light on invasive rodent success. *Zoological Research*, **44**(6): 1052–1063.

Xu LH, Auer G, Peona V, et al. 2019. Dynamic evolutionary history and gene content of sex chromosomes across diverse songbirds. *Nature Ecology & Evolution*, **3**(5): 834–844.

Xu LH, Zhou Q. 2020. The female-specific W chromosomes of birds have conserved gene contents but are not feminized. *Genes*, **11**(10): 1126.

Xu LL, Ren YD, Wu JH, et al. 2024a. Evolution and expression patterns of the neo-sex chromosomes of the crested ibis. *Nature Communications*, **15**(1): 1670.

Xu X, Wang C, Xu CZ, et al. 2024b. Genomic evolution of island birds from the view of the Swinhoe's pheasant (*Lophura swinhoii*). *Molecular Ecology Resources*, **24**(2): e13896.

Yang CT, Zhou Y, Marcus S, et al. 2021. Evolutionary and biomedical insights from a marmoset diploid genome assembly. *Nature*, **594**(7862): 227–233.

Yusuf L, Heatley MC, Palmer JPG, et al. 2020. Noncoding regions underpin avian bill shape diversification at macroevolutionary scales. *Genome Research*, **30**(4): 553–565.

Zhang GJ, Li C, Li QY, et al. 2014. Comparative genomics reveals insights into avian genome evolution and adaptation. *Science*, **346**(6215): 1311–1320.

Zhang YJ, Chu J, Cheng HY, et al. 2023. De novo reconstruction of satellite repeat units from sequence data. *Genome Research*, **33**(11): 1994–2001.

Zhao N, Guo HB, Jia L, et al. 2021. High-quality chromosome-level genome assembly of redlip mullet (*Planiliza haematocheila*). *Zoological Research*, **42**(6): 796–799.

Zhou H, Huang XH, Liu JJ, et al. 2024. De novo phased genome assembly, annotation and population genotyping of alectoris chukar. *Scientific Data*, **11**(1): 162.

Zhou Q, Zhang JL, Bachtrog D, et al. 2014. Complex evolutionary trajectories of sex chromosomes across bird taxa. *Science*, **346**(6215): 1246338.

Zhu F, Yin ZT, Zhao QS, et al. 2023. A chromosome-level genome assembly for the Silkie chicken resolves complete sequences for key chicken metabolic, reproductive, and immunity genes. *Communications Biology*, **6**(1): 1233.

Ma et al. *Zool. Res.* 2025, 46(1): 87−102
https://doi.org/10.24272/j.issn.2095-8137.2024.269
https://cstr.cn/32248.14.zr.2024.269

ZR | Zoological Research

Article Open Access

DNA2 knockout aggravates cerebral ischemia/reperfusion injury by reducing postsynaptic Homer1a

Ting Ma[1,2,3,4,#], Yu-Meng Li[5,#], Peng-Yu Ren[2,3,4], Shi-Quan Wang[5], Xiang-Long Liu[2,3,4,6], Wen-Bo Lv[2,3,4], Wu-Gang Hou[5], Wen-Qiang Zuo[5], Wei-Qiang Lin[7], Jian Sima[1,*], An-Qi Geng[2,3,4,*]

[1] *Laboratory of Aging Neuroscience and Neuropharmacology*, *School of Basic Medicine and Clinical Pharmacy*, *China Pharmaceutical University*, *Nanjing*, *Jiangsu* 210009, *China*

[2] *Research & Development Institute of Northwestern Polytechnical University in Shenzhen*, *Shenzhen*, *Guangdong* 518057, *China*

[3] *Xi'an Key Laboratory of Stem Cell and Regenerative Medicine*, *Xi'an Key Laboratory of Special Medicine and Health Engineering*, *Institute of Medical Research*, *Northwestern Polytechnical University*, *Xi'an*, *Shaanxi* 710129, *China*

[4] *Sanhang Institute for Brain Science and Technology*, *Northwestern Polytechnical University*, *Xi'an*, *Shaanxi* 710129, *China*

[5] *Department of Anesthesiology and Perioperative Medicine*, *Xijing Hospital*, *Fourth Military Medical University*, *Xi'an*, *Shaanxi* 710032, *China*

[6] *College of Pharmacy*, *Shaanxi University of Chinese Medicine*, *Xi'an*, *Shaanxi* 712046, *China*

[7] *International Institutes of Medicine*, *Fourth Affiliated Hospital*, *School of Medicine*, *Zhejiang University*, *Yiwu*, *Zhejiang* 322023, *China*

ABSTRACT

DNA2, a multifunctional enzyme with structure-specific nuclease, 5′-to-3′ helicase, and DNA-dependent ATPase activities, plays a pivotal role in the cellular response to DNA damage. However, its involvement in cerebral ischemia/reperfusion (I/R) injury remains to be elucidated. This study investigated the involvement of DNA2 in cerebral I/R injury using conditional knockout (cKO) mice (*Nestin*-Cre) subjected to middle cerebral artery occlusion (MCAO), an established model of cerebral I/R. Results demonstrated a gradual up-regulation of DNA2 expression, peaking at 72 h post-MCAO. Notably, *DNA2* cKO mice exhibited more pronounced brain injury, neurological deficits, and neuronal apoptosis within the penumbra following MCAO. Additionally, DNA2 expression was elevated in an oxygen-glucose deprivation/reoxygenation (OGD/R) cell culture model, and *DNA2* knockdown (KD) exacerbated neuronal apoptosis and oxidative stress. Transcriptome analysis of ischemic penumbra tissues via RNA sequencing revealed significant down-regulation of *Homer1* in *DNA2* cKO mice. Furthermore, *in vitro* experiments demonstrated that overexpression of *Homer1a* ameliorated *DNA2* KD-induced neuronal apoptosis. Collectively, these findings demonstrate that *DNA2* deficiency exacerbates cerebral I/R injury through the down-regulation of *Homer1a*, highlighting a novel regulatory axis in ischemic neuroprotection.

Keywords: DNA2; Homer1a; Cerebral I/R; OGD/R; Neuronal apoptosis

INTRODUCTION

Ischemic stroke, primarily resulting from atherosclerosis or thromboembolism, is a leading cause of global disability and mortality (Feigin et al., 2021; Tuo & Lei, 2024). Current therapeutic strategies focus on restoring cerebral blood flow through thrombolytic therapy to rescue penumbra cells and reduce infarct volume (Ma et al., 2019). However, the restoration of blood supply inevitably triggers secondary brain injury and increases the risk of hemorrhagic transformation and edema, known as ischemia/reperfusion (I/R) injury, characterized by inflammatory cascades, reactive oxygen species (ROS) production, and neuronal apoptosis (Chen et al., 2020; Zhang et al., 2022). Understanding the molecular processes governing penumbra biology is vital for identifying novel therapeutic targets to mitigate cerebral I/R injury.

Located in the nucleus, cytoplasm, and mitochondria, DNA replication helicase/nuclease 2 (DNA2) is a multifaceted

This is an open-access article distributed under the terms of the Creative Commons Attribution Non-Commercial License (http://creativecommons.org/licenses/by-nc/4.0/), which permits unrestricted non-commercial use, distribution, and reproduction in any medium, provided the original work is properly cited.

Copyright ©2025 Editorial Office of Zoological Research, Kunming Institute of Zoology, Chinese Academy of Sciences

Received: 20 August 2024; Accepted: 05 November 2024; Online: 06 November 2024

Foundation items: This work was supported by the National Natural Science Foundation of China (32070979), Shenzhen Science and Technology Program (JCYJ20220530161604009, JCYJ20240813150734043), Key Research and Development Program of Shaanxi (2024SF, YBXM, 050), Fundamental Research Funds for the Central Universities (31020190QD004, 3102019YX01001), Double First-Class Project of China Pharmaceutical University (CPUQNJC22_02), and Global Pharmaceutical Development Alliance Plan of China Pharmaceutical University (1302090024-05)

[#]Authors contributed equally to this work

*Corresponding authors, E-mail: simajian@cpu.edu.cn; anqi@nwpu.edu.cn

guardian of genome fidelity, critical in DNA repair, telomere maintenance, and mitochondrial DNA stability (Caston et al., 2023; Ma et al., 2022; Meng et al., 2019; Zheng et al., 2020). In coordination with flap endonuclease 1 (FEN1), DNA2 orchestrates the cleavage of RNA/DNA primers and 5' end Okazaki fragments, ensuring proper primer removal during maturation (Kao et al., 2004; Thakar et al., 2020). Based on evidence from yeast *DNA2* mutants, *DNA2* is thought to play a role in DNA double-strand break (DSB) repair (Budd & Campbell, 2000), with recent studies also demonstrating its involvement in dismantling single-stranded DNA (ssDNA)-RPA filaments during meiotic recombination-associated DNA synthesis, a process essential for meiotic DSB repair (Zhai et al., 2023). *DNA2* deficiency leads to telomeric DNA damage and defective DNA repair, indicating significance in safeguarding genomic stability (Falqu et al., 2020; Hudson & Rass, 2021; Li et al., 2018). Furthermore, post-translational modifications, such as phosphorylation by Cdk1 in response to DSBs, facilitate DNA2 recruitment to DSB sites, emphasizing its regulatory role in DNA repair mechanisms (Chen et al., 2011). Collectively, these findings highlight the critical function of DNA2 in preserving genome stability.

Axonal and dendritic injury following ischemic stroke profoundly disrupts neural circuit integrity, compounding neurological deficits (Wu et al., 2023b). Homer1, a postsynaptic density scaffolding protein, plays a crucial role in synaptic architecture and postsynaptic signaling transduction through its helical, Ena/VASP homolog (EVH) protein-binding, and leucine zipper structural domains (Fei et al., 2022; Stillman et al., 2022). Homer1a, a short spliced form of Homer1, is expressed at low levels under physiological states but is up-regulated in response to physiological and pathological stimuli, suggesting involvement in adaptive and pathological processes (Fei et al., 2015; Serchov et al., 2016; Vazdarjanova et al., 2002). Homer1a exhibits several neuroprotective functions, including the attenuation of neuronal calcium overload, modulation of mGluR1/5 functions to reduce traumatic brain injury, and regulation of mitogen-activated protein kinase (MAPK) signaling to suppress apoptosis (Luo et al., 2012, 2014). Homer1a also provides neuroprotection against N-methyl-D-aspartate (NMDA)-induced neuronal injury by modulating NMDA receptor activity (Wang et al., 2015) and preserves mitochondrial function by inhibiting the protein kinase R-like ER kinase (PERK) pathway, thereby mitigating oxygen-glucose deprivation-induced neuronal injury (Wei et al., 2019). Based on these findings, Homer1a has emerged as a potent neuroprotective molecule in various models of neural injury, operating through distinct molecular pathways.

This study investigated the role of DNA2 in cerebral I/R pathophysiology using *DNA2* conditional knockout (cKO) mice subjected to middle cerebral artery occlusion (MCAO), an established model for ischemic injury, based on behavioral assessments, whole-transcriptome sequencing, and histochemical analyses. Furthermore, an *in vitro* model using HT22 cells and primary neurons under oxygen-glucose deprivation/reoxygenation (OGD/R) conditions was used to investigate the potential mechanisms of DNA2-mediated regulation in cerebral I/R injury. Results indicated that *DNA2* deficiency exacerbates cerebral damage, with *Homer1a* identified as a critical downstream target of *DNA2* modulation, offering new insights into molecular targets for neuroprotection.

MATERIALS AND METHODS

Animals and MCAO model

C57BL/6J mice were obtained from the Laboratory Animal Center of Xi'an Jiaotong University, China. *Nestin*-Cre mice (003771) were obtained from Jackson Laboratory, while *DNA2*$^{fl/fl}$ mice were generously provided by Dr. Weiqiang Lin from the School of Medicine, Zhejiang University. Mouse genotyping primers are listed in Supplementary Table S1. All animals were housed in a sterile, temperature-controlled environment under a 12 h light/12 h dark cycle, with *ad libitum* access to food and water. All animal procedures adhered to the ethical guidelines of the Animal Care and Use Committee of Northwestern Polytechnical University of China (No. 202301126).

Mice were randomly divided into Sham, MCAO wild-type (WT), and MCAO cKO groups. The MCAO model was prepared as described previously (Chen et al., 2019). In brief, adult male mice (23–25 g, 8–10 weeks old) assigned to the MCAO groups were anesthetized using 1.4% isoflurane. A small midline neck incision was performed to expose the external carotid artery, into which a monofilament nylon suture (RWD Life Sciences, China) was inserted and advanced to occlude the middle cerebral artery. After 60 min, the filament was removed to allow for reperfusion and the incision was sutured. Body temperature was maintained at 37°C during anesthesia using a heating pad. Sham group mice underwent the same procedure but without insertion of the nylon monofilament. Successful MCAO was confirmed by observing mice exhibiting circling behavior toward the non-ischemic (left) side at the conclusion of ischemia.

Evaluation of neurological deficits and sensorimotor functions

The modified neurological severity scale (mNSS) and sensorimotor functional behavioral experiments were used to assess neurological impairments in mice 24 h and 72 h after the MCAO procedure. All assessments were performed by a researcher blinded to the treatment groups. The mNSS evaluates sensory, motor, reflex, and balance functions, with a total score of 18 points, where higher scores indicate more severe neurological deficits. The rotarod test (Zslab1, Zhongshi Dichuang Technology Development, China) was used to evaluate motor coordination and balance. Mice underwent pre-training sessions four times daily for three consecutive days to establish baseline performance. During the test, mice were placed on a rotating beam oriented opposite to the direction of rotation to discourage forward movement. Each trial lasted for a maximum of 5 min, with a 3 min rest between tests to prevent fatigue. The latency to fall from the bar was recorded for each test, and the average latency was calculated as the final result.

Grip strength was measured using a grip strength test meter (Bioseb, France). Each mouse was positioned on the tripod of the grip strength meter until it grasped the tripod with its forelimbs, with gently backward pulling then applied until it released its grip. The peak force recorded by the meter was noted for each trial, and the average of three measurements was calculated for statistical analysis.

The adhesive tape removal test was performed following the experimental procedures described by Bouët et al. (2007). Prior to the test, the forelimbs of mice were wiped with alcohol to reduce lipid viscosity and avoid influencing the behavioral

experiment. A piece of tape (0.3 cm×0.4 cm) was attached to the front paw of each mouse, covering the three pads of the thenar and hypothenar regions. Immediately after application, a stopwatch was used to record the time to the first contact with the tape and the time taken to fully remove it. These metrics were analyzed to evaluate sensorimotor function.

2,3,5-Triphenyltetrazolium chloride (TTC) staining

Following 72 h of reperfusion, mice were anesthetized with an intraperitoneal injection of sodium pentobarbital (60 mg/kg, Sigma-Aldrich, USA) and subsequently decapitated. Brain tissues were collected, rapidly frozen at −20°C for 20 min, sliced into 1 mm thick coronal sections, immersed in a 2% TTC (Solarbio, IT0160, China) solution for 20 min at 37°C, and fixed in 4% paraformaldehyde overnight. Infarct volume was calculated by subtracting the non-infarct volume of the same hemisphere from the volume of the contralateral hemisphere. Cerebral infarct volume was measured by serial scanning of the stained sections using ImageJ (v.1.8).

Nissl staining

After 72 h of reperfusion, brain tissues were fixed in 4% paraformaldehyde and subsequently immersed in 15% sucrose solution for 12 h and 30% sucrose solution overnight. The samples were embedded in OCT and sliced into 14 μm thick sections using a cryostat (Leica, Germany). The sections were dried overnight in a 55°C oven, then sequentially immersed in different concentrations of ethanol (100% for 5 min, followed by 95%, 70%, and 50% ethanol for 2 min each) and rinsed with distilled water for 12 s. Staining was performed with 0.1% cresyl violet (J&K Science, 176022, China) for 1 h in the absence of light. After staining, the sections were quickly rinsed in distilled water and sequentially immersed in 50%, 70%, 95%, and 100% ethanol for 12 s each. Finally, the sections were sealed with 4',6-diamino-2-phenylindole (DAPI) nuclear stain. Nissl-positives cells were detected using a fluorescence microscope (Olympus, Japan) and quantified with ImageJ (v.1.8).

Immunohistochemical (IHC) analysis

Standard perfusion and fixation protocols were employed to prepare 14 μm coronal brain sections, which were subjected to standard IHC analysis. Briefly, sections were rinsed three times with 1×phosphate-buffered saline (PBS), then permeabilized with 0.2% Triton X-100 for 30 min and blocked in 10% donkey serum with 0.2% Triton X-100 for 1 h at room temperature, followed by incubation with specific primary antibodies at 4°C overnight. After washing with PBS for three 10 min periods, the sections were incubated with appropriate secondary antibodies for 2 h at room temperature. After three rinses (10 min each) with 1×PBS, the sections were incubated with 1 μg/mL DAPI for 10 min. Following three rinses with 1×PBS, the sections were covered with Fluoromount-G® (SouthernBiotech, 0100-01, USA) and imaged using a confocal microscope (Olympus, Japan). Primary antibodies used included DNA2 (1:300, Rabbit, Proteintech, 18727-1-AP, China), NeuN (1:400, Mouse, Cell Signaling Technology, 94403S, USA), cleaved-Caspase3 (1:1 000, Rabbit, Cell Signaling Technology, Asp175, USA), γ-H2AX (1:1 000, Mouse, Millipore, JBW301, USA), and Homer1 (1:200, Rabbit, Proteintech, 12433-1-AP, China). Secondary antibodies included Cy2, Cy3, and Cy5 AffiniPure-conjugated antibodies (1:1 000, Jackson ImmunoResearch Laboratory, USA).

Terminal deoxynucleotidyl transferase dUTP nick end labeling (TUNEL) staining

Apoptosis was detected using a TUNEL assay kit (Beyotime, C1090, China). Briefly, tissue sections were incubated in 0.5% Triton X-100 in PBS for 5 min at room temperature and rinsed twice with PBS. The TUNEL detection solution was then added dropwise to the sections, followed by incubation for 60 min at 37°C in the absence of light. The reaction mixture was discarded, and the sections were rinsed with PBS four times (5 min each). Apoptosis was detected using a fluorescence microscope (Olympus, Japan) and quantified using ImageJ (v.1.8).

RNA sequencing (RNA-seq)

Ischemic penumbra tissues were collected 3 days after MCAO and sent to Novogene (China) for RNA-seq. The penumbra was isolated from the infarct center by first performing a coronal incision along the basal optic intersection of the brain, followed by a second coronal incision approximately 2 mm caudal to the first, and a third longitudinal incision approximately 1 mm to the right of the midline at the 2 o'clock position. The cortical region enclosed by these incisions constituted the penumbra tissue (Chen et al., 2017; Guo et al., 2021).

Total RNA was extracted from fresh brain tissues using TRIzol reagent (Takara, 9109, Japan), and sequencing libraries were prepared using the NEB Next Ultra™ RNA Library Prep Kit for Illumina (NEB, USA) following the manufacturer's recommendations, with index codes added to label each sample. The libraries were sequenced on the Illumina NovaSeq platform to generate 150 bp paired-end reads. Differential expression analysis was conducted with adjusted *P*-values calculated using the Benjamini-Hochberg method. Gene Ontology (GO) and Kyoto Encyclopedia of Genes and Genomes (KEGG) pathway enrichment analyses were conducted using the clusterProfiler R package, and a hierarchical clustering heatmap was visualized using the ggplot library.

Real-time quantitative reverse transcription polymerase chain reaction (RT-qPCR)

Total RNA from the ischemic penumbra tissue of the cortex was extracted using TRIzol reagent. A PrimeScript™ RT reagent kit with gDNA Eraser (Takara, RR036A, Japan) was used for reverse transcription of RNA to obtain cDNA. Target gene amplification was performed using TB Green® Premix Ex Taq™ II (Takara, RR820A, Japan). The Bio-Rad CFX Opus 96 real-time PCR system (Bio-Rad, USA) and CFX Manager (v.3.0) were used for the analysis. β-actin expression was set as an endogenous reference gene. All primers were synthesized by Tsingke Company (China). The oligonucleotide sequences are listed in Supplementary Table S2.

Western blotting (WB)

Cortical tissue (1–2 mm thick) from the ischemic penumbra, as well as HT22 cells and primary neurons, were subjected to protein extraction using RIPA lysis buffer. The cells were lysed on ice for 10 min with RIPA lysis buffer and centrifuged at 12 000 r/min for 15 min at 4°C. The resulting supernatant was collected and used to detect the expression of DNA2, Bcl2, Bax, and Homer1a, with protein concentration determined using BSA as a standard. Proteins were separated by sodium dodecyl sulfate-polyacrylamide gel electrophoresis (SDS-

PAGE) and transferred onto polyvinylidene fluoride (PVDF) membranes (Millipore, IPVH00010, USA) via electroblotting, adjusted based on the molecular weight of target protein. For proteins of similar molecular weights, such as Bax and Bcl2, different membranes with β-actin or α-tubulin as loading controls were used. After blocking, the membranes were incubated for 12 h at 4°C with the following primary antibodies: DNA2 (1:2 500, Rabbit, Proteintech, 18727-1-AP, China), Bcl2 (1:1 000, Rabbit, Proteintech, 26593-1-AP, China), Bax (1:3 000, Rabbit, Proteintech, 50599-2-Ig, China), Homer1a (1:1 000, Rabbit, Proteintech, 12433-1-AP, China), α-tubulin (1:100 000, Mouse, Proteintech, 11224-1-AP, China), and β-actin (1:2 000, Mouse, OriGene, TA811000, USA). Subsequently, the membranes were incubated with secondary antibodies for 1 h. Images were captured using a chemiluminescence imaging system, and gray values were quantified using ImageJ (v.1.8), normalizing the intensity of target protein bands to that of the loading control (β-actin or α-tubulin).

shRNA design and screening

Potential shRNA sequences were designed using the online tool at rnaidesigner.thermofisher.com/rnaiexpress/design.do. The shRNAs were expressed under the control of the mouse U6 promoter in the pNUTS vector, which contained a ubiquitin promoter-EGFP expression cassette. Plasmid pcDNA3.1-Homer1a-3flag-ZsGreen-Puro (overexpression (OE) *Homer1a*) and its corresponding negative control (Ctrl) were purchased from HANBIO Shanghai. The 19-mer shRNA sequences used in this study (shRNA loop underlined) included: sh*DNA2*-CDS: 5′–CTGTGAAGTTGAGGAGTAT-TTCAAGAGA-ATACTCCTCAACTTCACAG-3′; Scramble: 5′-CGGCTGAAACAAGAGTTGG-TTCAAGAGA-CCAACTCTT GTTTCAGCCG-3′.

Primary neuron culture

Primary neurons were obtained from the brains of C57BL/6J embryos at embryonic days 14–15, as reported previously (Grimm et al., 2018; Guo et al., 2021). Briefly, embryos were collected, followed by the careful removal of the meninges and blood vessels under a microscope. The cerebral cortex was then shredded and digested with pancreatic enzymes for 10 min. Neurons were resuspended in Neurobasal medium (Gibco, 21103-49, USA) supplemented with 2% B-27 (Gibco, 17504-044, USA) and 1% L-glutamine (Gibco, 25030-081, USA). The neurons were cultured in a 5% CO_2 incubator at 37°C for 7 days, with the culture medium renewed every 3 days.

OGD/R treatment

To model ischemia/reperfusion *in vitro*, OGD/R was performed as described previously (Zhang et al., 2020). In brief, HT22 cells in the OGD group were placed in a hypoxic chamber under anoxic conditions (94% N_2, 5% CO_2, and 1% O_2) and cultured in Dulbecco's Modified Eagle Medium (DMEM) without glucose and Fetal Bovine Serum (FBS) at 37°C for 6 h. The cells were then returned to normal culture conditions (5% CO_2, 95% air) and incubated in DMEM (high glucose supplemented with 10% FBS and 1% penicillin-streptomycin) for 3 h at 37°C. *DNA2*-shRNA (sh-*DNA2*) or negative control Scramble shRNA (Sc) was transfected into HT22 cells using GenEscort I (Wisegn, China) reagent 48 h prior to OGD/R treatment, following the experimental requirements.

For primary neurons, transfection was modified from a previous study (Buchser et al., 2006). Intracellular buffer (800 μL, 135 mmol/L KCl, 0.2 mmol/L $CaCl_2$, 2 mmol/L $MgCl_2$, 10 mmol/L HEPES, 5 mmol/L EGTA, pH 7.3) was added to the attached neurons in a 3.5 cm dish and subjected to electroporation using a Petri pulser electrode PP35-2P (45-0130, Harvard Apparatus/BTX, USA) with parameters: one 340 V pulse, 900 μs pulse length. After 60 h of electroporation with Sc, sh-*DNA2*, and OE-*Homer1a* plasmids, the Neurobasal medium was replaced with glucose-free culture medium and transferred to an incubator (94% N_2, 5% CO_2, and 1% O_2) at 37°C. After 9 h of OGD, the cells were transferred to Neurobasal medium and placed in a 37°C (5% CO_2 and 95% air) incubator for 3 h.

Detection of cell apoptosis using flow cytometry

Apoptosis was detected using an Annexin V-APC/7-AAD Apoptosis Detection Kit (Elabscience, E-CK-A218B, China). HT22 cells were transfected with shRNA to establish an OGD/R model. Subsequently, the cells were collected and treated with Annexin V-APC and 7-AAD in the dark for 20 min, following the manufacturer's instructions. Apoptosis rates were measured using a BD FACSCalibur flow cytometer (Becton, Dickinson and Company, USA) and analyzed using FlowJo (v.10.8).

Detection of oxidative stress

ROS levels in HT22 cells and primary neurons were detected using an ROS Assay Kit (BB-470515, Bestbio, China). Cells subjected to OGD/R were rinsed three times with serum-free medium. BBoxiProbe® dihydroethidium (DHE) was diluted 1:1 000 in serum-free medium and added to the cells, which were subsequently incubated at 37°C for 30 min. After incubation, the cells were washed three times with serum-free medium, and visualized under a fluorescence microscope (Olympus, Japan).

Cell counting kit 8 (CCK-8) assay

Cell viability was assessed using a CCK-8 Assay Kit (Mishushengwu, China). After OGD/R treatment, 10 μL of CCK-8 reagent was added to each well and incubated at 37°C for 1 h. Absorbance was then measured at 450 nm using a microplate reader.

Statistical analysis

GraphPad Prism (v.9.0) and SPSS (v.26.0) statistical software were used for data analysis. All experimental data are presented as the mean±standard deviation (SD). Group means were compared using Student's *t*-tests or one-way analysis of variance (ANOVA) with Dunnett's *post hoc* analysis. P-value<0.05 was considered statistically significant.

RESULTS

DNA2 is up-regulated in cerebral ischemic penumbra following MCAO

The role of DNA2 in cerebral I/R injury progression was analyzed using an MCAO model (Figure 1A, B). DNA2 expression in the ischemic penumbra was evaluated in WT mice, revealing a significant increase in protein levels at 12 h post-MCAO, with a peak at 72 h (Figure 1C, D). Based on this expression pattern, the 72 h time point was selected for subsequent experiments. IHC staining confirmed the up-regulation of DNA2 following MCAO (Figure 1E, F) and demonstrated colocalization of DNA2 and NeuN, a neuronal marker, within the ischemic penumbra (Supplementary

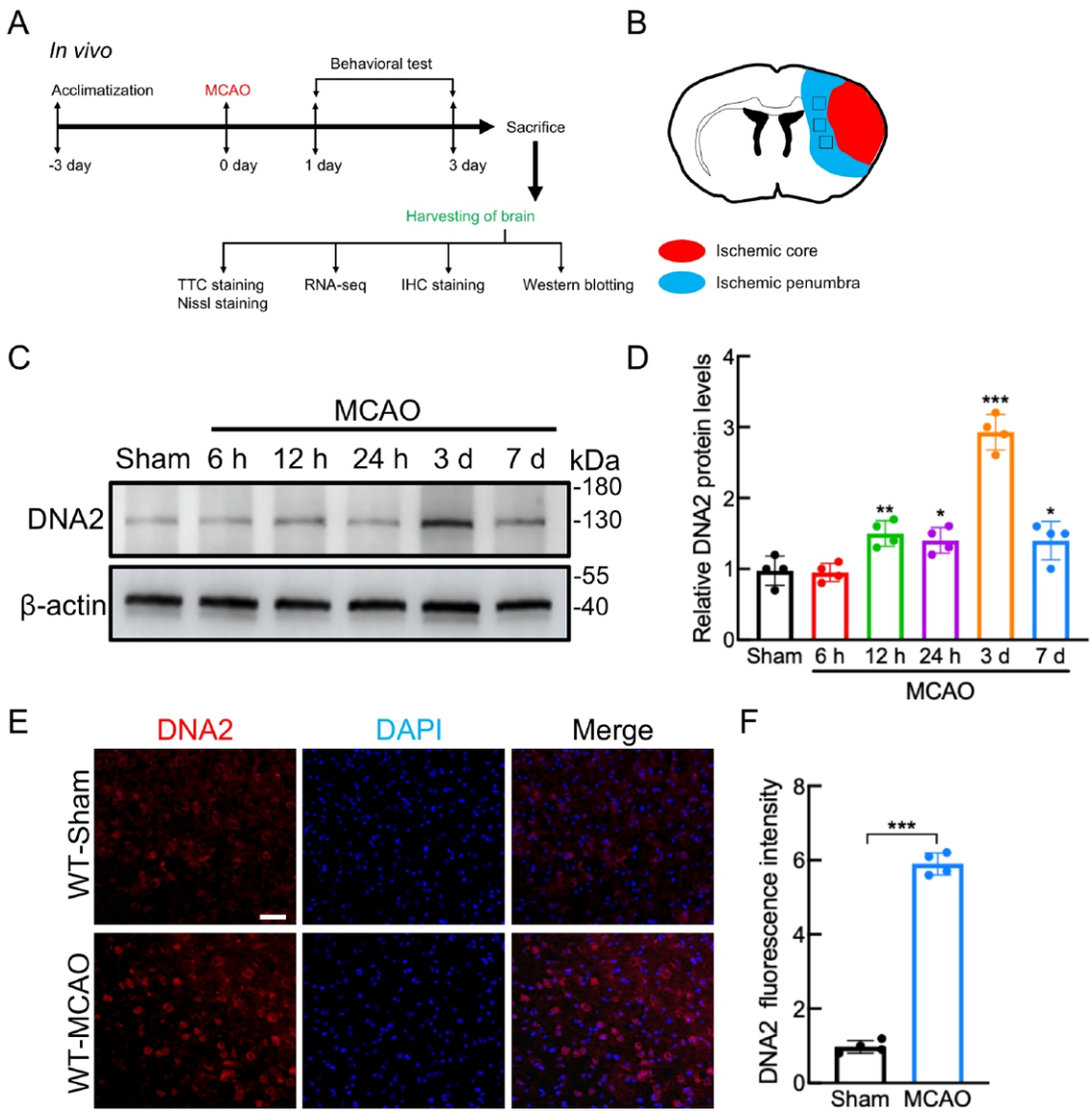


Figure 1 Expression pattern of DNA2 in ischemic penumbra following middle cerebral artery occlusion (MCAO)

A: Schematic of animal experiments. B: Schematic of ischemic core (red) and penumbra (blue). C: WB images showing levels of DNA2 in ischemic penumbra at indicated time intervals following MCAO. D: Quantification of DNA2 protein levels (n=4), normalized to β-actin, with Sham group set to 1. *: P<0.05; **: P<0.01; ***: P<0.001 (one-way ANOVA with Dunnett's *post hoc* analysis, $F(5,18)$=48.15). E: Representative images of IHC staining of DNA2 (red), cell nuclei counterstained with DAPI (blue) in ischemic penumbra from Sham or MCAO groups. Scale bar: 50 μm. F: Quantification of DNA2 fluorescence intensity (n=4). ***: P<0.001 (Student's t-tests, $t(6)$=28.94).

Figure S1). These findings indicate that DNA2 expression is up-regulated after MCAO and is predominantly localized in neurons.

***DNA2* suppression increases infarct volume and aggravates neurological deficits**

The functional role of DNA2 in cerebral I/R injury was examined using *DNA2* cKO mice (*Nestin*-Cre^{+}*DNA2*$^{fl/fl}$), with the genotype verified by PCR (Figure 2A, B). As expected, DNA2 levels in the ischemic penumbra were significantly reduced in cKO mice compared to WT mice (Figure 2C). MCAO experiments revealed that cKO mice exhibited a substantially larger infarct size compared to WT mice (Figure 2D, E). Neurological deficits, assessed using mNSS scores, were markedly worse in *DNA2* cKO mice at both 24 h and 72 h post-MCAO (Figure 2F). Sensorimotor dysfunction was further evaluated through neurobehavioral tests. Notably, *DNA2* cKO mice demonstrated impaired motor coordination, evidenced by reduced time spent on the rotarod (Figure 2G) and exhibited significantly weaker forelimb grip strength at both 24 and 72 h post-MCAO compared to WT mice (Figure 2H). The adhesive tape removal test showed no significant differences between *DNA2* cKO and WT mice at 24 h post-MCAO. However, at 72 h, *DNA2* cKO mice displayed delayed responses, taking longer to make contact and remove the tape from the center of their left paw (Figure 2I). These findings suggest that neuronal *DNA2* cKO exacerbates MCAO-induced brain damage and may lead to a slower recovery of sensorimotor function. To exclude the possibility that *DNA2* cKO may cause neurological deficits even without MCAO treatment, Sham groups of WT and cKO mice were compared. No significant differences were observed in infarct size, mNSS scores, or behavioral test results between the two groups (Supplementary Figure S2A–C). Consequently, Sham WT mice were used as the primary controls in subsequent

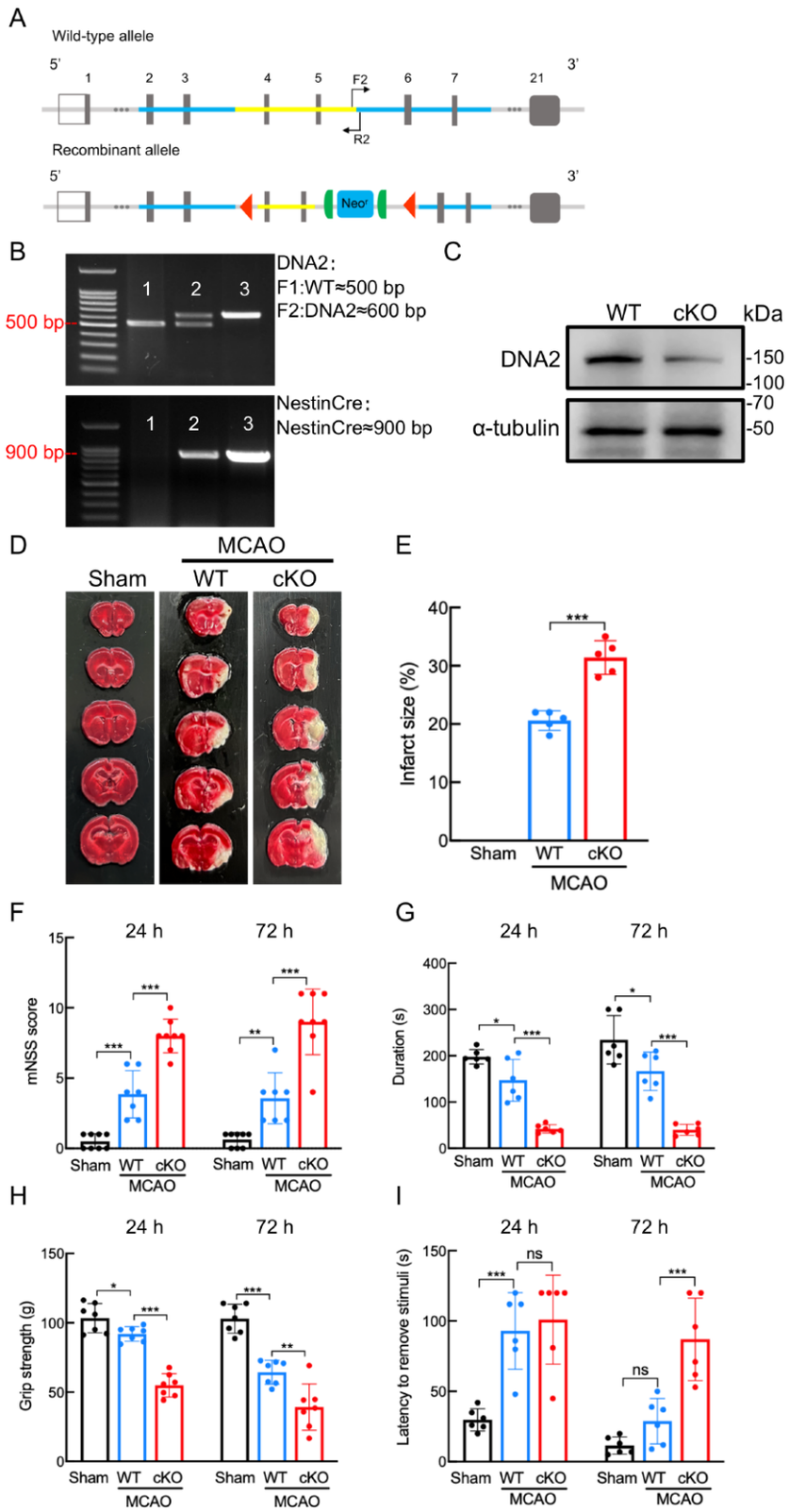


Figure 2 ***DNA2*** **deficiency exacerbates neurobehavioral deficits and brain damage in MCAO**

A: Schematic of *DNA2*$^{fl/fl}$ mouse line construction. B: Representative genotyping images of *DNA2*$^{fl/fl}$ mice using standard PCR method, with DNA gels showing genotypes of homozygous *DNA2*$^{fl/fl}$ (600 bp), WT (500 bp), and *Nestin*-Cre (900 bp) mice. C: Representative WB images of DNA2 protein levels in cerebral ischemic penumbra. D: Representative brain sections stained with TTC showing infarcts 72 h after MCAO. E: Quantitative analysis of infarct size presented as a percentage of contralateral hemisphere size 3 days after MCAO (n=5). ***: P<0.001 (Student's t-tests, t(8)=7.25). F: Neurological deficit scores of mice at 24 h and 72 h after MCAO (n≥6). 24 h: F(2,20)=78.23, 72 h: F(2,20)=48.34. G: Duration of mice on rotarod (n≥6). 24 h: F(2,15)=48.01, 72 h: F(2,15)=38.12. H: Comparison of forelimb grip strength in mice (n≥6). 24 h: F(2,18)=64.68, 72 h: F(2,18)=46.85. I: Time taken by mice to remove tape from their left paw (n≥6). 24 h: F(2,15)=15.22, 72 h: F(2,15)=24.33. ns: Not significant; *: P<0.05; **: P<0.01; ***: P<0.001 (one-way ANOVA with Dunnett's *post hoc* analysis in F, G, H, and I).

animal studies.

DNA2 cKO promotes neuronal apoptosis in cerebral ischemic penumbra following MCAO

Neuronal loss in the ischemic penumbra was assessed using Nissl staining, which revealed a significant reduction in neuronal cell numbers in WT mice post-MCAO. Notably, *DNA2* cKO mice exhibited greater neuronal loss compared to WT mice (Figure 3A, B). IHC analysis further demonstrated a reduction in NeuN-positive cells in WT mice compared to the Sham group, with an even more pronounced decrease in cKO mice (Figure 3C, D).

Given the critical role of neuronal loss in sensorimotor and cognitive dysfunction, the role of DNA2 in neuronal apoptosis was further evaluated. TUNEL staining showed an increase in TUNEL-positive cells in the ischemic penumbra of WT mice compared to Sham mice. *DNA2* cKO mice exhibited a significantly higher number of TUNEL-positive cells than WT mice (Figure 3C, E). Consistent with behavioral assessments, no significant differences were observed in the levels of the pro-apoptotic factor Bax and anti-apoptotic factor Bcl2 between the two Sham groups (Supplementary Figure S2D, E). However, post-MCAO, *DNA2* cKO mice demonstrated a significant up-regulation in Bax and down-regulation in Bcl2 compared to WT mice, highlighting a shift toward pro-apoptotic signaling in the absence of *DNA2* (Figure 3F, G).

DNA2 is a key enzyme involved in DNA damage repair, essential for processing DNA strand breaks and responding to replication stress (Caston et al., 2023). To assess DNA damage following MCAO, the DNA damage marker γ-H2AX was evaluated. IHC analysis revealed increased γ-H2AX activation in WT mice post-MCAO, with a substantially stronger γ-H2AX-positive signal in *DNA2* cKO mice (Figure 3H, I).

These findings suggest that the deletion of neuronal *DNA2* exacerbates DNA damage and promotes cerebral I/R-induced neuronal apoptosis, underscoring the potential importance of DNA2 in protecting against ischemic injury.

DNA2 is up-regulated in neuronal cells following OGD/R treatment

The role of DNA2 *in vitro* was investigated using OGD/R cell culture models with HT22 cells and primary neurons (Figure 4A). Cells were subjected to OGD for 3, 6, 9, and 12 h, followed by 3 h of reoxygenation. Morphological examination of HT22 cells revealed progressive cellular damage over time. Cell shrinkage was evident at 3 h, with sparse arrangement and a rounded morphology at 6 h, loss of intercellular connections, reduced cell numbers, and cellular remnants at 9 h, and further deterioration at 12 h compared to the control cells (Figure 4B).

Cell viability, as assessed using the CCK-8 assay, revealed a progressive decline during OGD/R treatment (Figure 4C). Immunoblotting indicated that DNA2 protein levels began to increase after 3 h of OGD, peaking at 6 h in HT22 cells (Figure 4D, E). Based on the observed peak in DNA2 expression at 6 h, this point was chosen for subsequent experiments.

DNA2 knockdown (KD) exacerbates OGD/R-induced neuronal apoptosis

DNA2 KD was investigated to assess its role in neuronal apoptosis *in vitro* under OGD/R conditions. Transfection of HT22 cells with shRNA targeting *DNA2* confirmed efficient KD (Figure 5A). ROS levels, measured using DHE staining and fluorescence imaging, showed no significant differences between the two Mock groups without OGD/R treatment (Supplementary Figure S3A, B). However, OGD/R significantly increased ROS levels in *DNA2* KD cells compared to those transfected with Sc shRNA (Figure 5B, C).

Following OGD/R treatment, *DNA2* KD cells exhibited increased Bax and decreased Bcl2 levels, with no changes observed in the absence of OGD/R (Figure 5D, E; Supplementary Figure S3C, D). Flow cytometry analysis further confirmed that *DNA2* KD markedly increased the percentage of OGD/R-induced total apoptotic neurons, from 10.86% in the Sc group to 16.04% in the sh-*DNA2* group (Figure 5F, G). Immunofluorescence staining for active Caspase3 also confirmed that *DNA2* KD exacerbated OGD/R-induced apoptosis in HT22 cells (Supplementary Figure S4A, B). Additionally, *DNA2* KD cells showed a significant increase in the number of γ-H2AX-positive cells, indicative of DNA damage (Supplementary Figure S4C, D).

Collectively, these results demonstrate that *DNA2* KD exacerbates OGD/R-induced oxidative stress, DNA damage, and neuronal apoptosis, underscoring the protective role of DNA2 in maintaining cellular integrity under ischemic conditions.

RNA-seq reveals neuronal synapses and oxidative stress as critical downstream pathways of *DNA2*

To elucidate the potential mechanisms underlying *DNA2* regulation of ischemic brain injury, RNA-seq analysis was performed on ischemic penumbra tissues from *DNA2* cKO and WT mice after 3 days of reperfusion. A total of 19 675 and 20 157 genes were detected in WT and cKO mice, respectively, with 18 392 genes detected in both groups (Figure 6A). Analysis identified 545 down-regulated and 607 up-regulated differentially expressed genes (DEGs) in the cKO group compared to WT (Figure 6B, C). GO analysis revealed significant enrichment of these DEGs in processes such as positive regulation of cytosolic calcium ion concentration, neuronal apoptotic processes, postsynaptic processes, neuron-to-neuron synapse functions, and negative regulation of the cellular response to oxidative stress (Figure 6D). Neuron-to-neuron synapse interactions are critical for neural signal transmission. Alterations during cerebral ischemia due to inadequate energy supply affect neurotransmitter transmission and synaptic plasticity. Consistently, Chord diagrams and KEGG analysis further highlighted the top 20 enriched pathways (Figure 6E, F), confirming the role of *DNA2* in the regulation of various pathways related to neuronal apoptosis, oxidative stress, and synaptic functions. Among the key genes identified, postsynaptic *Homer1* emerged as a critical regulator of synaptic processes (Figure 6E).

DNA2 cKO reduces *Homer1a* expression in mice with cerebral I/R injury

To identify downstream targets of *DNA2*, DEGs with high qPCR validation scores were analyzed, identifying *Homer1* as the most significantly down-regulated (Figure 7A). Within the *Homer1* family, comprising *Homer1a*, *Homer1b*, and *Homer1c*, only *Homer1a* exhibited a marked reduction in expression (Figure 7A). Homer1a, recognized for its neuroprotective properties, is typically up-regulated during ischemic and traumatic brain injuries, where it mitigates neuronal damage by reducing calcium influx (Fei et al., 2015; Rao et al., 2016). WB and IHC analyses further validated the

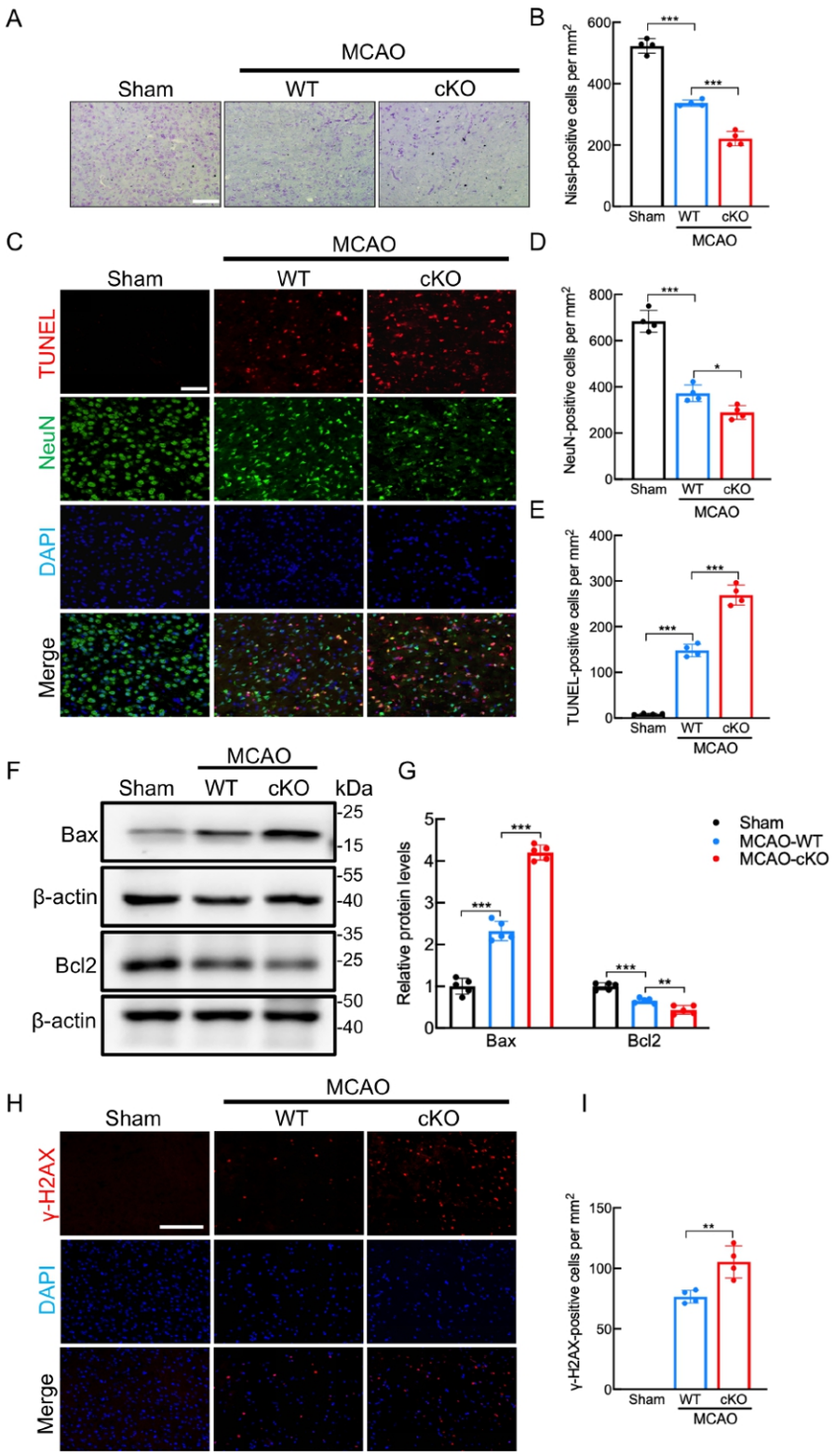


Figure 3 *DNA2* conditional knockout (cKO) aggravates MCAO-induced neuronal loss

A: Nissl-stained images of neurons in cerebral ischemic penumbra in WT and *DNA2* cKO mouse brains. Scale bar: 100 μm. B: Quantitative results of Nissl-positive neurons (n=4). ***: P<0.001 (one-way ANOVA with Dunnett's *post hoc* analysis, F(2,9)=226.4). C: IHC images showing NeuN (green) and TUNEL (red) staining in cerebral ischemic penumbra. Scale bar: 50 μm. D: Quantitative analysis of NeuN-positive cells in cerebral ischemic penumbra (n=4). *: P<0.05; ***: P<0.001 (one-way ANOVA with Dunnett's *post hoc* analysis, F(2,9)=117.7). E: Quantitative analysis of TUNEL-positive cells in cerebral ischemic penumbra (n=4). ***: P<0.001 (one-way ANOVA with Dunnett's *post hoc* analysis, F(2,9)=300.5). F: Immunoblotting images showing levels of Bax and Bcl2 at 72 h after MCAO or Sham treatment. G: Quantitative analysis of Bax and Bcl2 protein levels (n=5), normalized to β-actin, with Sham group set to 1. **: P<0.01, ***: P<0.001 (one-way ANOVA with Dunnett's *post hoc* analysis, Bax: F(2,12)=317.3, Bcl2: F(2,12)=57.34). H: Representative images of IHC staining of γ-H2AX (red) in ischemic penumbra from Sham or MCAO groups. Scale bar: 100 μm. I: Quantitative analysis of γ-H2AX-positive cells in cerebral ischemic penumbra (n=4). **: P<0.01 (Student's t-tests, t(6)=4.01).

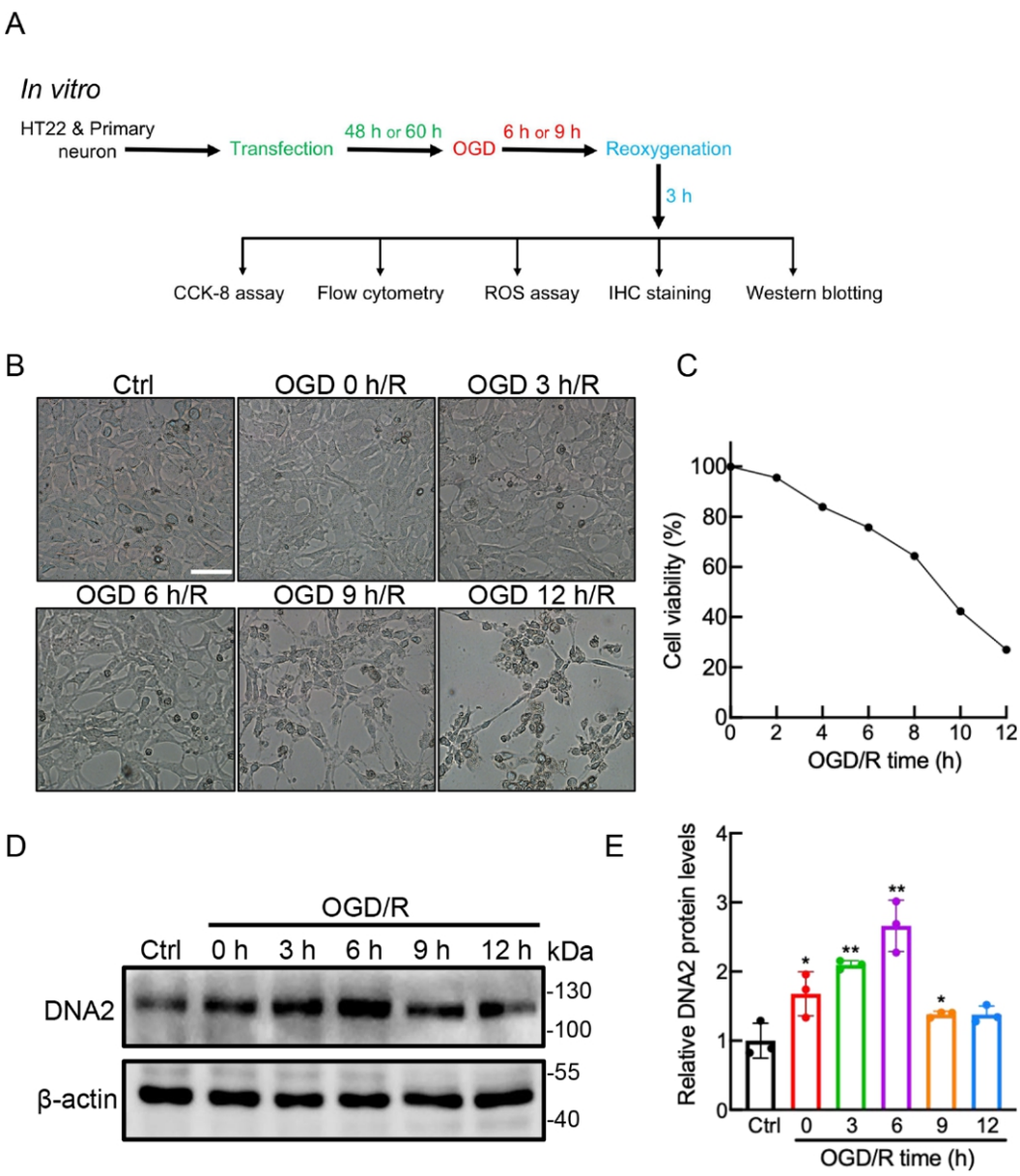


Figure 4 Expression pattern of DNA2 during oxygen-glucose deprivation/reoxygenation (OGD/R) in neuronal cultures

A: Schematic of *in vitro* OGD/R study design. B: Morphological characteristics of HT22 cells at various OGD/R time points. Scale bar: 50 μm. C: Comparison of cell survival ratios under different experimental conditions, determined using CCK-8 assays. D: Representative WB images showing DNA2 levels at various OGD/R time points in HT22 cells. E: Quantitative analysis of DNA2 protein levels, normalized to β-actin, with Ctrl group set to 1. Data are from at least three independent experiments. *: P<0.05; **: P<0.01 (one-way ANOVA with Dunnett's *post hoc* analysis, $F(5,12)=19.86$).

significant reduction in Homer1a expression in *DNA2* cKO mice compared to WT following MCAO (Figure 7B–E). These findings suggest that *DNA2* plays a critical role in modulating *Homer1a* expression, potentially contributing to its neuroprotective effects during cerebral I/R injury.

OE-*Homer1a* ameliorates *DNA2* KD-induced neuronal apoptosis in OGD/R models

Based on the above findings, the role of *Homer1a* in ameliorating OGD/R-induced neuronal damage under *DNA2* KD treatment was examined. Primary neurons were cultured and exposed to OGD for 3, 6, 9, and 12 h, followed by 3 h of reoxygenation. WB analysis revealed that DNA2 and Homer1a levels peaked at 9 h of OGD before returning to baseline (Figure 8A). A *Homer1a*-expressing plasmid was constructed, with WB confirming its overexpression efficacy (Supplementary Figure S5A). In primary neurons, the *DNA2* KD/OE-*Homer1a* group exhibited a notable down-regulation in Bax levels and an up-regulation in Bcl2 levels compared to the *DNA2* KD group alone (Figure 8B, C). These effects were consistently observed in HT22 cells (Supplementary Figure S5B, C). ROS assays revealed significantly lower levels of ROS in the *DNA2* KD/OE-*Homer1a* groups compared to the *DNA2* KD group alone in both primary neurons (Figure 8D, E) and HT22 cells (Supplementary Figure S5D, E). These results indicate that *Homer1a* overexpression mitigates *DNA2* KD-induced oxidative stress and neuronal apoptosis, highlighting its protective role in OGD/R-induced neuronal injury.

DISCUSSION

DNA2, first identified in yeast in the early 1980s (Kuo et al., 1983), is recognized for its helicase and nuclease activities as well as its crucial functions in DNA replication within both

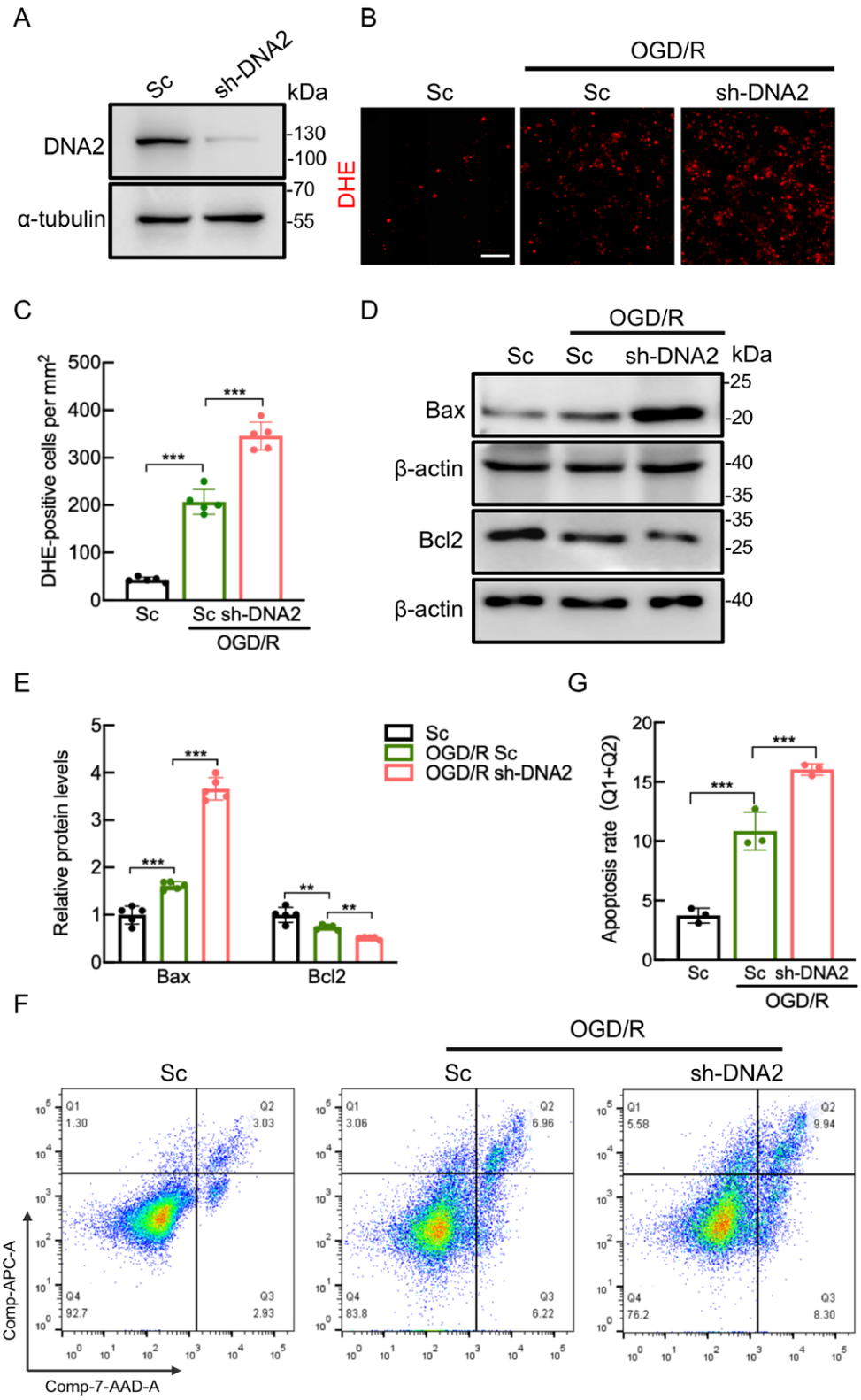


Figure 5 *DNA2* knockdown (KD) enhances apoptosis in HT22 cells subjected to OGD/R

A: Representative WB images depicting DNA2 protein levels in HT22 cells. B: Fluorescence images showing ROS levels in HT22 cells transfected with scrambled shRNA (Sc) and *DNA2* shRNA (sh-*DNA2*). Scale bar: 100 μm. C: Quantitative analysis of DHE-positive cells. Data are from at least five independent experiments. ***: P<0.001 (one-way ANOVA with Dunnett's *post hoc* analysis, $F(2,12)=217.4$). D: WB images showing expression levels of Bax and Bcl2 proteins in HT22 cells post-OGD/R. E: Quantitative analysis of Bax and Bcl2 protein levels, normalized to β-actin, with Sc group set to 1. Data are from at least five independent experiments. **: P<0.01; ***: P<0.001 (one-way ANOVA with Dunnett's *post hoc* analysis, Bax: $F(2,12)=296.5$, Bcl2: $F(2,12)=32.55$). F, G: Flow cytometry results of annexin V-APC/7-AAD staining, showing percentage of total neuronal apoptosis (sum of Q1 and Q2 quadrants), Q1: Early apoptosis, Q2: Late apoptosis, Q3: Necrosis, Q4: Viable cells. Data are from at least three independent experiments. ***: P<0.001 (one-way ANOVA with Dunnett's *post hoc* analysis, $F(2,6)=109.2$).

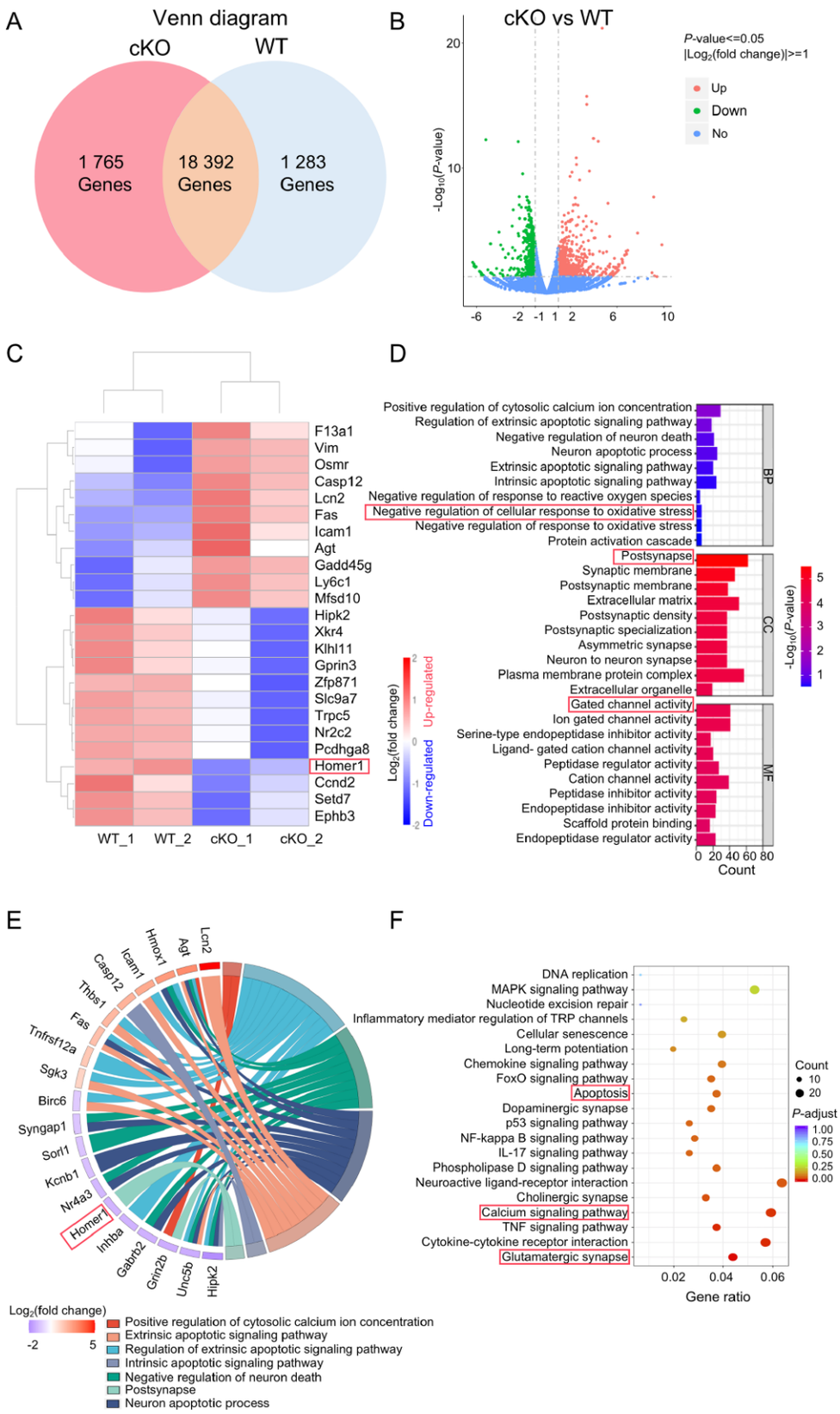


Figure 6 RNA-seq analysis of *DNA2* cKO mice compared to WT mice following MCAO

A: Venn diagram showing overlap of genes between cKO and WT groups. B: Volcano plot showing differentially expressed genes (DEGs) between DNA2 cKO and WT mice, highlighting significant changes. C: Heatmap of hierarchical cluster analysis for DEGs between cKO and WT mice, with red indicating up-regulated genes and blue indicating down-regulated genes. D: GO analysis of biological processes (BP), cellular components (CC), and molecular functions (MF), identifying key affected categories. E: Chord diagrams of GO enrichment analysis, showing gene names on the left semicircle and their corresponding functions on the right semicircle. F: Analysis of KEGG signaling pathways influenced by *DNA2* cKO. Red rectangles highlight key genes or signaling pathways identified by RNA-seq.

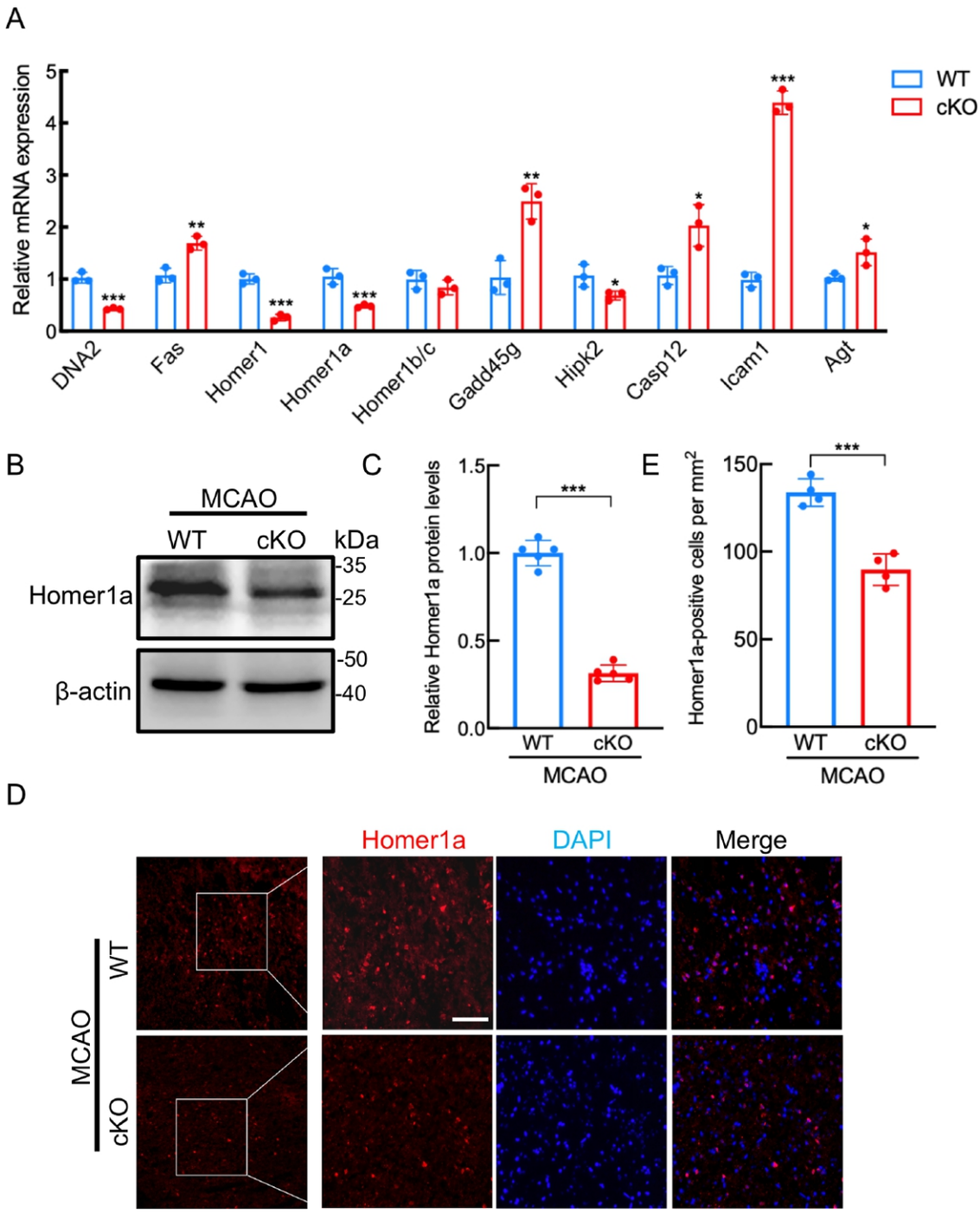


Figure 7 ***DNA2*** **cKO reduces Homer1a expression at 3 days post-MCAO**

A: Real-time qPCR analysis of gene expression, selected from RNA-seq data (n=3). *: P<0.05; **: P<0.01 ***: P<0.001 (Student's t-tests, *DNA2*: t(4)=10.06, *Fas*: t(4)=5.63, *Homer1*: t(4)=11.13, *Homer1a*: t(4)=7.72, *Homer1b/c*: t(4)=1.18, *Gadd45g*: t(4)=5.38, *Hipk2*: t(4)=2.84, *Casp12*: t(4)=3.80, *Icam1*: t(4)=22.42, *Agt*: t(4)=3.17). B: WB analysis of Homer1a protein levels in WT and cKO mice following MCAO. C: Quantitative analysis of Homer1a protein levels (n=5), normalized to β-actin, with WT group set to 1. ***: P<0.001 (Student's t-tests, t(8)=17.62). D: IHC images showing Homer1a expression (red) in cerebral ischemic penumbra of WT and cKO mice at 3 days post-MCAO, with nuclei counterstained using DAPI. Scale bar: 50 μm. E: Quantitative analysis of Homer1a-positive cells within ischemic penumbra (n=4). ***: P<0.001 (Student's t-tests, t(6)=7.41).

nuclear and mitochondrial compartments (Dumas et al., 1982; Park et al., 2021). DNA2 also serves as a guardian of genomic stability, mediating processes such as Okazaki fragment processing, DSB repair, and stalled replication fork protection (Cejka et al., 2010; Zhou et al., 2015). Despite these established functions, the precise role of DNA2 in cerebral I/R injury has remained elusive. This study provides novel evidence implicating DNA2 in cerebral I/R injury, with neuronal inhibition of DNA2 shown to exacerbate neuropathology.

Our findings showed that DNA2 expression peaked at 72 h post-MCAO, suggesting a dynamic response during the acute phase of ischemic injury. Schwab et al. (2021) reported that the up-regulation of DNA repair genes, such as *DNA2*, *ATG7*, and *NBN*, and the down-regulation of pro-apoptotic genes, are

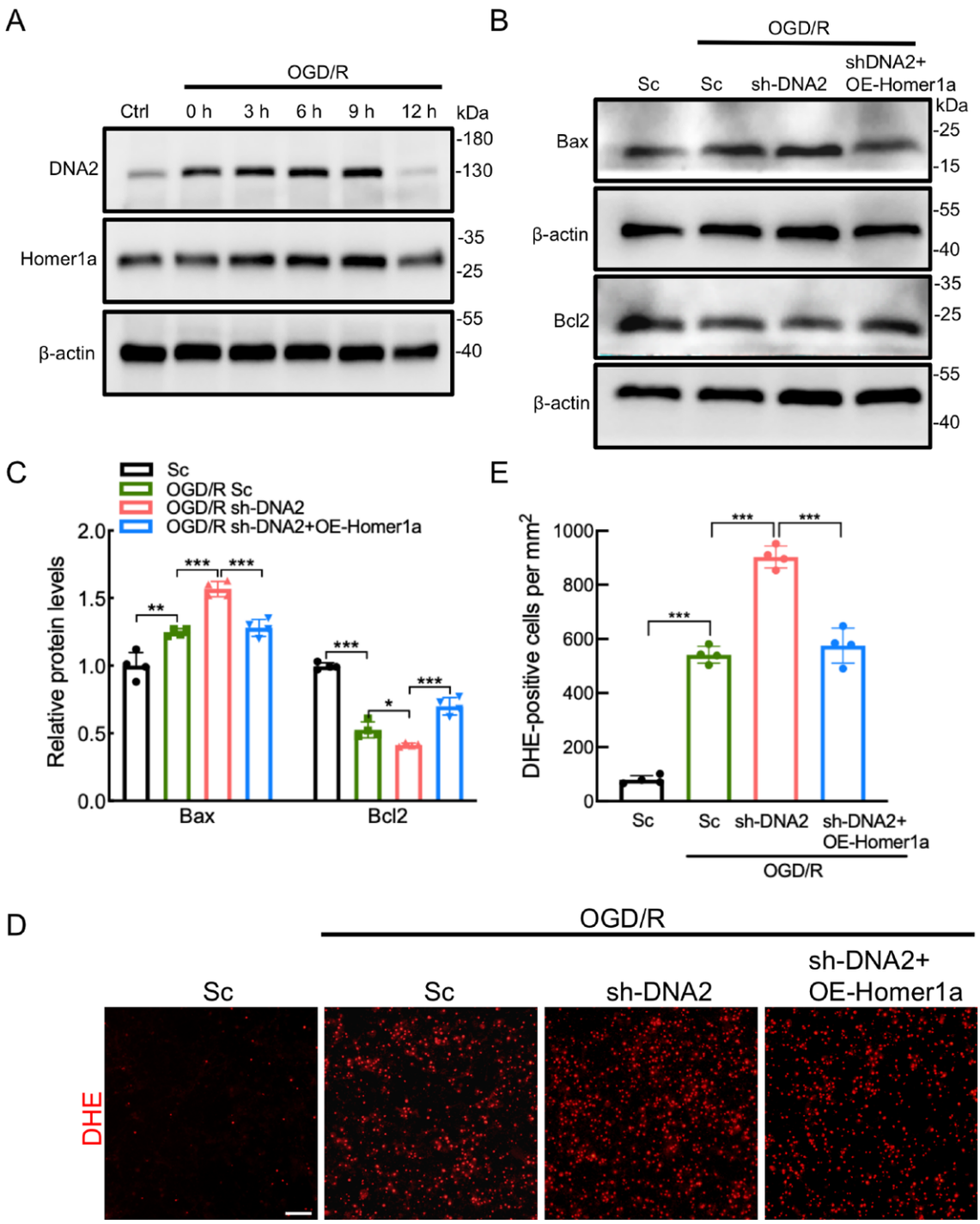


Figure 8 Overexpression (OE) of *Homer1a* mitigates apoptosis in primary neurons mediated by *DNA2* KD in OGD/R

A: Representative WB images showing levels of DNA2 and Homer1a at indicated time points during OGD/R in primary neurons. B: WB analysis of pro-apoptotic Bax and anti-apoptotic Bcl2 protein levels in primary neurons following OGD/R treatment. C: Quantitative analysis of Bax and Bcl2 protein levels, normalized to β-actin, with Sc group set to 1. Data are from at least four independent experiments. *: P<0.05; **: P<0.01; ***: P<0.001 (one-way ANOVA with Dunnett's *post hoc* analysis, Bax: $F(3,12)=49.50$, Bcl2: $F(3,12)=120.5$). D: Fluorescence images showing ROS levels in primary neurons from indicated groups. Scale bar: 100 μm. E: Quantitative analysis of ROS-positive cells using DHE probe (red). Data are from at least four independent experiments. ***: P<0.001 (one-way ANOVA with Dunnett's *post hoc* analysis, $F(3,12)=259.9$).

indicative of the involvement of the DNA repair pathway in brain injury. Consistent with this, the up-regulation of DNA2 observed in this study may represent an intrinsic protective mechanism against I/R injury. Further investigation of brain injury and neurological impairment in *DNA2* cKO mice following MCAO revealed significantly larger cerebral infarct size, higher mNSS score, and exacerbated sensorimotor dysfunction in the cKO group compared to WT mice. These results indicate that *DNA2* deficiency hinders sensorimotor function recovery post-MCAO and exacerbates neurological deficits associated with cerebral I/R injury. Moreover, substantial neuronal loss was observed in cKO mice after MCAO, further supporting the role of DNA2 in neuronal protection. These observations align with prior studies

showing that KO of *TRIM29*, another DNA damage-related gene, leads to neuronal arrangement disorders, increased neuronal apoptosis, neuroinflammatory responses, and aggravated sensorimotor dysfunction post-MCAO (Deng et al., 2023).

Ischemia followed by reperfusion induces excessive accumulation of ROS in the brain, triggering signaling pathways that lead to oxidative damage and neuronal apoptosis (Ferranti et al., 2020; Szabó et al., 2020; Wu et al., 2023a; Zhang et al., 2022). Our results indicated that *DNA2* KD significantly increased ROS levels and apoptosis in OGD/R-induced HT22 cells and primary neurons, suggesting a critical role for *DNA2* in regulating neuronal injury during I/R. To further assess the effects of *DNA2* cKO on neuronal apoptosis, TUNEL staining was used to evaluate neuronal loss in the ischemic penumbra, while Bax and Bcl2 protein levels, key indicators of cell apoptosis, were analyzed using WB. Results revealed that *DNA2* cKO significantly exacerbated neuronal apoptosis in the ischemic penumbra at 3 days post-MCAO. The reversibility of ischemic penumbra cell damage remains a fundamental pathological basis for emergency thrombolytic therapy in ischemic stroke patients (Frank et al., 2022; Radak et al., 2017). In animal MCAO models, docosahexaenoic acid (DHA) treatment has been shown to improve behavioral function, reduce infarct volume, preserve cortical neurons, and promote axonal regeneration in the penumbra. DHA also exerts protective effects against stroke symptoms, emphasizing its importance in preventing penumbra infarction and reducing residual neurological damage (Furlan et al., 1996). Whether neuroprotective agents such as DHA also regulate DNA2 function during ischemia remains an intriguing and unexplored question.

The neuroprotective mechanism of DNA2 remains largely unexplored, necessitating further investigations to unveil its downstream targets. *Homer1a*, encoded by the *Homer1* gene, is up-regulated following ischemic hypoxia and traumatic brain injury, suggesting its potential involvement in neuroprotection (Bockaert et al., 2021; Wu et al., 2022). Previous studies have elucidated the protective effects of Homer1a on neurons through the regulation of mGluR, NMDA receptors, calcium ion channels, and antioxidant stress responses (Rao et al., 2016; Wang et al., 2015). In this study, RNA-seq analysis identified down-regulation of *Homer1* in *DNA2* cKO mice. Subsequent qPCR validation confirmed a significant decrease in the *Homer1a* subtype compared to WT mice. These findings were further supported by WB and IHC analyses, which revealed markedly decreased Homer1a expression levels in *DNA2* cKO mice. To determine whether *Homer1a* acts as a downstream target of *DNA2*, the rescue potential of OE-*Homer1a* in *DNA2* KD-induced neuronal apoptosis was evaluated in HT22 cells and neurons. Results showed that OE-*Homer1a* effectively mitigated *DNA2* KD-induced neuronal apoptosis. This is consistent with previous studies showing that OE-*Homer1a* inhibits PI3K/AKT/mTOR signaling pathway activation, thereby preventing neuronal damage in traumatic brain injury models (Wang et al., 2020). Based on these findings, we propose that DNA2 expression dynamically increases following cerebral I/R injury, potentially exerting neuroprotective effects by inducing Homer1a expression. However, further investigations are needed to unravel the molecular mechanisms linking *DNA2* to *Homer1a*-mediated neuronal protection.

Although this study primarily focused on the *DNA2*-*Homer1a* axis, alternative pathways likely intersect with or complement its role in neuroprotection. Oxidative stress resulting from I/R injury frequently leads to DNA strand breaks, necessitating efficient DNA repair mechanisms to prevent neuronal death. DNA2 plays an essential role in repairing DSBs via the homologous recombination pathway. This study demonstrated that *DNA2* deletion exacerbated DNA damage in I/R models. Proteins involved in base excision repair (BER) and nucleotide excision repair (NER) pathways, such as PARP1 and XRCC1, are critical for protecting neurons against oxidative stress and DNA damage (Wu et al., 2021). PARP1 detects DNA damage and recruits repair proteins, while XRCC1 serves as a scaffold for BER enzymes, ensuring efficient repair (Hoch et al., 2017). Notably, evidence suggests that DNA2 cooperates with PARP1 to repair DNA and restore disrupted DNA replication (Pawłowska et al., 2017; Wanrooij & Burgers, 2015; Ying et al., 2012). Additionally, recent research has indicated that *Gastrodia elata Blume* (GEB) enhances DNA repair capabilities by up-regulating the expression of *DNA2*, *Mcm2*, and *Rpa2*, thereby improving neural progenitor cell activity under hypoxic conditions (Gong et al., 2022). These findings suggest that *DNA2* may contribute to neuronal resilience against I/R injury not only through its regulation of *Homer1a* but also by enhancing broader DNA damage repair mechanisms.

Mitochondria contain their own DNA (mtDNA), which encodes essential components of the electron transport chain (ETC) responsible for driving adenosine triphosphate (ATP) synthesis through oxidative phosphorylation (OXPHOS) (Elosua, 2019). Disruption of OXPHOS not only depletes ATP levels but also increases the production of ROS, thereby exacerbating I/R injury (Huang et al., 2023). DNA2, which has been found to localize in the mitochondria, may play a critical role in mtDNA repair. Previous studies have shown that *DNA2* enables cancer cells to counteract mtDNA oxidative damage caused by replication stress and DNA-damaging agents, highlighting its importance in maintaining activated OXPHOS (Thongon et al., 2021, 2024). Furthermore, h*DNA2* deficiency has been shown to worsen hydrogen peroxide-induced mtDNA oxidative damage (Zheng et al., 2008). Consistent with these findings, our study also demonstrated that *DNA2* KD aggravated OGD/R-induced neuronal oxidative damage. These results suggest that *DNA2* may alleviate I/R injury by regulating OXPHOS.

I/R injury triggers a cascade of cellular responses involving multiple signaling pathways, which can either exacerbate or mitigate neuronal damage. Pan et al. (2019) demonstrated that *Ginkgetin* alleviates cerebral I/R-induced autophagy and apoptosis by inhibiting the NF-κB/p53 signaling pathway. Similarly, Li et al. (2024) reported that *IL-17A* deficiency mitigates I/R injury by activating the ERK/MAPK pathway and enhancing synaptic plasticity in the hippocampus. Here, KEGG analysis of brain tissue from *DNA2* cKO mice revealed that DEGs were enriched in the NF-κB, p53, and MAPK pathways, indicating that *DNA2* may regulate these pathways. Further investigation into the interplay between *DNA2* and these signaling pathways could provide valuable insights into novel therapeutic approaches for reducing neuronal injury associated with cerebral I/R.

In addition to the *DNA2*-*Homer1a* axis, our study also highlighted new avenues for developing targeted therapies to reduce neuronal damage after I/R. Activating DNA2 during the acute phase of brain injury through small molecules or

pharmacological interventions could provide an effective strategy for mitigating neuronal damage. Similarly, Homer1a has a well-documented role in synaptic plasticity and calcium homeostasis, protecting neurons from excitotoxicity (Reshetnikov & Bondar, 2021). Studies have shown that OE-*Homer1a* mitigates neuronal damage by regulating calcium signaling and glutamate receptor activity (mGluR1/5), while reducing lactate dehydrogenase release in neurons (Luo et al., 2014; Rao et al., 2016; Su et al., 2014; Wu et al., 2022). A combined approach targeting both *DNA2* and *Homer1a* may offer a dual protective strategy, addressing both genomic stability and synaptic resilience. This approach may effectively minimize both the acute and secondary effects of stroke.

In conclusion, this study provides evidence that *DNA2* cKO exacerbates neurological impairment in mice following MCAO, highlighting its critical role in neuroprotection during cerebral I/R. However, this study has several limitations. Notably, the potential neuroprotective effects of OE-*DNA2* in the context of cerebral I/R injury have yet to be validated, and the precise molecular pathways through which *DNA2* regulates *Homer1a* expression require further elucidation. Addressing these limitations in future research will provide a more comprehensive understanding of DNA2 function in I/R injury and facilitate the development of targeted therapeutic strategies.

DATA AVAILABILITY

The raw RNA-seq data reported in this study are available from the NCBI database (BioProjectID PRJNA1182985), China National Center for Bioinformation database (GSA: CRA020250), and Science Data Bank database (DOI: 10.57760/sciencedb.16506).

SUPPLEMENTARY DATA

Supplementary data to this article can be found online.

COMPETING INTERESTS

The authors declare that they have no competing interests.

AUTHORS' CONTRIBUTIONS

Conceived or designed the study: A.G., J.S., and T.M.; performed the research: T.M., Y.L., P.R., and S.W.; analyzed the data: X.L., W.L., and W.Z.; wrote the paper: T.M., W.L., and W.H. All authors read and approved the final version of the manuscript.

REFERENCES

Bockaert J, Perroy J, Ango F. 2021. The complex formed by group I metabotropic glutamate receptor (mGluR) and Homer1a plays a central role in metaplasticity and homeostatic synaptic scaling. *The Journal of Neuroscience*, **41**(26): 5567–5578.

Bouët V, Freret T, Toutain J, et al. 2007. Sensorimotor and cognitive deficits after transient middle cerebral artery occlusion in the mouse. *Experimental Neurology*, **203**(2): 555–567.

Buchser WJ, Pardinas JR, Shi Y, et al. 2006. 96-well electroporation method for transfection of mammalian central neurons. *Biotechniques*, **41**(5): 619–624.

Budd ME, Campbell JL. 2000. The pattern of sensitivity of yeast *dna2* mutants to DNA damaging agents suggests a role in DSB and postreplication repair pathways. *Mutation Research/DNA Repair*, **459**(3): 173–186.

Caston RA, Fortini P, Chen K, et al. 2023. Maintenance of flap endonucleases for long-patch base excision DNA repair in mouse muscle and neuronal cells differentiated in vitro. *International Journal of Molecular Sciences*, **24**(16): 12715.

Cejka P, Cannavo E, Polaczek P, et al. 2010. DNA end resection by Dna2-Sgs1-RPA and its stimulation by Top3-Rmi1 and Mre11-Rad50-Xrs2. *Nature*, **467**(7311): 112–116.

Chen HS, He YC, Chen S, et al. 2020. Therapeutic targets of oxidative/nitrosative stress and neuroinflammation in ischemic stroke: applications for natural product efficacy with omics and systemic biology. *Pharmacological Research*, **158**: 104877.

Chen SC, Wang MD, Yang H, et al. 2017. LncRNA TUG1 sponges microRNA-9 to promote neurons apoptosis by up-regulated Bcl2l11 under ischemia. *Biochemical and Biophysical Research Communications*, **485**(1): 167–173.

Chen XF, Niu HY, Chung WH, et al. 2011. Cell cycle regulation of DNA double-strand break end resection by Cdk1-dependent Dna2 phosphorylation. *Nature Structural & Molecular Biology*, **18**(9): 1015–1019.

Chen ZZ, Hu Q, Xie QF, et al. 2019. Effects of treadmill exercise on motor and cognitive function recovery of MCAO mice through the caveolin-1/VEGF signaling pathway in ischemic penumbra. *Neurochemical Research*, **44**(4): 930–946.

Deng YM, Li ZY, Sun X, et al. 2023. TRIM29 (tripartite motif containing 29) alleviates NLRC4 (NLR Family CARD domain containing Protein 4) inflammasome related cerebral injury via promoting proteasomal degradation of NLRC4 in ischemic stroke. *Stroke*, **54**(5): 1377–1389.

Dumas LB, Lussky JP, Mcfarland EJ, et al. 1982. New temperature-sensitive mutants of *Saccharomyces cerevisiae* affecting DNA replication. *Molecular and General Genetics: MGG*, **187**(1): 42–46.

Elosua R. 2019. Mitochondrial DNA and cardiovascular diseases: a long road ahead. *European Journal of Preventive Cardiology*, **26**(9): 973–975.

Falquet B, Ölmezer G, Enkner F, et al. 2020. Disease-associated *DNA2* nuclease-helicase protects cells from lethal chromosome under-replication. *Nucleic Acids Research*, **48**(13): 7265–7278.

Fei F, Li J, Rao W, et al. 2015. Upregulation of Homer1a promoted retinal ganglion cell survival after retinal ischemia and reperfusion via interacting with Erk pathway. *Cellular and Molecular Neurobiology*, **35**(7): 1039–1048.

Fei XW, Dou YN, Wang L, et al. 2022. Homer1 promotes the conversion of A1 astrocytes to A2 astrocytes and improves the recovery of transgenic mice after intracerebral hemorrhage. *Journal of Neuroinflammation*, **19**(1): 67.

Feigin VL, Stark BA, Johnson CO, et al. 2021. Global, regional, and national burden of stroke and its risk factors, 1990–2019: a systematic analysis for the Global Burden of Disease Study 2019. *The Lancet Neurology*, **20**(10): 795–820.

Ferranti CS, Cheng J, Thompson C, et al. 2020. Fusion of lysosomes to plasma membrane initiates radiation-induced apoptosis. *Journal of Cell Biology*, **219**(4): e201903176.

Frank D, Zlotnik A, Boyko M, et al. 2022. The development of novel drug treatments for stroke patients: a review. *International Journal of Molecular Sciences*, **23**(10): 5796.

Furlan M, Marchal G, Derlon JM, et al. 1996. Spontaneous neurological recovery after stroke and the fate of the ischemic penumbra. *Annals of Neurology*, **40**(2): 216–226.

Gong X, Cheng J, Zhang KS, et al. 2022. Transcriptome sequencing reveals *Gastrodia elata* Blume could increase the cell viability of eNPCs under hypoxic condition by improving DNA damage repair ability. *Journal of Ethnopharmacology*, **282**: 114646.

Grimm A, Cummins N, Götz J. 2018. Local oxidative damage in the soma and dendrites quarantines neuronal mitochondria at the site of insult. *iScience*, **6**: 114–127.

Guo HY, Fan Z, Wang SQ, et al. 2021. Astrocytic A1/A2 paradigm participates in glycogen mobilization mediated neuroprotection on reperfusion injury after ischemic stroke. *Journal of Neuroinflammation*, **18**(1): 230.

Hoch NC, Hanzlikova H, Rulten SL, et al. 2017. *XRCC1* mutation is associated with PARP1 hyperactivation and cerebellar ataxia. *Nature*,

541(7635): 87–91.

Huang J, Chen L, Yao ZM, et al. 2023. The role of mitochondrial dynamics in cerebral ischemia-reperfusion injury. *Biomedicine & Pharmacotherapy*, **162**: 114671.

Hudson JJR, Rass U. 2021. *DNA2* in chromosome stability and cell survival-is it all about replication forks?. *International Journal of Molecular Sciences*, **22**(8): 3984.

Kao HI, Campbell JL, Bambara RA. 2004. Dna2p helicase/nuclease is a tracking protein, like FEN1, for flap cleavage during Okazaki fragment maturation. *Journal of Biological Chemistry*, **279**(49): 50840–50849.

Kuo CL, Nuang H, Campbell JL. 1983. Isolation of yeast DNA replication mutants in permeabilized cells. *Proceedings of the National Academy of Sciences of the United States of America*, **80**(21): 6465–6469.

Li YN, Zhang Q, Wang XP, et al. 2024. IL-17A deficiency alleviates cerebral ischemia-reperfusion injury via activating ERK/MAPK pathway in hippocampal CA1 region. *Brain Research Bulletin*, **208**: 110890.

Li ZK, Liu BC, Jin WW, et al. 2018. hDNA2 nuclease/helicase promotes centromeric DNA replication and genome stability. *The EMBO Journal*, **37**(14): e96729.

Luo P, Chen T, Zhao Y, et al. 2014. Postsynaptic scaffold protein Homer 1a protects against traumatic brain injury via regulating group I metabotropic glutamate receptors. *Cell Death & Disease*, **5**(4): e1174.

Luo P, Zhao YB, Li D, et al. 2012. Protective effect of Homer 1a on tumor necrosis factor-α with cycloheximide-induced apoptosis is mediated by mitogen-activated protein kinase pathways. *Apoptosis*, **17**(9): 975–988.

Ma H, Campbell BCV, Parsons MW, et al. 2019. Thrombolysis guided by perfusion imaging up to 9 hours after onset of stroke. *New England Journal of Medicine*, **380**(19): 1795–1803.

Ma LZ, Sun HT, Abeywardana T, et al. 2022. Structure-specific nucleases: role in Okazaki fragment maturation. *Trends in Genetics*, **38**(8): 793–796.

Meng Y, Liu CW, Shen L, et al. 2019. TRAF6 mediates human DNA2 polyubiquitination and nuclear localization to maintain nuclear genome integrity. *Nucleic Acids Research*, **47**(14): 7564–7579.

Pan JQ, Li X, Guo F, et al. 2019. Ginkgetin attenuates cerebral ischemia-reperfusion induced autophagy and cell death via modulation of the NF-κB/p53 signaling pathway. *Bioscience Reports*, **39**(9): BSR20191452.

Park S, Karatayeva N, Demin AA, et al. 2021. The secondary-structured DNA-binding activity of Dna2 endonuclease/helicase is critical to cell growth under replication stress. *The FEBS Journal*, **288**(4): 1224–1242.

Pawłowska E, Szczepanska J, Blasiak J. 2017. DNA2-an important player in DNA damage response or just another DNA maintenance protein?. *International Journal of Molecular Sciences*, **18**(7): 1562.

Radak D, Katsiki N, Resanovic I, et al. 2017. Apoptosis and acute brain ischemia in ischemic stroke. *Current Vascular Pharmacology*, **15**(2): 115–122.

Rao W, Peng C, Zhang L, et al. 2016. Homer1a attenuates glutamate-induced oxidative injury in HT-22 cells through regulation of store-operated calcium entry. *Scientific Reports*, **6**: 33975.

Reshetnikov VV, Bondar NP. 2021. The role of stress-induced changes of Homer1 expression in stress susceptibility. *Biochemistry (Moscow)*, **86**(6): 613–626.

Schwab N, Ju Y, Hazrati LN. 2021. Early onset senescence and cognitive impairment in a murine model of repeated mTBI. *Acta Neuropathologica Communications*, **9**(1): 82.

Serchov T, Heumann R, Van Calker D, et al. 2016. Signaling pathways regulating Homer1a expression: implications for antidepressant therapy. *Biological Chemistry*, **397**(3): 207–214.

Stillman M, Lautz JD, Johnson RS, et al. 2022. Activity dependent dissociation of the Homer1 interactome. *Scientific Reports*, **12**(1): 3207.

Su JJ, Pan H, Zhou HG, et al. 2014. Acid-sensing ion channels activation and hypoxia upregulate Homer1a expression. *CNS Neuroscience & Therapeutics*, **20**(3): 264–274.

Szabó MR, Pipicz M, Csont T, et al. 2020. Modulatory effect of myokines on reactive oxygen species in ischemia/reperfusion. *International Journal of Molecular Sciences*, **21**(24): 9382.

Thakar T, Leung W, Nicolae CM, et al. 2020. Ubiquitinated-PCNA protects replication forks from DNA2-mediated degradation by regulating Okazaki fragment maturation and chromatin assembly. *Nature Communications*, **11**(1): 2147.

Thongon N, Ma FY, Baran N, et al. 2024. Targeting DNA2 overcomes metabolic reprogramming in multiple myeloma. *Nature Communications*, **15**(1): 1203.

Thongon N, Santoni A, Lui J, et al. 2021. P-106: targeting DNA2 overcomes myeloma cells' metabolic reprogramming in response to DNA damage. *Clinical Lymphoma Myeloma and Leukemia*, **21**: S96–S97.

Tuo QZ, Lei P. 2024. Ferroptosis in ischemic stroke: animal models and mechanisms. *Zoological Research*, **45**(6): 1235–1248.

Vazdarjanova A, Mcnaughton BL, Barnes CA, et al. 2002. Experience-dependent coincident expression of the effector immediate-early genes *Arc* and *Homer 1a* in hippocampal and neocortical neuronal networks. *The Journal of Neuroscience*, **22**(23): 10067–10071.

Wang Y, Rao W, Zhang C, et al. 2015. Scaffolding protein Homer1a protects against NMDA-induced neuronal injury. *Cell Death & Disease*, **6**(8): e1843.

Wang Y, Zhao MM, Shang L, et al. 2020. Homer1a protects against neuronal injury via PI3K/AKT/mTOR signaling pathway. *International Journal of Neuroscience*, **130**(6): 621–630.

Wanrooij PH, Burgers PM. 2015. Yet another job for Dna2: checkpoint activation. *DNA Repair*, **32**: 17–23.

Wei JL, Wu XQ, Luo P, et al. 2019. Homer1a attenuates endoplasmic reticulum stress-induced mitochondrial stress after ischemic reperfusion injury by inhibiting the PERK pathway. *Frontiers in Cellular Neuroscience*, **13**: 101.

Wu H, Li Y, Zhang Q, et al. 2023a. Crocetin antagonizes parthanatos in ischemic stroke via inhibiting NOX2 and preserving mitochondrial hexokinase-I. *Cell Death & Disease*, **14**(1): 50.

Wu QL, Cui LY, Ma WY, et al. 2023b. A novel small-molecular CCR5 antagonist promotes neural repair after stroke. *Acta Pharmacologica Sinica*, **44**(10): 1935–1947.

Wu W, Hill SE, Nathan WJ, et al. 2021. Neuronal enhancers are hotspots for DNA single-strand break repair. *Nature*, **593**(7859): 440–444.

Wu XQ, Su N, Fei Z, et al. 2022. Homer signaling pathways as effective therapeutic targets for ischemic and traumatic brain injuries and retinal lesions. *Neural Regeneration Research*, **17**(7): 1454–1461.

Ying SM, Hamdy FC, Helleday T. 2012. Mre11-dependent degradation of stalled DNA replication forks is prevented by BRCA2 and PARP1. *Cancer Research*, **72**(11): 2814–2821.

Zhai BY, Zhang SX, Li B, et al. 2023. Dna2 removes toxic ssDNA-RPA filaments generated from meiotic recombination-associated DNA synthesis. *Nucleic Acids Research*, **51**(15): 7914–7935.

Zhang Q, Jia M, Wang YF, et al. 2022. Cell death mechanisms in cerebral ischemia-reperfusion injury. *Neurochemical Research*, **47**(12): 3525–3542.

Zhang TS, Tian C, Wu JR, et al. 2020. MicroRNA-182 exacerbates blood-brain barrier (BBB) disruption by downregulating the mTOR/FOXO1 pathway in cerebral ischemia. *The FASEB Journal*, **34**(10): 13762–13775.

Zheng L, Meng Y, Campbell JL, et al. 2020. Multiple roles of DNA2 nuclease/helicase in DNA metabolism, genome stability and human diseases. *Nucleic Acids Research*, **48**(1): 16–35.

Zheng L, Zhou M, Guo ZG, et al. 2008. Human DNA2 is a mitochondrial nuclease/helicase for efficient processing of DNA replication and repair intermediates. *Molecular Cell*, **32**(3): 325–336.

Zhou C, Pourmal S, Pavletich NP. 2015. Dna2 nuclease-helicase structure, mechanism and regulation by Rpa. *eLife*, **4**: e09832.

Li et al. *Zool. Res.* 2025, 46(1): 103−121
https://doi.org/10.24272/j.issn.2095-8137.2024.298
https://cstr.cn/32248.14.zr.2024.298

ZR | Zoological Research

Article Open Access

Identification of novel rodent and shrew orthohepeviruses sheds light on hepatitis E virus evolution

Fu-Li Li[1,2,#], Bo Wang[3,#], Pei-Yu Han[1], Bei Li[4], Hao-Rui Si[4], Yan Zhu[4], Hong-Min Yin[1], Li-Dong Zong[1], Yi Tang[1], Zheng-Li Shi[4], Ben Hu[4,*], Xing-Lou Yang[5,*], Yun-Zhi Zhang[1,*]

[1] *Institute of Preventive Medicine*, *School of Public Health*, *Dali University*, *Yunnan Key Laboratory of Screening and Research on Anti-pathogenic Plant Resources from Western Yunnan*, *Yunnan Key Laboratory of Zoonotic Disease Cross-border Prevention and Quarantine*, *Dali*, *Yunnan* 671000, *China*

[2] *Second People's Hospital of Qujing*, *Qujing*, *Yunnan* 655000, *China*

[3] *Programme in Emerging Infectious Diseases*, *Duke-NUS Medical School*, *Singapore* 169857, *Singapore*

[4] *CAS Key Laboratory of Special Pathogens*, *Wuhan Institute of Virology*, *Chinese Academy of Sciences*, *Wuhan*, *Hubei* 430071, *China*

[5] *Key Laboratory of Genetic Evolution & Animal Models*, *Yunnan International Joint Laboratory of Zoonotic Viruses*, *Yunnan Key Laboratory of Biodiversity Information*, *Kunming Institute of Zoology*, *Chinese Academy of Sciences*, *Kunming*, *Yunnan* 650223, *China*

ABSTRACT

The family *Hepeviridae* has seen an explosive expansion in its host range in recent years, yet the evolutionary trajectory of this zoonotic pathogen remains largely unknown. The emergence of rat hepatitis E virus (HEV) has introduced a new public health threat due to its potential for zoonotic transmission. This study investigated 2 464 wild small mammals spanning four animal orders, eight families, 21 genera, and 37 species in Yunnan Province, China. Using broadly reactive reverse transcription-polymerase chain reaction (RT-PCR), we systematically screened the presence and prevalence of *Orthohepevirus* and identified 192 positive specimens from 10 species, corresponding to an overall detection rate of 7.79%. Next-generation sequencing enabled the recovery of 24 full-length genomic sequences from eight host species, including *Bandicota bengalensis*, *Eothenomys eleusis*, and *Episoriculus caudatus*, representing newly reported host species for *Orthohepevirus* strains. Phylogenetic and sequence analyses revealed extensive genetic diversity within orthohepeviruses infecting rodents and shrews. Notably, among the identified strains, 20 were classified as *Rocahepevirus ratti* C1, two as C3, and one as *Rocahepevirus eothenomi*, while the remaining strain exhibited significant divergence, precluding classification. Evolutionary analyses highlighted close associations between orthohepeviruses and their respective host taxa, with distinct phylogenetic clustering patterns observed across different host orders. These findings emphasize the critical roles of co-speciation and cross-species transmission in shaping the evolutionary trajectories of the genera *Paslahepevirus* and *Rocahepevirus*.

Keywords: Hepatitis E Virus (HEV); *Orthohepevirus*; *Rocahepevirus* (HEV-C); Rodent; Shrew; Genomic Characterization; Genetic Diversity; Molecular Evolution

INTRODUCTION

Hepatitis E virus (HEV), a small quasi-enveloped, positive-sense, single-stranded RNA virus belonging to the family *Hepeviridae*, represents a significant global cause of acute viral hepatitis (Wang & Meng, 2021b). Four major HEV genotypes (HEV-1 to HEV-4) within the species *Paslahepevirus balayani* infect humans, exhibiting distinct epidemiological patterns. HEV-1 and HEV-2 are predominantly transmitted to humans through the fecal-oral route, primarily in developing countries via drinking contaminated water sources. Conversely, sporadic cases of HEV-3 and HEV-4 infection in industrialized nations have been linked to the consumption of undercooked or raw meat products (Wang et al., 2018a). Although acute hepatitis E is typically self-limiting, HEV-1 infections during pregnancy are

This is an open-access article distributed under the terms of the Creative Commons Attribution Non-Commercial License (http://creativecommons.org/licenses/by-nc/4.0/), which permits unrestricted non-commercial use, distribution, and reproduction in any medium, provided the original work is properly cited.

Copyright ©2025 Editorial Office of Zoological Research, Kunming Institute of Zoology, Chinese Academy of Sciences

Received: 12 September 2024; Accepted: 09 December 2024; Online: 10 December 2024

Foundation items: This study was supported by the National Natural Science Foundation of China (U2002218, 81874274), Yunnan Health Training Project of High Level Talents (L-2017027), Project of Cross-border Control and Quarantine Innovation Group of Zoonosis of Dali University (ZKPY2019302) to Y.Z.Z, Open Project of Yunnan Key Laboratory of Biodiversity Information (BIKF22-02), Youth Innovation Promotion Association of the Chinese Academy of Sciences, and Yunnan Revitalization Talent Support Program Young Talent Project to X.L.Y.

[#]Authors contributed equally to this work

*Corresponding authors, E-mail: huben@wh.iov.cn; yangxinglou@mail.kiz.ac.cn; zhangyunzhi1818@163.com

particularly severe. Pregnant women, especially in their third trimester, face an elevated risk of fulminant hepatic failure, with mortality rates up to 30% (Wang et al., 2022). Moreover, HEV-3 infections in immunocompromised individuals, including solid organ transplant recipients and chemotherapy patients, frequently progress to chronic hepatitis, necessitating antiviral intervention (Choi et al., 2018). Beyond its role in acute and chronic liver diseases, HEV has emerged as a pathogen of growing concern due to its association with extrahepatic complications, including neurological and renal disorders (Kamar et al., 2016; Tian et al., 2022).

HEV is unique among hepatotropic viruses due to its documented zoonotic transmission, ranking sixth in spillover potential among 887 wildlife-associated viruses (Grange et al., 2021; Rasche et al., 2019; Sander et al., 2018). Since the initial discovery of HEV in domestic pigs (termed swine HEV) in 1997 in the United States and the subsequent recognition of its zoonotic capacity, various genetically related human HEV homologs have been recovered in over a dozen animal hosts (Meng et al., 1997, 1998; Wang & Meng, 2021a). Although domestic pigs, wild boars, and sika deer are the primary animal reservoirs for HEV, numerous strains from other animal species have demonstrated the ability to breach species barriers and infect humans (Kinast et al., 2022; Wang & Meng, 2021a). Among these, HEV variants from rats (termed rat HEV) have attracted increasing scientific attention. Despite considerable genetic divergence from human HEV, multiple independent studies have documented zoonotic infections caused by rat HEV, including 16 cases in Hong Kong, three cases in Spain, one case in France, and one case in Canada (Andonov et al., 2019; Rivero-Juarez et al., 2022; Rodriguez et al., 2023; Sridhar et al., 2018, 2021b, 2022). These findings suggest that rat HEV likely represents an underestimated source of human infection that warrants further investigation. Moreover, a recent study highlighted a critical distinction in the antigenic properties of rat HEV compared to human HEV, revealing that prior exposure to human HEV does not confer immunity against rat HEV infection (Sridhar et al., 2021a).

Rat HEV was first identified in Norway/Brown rats (family Muridae, species *Rattus norvegicus*) in Germany in 2010 (Johne et al., 2010). Since then, genetically diverse rat HEV strains have been detected in multiple murine species worldwide (summarized in Wang et al. (2020)). Interestingly, evidence suggests that Asian house shrews (family Soricidae, species *Suncus murinus*) serve as reservoirs for rat HEV (Guan et al., 2013; Wang et al., 2017a), despite the remarkable evolutionary divergence between their representative taxonomic orders, Rodentia and Eulipotyphla (Rasche et al., 2019). In contrast, a 254-nt HEV genomic fragment identified in Oliver's shrew (family Soricidae, species *Crocidura olivieri*) from Kenya displayed substantial phylogenetic divergence from rat HEV, implying the existence of distinct HEV variants in shrews (Onyuok et al., 2019). Taxonomically, rat HEV is classified within the genus *Rocahepevirus* (HEV-C), which includes at least two recognized species, *R. ratti* and *R. eothenomi*. This genus predominantly includes HEV variants found in rodents, insectivores, and carnivores. Within *R. ratti*, three genotypes have been proposed based on evolutionary relationships and host tropism: HEV-C1 (rats and house shrews), HEV-C2 (ferrets), and HEV-C3 (field mice) (Wang & Yang, 2022). Nonetheless, some HEV-C variants identified in wild rodents, such as hamsters and field mice, remain unassigned due to their ambiguous phylogenetic placement (Wang et al., 2020).

Thus far, HEV-C RNA has been reported in nearly 20 rodent species, representing only a small fraction of the immense rodent diversity, accounting for approximately 1% of a total of 2 277 named species within the order Rodentia (Wang et al., 2020). This limited representation strongly suggests that the host range and genetic diversity of HEV-C variants are likely to expand as additional wild rodent species and small mammals are investigated. Importantly, while the evolutionary origin and lineage of human HEV (genus *Paslahepevirus*) remain unknown, the broad host range and significant genetic diversity of HEV-C have prompted hypotheses implicating the genus *Rocahepevirus* as a crucial contributor to the genealogy of human HEV (Rasche et al., 2019; Sander et al., 2018). Moreover, considering the broad host spectrum of orthohepeviruses (subfamily *Orthohepevirinae*), advances in sequencing techniques are expected to uncover increasingly divergent HEV-related viruses in other mammalian orders (Papp et al., 2022; Wu et al., 2018), further emphasizing the zoonotic potential of these viruses and raising public health concerns.

We previously detected and characterized novel HEV-C genomes in Chevrier's field mice (family Muridae, species *Apodemus chevrieri*) and Pere David's voles (family Cricetidae, species *Eothenomys melanogaster*) (Wang et al., 2018c), designated as species *R. ratti* genotype HEV-C3 and species *R. eothenomi*, respectively, based on the 2021 International Committee on Taxonomy of Viruses (ICTV) *Hepeviridae* Study Group (Purdy et al., 2022; Wang & Yang, 2022). In the present study, we sampled 2 464 wild small mammals across Yunnan Province, China, consisting of four animal orders, eight families, 21 genera, and 37 species. This systematic investigation revealed additional genetically diverse *Orthohepevirus* variants, which were subsequently subjected to detailed analysis of genetic diversity, genomic characterization, and molecular evolution. Our results expand the known host range within the family *Hepeviridae* and underscore the importance of virus-host co-speciation and cross-species transmission events in shaping the evolutionary trajectories of the genera *Paslahepevirus* and *Rocahepevirus*.

MATERIALS AND METHODS

Ethics statement

The collection of wild small mammals was conducted by veterinarians with approval from the Human and Animal Ethics Committee of Dali University (Human and Animal Ethics Approval Number: DLDXLL2013002).

Sample collection

Between April 2014 and September 2019, a total of 2 464 wild small mammals were collected from 10 prefectures or cities in 16 counties or districts of Yunnan Province in southwestern China (Figure 1A), including (west to east): Ruili City and Lianghe County (Dehong Prefecture), Deqin County (Diqing Prefecture), Nanjian County, Xiangyun County, and Yunlong County (Dali Prefecture), Gucheng District (Lijiang City), Yuanmou County (Chuxiong Prefecture), Yuanjiang County (Yuxi City), Jinghong City, Menghai County, and Mengla County (Xishuangbanna Prefecture), Luxi County (Honghe Prefecture), Yiliang County (Kunming City), Yongshan County, and Zhaoyang District (Zhaotong City) (Table 1). The small mammals were trapped using rat traps using fried dough

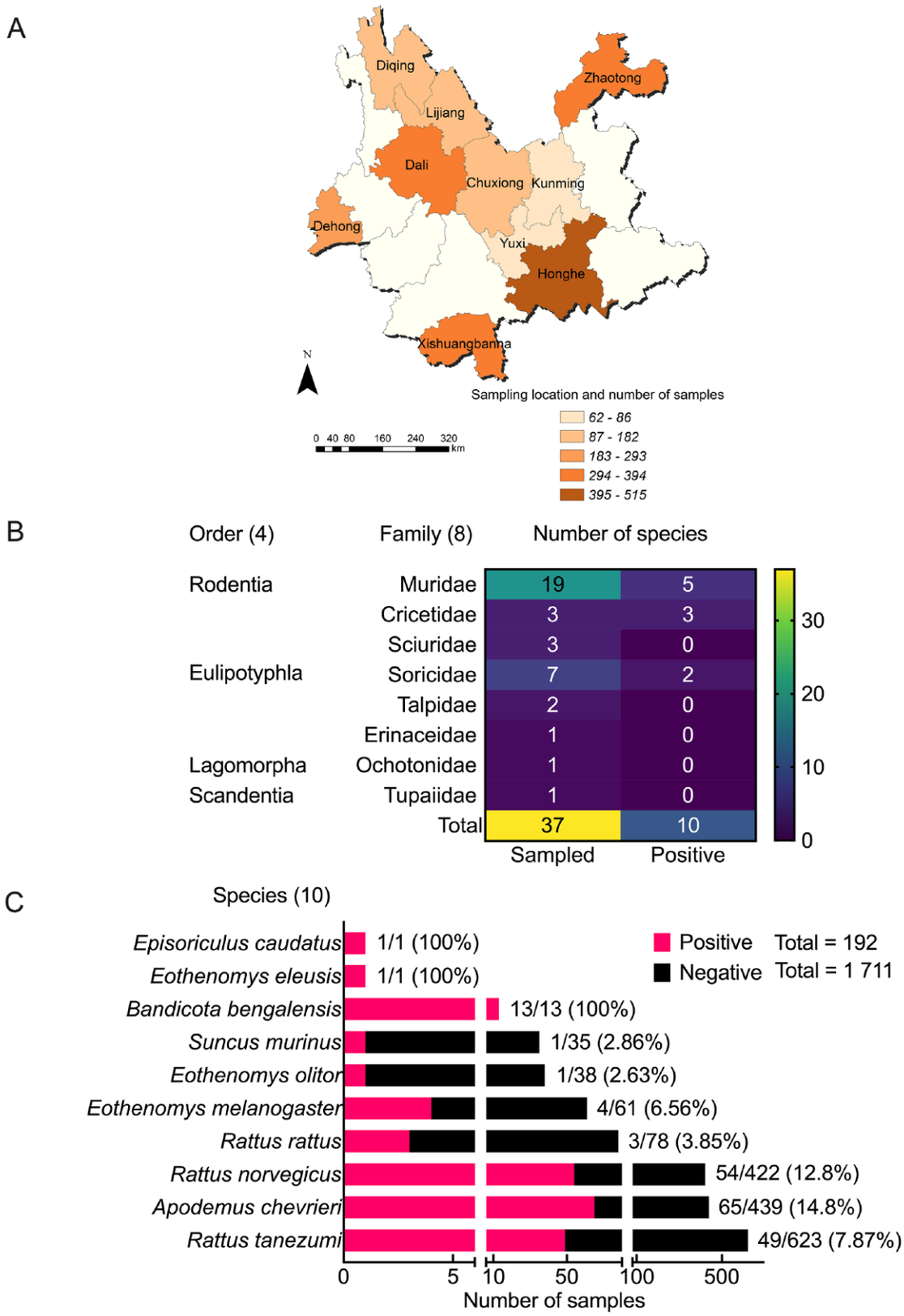


Figure 1 Sampling locations and corresponding sampling numbers in Yunnan, China

A: Global map on the left was generated using QGIS v.3.22 and free vector and raster map data from Natural Earth. China and Yunnan are highlighted in red and orange, respectively. Map of Yunnan on the right and its 10 prefectures and cities was created in ArcGIS. Each sampling site is color-coded in varying shades of orange, reflecting number of samples collected. B: Numbers of *Orthohepevirus*-positive animal species, characterized by family, surveyed in this study. Animal orders and corresponding numbers are listed on the left. C: Comparison of *Orthohepevirus*-positive and -negative samples across 10 *Orthohepevirus*-positive animal species identified in this study. Percentage of positivity indicates proportion of *Orthohepevirus*-positive samples relative to total samples collected from each host species.

Table 1 Sampling information and detection of orthohepevirus in small mammals in Yunnan province from April 2014 to September 2019

Animal order	Family	Genus	Species	Genbank common name	NCBI taxonomy ID	No. of positive samples (%)	Sampling site(s) (year)
	Muridae	*Apodemus*	*agrarius*	Striped field mouse	txid39030	0/6 (0)	Yongshan (2018)
			chevrieri	Chevrier's field mouse	txid129246	65/439 (14.8%)	Lijiang (2014/2015[c]), Luxi (2014/2015/2016), Yiliang (2016), Zhaoyang (2016[c]), Xiangyun (2016/2017), Yuanmou (2016/2017), Yongshan (2018[c]), Yunlong (2019), Deqin (2018[c])
			draco	South China field mouse	txid129247	0/11 (0)	Menghai (2016), Yuanmou (2016)
			latronum	Sichuan field mouse	txid214933	0/40 (0)	Ruili (2017), Deqin (2018), Jinghong (2018), Yongshan (2018)
			sylvaticus	European woodmouse	txid10129	0/10 (0)	Jinghong (2018)
		Bandicota	*bengalensis*	lesser bandicoot rat	txid69079	13/13 (100%)	Ruili (2017)
			indica	Greater bandicoot rat	txid456472	0/42 (0)	Lianghe (2016), Yuanjiang (2017), Ruili (2017)
		Berylmys	*bowersi*	Bower's white-toothed rat	txid83759	0/1 (0)	Yuanmou (2017)
		Mus	*caroli*	Ryukyu mouse	txid10089	0/113 (0)	Lianghe (2016), Yiliang (2016), Yuanmou (2016), Xiangyun (2017), Yuanjiang (2017), Jinghong (2018)
			musculus	house mouse	txid10090	0/65 (0)	Luxi (2014), Yiliang (2016), Zhaoyang (2016), Xiangyun (2016/2017), Menghai (2016), Ruili (2017)
			pahari	shrew mouse	txid10093	0/84 (0)	Lianghe (2016), Yiliang (2016), Yuanmou (2016), Yongshan (2018)
		Micromys	*minutus*	European harvest mouse	txid13151	0/50 (0)	Yiliang (2016), Luxi (2016), Jinghong (2018), Yongshan (2018)
		Niviventer	*confucianus*	Chinese white-bellied rat	txid248811	0/56 (0)	Lianghe (2016), Yiliang (2016), Yuanmou (2017), Xiangyun (2017), Ruili (2017), Deqin (2018), Yongshan (2018), Yunlong (2019)
			coxingi	Coxing's white-bellied rat	txid357352	0/3 (0)	Yongshan (2018)
			fulvescens	Chestnut white-bellied rat	txid83774	0/67 (0)	Lianghe (2016), Ruili (2017), Nanjian (2017), Jinghong (2018), Yongshan (2018), Yunlong (2019)
		Rattus	*nitidus*	White-footed indochinese rat	txid508668	0/11 (0)	Yiliang (2016), Zhaoyang (2016), Menghai (2016), Yongshan (2018)
			norvegicus	Norway rat	txid10116	54/422 (12.8%)	Luxi (2014/2015/2016/2017[c]), Zhaoyang (2016), Yiliang (2016[c]), Zhaoyang (2016), Yuanmou (2016/2017), Yuanjiang (2017[c]), Xiangyun (2017[c]), Yongshan (2018)
			rattus	black rat	txid10117	3/78 (3.85%)	Lianghe (2016[c]), Menghai (2016), Ruili (2017), Yuanjiang (2017), Ruili (2017), Nanjian (2017), Yongshan (2018), Jinghong (2018)
			tanezumi	Oriental house rat	txid35732	49/623 (7.87%)	Lijiang (2014), Lianghe (2016[c]), Menghai (2016[c]), Ruili (2017[c]), Yuanjiang (2017[c]), Xiangyun (2016), Mengla (2016), Yiliang (2016), Zhaoyang (2016), Yuanmou (2016/2017), Luxi (2017), Nanjian (2017), Deqin (2018[c]), Yongshan (2018), Jinghong (2018[c]), Yunlong (2019)
	Cricetidae	*Eothenomys*	*eleusis*	Kachin red-backed vole	txid259053	1/1 (100%)	Luxi (2017)
			melanogaster	Pere David's vole	txid82468	4/61 (6.56%)	Luxi (2014)
			olitor	Chaotung vole	txid259051	1/38 (2.63%)	Zhaoyang (2016)
	Sciuridae	*Dremomys*	*pernyi*	Perny's long-nosed squirrel	txid234634	0/22 (0)	Yongshan (2018)
		Sciurotamias	*davidianus*	Pere David's rock squirrel	txid226849	0/16 (0)	Deqin (2018)
		Tamiops	*mcclellandii*	Himalayan striped squirrel	txid461710	0/2 (0)	Deqin (2018)

Continued

Animal order	Family	Genus	Species	Genbank common name	NCBI taxonomy ID	No. of positive samples (%)	Sampling site(s) (year)
Eulipotyphla	Soricidae	*Anourosorex*	*squamipes*	mole shrew	txid127560	0/52 (0)	Luxi (2016), Zhaoyang (2016), Ruili (2017), Nanjian (2018), Yongshan (2018)
		Crocidura	*attenuata*	Asian gray shrew	txid167044	0/37 (0)	Lianghe (2016), Zhaoyang (2016), Menghai (2016), Yuanmou (2016), Xiangyun (2017), Yuanjiang (2017), Nanjian (2017), Jinghong (2018), Yongshan (2018), Yunlong (2019)
			suaveolens	Lesser white-toothed shrew	txid52631	0/3 (0)	Yongshan (2018)
		Episoriculus	*caudatus*	Hodgson's brown-toothed shrew	txid62291	1/1 (100%)	Yongshan (2018)
		Sorex	*araneus*	European shrew	txid42254	0/11 (0)	Menghai (2016), Xiangyun (2016/2017), Jinghong (2018)
			excelsus	lofty shrew	txid62901	0/2 (0)	Yongshan (2018)
		Suncus	*murinus*	Asian house shrew	txid9378	1/35 (2.86%)	Lianghe (2016[c]), Mengla (2016), Menghai (2016), Ruili (2017), Yongshan (2018)
	Talpidae	*Euroscaptor*	*longirostris*	long-nosed mole	txid481574	0/1 (0)	Yunlong (2019)
		Nasillus	*gracilis*	NA[a]	NA[b]	0/5 (0)	Yongshan (2018)
	Erinaceidae	*Hylomys*	*suillus*	short-tailed gymnure	txid48897	0/20 (0)	Lianghe (2016), Ruili (2017)
Lagomorpha	Ochotonidae	*Ochotona*	*thibetana*	Moupin pika	txid130843	0/1 (0)	Deqin (2018)
Scandentia	Tupaiidae	*Tupaia*	*belangeri*	northern tree shrew	txid37347	0/22 (0)	Yuanmou (2016/2017), Xiangyun (2017), Ruili (2017), Jinghong (2018), Yunlong (2019)
Total	8 families	21 genera	37 species			192/2,464 (7.79%)	

[a]: Species not found in the NCBI Taxonomy database for the common name. [b]: Species not found in the NCBI Taxonomy database for taxonomy ID. [c]: Positive sampling site and year.

sticks as bait, as described previously (Guo et al., 2019, 2023; Huang et al., 2023). Animals captured alive were anesthetized and humanely euthanized to minimize suffering (Han et al., 2024; Shomer et al., 2020; Tang et al., 2024). Blood and various tissue samples, including heart, liver, spleen, lung, kidney, and intestine, were collected from each animal. All samples were temporarily stored in liquid nitrogen, transported to the laboratory, and subsequently maintained at –80°C for storage until use.

Precise species identification was conducted through morphological observations by trained field biologists and confirmed by DNA sequencing of the mitochondrial cytochrome b (cyt *b*) gene, as described in previous studies (Guo et al., 2019, 2023; Huang et al., 2023; Wang et al., 2017c). The collected animal specimens were ultimately classified into four different orders, eight families, 21 genera, and 37 species, with most belonging to the family Muridae, including *R. tanezumi* (*n*=623), *R. norvegicus* (*n*=422), *A. chevrieri* (*n*=439), and other murine species (*n*=650) (Table 1).

Viral RNA extraction and *Orthohepevirus* detection

RNA extraction from ground animal liver samples was performed using a High Pure Viral RNA Kit (Roche Life Science, Switzerland). Orthohepevirus RNA was screened through hemi-nested reverse transcription polymerase chain reaction (RT-PCR), employing generic primers targeting conserved regions within the HEV RNA-dependent RNA polymerase (RdRp) region, as detailed in previous studies (Wang et al., 2017a, 2017c, 2018c). RT-PCR was conducted using the SuperScript™ III One-Step RT-PCR System with Platinum™ (Thermo Fisher Scientific, USA). The PCR products were analyzed on ethidium bromide-stained agarose gels, purified using a MinElute Gel Extraction Kit (Qiagen, Germany), and sequenced using the ABI 3100 Sequencer (USA) with both forward and reverse primers. If direct sequencing failed, the amplicons were cloned into the pGEM-T Easy Vector (Promega, USA) for subsequent sequencing.

Full-length genome sequencing of *Orthohepevirus* strains

Full-length genomes of all *Orthohepevirus*-positive specimens were amplified using next-generation sequencing (NGS). Consequently, 24 viral genomes were successfully obtained from eight out of 10 *Orthohepevirus*-positive animal species (excluding *Eothenomys olitor* and *Eothenomys melanogaster*). Failure to amplify the other *Orthohepevirus* genome was likely due to lower viral loads in the liver samples. Briefly, viral RNA of liver specimens from selected animals was re-extracted and amplified through high-throughput sequencing. The reads of the original samples were assembled without reference using MEGAHIT v.1.2.9 (Li et al., 2015). Assembled contigs classified as *Orthohepevirus* were searched using BLASTn (https://blast.ncbi.nlm.nih.gov) against the NCBI GenBank. Based on the resulting alignments, the approximate positions of the target contigs to the HEV reference Burma strain (GenBank accession no. M73218) were determined, and the consensus sequences of *Orthohepevirus* strains containing gaps were obtained. Viral genome-specific primers, based on the position of gaps, were designed to obtain full-length or nearly complete *Orthohepevirus* genomes (Supplementary Table S1). RT-PCR was performed using the SuperScript™ III One-Step RT-PCR System with Platinum™ (Thermo Fisher Scientific, USA). Genome ends were amplified using a SMARTer RACE 5′/3′ Kit (Takara Bio, Japan), following the manufacturer's instructions. Ultimately, full-length or nearly

complete genomic sequences of *Orthohepevirus* strains were assembled, and three typical HEV open reading frames (ORFs) and other putative ORFs were annotated using Geneious Prime v.2024.0.3 (Biomatters, New Zealand). The functional domains or motifs of *Orthohepevirus* strains identified in this study were inferred according to previous studies (Drexler et al., 2012; Koonin et al., 1992; Wang & Yang, 2022).

Sequence identity and recombination analyses

Geneious Prime v.2024.0.3 (Biomatters, New Zealand) was used for sequence analysis, splicing, and assembly. Following the ICTV recommendations on HEV classification, genetic size-based classification was performed using BLASTn. ORF Finder was used to predict the ORFs of the obtained *Orthohepevirus* genome sequences, and Motif Scan (http://myhits.isb-sib.ch) was used to identify homology to known protein domains. Complete genomic sequences of rodent and shrew orthohepeviruses were compared with the representative strains of the five genera *Paslahepevirus*, *Rocahepevirus*, *Avihepevirus*, *Chirohepevirus*, *Piscihepevirus* within the family *Hepeviridae*. Viral sequences were downloaded from the NCBI Nucleotide GenBank (https://www.ncbi.nlm.nih.gov/nucleotide/) for nucleotide and amino acid level identity comparison using BioEdit v.7.2 (Informer Technologies, USA) (Supplementary Table S2). To identify possible recombination, the full-length sequences of specific *Orthohepevirus* were scanned and analyzed using SimPlot v.3.5.1 with a sliding window size of 200 and a step size of 20 amino acids (Lole et al., 1999; Wang et al., 2018a, 2019).

Phylogenetic and evolutionary analyses

Phylogenetic analyses incorporated the rodent and shrew orthohepeviruses identified in this study alongside genomic sequences representing five genera within the *Hepeviridae* family. Multiple Alignment using the Fast Fourier Transform (MAFFT) algorithm in Geneious Prime v.2024.0.3 (Biomatters, New Zealand) was applied to align the complete genome sequences. Molecular Evolutionary Genetics Analysis (MEGA) v.11.0.13 for macOS was used to construct phylogenetic trees of the nucleotide sequences of complete genomes and amino acid sequences of the ORF1 and ORF2 regions. The trees were rooted using the divergent cutthroat trout *Piscihepevirus* Heenan88 strain (GenBank accession number HQ731075). Posterior probabilities were denoted at specific branches, with scale bars representing the number of substitutions per site. Viral designations included their classification and GenBank accession numbers. Trees were annotated and visualized using FigTree v.14.4.

To investigate the evolutionary and genetic relationships between orthohepeviruses and their animal hosts, phylogenetic trees were also constructed using MEGA v.11.0.13. The optimal substitution models were determined based on the Find Best-Fit Substitution Model. Phylogenetic trees were generated based on the amino acid sequences of concatenated ORF1 and ORF2 from representative *Hepeviridae* members, as well as on the amino acid sequences of the cyt *b* gene from corresponding host species. Mitochondrial sequences for each host were downloaded from the NCBI Nucleotide GenBank (https://www.ncbi.nlm.nih.gov/nucleotide/), and the cyt *b* gene was extracted using Geneious Prime v.2024.0.3 (Biomatters, New Zealand). Host taxonomic information was obtained from the NCBI Taxonomy GenBank (https://www.ncbi.nlm.nih.gov/taxonomy). The virus and host phylogenetic trees were rooted with *Piscihepevirus* and fish (*Oncorhynchus clarkii*), respectively.

Statistical analysis

All statistical analyses were performed using GraphPad Prism v.10.2.1 for macOS. Detection rates in wild small mammals were analyzed and compared using SAS v.9.4 (SAS Institute, USA). Maps were generated using Geographic Information System (GIS) tools, including ArcGIS v.10.2 (ESRI, USA) and Quantum Geographic Information System (QGIS) v.3.36 (https://qgis.org/) with free vector and raster map data obtained from Natural Earth (https://www.naturalearthdata.com/).

RESULTS

Sampling and *Orthohepevirus* screening

From April 2014 to September 2019, a comprehensive study was conducted in Yunnan Province, encompassing 10 prefectures and cities. During this period, 2 464 wild small mammals were collected, representing four orders, eight families, 21 genera, and 37 species (Table 1; Figure 1A). Among these, *Orthohepevirus* RNA was detected in five of the 19 species within the Muridae family (order Rodentia), all three species of the Cricetidae family (order Rodentia), and two of the seven species in the Soricidae family (order Eulipotyphla). In contrast, the remaining five families (Sciuridae, Talpidae, Erinaceidae, Ochotonidae, and Tupaiidae) and two orders (Lagomorpha and Scandentia) tested negative for *Orthohepevirus* (Figure 1B).

Overall, 192 samples tested positive for *Orthohepevirus*, yielding an overall detection rate of 7.79%. Furthermore, *Orthohepevirus* was identified in 10 of the 37 captured species, including *Apodemus chevrieri* (Chevrier's field mouse), *Bandicota bengalensis* (lesser bandicoot rat), *Rattus norvegicus* (Norway rat), *Rattus rattus* (black rat), *Rattus tanezumi* (Oriental house rat), *Eothenomys eleusis* (Kachin red-backed vole), *Eothenomys melanogaster* (Pere David's vole), *Eothenomys olitor* (Chaotung vole), *Episoriculus caudatus* (Hodgson's brown-toothed shrew), and *Suncus murinus* (Asian house shrew) (Table 1; Figure 1C).

Detection rates varied significantly across species. Within the Muridae family (order Rodentia), the detection rates for *A. chevrieri*, *B. bengalensis*, *R. norvegicus*, *R. rattus*, and *R. tanezumi* were 14.81% (65/439), 100% (13/13), 12.80% (54/422), 3.85% (3/78), and 7.87% (49/623), respectively. Within the Cricetidae family (order Rodentia), the detection rates for *E. eleusis*, *E. melanogaster*, and *E. olitor* were 100% (1/1), 6.56% (4/61), and 2.63% (1/38), respectively. Within the Soricidae family (order Eulipotyphla), the detection rates for *E. caudatus* and *S. murinus* were 100% (1/1) and 2.86% (1/35), respectively (Figure 1C). These findings underscore the extensive distribution of *Orthohepevirus* among wild small mammals, particularly rodents and shrews, in Yunnan Province. The observed patterns highlight the need for a deeper understanding of *Orthohepevirus* infection dynamics and their potential public health implications.

Epidemiological and geographical characteristics of *Orthohepevirus* detection

In Yunnan Province, the Muridae family (order Rodentia) constituted the majority of collected specimens, with the most prevalent species being *R. tanezumi* (623, 25.28%), *A.*

chevrieri (439, 17.82%), and *R. norvegicus* (422, 17.13%) (Figure 2A). Among *Orthohepevirus*-positive species, *A. chevrieri* (65, 33.85%), *R. norvegicus* (54, 28.13%), and *R. tanezumi* (49, 25.52%) accounted for the highest proportions (Figure 2B), suggesting a key role for these rodents in the transmission cycle of *Orthohepevirus* within the region.

Geographically, the distribution of *Orthohepevirus* infections exhibited distinct patterns across the ten prefectures and cities. Lijiang City recorded the highest detection rate at 32.41% (59/182), followed by Dehong Prefecture at 14.33% (42/293), Honghe Prefecture at 10.68% (55/515), Yuxi City at 9.68% (6/62), and Xishuangbanna Prefecture at 4.88% (18/369). Conversely, lower detection rates were observed in Kunming City, Zhaotong City, Diqing Prefecture, and Dali Prefecture, ranging from 0.67% to 1.84%, with no detections reported in Chuxiong Prefecture (Figure 2C; Supplementary Table S3). Species-specific analysis at the regional level revealed further insights. In Dehong Prefecture, *R. tanezumi* (25/42) and *B. bengalensis* (13/42) were the dominant *Orthohepevirus*-positive species, while *R. norvegicus* (51/55) was the primary positive species in Honghe Prefecture (Figure 2D; Supplementary Table S4).

Statistical analysis revealed significant variations in detection rates across different regions (χ^2=207.8364, P<0.0001) and species (Z=122.8027, P<0.0001). Collectively, these results underscore the spatial disparity and heterogeneity in the distribution of *Orthohepevirus* infections, as well as the prevalence of dominant *Orthohepevirus*-positive animal species across diverse regions in Yunnan.

Genomic characterization of newly discovered *Orthohepevirus* strains

Since the initial identification of rat HEV-C strain R63 (GenBank accession no. GU345042) in Germany in 2010 as the prototype isolate of *Orthohepevirus C* (now reclassified as *Rocahepevirus*) (Smith et al., 2014), 88 full-length or nearly complete HEV-C genomic sequences have been detected and deposited in the NCBI GenBank database (as of 4 March 2024) (Supplementary Table S2) (Wang et al., 2020). To elucidate the genetic characteristics of the *Orthohepevirus* strains detected, high-throughput sequencing was conducted, yielding 24 full-length or nearly complete genomic sequences from selected small mammal species (Supplementary Table S5). This effort expanded the total number of complete HEV-C genomic sequences to 112, distributed across four animal orders, six families, and 27 species. The majority of these viruses were detected in *R. norvegicus* (28), *R. rattus* (10), and *Mustela putorius* (11) (Figure 3A). However, the classification of *Orthohepevirus* detected in Eulipotyphla as HEV-C remains unresolved. One HEV-C sequence was identified in a common kestrel (order Falconiformes, species *Falco tinnunculus*), likely representing a spillover event from HEV-C carried by common voles (*Microtus arvalis*) (Reuter et al., 2016; Wang et al., 2020). Seven HEV-C strains were isolated from humans, indicating zoonotic potential. Significantly, this study is the first to report *Orthohepevirus* variants in the lesser bandicoot rat (family Muridae, species *B. bengalensis*), Kachin red-backed vole (family Cricetidae, species *E. eleusis*), and Hodgson's brown-toothed shrew (family Soricidae, species *E. caudatus*).

Of the 24 *Orthohepevirus* strains analyzed, 17 yielded full-length genomic sequences, distributed across seven rodent species in eight different regions, including *A. chevrieri* in Deqin County (AcDQ34) and Yongshan County (AcYS245), *R. tanezumi* in Jinghong City (RtJH59 and RtJH124) and Menghai County (RtMH71 and RtMH77), *R. norvegicus* in Luxi County (RnLX 20, RnLX 33, RnLX36, and RnLX91), Yuanjiang County (RnYJ25), and Yiliang County (RnYL10), *R. rattus* in Lianghe County (RnLH15 and RrLH258), *B. bengalensis* in Ruili City (BbRL274), *S. murinus* in Lianghe County (SmLH25), and *E. caudatus* in Yongshan County (EcYS16). Genome lengths varied, with the longest sequence (7 092 nt) identified in strain EcYS16 and the shortest (6 881 nt) in strain RrLH15. Seven nearly complete HEV-C sequences were also identified in four rodent species, including *R. norvegicus* in Xiangyun County (RnXY58) and Luxi County (RnLX92), *R. tanezumi* in Ruili County (RtRL51), *B. bengalensis* in Ruili City (RL26, RL60, and RL323), and *E. eleusis* in Luxi County (EeLX101). The genome lengths of these HEV-C strains ranged from 6 628 nt (RtRL51) to 6 977 nt (RnLX92) (Figure 3B; Supplementary Table S5).

Analysis revealed considerable variation in the 5' untranslated region (UTR) among the strains. All seven nearly complete viral genomes lacked a 5' UTR, likely due to challenges with NGS reads and contig assembly. In contrast, the 3' UTR was successfully amplified in almost all strains, except for RtRL51 (Figure 3B). Interestingly, an additional ORF (ORF4), typically present in HEV-C1 and HEV-C2 strains (Reuter et al., 2020; Wang et al., 2020), was observed in all sequences except EcYS16 (Figure 3B). Our previous study also demonstrated the absence of ORF4 in *E. melanogaster* and *E. Inez* (order Rodentia, family Cricetidae) (Wang et al., 2018c). Thus, whether ORF4 is evolutionarily conserved across HEV-C strains is still obscure. Furthermore, current knowledge regarding the functional mechanisms of ORF4 in HEV-C remains unclear, although recent evidence suggests it is not necessary for the active replication of rat HEV (Tanggis et al., 2018).

Genetic diversity of *Orthohepevirus* variants identified in rodents

To assess the genetic diversity of the *Orthohepevirus* variants identified in Yunnan, comparative sequence analyses were performed on the 24 *Orthohepevirus* genomes alongside representative members of the family *Hepeviridae* (Figures 4, 5). Compared to the HEV-1 reference Burma strain (GenBank accession no. M73218) from *Paslahepevirus balayani*, all 24 *Orthohepevirus* strains exhibited approximately 50% identity at both the nucleotide and amino acid levels, highlighting their significant genetic divergence from human HEV (Figure 4A). As most *Orthohepevirus* genomes (22 out of 24) in our study were detected in rodents (Figure 3A), they were further compared with the HEV-C1 reference R63 strain (GenBank accession no. GU345042) from *R. ratti*. With the exception of the AcDQ34, AcYS245, EeLX101, and EcYS16 strains, the remaining 20 *Orthohepevirus* strains demonstrated relatively high sequence identities with R63, exceeding 75% at the nucleotide level and 88% at the amino acid level. This included the SmLH25 strain from the Asian house shrew (*S. murinus*) (Figure 4B), reaffirming that Asian house shrews act as reservoirs for rat HEV-C1 (Guan et al., 2013; He et al., 2018; Wang et al., 2017a). Genetic divergence among the 20 HEV-C1 genomes was also assessed. Nucleotide sequence identities ranged from 76.1% to 99.7%, while amino acid sequences ranged from 98.2% to 99.9%. Notably, four HEV-C1 strains identified in the lesser bandicoot rat (*B.*

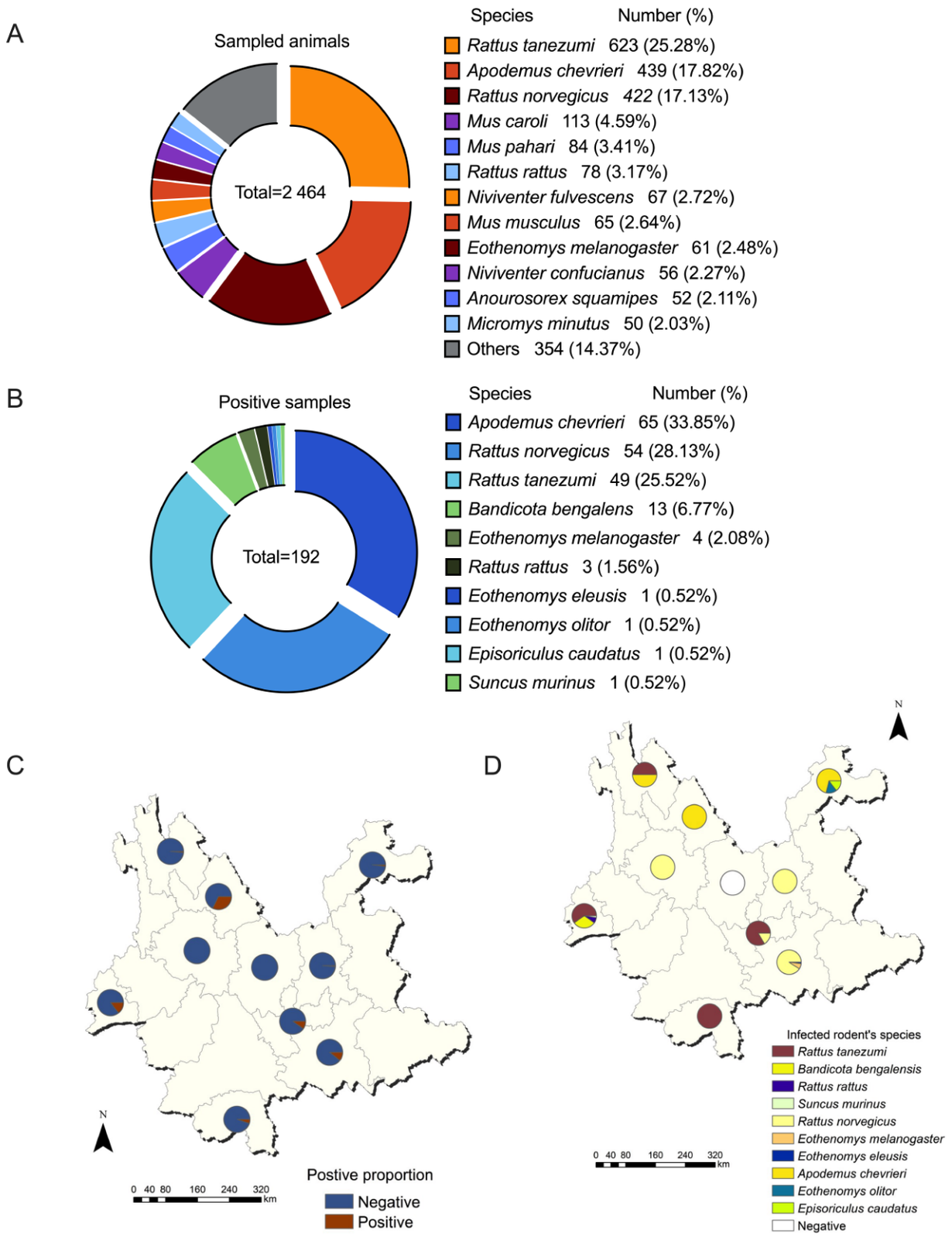


Figure 2 Compositions of sampled animals and *Orthohepevirus*-positive samples and spatial distribution of *Orthohepevirus*-infected animals at each surveillance site

A: Distribution of major sampled animal species and their respective sample counts. Percentage indicates proportion of samples obtained from each animal species relative to the total specimens collected. B: Distribution of *Orthohepevirus*-positive animal species and corresponding number of *Orthohepevirus*-positive samples within each host species. Percentage denotes proportion of *Orthohepevirus*-positive samples in each animal species relative to total *Orthohepevirus*-positive samples. C: Representation of spatial distribution of captured animals at each surveillance site, with blue (negative) and red (positive) denoting *Orthohepevirus* infection status. D: Distribution of host species of *Orthohepevirus*-infected rodents at each surveillance site, categorized and visualized with distinct colors.

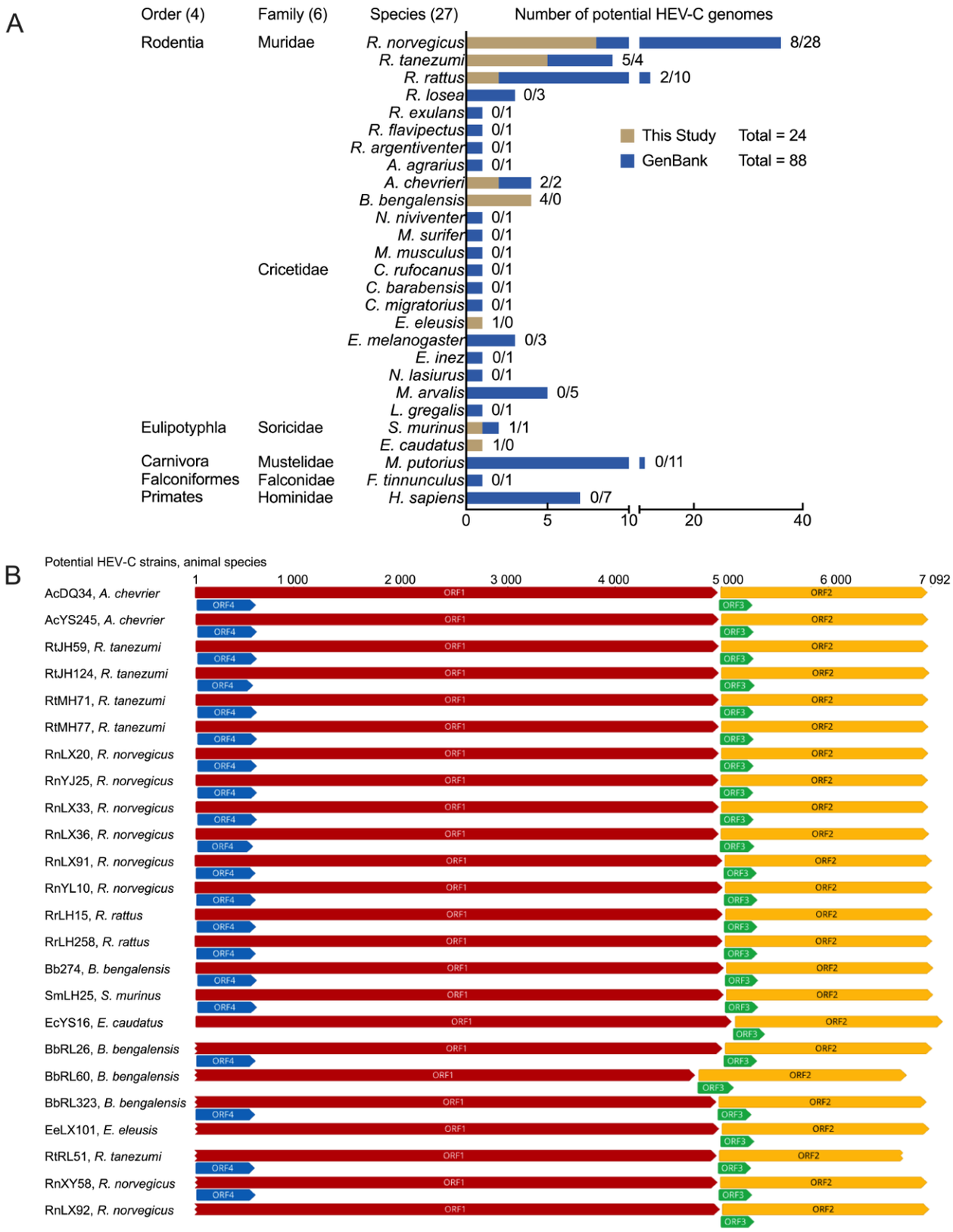


Figure 3 Genomic characterization of *Orthohepevirus* strains

A: Comparative analysis of numbers of potential *Rocahepevirus* (HEV-C) genomes identified in this study and those available in the NCBI GenBank database. Left side depicts animal species, family, and order, along with their respective counts. B: Schematic representation of full-length genomic organization of 24 potential HEV-C strains. Designations of viruses and their corresponding host species are provided on the left. Different colors represent three typical HEV ORFs: red, yellow, and green, respectively. Putative HEV-C ORF-4 is depicted in blue. Genome scale is indicated in bases at the top.

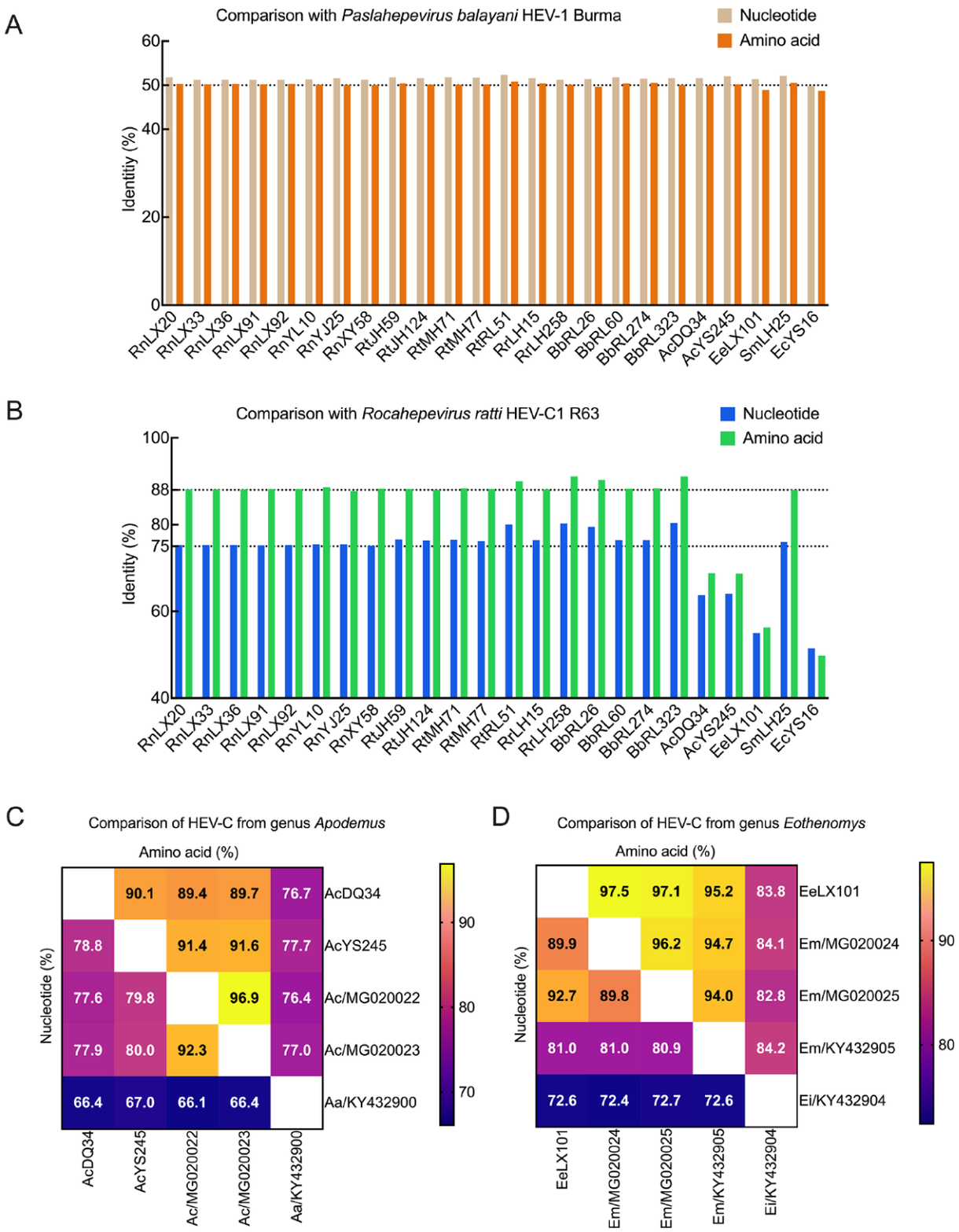


Figure 4 Comparison of *Orthohepevirus* strains with known representative members within the family *Hepeviridae*

A: Comparison of nucleotide (complete genome) and amino acid (concatenated ORF1 and ORF2) sequence identity percentages between 24 *Orthohepevirus* strains and HEV-1 reference Burma strain (GenBank accession no. M73218) from *Paslahepevirus balayani*. Identity of 50% is indicated by a dashed line. B: Comparison of nucleotide and amino acid sequence identity percentages between 24 *Orthohepevirus* strains and HEV-C1 reference R63 strain (GenBank accession no. GU345042) from *Rocahepevirus ratti*. Identities of 75% and 88% are indicated by dashed lines. C: Comparison of nucleotide and amino acid sequence identity percentages between two HEV-C strains (AcDQ34 and AcYS245) identified here and three HEV-C strains (GenBank accession no. MG020022, MG020023, and KY432800) from rodents (genus *Apodemus*). Colored heatmap was automatically generated based on the range of values in GraphPad Prism v.10. D: Comparison of nucleotide and amino acid sequence identity percentages between one HEV-C strain (EeLX101) identified here and four HEV-C strains (GenBank accession no. MG020024, MG020025, KY432904, and KY432905) from rodents (genus *Eothenomys*).

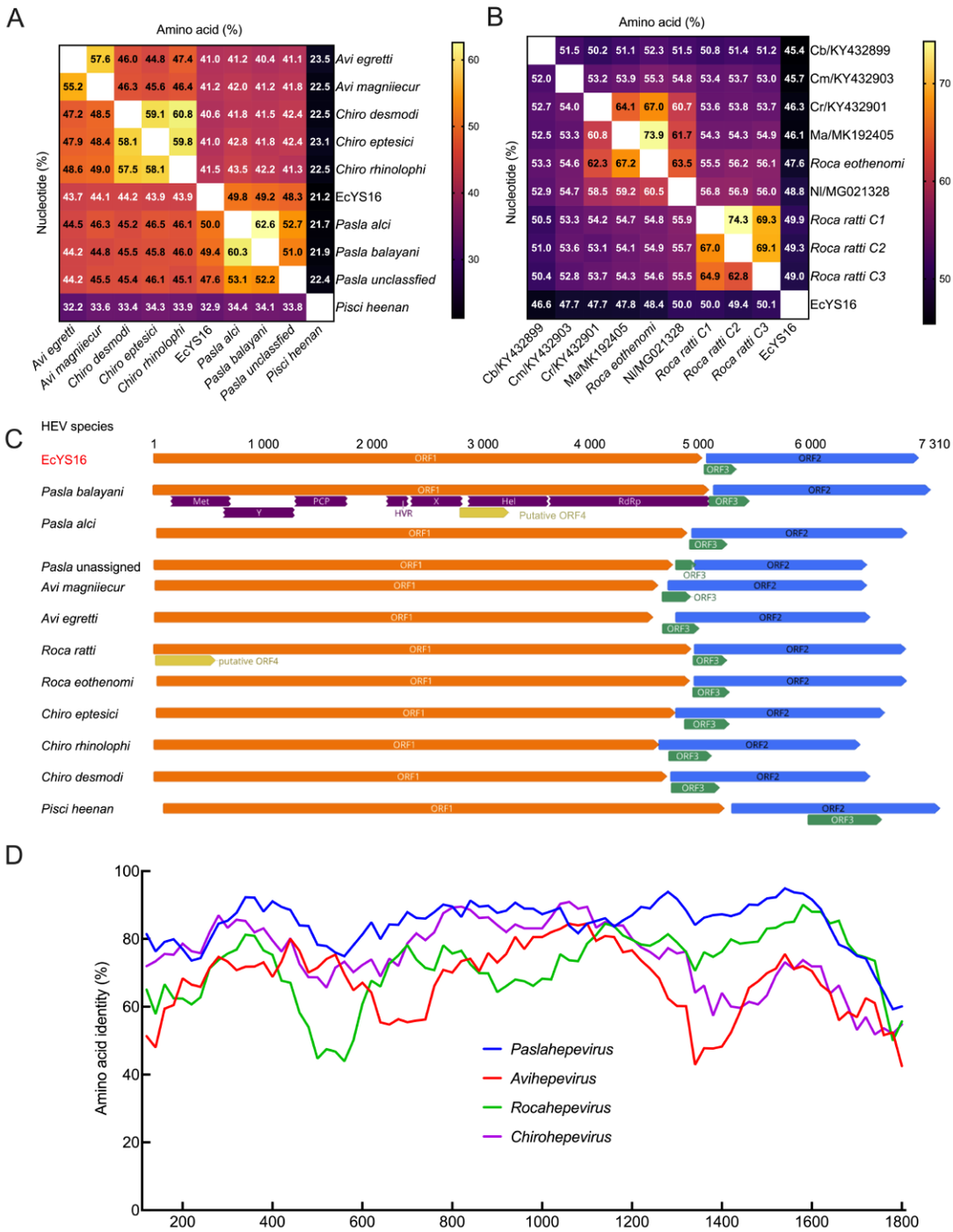


Figure 5 Comparative genomic analyses of the EcYS16 strain

A: Comparison of nucleotide (complete genome) and amino acid (concatenated ORF1 and ORF2) sequence identity percentages between EcYS16, identified in this study, and nine assigned or unassigned *Orthohepevirus* species within the family *Hepeviridae*. GenBank accession numbers of *Orthohepevirus* strains for each species used for sequence analyses: KX589065 (*Avihepevirus egretti*), AY535004 (*Avihepevirus magniiecur*), MW249011 (*Chirohepevirus desmoidi*), JQ001749 (*Chirohepevirus eptesici*), KJ562187 (*Chirohepevirus rhinolophi*), KF951328 (*Paslahepevirus alci*), M73218 (*Paslahepevirus balayani*), KR905549 (tree shrew HEV), HQ731075 (*Piscihepevirus heenan*). Color heatmap was automatically generated based on the range of values in GraphPad Prism v.10. B: Comparison of nucleotide and amino acid sequence identity percentages between EcYS16 and nine representative *Rocahepevirus* strains from various animal species. GenBank accession numbers of *Rocahepevirus* strains species and genotypes used for sequence analyses: GU345042 (*Rocahepevirus ratti* genotype C1), JN998606 (*Rocahepevirus ratti* genotype C2), (*Rocahepevirus ratti* genotype C3), MG020022 (*Rocahepevirus eothenomi*). C: Schematic representation of full-length genomic organization of EcYS16 and representative members within the family *Hepeviridae*. Virus species are shown on the left. Different colors represent three typical HEV ORFs and motifs of ORF1. Putative HEV-C ORF-4 is depicted in yellow. Genome scale is indicated in bases at the top. D: Amino acid identity plot of concatenated ORF1 and ORF2 of EcYS16 and selective *Orthohepevirus* strains. Identity plot was created in SimPlot v.3.5.1 with a window size of 200 and a step size of 20 amino acids.

bengalensis) were reported for the first time in this study, with sequence identities ranging from 77.5% to 98.8% at the nucleotide level and from 88.5% to 99.9% at the amino acid level. Overall, these findings underscore the significant genetic diversity of HEV-C1 carried by this species.

We previously identified two *Orthohepevirus* strains (GenBank accession no. MG020022 and MG020023) from the Chevrier's field mouse (*A. chevrieri*, family Muridae) in Yunnan (Wang et al., 2018c), classified as HEV-C3 in *R. ratti* (Wang & Yang, 2022). Subsequently, an *Orthohepevirus* strain was detected in a closely related species, the striped field mouse (*A. argrarius*, family Muridae) (Wu et al., 2018). These HEV-C strains clustered within the *Rocahepevirus* clade (Wang et al., 2020). To further investigate, sequence comparisons were performed between the two newly identified HEV-C strains, AcDQ34 and AcYS245, and known HEV-C strains from the genus *Apodemus*. Results showed that the four *A. chevrieri* HEV-C strains exhibited sequence identities ranging from 77.6% to 92.3% at the nucleotide level and from 89.4% to 96.9% at the amino acid level. In contrast, the single HEV-C strain from *A. argrarius* showed comparatively greater divergence, with identities below 67% at the nucleotide level and below 77.7% at the amino acid level (Figure 4C). Additionally, two *Orthohepevirus* strains (GenBank accession no. MG020024 and MG020025) identified in Pere David's vole (*E. melanogaster*, family Cricetidae) and two *Orthohepevirus* strains (GenBank accession no. KY432904 and KY432905) identified in Pere David's vole and Kolan vole (*E. inez*, family Cricetidae) were classified as the species *R. eothenomi*. Similarly, the four HEV-C strains from *Eothenomys* were compared with the novel EeLX101 strain identified in Kachin red-backed vole (*E. eleusis*, family Cricetidae). Analysis revealed that EeLX101 showed higher sequence identities to *E. melanogaster* HEV-C strains (ranging from 80.9% to 92.7% at the nucleotide level and from 94.0% to 97.5% at the amino acid level) compared to the *E. inez* HEV-C strain (72.6% at the nucleotide level and 83.8% at the amino acid level) (Figure 4D). These results suggest that sequence divergence of HEV-C in rodents is likely correlated with host species demarcation.

Comparative sequence analyses of novel *Orthohepevirus* variants identified in Eulipotyphla

In addition to *Orthohepevirus* variants in rodents, EcYS16 was detected in Hodgson's brown-toothed shrews (*E. caudatus*, family Soricidae), a member of the mammal order Eulipotyphla. While Asian house shrews (*S. murinus*, family Soricidae) have been established as reservoirs of rat HEV-C1 (Guan et al., 2013; He et al., 2018; Wang et al., 2017a), the discovery of a phylogenetically distinct 254-nt orthohepevirus genomic fragment in Oliver's shrew (Crocidura olivieri, family Soricidae) in Kenya highlights the genetic diversity of orthohepeviruses within the family Soricidae (Onyuok et al., 2019). Notably, our sequence analysis revealed substantial divergence between EcYS16 and rat HEV-C1, with nucleotide and amino acid sequence identities of only 51.5% and 49.8%, respectively (Figure 4B). To clarify the taxonomic placement of EcYS16, comprehensive comparative analyses were conducted with nine assigned and unassigned *Orthohepevirus* species within the family *Hepeviridae* (Wang & Yang, 2022) (Figure 5A). Considering the evolutionary proximity between the mammalian orders Eulipotyphla and Rodentia, and the genetic complexity of *Orthohepevirus* variants found in these two groups, EcYS16 was also independently compared with nine representative *Rocahepevirus* variants (Figure 5B) (Wang et al., 2020).

Comparisons of EcYS16 with nine *Orthohepevirus* species revealed low sequence homologies, with identities of less than 50.0% at the nucleotide level and 49.8% at the amino acid level across orthohepeviruses (subfamily *Orthohepevirinae*) from both mammals and birds. Homology was even lower with *Piscihepevirus* (subfamily *Parahepevirinae*) from fish, at 32.9% (nucleotide) and 21.2% (amino acid) (Figure 5A) (Purdy et al., 2022). Similarly, comparisons with nine representative *Rocahepevirus* variants from various small mammal species revealed significant divergence, with sequence identities less than 50.1% at both the nucleotide and amino acid levels (Figure 5B), comparable to discrepancies observed between distinct *Orthohepevirus* genera (Wang & Yang, 2022). Interestingly, the EcYS16 genome was longer than that of other mammalian orthohepeviruses, except for human HEV (Figure 5C). Recombination analysis indicated that EcYS16 had the highest amino acid sequence identity with *Paslahepevirus* variants across most of the viral genome. While recombination events involving *Avihepevirus*, *Chirohepevirus*, and *Rocahepevirus* could potentially explain the occurrence of EcYS16, the relatively low genomic sequence identity (~50%) necessitates cautious interpretation. Of note, no instances of intrageneric or intraspecific recombination of *Orthohepevirus* were documented (Figure 5D). Overall, our comparative analyses strongly suggest that EcYS16, discovered in *E. caudatus*, is genetically divergent from known orthohepeviruses. Whether this novel *Orthohepevirus* represents a new species or even a new genus requires further formal classification based on ICTV *Hepeviridae* guidelines (Purdy et al., 2022).

Phylogenetic relationships of rodent and shrew orthohepeviruses

To elucidate the phylogenetic connections among the newly identified rodent and shrew orthohepeviruses found in Yunnan, a phylogenetic tree was constructed using nucleotide sequences of full-length genomes. Analysis included representative members from the five genera within the family *Hepeviridae* (Figure 6A). Among the 24 *Orthohepevirus* strains identified in this study, 23 clustered within the *Rocahepevirus* clade. Specifically, 20 strains from *R. norvegicus* (9), *R. tanezumi* (5), *R. rattus* (1), and *S. murinus* (1) were grouped with the *R. ratti* genotype HEV-C1, indicating a strong phylogenetic link between these animal species and rat HEV-C1. These 16 HEV-C1 strains formed at least three distinct clades, reflecting substantial genetic diversity.

Two *Orthohepevirus* strains, AcYS245 and AcDQ34, from *A. chevrieri* clustered with the *R. ratti* genotype HEV-C3, which includes orthohepeviruses previously identified in *A. chevrieri* and *A. argrarius.* Additionally, the *Orthohepevirus* strain EeLX101 from *E. eleusis* clustered with the *R. eothenomi* clade, alongside orthohepeviruses from *E. melanogaster* and *E. inez* (Figure 6A). To date, all known HEV-C3 and *R. eothenomi Orthohepevirus* variants have been discovered in Yunnan (Wang et al., 2018c; Wu et al., 2018); however, orthohepeviruses from individual animal species also exhibited considerable genetic heterogeneity, reflecting long-term evolutionary relationships between the viruses and their hosts (Rasche et al., 2019).

The *Orthohepevirus* strain EcYS16 from *E. caudatus*

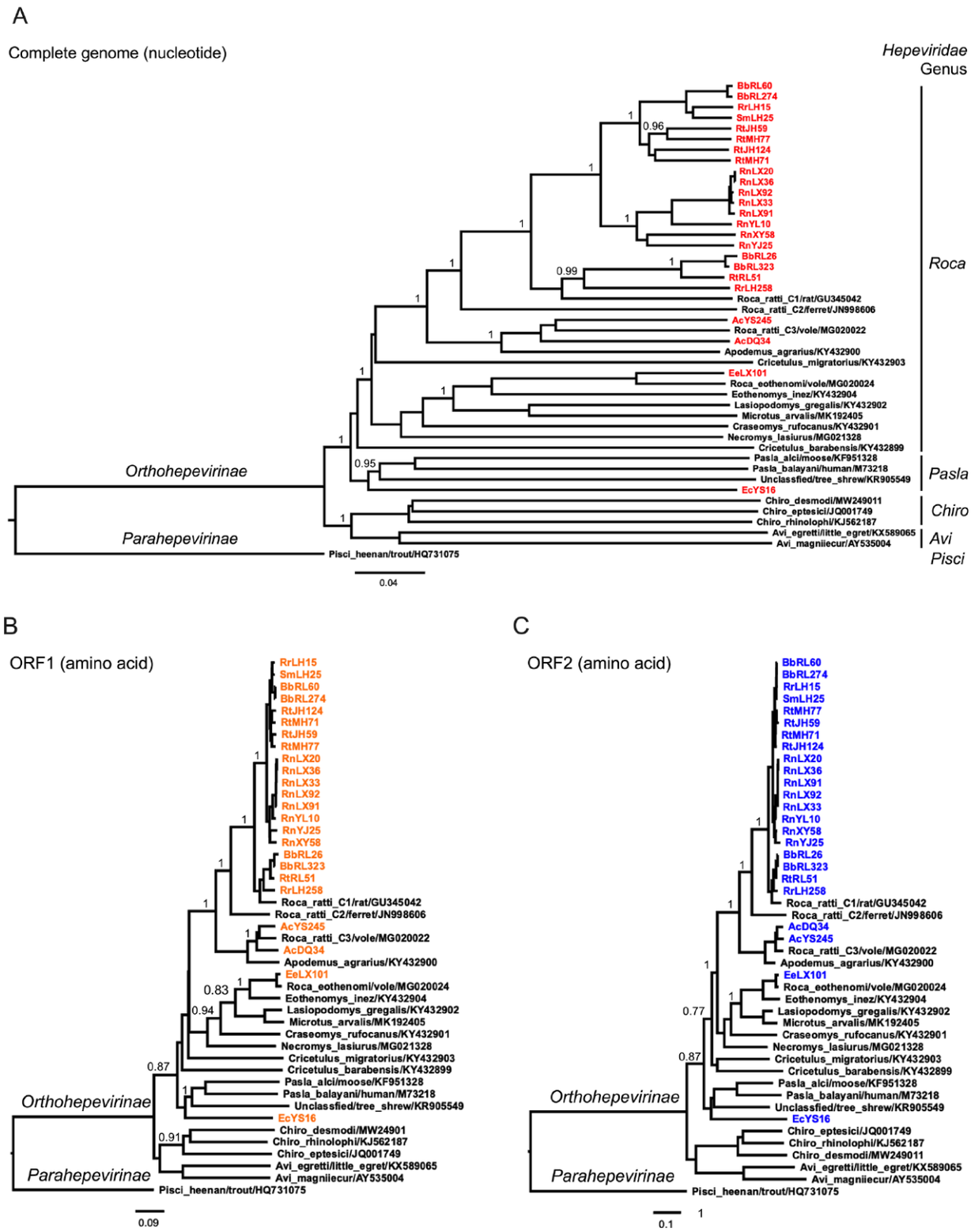


Figure 6 Phylogenetic relationships of novel orthohepeviruses

A: Neighbor-joining tree constructed using *P*-distance model with pairwise deletion, based on nucleotide sequences of complete genomes of 24 orthohepeviruses and 23 representative members within the family *Hepeviridae*. Viruses newly identified in this study are highlighted in red. Evolutionary analyses were performed in MEGA v.11 with 1 000 bootstrap reiterations. Tree was rooted using divergent *Piscihepevirus*. Posterior probabilities are denoted at specific branches. Scale bars represent number of substitutions per site. Virus designations include viral classification and GenBank accession number. The tree was annotated and visualized using FigTree v.14.4. Specific genus of the family *Hepeviridae* is shown on the right. B: Neighbor-joining tree using Poisson model with pairwise deletion, based on amino acid sequences of ORF1 of 24 novel orthohepeviruses and 23 representative members within the family *Hepeviridae*. Viruses newly identified in this study are highlighted in orange. C: Neighbor-joining tree using Poisson model with pairwise deletion, based on amino acid sequences of ORF2 of 24 novel orthohepeviruses and 23 representative members within the family *Hepeviridae*. Viruses newly identified in this study are highlighted in blue.

exhibited a complex and distinct phylogenetic placement. Although it is clustered with the *Paslahepevirus* clade, it occupied an external branch with considerable phylogenetic distance. The genus *Paslahepevirus* currently includes *Paslahepevirus balayani* (infecting humans, pigs, deer, wild boar, rabbits, and camels), *Paslahepevirus alci* (in moose), and tree shrew *Orthohepevirus* (Wang & Yang, 2022). The significant genetic divergence of EcYS16 raises the possibility that this shrew *Orthohepevirus* discovered could represent a new *Paslahepevirus* species, although formal classification remains to be determined.

Further phylogenetic analyses based on amino acid sequences of ORF1 and ORF2 (Figure 6B, C) corroborated the topological positions of the 24 *Orthohepevirus* strains in the phylogenetic tree of the complete genome (Figure 6A). However, the placements of *Orthohepevirus* strains from the striped dwarf hamster (*Cricetulus barabensis*) and grey dwarf hamster (*Cricetulus migratorius*) showed ambiguous topology, despite consistently clustering within the *Rocahepevirus* clade (Figure 6B, C).

Overall, the phylogenetic analyses demonstrated that 23 of the 24 *Orthohepevirus* strains identified in this study were classified within the genus *Rocahepevirus*, including the virus detected in *S. murinus*. However, the taxonomic assignment of the *Orthohepevirus* detected in *E. caudatus* remains unresolved, warranting further investigation.

Evolutionary analyses of orthohepeviruses and their hosts

To explore the evolutionary trajectories of orthohepeviruses, particularly the EcYS16 strain detected in Hodgson's brown-toothed shrew, we conducted a comparative examination of the phylogenetic relationships between orthohepeviruses and their host cyt *b* gene (Figure 7). Representative *Orthohepevirus* strains originating from mammals and birds within the subfamily *Orthohepevirinae* were included, with *Piscihepevirus* (subfamily *Parahepevirinae*) from fish serving as an outgroup. A phylogenetic tree based on concatenated ORF1 and ORF2 sequences revealed four distinct clades within *Orthohepevirinae*, each corresponding to a virus genus, consistent with the ICTV *Hepeviridae* guidelines (Figure 7A) (Purdy et al., 2022). Notably, the genus *Rocahepevirus* exhibited considerable genetic diversity, with strains identified in species such as the hairy-tailed bolo mouse (*Necromys lasiurus*), grey red-backed vole (*Craseomys rufocanus*), narrow-headed vole (*Lasiopodomys gregalis*), common vole (*Microtus arvalis*), Armenian hamster (*C. migratorius*), and striped dwarf hamster (*C. barabensis*). These highly divergent HEV-C strains may represent new species or genotypes due to their genetic divergence, warranting further investigation. While *Paslahepevirus* and *Rocahepevirus* include viruses infecting multiple animal orders, *Chirohepevirus* and *Avihepevirus* remain confined to their respective host orders. Consistent with the phylogenetic analyses based on complete genomes and individual ORF1 and ORF2 sequences (Figure 6), EcYS16 from *E. caudatus* clustered alongside the genus *Paslahepevirus*, albeit with a substantial phylogenetic distance from its common ancestor (Figure 7A).

In the phylogenetic tree of host cyt *b* sequences, the topology closely mirrored virus classification (Figure 7B). For instance, HEV-C strains from rodent families Muridae and Cricetidae were segregated according to the evolutionary lineages of their hosts. Similarly, *Chirohepevirus* and *Avihepevirus* aligned with their respective host orders, Chiroptera and Galliformes. This strong correlation suggests a long history of co-speciation between orthohepeviruses and their hosts.

However, cross-species transmission of orthohepeviruses has been observed in several instances, highlighting the ability of these viruses to infect multiple host species. House shrews (*Suncus murinus*, order Eulipotyphla) act as reservoirs for rat HEV-C1, while ferret HEV-C2 strains (from *Mustela putorius*, order Carnivora) phylogenetically cluster with rodent HEV-C strains, indicating that rodent HEV-C has spilled over to these species (Figure 7B). Swine (*Sus scrofa*) are natural reservoirs for HEV-3 and HEV-4, which can infect a range of hosts, including deer, humans, and other species (Wang et al., 2017b; Wang & Yang, 2022). A divergent HEV strain identified in moose (*Alces alces*), closely related to red deer (*Cervus elaphus*) in host taxonomy, further supports the cross-species transmission of swine HEV-3 to deer (Lin et al., 2014). In addition, genetically diverse swine HEV strains detected in wild boars have been classified as HEV-5 and HEV-6, reflecting the long-term evolution of swine HEV within its natural hosts (Figure 7B). These findings suggest that humans, or their primate precursors, may have acquired HEV-3 and HEV-4 from swine during the rise of intensive livestock farming (Sander et al., 2018). Conversely, HEV-1 and HEV-2, which exclusively infect humans and some primates, likely originated through virus-host co-speciation in human ancestors, considering their markedly different host range, geographical distribution, and infection patterns (Akanbi et al., 2019; Brayne et al., 2017; Wang et al., 2018b). The evolutionary history of HEV-3r in rabbits (*Oryctolagus cuniculus*, order Lagomorpha) remains enigmatic (Mahsoub et al., 2023; Wang et al., 2023), leaving open the possibility of more distant orthohepeviruses within this animal order. The discovery of the divergent EcYS16 strain in this study strongly suggests that Eulipotyphla and possibly Carnivora may also harbor distinct orthohepeviruses associated with their specific host taxa. Indeed, short sequence fragments of orthohepeviruses have been detected in red foxes (*Vulpes vulpes*), which are highly divergent from rodent HEV-C (Bodewes et al., 2013).

In conclusion, our evolutionary analyses of orthohepeviruses and their hosts demonstrated that both co-speciation and cross-species transmission have significantly influenced the diversity and evolution of the family *Hepeviridae*, particularly within the genera *Paslahepevirus* and *Rocahepevirus*.

DISCUSSION

This study provided a comprehensive analysis of the genomic diversity and phylogenetic relationships of rodent and shrew orthohepeviruses identified in Yunnan, China. Our findings revealed previously uncharacterized viral strains in specific small mammal species, which demonstrated significant phylogenetic divergence from known orthohepeviruses. These results not only expand the recognized host range within the family *Hepeviridae* but also offer valuable insights into the evolutionary dynamics of HEV within diverse hosts.

Yunnan is renowned for its exceptional biodiversity, supported by unique geographical, ecological, and environmental conditions that sustain diverse and thriving small mammal populations. However, the association between regions with high biodiversity and the emergence of infectious

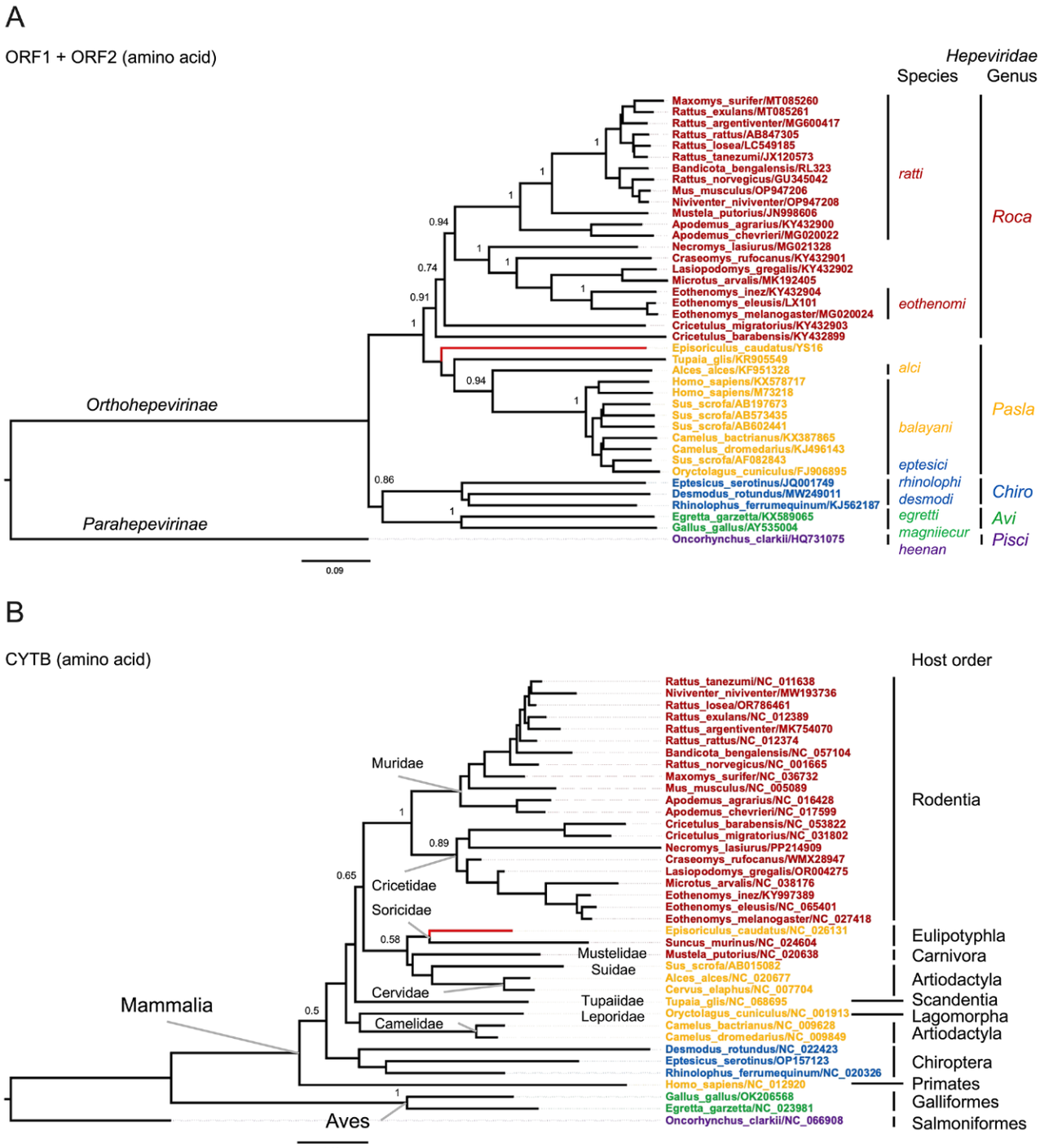


Figure 7 Evolutionary analyses of orthohepeviruses and their host

A: Maximum-likelihood tree generated based on amino acid sequences of concatenated ORF1 and ORF2 of 40 representative members of the family *Hepeviridae*, discovered in various animal species. Evolutionary analyses were conducted in MEGA v.11 with 1 000 bootstrap reiterations. The Le Gascuel (LG) amino acid substitution model with gamma distribution (G) and different frequencies (F) (LG+G+F) was selected based on the Find Best-Fit Substitution Model. Tree was rooted with the divergent *Piscihepevirus*. Posterior probabilities are denoted at specific branches. Scale bars represent number of substitutions per site. Viruses from distinct species are colored in dark red, orange, blue, green, and purple. *Orthohepevirus* clade from *Episoriculus caudatus* is in red. Virus designations include host species and GenBank accession number of each virus. Tree was annotated and visualized in FigTree v.14.4. B: Maximum-likelihood tree generated based on amino acid sequences of cyt *b* gene of corresponding host species. Evolutionary analyses were conducted in MEGA v.11 with 1 000 bootstrap reiterations. General Reversible Mitochondrial (mtREV) amino acid substitution model with gamma distribution (G) (mtREV + G) was selected based on the Find Best-Fit Substitution Model. Tree was rooted with fish (*Oncorhynchus clarkii*). Host cyt *b* from distinct species are colored relative to virus classification. Clade of cyt *b* from *Episoriculus caudatus* is in red. Host cyt *b* designations include species name and GenBank accession number of cyt *b* gene of each host. Order of host is shown on the right. Specific taxonomy (class and family) of host is indicated on the phylogenetic tree.

diseases linked to zoonotic pathogens originating from wildlife also establishes Yunnan as a prominent "hotspot" for emerging infectious diseases (Olival et al., 2017). For instance, the Chinese horseshow bat (*Rhinolophus sinicus*), native to Yunnan, has been implicated as a likely reservoir for severe acute respiratory coronavirus 1 (SARS-CoV-1) (Hu et al., 2017). This illustrates the importance of conducting on-the-ground viral surveillance in biodiverse regions identified as emerging disease hotspots to identify novel zoonotic pathogens before they pose significant public health threats.

Comprehensive classification of viruses typically necessitates full-length genome sequencing, with phylogenetic analyses based solely on partial viral fragments potentially leading to a misrepresentation of evolutionary lineages (Smith et al., 2014). To address this, we amplified 24 complete *Orthohepevirus* genomes from eight distinct animal species. Notably, this study represents the first identification of the Kachin red-backed vole (*E. eleusis*) and Hodgson's brown-toothed shrew (*E. caudatus*) as hosts of orthohepeviruses. Among the newly identified *Orthohepevirus*, most (20 out of 24) were classified within the *R. ratti* genotype C1, a lineage with a well-documented zoonotic potential in various regions, including Hong Kong, Canada, Spain, and France (Andonov et al., 2019; Rivero-Juarez et al., 2022; Rodriguez et al., 2023; Sridhar et al., 2018). Experimental studies have also confirmed the ability of rat HEV-C1 to infect non-human primates such as rhesus and cynomolgus monkeys, further highlighting its zoonotic capacity (Yang et al., 2022). Swine have also been proposed as a significant vector for rat HEV transmission to humans (Rios-Muñoz et al., 2024; Yadav et al., 2024b). Interestingly, a recent experimental study showed that rat HEV inoculation can lead to mild infection in chickens, indicating potential cross-species transmission (Yadav et al., 2024a). Despite these findings, key questions remain regarding the mechanisms underlying zoonotic transmission of rat HEV-C1. Notably, the genetic determinants that facilitate interspecies infection and the extent of cross-species transmission of specific rat HEV-C1 strains remain to be elucidated (Kinast et al., 2022; Wang et al., 2024).

Rat HEV-C1 is widely recognized as a genetically diverse lineage carried by various *Rattus* species. Our study revealed significant sequence variation among rat HEV-C1 strains, raising the possibility that single nucleotide polymorphisms (SNPs) and amino acid substitutions may play roles in host adaptation or influence strain-specific characteristics, such as virulence, transmission efficiency, and host specificity. Comparative analyses of SNPs and amino acid mutations across strains from different hosts and regions could uncover patterns linked to specific hosts or zoonotic potential, providing valuable insights into viral evolution and host-virus interactions (Harms et al., 2018; van Tong et al., 2016). In addition to *Rattus* species, our study identified genetic heterogeneity in rat HEV-C1 strains carried by the lesser bandicoot rat (*B. bengalensis*), mirroring observations in the white-bellied rat (*Niviventer niviventer*), red spiny rat (*Maxomys surifer*), and house mouse (*Mus musculus*). These findings suggest the close relatedness among *Rocahepevirus* strains within the family Muridae. Furthermore, two additional viral strains of *R. ratti* genotype C3 were identified in Chevrier's field mouse (*A. chevrieri*), exhibiting notable sequence divergence from our two previously identified *A. chevrieri* HEV-C3 strains in Yunnan (Wang et al., 2018c). Beyond Muridae, the Kachin red-backed vole (*E. eleusis*) was found to harbor *Rocahepevirus* strains that clustered with viral from Pere David's vole (*E. melanogaster*) and Kolan vole (*E. inez*), forming a distinct phylogenetic clade of *E. eothenomi* species within the genus *Rocahepevirus*. Intriguingly, most viral strains detected in the family Cricetidae clustered together, with the exception of two strains each from the grey red-backed vole (*Craseomys rufocanus*) and striped dwarf hamster (*C. barabensis*), which were basal to all other *Rocahepevirus* species in the phylogenetic tree. However, the definitive taxonomy of these strains requires further investigation.

The house shrew (*S. murinus*) is recognized as a reservoir for rat HEV-C1 (Guan et al., 2013; He et al., 2018; Wang et al., 2017a). Until now, only a single complete genome sequence of house shrew HEV-C1 has been available in GenBank (accession number OP947209). In this study, an additional HEV-C1 genome was amplified from the house shrew, demonstrating only 77.3% sequence identity with the previously reported strain. This substantial genetic divergence underscores the susceptibility of house shrews to infection by genetically diverse HEV-C1 variants. Conversely, the *Orthohepevirus* strain identified in Hodgson's brown-toothed shrew (*E. caudatus*) was phylogenetically distant from HEV-C1, instead clustering with the genus *Paslahepevirus*. Similarly, a partial *Orthohepevirus* sequence from Oliver's shrew (*C. olivieri*) in Kenya was shown to diverge significantly from the genus *Rocahepevirus* (Onyuok et al., 2019). These findings indicate that members of the order Eulipotyphla may carry unique orthohepeviruses. Given the genetic and phylogenetic divergence observed, the *E. caudatus Orthohepevirus* strain identified here may represent a new species within the genus *Paslahepevirus*.

The tree shrew (order Scandentia, family Tupaiidae) has recently emerged as a promising animal model for studying the infection and pathogenesis of human hepatitis viruses, including hepatitis B and C (Kayesh et al., 2021; Xiao et al., 2017). Notably, a highly divergent *Paslahepevirus* strain has been identified in the common tree shrew (*Tupaia glis*), presenting an opportunity to develop a tree shrew HEV infection model. However, the utility of tree shrews for investigating human HEV pathogenesis remains to be established. Furthermore, given the diversity of species within the order Scandentia, it is conceivable that genetically diverse orthohepeviruses may exist beyond the common tree shrew. Despite this potential, in our study, all 22 northern tree shrews (*Tupaia belangeri*) tested negative for *Paslahepevirus*. Nonetheless, the search for additional divergent orthohepeviruses in tree shrews remains an open avenue for future exploration (Yadav & Kenney, 2022).

The evolutionary analyses presented in this study strongly suggest that animals within each taxonomic order harbor specific HEV-related viruses due to long-term co-speciation of their hosts. However, cross-species viral transmission events have also occurred frequently throughout the evolutionary history of HEV, as exemplified by shrew HEV-C1, ferret HEV-C2, rabbit HEV-3r, and human HEV-3 and HEV-4. Notably, identification of HEV homologs in wild primates holds promise for gaining a deeper understanding of the evolutionary history and origin of human HEV (Drexler et al., 2012). Moreover, considering the abundance and geographical distribution of small mammal orders, such as Rodentia, Eulipotyphla, Carnivore, Scandentia, Lagomorpha, and Chiroptera (Blanga-Kanfi et al., 2009), the discovery of novel orthohepeviruses is

highly anticipated. Advances in molecular techniques for virus identification are likely to accelerate this process, expanding the known host range of the family *Hepeviridae* in the near future (Meng, 2016).

Our study had several limitations that warrant recognition. First, a full-length genome of the only *Orthohepevirus*-positive sample from the Chaotung vole (*E. olitor*) was not obtained, limiting our ability to conduct comprehensive comparative and evolutionary analyses of *Rocahepevirus* strains within the genus *Eothenomys*. Second, the lack of properly preserved animal tissues precluded histopathological examinations of liver tissues from *Orthohepevirus*-positive specimens. Additionally, virus concentrations in different solid organs of *Orthohepevirus*-positive specimens were not compared, hindering investigation of potential liver damage and extra-hepatic injuries caused by novel *Rocahepevirus* strains (Kamar et al., 2016; Tian et al., 2022). Third, functional *in vitro* or *in vivo* studies of the novel *Orthohepevirus* strains identified in rodents and shrews were not undertaken. Consequently, critical aspects of the molecular biology and pathogenicity of these viruses remain unexplored, necessitating future research using cell culture systems and animal models.

In conclusion, the detection and genomic characterization of genetically divergent *Orthohepevirus* strains in various rodent and shrew species in Yunnan, China, highlight the critical roles of co-speciation and cross-species transmission in shaping the evolutionary history of the genera *Paslahepevirus* and *Rocahepevirus*. Identifying *Orthohepevirus* strains across diverse animal orders holds significance in unraveling and understanding the pathogenesis, evolution, and zoonotic transmission of HEV.

DATA AVAILABILITY

The nucleotide sequences from all rodent and shrew orthohepeviruses described in this study were deposited into the NCBI GenBank database under accession numbers PP533449 to PP533472, with PP533472 representing the full-length genomic sequence of the *Orthohepevirus* strain EcYS16 from Hodgson's brown-toothed shrew (*Episoriculus caudatus*). The nucleotide sequences were also deposited in the Genome Sequence Archive (GSA) database (ID number 0005084) and Science Data Bank (DOI number 10.57760/sciencedb.j00139.00149).

SUPPLEMENTARY DATA

Supplementary data to this article can be found online.

COMPETING INTERESTS

The authors declare that they have no competing interests.

AUTHORS' CONTRIBUTIONS

Y.Z.Z., X.L.Y., B.H., and Z.L.S. administrated and supervised the project. F.L.L., B.W., P.Y.H., B.L., H.R.S., Y.Z., H.M.Y., L.R.Z., and Y.T. performed all experiments. F.L.L. and B.W. designed the study, analyzed the data, and drafted the original manuscript. B.H., X.L.Y., and Y.Z.Z. edited the manuscript. All authors read and approved the final version of the manuscript.

REFERENCES

Akanbi OA, Harms D, Wang B, et al. 2019. Complete genome sequence of a hepatitis E virus genotype 1e strain from an outbreak in Nigeria, 2017. *Microbiology Resource Announcements*, **8**(1): e01378–18.

Andonov A, Robbins M, Borlang J, et al. 2019. Rat hepatitis E virus linked to severe acute hepatitis in an immunocompetent patient. *The Journal of Infectious Diseases*, **220**(6): 951–955.

Blanga-Kanfi S, Miranda H, Penn O, et al. 2009. Rodent phylogeny revised: analysis of six nuclear genes from all major rodent clades. *BMC Evolutionary Biology*, **9**(1): 71.

Bodewes R, van der Giessen J, Haagmans BL, et al. 2013. Identification of multiple novel viruses, including a parvovirus and a hepevirus, in feces of red foxes. *Journal of Virology*, **87**(13): 7758–7764.

Brayne AB, Dearlove BL, Lester JS, et al. 2017. Genotype-specific evolution of hepatitis E virus. *Journal of Virology*, **91**(9): e02241–16.

Choi M, Hofmann J, Köhler A, et al. 2018. Prevalence and clinical correlates of chronic hepatitis e infection in German renal transplant recipients with elevated liver enzymes. *Transplantation Direct*, **4**(2): e341.

Drexler JF, Seelen A, Corman VM, et al. 2012. Bats worldwide carry hepatitis E virus-related viruses that form a putative novel genus within the family *Hepeviridae*. *Journal of Virology*, **86**(17): 9134–9147.

Grange ZL, Goldstein T, Johnson CK, et al. 2021. Ranking the risk of animal-to-human spillover for newly discovered viruses. *Proceedings of the National Academy of Sciences of the United States of America*, **118**(15): e2002324118.

Guan DW, Li W, Su J, et al. 2013. Asian musk shrew as a reservoir of rat hepatitis E virus, China. *Emerging Infectious Diseases*, **19**(8): 1341–1343.

Guo H, Cai CL, Wang B, et al. 2019. Novel hepacivirus in Asian house shrew, China. *Science China Life Sciences*, **62**(5): 701–704.

Guo L, Li B, Han PY, et al. 2023. Identification of a Novel Hepacivirus in Southeast Asian Shrew (*Crocidura fuliginosa*) from Yunnan Province, China. *Pathogens*, **12**(12): 1400.

Han PY, Xu FH, Tian JW, et al. 2024. Molecular prevalence, genetic diversity, and tissue tropism of *Bartonella* species in small mammals from Yunnan Province, China. *Animals (Basel)*, **14**(9): 1320.

Harms D, Wang B, Papp CP, et al. 2018. Capturing virus evolution by proteomic bioinformatics: hunting for characteristic mutations in the hepatitis E virus genome. *Virulence*, **9**(1): 13–16.

He WQ, Wen YQ, Xiong YQ, et al. 2018. The prevalence and genomic characteristics of hepatitis E virus in murine rodents and house shrews from several regions in China. *BMC Veterinary Research*, **14**(1): 414.

Hu B, Zeng LP, Yang XL, et al. 2017. Discovery of a rich gene pool of bat SARS-related coronaviruses provides new insights into the origin of SARS coronavirus. *PLoS Pathogens*, **13**(11): e1006698.

Huang H, Fu M, Han PY, et al. 2023. Clinical and molecular epidemiology of hemorrhagic fever with renal syndrome caused by orthohantaviruses in Xiangyun County, Dali Prefecture, Yunnan Province, China. *Vaccines (Basel)*, **11**(9): 1477.

Johne R, Plenge-Bönig A, Hess M, et al. 2010. Detection of a novel hepatitis E-like virus in faeces of wild rats using a nested broad-spectrum RT-PCR. *Journal of General Virology*, **91**(3): 750–758.

Kamar N, Marion O, Abravanel F, et al. 2016. Extrahepatic manifestations of hepatitis E virus. *Liver International*, **36**(4): 467–472.

Kayesh MEH, Sanada T, Kohara M, et al. 2021. Tree shrew as an emerging small animal model for human viral infection: a recent overview. *Viruses*, **13**(8): 1641.

Kinast V, Klöhn M, Nocke MK, et al. 2022. Hepatitis E virus species barriers: seeking viral and host determinants. *Current Opinion in Virology*, **56**: 101274.

Koonin EV, Gorbalenya AE, Purdy MA, et al. 1992. Computer-assisted assignment of functional domains in the nonstructural polyprotein of hepatitis E virus: delineation of an additional group of positive-strand RNA plant and animal viruses. *Proceedings of the National Academy of Sciences of the United States of America*, **89**(17): 8259–8263.

Li DH, Liu CM, Luo RR, et al. 2015. MEGAHIT: an ultra-fast single-node solution for large and complex metagenomics assembly via succinct *de Bruijn* graph. *Bioinformatics*, **31**(10): 1674–1676.

Lin J, Norder H, Uhlhorn H, et al. 2014. Novel hepatitis E like virus found in

Swedish moose. *Journal of General Virology*, **95**(Pt 3): 557–570.
Lole KS, Bollinger RC, Paranjape RS, et al. 1999. Full-length human immunodeficiency virus type 1 genomes from subtype C-infected seroconverters in India, with evidence of intersubtype recombination. *Journal of Virology*, **73**(1): 152–160.
Mahsoub HM, Heffron CL, Hassebroek AM, et al. 2023. Fetal loss in pregnant rabbits infected with genotype 3 hepatitis E virus is associated with altered inflammatory responses, enhanced virus replication, and extrahepatic virus dissemination with positive correlations with increased estradiol level. *mBio*, **14**(2): e00418–23.
Meng XJ. 2016. Expanding host range and cross-species infection of hepatitis E virus. *PLoS Pathogens*, **12**(8): e1005695.
Meng XJ, Halbur PG, Shapiro MS, et al. 1998. Genetic and experimental evidence for cross-species infection by swine hepatitis E virus. *Journal of Virology*, **72**(12): 9714–9721.
Meng XJ, Purcell RH, Halbur PG, et al. 1997. A novel virus in swine is closely related to the human hepatitis E virus. *Proceedings of the National Academy of Sciences of the United States of America*, **94**(18): 9860–9865.
Olival KJ, Hosseini PR, Zambrana-Torrelio C, et al. 2017. Host and viral traits predict zoonotic spillover from mammals. *Nature*, **546**(7660): 646–650.
Onyuok SO, Hu B, Li B, et al. 2019. Molecular detection and genetic characterization of novel RNA viruses in wild and synanthropic rodents and shrews in Kenya. *Frontiers in Microbiology*, **10**: 2696.
Papp CP, Biedermann P, Harms D, et al. 2022. Advanced sequencing approaches detected insertions of viral and human origin in the viral genome of chronic hepatitis E virus patients. *Scientific Reports*, **12**(1): 1720.
Purdy MA, Drexler JF, Meng XJ, et al. 2022. ICTV virus taxonomy profile: *Hepeviridae* 2022. *Journal of General Virolog*, **103**(9).
Rasche A, Sander AL, Corman VM, et al. 2019. Evolutionary biology of human hepatitis viruses. *Journal of Hepatology*, **70**(3): 501–520.
Reuter G, Boros Á, Mátics R, et al. 2016. Divergent hepatitis E virus in birds of prey, common kestrel (*Falco tinnunculus*) and red-footed falcon (*F. vespertinus*), Hungary. *Infection, Genetics and Evolution*, **43**: 343–346.
Reuter G, Boros Á, Pankovics P. 2020. Review of hepatitis E virus in rats: evident risk of species *Orthohepevirus C* to human zoonotic infection and disease. *Viruses*, **12**(10): 1148.
Rios-Muñoz L, Gonzálvez M, Caballero-Gomez J, et al. 2024. Detection of rat hepatitis E virus in pigs, Spain, 2023. *Emerging Infectious Diseases*, **30**(4): 823–826.
Rivero-Juarez A, Frias M, Perez AB, et al. 2022. *Orthohepevirus* C infection as an emerging cause of acute hepatitis in Spain: first report in Europe. *Journal of Hepatology*, **77**(2): 326–331.
Rodriguez C, Marchand S, Sessa A, et al. 2023. *Orthohepevirus C* hepatitis, an underdiagnosed disease?. *Journal of Hepatology*, **79**(1): e39–e41.
Sander AL, Corman VM, Lukashev AN, et al. 2018. Evolutionary origins of enteric hepatitis viruses. *Cold Spring Harbor Perspectives in Medicine*, **8**(12): a031690.
Shomer NH, Allen-Worthington KH, Hickman DL, et al. 2020. Review of rodent euthanasia methods. *Journal of the American Association for Laboratory Animal Sciencei*, **59**(3): 242–253.
Smith DB, Simmonds P, Members of the International Committee on the Taxonomy of Viruses Study Group, et al. 2014. Consensus proposals for classification of the family *Hepeviridae. Journal of General Virology*, **95**(Pt 10): 2223–2232.
Sridhar S, Situ JW, Cai JP, et al. 2021a. Multimodal investigation of rat hepatitis E virus antigenicity: implications for infection, diagnostics, and vaccine efficacy. *Journal of Hepatology*, **74**(6): 1315–1324.
Sridhar S, Yip CCY, Lo KHY, et al. 2022. Hepatitis E virus species c infection in humans, Hong Kong. *Clinical Infectious Diseases*, **75**(2): 288–296.
Sridhar S, Yip CCY, Wu SS, et al. 2018. Rat hepatitis E Virus as cause of persistent hepatitis after liver transplant. *Emerging Infectious Diseases*, **24**(12): 2241–2250.
Sridhar S, Yip CCY, Wu SS, et al. 2021b. Transmission of rat hepatitis E virus infection to humans in Hong Kong: a clinical and epidemiological analysis. *Hepatology*, **73**(1): 10–22.
Tang Y, Zhao K, Yin HM, et al. 2024. Identification and genomic characterization of two novel hepatoviruses in shrews from Yunnan Province, China. *Viruses*, **16**(6): 969–969.
Tanggis, Kobayashi T, Takahashi M, et al. 2018. An analysis of two open reading frames (ORF3 and ORF4) of rat hepatitis E virus genome using its infectious cDNA clones with mutations in ORF3 or ORF4. *Virus Research*, **249**: 16–30.
Tian DB, Li W, Heffron CL, et al. 2022. Hepatitis E virus infects brain microvascular endothelial cells, crosses the blood-brain barrier, and invades the central nervous system. *Proceedings of the National Academy of Sciences of the United States of America*, **119**(24): e2201862119.
van Tong H, Hoan NX, Wang B, et al. 2016. Hepatitis E virus mutations: functional and clinical relevance. *EBioMedicine*, **11**: 31–42.
Wang B, Akanbi OA, Harms D, et al. 2018a. A new hepatitis E virus genotype 2 strain identified from an outbreak in Nigeria, 2017. *Virology Journal*, **15**(1): 163.
Wang B, Cai CL, Li B, et al. 2017a. Detection and characterization of three zoonotic viruses in wild rodents and shrews from Shenzhen city, China. *Virologica Sinica*, **32**(4): 290–297.
Wang B, Harms D, Hofmann J, et al. 2017b. Identification of a novel hepatitis E virus genotype 3 strain isolated from a chronic hepatitis E virus infection in a kidney transplant recipient in Switzerland. *Genome Announcements*, **5**(20): e00345–17.
Wang B, Harms D, Papp CP, et al. 2018b. Comprehensive molecular approach for characterization of hepatitis e virus genotype 3 variants. *Journal of Clinical Microbiology*, **56**(5): e01686–17.
Wang B, Harms D, Yang XL, et al. 2020. *Orthohepevirus* C: an expanding species of emerging hepatitis E virus variants. *Pathogens*, **9**(3): 154.
Wang B, Krüger L, Machnowska P, et al. 2019. Characterization of a hepatitis C virus genotype 1 divergent isolate from an HIV-1 coinfected individual in Germany assigned to a new subtype 1o. *Virology Journal*, **16**(1): 28.
Wang B, Li W, Zhou JH, et al. 2018c. Chevrier's field mouse (*Apodemus chevrieri*) and Père David's vole (*Eothenomys melanogaster*) in China carry orthohepeviruses that form two putative novel genotypes within the species *Orthohepevirus C*. *Virologica Sinica*, **33**(1): 44–58.
Wang B, Mahsoub HM, Li W, et al. 2023. Ribavirin treatment failure-associated mutation, Y1320H, in the RNA-dependent RNA polymerase of genotype 3 hepatitis E virus (HEV) enhances virus replication in a rabbit HEV infection model. *mBio*, **14**(2): e03372–22.
Wang B, Meng XJ. 2021a. Hepatitis E virus: host tropism and zoonotic infection. *Current Opinion in Microbiology*, **59**: 8–15.
Wang B, Meng XJ. 2021b. Structural and molecular biology of hepatitis E virus. *Computational and Structural Biotechnology Journal*, **19**: 1907–1916.
Wang B, Subramaniam S, Tian DB, et al. 2024. Phosphorylation of Ser711 residue in the hypervariable region of zoonotic genotype 3 hepatitis E virus is important for virus replication. *MBio*, **15**(11): e02635–24.
Wang B, Tian DB, Sooryanarain H, et al. 2022. Two mutations in the ORF1 of genotype 1 hepatitis E virus enhance virus replication and may associate with fulminant hepatic failure. *Proceedings of the National Academy of Sciences of the United States of America*, **119**(34): e2207503119.
Wang B, Yang XL. 2022. *Chirohepevirus* from bats: insights into hepatitis E virus diversity and evolution. *Viruses*, **14**(5): 905.
Wang B, Yang XL, Li W, et al. 2017c. Detection and genome

characterization of four novel bat hepadnaviruses and a hepevirus in China. *Virology Journal*, **14**(1): 40.

Wu ZQ, Lu L, Du J, et al. 2018. Comparative analysis of rodent and small mammal viromes to better understand the wildlife origin of emerging infectious diseases. *Microbiome*, **6**(1): 178.

Xiao J, Liu R, Chen CS. 2017. Tree shrew (*Tupaia belangeri*) as a novel laboratory disease animal model. *Zoological Research*, **38**(3): 127–137.

Yadav KK, Boley PA, Khatiwada S, et al. 2024a. The zoonotic LCK-3110 strain of *Rocahepevirus ratti* leads to mild infection in chickens after experimental inoculation. *Virus Res Research*, **350**: 199477.

Yadav KK, Boley PA, Lee CM, et al. 2024b. Rat hepatitis E virus cross-species infection and transmission in pigs. *PNAS Nexus*, **3**(7): pgae259.

Yadav KK, Kenney SP. 2022. Hepatitis E virus zoonotic axis. *In*: Sing A. Zoonoses: Infections Affecting Humans and Animals. Cham: Springer, 1–28.

Yang FM, Li YY, Li YJ, et al. 2022. Experimental cross-species transmission of rat hepatitis e virus to rhesus and cynomolgus monkeys. *Viruses*, **14**(2): 293.

Wu et al. *Zool. Res.* 2025, 46(1): 122−138
https://doi.org/10.24272/j.issn.2095-8137.2024.211
https://cstr.cn/32248.14.zr.2024.211

ZR | Zoological Research

Article Open Access

Transcription coactivator YAP1 promotes CCND1/CDK6 expression, stimulating cell proliferation in cloned cattle placentas

Shan-Shan Wu[1,2,#], Xiao-Yu Zhao[1,2,#], Lei Yang[1,2], Chao Hai[1,2], Di Wu[1,2], Xue-Fei Liu[1,2], Li-Shuang Song[1,2], Chun-Ling Bai[1,2], Guang-Hua Su[1,2,*], Guang-Peng Li[1,2,*]

[1] *State Key Laboratory of Reproductive Regulation and Breeding of Grassland Livestock (R2BGL)*, *Inner Mongolia University*, *Hohhot*, *Inner Mongolia* 010070, *China*

[2] *College of Life Sciences*, *Inner Mongolia University*, *Hohhot*, *Inner Mongolia* 010070, *China*

ABSTRACT

Somatic cell nuclear transfer (SCNT) has been successfully employed across various mammalian species, yet cloned animals consistently exhibit low pregnancy rates, primarily due to placental abnormalities such as hyperplasia and hypertrophy. This study investigated the involvement of the Hippo signaling pathway in aberrant placental development in SCNT-induced bovine pregnancies. SCNT-derived cattle exhibited placental hypertrophy, including enlarged abdominal circumference and altered placental cotyledon morphology. RNA sequencing analysis indicated significant dysregulation of Hippo signaling pathway genes in SCNT placentas. Co-expression of YAP1 and CCND1 was observed in cloned blastocysts, placental tissues, and bovine placental mesenchymal stem cells (bPMSCs). Manipulation of YAP1 expression demonstrated the capacity to regulate bPMSC proliferation. Experimental assays confirmed the direct binding of YAP1 to CCND1, which subsequently promoted CCND1 expression in bPMSCs. Furthermore, inhibition of CDK6, a downstream target of CCND1, attenuated SCNT bPMSC proliferation. This study identified YAP1 as a key regulatory component within the Hippo signaling pathway that drives placental hyperplasia in cloned cattle through up-regulation of CCND1-CDK6 expression, facilitating cell cycle progression. These findings offer potential avenues for enhancing cloning efficiency, with implications for evolutionary biology and the conservation of valuable germplasm resources.

Keywords: Somatic cell nuclear transfer; Cloned cattle; Placental hypertrophy; Cell proliferation; CCND1-CDK6; YAP1

This is an open-access article distributed under the terms of the Creative Commons Attribution Non-Commercial License (http://creativecommons.org/licenses/by-nc/4.0/), which permits unrestricted non-commercial use, distribution, and reproduction in any medium, provided the original work is properly cited.

Copyright ©2025 Editorial Office of Zoological Research, Kunming Institute of Zoology, Chinese Academy of Sciences

INTRODUCTION

Somatic cell nuclear transfer (SCNT) is a powerful technique in animal biotechnology, enabling the rapid duplication and enhancement of desirable traits in livestock, thus making invaluable contributions to animal breeding programs (Matoba & Zhang, 2018). SCNT technology also has broad applications in the fields of transgenic animal reproduction, evolution, germplasm preservation, endangered species protection, organ transplantation, and fundamental biological research (Matoba & Zhang, 2018; Oback, 2008; Ogura et al., 2013; Vajta, 2007).

Despite its potential, SCNT-based cloning in animals continues to show low efficiency, with birth success rates remaining limited (Yang et al., 2007). For instance, survival rates for SCNT-derived sheep, cattle, pigs, and mice have been reported to range from 0.5% to 18% (Tsunoda & Kato, 2002). A nine-year survey in Japan observed an average success rate of 4.3% in cloned cattle (Watanabe & Nagai, 2011), while a recent 2022 review confirmed critically low success rates across species, fluctuating between 0.1% and 5% (Samiec, 2022).

The low efficiency in generating SCNT-derived progeny is predominantly linked to the limited capacity of nuclear donor

Received: 08 September 2024; Accepted: 22 October 2024; Online: 23 October 2024

Foundation items: This study was supported by the National Natural Science Foundation of China (32060755), Natural Science Foundation of Inner Mongolia (2024MS03001), Inner Mongolia Autonomous Region Open Competition Projects (2022JBGS0018), Program for Young Talents of Science and Technology in Universities of Inner Mongolia Autonomous Region (NJYT23090), Inner Mongolia Autonomous Region Science and Technology Leading Team (2022LJRC0006), Inner Mongolia Autonomous Region Science and Technology Major Project (2021ZD0009), Major Agricultural Science and Technology Project of the Ministry of Agriculture and Rural Affairs (NK2022130203), Central Government Guides Local Science and Technology Development Funds (2022ZY0212), Inner Mongolia Autonomous Region High-level Talent Support Program, and Inner Mongolia University Chief Scientist Program

[#]Authors contributed equally to this work

*Corresponding authors, E-mail: guanghuasu@imu.edu.cn; gpengli@imu.edu.cn

cells (NDCs) to undergo epigenetic reprogramming of their transcriptomic and proteomic profiles within nuclear-transferred embryos. The efficiency of this reprogramming process is highly dependent on the histological origin of the NDCs, their levels of stemness and differentiation, and the synchronization of their cell cycle to the G0/G1 phases (Gorczyca et al., 2021; Huang et al., 2023; Min et al., 2015; Samiec & Skrzyszowska, 2010). Additionally, incompatibilities in meiotic, epigenomic, and cytoplasmic maturation processes within *in vitro* cultured nuclear recipient oocytes (NROs) often lead to aberrant activation of the embryo-specific developmental program in nuclear-transferred oocytes (Canel et al., 2010; Gorczyca et al., 2022; Ross et al., 2009; Skrzyszowska et al., 2008). Equally significant are issues related to asynchronous or non-synergistic interactions among inter-genomic, inter-epigenomic, inter-transcriptomic, and inter-proteomic pathways between nuclear and mitochondrial compartments, which derive from both NDCs and enucleated NROs used to propagate SCNT-derived embryos (Jiao et al., 2007; Samie & Skrzyszowska, 2005; Yan et al., 2010). Cloned embryos, fetuses, and offspring are susceptible to various developmental abnormalities throughout gestation, including large offspring syndrome, early embryonic and fetal losses, elevated perinatal mortality, prolonged gestation, increased abdominal girth, excessive amniotic fluid, and enlarged placenta (Hwang et al., 2015; Svarcova et al., 2007).

Overcoming the hurdles of low efficiency and abnormal development in cloned mammals has become a central focus in SCNT research (Samiec, 2022; Sangalli et al., 2023). Placental abnormalities are major contributors to the low success rates of cloned pregnancies (Chavatte-Palmer et al., 2006), impairing nutrient transport and fetal development (Whitworth & Prather, 2010). During the blastocyst stage, embryonic differentiation leads to the formation of the inner cell mass (ICM) and trophectoderm (TE), with the latter developing into the placenta. The placenta plays a crucial role in nutrient transport and hormone synthesis, directly influencing fetal growth and development (Tanaka et al., 2001).

Placental enlargement in SCNT animals is attributed to multiple factors, including dysregulated hormone secretion, abnormal DNA methylation and RNA expression (Arnold et al., 2008; Malin et al., 2022), and most notably, abnormal chromatin histone modifications and imprinting gene expression (Ogura et al., 2021; Ticiani et al., 2020). Wang et al. (2020) found that histone H3 lysine 27 trimethylation (H3K27me3) is associated with the up-regulation of imprint coding genes, such as Scm-like with four MBT domains 2 (*Sfmbt2*), GRB2-associated binding protein 1 (*Gab1*), and SPARC-related modular calcium binding (*Smoc1*), in cloned mouse placentas. Similarly, Arnold et al. (2017) reported increased levels of histone H3 lysine 4 dimethylation (H3K4me2) in the placental tissues of cloned cattle fetuses at day 60 of pregnancy, with relatively lower, though not significantly, levels of H3K9me2. Zhou et al. (2020) demonstrated that H3K4me3 loss during embryonic development enhances the growth of cloned cattle embryos. Studies have also identified aberrant hormone expression, including progesterone and placental lactogens, as a crucial factor contributing to placental enlargement in cloned placentas (Bajoria et al., 2002; Hill, 2014). Currently, however, research on effective repair strategies for placental abnormalities in cloned animals remains scarce. Most studies have focused on genetic interventions aimed at rescuing abnormal epigenetic reprogramming, specifically through the modulation of DNA methylation and histone modifications, alongside the targeted overexpression or suppression of genes involved in embryonic development (Srirattana et al., 2022). Our earlier studies identified abnormal expression of circular RNAs (circRNAs), long non-coding RNAs (lncRNAs), microRNAs (miRNAs), and competing endogenous RNAs (CeRNAs) in SCNT-derived bovine placentas, particularly those regulated by the DNA methylation hydroxylase Tet methylcytosine dioxygenase 1 (TET1), influenced by BTA-miR-1298 and lncRNAMSTRG.119672 (Gao et al., 2019; Su et al., 2019).

Mesenchymal stem cells (MSCs) exhibit pluripotency and paracrine signaling capabilities, allowing differentiation into cell types closely related to placental formation. Placental MSCs (PMSCs), in particular, contribute to early placental angiogenesis by differentiating into cells that form vascular structures (Boss et al., 2018). PMSCs further support placental function through paracrine interaction with other constituent placental cells, improving angiogenesis, enhancing uterine spiral artery remodeling, and regulating uteroplacental immune dynamics (Liu et al., 2021; Magatti et al., 2019; Wu et al., 2020). Successful placental growth requires a precise balance among cell proliferation, differentiation, and apoptosis (Peter, 2013). Placental formation and development are regulated by a variety of signaling pathways and growth factors, some of which may induce abnormal or accelerated cell proliferation, although comprehensive research on this topic remains limited.

Several cell signaling pathways, including the Hippo/Yap1, PI3K/Akt, Notch, and Wnt/β-catenin signaling pathways, are key regulators of organ size and placental development (Camargo et al., 2007; Dong et al., 2007). Among these, the Hippo signaling pathway plays a central role in promoting cell proliferation and suppressing cell differentiation through positive regulation of the Yes1-associated transcriptional regulator (*Yap1*), an essential factor in organ size control (Heallen et al., 2011; Moon et al., 2018). In human placental tissues, the Hippo pathway also plays a crucial role in placental development by promoting cell proliferation and maintaining stemness (Meinhardt et al., 2020). CCND1 and CDK6 act as important regulators of cellular proliferation, particularly during the G1 phase of the cell cycle, facilitating the G1-S transition that drives cell division (Li et al., 2018a). In SCNT cattle, placental overgrowth-characterized by increased cell numbers, hypertrophy, and stromal expansion-may contribute to placental enlargement, although further studies are needed to determine the involvement of the Hippo pathway in this condition.

Evolution has shaped the role of the Hippo signaling pathway in placental development, and disruptions in this pathway can lead to the development of abnormalities. Exploring these regulatory mechanisms can provide insights into both evolutionary biology and developmental processes. Furthermore, the preservation and utilization of germplasm resources are essential for maintaining genetic diversity and adaptability in agricultural species. Effective advancements in SCNT technology can support the conservation and propagation of valuable genetic traits, ensuring species resilience under changing environments. This study is important for revealing the regulatory mechanisms underlying placental gigantism in SCNT-derived animals and for

improving cloning efficiency, contributing to the advancement of cloned animal production.

MATERIALS AND METHODS

Ethics statement

All animals used in the study were treated following the Council of China Animal Welfare guidelines. All protocols were approved by the Institutional Animal Care and Use Committee at Inner Mongolia University (approval number: IMU-CATTLE-2022-063).

Analysis of gestational indicators in recipient cows of cloned cattle and determination of postpartum placental phenotypes

All cattle used in this study were raised under consistent conditions at the NeiDaShengMu High-Tech Livestock Farming Company facility in Hohhot city and Heling District. The cloned cattle group was derived from donor ear-tip fibroblasts obtained from a high-quality 2-year-old bull, while the control (CON) group consisted of cattle naturally impregnated through artificial insemination. Both groups included pregnant cows aged 18–22 months, all fed the same forage and maintained under the same conditions. In the CON group, gestation period calculations began from the breeding date immediately following estrus, with the birth date of the calf marking the end of gestation (gestation period = calf birth date − cow breeding date). In the SCNT group, gestation period calculations began from the estrus date. Cloned embryos were transferred into recipient uteruses 7 days post-estrus (gestation period = calf birth date − cow estrus date). By using estrus as the starting point in both groups, the initial reference time remained consistent across comparisons. After delivery, placental tissue samples from both the CON and SCNT groups were collected for phenotypic assessment. Placental parameters were recorded, including number, length, and width of cotyledons, as well as birth weight of the cloned calves. All data were subsequently subjected to statistical analysis.

RNA sequencing (RNA-seq) of placental tissue

Placental tissue samples were obtained from three CON cattle and three SCNT cattle. Total RNA was extracted, followed by RNA-seq library construction. Sequencing was performed on the Illumina NovaSeq 6000 Sequencing Platform (USA). The RNA-seq data were subjected to quality control using the Fastx-toolkit (v.0.014) and Fastp (v.0.19.5, http://github.com/OpenGene/fastp) software (reference gene source: *Bos taurus*; reference genome version: ARS-UCD1.2). Read mapping to the genome was performed using Bowtie alignment software. Differential expression analysis was conducted using DESeq2 (http://bioconductor.org/packages/stats/bioc/DESeq2/), applying a filtering threshold of $|\log_2 FC| \geq 1$ and $P<0.05$ to identify differentially expressed genes (DEGs). Gene Ontology (GO, https://geneontology.org/) and Kyoto Encyclopedia of Genes and Genomes (KEGG, https://www.genome.jp/kegg/) pathway analyses were performed using the DAVID database.

Isolation, cultivation, and differentiation analysis of bovine PMSCs (bPMSCs)

The isolation and culture protocols for bPMSCs followed previous research (Lankford et al., 2017). Briefly, placental chorionic membrane tissue was washed in phosphate-buffered saline (PBS, Gibco, USA) containing 2% penicillin-streptomycin (Gibco, USA), dissected into small fragments, and digested with an enzyme solution comprising 0.25% trypsin (Gibco, USA) and 1% Type IV collagenase (Gibco, USA) at a 1:1 ratio. Tissue digestion was carried out in three cycles at 37°C, each lasting 30 min. The digested cell suspension was then seeded in Dulbecco's Modified Eagle Medium/Nutrient Mixture F-12 (DMEM-F12, Gibco, USA) enriched with 20% fetal bovine serum (FBS, Gibco, USA) and 1% penicillin-streptomycin and incubated at 37°C in a humidified 5% CO_2 environment. Cells were subcultured upon reaching 95% confluence, typically at a 1:3 ratio, or cryopreserved for future use. Differentiation assays for MSCs involved the use of adipogenic induction culture A medium (DMEM-F12, 10% FBS, 1% glutamine (Gibco, USA), 0.2% insulin (Sigma, USA), 0.1% dexamethasone (Sigma, USA), 0.1% IBMX (Sigma, USA), and 0.1% rosiglitazone (Sigma, USA)) and adipogenic induction culture B medium (DMEM-F12, 10% FBS, 1% glutamine, and 0.2% insulin), with alternate treatments over 3–5 cycles (12–20 days) to induce adipogenic differentiation. The cells were stained with Oil Red O staining solution and imaged under a microscope (ZEISS, Germany). For osteogenic differentiation, bPMSCs were cultured in osteogenic induction culture medium (DMEM-F12, 15% FBS, 1% 1 mol/L β-glycerophosphate (Gibco, USA), 2% dexamethasone (Gibco, USA), and 2% ascorbate (Gibco, USA)) for 12–28 days, with differentiation evaluated using Alizarin Red S staining under microscopy. In this study, Yap1 expression was inhibited in CON and SCNT bPMSCs by the addition of 100 nmol/L verteporfin (CL318952, MCE, USA) during culture. Additionally, SCNT bPMSCs were further validated by treatment with the CDK4/CDK6 inhibitor BSJ-03-204 (effective inhibitory concentration of 26.9 nmol/L for CDK4/CCND1 and 10.4 nmol/L for CDK6/CCND1) (HY-136250, MCE, USA).

Construction of lentiviral vectors for YAP1 overexpression/knockdown and establishment of stable cell lines

To construct the YAP1 overexpression vector, YAP1 DNA was inserted into the PCDH-CMV-EF1-T2A-Puro vector. Four short hairpin RNAs (shRNAs) targeting the YAP1 gene were designed using the Invitrogen and Gene Link interference fragment design platform (Dalian Baio Biological, China) (Supplementary Table S1). These shRNAs were converted into double-stranded DNA and inserted into the PLKO.1-CopGFE-Puro vector to create the YAP1 knockdown vector. The resulting vectors were subsequently transformed into Stbl3 *Escherichia coli* competent cells, sequenced for verification, and subsequently used for YAP1 overexpression and knockdown experiments.

For lentivirus production, Lipofectamine 2000 (Invitrogen, 11668019, USA) was used to co-transfect 293T cells with the auxiliary packaging plasmids psPAX2 and pMD2G, along with the lentiviral shuttle plasmids PCDH-CMV-EF1-T2A-Puro-YAP1 or PLKO.1-CopGFP-Puro-shYAP1, at a shuttle plasmid-to-pMD2G:psPAX2 ratio of 5:2:3. After 6 h of transfection, the culture medium was replaced with fresh complete medium (DMEM-F12 supplemented with 10% FBS and 1% penicillin-streptomycin). The cells were cultured at 37°C with 5% CO_2 under high humidity for 24 h and 48 h, after which cell supernatants enriched with YAP1-overexpressing/knockdown lentivirus particles were collected. The lentivirus was concentrated using the PEG-8000 method, and the resulting

lentiviral pellet was dissolved in an appropriate amount of PBS and aliquoted for storage at −80°C. For bPMSC infection, the concentrated viral suspension was applied to the cells. After 48 h of transfection, fluorescence was observed under an inverted fluorescence microscope (ZEISS, Germany).

Preparation of *in vitro* fertilization (IVF) and SCNT embryos

IVF embryos were generated following the procedures outlined in our previous study (Su et al., 2021a). Cumulus-oocyte complexes (COCs) were collected from ovarian follicles, measuring 3–8 mm in diameter, obtained from a slaughterhouse. *In vitro* maturation (IVM) of the oocytes was achieved using an IVM medium (M199 Gibco USA, 10 mmol/L HEPES sigma USA, 10% FBS, 0.01 μg/mL FSH sigma USA, 1 μg/mL LH sigma USA, and 0.01 μg/mL E2 sigma USA). For fertilization, frozen-thawed semen from verified fertile bulls was used. Post-fertilization, the embryos were washed and cultured in BO-IVC medium (71005, IVF Bioscience, UK) at 38.5°C under 5% CO_2 saturation and high humidity.

SCNT was performed as described in our previous study (Su et al., 2021b). Briefly, donor fibroblasts were introduced into the perivitelline space of enucleated oocytes. Successfully reconstructed embryos underwent electrofusion 30 min later and were subsequently cultured in SOF medium at 38.5°C under 5% CO_2 saturation and high humidity for 30 min. All fused embryos were activated in 5 μmol/L ionomycin (sigma USA) for 5 min, followed by incubation in 10 μg/mL cycloheximide (Sigma, USA) for 5 h. The embryos were then transferred to SOF development medium, covered with mineral oil, and cultured at 38.5°C under 5% CO_2 saturation and high humidity. After 48 h, the cells were co-cultured on a granulosa cell layer to support development to the blastocyst stage.

Reverse transcription-quantitative real-time polymerase chain reaction (RT-qPCR)

mRNA from blastocyst-stage embryos was extracted using an Arcturus PicoPure RNA Isolation Kit (65032D, Thermo, USA) following the provided instructions. The isolated mRNA was subsequently reverse-transcribed into cDNA using a PrimeScript II 1st Strand cDNA Synthesis Kit (6210A, Takara, China). For placental tissues and PMSCs, total RNA was extracted using RNAiso Plus, and cDNA synthesis was performed via the HiScript® II Q RT SuperMix for qPCR (+gDNA wiper) (R223-01, Vazyme, China). RT-qPCR assays were carried out using ChamQ Universal SYBR QPCR Master Mix (Q711-02, Vazyme, China) (Supplementary Table S2). The RT-qPCR system and conditions are shown in Supplementary Tables S3 and S4, respectively. Data analysis was conducted using Roche software (LightCycler 480, USA), with Gapdh employed as the reference gene for data normalization. Relative gene expression levels were determined via the $2^{-\triangle\triangle Ct}$ method, and statistical analysis was performed using GraphPad Prism v.8.

Immunofluorescence staining analysis

Cells and embryos were fixed in 4% paraformaldehyde at room temperature for 20 min, followed by three 5 min washes in PBS. The samples were subsequently incubated in permeabilization solution (0.1% Triton X-100) at room temperature for 30 min, then placed in 3% BSA blocking buffer at room temperature for 1 h, followed by three 5 min washes in PBS. The samples were then incubated with primary antibodies overnight at 4°C, including anti-mouse CD105 (sc-18838; 1:100, Santa Cruz Biotechnology, USA), mouse anti-CD90 (sc-53116; 1:100, Santa Cruz Biotechnology, USA), mouse anti-CD44 (sc-7297; 1:100, Santa Cruz Biotechnology, USA), mouse anti-CD29 (sc-374429; 1:100, Santa Cruz Biotechnology, USA), rabbit anti-YAP1 (14074; 1:200, Cell Signaling Technology, USA), and mouse anti-CCND1 (sc-8396; 1:100, Santa Cruz Biotechnology, USA). The samples were then washed three times in PBS (5 min each) and incubated with secondary antibodies, including CoraLite594-conjugated goat anti-rabbit IgG (H+L) (SA00013-4; 1:1 000, Proteintech, China) or CoraLite488-conjugated goat anti-rabbit IgG (H+L) (SA00013-2; 1:1 000, Proteintech, China), at room temperature for 1 h. After removing the secondary antibodies, the samples were washed three times in PBS (5 min each). 4’,6-Diamidino-2-phenylindole (DAPI, D9542, Sigma, USA) was added for nuclear staining, with samples incubated at room temperature in the dark for 15 min, then mounted on glass slides with a fluorescence quenching reagent. After sealing, images were captured using a confocal laser scanning microscope (Nikon A1 plus, Japan). All experiments were performed under the same conditions and parameters for each group.

For immunofluorescence of tissue sections, the paraffin-embedded sections were first deparaffinized, followed by antigen retrieval in 1× citrate buffer repair solution for 20 min. The sections were immersed in a 3% H_2O_2 solution in a light-protected environment at room temperature to block endogenous peroxidase activity. The sections were then placed in a 3% BSA solution for 1 h to block nonspecific binding and incubated overnight at 4°C with primary antibodies, including rabbit anti-YAP1 (14074; 1:200, Cell Signaling Technology, USA) and mouse anti-CCND1 (sc-8396; 1:100, Santa Cruz Biotechnology, USA), followed by incubation with fluorescent-conjugated secondary antibodies at room temperature for 1 h. Finally, the nuclei were stained with DAPI.

Western blot detection

Placental tissues were homogenized with a tissue grinder and placed in protein lysis buffer (990 μL of RIPA and 10 μL of PMSF). PMSCs were similarly collected, resuspended in protein lysis buffer, and incubated on ice for 30 min. The lysates were centrifuged at 4°C and 12 000 r/min for 30 min, and the supernatant was collected as the protein sample. Nuclear and cytoplasmic proteins were extracted using NE-PER Nuclear and Cytoplasmic Extraction Reagent (78835, Thermo, USA). Protein concentrations were determined using a Pierce™ BCA Protein Assay Kit (23225, Thermo, USA). For each sample, 30 μg of protein was mixed with 5× protein loading buffer containing DTT at a 4:1 volume ratio, boiled for 10 min, and then stored at −80°C. Proteins were separated using 10% sodium dodecyl-sulfate polyacrylamide gel electrophoresis (SDS-PAGE) based on molecular weight. After electrophoresis, the proteins were transferred to polyvinylidene fluoride (PVDF) membranes, which were blocked at room temperature in 5% skim milk solution (2.5 g of skim milk powder and 50 mL of TBST) for 1 h. The membranes were then incubated overnight at 4°C with diluted primary antibodies (see Supplementary Table S5 for details). After discarding the primary antibodies, the membranes were washed four times (5 min each) with 1× TBST wash buffer on a rocking platform, then incubated with diluted secondary

antibodies, including HRP-conjugated AffiniPure goat anti-mouse IgG (H+L) (SA00001-1; 1:5 000, Proteintech, China) and HRP-conjugated AffiniPure goat anti-rabbit IgG (H+L) (SA00001-2; 1:5 000, Proteintech, China), at room temperature on a rocking platform for 1 h. After the secondary antibodies were discarded, the membranes were washed three times (10 min each) in 1× TBST wash buffer on a rocking platform. The chemiluminescent substrate was prepared by mixing luminol reagent and peroxide solution at a 1:1 ratio (32209, Thermo, USA) and applied evenly to the membrane surface. The membranes were then enclosed in self-sealing bags, ensuring the removal of any air bubbles. Exposure was performed using a chemiluminescent gel imaging system. Images were saved in the desired format, and grayscale quantification was performed using ImageJ software.

Hematoxylin and eosin (H&E) staining and immunohistochemical analysis of bovine placental tissues

Placental tissues from both CON and SCNT cattle were embedded in paraffin, cut into 5 μm-thick sections, mounted on adhesive slides, and dried at 42°C. The sections were then subjected to a series of ethanol treatments (100%, 95%, 85%, and 70%), followed by appropriate hematoxylin staining, differentiation in 1% hydrochloric acid in ethanol (concentrated hydrochloric acid and 75% ethanol), dehydration, and the addition of eosin staining solution. After subsequent treatments in 95% and 100% ethanol and incubation in xylene, the sections were sealed with neutral resin. Immunohistochemical staining involved deparaffinization and rehydration of paraffin-embedded sections, antigen retrieval, serum blocking, incubation with primary and secondary antibodies, and immunofluorescence staining of the same sections. DAB staining reagent (AR1022, Boster, China) was added to the sections, and staining time was observed under a microscope to determine the appropriate duration. Hematoxylin was used to stain the cell nuclei, followed by differentiation and bluing with differentiation solution and bluing reagent, respectively. After dehydration, the sections were sealed, and images were obtained using a microscope (Nikon ECLIPSE 80i, Japan).

Cell proliferation assay

CON and SCNT bPMSCs were seeded in 96-well plates at a density of 2×10^3/100 μL per well and cultured at 37°C with 5% CO_2 saturation for 24, 48, 72, 96, and 120 h. At different time points, 10 μL of Cell Counting Kit-8 (CCK-8) reagent (K1018, Apexbio, USA) was added to each well, followed by 2 h of incubation in the dark at 37°C with 5% CO_2. Optical density (OD) at 450 nm was subsequently measured using a microplate reader (Thermo, USA). Following the manufacturer's instructions, bPMSC proliferation was assessed using an EdU Imaging Kit (Cy3) (K1075, Apexbio, USA). EdU was added to the culture medium of both CON and SCNT bPMSCs, which were subsequently incubated overnight to label the cells. The cells were then fixed with 4% paraformaldehyde at room temperature for 15 min, followed by permeabilization with 0.5% Triton X-100 at room temperature for 20 min. The cells were subsequently incubated with 1× EdU buffer additive working solution and Click reaction solution at room temperature in the dark for 30 min. Finally, the cell nuclei were stained with DAPI, and image acquisition was performed via confocal microscopy (Nikon A1R, Japan).

Flow cytometry was used to analyze the cell cycle of the bPMSCs. Initially, cells were collected and placed in prechilled 70% ethanol for overnight fixation at 4°C. The cells were then incubated in a premade propidium iodide staining solution at 37°C for 30 min in the dark. Cell cycle analysis was carried out using a Cytoflex flow cytometer, and the percentages of cells in the G0/G1 and S phases were calculated and analyzed with FlowJo software.

Chromatin Immunoprecipitation (ChIP) and ChIP-qPCR analysis

ChIP was conducted using a Simple ChIP Plus Enzymatic Chromatin IP Kit (9005, Cell Signaling Technology, USA), following the manufacturer's instructions. In brief, cells were exposed to 1% formaldehyde at room temperature for 10 min to cross-link chromatin, with the reaction stopped by the addition of glycine. After the samples were collected and chromatin was enzymatically fragmented using the provided mixed buffer. Agarose gel electrophoresis verified that the chromatin fragments fell within the 150–900 bp range. Fragmented chromatin was subsequently subjected to ChIP using a YAP1 antibody (14074, Cell Signaling Technology, USA, 14074, 10 μg/tube) and IgG (included in the kit, 2 μg/tube). Precipitated DNA samples were quantified using quantitative real-time PCR (qPCR), with results expressed as a percentage of input DNA.

Luciferase assay

Using the 2 000 bp upstream region of the CCND1 gene as the promoter sequence from NCBI, YAP1 binding sites on the CCND1 promoter were predicted using the JASPAR database (http://jaspar.binf.ku.dk/cgi-bin/jaspar_db.pl) and corresponding binding primers were designed accordingly (Supplementary Table S6). A recombinant plasmid containing the CCND1 luciferase reporter gene was subsequently constructed using the psiCHECK-2 vector. The CCND1 promoter region (upstream 2 000 bp) was divided into three segments based on predicted binding sites: (-579-1), (-1458-579), and (-2000-1458). Recombinant plasmids psiCHECK-2-pCCND1, psiCHECK-2-(pCCND1-579-1), psiCHECK-2-(pCCND1-1458-579), and psiCHECK-2-(pCCND1-2000-1458) were then generated. Luciferase reporter gene activity was then measured using the Dual-Luciferase Reporter Assay System and a luminometer (Thermo, USA), following the manufacturer's instructions.

Coimmunoprecipitation detection

The bPMSCs were prepared by adding prechilled IP lysis/wash buffer, followed by incubation on ice for 5 min. Cells were then collected, sonicated, and centrifuged at 4°C and 13 000 ×*g* for 10 min. The resulting supernatant was used to determine protein concentration. Immunoprecipitation was conducted using a Pierce Co-Immunoprecipitation (Co-IP) Kit (26149, Thermo, USA) according to the manufacturer's instructions. Antibodies were incubated with the resin and covalently crosslinked. The antibody-conjugated resin was then incubated with 200 μL of bPMSC protein lysate at 4°C overnight. After washing, the antibody-bound protein complexes were eluted, and protein blot analysis was performed as described previously.

Quantification and statistical analysis

All values are expressed as means ± standard error of the mean (SEM). GraphPad Prism v.8 was used to analyze the significance of differences, with one-way analysis of variance

(ANOVA) used for multiple group comparisons and Student's *t*-test used for two-group comparisons. *P*-values less than 0.05 were considered statistically significant (*: $P<0.05$; **: $P<0.01$; ***: $P<0.001$, or as indicated in the figure legends). All experiments were repeated three times for both technical and biological replicates.

RESULTS

Abnormal placental tissue and placental RNA-seq analysis in SCNT cattle

Comparative analysis of cloned and CON cattle during gestation and the perinatal period revealed that cloned cattle experienced prolonged gestation periods, increased abdominal circumferences during the perinatal period, and significantly higher birth weights of SCNT calves (Supplementary Figure S1A–F). Postpartum assessment of placental cotyledons demonstrated a significant reduction in cotyledon number in SCNT cattle ($P<0.05$), accompanied by a marked increase in cotyledon length and width ($P<0.001$) (Figure 1A–D; Supplementary Figure S1C). Histological examination indicated substantial changes, including a significant increase in binucleate trophoblast giant cells within SCNT placental tissue, disordered arrangement of uterine epithelial cells (UE), and a significant increase in interstitial villi within the chorionic membrane (Figure 1E, F; Supplementary Figure S1G). To investigate the underlying molecular mechanisms contributing to placental enlargement in SCNT cattle, RNA-seq was performed on SCNT placental tissue, identifying many DEGs. These DEGs were primarily involved in biological functions such as cell morphogenesis, cell motility, cell migration, cell localization, cellular stress response, cell cycle, and cytoskeletal organization (Supplementary Figure S1H, I). These genes were also significantly enriched in the PI3K-AKT and Hippo pathways (Figure 1G), suggesting a potential link between placental overgrowth in cloned cattle and dysregulated gene expression within these pathways. Focusing on genes with co-regulatory roles in both the PI3K-AKT and Hippo pathways, further analysis identified three genes with significant differential expression, including cyclin D1 (*Ccnd1*), protein phosphatase 2 regulatory subunit B (*Ppp2r2b*), and fibroblast growth factor 1 (*Fgf1*), with *Ccnd1* exhibiting the most pronounced expression change (Figure 1H–J; Supplementary Figure S1J, K).

Colocalized expression regulation analysis of *Yap1* and *CCND1* in SCNT and CON cattle placental tissues

To explore the regulatory mechanisms behind placental enlargement in SCNT cattle, bPMSCs were isolated from both SCNT and CON cattle for experimental analysis. The isolated bPMSCs exhibited a spindle-like elongated morphology and a whirlpool-like growth pattern (Supplementary Figure S2A). Surface marker profiling confirmed these cells were positive for CD29, CD44, CD90, and CD105 but negative for the hematopoietic stem cell marker CD34 (Supplementary Figure S2B). Furthermore, these bPMSCs successfully differentiated into osteogenic and adipogenic lineages *in vitro* (Supplementary Figure S2C, D), validating their suitability for further experimental research.

Given the significant enrichment of the Hippo and PI3K-AKT signaling pathways observed in the RNA-seq data from SCNT placental tissues, further research was conducted on two key regulatory factors within these pathways, *Yap1* and *Ccnd1*. The Hippo pathway is known to influence organ size and volume, while CCND1 plays a critical role in cell cycle regulation (Cheraghi et al., 2015; Heallen et al., 2011). Immunofluorescence analysis demonstrated colocalization of Yap1 and CCND1 in SCNT and CON placental tissues (Figure 2A), bPMSCs (Figure 2C), and preimplantation blastocysts (Figure 2E), with higher immunofluorescence intensities for YAP1 and CCND1 in the SCNT groups (Figure 2B, D, F). Immunohistochemical analyses further corroborated these findings, showing significantly elevated YAP1 and CCND1 protein levels in SCNT placental tissues compared to the CON group (Supplementary Figure S3A, B). RT-qPCR analysis confirmed that *Yap1* and *Ccnd1* expression levels in SCNT placental tissues, bPMSCs, and preimplantation blastocysts were significantly higher than in the CON group (Supplementary Figure S3C–E). Additionally, stage-specific Immunofluorescence of YAP1 during preimplantation embryo development revealed prominent nuclear expression. Specifically, YAP1 expression was significantly elevated at the 8-cell stage compared to the CON group and further increased at the 16-cell and blastocyst stages (Supplementary Figure S3F, G). These results demonstrate that YAP1 and CCND1 are expressed at higher levels in the placental tissues, bPMSCs, and preimplantation embryos of the SCNT group compared to the CON group, with these expression differences emerging in the early developmental stages of the cloned embryos.

Elevated YAP1 and CCND1 expression in SCNT bPMSCs and cell proliferation and cell cycle regulation

The above findings demonstrated that YAP1 and CCND1 exhibit colocalized expression patterns in tissues, bPMSCs, and embryos. Given that YAP1 regulates cell proliferation and cell cycle progression, impacting organ size (Heallen et al., 2011), we further investigated whether YAP1 regulates CCND1 and subsequently affects cell proliferation in SCNT-derived bPMSCs, potentially contributing to abnormal placental development in cloned cattle.

Fluorescence EdU analysis revealed a significantly higher proportion of newly synthesized DNA in SCNT bPMSCs compared to CON bPMSCs ($P<0.01$), indicating a markedly enhanced proliferative capacity in the SCNT group (Figure 3A, B). Cell cycle analysis showed a significant reduction in the proportion of SCNT bPMSCs in the G0/G1 phase and a corresponding increase in the S-phase population relative to CON bPMSCs (Figure 3C; Supplementary Figure S4A). To further assess proliferation dynamics, CCK-8 assays were conducted at 0, 24, 48, 72, 96, and 120 h. At 24 h, no significant difference was observed between SCNT and CON bPMSCs ($P>0.05$); however, SCNT bPMSCs displayed significantly enhanced proliferation at 48–72 h ($P<0.05$) and at 96–120 h ($P<0.01$) (Figure 3D). Collectively, these findings suggest that SCNT bPMSCs exhibit accelerated cell division and proliferative capacity.

Previous research has shown that the YAP1 protein, when dephosphorylated, is translocated into the nucleus, where it activates the transcription of downstream target genes, driving cell growth, proliferation, differentiation, and migration (Mizuno et al., 2012). To investigate YAP1 signaling in SCNT and CON bPMSCs and placental tissues, we analyzed the distribution and phosphorylation status of YAP1 in both the cytoplasm and nucleus. Western blot analysis revealed a significant increase

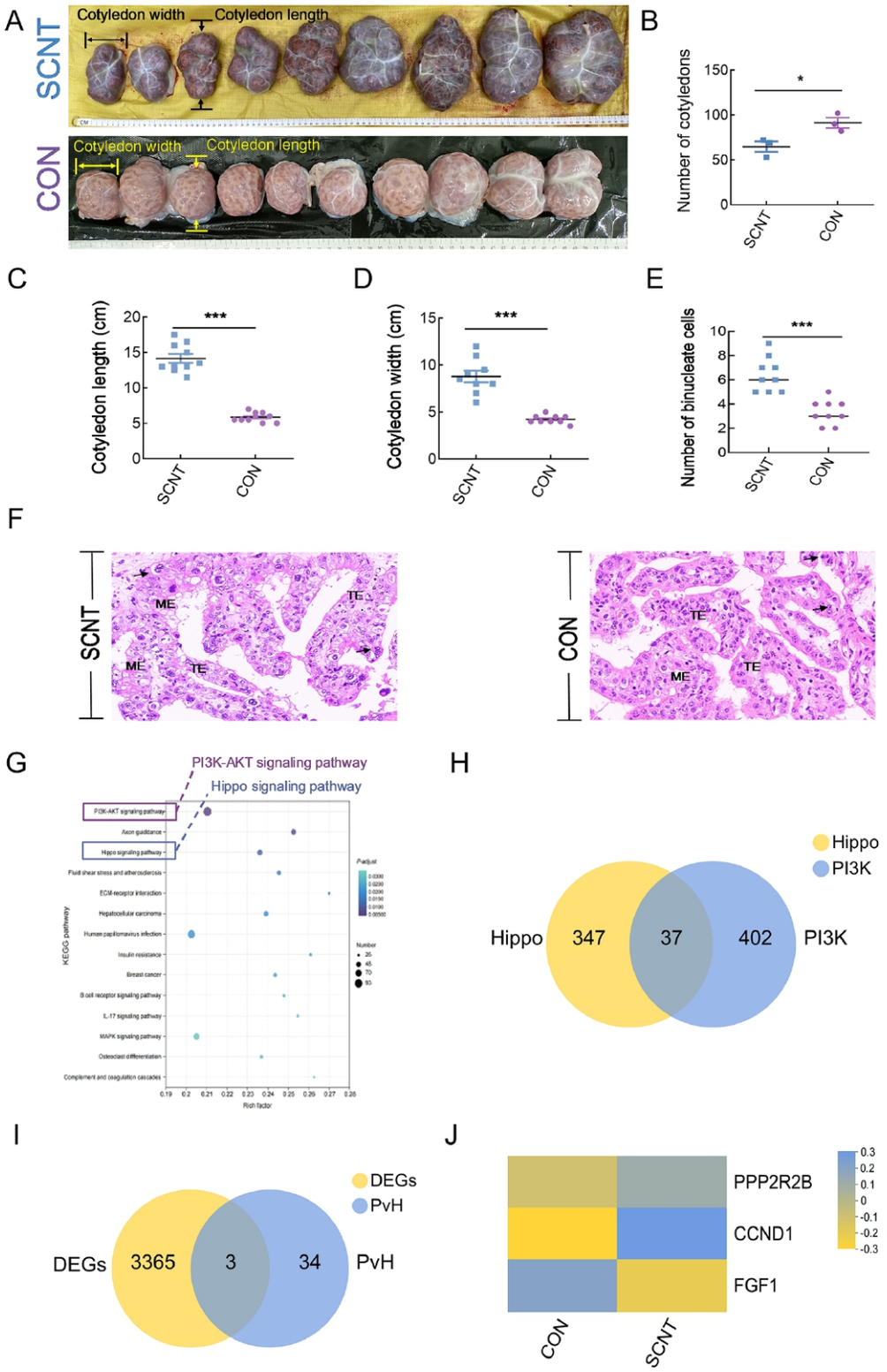


Figure 1 Morphological analysis of placental tissues and RNA-seq transcriptome of cloned and control (CON) cattle

A: Morphological size and distribution of placental cotyledons in SCNT and CON groups. B: Statistical analysis of number of placental cotyledons in SCNT and CON groups. C: Comparison of cotyledon length between SCNT and CON groups. D: Comparison of cotyledon width between SCNT and CON groups. E: Statistical analysis of number of binucleated cells in SCNT and CON bovine placentas. F: Histological staining of chorionic membrane structure in SCNT and CON bovine placentas (H&E staining, TE, trophoblast epithelium; ME, mesenchyme; arrows, binucleate giant cells); Scale bars: 100 μm. G: KEGG enrichment analysis of DEGs in placental tissues of SCNT and CON groups. H: Significant DEGs involved in PI3K-AKT and Hippo signaling pathways in placental tissues of SCNT and CON groups. I: Selection of significant DEGs commonly regulated in PI3K-AKT and Hippo signaling pathways in placental tissues of SCNT and CON groups. J: Cluster analysis of *CCND1*, *PPP2R2B*, and *FGF1* genes in placental tissues of SCNT and CON groups. Graphs show mean±SEM, data are representative of three independent experiments. “PvH” refers to DEGs within PI3K-Akt and Hippo signaling pathways. *: $P<0.05$; **: $P<0.01$; ***: $P<0.001$; ns: Not significant.

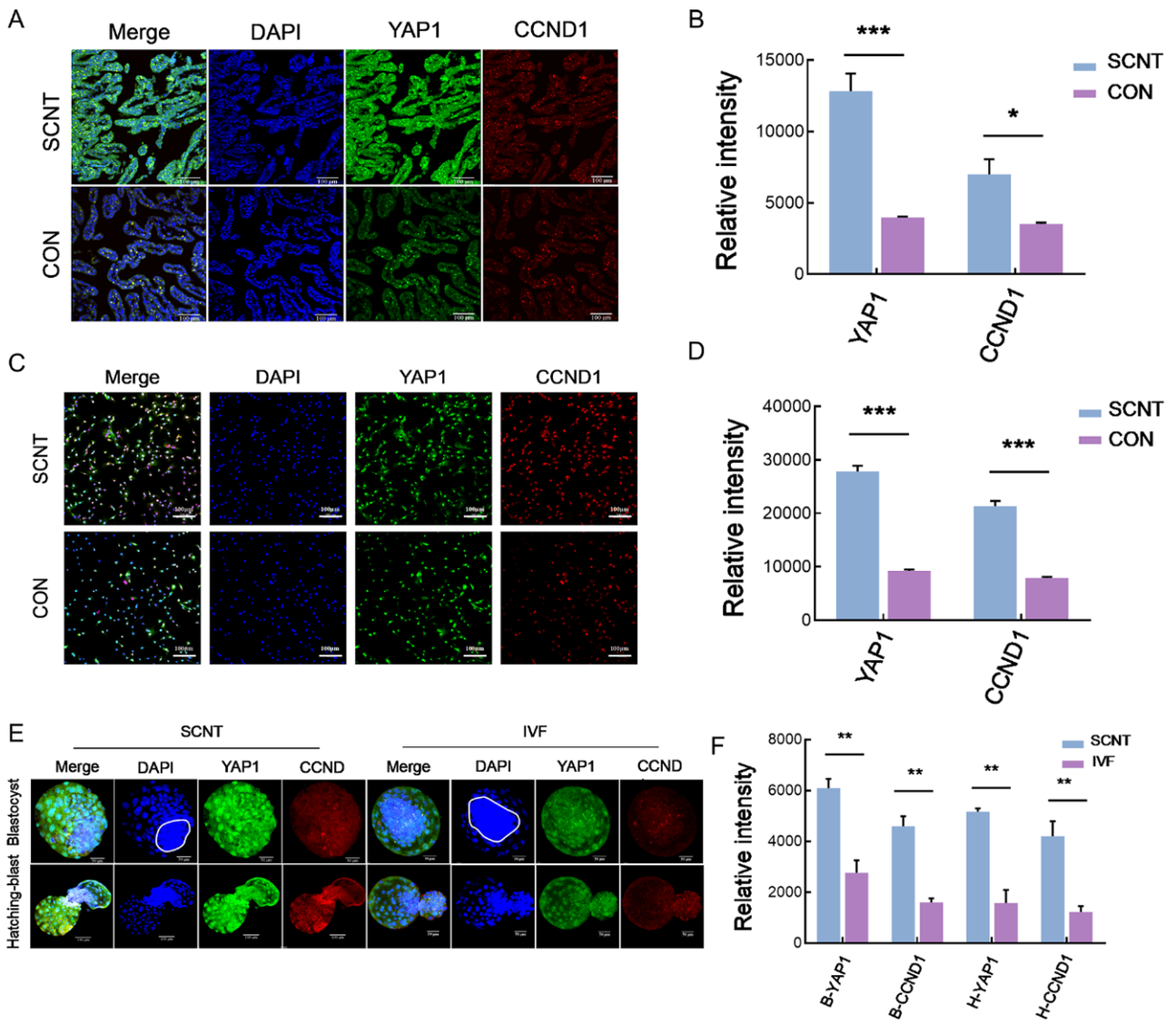


Figure 2 Detection of YAP1 and CCND1 expression levels in placental tissues, bPMSCs, and blastocyst-stage embryos of SCNT and IVF groups

A: Immunofluorescence (IF) detection of YAP1 and CCND1 protein expression in SCNT and CON placental tissues; Scale bars: 100 μm. B: IF relative intensity analysis of YAP1 and CCND1 in SCNT and CON placental tissues. C: IF detection of YAP1 and CCND1 expression in bPMSCs of SCNT and CON groups; Scale bars: 200 μm. D: IF relative intensity analysis of YAP1 and CCND1 in bPMSCs of SCNT and CON groups. E: IF detection of YAP1 and CCND1 expression in SCNT and IVF blastocysts; inner cell mass (ICM) region of blastocysts is marked with a white circle. Scale bars: 50 μm. F: IF relative intensity analysis of YAP1 and CCND1 in SCNT and IVF blastocysts. Graphs show mean±SEM, data are representative of three independent experiments. *: P<0.05; **: P<0.01; ***: P<0.001.

in YAP1 and CCND1 protein expression in SCNT bPMSCs (P<0.001). Nuclear YAP1 (Nuc-YAP1) and cytoplasmic YAP1 (Cyto-YAP1) levels in SCNT bPMSCs were significantly higher than those in the CON group (P<0.05), while phosphorylated YAP1 at serine 127 (P-YAP1-S127) and serine 397 (P-YAP1-S397) was significantly lower (Figure 3E, F). These findings were validated in placental tissue, which showed consistent expression trends at the cellular level (Supplementary Figure S4B, C). These results indicate that YAP1 levels are significantly higher in SCNT bPMSCs than in CON bPMSCs, with reduced phosphorylation, suggesting increased nuclear localization and functional activity of YAP1. The expression of CCND1 in SCNT bPMSCs showed a similar trend to that of YAP1, further suggesting a positive regulatory relationship between YAP1 and CCND1 in these cells.

To further explore the mechanisms driving cell proliferation, we examined cyclin-dependent kinases (CDKs), cell cycle inhibitory genes, and proliferation markers known to influence this process. CCND1, as a regulatory subunit, forms complexes with CDK4 or CDK6 (Aggarwal et al., 2010). These cyclin-dependent kinases are indispensable for G1 to S phase transition. CCND1 is also recognized as an oncogene, and its overexpression can lead to uncontrolled cell proliferation and malignancy (Wang et al., 2006; Zhong et al., 2010). Here, RT-qPCR and western blot analyses confirmed significant up-regulation of cell proliferation-related proteins, including CDK4, CDK6, proliferating cell nuclear antigen (PCNA), MYC proto-oncogene, Bhlh transcription factor (C-MYC), and Ki-67 (Ki67) in the SCNT group. Conversely, the expression of cyclin-inhibiting genes, such as cyclin-dependent kinase inhibitor 2A (CDKN2A), CDKN2B, and CDKN2C, was significantly down-regulated in the SCNT group (Figure 3G–I).

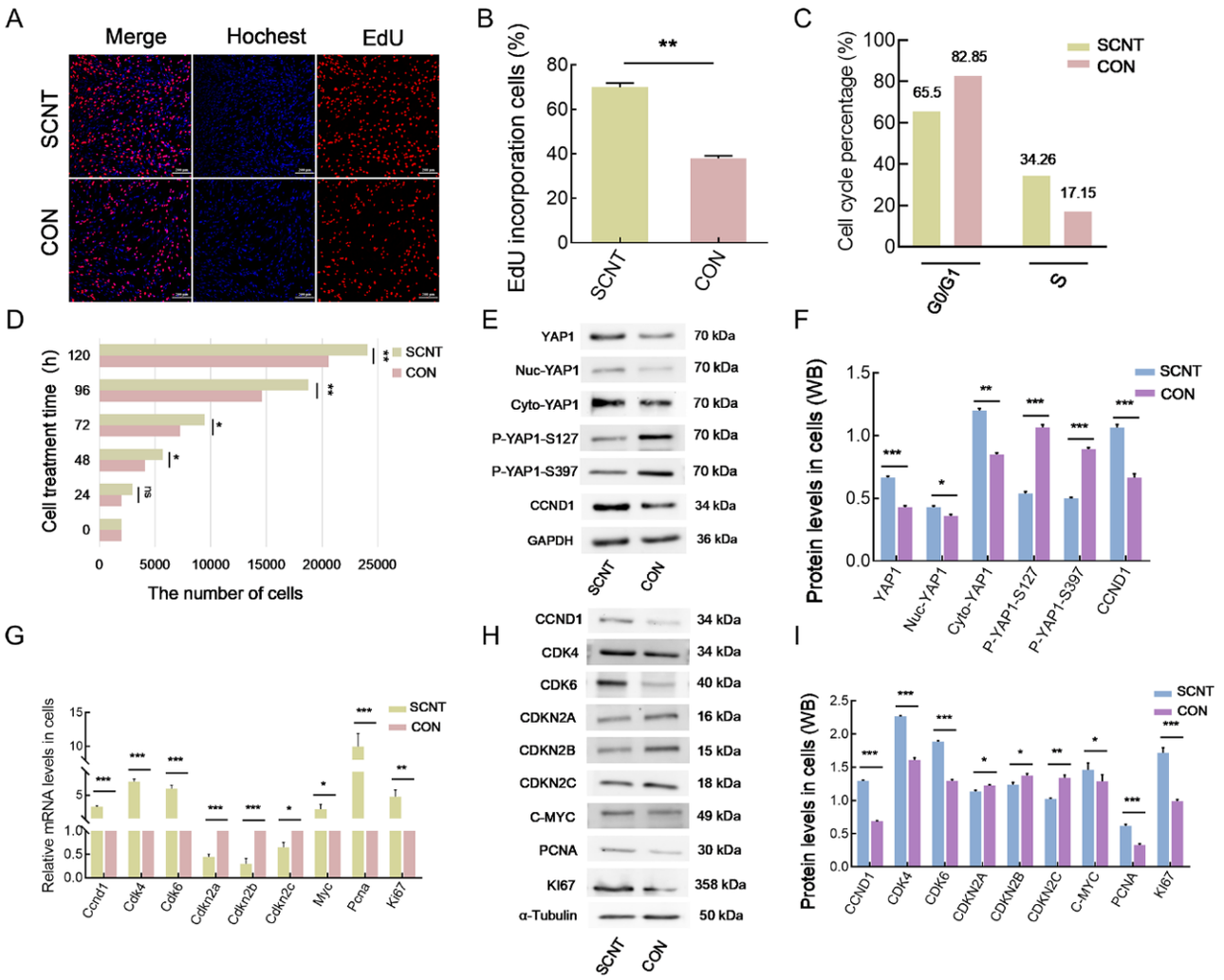


Figure 3 Proliferation analysis of bPMSCs and expression analysis of cell cycle-related genes in SCNT and CON groups

A: EdU proliferation assay of SCNT and CON bPMSCs. Scale bars: 200 μm. B: Statistical analysis of EdU proliferation data in SCNT and CON bPMSCs. C: Cell cycle distribution analysis of SCNT and CON bPMSCs. D: Proliferation assay of SCNT and CON bPMSCs at 0, 24, 48, 72, 96, and 120 h by CCK-8 assay, respectively. E: Western blot analysis of CCND1, YAP1, and phosphorylated YAP1 protein levels in SCNT and CON bPMSCs, respectively. F: Grayscale analysis of CCND1, YAP1, and phosphorylated YAP1 proteins in SCNT and CON bPMSCs. G: RT-qPCR analysis of mRNA expression levels of cell cycle-related genes (*Ccnd1*, *Cdk4*, *Cdk6*, *Cdkn2a*, *Cdkn2b*, *Cdkn2c*, *Myc*, *Pcna*, and *Ki67*) in SCNT and CON bPMSCs. H: Western blot analysis of protein expression levels of cell cycle-related proteins (CCND1, CDK4, CDK6, CDKN2A, CDKN2B, CDKN2C, MYC, PCNA, and KI67) in SCNT and CON bPMSCs. I: Grayscale analysis of cell cycle-related proteins in SCNT and CON bPMSCs. Graphs show mean±SEM, data are representative of three independent experiments. *: P<0.05; **: P<0.01; ***: P<0.001; ns: Not significant.

In summary, SCNT bPMSCs presented enhanced DNA synthesis, accelerated cell cycle progression, and increased expression of CCND1-associated cyclin-dependent kinases and proliferation-related genes compared to CON bPMSCs.

Regulation of YAP1 gene expression affects bPMSC proliferation

In light of the colocalization relationship between CCND1 and YAP1, we further investigated whether YAP1 regulates the proliferation of bPMSCs in cloned cattle and its potential interaction with CCND1. Overexpression and knockdown vectors for YAP1 were first constructed and transfected into SCNT and CON bPMSCs, establishing YAP1-overexpressing ($CON^{OE\text{-}YAP1}$) and YAP1-knockdown ($CON^{sh\text{-}YAP1}$, $SCNT^{sh\text{-}YAP1}$) bPMSCs for subsequent validation studies (Supplementary Figure S5A, B). Western blot and qPCR analyses confirmed successful YAP1 transfection in bPMSCs, showing a significant increase in YAP1 mRNA and protein expression levels in both the nucleus and cytoplasm of $CON^{OE\text{-}YAP1}$ cells (Supplementary Figure S5C–F). Furthermore, four YAP1-targeted shRNAs were designed, and the lentiviral-mediated plasmid pLKO.1-copGFP-shYAP1 was transfected into SCNT/CON bPMSCs. Of these, shYAP1-4 exhibited the highest efficiency in inhibiting YAP1 mRNA and protein expression, allowing the selection of stably transfected $SCNT^{sh\text{-}YAP1}$ and $CON^{sh\text{-}YAP1}$ cell lines via puromycin treatment. Additionally, the application of the YAP1 inhibitor verteporfin in SCNT bPMSCs restored YAP1 expression to levels comparable to those in the CON group (Supplementary Figure S5C–E).

The proliferation capacities of $SCNT^{sh\text{-}YAP1}$, $SCNT^{Verteporfin}$, $CON^{OE\text{-}YAP1}$, $CON^{sh\text{-}YAP1}$, and $CON^{Verteporfin}$ bPMSCs were assessed and compared to CON and SCNT bPMSCs. Results indicated that the proportion of newly synthesized DNA to total DNA in $CON^{OE\text{-}YAP1}$ bPMSCs was significantly higher than that in CON bPMSCs and similar to the level observed in SCNT bPMSCs. In contrast, the proportion of newly synthesized

DNA to total DNA in $CON^{sh\text{-}YAP1}$ and $CON^{Verteporfin}$ bPMSCs was significantly lower than in CON bPMSCs. Additionally, the proportion of newly synthesized DNA to total DNA in $SCNT^{sh\text{-}YAP1}$ and $SCNT^{Verteporfin}$ bPMSCs was significantly lower than that in SCNT bPMSCs and similar to the levels observed in CON bPMSCs (Figure 4A, B). Further proliferation assays over 24, 48, 72, 96, and 120 h revealed that the $CON^{OE\text{-}YAP1}$ bPMSCs displayed a significantly enhanced proliferative capacity compared to CON bPMSCs, similar to that of SCNT bPMSCs. Conversely, both $CON^{sh\text{-}YAP1}$ and $CON^{Verteporfin}$ bPMSCs demonstrated significantly lower proliferative capacity than that of CON (Figure 4C). Additionally, the proliferative capacity of $SCNT^{sh\text{-}YAP1}$ and $SCNT^{Verteporfin}$ bPMSCs was significantly lower than that of SCNT bPMSCs and similar to that of CON bPMSCs (Figure 4C). RT-qPCR analysis of cell cycle and cell proliferation-related gene expression in $CON^{OE\text{-}YAP1}$ bPMSCs revealed up-regulation of *Ccnd1*, *Cdk4*, *Cdk6*, *Myc*, *Pcna*, and *Ki67* to levels comparable to those in SCNT bPMSCs. Simultaneously, the expression levels of *Cdkn2a*, *Cdkn2b*, and *Cdkn2c* were reduced (Supplementary Figure S5G).

Cell cycle analysis revealed that the proportion of $CON^{OE\text{-}YAP1}$ bPMSCs in the G0/G1 phase was significantly lower than that of CON bPMSCs, while the proportion of cells in the S phase was significantly higher, similar to the distribution observed in SCNT bPMSCs. Conversely, the proportion of cells in the G0/G1 phase in $CON^{sh\text{-}YAP1}$ and $CON^{Verteporfin}$ bPMSCs was significantly higher than that in CON bPMSCs, while the proportion of cells in the S phase was significantly lower. In $SCNT^{sh\text{-}YAP1}$ and $SCNT^{Verteporfin}$ bPMSCs, the proportion of cells in the G0/G1 phase was significantly higher than that in SCNT bPMSCs, while the proportion of cells in the S phase was significantly lower, similar to the distribution observed in CON bPMSCs (Figure 4D; Supplementary Figure S6).

YAP1-mediated regulation of CCND1 expression in bPMSCs

Considering the proliferative effect of YAP1 overexpression and the inhibitory effect of YAP1 knockdown on bPMSCs, we conducted RT-qPCR and western blot analyses to further confirm the impact of YAP1 expression changes on CCND1 expression. In CON, $CON^{OE\text{-}YAP1}$, $CON^{sh\text{-}YAP1}$, and $CON^{Verteporfin}$ bPMSCs, YAP1 and CCND1 mRNA and protein expression levels followed a similar expression pattern (Figure 5A–C). However, YAP1 knockdown in SCNT bPMSCs led to a significant down-regulation in CCND1 expression, similar to the levels observed in CON bPMSCs (Figure 5D–F). These findings indicate that YAP1 positively regulates CCND1 expression in bPMSCs.

To further validate the specific regulatory relationship between YAP1 and CCND1, Co-IP, luciferase, and ChIP-qPCR assays were conducted. The Co-IP results demonstrated co-expression of YAP1 and CCND1 protein in bPMSCs (Input). In control assays using IgG, neither YAP1 nor CCND1 was precipitated, indicating that these proteins did not bind to IgG. However, immunoprecipitation targeting the YAP1 protein successfully precipitated CCND1 (Figure 5G), and vice versa (Figure 5H), indicating a direct interaction between YAP1 and CCND1 proteins.

The impact of *Yap1* on *Ccnd1* promoter activity was assessed using a dual-luciferase reporter system, with the *Ccnd1* promoter inserted into the psiCHECK-2 vector. SCNT bPMSCs with elevated *Yap1* expression exhibited significantly increased activity of the psiCHECK-2-pCCND1 and psiCHECK-2-(pCCND1-1458-579) promoters, with the psiCHECK-2-(pCCND1-579-1) promoter showing a marked increase. However, no significant activity change was observed with the psiCHECK-2-(pCCND1-2000-1458) promoter. In SCNT bPMSCs, *Ccnd1* promoter activity was significantly increased, indicating that YAP1 has a promoting effect on the *Ccnd1* promoter (Figure 5I). These findings suggest that YAP1 promotes *Ccnd1* expression by binding to the proximal promoter (pCCND1-579-1). ChIP-qPCR analysis confirmed increased YAP1 binding to the *Ccnd1* promoter in SCNT bPMSCs with elevated YAP1 expression (Figure 5J). These results indicate that YAP1 up-regulates *Ccnd1* expression by binding directly to its proximal promoter.

YAP1 promotes G0/G1-S transition in bPMSCs via the CCND1-CDK6 pathway

To further investigate the mechanism by which YAP1 promotes SCNT bPMSC proliferation through CCND1 up-regulation, we exposed SCNT bPMSCs to the CDK4/CDK6 inhibitor BSJ-03-204 (inhibitory concentrations of 26.9 nmol/L for CDK4/CCND1 and 10.4 nmol/L for CDK6/CCND1) and assessed their cell proliferative capacity. Western blot and RT-qPCR analyses demonstrated that YAP1 overexpression in the CON group led to increased CDK4 and CDK6 expression (Figure 6A–C). Furthermore, inhibition of CDK6 (SCNT-CDK6) significantly reduced the proportion of S-phase cells among SCNT bPMSCs, resulting in proliferation levels similar to those observed in CON bPMSCs. Inhibition of CDK4 (SCNT-CDK4) also reduced the proportion of S-phase cells, although the effect was less pronounced than that of CDK6 (Figure 6D–F). These findings indicate that YAP1 drives the G0/G1-S phase transition in SCNT bPMSCs predominantly via the CCND1-CDK6 pathway.

DISCUSSION

SCNT has emerged as a valuable and promising tool with significant implications for agricultural and medical applications. Advances in SCNT and related biotechnology have played a critical role in germplasm conservation, maintaining genetic diversity and enhancing adaptability in agricultural species. Despite the potential benefits offered by assisted reproductive technologies in cattle, pregnancies derived from cloning technologies present numerous challenges, including abnormal placental phenotypes and health issues in newborns and surrogate mothers. Furthermore, the reproductive efficiency of SCNT remains suboptimal, with success rates consistently below 5%, compounded by low pregnancy rates, high incidences of pregnancy loss, and a multitude of fetal and placental abnormalities (Arnold et al., 2008; Matoba & Zhang, 2018; Yang et al., 2007). In SCNT mouse models, placental tissues exhibit pronounced trophoblast layer expansion, accompanied by destruction of the labyrinth layer, trophoblast cell hypertrophy, and abnormal increase in glycogen cell number, ultimately resulting in the abnormal proliferation of placental tissue (Wakisaka-Saito et al., 2006; Whitworth & Prather, 2010). Similarly, morphological analyses of SCNT-derived pig placentas have highlighted severe abnormalities, including reduced columnar epithelial cells, decreased placental villi density, underdeveloped nutritive layer cells, impaired vascularization, and reduced placental weight (Chae et al.,

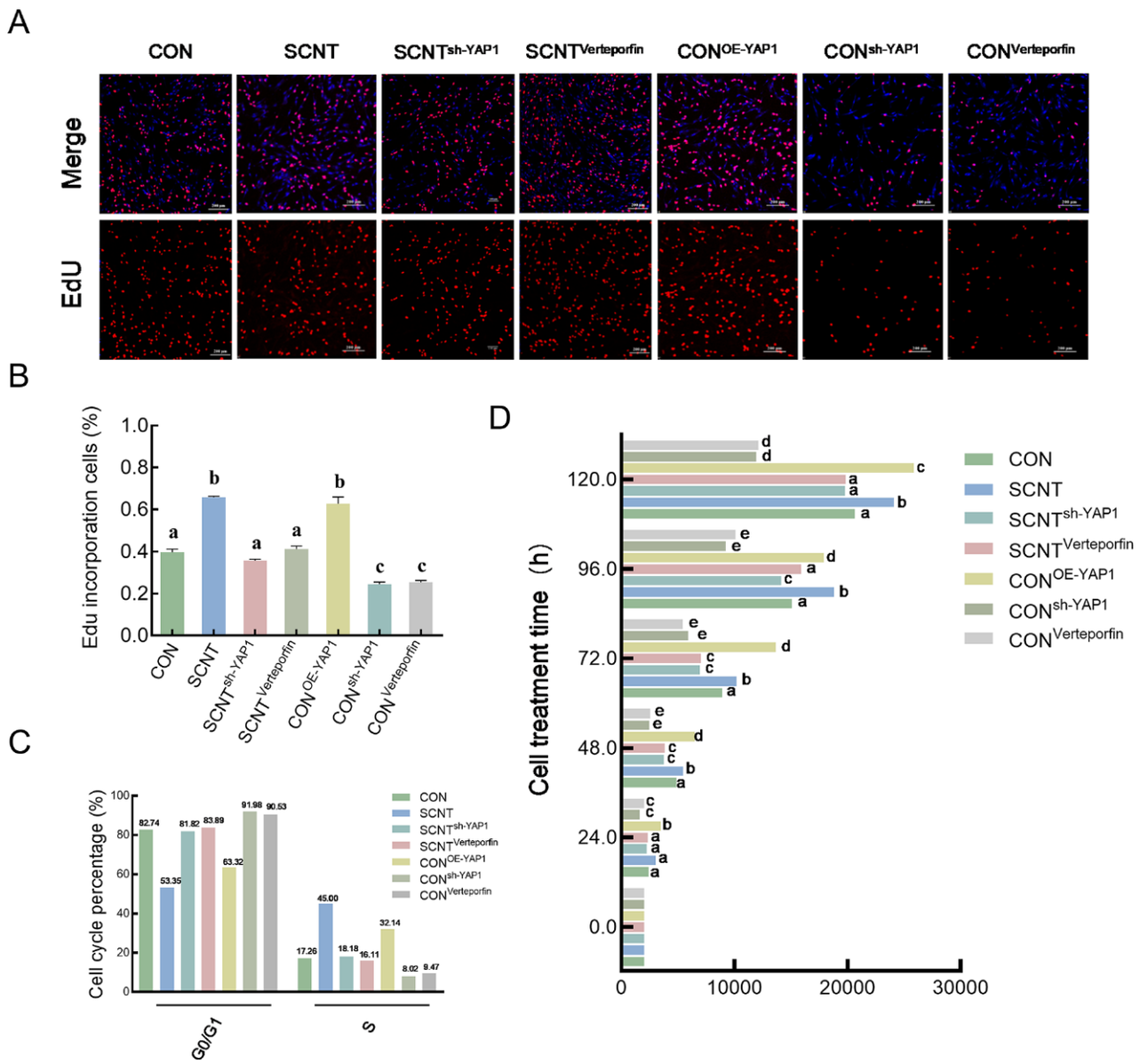


Figure 4 YAP1 promotes bPMSC proliferation

A: Proliferative capacity assay of different YAP1 overexpression and YAP1 gene knockout bPMSC groups by EdU. Scale bars: 200 μm. B: Statistical analysis of proliferation detected by EdU assay in bPMSCs with YAP1 overexpression and YAP1 gene knockout. C: Proliferation assay of different YAP1 overexpression and YAP1 gene knockout bPMSC groups by CCK-8 method at 0, 24, 48, 72, 96, and 120 h, respectively. D: Statistical analysis of cell cycle distribution in different YAP1 overexpression and YAP1 gene knockout bPMSCs groups. sh-YAP1 and verteporfin represent down-regulation of YAP1 expression, while OE-YAP1 represents overexpression of YAP1.Graphs show mean±SEM, data are representative of three independent experiments. Same letters indicate no significant differences (P>0.05), and different letters indicate significant differences (P<0.05).

2006; Lee et al., 2007; Park et al., 2009). In SCNT-derived cattle, placental abnormalities are also present and widespread. Notably, over 50% of pregnancies result in miscarriage during the first trimester (Hill et al., 2000). Furthermore, early-stage pregnancies frequently exhibit reduced placental cotyledons, increased placental dysplasia, and reduced vascularization (Hill, 2014). Between days 30 and 90 of gestation, SCNT-derived bovine placentas often show abnormal villous epithelium development, allantoic dysplasia, and vascular defects, leading to a decrease in cotyledon number (Biase et al., 2016; Chavatte-Palmer et al., 2006). Between days 100 and 150, cotyledon count in cloned bovine placentas decreases further, while uterine caruncle weight increases significantly (Chavatte-Palmer et al., 2006). In addition, crypt expansion on the caruncle surface aggregates individual villi into composite structures, further exacerbating placental abnormalities (Miglino et al., 2007).

In this study, SCNT cattle exhibited significantly prolonged gestation periods and markedly increased abdominal circumference during the perinatal period. Birth weights of SCNT calves were significantly higher than those in the CON group. Additionally, morphological analysis of SCNT placentas revealed a substantial reduction in the number of cotyledons (>2 cm), accompanied by a significant increase in cotyledon length and width. Histological assessment of placental tissue identified several abnormalities, including a significant increase in binucleate giant cells, disordered arrangement of cuboidal uterine epithelial cells, and a pronounced increase in

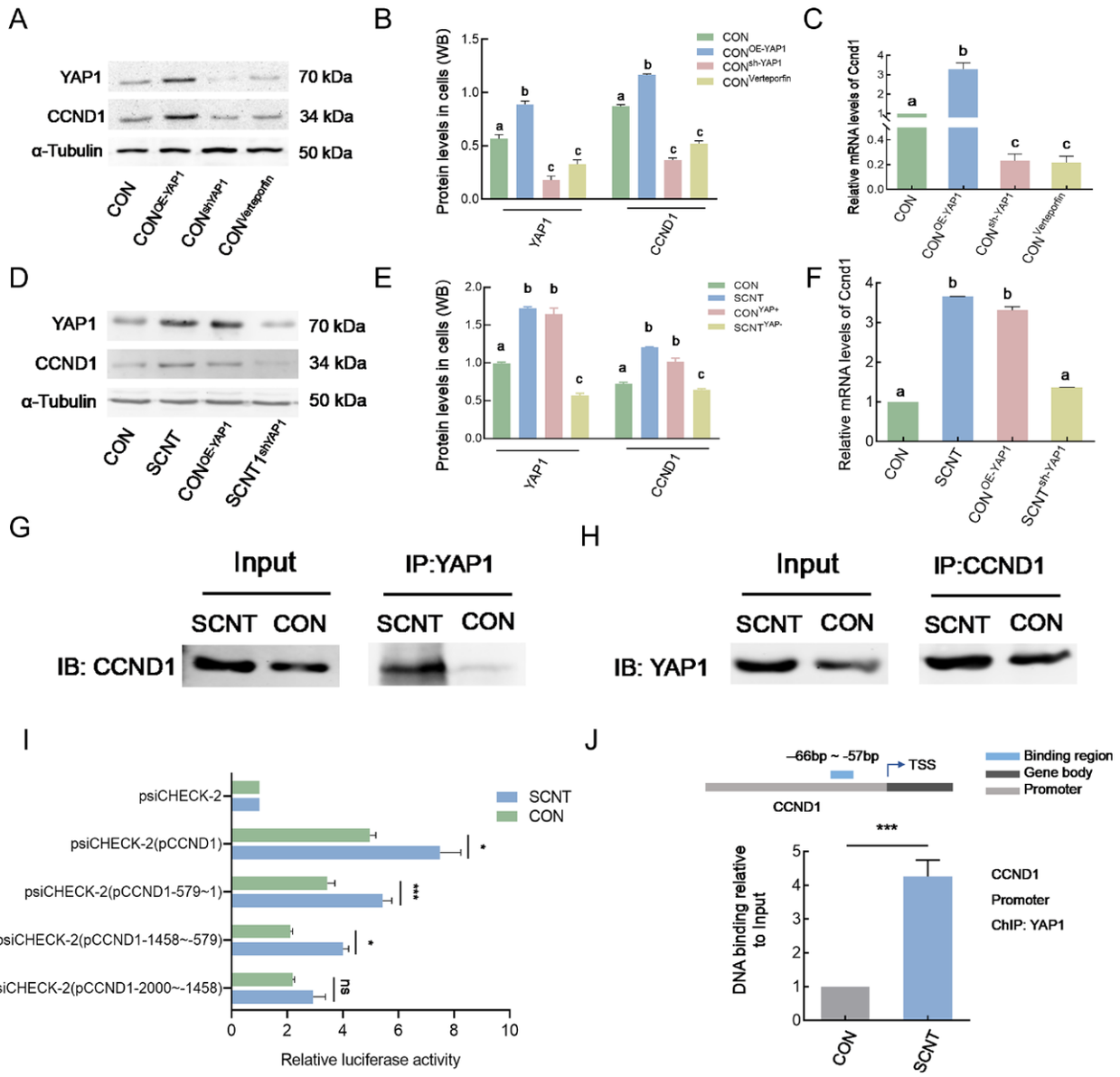


Figure 5 Regulatory role of YAP1 and CCND1 in bPMSCs

A: Western blot analysis of CCND1 protein expression in CON bPMSCs with YAP1 gene overexpression or knockout. B: Quantitative analysis of CCND1 protein expression in CON bPMSCs using densitometry (gray intensity analysis). C: RT-qPCR detection of *CCND1* mRNA expression in CON bPMSCs with *YAP1* gene overexpression or knockout. D: Western blot analysis of CCND1 protein expression in bPMSCs with YAP1 gene overexpression or knockout. E: Quantitative analysis of CCND1 protein expression in bPMSCs by densitometry. F: qPCR detection of *CCND1* mRNA expression in bPMSCs with YAP1 gene overexpression or knockout. G: Immunoprecipitation of YAP1 protein in bPMSCs. H: Immunoprecipitation of CCND1 protein in bPMSCs. I: Dual-luciferase reporter assay to validate promoting effects of YAP1 on CCND1 promoter activity. J: Chromatin immunoprecipitation (ChIP) verification of YAP1 binding to CCND1 promoter. sh-YAP1 and verteporfin represent down-regulation of YAP1 expression, while OE-YAP1 represents overexpression of YAP1. Graphs show mean±SEM, data are representative of three independent experiments. Different significance levels are indicated by asterisks (*: P<0.05; **: P<0.01; ***: P<0.001; ns: Not significant).

cotyledon interstitial villi. Cattle and other ruminants possess cotyledonary placentas, wherein placental functionality depends on the proper formation and arrangement of cotyledons and uterine caruncles. During SCNT pregnancies, the number of placental cotyledons is significantly reduced, alongside a noticeable enlargement of uterine caruncles (Fletcher et al., 2007; Young et al., 1998). This reduction in placental cotyledons, coupled with caruncular hypertrophy, likely reflects compromised placental function, which may contribute to developmental abnormalities in cloned fetuses (Fletcher et al., 2007; Young et al., 1998). The increase in binucleate giant cells in SCNT placentas likely results from an increase in the number of trophoblast cells from the fetal-nourishing outer layer and maternal uterine epithelial cells, leading to placental enlargement, thickening, and a characteristic fist-like morphology (Lee et al., 2004; Ravelich et al., 2006). The disordered arrangement of uterine epithelial cells in SCNT-derived cattle may disrupt metabolic processes, impairing placental function (Constant et al., 2006; Pool et al., 2019). Mesenchymal tissue, a key regulator of organ-specific morphogenesis, exhibits marked alterations in SCNT cattle (Constant et al., 2006; Pool et al., 2019). Specifically, the significant increase in chorionic interstitial villi suggests potential stromal regulatory mechanisms contributing to

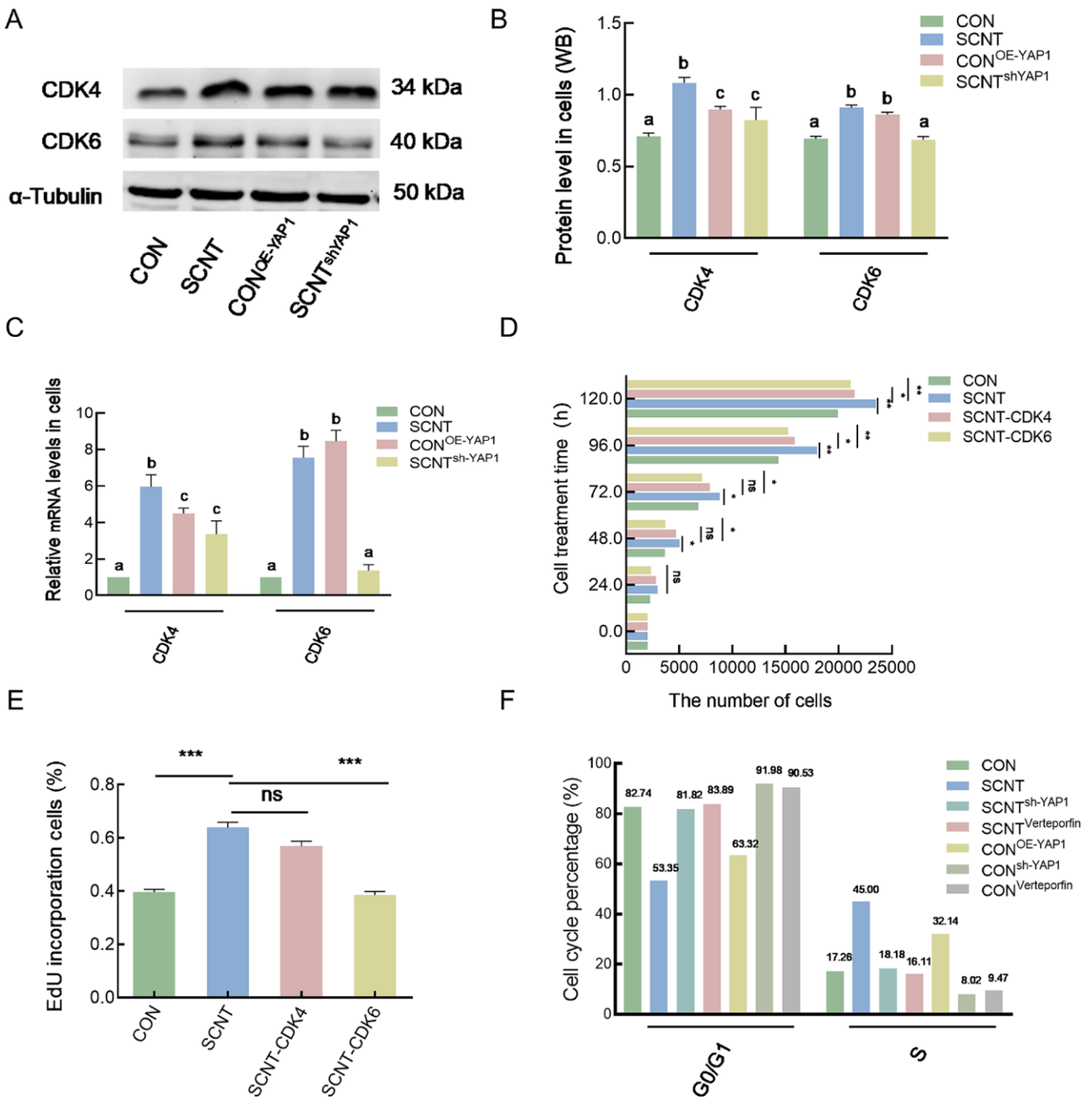


Figure 6 YAP1 promoted G0/G1-S transition of bPMSCs through CCND1-CDK6 pathway

A: Western blot analysis of CDK4 and CDK6 protein expression in bPMSCs with YAP1 gene overexpression or knockout. B: Quantitative analysis of CDK4 and CDK6 protein expression in bPMSCs by densitometry. C: RT-qPCR detection of *CDK4* and *CDK6* mRNA expression in bPMSCs with YAP1 gene overexpression or knockout. D: Proliferation assessment of bPMSCs treated with BSJ-03-204 (CDK4 26.9 nmol/L, CDK6 10.4 nmol/L) at 0, 24, 48, 72, 96, and 120 h by CCK-8 method. E: EdU proliferation assay of bPMSCs. F: Cell cycle analysis of bPMSCs. sh-YAP1 represents down-regulation of YAP1 expression, while OE-YAP1 represents overexpression of YAP1. Graphs show mean±SEM, data are representative of three independent experiments. Significance levels are indicated by asterisks (*: P<0.05; **: P<0.01; ***: P<0.001; ns: Not significant). Different letters denote significant differences (P<0.05) between groups.

placental hypertrophy (Constant et al., 2006; Pool et al., 2019). Placental overgrowth may precede and potentially drive fetal overgrowth, suggesting that fetal overgrowth may arise as a consequence rather than a cause of placental hypertrophy. Overall, these findings indicate that SCNT placental tissues in cattle exhibit pronounced abnormalities characteristic of large offspring syndrome and large placental syndrome. These abnormalities are closely associated with disrupted placental structure and function, potentially driven by metabolic dysregulation and aberrant cell signaling.

Previous studies have identified multiple factors contributing to placental hypertrophy in SCNT animals, including abnormal imprinting gene expression, dysregulated hormone secretion, epigenetic modifications, RNA dysregulation, and abnormal signal regulation. Abnormal gene expression during placental development has been highlighted as a major driver of pathological changes in cloned placentas (Inoue et al., 2002; Rivera, 2021). Everts et al. (2008) reported that DEGs in the developing placenta of SCNT bovines are enriched in cell cycle regulation and apoptosis. Similarly, Salilew-Wondim

et al. (2013) identified 58 DEGs through microarray analysis of placentas from IVF, SCNT, and artificially inseminated cattle, showing enrichment in organ development; extracellular structure, matrix tissue, and the development, regulation, and maintenance of blood vessels and the vascular system. The molecular mechanisms underlying placental development and function are highly complex and involve many interconnected regulatory pathways. In the placenta of SCNT cattle, disruptions have been observed in extracellular matrix and adhesion, immune-related signaling pathways, and nutrient transport-related pathways (Ledgard et al., 2009). In our previous research, multi-omics analyses suggested that placental hypertrophy in SCNT cattle may be associated with abnormalities in urea and ion transmembrane transport signaling pathways (Gao et al., 2019). These disruptions in regulatory networks profoundly affect placental development and formation, potentially leading to fetal malformation or miscarriage. Excessive placental proliferation has emerged as a crucial factor contributing to the functional abnormalities observed in cloned placentas. In this study, transcriptome sequencing of SCNT and CON bovine placentas revealed that DEGs in SCNT placentas were predominantly enriched in energy metabolism, growth hormone signaling, cell differentiation, cell cycle-related signaling pathways, as well as the Hippo and PI3K-Akt signaling pathways. Among the DEGs, *Ccnd1* was identified as a key gene involved in both the Hippo and PI3K-Akt signaling pathways. The Hippo signaling pathway plays a vital role in tissue development, regeneration, and stem cell maintenance. Its core component, *Yap1*, regulates organ size, tissue regeneration, and cell proliferation (Yu et al., 2015). The biological functions of the Hippo signaling pathway closely overlap those of the TGF-β signaling pathway. In human placental tissues, Yap1 has been shown to specifically bind to Smad7, facilitating its recruitment to active TGFβRi and enhancing Smad7-mediated inhibition of Smad3/4 transcription (Mauviel et al., 2012). Research by Hiemer et al. (2014) demonstrated that the nuclear localization of Yap1 varies among breast cancer cell lines, influencing their sensitivity to TGF-β-induced growth arrest. The Wnt signaling pathway, which plays a central role in cell regulation, stem cell expansion, and regeneration, is closely linked to β-catenin as a key regulatory factor (Nusse & Clevers, 2017). Yap1 can directly bind to β-catenin, preventing its nuclear translocation and thereby inhibiting Wnt signaling (Azzolin et al., 2014). Deng et al. (2018) further confirmed that overexpression of Yap1 significantly increases the expression of Wnt/β-Catenin target genes *Lgr5* and *cyclinD1*. Additionally, Yap1 mediates the regulatory effects of both Wnt/β-catenin and insulin-like growth factor signaling on cardiomyocyte proliferation (Heallen et al., 2011). Despite these insights, studies specifically addressing the regulatory roles of YAP1 in the placentas of SCNT animals are limited.

In this study, PMSCs were isolated from both cloned and CON cattle. Cell proliferation assays demonstrated a significantly greater proliferative capacity in SCNT-derived bPMSCs compared to CON-derived bPMSCs, consistent with previous research (Miglino et al., 2007). In addition, YAP1 protein expression was significantly greater in SCNT blastocysts, placental tissues, and PMSCs compared to CON placental tissues, while phosphorylated YAP1 levels were markedly reduced in SCNT placental tissues and PMSCs. This reduction was associated with a significant increase in functional nuclear YAP1 protein in SCNT placental tissues. The Hippo signaling pathway is known to negatively regulate cell proliferation by inhibiting *Yap1*, thereby promoting cell differentiation and regulating organ size (Heallen et al., 2011; Zhang, 2015). Camargo et al. (2007) demonstrated that *Yap1*-specific overexpression in the mouse liver results in a greater than 4-fold increase in liver size, while termination of Yap1 overexpression restores the liver to normal size. Conversely, *Yap1* deficiency in the heart impedes cardiomyocyte proliferation, leading to incomplete cardiac development (Gong et al., 2021; Patel et al., 2017; von Gise et al., 2012; Weiler et al., 2017). Our findings suggest that overactivation of *Yap1* may be a key factor influencing placental hypertrophy in SCNT cattle. Previous studies have also shown that YAP1 can induce the cell cycle regulatory gene *Ccnd1*, linking YAP1 activation to abnormal cell cycle regulation. Down-regulation of *Yap1* has been shown to inhibit bladder cancer cell proliferation and induce cell cycle arrest in the G1 phase by reducing the expression of CCND1 and other G1 phase-related molecules. Notably, this arrest can be reversed by the up-regulation of *Yap1* expression (Mizuno et al., 2012; Wang et al., 2013; Wu et al., 2019). In this study, YAP1 overexpression in SCNT bPMSCs was accompanied by a significant reduction in phosphorylated YAP1 levels, while CCND1 exhibited a parallel increase in expression. Given the role of CCND1 in regulating cell proliferation and promoting G1/S cell cycle progression, SCNT bPMSCs demonstrated enhanced DNA synthesis, accelerated cell division, and rapid cell cycle progression. Furthermore, cyclin-dependent kinases and cell proliferation-related genes were expressed at significantly higher levels in SCNT bPMSCs compared to CON bPMSCs, indicating a markedly greater proliferative capacity.

To explore whether the enhanced proliferation of bPMSCs is attributable to the regulation of CCND1 by YAP1, these findings were validated using YAP1 overexpression and knockdown bPMSC models. Results confirmed that YAP1 plays a pivotal role in regulating bPMSC proliferation. Deletion of the YAP1 gene significantly reduced the proportion of S-phase cells, resulting in proliferation levels similar to those observed in CON bPMSCs. These findings suggest that YAP1 promotes SCNT bPMSC proliferation via the regulation of CCND1. Co-IP, luciferase, and ChIP interaction assays revealed that YAP1 binds to the proximal promoter of CCND1 (pCCND1-579-1) in SCNT bPMSCs, thereby promoting CCND1 expression. Additionally, CCND1 forms a complex with CDK6, facilitating G1-S cell cycle progression in SCNT bPMSCs. Within the cell, the activated CCND1-CDK4/CDK6 complex translocates to the nucleus and promotes the transcription of *E2F* transcription factors. These transcription factors regulate genes required for cell proliferation, driving cells into the S phase. The expression of CCND1 peaks in the late G1 phase, followed by its nuclear export during the S phase and subsequent ubiquitination and degradation (Chen et al., 2021; Wang et al., 2006; Zhong et al., 2010). Studies have demonstrated that reducing YAP1 or inhibiting its nuclear transport in breast cancer cells significantly reduces CDK6 expression and restores sensitivity to CDK4/6 inhibitors, thereby impacting the sensitivity of cancer cells to CDK4/6 inhibitors (Li et al., 2018b). In addition, the Hippo signaling pathway plays a crucial role in placental development by promoting cell proliferation and maintaining stemness (Meinhardt et al., 2020). However, its involvement in SCNT bovine placental hypertrophy has not been fully characterized. In this study, we demonstrated that YAP1 forms a complex

with CDK6 by binding to the *CCND1* proximal promoter (pCCND1-579-1) in SCNT placentas, driving G0/G1-S cell cycle progression in SCNT bPMSCs. These findings provide the first mechanistic insights into the role of the Hippo signaling pathway in controlling placental cell proliferation in SCNT animals, providing a foundation for understanding placental development in cloned cattle and advancing somatic cloning research.

CONCLUSIONS

This study revealed that the Hippo signaling pathway, specifically YAP1, regulates placental hyperplasia in cloned cattle by promoting CCND1-CDK6 expression and facilitating cell cycle progression. Understanding these molecular mechanisms has theoretical and practical implications, offering a potential avenue for enhancing cloning efficiency and advancing efforts in species conservation.

DATA AVAILABILITY

The datasets produced and/or analyzed in the current study are available from the corresponding author upon reasonable request. The raw RNA-seq data analyzed in this study are available from NCBI database (BioProjectID PRJNA1177607), China National Center for Bioinformation database of Genome Sequence Archive (GSA) (CRA014398), and Science Data Bank database (doi: 10.57760/sciencedb.j00139.00114).

SUPPLEMENTARY DATA

Supplementary data to this article can be found online

COMPETING INTERESTS

The author declare that they have no competing interests.

AUTHORS' CONTRIBUTIONS

G.H.S. and G.P.L. initiated and supervised the study; S.S.W. and X.Y.Z. performed most experiments and analyses; L.Y. and G.H.S. prepared the somatic cell nucleus transfer embryos; C.H. and D.W. performed RNA-seq experiments and data analysis; X.F.L., L.S.S., and C.L.B. provided instructive suggestions and revised the manuscript; S.S.W. and G.H.S. wrote the manuscript. All authors read and approved the final version of the manuscript.

ACKNOWLEDGMENTS

We utilized templates from BioRender software as the foundation for our figures.

REFERENCES

Aggarwal P, Vaites LP, Kim JK, et al. 2010. Nuclear cyclin D1/CDK4 kinase regulates *CUL4* expression and triggers neoplastic growth via activation of the PRMT5 methyltransferase. *Cancer Cell*, **18**(4): 329–340.

Arnold DR, Fortier AL, Lefebvre R, et al. 2008. Placental insufficiencies in cloned animals - A workshop report. *Placenta*, **29**(Suppl 1): 108–110.

Arnold DR, Gaspar RC, da Rocha CV, et al. 2017. Nuclear transfer alters placental gene expression and associated histone modifications of the placental-specific imprinted gene pleckstrin homology-like domain, family A, member 2 (*PHLDA2*) in cattle. *Reproduction, Fertility and Development*, **29**(3): 458–467.

Azzolin L, Panciera T, Soligo S, et al. 2014. YAP/TAZ incorporation in the β-catenin destruction complex orchestrates the Wnt response. *Cell*, **158**(1): 157–170.

Bajoria R, Sooranna SR, Ward BS, et al. 2002. Prospective function of placental leptin at maternal-fetal interface. *Placenta*, **23**(2-3): 103–115.

Biase FH, Rabel C, Guillomot M, et al. 2016. Massive dysregulation of genes involved in cell signaling and placental development in cloned cattle conceptus and maternal endometrium. *Proceedings of the National Academy of Sciences of the United States of America*, **113**(51): 14492–14501.

Boss AL, Chamley LW, James JL. 2018. Placental formation in early pregnancy: how is the centre of the placenta made?. *Human Reproduction Update*, **24**(6): 750–760.

Camargo FD, Gokhale S, Johnnidis JB, et al. 2007. YAP1 increases organ size and expands undifferentiated progenitor cells. *Current Biology*, **17**(23): 2054–2060.

Canel N, Bevacqua R, Fernández-Martín R, et al. 2010. Activation with ionomycin followed by dehydroleucodine and cytochalasin B for the production of parthenogenetic and cloned bovine embryos. *Cellular Reprogramming*, **12**(4): 491–499.

Chae JI, Cho SK, Seo JW, et al. 2006. Proteomic analysis of the extraembryonic tissue from cloned porcine embryos. *Molecular & Cellular Proteomics*, **5**(9): 1559–1566.

Chavatte-Palmer P, de Sousa N, Laigre P, et al. 2006. Ultrasound fetal measurements and pregnancy associated glycoprotein secretion in early pregnancy in cattle recipients carrying somatic clones. *Theriogenology*, **66**(4): 829–840.

Chen ZG, Xie YY, Luo HC, et al. 2021. NAP1L1 promotes proliferation and chemoresistance in glioma by inducing CCND1/CDK4/CDK6 expression through its interaction with HDGF and activation of c-Jun. *Aging*, **13**(24): 26180–26200.

Cheraghi S, Razi M, Malekinejad H. 2015. Involvement of cyclin D1 and E2f1 in zearalenone-induced DNA damage in testis of rats. *Toxicon*, **106**: 108–116.

Constant F, Guillomot M, Heyman Y, et al. 2006. Large offspring or large placenta syndrome? Morphometric analysis of late gestation bovine placentomes from somatic nuclear transfer pregnancies complicated by hydrallantois. *Biology of Reproduction*, **75**(1): 122–130.

Deng FH, Peng L, Li ZJ, et al. 2018. YAP triggers the Wnt/β-catenin signaling pathway and promotes enterocyte self-renewal, regeneration and tumorigenesis after DSS-induced injury. *Cell Death & Disease*, **9**(2): 153.

Dong JX, Feldmann G, Huang JB, et al. 2007. Elucidation of a universal size-control mechanism in *Drosophila* and mammals. *Cell*, **130**(6): 1120–1133.

Everts RE, Chavatte-Palmer P, Razzak A, et al. 2008. Aberrant gene expression patterns in placentomes are associated with phenotypically normal and abnormal cattle cloned by somatic cell nuclear transfer. *Physiological Genomics*, **33**(1): 65–77.

Fletcher CJ, Roberts CT, Hartwich KM, et al. 2007. Somatic cell nuclear transfer in the sheep induces placental defects that likely precede fetal demise. *Reproduction*, **133**(1): 243–255.

Gao GQ, Wang SY, Zhang JQ, et al. 2019. Transcriptome-wide analysis of the SCNT bovine abnormal placenta during mid- to late gestation. *Scientific Reports*, **9**(1): 20035.

Gong R, Jiang ZK, Zagidullin N, et al. 2021. Regulation of cardiomyocyte fate plasticity: a key strategy for cardiac regeneration. *Signal Transduction and Targeted Therapy*, **6**(1): 31.

Gorczyca G, Wartalski K, Romek M, et al. 2022. The molecular quality and mitochondrial activity of porcine cumulus-oocyte complexes are affected by their exposure to three endocrine-active compounds under 3D In vitro maturation conditions. *International Journal of Molecular Sciences*, **23**(9): 4572.

Gorczyca G, Wartalski K, Wiater J, et al. 2021. Anabolic steroids-driven regulation of porcine ovarian putative stem cells favors the onset of their neoplastic transformation. *International Journal of Molecular Sciences*, **22**(21): 11800.

Heallen T, Zhang M, Wang J, et al. 2011. Hippo pathway inhibits wnt signaling to restrain cardiomyocyte proliferation and heart size. *Science*,

332(6028): 458–461.

Hiemer SE, Szymaniak AD, Varelas X. 2014. The transcriptional regulators TAZ and YAP direct transforming growth factor β-induced tumorigenic phenotypes in breast cancer cells. *Journal of Biological Chemistry*, **289**(19): 13461–13474.

Hill JR. 2014. Incidence of abnormal offspring from cloning and other assisted reproductive technologies. *Annual Review of Animal Biosciences*, **2**: 307–321.

Hill JR, Burghardt RC, Jones K, et al. 2000. Evidence for placental abnormality as the major cause of mortality in first-trimester somatic cell cloned bovine fetuses. *Biology of Reproduction*, **63**(6): 1787–1794.

Huang YM, Zhang JC, Li XM, et al. 2023. Chromatin accessibility memory of donor cells disrupts bovine somatic cell nuclear transfer blastocysts development. *The FASEB Journal*, **37**(9): e23111.

Hwang JY, Oh JN, Park CH, et al. 2015. Dosage compensation of X-chromosome inactivation center-linked genes in porcine preimplantation embryos: non-chromosome-wide initiation of X-chromosome inactivation in blastocysts. *Mechanisms of Development*, **138**: 246–255.

Inoue K, Kohda T, Lee J, et al. 2002. Faithful expression of imprinted genes in cloned mice. *Science*, **295**(5553): 297–297.

Jiao F, Yan JB, Yang XY, et al. 2007. Effect of oocyte mitochondrial DNA haplotype on bovine somatic cell nuclear transfer efficiency. *Molecular Reproduction and Development*, **74**(10): 1278–1286.

Lankford L, Chen YJ, Saenz Z, et al. 2017. Manufacture and preparation of human placenta-derived mesenchymal stromal cells for local tissue delivery. *Cytotherapy*, **19**(6): 680–688.

Ledgard A, Lee RSF, Couldrey C, et al. 2009. Dickkopf-1 expression during early bovine placentation and its down-regulation in somatic cell nuclear transfer (SCNT) pregnancies. *Journal of Reproduction and Development*, **55**(5): 467–474.

Lee RSF, Peterson AJ, Donnison MJ, et al. 2004. Cloned cattle fetuses with the same nuclear genetics are more variable than contemporary half-siblings resulting from artificial insemination and exhibit fetal and placental growth deregulation even in the first trimester. *Biology of Reproduction*, **70**(1): 1–11.

Lee SY, Park JY, Choi YJ, et al. 2007. Comparative proteomic analysis associated with term placental insufficiency in cloned pig. *Proteomics*, **7**(8): 1303–1315.

Li NN, Zeng J, Sun FZ, et al. 2018a. *p27* inhibits CDK6/CCND1 complex formation resulting in cell cycle arrest and inhibition of cell proliferation. *Cell Cycle*, **17**(19-20): 2335–2348.

Li ZQ, Razavi P, Li Q, et al. 2018b. Loss of the FAT1 tumor suppressor promotes resistance to CDK4/6 inhibitors via the hippo pathway. *Cancer Cell*, **34**(6): 893–905. e8.

Liu Y, Shi HR, Wu D, et al. 2021. The protective benefit of heme oxygenase-1 gene-modified human placenta-derived mesenchymal stem cells in a N-nitro-L-arginine methyl ester-induced preeclampsia-like rat model: possible implications for placental angiogenesis. *Stem Cells and Development*, **30**(19): 991–1002.

Magatti M, Stefani FR, Papait A, et al. 2019. Perinatal mesenchymal stromal cells and their possible contribution to fetal-maternal tolerance. *Cells*, **8**(11): 1401.

Malin K, Witkowska-Piłaszewicz O, Papis K. 2022. The many problems of somatic cell nuclear transfer in reproductive cloning of mammals. *Theriogenology*, **189**: 246–254.

Matoba S, Zhang Y. 2018. Somatic cell nuclear transfer reprogramming: mechanisms and applications. *Cell Stem Cell*, **23**(4): 471–485.

Mauviel A, Nallet-Staub F, Varelas X. 2012. Integrating developmental signals: a Hippo in the (path)way. *Oncogene*, **31**(14): 1743–1756.

Meinhardt G, Haider S, Kunihs V, et al. 2020. Pivotal role of the transcriptional co-activator YAP in trophoblast stemness of the developing human placenta. *Proceedings of the National Academy of Sciences of the United States of America*, **117**(24): 13562–13570.

Miglino MA, Pereira FTV, Visintin JA, et al. 2007. Placentation in cloned cattle: structure and microvascular architecture. *Theriogenology*, **68**(4): 604–617.

Min B, Cho S, Park JS, et al. 2015. Transcriptomic features of bovine blastocysts derived by somatic cell nuclear transfer. *G3 Genes| Genomes| Genetics*, **5**(12): 2527–2538.

Mizuno T, Murakami H, Fujii M, et al. 2012. YAP induces malignant mesothelioma cell proliferation by upregulating transcription of cell cycle-promoting genes. *Oncogene*, **31**(49): 5117–5122.

Moon S, Park SY, Park HW. 2018. Regulation of the Hippo pathway in cancer biology. *Cellular and Molecular Life Sciences*, **75**(13): 2303–2319.

Nusse R, Clevers H. 2017. Wnt/β-Catenin signaling, disease, and emerging therapeutic modalities. *Cell*, **169**(6): 985–999.

Oback B. 2008. Climbing mount efficiency-small steps, not giant leaps towards higher cloning success in farm animals. *Reproduction in Domestic Animals*, **43**(S2): 407–416.

Ogura A, Inoue K, Wakayama T. 2013. Recent advancements in cloning by somatic cell nuclear transfer. *Philosophical Transactions of the Royal Society B: Biological Sciences*, **368**(1609): 20110329.

Ogura A, Matoba S, Inoue K. 2021. 25th ANNIVERSARY OF CLONING BY SOMATIC-CELL NUCLEAR TRANSFER: epigenetic abnormalities associated with somatic cell nuclear transfer. *Reproduction*, **162**(1): F45–F58.

Park JY, Kim JH, Choi YJ, et al. 2009. Comparative proteomic analysis of malformed umbilical cords from somatic cell nuclear transfer-derived piglets: implications for early postnatal death. *BMC Genomics*, **10**: 511.

Patel SH, Camargo FD, Yimlamai D. 2017. Hippo signaling in the liver regulates organ size, cell fate, and carcinogenesis. *Gastroenterology*, **152**(3): 533–545.

Peter AT. 2013. Bovine placenta: a review on morphology, components, and defects from terminology and clinical perspectives. *Theriogenology*, **80**(7): 693–705.

Pool M, Leuvenink H, Moers C. 2019. Reparative and regenerative effects of mesenchymal stromal cells-promising potential for kidney transplantation?. *International Journal of Molecular Sciences*, **20**(18): 4614.

Ravelich SR, Shelling AN, Wells DN, et al. 2006. Expression of TGF-β1, TGF-β2, TGF-β3 and the receptors TGF-βRI and TGF-βRII in placentomes of artificially inseminated and nuclear transfer derived bovine pregnancies. *Placenta*, **27**(2-3): 307–316.

Rivera RM. 2021. 209 Large offspring syndrome: effects of in vitro production on embryo epigenetics and development. *Journal of Animal Science*, **99**(S1): 114–115.

Ross PJ, Rodriguez RM, Iager AE, et al. 2009. Activation of bovine somatic cell nuclear transfer embryos by PLCZ cRNA injection. *Reproduction*, **137**(3): 427–437.

Salilew-Wondim D, Tesfaye D, Hossain M, et al. 2013. Aberrant placenta gene expression pattern in bovine pregnancies established after transfer of cloned or in vitro produced embryos. *Physiological Genomics*, **45**(1): 28–46.

Samiec M. 2022. Molecular mechanism and application of somatic cell cloning in mammals-past, present and future. *International Journal of Molecular Sciences*, **23**(22): 13786.

Samiec M, Skrzyszowska M. 2005. Molecular conditions of the cell nucleus remodelling/reprogramming process and nuclear-transferred embryo development in the intraooplasmic karyoplast injection technique: a review. *Czech Journal of Animal Science*, **50**(5): 185–195.

Samiec M, Skrzyszowska M. 2010. Preimplantation developmental capability of cloned pig embryos derived from different types of nuclear donor somatic cells. *Annals of Animal Science*, **10**(4): 385–398.

Sangalli JR, Sampaio RV, De Bem THC, et al. 2023. Cattle cloning by

somatic cell nuclear transfer. *In*: Moura MT. Somatic Cell Nuclear Transfer Technology. New York: Humana, 225–244.

Skrzyszowska M, Samiec M, Słomski R, et al. 2008. Development of porcine transgenic nuclear-transferred embryos derived from fibroblast cells transfected by the novel technique of nucleofection or standard lipofection. *Theriogenology*, **70**(2): 248–259.

Srirattana K, Kaneda M, Parnpai R. 2022. Strategies to improve the efficiency of somatic cell nuclear transfer. *International Journal of Molecular Sciences*, **23**(4): 1969.

Su GH, Wang LN, Gao GQ, et al. 2021a. C23 gene regulates the nucleolin structure and biosynthesis of ribosomes in bovine intraspecific and interspecific somatic cell nuclear transfer embryos. *The FASEB Journal*, **35**(11): e21993.

Su GH, Wu SS, Wu ML, et al. 2021b. Melatonin improves the quality of frozen bull semen and influences gene expression related to embryo genome activation. *Theriogenology*, **176**: 54–62.

Su XH, Gao GQ, Wang SY, et al. 2019. CircRNA expression profile of bovine placentas in late gestation with aberrant SCNT fetus. *Journal of Clinical Laboratory Analysis*, **33**(6): e22918.

Svarcova O, Laurincik J, Avery B, et al. 2007. Nucleolar development and allocation of key nucleolar proteins require de novo transcription in bovine embryos. *Molecular Reproduction and Development*, **74**(11): 1428–1435.

Tanaka S, Oda M, Toyoshima Y, et al. 2001. Placentomegaly in cloned mouse concepti caused by expansion of the spongiotrophoblast layer. *Biology of Reproduction*, **65**(6): 1813–1821.

Ticiani E, Rodrigues VHV, Willhelm BR, et al. 2020. Evidence of metabolic compartmentation in the bovine placenta and significance for the regulation of placental function and fetal growth in pregnancies bearing *in vivo*-or *in vitro*-produced embryos. *Livestock Science*, **236**: 104024.

Tsunoda Y, Kato Y. 2002. Recent progress and problems in animal cloning. *Differentiation*, **69**(4-5): 158–161.

Vajta G. 2007. Somatic cell nuclear transfer in its first and second decades: successes, setbacks, paradoxes and perspectives. *Reproductive Biomedicine Online*, **15**(5): 582–590.

von Gise A, Lin ZQ, Schlegelmilch K, et al. 2012. YAP1, the nuclear target of Hippo signaling, stimulates heart growth through cardiomyocyte proliferation but not hypertrophy. *Proceedings of the National Academy of Sciences of the United States of America*, **109**(7): 2394–2399.

Wakisaka-Saito N, Kohda T, Inoue K, et al. 2006. Chorioallantoic placenta defects in cloned mice. *Biochemical and Biophysical Research Communications*, **349**(1): 106–114.

Wang CG, Li ZP, Lu YN, et al. 2006. Cyclin D1 repression of nuclear respiratory factor 1 integrates nuclear DNA synthesis and mitochondrial function. *Proceedings of the National Academy of Sciences of the United States of America*, **103**(31): 11567–11572.

Wang LY, Li ZK, Wang LB, et al. 2020. Overcoming intrinsic H3K27me3 imprinting barriers improves post-implantation development after somatic cell nuclear transfer. *Cell Stem Cell*, **27**(2): 315–325. e5.

Wang Y, Xie CY, Li QC, et al. 2013. Clinical and prognostic significance of Yes-associated protein in colorectal cancer. *Tumor Biology*, **34**(4): 2169–2174.

Watanabe S, Nagai T. 2011. Survival of embryos and calves derived from somatic cell nuclear transfer in cattle: a nationwide survey in Japan. *Animal Science Journal*, **82**(2): 360–365.

Weiler SME, Pinna F, Wolf T, et al. 2017. Induction of chromosome instability by activation of yes-associated protein and forkhead box M1 in liver cancer. *Gastroenterology*, **152**(8): 2037–2051. e22.

Whitworth KM, Prather RS. 2010. Somatic cell nuclear transfer efficiency: how can it be improved through nuclear remodeling and reprogramming?. *Molecular Reproduction and Development*, **77**(12): 1001–1015.

Wu D, Liu Y, Liu XX, et al. 2020. Heme oxygenase-1 gene modified human placental mesenchymal stem cells promote placental angiogenesis and spiral artery remodeling by improving the balance of angiogenic factors *in vitro*. *Placenta*, **99**: 70–77.

Wu YJ, Zheng QQ, Li Y, et al. 2019. Metformin targets a YAP1-TEAD4 complex via AMPKα to regulate CCNE1/2 in bladder cancer cells. *Journal of Experimental & Clinical Cancer Research*, **38**(1): 376.

Yan ZH, Zhou YY, Fu J, et al. 2010. Donor-host mitochondrial compatibility improves efficiency of bovine somatic cell nuclear transfer. *BMC Developmental Biology*, **10**: 31.

Yang XZ, Smith SL, Tian XC, et al. 2007. Nuclear reprogramming of cloned embryos and its implications for therapeutic cloning. *Nature Genetics*, **39**(3): 295–302.

Young LE, Sinclair KD, Wilmut I. 1998. Large offspring syndrome in cattle and sheep. *Reviews of Reproduction*, **3**(3): 155–163.

Yu FX, Zhao B, Guan KL. 2015. Hippo pathway in organ size control, tissue homeostasis, and cancer. *Cell*, **163**(4): 811–828.

Zhang L. 2015. Control of growth and beyond: a special issue on Hippo signaling. *Acta Biochimica et Biophysica Sinica*, **47**(1): 1.

Zhong ZJ, Yeow WS, Zou CH, et al. 2010. Cyclin D1/cyclin-dependent kinase 4 interacts with filamin a and affects the migration and invasion potential of breast cancer cells. *Cancer Research*, **70**(5): 2105–2114.

Zhou C, Zhang JC, Zhang M, et al. 2020. Transcriptional memory inherited from donor cells is a developmental defect of bovine cloned embryos. *The FASEB Journal*, **34**(1): 1637–1651.

Yu et al. *Zool. Res.* 2025, 46(1): 139−151
https://doi.org/10.24272/j.issn.2095-8137.2024.284
https://cstr.cn/32248.14.zr.2024.284

ZR | Zoological Research

Article Open Access

Reciprocal translocation experiments reveal gut microbiome plasticity and host specificity in a Qinghai-Xizang Plateau lizard

Wei Yu[1,2,#], Jing Yang[2,#], Li-Wei Teng[1,3,#], Xiao-Long Zhao[2,4], Ze-Yu Zhu[1,2], Shuang Cui[1], Wei-Guo Du[2], Zhen-Sheng Liu[1,3,*], Zhi-Gao Zeng[2,*]

[1] *College of Wildlife and Protected Area*, *Northeast Forestry University*, *Harbin*, *Heilongjiang* 150040, *China*
[2] *Key Laboratory of Animal Ecology and Conservation Biology*, *Institute of Zoology*, *Chinese Academy of Sciences*, *Beijing* 100101, *China*
[3] *Key Laboratory of Conservation Biology*, *National Forestry and Grassland Administration*, *Harbin*, *Heilongjiang* 150040, *China*
[4] *School of Ecological and Environmental Sciences*, *Institute of Eco-Chongming*, *Shanghai Institute of Wildlife Epidemics*, *East China Normal University*, *Shanghai* 200241, *China*

ABSTRACT

Animal adaptation to environmental challenges is a complex process involving intricate interactions between the host genotype and gut microbiome composition. The gut microbiome, highly responsive to external environmental factors, plays a crucial role in host adaptability and may facilitate local adaptation within species. Concurrently, the genetic background of host populations influences gut microbiome composition, highlighting the bidirectional relationship between host and microbiome. Despite this, our understanding of gut microbiome plasticity and its role in host adaptability remains limited, particularly in reptiles. To clarify this issue, we conducted a reciprocal translocation experiment with gravid females of the Qinghai toad-headed lizards (*Phrynocephalus vlangalii*) between high-altitude (2 600 m a.s.l.) and superhigh-altitude (3 600 m a.s.l.) environments on Dangjin Mountain of the Qinghai-Xizang Plateau, China. One year later, we assessed the phenotypes and gut microbiomes of their offspring. Results revealed significant plasticity in gut microbiome diversity and structure in response to contrasting elevations. High-altitude conditions increased diversity, and maternal effects appeared to enable high-altitude lizards to maintain elevated diversity when exposed to superhigh-altitude environments. Additionally, superhigh-altitude lizards displayed distinct gut microbiome structures with notable host specificity, potentially linked to their lower growth rates. Overall, these findings underscore the importance of the gut microbiome in facilitating reptilian adaptation to rapid environmental changes across altitudinal gradients. Furthermore, this study provides critical insights into microbial mechanisms underpinning local adaptation and adaptative plasticity, offering a foundation for future research on host-microbiome interactions in evolutionary and ecological contexts.

Keywords: Gut microbiome; Plasticity; Host specificity; *Phrynocephalus vlangalii*; Reciprocal translocated experiment

INTRODUCTION

The gut microbiome is critical for host fitness and health, underpinning numerous biological processes and mediating interactions between organisms and their environments (Gensollen et al., 2016; Melaku et al., 2021; Zhang et al., 2020). Its composition and abundance are shaped by a complex interplay of dietary inputs, genetic factors, and environmental dynamics, reflecting the multifaceted nature of host-microbiome relationships (Chen et al., 2022; He et al., 2018; Moeller et al., 2020; Smith et al., 2015; Vasconcelos et al., 2023; Williams et al., 2022). Changes in environmental conditions and host genetics create selective pressures that influence microbial community dynamics (Carrier & Reitzel, 2018; Fietz et al., 2018; Nielsen et al., 2023). However, despite extensive research, the plasticity and specificity of the gut microbiome remain poorly understood, particularly in the context of environmental adaptation.

Organisms adapt to environmental variation through various

This is an open-access article distributed under the terms of the Creative Commons Attribution Non-Commercial License (http://creativecommons.org/licenses/by-nc/4.0/), which permits unrestricted non-commercial use, distribution, and reproduction in any medium, provided the original work is properly cited.

Copyright ©2025 Editorial Office of Zoological Research, Kunming Institute of Zoology, Chinese Academy of Sciences

Received: 29 October 2024; Accepted: 20 January 2025; Online: 21 January 2025

Foundation items: This work was supported by the National Natural Science Foundation of China (31861143023, 31872252) and Strategic Priority Research Program of the Chinese Academy of Sciences (XDA20050201)

[#]Authors contributed equally to this work

*Corresponding authors, E-mail: zhenshengliu@163.com; zengzhg@ioz.ac.cn

mechanisms such as local adaptation and phenotypic plasticity, which often coexist in nature (Becheler et al., 2022; Catullo et al., 2019; Čupić et al., 2023; Ma et al., 2018; Petipas et al., 2021; Swanson et al., 2023). Local adaptation involves the evolution of traits suited to specific environmental conditions, providing a heritable advantage in distinct habitats (Johnson et al., 2022; Kawecki & Ebert, 2004). Conversely, phenotypic plasticity enables a single genotype to express different phenotypes in response to varying environmental stimuli (Catullo et al., 2019; Pigliucci, 2005), which may persist throughout an individual's life (Baldo et al., 2023). Recent studies have increasingly focused on the molecular pathways underlying phenotypic plasticity and its role in ecological and evolutionary processes (Krist et al., 2021; Regan & Sheldon, 2023; Schuster et al., 2021; Sun et al., 2021). Reciprocal translocation experiments, derived from common garden experiments, involve the transfer of individuals between native and non-native habitats to investigate the influence of genetic and environmental factors on population-level variation (Hao et al., 2021; Ho et al., 2020; Johnson et al., 2022; Lane et al., 2019). Multiple studies have employed this approach to examine variation in growth, behavior, and survival among animal populations (Iraeta et al., 2006, 2008; Niewiarowski & Roosenburg, 1993; Ortega et al., 2017; Sears, 2005). However, most studies have focused on organismal responses to environmental changes, overlooking the potential contributions of the gut microbiome to adaptive processes.

Host adaptation is influenced by both the host genome and gut microbiome, both of which contribute to survival and fitness in changing environments (Martínez et al., 2018; Rennison et al., 2019; Uren Webster et al., 2018). Unlike the relatively stable genome, the gut microbiome is highly dynamic, responding rapidly to external factors through plastic changes that facilitate adaptation (Baniel et al., 2021; Carrier & Reitzel, 2018; Khakisahneh et al., 2020; Nielsen et al., 2023; Yang et al., 2024). This microbial flexibility plays a key role in phenotypic plasticity (Alberdi et al., 2016; Baniel et al., 2021; Carrier & Reitzel, 2018; Khakisahneh et al., 2020), enabling hosts to adjust dietary and metabolic processes to align with environmental demands (Baniel et al., 2021; Hicks et al., 2018; Mallott et al., 2022). Ectotherms, in particular, demonstrate highly dynamic gut microbiomes, which typically enhance their ability to thrive in novel environments (Bletz et al., 2016; Fontaine et al., 2022; Piazzon et al., 2020; Zhu et al., 2024a). Beyond this plasticity, the composition of the microbiome is closely linked to the phylogeny of the host (Ley et al., 2008; Rennison et al., 2019), potentially influencing evolutionary trajectories and driving reproductive isolation, thereby constraining local adaptation within host populations (Fietz et al., 2018; Greyson-Gaito et al., 2020; Rennison et al., 2019). Host specificity in gut microbiomes further underscores their adaptive importance (Chen et al., 2023; Mazel et al., 2024), with ectotherms frequently showing preferential associations with specific bacterial species (Powell et al., 2016; Sauers & Sadd, 2019). These microbial partnerships can provide adaptive benefits, enhancing host survival and ecological success (Chung et al., 2012; Sauers & Sadd, 2019). However, while the adaptive role of microbiome plasticity is well recognized, its effects on host phenotypic plasticity and local adaptation remain underexplored, leaving critical gaps in our understanding of adaptive evolution.

The Qinghai toad-headed lizard (*Phrynocephalus vlangalii*) is an endemic viviparous reptile inhabiting the northeastern Qinghai-Xizang Plateau in China, across a broad altitudinal range of 2 000 to 4 500 m a.s.l. (Zhao et al., 1999). Populations living at these contrasting elevations experience abrupt environmental gradients, making them ideal models for studying adaptive evolution (Serén et al., 2023). While previous studies have explored behavioral adaptations (Zhao et al., 2022; Zhu et al., 2020), physiological responses (Zhu et al., 2020, 2021), life history traits (Lu et al., 2018a, 2018b; Yu et al., 2023), and genomic features (Sun et al., 2018; Wu et al., 2022) in this species, few studies have explored the plasticity and specificity of their gut microbiomes, critical factors in adaptation to extreme environments given the direct impact of the gut microbiome on physiology, immune responses, and behavior (Du et al., 2022; Ho et al., 2020; Zeng et al., 2020). Environmental stressors encountered by *P. vlangalii* populations likely drive adaptation through a combination of genetic factors and the plasticity and host specificity of their gut microbiomes, which can directly impact survival and fitness (Alberdi et al., 2016; Baniel et al., 2021; Carrier & Reitzel, 2018). For example, in the eastern water dragon (*Intellagama lesueurii*), the gut microbiome exhibits plasticity in response to dietary changes associated with urbanization, specifically increased plant and fat intake (Littleford-Colquhoun et al., 2019). Similarly, the eastern river shrimp (*Macrobrachium nipponense*) shows gut microbiome plasticity when transitioning between lake and river habitats (Chen et al., 2017). The genetic background of hosts also shapes the gut microbiomes, contributing to host specificity. For example, populations of Mexican tetras (*Astyanax mexicanus*) from distinct habitats maintain different microbiome profiles even under uniform laboratory conditions, reflecting differences in host genetics (Riddle et al., 2024).

Populations of *P. vlangalii* inhabiting different altitudes display marked differences in gut microbiome composition (Zhang et al., 2018), suggesting the influence of both environmental plasticity and genetic backgrounds on microbial community structure. Reciprocal translocation experiments offer a robust approach for exploring the contributions of phenotypic plasticity and genetic determination to adaptive traits (Johnson et al., 2022; Kawecki & Ebert, 2004). To investigate the role of gut microbiome plasticity and host specificity in adaptation, a reciprocal translocation experiment was conducted on *P. vlangalii* populations at two contrasting altitudes. We hypothesize that, following translocation, the gut microbiota of individuals introduced to a novel environment will adapt to resemble that of the local population. However, genetic differences between populations may also assert a strong influence, leading to distinct microbial profiles compared to those of native individuals. In addition, the interaction between microbiome plasticity and host specificity may affect the host phenotype, potentially driving changes in migrant traits to align with those of the local population. By integrating environmental and genetic perspectives, this approach aims to elucidate the mechanisms underlying the interactions among environmental factors, genetic variations, and gut microbiome plasticity.

MATERIALS AND METHODS

Reciprocal translocation experiment

Between early June and early July 2020, 60 late-pregnant *P. vlangalii* females were captured from two distinct altitudinal

sites on Dangjin Mountain, Aksai County, Gansu Province, China. These locations were categorized as superhigh altitude (3 600 m a.s.l.) and high altitude (2 600 m a.s.l.), based on the global elevation classification system of Price et al. (2013). The superhigh-altitude site (N39°18'53", E94°15'40") was situated near the summit of the south slope of Dangjin Mountain in an alpine steppe ecosystem. In contrast, the high-altitude site (N39°24'42", E94°14'12") was situated at the northern base of the mountain within a temperate steppe zone (Zhu et al., 2024b). Despite being separated by only 30 km, the two locations exhibited marked climatic differences. Superhigh-altitude conditions were characterized by lower average daily temperatures and higher average daily humidity compared to high-altitude areas. While overall light intensity was similar between the sites, the timing of peak light intensity varied. At the high-altitude site, maximum light intensity occurred between 1000h and 1200h, while in the superhigh-altitude site, maximum light intensity peaked between 1300h and 1600h (Yu et al., 2023).

A reciprocal translocation experiment was conducted with a 2×2 factorial design that combined two populations of *P. vlangalii* (superhigh- and high-altitude females) with two environmental conditions (superhigh- and high-altitude habitats) (Figure 1A). The experimental groups were categorized as follows: high-high lizards (high-altitude lizards in their native environment), superhigh-superhigh lizards (superhigh-altitude lizards in their native environment), high-superhigh lizards (high-altitude lizards translocated to superhigh-altitude habitats), and superhigh-high lizards (superhigh-altitude lizards translocated to high-altitude habitats). At each study site, outdoor semi-natural circular enclosures (radius r=0.85 m) were constructed using transparent plastic sheets. These enclosures replicated the natural vegetation of their respective habitats and were covered with nets to prevent predation by birds.

Following capture, each lizard was measured for snout-vent length (SVL) using digital vernier calipers (PD-151, Prokit's Industries Co., Ltd., Taiwan, China) and for body mass (BM) with an electronic balance (ES-08B, Shanghai Hochoice Apparatus Manufacturer Co., Ltd., Shanghai, China). Individual identification was achieved through toe-clipping, and lizards were assigned to enclosures based on the experimental design, with two individuals per enclosure. Of the 60 pregnant females captured from the high-altitude population, half were placed in high-altitude enclosures, while the remainder were translocated to superhigh-altitude enclosures. Similarly, 60 pregnant females captured from the superhigh-altitude population were divided between superhigh-altitude and high-altitude enclosures. Consistent rearing was maintained in each enclosure, with food (*Tenebrio molitor* larvae and adults) provided *ad libitum* every two days.

Between July and August 2020, the captured females gave birth to their neonates, which were toe-clipped for individual identification. The neonates were measured for SVL and BM at birth and before overwintering. Cannibalism was not observed in this species, and stomach content analyses revealed no evidence of conspecific consumption (Zhao et al., 1999). Previous studies have indicated that mothers and offspring of this species share burrows (Qi et al., 2012). Through regular monitoring of enclosures, interactions between mothers and offspring were documented. Phenotypic data were collected from the offspring to evaluate developmental outcomes. As *P. vlangalii* is a viviparous species, it was not possible to establish germ-free conditions. To address this limitation, gut microbiota data from the offspring were analyzed to minimize the potential confounding effects of historical colonization.

In May and September 2021, the SVL and BM of juveniles were measured again. Resting metabolic rates were recorded in August 2021. Survival status was documented during these measurements, with survival coded as 1 and death as 0. Growth rates for SVL and BM were calculated for each individual using the formula $\ln(\text{measurement}_2/\text{measurement}_1)/(\text{date}_2\text{-date}_1)$ (Sun et al., 2018). Body condition was quantified using the scaled mass index (SMI) (Peig & Green, 2009), which accounts for the allometric relationship between SVL and BM. This index normalizes each individual's mass to the mean body size of the population. Data for males and females were analyzed separately, with sex identified based on ventral tail-tip coloration (orange for females, black for males) (Glavaš et al., 2020; Peig & Green, 2009; Zhao et al., 1999). The SMI was calculated using the following formula:

$$\hat{M}_i = M_i \left[\frac{L_0}{L_i} \right]^{b_{SMA}} \quad (1)$$

where M_i and L_i are the BM and SVL of lizard i, respectively; L_0 is an arithmetic mean value for the study population; b_{SMA} is the scaling exponent estimated by the SMA regression of M on L; and $\widehat{M}_i$ is the predicted BM for lizard i when the SVL is L_0.

From 19 to 25 August 2021, 32 lizard juveniles (eight per group) were randomly selected for field measurements of carbon dioxide production rates using closed-flow respirometry (FOXBOX, Sable Systems International, Henderson, GA, USA). These measures were conducted to estimate resting metabolic rates, which provide a critical measure of maintenance energy costs in ectotherms (Jiang et al., 2024; Rutschmann et al., 2024). Before testing, lizards were fasted for 48 h to standardize metabolic conditions and acclimated to temperatures of 18, 27, and 36°C (in random order) for 1 h. The temperature of 36°C closely approximates the preferred temperature of both studied populations (Zhu et al., 2024b). Closed-flow respirometry was performed in a 286 mL thermostatic chamber to measure carbon dioxide production and construct a thermal function curve for the metabolic rates of juveniles at set temperatures. To avoid possible biases from repeated measurements at the same temperature, the body temperature of each lizard was measured once a day. To minimize the impact of circadian rhythms, resting metabolic rate was only measured between 0900h and 1800h each day. The resting metabolic rate was calculated using the following formula:

$$\text{RMR} = \text{VCO}_2 \times \text{volume}/\text{body mass} \quad (2)$$

where VCO_2 is the CO_2 production rate, measured as percentage per hour (%/h), in a closed-circuit system. After the experiment, the female lizards were returned to their original field enclosures. All collection and handling procedures were approved by the Animal Ethics Committee of the Institute of Zoology, Chinese Academy of Sciences (IOZ-IACUC-2023-153).

Fecal collection and gut microbiota analysis

From 16 to 21 August 2021, fecal samples were collected from lizards to analyze their gut microbiome. Sampling was

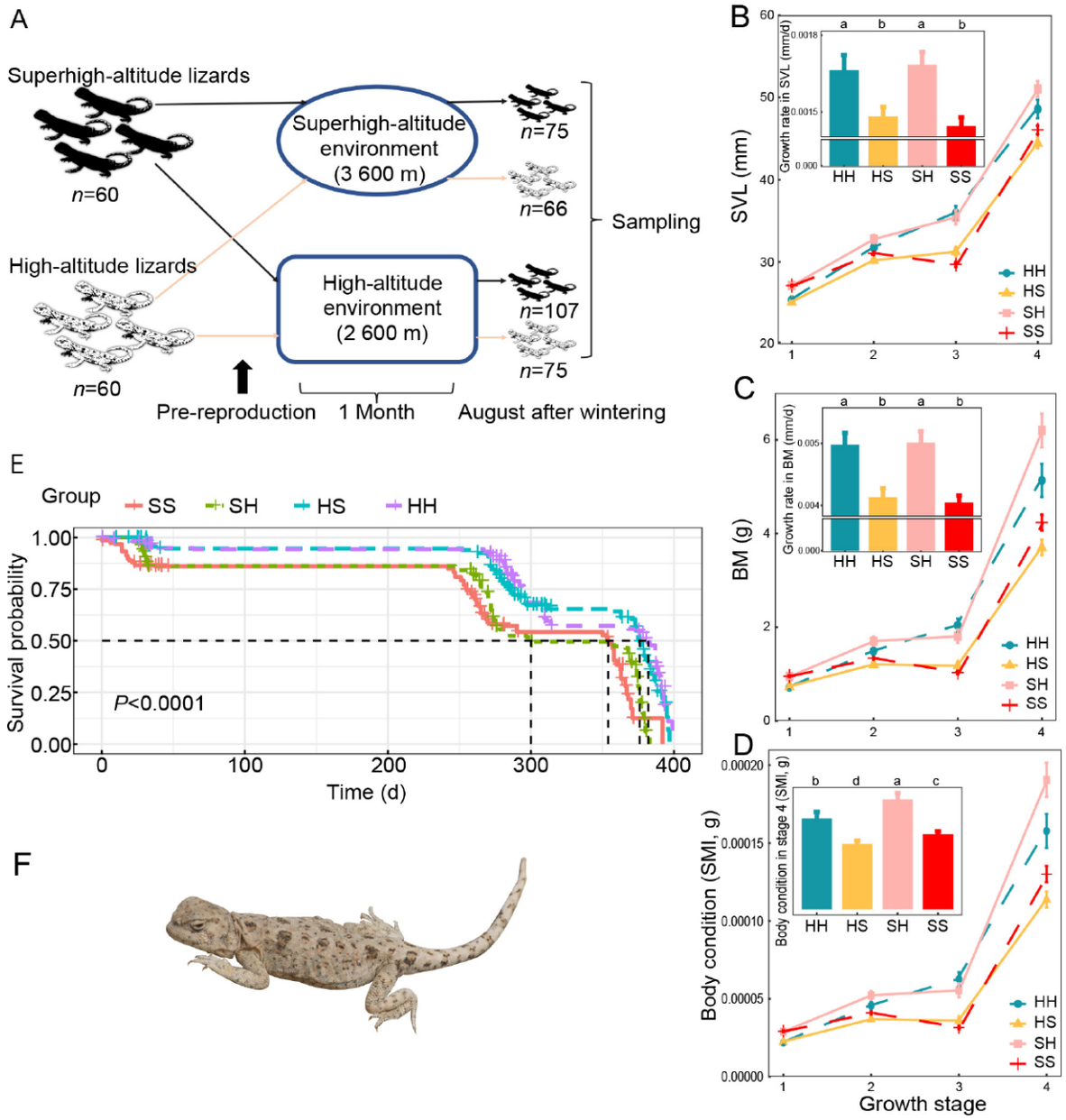


Figure 1 Experimental design and phenotypic changes

A: Reciprocal translocation experimental design. B–E: Phenotypic changes in each group in reciprocal translocation experiment: B: Snout-vent length (SVL); C: Body mass (BM); D: Body condition (SMI, scaled mass index); E: Kaplan-Meier survival curve, with time on the X-axis representing number of days after lizard births (July–September 2020). F: Photo of *Phrynocephalus vlangalii* (by Wei Yu). [a] & [b] represent differences between different treatment groups. Data are shown as mean±standard error (SE). HH and HS represent high-altitude lizards inhabiting native high-altitude environments and translocated to superhigh-altitude environments, respectively. SS and SH represent superhigh-altitude lizards inhabiting native superhigh-altitude environments and translocated to high-altitude environments, respectively. Numbers 1–4 on the X-axis represent four stages of lizard growth, respectively: after birth in 2020 (1), before wintering in 2020 (2), after emerging from hibernation in 2021 (3), and before wintering in 2021 (4).

conducted on sunny days between 1100h to 1600h. During this period, each lizard was individually transferred to a small, sterilized plastic container placed near its enclosure. Fecal matter produced during the observation period was promptly collected, ensuring minimal contamination. A total of 32 fecal samples were collected, with eight samples from each experimental group. The samples were immediately transferred to sterile tubes containing RNAlater for preservation. After collection, each lizard was returned to its enclosure. The collected samples were transported to the Institute of Zoology, Chinese Academy of Sciences, Beijing, and stored at –80°C for testing and analysis of gut microbiota.

DNA extraction, amplification, and sequencing were performed by Personal Biotechnology (China). Complete DNA samples were initially extracted using the E.Z.N.A™ Mag-Bind Soil DNA Kit (M5635, Omega, USA) following the manufacturer's protocols. DNA quality and concentration were assessed using a Quantifluor-ST fluorometer (Promega, E6090, USA) and Quant-iT PicoGreen dsDNA Assay Kit (Invitrogen, P7589, USA) at 260 nmol/L and 280 nmol/L, respectively. Additionally, DNA integrity was confirmed through 1.2% agarose gel electrophoresis.

The bacterial 16S rRNA gene V3–V4 hypervariable region was amplified using forward (338F: 5'-ACTCCTACGGGAG GCAGCA-3') and reverse primers (806R: 5'-GGACTACHVG GGTWTCTAAT-3'). The polymerase chain reaction (PCR) (25 mL) consisted of 1 mL of template DNA, 1 mL of amplicon PCR forward primer (10 mmol/L), 1 mL of amplicon PCR reverse primer (10 mmol/L), 2 mL of dNTP (2.5 mmol/L), 0.25 mL of Fast Pfu DNA Polymerase, 5 mL of 2×buffer, and 14.75 mL of ddH_2O. Thermal cycling was performed as follows: initial denaturation at 98°C for 5 min, followed by 25 cycles of denaturation at 98°C for 30 s, annealing at 52°C for 30 s, and extension at 72°C for 45 s, with a final extension step at 72°C for 5 min. Subsequently, PE250 paired-end sequencing was performed using the Illumina MiSeq platform (Illumina San Diego, USA) after the DNA libraries were mixed.

Raw sequencing reads were processed using QIIME 2 (v.2020.11.1) (Bolyen et al., 2019). Adapters were trimmed using Cutadapt (v.3.1) to remove sequences with at least 90% base overlap (Martin, 2011). The Divisive Amplicon Denoising Algorithm DADA2 (v.1.18.0) pipeline was utilized for sequence quality control, including filtering low-quality reads, denoising reads, merging forward and reverse reads, removing chimeric reads, and identifying amplicon sequence variants (ASVs) (Callahan et al., 2016). MAFFT (v.7.475) (Katoh et al., 2002) and FastTree (v.2.1.10) (Price et al., 2009) were used to align sequences and construct the phylogenetic tree. Taxonomic classification of ASVs was performed using the Greengenes reference database (v.13-8-99) (Desantis et al., 2006).

Statistical analysis

All statistical analyses were performed using R (v4.2.2). Data normality was assessed with the Shapiro-Wilk test, and homogeneity of variance was evaluated using the Bartlett test. Where necessary, data were normalized by exponential or logarithmic transformation. To explore the effects of population and rearing environment on juvenile growth rate, a linear mixed model was employed, with population and rearing environment as fixed factors and enclosures as random factors. Generalized linear mixed models, with a gamma distribution family, were used to analyze the effects of population and rearing environment on body condition (measured by SMI), with population, rearing environment, and growth stage as fixed factors and enclosures as random factors. Model selection was conducted using Akaike Information Criterion (AIC) (Supplementary Table S1), and *post hoc* tests were performed using the emmeans package. Repeated measures analysis of variance, conducted using the ez package in R, was used to investigate the effects of population and rearing environment on offspring resting metabolic rate, with population and rearing environment as fixed factors and rearing temperature as repeated measurement factors. Survival analysis was conducted using the Cox proportional risk model to detect the effects of population and rearing environment on survival probabilities, with model selection based on AIC. Kaplan-Meier survival curves were generated to visualize differences in survival rates between groups.

Microbial alpha diversity (Chao1 richness and Shannon diversity) was calculated using the vegan package, with the effects of population and environment assessed through linear models. Paired comparisons were performed using the nonparametric Wilcoxon rank sum test (Wilcoxon, 1945). For beta diversity, the Bray-Curtis distance was calculated, and permutational multivariate analysis of variance (PERMANOVA) was used to evaluate the influence of population and environment on microbial community composition. Principal coordinate analysis (PCoA) was conducted to visualize beta diversity patterns, with PC1 and PC2 compared using a *t*-test. Differences in intergroup microbial structure were compared using analysis of similarities (ANOSIM). Relative abundances at the phylum and gene levels were visualized using a bar chart. Differences in microbial composition among groups were explored using nonparametric tests implemented using the PMCMRplus package.

Gut microbiota plasticity was evaluated by determining whether microbial compositions of translocated lizards shifted toward those of native lizards. Host specificity was defined as the stability of microbial communities within a host, independent of environmental variation. Linear discriminant analysis effect size (LEfSe) was used to identify biomarkers distinguishing the gut microbiota of local and non-native lizards at both superhigh and high altitudes, providing insights into microbial abundance patterns specific to each host environment.

Spearman correlation analysis, conducted using the psych package, was used to determine the relationships between gut microbial composition (at the phylum, class, and genus levels) and growth rate (SVL and BM) or body condition. This approach was selected for its suitability in analyzing non-normally distributed data and its ability to capture monotonic relationships. Results were visualized using heatmaps.

To explore the functional implications of the observed plasticity and host specificity, differences in the abundance of microbial communities in the intestines and their corresponding functions were analyzed. *T*-test was used to compare differences in the relative abundance of microbes in the different Kyoto Encyclopedia of Genes and Genomes (KEGG) functional categories, and results were visualized with extended error bar plots, highlighting key differences in microbial function across groups.

RESULTS

Specific growth rate

The SVL growth rate in juvenile lizards was affected by the rearing environment ($F_{1,\ 55.89}$=17.96, P<0.001), but not by the population source ($F_{1,\ 90.95}$=0.30, P=0.59). Similarly, the BM growth rate was affected by the rearing environment ($F_{1,\ 57.60}$=29.95, P<0.001), but not by the population source ($F_{1,\ 92.56}$=0.39, P=0.54). Juveniles reared in the high-altitude environment exhibited accelerated growth in both SVL and BM, whereas those in the superhigh-altitude environment experienced reduced growth rates (Figure 1B, C).

Body condition and resting metabolic rates

Resting metabolic rates were not significantly affected by population source ($F_{1,\ 28}$=1.01, P=0.32), rearing environment ($F_{1,\ 28}$=2.97, P=0.10), or their interaction ($F_{1,\ 28}$=2.85, P=0.10; Supplementary Figure S1). However, resting metabolic rates increased significantly with rising temperatures in both the superhigh- and high-altitude environments ($F_{2,\ 56}$=163.33, P<0.001; Supplementary Figure S1).

The body condition (SMI) of lizards was significantly influenced by population source (χ^2=1 339.6, P<0.001), rearing environment (χ^2=20 543.7, P<0.001), growth stage

(χ^2=127 174.5, P<0.001), and the interaction between population and environment (χ^2=112.8, P<0.001; Figure 1D). At the end of the experiment, significant differences in body condition were observed among treatment groups (P<0.001), with SMI size rankings as follows: superhigh-high lizards>high-high lizards>superhigh-superhigh lizards>high-superhigh lizards (Figure 1D).

Survival rate

The survival rate of lizards was significantly impacted by population source (χ^2=53.63, P<0.001), but not by rearing environment (χ^2=0.24, P=0.62; Figure 1E). High-altitude lizards exhibited higher survival rates than superhigh-altitude lizards, regardless of rearing environment (P<0.001; Supplementary Figure S2A, D, E). Translocation did not significantly affect survival rates, regardless of population source (P>0.05; Supplementary Figure S2B, C).

Microbial alpha diversity

Gut microbiome alpha diversity, measured through Chao1 richness and Shannon diversity, revealed significant patterns. High-high lizards exhibited significantly higher gut Chao1 richness than superhigh-superhigh lizards (W=58, P<0.01), but no significant difference was observed in gut Shannon diversity between the two populations (W=46, P=0.16; Figure 2A, B). Linear model analyses indicated that rearing environment significantly affected gut Chao1 richness ($F_{1,\ 28}$=12.03, P<0.01), but not by population source ($F_{1,\ 28}$=1.72, P=0.20) or their interaction ($F_{1,\ 28}$=0.04, P=0.85). Similarly, gut Shannon diversity was affected by rearing environment ($F_{1,\ 28}$=8.97, P<0.01) but not by population source ($F_{1,\ 28}$=1.66, P=0.21) or their interaction ($F_{1,\ 28}$=0.02, P=0.88). High-altitude environments increased both the gut Shannon diversity (W=52, P<0.05) and Chao1 richness (W=64, P<0.001) in superhigh-altitude lizards (Figure 2A, B). Conversely, superhigh-altitude environments did not significantly affect the gut Shannon diversity (W=44, P=0.23) or Chao1 richness (W=50, P=0.06) of high-altitude lizards, although slight decreases were observed (Figure 2A, B).

Microbial beta diversity

Significant differences in gut microbiome structure were observed between superhigh- and high-altitude lizards ($F_{1,\ 14}$=2.19, P<0.001; Figure 2C; Supplementary Figure S3). After reciprocal translocations, the gut microbiome structure in both populations underwent substantial changes. These changes were significantly impacted by population source ($F_{1,\ 28}$=1.47, P<0.01) and rearing environment ($F_{1,\ 28}$=2.24, P<0.001), with no significant interaction between the two factors ($F_{1,\ 28}$=0.03, P=0.49; Figure 2C). Even at superhigh altitudes, the gut microbiome structures of the two populations

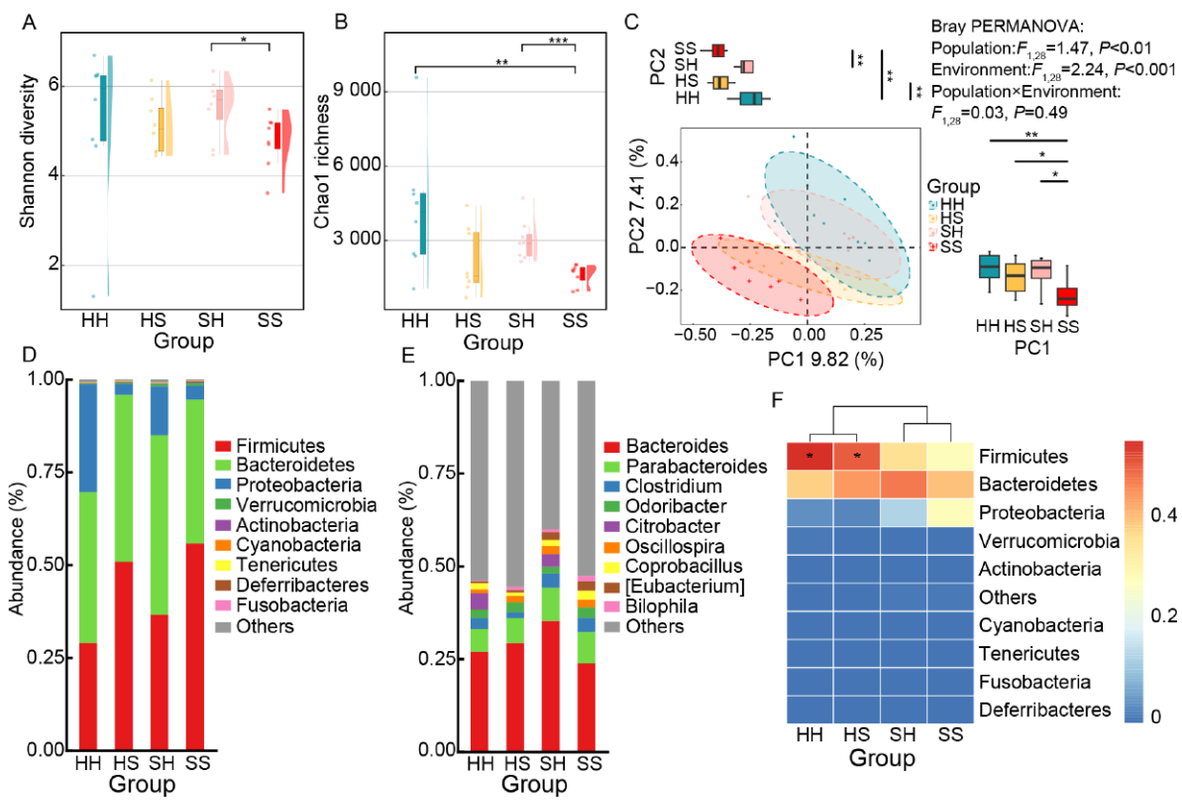


Figure 2 Gut microbiota diversity and composition in lizards

A, B: Changes in alpha diversity of gut microbiota in each group during reciprocal translocation experiments. A: Shannon diversity; B: Chao1 richness. C: Principal coordinates analysis (PCoA) and PERMANOVA analysis based on Bray-Curtis distance of each group in reciprocal translocation experiment, with two sets of grouped boxplots representing PC1 and PC2, illustrating distinctions among groups. D, E: Relative abundance of gut microbial composition. D: Phylum; E: Genus. F: Heatmap of inter-group differences in gut microbiota abundance at phylum level for *Phrynocephalus vlangalii*. Top hierarchical clustering tree indicates clustering relationships between groups, with asterisks denoting strong correlations between gut microbiota and samples. Asterisks indicate significant differences between two groups, *: P<0.05; **: P<0.01; ***: P<0.001. Data are mean±standard error (SE). HH and HS represent high-altitude lizards inhabiting native high-altitude environments and translocated to superhigh-altitude environments, respectively. SS and SH represent superhigh-altitude lizards inhabiting native superhigh-altitude environments and translocated to high-altitude environments, respectively.

remained distinct (Figure 2C; Supplementary Figure S3).

Gut microbiota composition

Analysis of fecal samples from the lizards revealed the presence of 24 phyla and 194 genera in their gut microbiota. The dominant phyla across both superhigh- and high-altitude lizards were *Firmicutes*, *Bacteroidetes*, and *Proteobacteria*, with their relative abundances corresponding to the respective rearing environments (Figure 2D). *Firmicutes* was particularly predominant in lizards originating from superhigh-altitude environments, while *Proteobacteria* showed lower relative abundance (Figure 2D; Supplementary Figure S4). Notably, the genus *Citrobacter* was significantly more abundant in high-altitude environments, irrespective of where the population originated, and less prevalent in superhigh-altitude environments (Figure 2E; Supplementary Figure S5).

Plasticity of gut microbiota

LEfSe analysis identified key biomarkers distinguishing superhigh- and high-altitude local populations, consistent with observed abundance differences between groups at the phylum and genus levels (Figure 3; Supplementary Figures S4, S5). The genera *Bacteroides* and *Citrobacter* were identified as key biomarkers for local high-altitude populations, while the phylum *Firmicutes* was the primary biomarker for the superhigh-altitude populations (Figure 3A). Translocation experiments demonstrated gut microbiota plasticity. In high-altitude lizards translocated to superhigh altitudes, *Citrobacter* abundance decreased significantly, while *Firmicutes* abundance increased significantly (Figure 3B). Conversely, in superhigh-altitude lizards translocated to high altitudes, *Firmicutes* abundance showed a marked decrease, while *Bacteroides* showed a marked increase (Figure 3C). LEfSe analysis further revealed that the class *Erysipelotrichia* was a host-specific bacterial group uniquely associated with superhigh-altitude lizards (Figure 3A, D).

Functional prediction of gut microbiota

KEGG enrichment analysis revealed significant shifts in metabolic pathways associated with gut microbial plasticity following translocation. When high-altitude lizards were translocated to superhigh-altitude environments, the beta-alanine metabolism pathway was significantly up-regulated, while the steroid biosynthesis pathway was significantly down-regulated (Figure 4B). When superhigh-altitude lizards were translocated to high-altitude environments, four metabolic pathways were significantly up-regulated, including folate biosynthesis, riboflavin metabolism, beta-alanine metabolism, and oxidative phosphorylation, and five metabolic pathways were significantly down-regulated, including base excision repair, D-arginine and D-ornithine metabolism, steroid biosynthesis, proteasome, meiosis-yeast (Figure 4C). No differential metabolic pathways were observed between the superhigh- and high-altitude populations within the high-altitude environment. However, in the superhigh-altitude environment, seven metabolic pathways were enriched in high-altitude lizards, and five metabolic pathways were enriched in superhigh-altitude lizards (Figure 4D). Notably, high-altitude lizards exhibited enrichment in the riboflavin metabolism pathway, while superhigh-altitude lizards showed enrichment in the fructose and mannose metabolism pathway.

DISCUSSION

Phenotypic plasticity is a key mechanism by which species adapt to novel and fluctuating environments (Alberdi et al., 2016; Fontaine & Kohl, 2023; Khakisahneh et al., 2020; Marsh et al., 2022; Uren Webster et al., 2018). Extensive research has highlighted the importance of plasticity in life history traits, behavior, physiology, and molecular mechanisms in environmental adaptation (Du, 2006; Iraeta et al., 2006, 2008; Lane et al., 2019; Sears, 2005; Sun et al., 2018, 2022; Wong et al., 2021). However, the plasticity of the gut microbiome and its influence on host adaptability remain underexplored, particularly in the context of rapidly changing environments. This study explored the plasticity and host specificity of the gut microbiome in *P. vlangalii* and their potential implications for host fitness. The findings aligned with our predictions that the gut microbiome of *P. vlangalii* exhibited remarkable plasticity and underwent substantial alterations following translocation. Both environmental plasticity and population genetic factors significantly influenced the gut microbiome structure. Furthermore, specific microbial markers and functional pathways associated with microbiota plasticity demonstrated possible effects on host fitness, suggesting a functional role of gut microbial adaptation in host resilience to environmental shifts.

To mitigate the potential confounding effects of historical colonization, which could obscure the plasticity of the gut microbiome in response to new environments, our analysis focused exclusively on the offspring of translocated lizards. Historical colonization refers to the stable microbial community present before translocation, which may persist and influence subsequent microbial changes (Uren Webster et al., 2020). Although this approach limits direct observations of initial microbial shifts in adults, it provides a more accurate assessment of how gut microbiota respond to environmental changes without pre-existing microbial interference. Overall, these results highlight the dual influence of environmental plasticity and host specificity in shaping the gut microbiome of *P. vlangalii*, with changes in the gut microbiome likely playing pivotal roles in enhancing host fitness.

Our findings revealed that gut microbiome diversity was higher in the high-altitude lizards than in the superhigh-altitude lizards (Figure 2B). The dominant phyla in both populations were *Bacteroidetes* and *Firmicutes* (Figure 2D), consistent with previous research (Zhang et al., 2018). However, the gut microbiome of high-altitude lizards was distinguished by the significant presence of *Citrobacter* within the phylum *Proteobacteria* (Figure 2D, E). LEfSe analysis identified *Citrobacter* and *Bacteroides* as key biomarkers in high-altitude lizards, whereas *Firmicutes* was the key biomarker in superhigh-altitude lizards (Figure 3A). Mechanistically, *Citrobacter* has been shown to enhance host energy storage by modulating the gut microbial community (Melaku et al., 2021; Zhang et al., 2020), while *Bacteroides* has been shown to induce gut IgA production for immune regulation (Yang et al., 2020). The enrichment of these microbes in high-altitude lizards highlights their potential importance in optimizing energy metabolism and strengthening immunity under these environmental conditions. Additionally, functional enrichment analysis indicated that the nine metabolic pathways enriched in the gut microbiome of lizards at high altitudes were mainly related to energy production, lipid, and protein synthesis (Figure 4A). A more diverse gut microbiome may enhance energy regulation and fat storage, as suggested in previous studies (Sommer et al., 2016; Wang et al., 2020). This functional capacity aligns with the observed higher growth rates, improved body condition (SMI), and greater

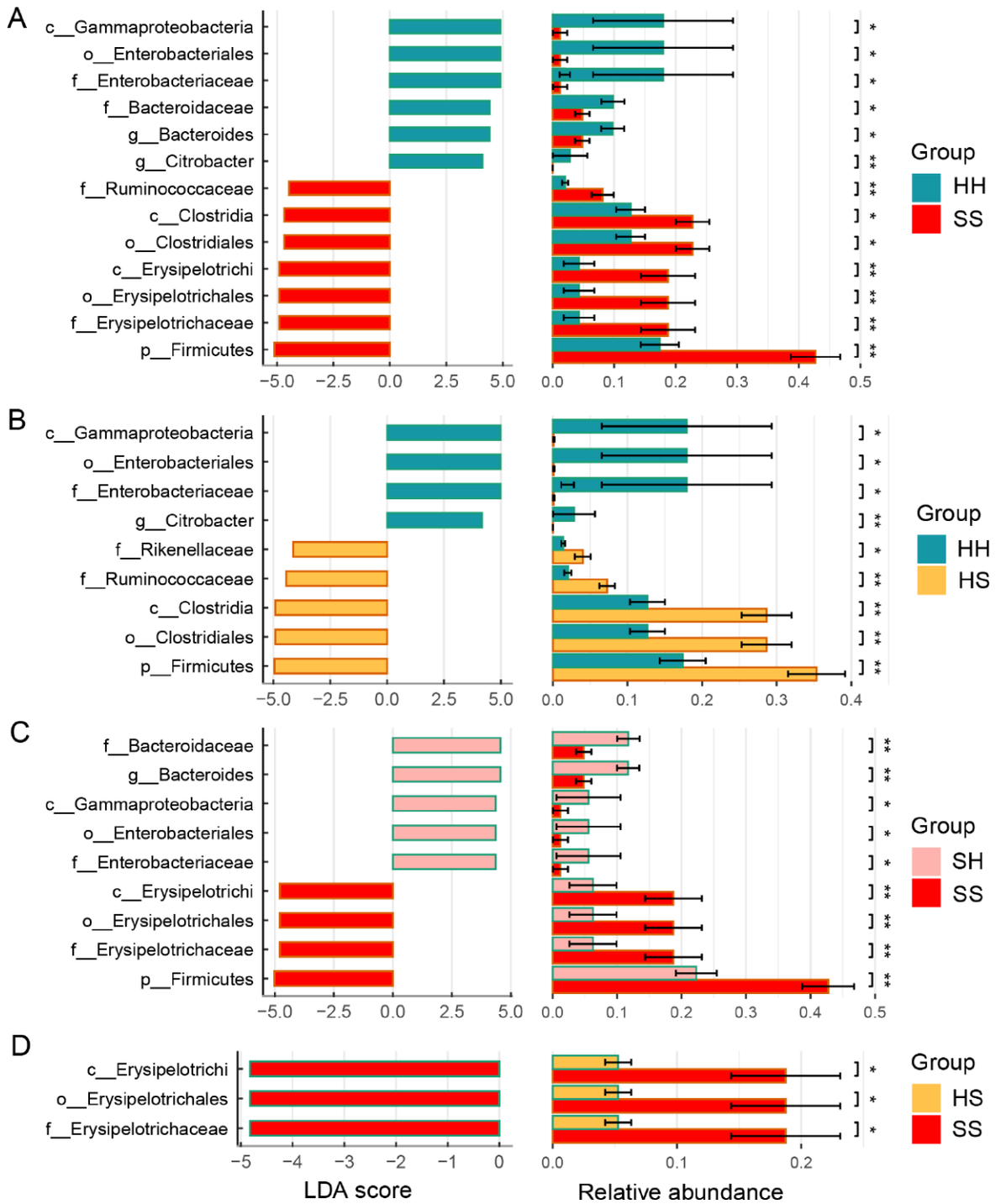


Figure 3 Differences in bacterial taxa of *Phrynocephalus vlangalii* determined using linear discriminant analysis of effect size (LEfSe)

A: Comparisons between source populations. B, C: Comparisons of plasticity. D: Host-specificity comparisons. Left: LDA score plots, Right: Corresponding Kruskal-Wallis single-factor tests of abundance among groups. Asterisks indicate significant differences between two groups, *: $P<0.05$; **: $P<0.01$; ***: $P<0.001$. HH and HS represent high-altitude lizards inhabiting native high-altitude environments and translocated to superhigh-altitude environments, respectively. SS and SH represent superhigh-altitude lizards inhabiting native superhigh-altitude environments and translocated to high-altitude environments, respectively.

survival rates in high-altitude lizards compared to superhigh-altitude lizards (Figure 1; Supplementary Figure S2A). The elevated presence of *Citrobacter* and the increased Shannon diversity in high-altitude lizards may contribute to more effective energy management and better overall fitness. Interestingly, high-altitude lizards tend to experience lower parasitic infection rates (Megía-Palma et al., 2020), which may influence the composition of their gut microbial communities. However, further investigation is needed to elucidate the interplay between parasitic infections and gut microbiome composition in these populations.

Do environmental changes drive the gut microbiota of translocated lizards to resemble those of native populations? Our reciprocal translocation experiments demonstrated that the alpha diversity of the gut microbiota in *P. vlangalii* was influenced only by rearing environment, highlighting the

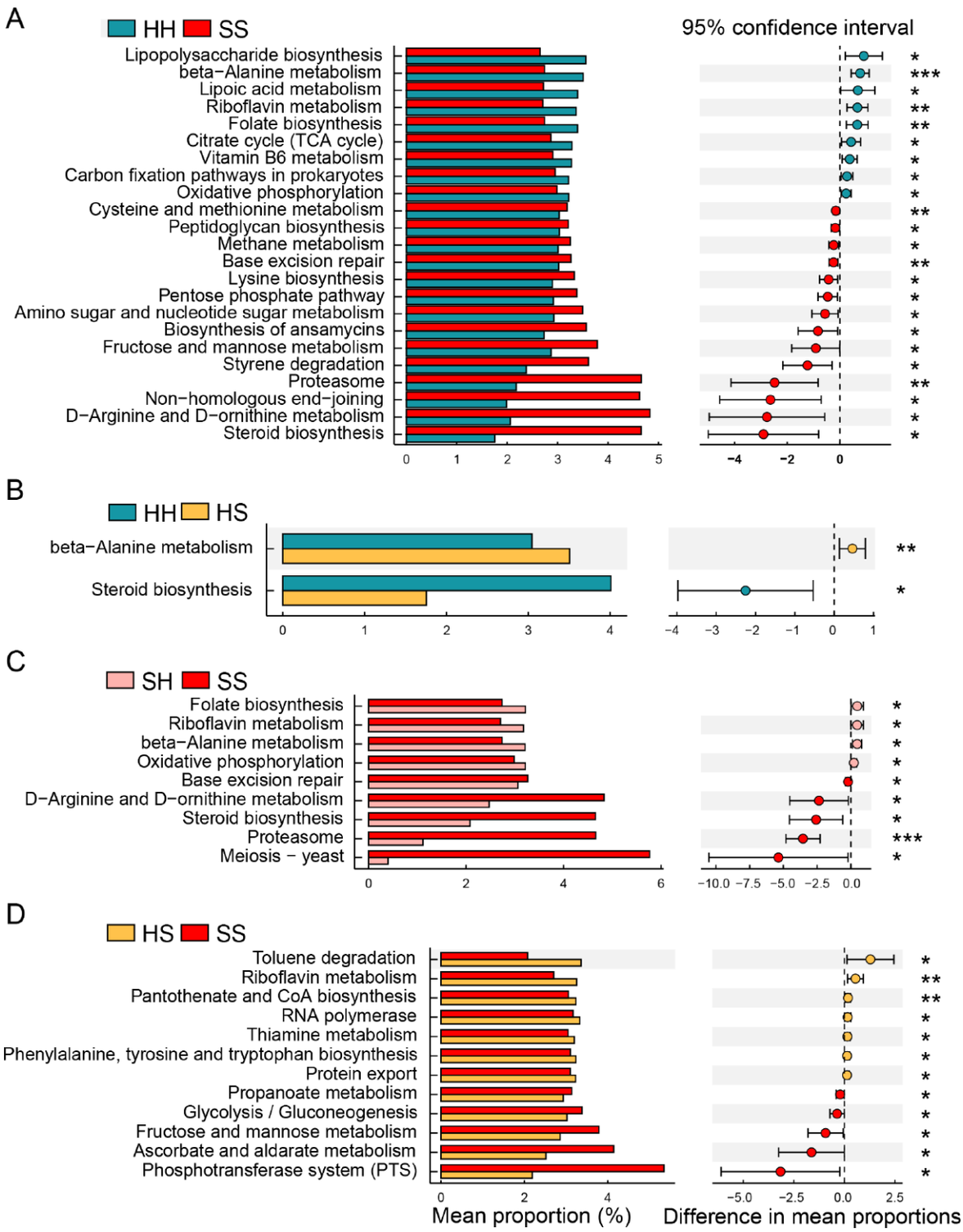


Figure 4 Relative abundance of KEGG orthologs in *Phrynocephalus vlangalii* detected by PICRUSt2 analysis

A: Comparisons between source populations. B, C: Comparisons of plasticity. D: Host-specificity comparisons (no significant difference in KEGG ortholog relative abundance between HH and SH). Asterisks indicate significant differences between two groups, *: P<0.05; **: P<0.01; ***: P<0.001. HH and HS represent high-altitude lizards inhabiting native high-altitude environments and translocated to superhigh-altitude environments, respectively. SS and SH represent superhigh-altitude lizards inhabiting native superhigh-altitude environments and translocated to high-altitude environments, respectively.

remarkable plasticity of gut microbes to altitudinal shifts (Figure 2A, B). This finding underscores the crucial role of environmental factors, particularly altitude, in shaping gut microbiota composition. For instance, lizards residing at high altitudes (2 900 m) exhibited greater microbial diversity than their counterparts at superhigh altitudes (4 250 m), consistent with previous research linking altitudinal gradients with microbial diversity (Zhang et al., 2018).

Our results further revealed a significant increase in alpha diversity (Chao1 richness and Shannon index) in superhigh-

altitude lizards translocated to high-altitude environments. This increase may be attributed to the improved environmental conditions, such as higher temperature and oxygen availability at lower altitudes. Conversely, the alpha diversity of high-altitude lizards remained stable even after translocation to superhigh altitudes, maintaining higher levels. This stability may be related to maternal microbial transmission, which has been shown to influence gut microbiota composition and persist into adulthood (Ren et al., 2017).

Environmental factors played a dominant role in determining the composition of gut microbiota, as evidenced by a hierarchical clustering heatmap of species composition (Figure 2F). Both superhigh- and high-altitude lizards exhibited significant changes in beta diversity following translocation, reflecting strong microbial plasticity (Figure 2C; Supplementary Figure S3). However, high-altitude lizards translocated to superhigh altitudes displayed no changes along the PC2 axis, indicating that certain gut microbial components did not change with the environment and were host specific (Figure 2C). Analysis of population sources and rearing environments revealed that the structure of the gut microbial communities was shaped by both environmental plasticity and host specificity (Figure 2C; Supplementary Figure S3). High-altitude environments were associated with enhanced microbial diversity, while high-altitude lizards appeared to sustain elevated diversity levels even under superhigh-altitude conditions, likely due to maternal effects. Overall, these findings indicate that gut microbial composition in *P. vlangalii* is shaped by both plastic responses to environmental conditions and intrinsic host-specific factors. While the gut microbiota of translocated lizards adjusts to resemble that of native populations, host-specific components persist.

Our findings reveal that after high-altitude lizards were translocated to superhigh altitudes, their growth rates and body condition declined, while survival remained unaffected (Figure 1; Supplementary Figure S2B). This decline coincided with a significant reduction in the abundance of *Citrobacter* and a marked increase in the abundance of *Firmicutes* (Figures 2D, E, 3B; Supplementary Figure S5). *Citrobacter* is known to enhance host energy storage by influencing the gut microbial community and increasing the availability of glucose and lipids, crucial for growth and metabolic function (Zhang et al., 2020). Conversely, *Firmicutes*, involved in the production of short-chain fatty acids (SCFAs) such as butyrate, which modulate immune function, exhibited a negative correlation with growth in both BM and SVL (Ridaura et al., 2013; Turnbaugh et al., 2006). This negative correlation may reflect a trade-off where heightened immune activity diverts resources from growth and metabolic demands. These findings were supported by metabolic analysis. Notably, after high-altitude lizards were translocated to superhigh altitudes, beta-alanine metabolism significantly increased, while steroid biosynthesis significantly decreased (Figure 4B). This metabolic shift likely reduces fat storage, potentially promoting growth (Nie et al., 2023). However, the reduced body condition observed at superhigh altitudes compared to high altitudes (Figure 1D: HH>HS) indicates that these changes may not fully mitigate the challenges of superhigh-altitude environments. In contrast, when superhigh-altitude lizards were translocated to high altitudes, their growth rates and body condition improved, although their survival rates remained unchanged (Figure 1B–D; Supplementary Figure S2C). This improvement was accompanied by a significant decrease in the abundance of *Firmicutes* and a marked increase in the abundance of *Bacteroides* (Figures 2D, E, 3C; Supplementary Figure S4). While *Firmicutes* contributes SCFAs with immune modulatory functions, *Bacteroidetes* promotes IgA production, enhancing immune regulation (Ridaura et al., 2013; Turnbaugh et al., 2006). The high-altitude environment fostered greater microbial diversity, as evidenced by increased Chao1 indices when superhigh-altitude lizards were translocated to high altitudes (Figure 2B). Enhanced microbial diversity is associated with improved energy metabolism and fat storage (Sommer et al., 2016; Wang et al., 2020). Briefly, we identified considerable plasticity in the gut microbiome of *P. vlangalii*. High-altitude environments induced greater gut microbiome diversity, while superhigh-altitude environments induced the opposite trend. Our results also indicated that *Citrobacter* may be beneficial for host growth, while *Erysipelotrichia* and *Firmicutes* were negatively correlated with host growth (Supplementary Figure S6), potentially reflecting adaptations to resource-limited environments (Zhu et al., 2024a). Evaluating the ecological significance of these phenotypic changes is challenging due to the complexity of underlying biological mechanisms. Future studies should prioritize experimental manipulation of the gut microbiome to validate its effects on growth and other physiological traits. Integrating host metabolomics and transcriptomics will provide deeper insights into how the gut microbiome influences host survival, physiological functions, and adaptive significance of phenotypic plasticity.

Our findings also demonstrated that the gut microbiota of both superhigh- and high-altitude lizards exhibited strong host specificity. Notably, growth rates did not significantly differ between populations, regardless of the rearing environment. However, superhigh-altitude lizards exhibited lower survival rates but better body condition compared to their high-altitude counterparts (Figure 1B–D; Supplementary Figure S2D, E). Beta diversity analysis revealed that population origin significantly influenced the gut microbiome structure, with clear differences along the PC2 axis in the superhigh-altitude environment between the two populations (Figure 2C). This stable association between the gut microbiome and population origin underscores the host specificity of the gut microbial community in these lizards. While these findings suggest a potential influence of both altitude and population origin on microbial community structure, sampling additional populations across varying altitudes could further clarify whether these effects are altitude-specific or site-dependent.

LEfSe analysis identified *Erysipelotrichaceae* as a key biomarker in the gut microbiome of superhigh-altitude lizards (Figure 3D). This bacterial family has been implicated in lipid metabolism disorders and inflammation (Kaakoush, 2015; Wu et al., 2021), potentially contributing to the lower survival rates observed in superhigh-altitude lizards (Supplementary Figure S2D, E). Furthermore, metabolic pathway analysis revealed distinct patterns between the two populations. High-altitude lizards exhibited enrichment in seven metabolic pathways, primarily related to protein production (Figure 3D). Conversely, superhigh-altitude lizards showed enrichment in five metabolic pathways, including the propanoate metabolism pathway, which is related to obesity (Jiao et al., 2018). These findings may partially explain the better body condition observed in superhigh-altitude lizards. Furthermore, a significant negative correlation was detected between *Erysipelothrix* abundance

and host growth (Supplementary Figure S6B). This association suggests that the host-specific gut microbiota of superhigh-altitude lizards may limit their growth rate, reflecting a trade-off between maintaining body condition and achieving growth in resource-limited environments.

In summary, our findings revealed significant differences in the gut microbiome between superhigh- and high-altitude populations of *P. vlangalii*, primarily driven by environmental factors related to altitude. Translocation experiments demonstrated pronounced plasticity in the gut microbiome, emphasizing its adaptability to environmental changes and its potential influence on host fitness. Notably, the closer the gut microbiome of translocated lizards resembled that of the local altitude population, the better their growth, body condition, and survival performance. In superhigh-altitude lizards, the host-specific gut microbiota composition, characterized by the presence of *Erysipelotrichaceae* and enrichment in lipid metabolism pathways associated with obesity, likely contributed to their lower survival rates despite better body condition compared to high-altitude lizards. These findings underscore the critical role of gut microbiota in mediating host physiological responses and highlight the vulnerability of superhigh-altitude populations to environmental pressures that shape gut microbiomes. Future studies should include mid-term monitoring of gut microbiota in translocated populations to assess whether microbial communities gradually converge with those of the local population or whether there is a persistent historical legacy effect (Baldo et al., 2023). Such insights will provide a deeper understanding of the long-term dynamics of gut microbiota in response to environmental changes. While this study did not deeply explore the mechanisms by which gut microbes influence adaptive phenotypes, existing studies have shown that gut microbes can affect host phenotypes by regulating metabolism and physiological functions (Sommer et al., 2016; Wang et al., 2020). Future studies should focus on the potential of microbial transplantation to facilitate phenotypic transitions between high- and low-altitude environments and assess its role in enhancing adaptability. Such studies will help clarify the functional contributions of gut microbiota to host adaptation in diverse and challenging ecosystems.

DATA AVAILABILITY

The metadata and raw sequence reads have been deposited in the NCBI SRA database (PRJNA1141194), China National Center for Bioinformation (PRJCA032768), and Science Data Bank databases (DOI: 10.57760/sciencedb.j00139.00134).

SUPPLEMENTARY DATA

Supplementary data to this article can be found online.

COMPETING INTERESTS

The authors declare that they have no competing interests.

AUTHORS' CONTRIBUTIONS

Z.G.Z., Z.S.L., L.W.T., W.G.D., and W.Y. conceived and designed the studies. W.Y., J.Y., Z.Y.Z., X.L.Z., and S.C. collected and analyzed the data; W.Y., J.Y., L.W.T., S.C., and Z.G.Z. wrote the manuscript, and all authors contributed to revisions. All authors read and approved the final version of the manuscript.

ACKNOWLEDGMENTS

We thank Bao-Jun Sun for advice on experimental design and manuscript preparation and Shuo Liu for help with data analysis. We thank Zhong-Wen Jiang for suggestions on manuscript revisions.

REFERENCES

Alberdi A, Aizpurua O, Bohmann K, et al. 2016. Do vertebrate gut metagenomes confer rapid ecological adaptation?. *Trends in Ecology & Evolution*, **31**(9): 689–699.

Baldo L, Tavecchia G, Rotger A, et al. 2023. Insular holobionts: persistence and seasonal plasticity of the Balearic wall lizard (*Podarcis lilfordi*) gut microbiota. *PeerJ*, **11**: e14511.

Baniel A, Amato KR, Beehner JC, et al. 2021. Seasonal shifts in the gut microbiome indicate plastic responses to diet in wild geladas. *Microbiome*, **9**(1): 26.

Becheler R, Haverbeck D, Clerc C, et al. 2022. Variation in thermal tolerance of the Giant Kelp's gametophytes: suitability of habitat, population quality or local adaptation?. *Frontiers in Marine Science*, **9**: 802535.

Bletz MC, Goedbloed DJ, Sanchez E, et al. 2016. Amphibian gut microbiota shifts differentially in community structure but converges on habitat-specific predicted functions. *Nature Communications*, **7**: 13699.

Bolyen E, Rideout JR, Dillon MR, et al. 2019. Reproducible, interactive, scalable and extensible microbiome data science using QIIME 2. *Nature Biotechnology*, **37**(8): 852–857.

Callahan BJ, Mcmurdie PJ, Rosen MJ, et al. 2016. DADA2: high-resolution sample inference from Illumina amplicon data. *Nature Methods*, **13**(7): 581–583.

Carrier TJ, Reitzel AM. 2018. Convergent shifts in host-associated microbial communities across environmentally elicited phenotypes. *Nature Communications*, **9**(1): 952.

Catullo RA, Llewelyn J, Phillips BL, et al. 2019. The potential for rapid evolution under anthropogenic climate change. *Current Biology*, **29**(19): R996–R1007.

Chen CY, Chen PC, Weng FCH, et al. 2017. Habitat and indigenous gut microbes contribute to the plasticity of gut microbiome in oriental river prawn during rapid environmental change. *PLoS One*, **12**(7): e0181427.

Chen HY, Li CQ, Chen SY, et al. 2023. Metagenomic analysis reveals hidden links between gut microbes and habitat adaptation among cave and surface dwelling *Sinocyclocheilus* species. *Zoological Research*, **44**(4): 793–807.

Chen JQ, Zhang LW, Zhao RM, et al. 2022. Gut microbiota differs between two cold-climate lizards distributed in thermally different regions. *BMC Ecology and Evolution*, **22**(1): 120.

Chung H, Pamp SJ, Hill JA, et al. 2012. Gut immune maturation depends on colonization with a host-specific microbiota. *Cell*, **149**(7): 1578–1593.

Čupić M, Marčić Z, Lukić M, et al. 2023. The first cavefish in the Dinaric Karst? Cave colonization made possible by phenotypic plasticity in *Telestes karsticus*. *Zoological Research*, **44**(4): 821–833.

Desantis TZ, Hugenholtz P, Larsen N, et al. 2006. Greengenes, a chimera-checked 16S rRNA gene database and workbench compatible with ARB. *Applied and Environmental Microbiology*, **72**(7): 5069–5072.

Du WG. 2006. Phenotypic plasticity in reproductive traits induced by food availability in a lacertid lizard, *Takydromus septentrionalis*. *Oikos*, **112**(2): 363–369.

Du XX, Li FG, Kong FL, et al. 2022. Altitude-adaption of gut microbiota in Tibetan chicken. *Poultry Science*, **101**(9): 101998.

Fietz K, Rye Hintze CO, Skovrind M, et al. 2018. Mind the gut: genomic insights to population divergence and gut microbial composition of two marine keystone species. *Microbiome*, **6**(1): 82.

Fontaine SS, Mineo PM, Kohl KD. 2022. Experimental manipulation of microbiota reduces host thermal tolerance and fitness under heat stress in a vertebrate ectotherm. *Nature Ecology & Evolution*, **6**(4): 405–417.

Fontaine SS, Kohl KD. 2023. The microbiome buffers tadpole hosts from heat stress: a hologenomic approach to understand host-microbe interactions under warming. *Journal of Experimental Biology*, **226**(1): jeb245191.

Gensollen T, Iyer SS, Kasper DL, et al. 2016. How colonization by microbiota in early life shapes the immune system. *Science*, **352**(6285): 539–544.

Glavaš OJ, Počanić P, Lovrić V, et al. 2020. Morphological and ecological divergence in two populations of European glass lizard, *Pseudopus apodus* (Squamata: Anguidae). *Zoological Research*, **41**(2): 172–181.

Greyson-Gaito CJ, Bartley TJ, Cottenie K, et al. 2020. Into the wild: microbiome transplant studies need broader ecological reality. *Proceedings of the Royal Society B: Biological Sciences*, **287**(1921): 20192834.

Hao X, Wang CX, Han XZ, et al. 2021. A reciprocal egg-swap experiment reveals sources of variation in developmental success among populations of a desert lizard. *Oecologia*, **196**(1): 27–35.

He XP, Chaganti SR, Heath DD. 2018. Population-specific responses to interspecific competition in the gut microbiota of two atlantic salmon (*Salmo salar*) populations. *Microbial Ecology*, **75**(1): 140–151.

Hicks AL, Lee KJ, Couto-Rodriguez M, et al. 2018. Gut microbiomes of wild great apes fluctuate seasonally in response to diet. *Nature Communications*, **9**(1): 1786.

Ho WC, Li DY, Zhu Q, et al. 2020. Phenotypic plasticity as a long-term memory easing readaptations to ancestral environments. *Science Advances*, **6**(21): eaba3388.

Iraeta P, Monasterio C, Salvador A, et al. 2006. Mediterranean hatchling lizards grow faster at higher altitude: a reciprocal transplant experiment. *Functional Ecology*, **20**(5): 865–872.

Iraeta P, Salvador A, Díaz JA. 2008. A reciprocal transplant study of activity, body size, and winter survivorship in juvenile lizards from two sites at different altitude. *É coscience*, **15**(3): 298–304.

Jiang ZW, Ma L, Tao SA, et al. 2024. Analysis of resting status reveals distinct elevational variation in metabolisms of lizards. *Ecology*, **105**(10): e4414.

Jiao N, Baker SS, Nugent CA, et al. 2018. Gut microbiome may contribute to insulin resistance and systemic inflammation in obese rodents: a meta-analysis. *Physiological Genomics*, **50**(4): 244–254.

Johnson LC, Galliart MB, Alsdurf JD, et al. 2022. Reciprocal transplant gardens as gold standard to detect local adaptation in grassland species: new opportunities moving into the 21st century. *Journal of Ecology*, **110**(5): 1054–1071.

Kaakoush NO. 2015. Insights into the role of *Erysipelotrichaceae* in the human host. *Frontiers in Cellular and Infection Microbiology*, **5**: 84.

Katoh K, Misawa K, Kuma KI, et al. 2002. MAFFT: a novel method for rapid multiple sequence alignment based on fast Fourier transform. *Nucleic Acids Research*, **30**(14): 3059–3066.

Kawecki TJ, Ebert D. 2004. Conceptual issues in local adaptation. *Ecology Letters*, **7**(12): 1225–1241.

Khakisahneh S, Zhang XY, Nouri Z, et al. 2020. Gut microbiota and host thermoregulation in response to ambient temperature fluctuations. *mSystems*, **5**(5): e00514–20.

Krist M, Munclinger P, Briedis M, et al. 2021. The genetic regulation of avian migration timing: combining candidate genes and quantitative genetic approaches in a long-distance migrant. *Oecologia*, **196**(2): 373–387.

Lane JE, Czenze ZJ, Findlay-Robinson R, et al. 2019. Phenotypic plasticity and local adaptation in a wild hibernator evaluated through reciprocal translocation. *The American Naturalist*, **194**(4): 516–528.

Ley RE, Hamady M, Lozupone C, et al. 2008. Evolution of mammals and their gut microbes. *Science*, **320**(5883): 1647–1651.

Littleford-Colquhoun BL, Weyrich LS, Jackson N, et al. 2019. City life alters the gut microbiome and stable isotope profiling of the eastern water dragon (*Intellagama lesueurii*). *Molecular Ecology*, **28**(20): 4592–4607.

Lu HL, Xu CX, Jin YT, et al. 2018a. Proximate causes of altitudinal differences in body size in an agamid lizard. *Ecology and Evolution*, **8**(1): 645–654.

Lu HL, Xu CX, Zeng ZG, et al. 2018b. Environmental causes of between-population difference in growth rate of a high-altitude lizard. *BMC Ecology*, **18**(1): 37.

Ma L, Sun BJ, Cao P, et al. 2018. Phenotypic plasticity may help lizards cope with increasingly variable temperatures. *Oecologia*, **187**(1): 37–45.

Mallott EK, Skovmand LH, Garber PA, et al. 2022. The faecal metabolome of black howler monkeys (*Alouatta pigra*) varies in response to seasonal dietary changes. *Molecular Ecology*, **31**(15): 4146–4161.

Marsh KJ, Raulo AM, Brouard M, et al. 2022. Synchronous seasonality in the gut microbiota of wild mouse populations. *Frontiers in Microbiology*, **13**: 809735.

Martin M. 2011. Cutadapt removes adapter sequences from high-throughput sequencing reads. *EMBnet. Journal*, **17**(1): 10–12.

Martínez I, Maldonado-Gomez MX, Gomes-Neto JC, et al. 2018. Experimental evaluation of the importance of colonization history in early-life gut microbiota assembly. *eLife*, **7**: e36521.

Mazel F, Guisan A, Parfrey LW. 2024. Transmission mode and dispersal traits correlate with host specificity in mammalian gut microbes. *Molecular Ecology*, **33**(1): e16862.

Megía-Palma R, Arregui L, Pozo I, et al. 2020. Geographic patterns of stress in insular lizards reveal anthropogenic and climatic signatures. *Science of the Total Environment*, **749**: 141655.

Melaku M, Zhong RQ, Han H, et al. 2021. Butyric and citric acids and their salts in poultry nutrition: effects on gut health and intestinal microbiota. *International Journal of Molecular Sciences*, **22**(19): 10392.

Moeller AH, Ivey K, Cornwall MB, et al. 2020. The lizard gut microbiome changes with temperature and is associated with heat tolerance. *Applied and Environmental Microbiology*, **86**(17): e01181–20.

Nie ZJ, Xu XT, Shao NL, et al. 2023. Integrative analysis of microbiome and metabolome reveals the linkage between gut microbiota and carp growth. *Environmental Research*, **220**: 115133.

Nielsen DP, Harrison JG, Byer NW, et al. 2023. The gut microbiome reflects ancestry despite dietary shifts across a hybrid zone. *Ecology Letters*, **26**(1): 63–75.

Niewiarowski PH, Roosenburg W. 1993. Reciprocal transplant reveals sources of variation in growth rates of the lizard *Sceloporus undulatus*. *Ecology*, **74**(7): 1992–2002.

Ortega J, López P, Martín J. 2017. Environmental drivers of growth rates in Guadarrama wall lizards: a reciprocal transplant experiment. *Biological Journal of the Linnean Society*, **122**(2): 340–350.

Peig J, Green AJ. 2009. New perspectives for estimating body condition from mass/length data: the scaled mass index as an alternative method. *Oikos*, **118**(12): 1883–1891.

Petipas RH, Geber MA, Lau JA. 2021. Microbe-mediated adaptation in plants. *Ecology Letters*, **24**(7): 1302–1317.

Piazzon MC, Naya-Català F, Perera E, et al. 2020. Genetic selection for growth drives differences in intestinal microbiota composition and parasite disease resistance in Gilthead sea bream. *Microbiome*, **8**(1): 168.

Pigliucci M. 2005. Evolution of phenotypic plasticity: where are we going now?. *Trends in Ecology & Evolution*, **20**(9): 481–486.

Powell E, Ratnayeke N, Moran NA. 2016. Strain diversity and host specificity in a specialized gut symbiont of honeybees and bumblebees. *Molecular Ecology*, **25**(18): 4461–4471.

Price MF, Byers AC, Friend DA, et al. 2013. Mountain Geography: Physical and Human Dimensions. Berkeley: University of California Press.

Price MN, Dehal PS, Arkin AP. 2009. FastTree: computing large minimum evolution trees with profiles instead of a distance matrix. *Molecular Biology and Evolution*, **26**(7): 1641–1650.

Qi Y, Noble DWA, Fu JZ, et al. 2012. Spatial and social organization in a burrow-dwelling lizard (*Phrynocephalus vlangalii*) from China. *PLoS One*, **7**(7): e41130.

Regan CE, Sheldon BC. 2023. Phenotypic plasticity increases exposure to extreme climatic events that reduce individual fitness. *Global Change Biology*, **29**(11): 2968–2980.

Ren TT, Boutin S, Humphries MM, et al. 2017. Seasonal, spatial, and maternal effects on gut microbiome in wild red squirrels. *Microbiome*, **5**(1): 163.

Rennison DJ, Rudman SM, Schluter D. 2019. Parallel changes in gut microbiome composition and function during colonization, local adaptation and ecological speciation. *Proceedings of the Royal Society B: Biological Sciences*, **286**(1916): 20191911.

Ridaura VK, Faith JJ, Rey FE, et al. 2013. Gut microbiota from twins discordant for obesity modulate metabolism in mice. *Science*, **341**(6150): 1241214.

Riddle MR, Nguyen NK, Nave M, et al. 2024. Host evolution shapes gut microbiome composition in *Astyanax mexicanus*. *Ecology and Evolution*, **14**(4): e11192.

Rutschmann A, Perry C, Le Galliard JF, et al. 2024. Ecological responses of squamate reptiles to nocturnal warming. *Biological Reviews*, **99**(2): 598–621.

Sauers LA, Sadd BM. 2019. An interaction between host and microbe genotypes determines colonization success of a key bumble bee gut microbiota member. *Evolution*, **73**(11): 2333–2342.

Schuster L, White CR, Marshall DJ. 2021. Plastic but not adaptive: habitat‐driven differences in metabolic rate despite no differences in selection between habitats. *Oikos*, **130**(6): 931–942.

Sears MW. 2005. Resting metabolic expenditure as a potential source of variation in growth rates of the sagebrush lizard. *Comparative Biochemistry and Physiology Part A: Molecular & Integrative Physiology*, **140**(2): 171–177.

Serén N, Megía‐Palma R, Simčič T, et al. 2023. Functional responses in a lizard along a 3.5‐km altitudinal gradient. *Journal of Biogeography*, **50**(12): 2042–2056.

Smith CCR, Snowberg LK, Gregory Caporaso J, et al. 2015. Dietary input of microbes and host genetic variation shape among-population differences in stickleback gut microbiota. *The ISME Journal*, **9**(11): 2515–2526.

Sommer F, Ståhlman M, Ilkayeva O, et al. 2016. The gut microbiota modulates energy metabolism in the hibernating brown bear *Ursus arctos*. *Cell Reports*, **14**(7): 1655–1661.

Sun BJ, Ma L, Li SR, et al. 2018. Phenology and the physiological niche are co‐adapted in a desert‐dwelling lizard. *Functional Ecology*, **32**(11): 2520–2530.

Sun BJ, Ma L, Wang Y, et al. 2021. Latitudinal embryonic thermal tolerance and plasticity shape the vulnerability of oviparous species to climate change. *Ecological Monographs*, **91**(3): 1–17.

Sun BJ, Williams CM, Li T, et al. 2022. Higher metabolic plasticity in temperate compared to tropical lizards suggests increased resilience to climate change. *Ecological Monographs*, **92**(2): e1512.

Swanson NE, Gluesenkamp AG, Donny AE, et al. 2023. Developmental environment contributes to rapid trait shifts among newly colonized subterranean habitats. *Zoological Research*, **44**(4): 808–820.

Turnbaugh PJ, Ley RE, Mahowald MA, et al. 2006. An obesity-associated gut microbiome with increased capacity for energy harvest. *Nature*, **444**(7122): 1027–1031.

Uren Webster TM, Consuegra S, Hitchings M, et al. 2018. Interpopulation variation in the *Atlantic salmon* microbiome reflects environmental and genetic diversity. *Applied and Environmental Microbiology*, **84**(16): e00691–18.

Uren Webster TM, Rodriguez-Barreto D, Castaldo G, et al. 2020. Environmental plasticity and colonisation history in the *Atlantic salmon* microbiome: a translocation experiment. *Molecular Ecology*, **29**(5): 886–898.

Vasconcelos DS, Harris DJ, Damas-Moreira I, et al. 2023. Factors shaping the gut microbiome of five species of lizards from different habitats. *PeerJ*, **11**: e15146.

Wang YJ, Zhou R, Yu QL, et al. 2020. Gut microbiome adaptation to extreme cold winter in wild plateau pika (*Ochotona curzoniae*) on the Qinghai-Tibet Plateau. *FEMS Microbiology Letters*, **367**(16): fnaa134.

Wilcoxon F. 1945. Individual comparisons by ranking methods. *Biometrics Bulletin*, **1**(6): 80–83.

Williams CE, Kueneman JG, Nicholson DJ, et al. 2022. Sustained drought, but not short-term warming, alters the gut microbiomes of wild *Anolis* lizards. *Applied and Environmental Microbiology*, **88**(19): e0053022.

Wong KH, Goodbody-Gringley G, De Putron SJ, et al. 2021. Brooded coral offspring physiology depends on the combined effects of parental press and pulse thermal history. *Global Change Biology*, **27**(13): 3179–3195.

Wu JY, Liu M, Zhou MQ, et al. 2021. Isolation and genomic characterization of five novel strains of *Erysipelotrichaceae* from commercial pigs. *BMC Microbiology*, **21**(1): 125.

Wu N, Liu JL, Wang S, et al. 2022. Comparative analysis of mitochondrial genomes in two subspecies of the sunwatcher toad-headed agama (*Phrynocephalus helioscopus*): prevalent intraspecific gene rearrangements in *Phrynocephalus*. *Genes*, **13**(2): 203.

Yang C, Mogno I, Contijoch EJ, et al. 2020. Fecal IgA levels are determined by strain-level differences in *Bacteroides ovatus* and are modifiable by gut microbiota manipulation. *Cell Host & Microbe*, **27**(3): 467–475. e6.

Yang J, Liu WQ, Han XZ, et al. 2024. Gut microbiota modulation enhances the immune capacity of lizards under climate warming. *Microbiome*, **12**(1): 37.

Yu W, Zhu ZY, Zhao XL, et al. 2023. Altitudinal variation in life-history features of a Qinghai-Tibetan Plateau lizard. *Current Zoology*, **69**(3): 284–293.

Zeng B, Zhang SY, Xu HL, et al. 2020. Gut microbiota of Tibetans and Tibetan pigs varies between high and low altitude environments. *Microbiological Research*, **235**: 126447.

Zhang ML, Li M, Sheng Y, et al. 2020. *Citrobacter* species increase energy harvest by modulating intestinal microbiota in fish: nondominant species play important functions. *mSystems*, **5**(3): e00303–20.

Zhang W Y, Li N, Tang X L, et al. 2018. Changes in intestinal microbiota across an altitudinal gradient in the lizard *Phrynocephalus vlangalii*. *Ecology and Evolution*, **8**(9): 4695–4703.

Zhao EM, Zhao K, Zhou K. 1999. Fauna Sinica, Reptilia. *In*: Vol. 2 (Squamata, Lacertilia). Beijing: Beijing Science Press, 189–191. (in Chinese)

Zhao XL, Yu W, Zhu ZY, et al. 2022. Factors influencing home ranges of the qinghai toad-headed lizard (*Phrynocephalus vlangalii*) on the Dangjin Mountain, Gansu. *Asian Herpetological Research*, **13**(2): 137–144.

Zhu W, Chang LM, Shi SC, et al. 2024a. Gut microbiota reflect adaptation of cave-dwelling tadpoles to resource scarcity. *The ISME Journal*, **18**(1): wrad009.

Zhu XX, Qiu X, Tang XL, et al. 2021. Tail display is regulated by anaerobic metabolism in an Asian agamid lizard. *Integrative Zoology*, **16**(5): 729–740.

Zhu XX, Yao ZY, Qi Y. 2020. Tail display intensity is restricted by food availability in an Asian agamid lizard (*Phrynocephalus vlangalii*). *Asian Herpetological Research*, **11**(3): 240–248.

Zhu Z, Du W, Zhang C, et al. 2024b. Altitudinal variation in thermal vulnerability of Qinghai-Tibetan Plateau lizards under climate warming. *Current Zoology*: zoae031.

He et al. *Zool. Res.* 2025, 46(1): 152−164
https://doi.org/10.24272/j.issn.2095-8137.2024.333
https://cstr.cn/32248.14.zr.2024.333

ZR | Zoological Research

Article Open Access

sRNA113 regulates *Pseudomonas plecoglossicida* motility to affect immune response against infection in pearl gentian grouper

Li He[1], Mei-Qin Mao[1], Ling-Min Zhao[1], Qi Li[1], Hui Ge[2], Jiao-Nan Zhang[3], Jiao-Lin Zhang[3], Qing-Pi Yan[1,*]

[1] *Fisheries College*, *Jimei University*, *Xiamen*, *Fujian* 361021, *China*

[2] *Fisheries Research Institute of Fujian*, *Xiamen*, *Fujian* 361000, *China*

[3] *Key Laboratory of Special Aquatic Feed for Fujian*, *Fujian Tianma Technology Company Limited*, *Fuzhou*, *Fujian* 350308, *China*

ABSTRACT

Small RNAs (sRNAs) are a class of molecules capable of perceiving environmental changes and exerting post-transcriptional regulation over target gene expression, thereby influencing bacterial virulence and host immune responses. *Pseudomonas plecoglossicida* is a pathogenic bacterium that poses a significant threat to aquatic animal health. However, the regulatory mechanisms of sRNAs in *P. plecoglossicida* remain unclear. This study focused on sRNA113, previously identified as a potential regulator of the *fliP* gene, a key component of the lateral flagellar type III secretion system. To investigate the effects of sRNA113 on *P. plecoglossicida* virulence, as well as its role in regulating pathogenic processes and host immune responses, mutant strains lacking this sRNA were generated and analyzed. Deletion of sRNA113 resulted in the up-regulation of lateral flagellar type III secretion system-related genes in *P. plecoglossicida*, which enhanced bacterial swarming motility, biofilm formation, and chemotaxis ability *in vitro*. *In vivo* infection experiments with pearl gentian grouper revealed that sRNA113 deletion enhanced the pathogenicity of *P. plecoglossicida*. This heightened virulence was attributed to the up-regulation of genes associated with the lateral flagellar type III secretion system, resulting in higher bacterial loads within host tissues. This amplification of pathogenic activity intensified tissue damage, disrupted immune responses, and impaired the ability of the host to clear infection, ultimately leading to mortality. These findings underscore the critical role of sRNA113 in regulating the virulence of *P. plecoglossicida* and its interaction with host immune defenses. This study provides a foundation for further exploration of sRNA-mediated mechanisms in bacterial pathogenesis and host-pathogen interactions, contributing to a deeper understanding of virulence regulation and immune evasion in aquatic pathogens.

Keywords: *Pseudomonas plecoglossicida*; sRNA; Virulence; Pearl gentian grouper; Immune response

INTRODUCTION

Pseudomonas plecoglossicida, a gram-negative opportunistic pathogen, poses a substantial threat to the aquaculture industry (Akayli et al., 2011; Nishimori et al., 2000; Sun et al., 2020). This pathogen typically exhibits pathogenicity within the temperature range of 16–19℃, where it induces visceral white nodules disease (VWND) in various fish species, such as ayu (*Plecoglossus altivelis*) (Wu et al., 2022), large yellow croaker (*Larimichthys crocea*) (Zhang et al., 2014), and orange-spotted grouper (*Epinephelus coioides*) (Yang et al., 2023a). VWND is characterized by the development of granulomatous inflammation in internal organs, most notably the spleen (Mao et al., 2024), and is associated with high mortality and morbidity rates, leading to significant economic losses within the aquaculture industry in China (Mao et al., 2024). Given these challenges, a thorough understanding of the molecular mechanisms driving *P. plecoglossicida* pathogenicity and the host immune responses elicited during infection is crucial. Such insights are essential for developing effective strategies to mitigate disease impacts and for ensuring the sustainable advancement of aquaculture.

Currently, there is significant emphasis on the investigation of virulence factors and genes in *P. plecoglossicida*, with particular focus on the two-component system (He et al.,

Received: 30 September 2024; Accepted: 22 November 2024; Online: 23 November 2024

Foundation items: This work was supported by the National Natural Science Foundation of China (32373181), National Key Research and Development Program (2023YFD2400700), Science and Technology Plan Project of Fujian Province (2022L3059), High-quality Development of Marine and Fishery Industry Special Fund Project of Fujian Province (FJHYF-L-2023-5), and Open Fund of Fujian Province Key Laboratory of Special Aquatic Formula Feed (TMKJZ2302)

*Corresponding author, E-mail: yanqp@jmu.edu.cn

This is an open-access article distributed under the terms of the Creative Commons Attribution Non-Commercial License (http://creativecommons.org/licenses/by-nc/4.0/), which permits unrestricted non-commercial use, distribution, and reproduction in any medium, provided the original work is properly cited.

Copyright ©2025 Editorial Office of Zoological Research, Kunming Institute of Zoology, Chinese Academy of Sciences

2023c; Zhou et al., 2023), secretion system (Yang et al., 2023b; Zhang et al., 2017), outer membrane protein (He et al., 2024), transport system (Huang et al., 2021), and flagella (Yang et al., 2023a). These studies have demonstrated that the pathogenicity of *P. plecoglossicida* arises from the tightly coordinated regulation of diverse virulence factors, enabling bacteria to effectively adapt to varying environmental conditions and interact with the immune system of the host (Mao et al., 2024; Tao et al., 2024b). Among these virulence factors, flagella play a crucial role in the infection process, as their motility enables bacterial invasion and adhesion to host tissues, while simultaneously activating host pattern recognition receptors to trigger the immune response (Nedeljković et al., 2021). Genomic analyses have identified two distinct flagellar systems in *P. plecoglossicida*, namely polar and lateral flagella (Mao et al., 2013). Polar flagella primarily enable swimming motility in liquid environments, whereas lateral flagella are associated with swarming motility on viscous or solid surfaces (Lau et al., 2021; McCarter, 2004). Notably, our previous research demonstrated that the expression of genes involved in lateral flagellar assembly in *P. plecoglossicida* was significantly up-regulated following host infection (Luo et al., 2020). Furthermore, we identified *fliP* as a crucial component of the export apparatus (FlhABFliPQR) within the type III secretion system of lateral flagella, playing a pivotal role in the pathogenicity of *P. plecoglossicida* (He et al., 2023b). However, the regulatory mechanisms controlling *fliP* expression remain unclear. Understanding these regulatory pathways is essential for elucidating how *P. plecoglossicida* modulates its pathogenicity and influences immune response during infection.

The post-transcriptional regulation of sRNAs represents a highly efficient and adaptive mechanism that pathogens employ to acclimate to the host environment and modulate virulence gene expression. This efficiency stems from the translational independence and rapid responsiveness of sRNAs compared to that of proteins and mRNAs (Jørgensen et al., 2020). Recent studies have identified hundreds of sRNAs across diverse bacterial species, which regulate crucial processes such as carbon, nitrogen, and iron metabolism regulation, biofilm formation control, quorum sensing modulation, drug resistance development facilitation, virulence factor expression orchestration, and oxidative stress response management (Liu et al., 2022; Xiong et al., 2021). The molecular mechanism underlying sRNA-mediated regulation involves the formation of base pairs between sRNAs and target mRNAs, leading to either positive or negative regulation of gene expression (Dutta & Srivastava, 2018). Notably, numerous sRNAs have been identified as regulators of flagellar expression in bacterial species, including 25 sRNAs in *Escherichia coli* (Bak et al., 2015) and 20 sRNAs in *P. aeruginosa* (Gill et al., 2018). Despite these advances, there is limited information regarding sRNAs in *P. plecoglossicida*.

This study employed bioinformatic analyses to identify a novel sRNA, designated as sRNA113, with potential regulatory influence over *fliP* expression in *P. plecoglossicida*, a key gene associated with the lateral flagellar type III secretion system. Further investigation is required to elucidate the precise mechanism by which sRNA113 modulates *fliP* expression and its role in influencing immune responses during infection. This study aims to clarify the molecular mechanism by which sRNA113 regulates the lateral flagella to mediate *P. plecoglossicida* virulence and its effects on the host immune response. These findings are expected to advance our understanding of the molecular regulatory mechanism underlying bacterial virulence in this pathogen.

MATERIALS AND METHODS

Ethics statement

All animal experiments were approved by the Animal Ethics Committee of Jimei University (permit number JMULAC2011-58) and were carried out in compliance with the National Institutes of Health's Guide for the Care and Use of Laboratory Animals and followed the ARRIVE guidelines (https://arriveguidelines.org/).

Bacterial strains and culture conditions

The *P. plecoglossicida* NZBD9 strain was isolated from large yellow croaker with VWND and maintained in our laboratory (Huang et al., 2018). NZBD9 cultures were grown in Luria-Bertani (LB) broth at 18℃ with shaking at 220 r/min. The *Escherichia coli* strain DH5α (Tsingke Biotech, China) was used as a host for maintenance of recombinant plasmids. All *E. coli* strains were cultured at 37℃ with shaking at 220 r/min in LB broth or on LB plates (containing 1.5% agar). Selection agents were incorporated into the media as required, with kanamycin (50 μg/mL) used for the generation of deletion strain and tetracycline (10 μg/mL) employed for the maintenance of complementation strain.

Identification of lateral flagellar regulator sRNA113 in *P. plecoglossicida* NZBD9

To investigate the regulatory mechanisms of sRNAs influencing *fliP* expression in *P. plecoglossicida*, prokaryotic transcriptome data were analyzed using Rockhopper software (http://cs.wellesley.edu/~btjaden/Rockhopper/) (He et al., 2023a). This analysis predicted sRNA candidates with potential regulatory roles. Among these, a novel sRNA, designated sRNA113, was identified using the RNAhybrid program (http://bibiserv.techfak.uni-bielefeld.de/rnahybrid), which predicted interactions between sRNA113 and *fliP* mRNA expression in *P. plecoglossicida* (Silva et al., 2019). The secondary structure of sRNA113 was further predicted using the RNAfold Web Server (http://rna.tbi.univie.ac.at/cgi-bin/RNAWebSuite/RNAfold.cgi) (Hofacker, 2003). In addition, the overnight-cultured NZBD9 bacterial solution was inoculated in LB broth, LB plates containing 0.5% agar, and LB plates containing 1.5% agar, respectively. After 24 h of culture, bacterial samples were collected for RNA extraction. The relative expression levels of sRNA13 and *flhABfliPQRMN* genes were quantified using reverse transcription quantitative real-time polymerase chain reaction (RT-qPCR).

Construction of mutant strains

To generate the sRNA113 deletion strain (Δ113) of *P. plecoglossicida* NZBD9, a scarless deletion method based on the suicide plasmid pK18*mobSacB* was used (Wang et al., 2018). First, a 545 bp upstream fragment and a 631 bp downstream fragment flanking sRNA113 were amplified from the chromosomal DNA of NZBD9 using PCR. The Δ113 fragment was then amplified by overlapping PCR and cloned into the *EcoR*I/*Xba*I sites of pK18*mobSacB* to obtain the recombinant plasmid pK18*mobSacB*-Δ113. This plasmid was electroporated into NZBD9 using a MicroPulser Electroporator (Bio-Rad, USA). Transformants were sequentially subjected to

homologous recombination on LB plates containing 50 μg/mL kanamycin and 10% sucrose, followed by colony PCR and DNA sequencing to confirm the Δ113 strain. For construction of the complementation strain C-Δ113, the sRNA113 fragment was amplified by PCR and cloned into the *BsrG*Ⅰ/*Nsi*Ⅰ sites of the expressive vector pCM130/tac to generate the complement plasmid pCM130/tac-113. This plasmid was transformed into the Δ113 strain to obtain the C-Δ113 strain, which was also validated using colony PCR and DNA sequencing. Total RNA was extracted from the three strains for RT-qPCR analysis to confirm strain construction and assess the expression of lateral flagella-related *flhABfliPQRMN* genes. All primers used in this study are listed in Supplementary Table S1.

Growth curve assay

Bacterial growth was assessed using a growth curve assay according to established protocols, with minor modifications (He et al., 2022a). Overnight cultures of NZBD9, Δ113, and C-Δ113 strains in LB broth were standardized to an optical density at 600 nm (OD_{600}) of 0.2 and diluted 10^5-fold using sterile fresh LB broth. A 200 μL aliquot of the diluted bacterial suspension was inoculated into each well of a 96-well plate, with eight biological replicates per strain. The OD_{600} was measured hourly for 36 h using a Synergy H1 Microplate Reader (Biotek, USA). The growth curves were plotted using GraphPad Prism (v.8.0.1). The assay was repeated three times.

Swarming motility assay

Swarming motility was evaluated following previously described protocols, with slight modifications (Zheng et al., 2023). Cultures of the NZBD9, Δ113, and C-Δ113 strains grown in LB broth were adjusted to an initial OD_{600} value of 0.3. A 1 μL aliquot of each bacterial suspension was inoculated onto the center of LB swarming plates (containing 0.5% agar), with three biological replicates per strain. After 24 h of incubation at 18℃, the migration distance of the colonies was quantified using a multifunctional colony counter (Shineso Biotech, China). The assay was repeated three times.

Quantification of biofilm formation

The biofilm formation assay was conducted following previously established protocols, with slight modifications (Li et al., 2021a). Bacterial suspensions of the NZBD9, Δ113, and C-Δ113 strains were prepared at an initial OD_{600} value of 0.3. A 100 μL aliquot of each suspension was inoculated into a 96-well plate, with six biological replicates per strain, and incubated at 18℃ for 24 h. After incubation, wells were gently rinsed with phosphate-buffered saline (PBS), with the remaining biofilm cells air-dried and stained with 1% crystal violet for 10 min. The stained biofilms were dissolved in 200 μL of 33% acetic acid, and their absorbance was quantified at 590 nm. The assay was repeated three times.

Adherence assay

The bacterial adherence assay was conducted according to previously described methods (Yuan et al., 2022). In brief, sterile mucus (20 μL) was collected from the body surface of pearl gentian groupers and evenly applied to slides. The slides were dried overnight and fixed with 4% methanol. Bacterial suspensions of the NZBD9, Δ113, and C-Δ113 strains at an OD_{600} of 0.3 were applied to slides, with three biological replicates per strain, followed by incubation at 18°C for 2 h. Non-adherent bacteria were subsequently removed with PBS, while the adherent bacteria were fixed with 4% methanol, stained with crystal violet (0.1%) for 3 min, and subsequently washed with sterile PBS. Microscopic analysis and imaging were conducted using a Leica microscope (Leica, Germany). Adherence was quantified by counting bacteria in 30 randomly selected fields per slide using a multifunctional colony counter (Shineso Biotech, China). The assay was repeated three times.

Chemotaxis assay

Bacterial chemotaxis was assessed following previously outlined protocols (Reyes-Darias et al., 2016). Bacterial suspensions of NZBD9, Δ113, and C-Δ113 strains were adjusted to an OD_{600} of 1.0 using sterile PBS. Mucus was obtained from the body surface of pearl gentian groupers. Capillary tubes (0.3 mm×100 mm, sealed at one end) were filled with mucus through capillary action and carefully inserted into a syringe containing 300 μL of bacterial suspension, with three biological replicates for each strain, and subsequently placed in a horizontal position and incubated at 18℃ for 1 h. After incubation, the bacteria-mucus mixtures in the capillaries were aspirated into 995 μL of PBS for 10-fold gradient dilution. A 100 μL aliquot of each bacterial suspension per gradient was coated onto LB plates to enumerate colony-forming units (CFUs). The assay was repeated three times.

Fish rearing

Pearl gentian groupers (*E. fuscoguttatus* ♀×*E. lanceolatus* ♂), each weighting approximately 50 g, were purchased from a fish farm in Tongan, Fujian Province, China. The fish were cultured in a recirculating aquaculture system at 18±1℃ for over 14 d. The fish were fed daily with a commercial diet during the resting period.

Fish challenge and sample collection

For the mortality assay, a total of 120 fish were randomly allocated into four groups: NZBD9 strain-infected group, Δ113 strain-infected group, C-Δ113 strain-infected group, and PBS-injected group. Fish in the NZBD9, Δ113, and C-Δ113 strain-infected groups were intraperitoneally administered with the corresponding bacterial solution (5×10^4 CFU/fish, 200 μL per fish), while the control group was injected with an equal volume of sterilized PBS (Figure 1A). Daily mortality was recorded for 10 days. Before injection and sampling, fish were anesthetized with 20 mg/L MS-222 (Sigma, USA) to minimize stress and ensure humane handling.

For sample collection, 210 fish were randomly selected and assigned to three groups: NZBD9 strain-infected group, Δ113 strain-infected group, and PBS-injected group, with three replicates per group. The challenge protocol followed the same method as the mortality assay. Samples were collected from three fish per group at 0–6 days post-infection (dpi). Tissues, including spleen, intestine, liver, and head kidney, were harvested for quantitative real-time PCR (qPCR) analysis of bacterial load and RT-qPCR analysis of gene expression. The four tissues collected at 4 dpi for histopathological observations were immediately immersed in fixation buffer.

Bacterial load analysis

Approximately 30 mg of each tissue sample was used for DNA extraction using an EasyPure Marine Animal Genomic DNA Kit (TransGen Biotech, China) in accordance with the manufacturer's instructions. Bacterial load was determined by

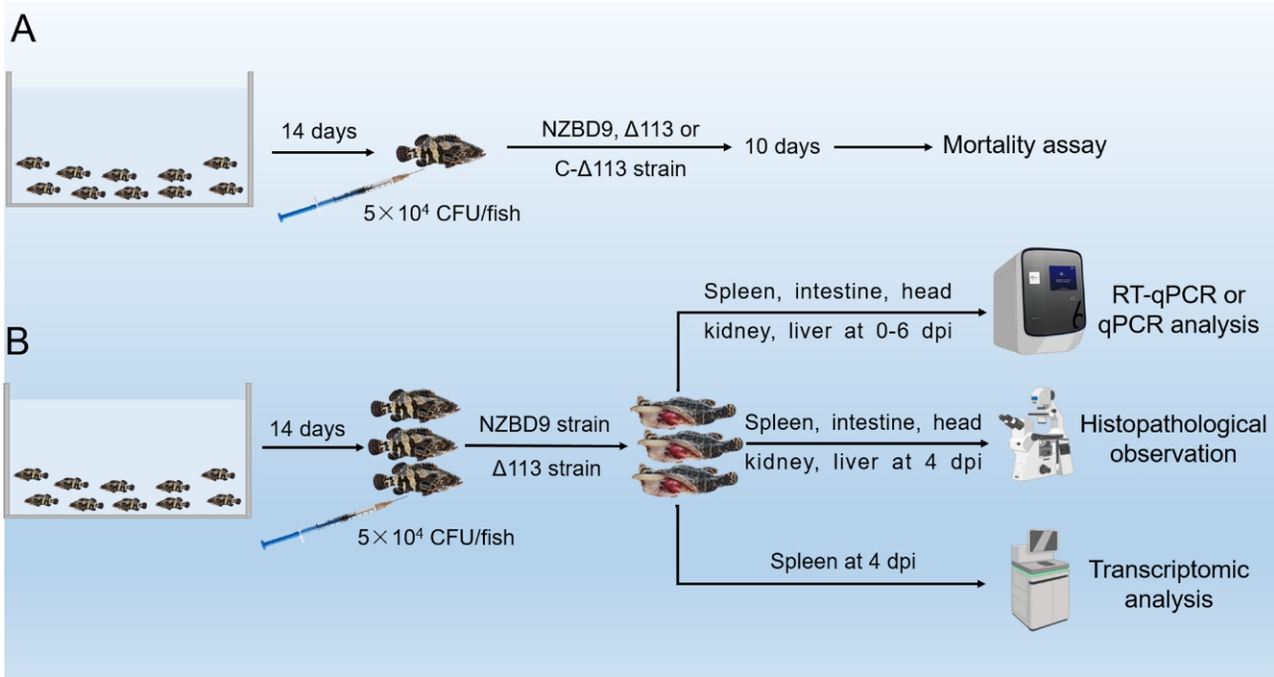


Figure 1 Schematic of experimental procedures and sampling methods

A: Schematic of mortality assay. B: Schematic of infection process and corresponding sampling workflow.

quantifying DNA copies of the single-copy gene *gyrB*. The extracted DNA served as a template, using primers *gyrB*-F/*gyrB*-R for qPCR amplification. Bacterial load of *P. plecoglossicida* in each sample was calculated following previously reported methods (Izumi et al., 2007).

Histology

Tissue samples underwent a standard histological processing procedure, including dehydration through a series of alcohol concentrations, clearing with xylene, and embedding in paraffin wax. Serial sections were cut to a thickness of 10 μm and stained using a hematoxylin & eosin (H&E) staining kit (Beyotime, China) according to the manufacturer's protocols. The stained sections were then observed and imaged using a Leica microscope (Germany).

RNA-seq analysis

Total RNA was extracted from spleen samples (100 mg) of the Δ113 strain-infected and NZBD9 strain-infected groups using TRIzol® Reagent (Invitrogen, USA) following the manufacturer's protocols. RNA concentration and purity were detected using a NanoDrop 2000 spectrophotometer (Thermo Scientific, USA), while RNA integrity was evaluated through agarose gel electrophoresis. The RNA integrity number (RIN) was determined using the Agilent 2100 Bioanalyzer (Agilent, USA). High-quality RNA was subsequently used to construct cDNA libraries using a TruSeq^{TM} RNA Sample Prep Kit (Illumina, USA). Sequencing was conducted on the Illumina NovaSeq6000 platform (2×150 bp read length) by Majorbio Biopharm (China). Raw reads underwent quality control to produce clean reads, which were *de novo* assembled using Trinity (v.2.8.5). The initial assembly was filtered and optimized with TransRate (v.1.0.3) and assessed for assembly completeness using BUSCO (v.3.0.2), resulting in the generation of a comprehensive transcript database for pearl gentian grouper.

Gene expression levels and variations were quantified using transcripts per million (TPM). Differentially expressed genes (DEGs) between the two groups were identified using DESeq2 (v.1.24.0) with the criteria of *P*-adjust<0.05 and $|\text{Log}_2\text{fold change}|\geq 1$. GOATOOLS (v.0.6.5) was used for Gene Ontology (GO) enrichment analysis and KOBAS was used for Kyoto Encyclopedia of Genes and Genomes (KEGG) pathway enrichment analysis. To validate the RNA-seq results, eight DEGs were selected from the dataset for further confirmation by RT-qPCR.

RT-qPCR

Total RNA was reverse-transcribed using the PrimeScript™ RT Reagent Kit with gDNA Eraser (TaKaRa, China) following the manufacturer's instructions. RT-qPCR was performed using PerfectStart® Green qPCR SuperMix (TransGen Biotech, China) on a QuantStudio 6 Flex Real-Time PCR System (Life Technologies, USA). The reaction mixture comprised 10 μL of PerfectStart® Green qPCR SuperMix, 1 μL each of forward and reverse primers, 2 μL of cDNA, and 6 μL of nuclease-free water. The 16S rRNA gene of *P. plecoglossicida* and the *β-actin* gene of pearl gentian grouper were selected as the internal reference genes. Gene expression levels were calculated using the $2^{-\Delta\Delta CT}$ method. All primers used in this study were synthesized by Sangon Biotech (China), with sequences provided in Supplementary Table S1.

Statistical analysis and drawing

Illustrations were created using Adobe Illustrator (San Jose, USA), TBtools (v.2.084), and GraphPad Prism (v.8.0.1) (Li et al., 2022). Normal distribution was determined using the Shapiro-Wilk test. Statistical differences in normally distributed data were analyzed using one-way analysis of variance (ANOVA) followed by Tukey's test or two-way ANOVA followed by Sidak's multiple comparisons test in GraphPad Prism. All data are presented as mean±standard deviation (SD). Visual materials were sourced from BioRender (https://app.biorender.com) and SCIDraw (https://scidraw.io/).

RESULTS

Identification of the lateral flagellar regulator sRNA113 in *P. plecoglossicida* NZBD9

An 83 bp sRNA, designated sRNA113, was predicted to be located at chromosome 1589231–1589313 in *P. plecoglossicida*. The predicted secondary structure of sRNA113 is depicted in Figure 2A. To investigate the potential role of sRNA113 in regulating *fliP* expression, its expression and that of the lateral flagellar operon (*flhABfliPQRMN*) were analyzed under varying culture conditions, including in LB broth and on LB plates containing 0.5% and 1.5% agar. Results showed that the expression of sRNA113 was significantly down-regulated on LB plates containing 0.5% agar (Figure 2B), while *flhABfliPQRMN* gene expression was significantly up-regulated (Figure 2C), suggesting a negative correlation between the expression of *fliP* and sRNA113 in *P. plecoglossicida*. To further explore the regulatory function of sRNA113, an sRNA113 deletion strain (Δ113) and complementation strain (C-Δ113) were constructed. Gel electrophoresis confirmed successful strain construction, as shown in Supplementary Figure S1.

Effects of sRNA113 on swarming motility and expression of lateral flagellar genes in *P. plecoglossicida*

The influence of sRNA113 on swarming motility was evaluated by measuring colony diameters after 24 h of cultivation on swarming plates (Figure 3A). Results revealed a significant increase in colony diameter for the Δ113 strain (8.20± 0.19 mm) compared to the NZBD9 strain (6.24±0.59 mm). The colony diameter of the C-Δ113 strain (6.79±0.57 mm) was intermediate between those of the Δ113 and NZBD9 strains

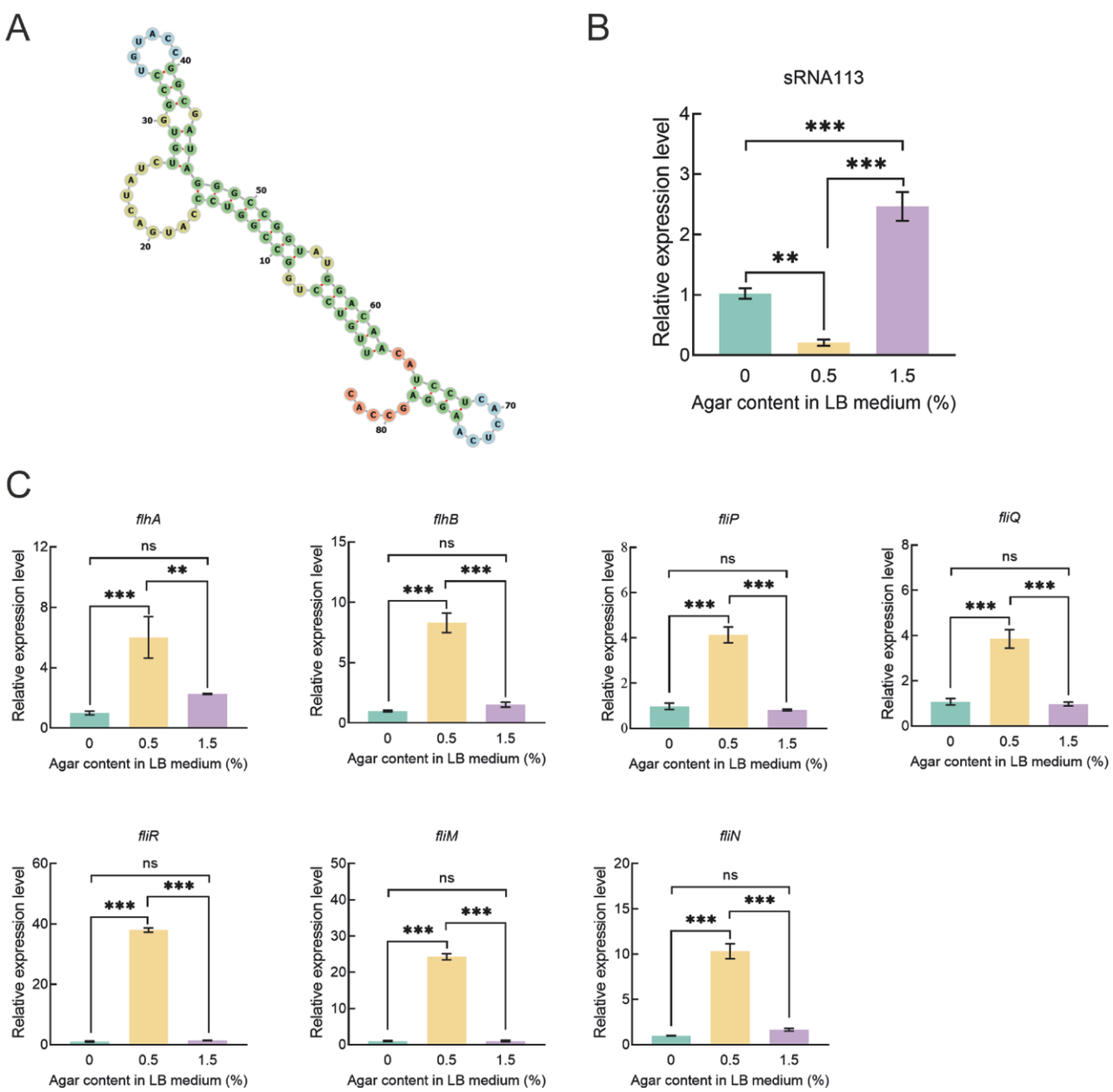


Figure 2 Identification of lateral flagellar regulator sRNA113 in *Pseudomonas plecoglossicida* NZBD9

A: Predicted secondary structure of sRNA113. B: Expression levels of sRNA113 in *P. plecoglossicida* cultured in LB medium with varying agar content. C: Expression levels of *flhABfliPQRMN* genes in *P. plecoglossicida* under the same conditions. Error bars represent SD of the mean (n=3). ns: Not significant; *: P<0.05; **: P<0.01; ***: P<0.001.

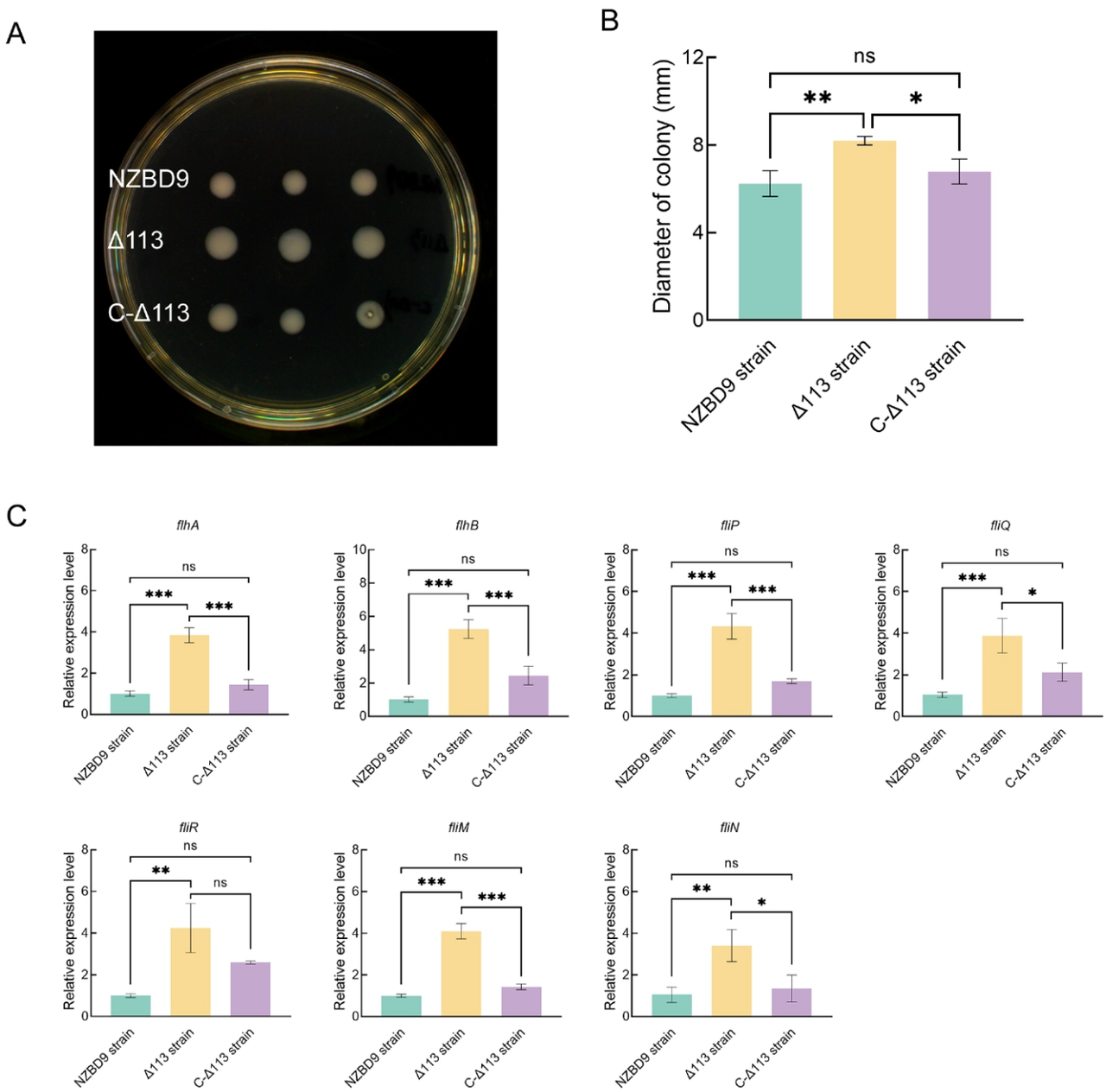


Figure 3 Effects of sRNA113 on swarming motility and expression of lateral flagellar *flhABfliPQRMN* genes in *Pseudomonas plecoglossicida*

A: Colonies of NZBD9, Δ113, and C-Δ113 strains on swarming plate (0.5% agar). B: Colony diameters of NZBD9, Δ113, and C-Δ113 strains. C: Expression levels of lateral flagellar *flhABfliPQRMN* genes in NZBD9, Δ113, and C-Δ113 strains. Error bars represent SD of the mean (n=3). ns: Not significant; *: P<0.05; **: P<0.01; ***: P<0.001.

(Figure 3B). Additionally, the expression of lateral flagella-related *flhABfliPQRMN* genes was significantly elevated in the Δ113 strain compared to both the NZBD9 and C-Δ113 strains (Figure 3C).

Effects of sRNA113 on biofilm formation, chemotactic ability, and adhesion of *P. plecoglossicida*

The deletion sRNA113 had no discernible impact on *P. plecoglossicida* growth (Figure 4A), indicating that sRNA113 is not directly involved in bacterial proliferation. This finding implies that the observed variations in biological characteristics in subsequent experiments were unrelated to growth differences. The biofilm formation assay showed that sRNA113 deletion significantly improved biofilm formation ability in *P. plecoglossicida* (Figure 4B). Similarly, the bacterial chemotaxis assay demonstrated a marked increase in the number of chemotactic cells in the Δ113 strain compared to the NZBD9 and C-Δ113 strains (Figure 4C). To evaluate bacterial adhesion, microscopy (1 000×) was employed to observe adhesion to the surface mucus of fish (Figure 4D). Analysis confirmed that the Δ113 strain exhibited significantly greater adhesion compared to the NZBD9 strain (Figure 4E).

Effects of sRNA113 on *P. plecoglossicida* pathogenicity in pearl gentian grouper

To assess the role of sRNA113 in pathogenicity, the cumulative survival of pearl gentian groupers infected with NZBD9, Δ113, and C-Δ113 strains was monitored over 10 days. As shown in Figure 5A, fish infected with the Δ113 strain exhibited a cumulative survival rate of 30% at 4 dpi, which

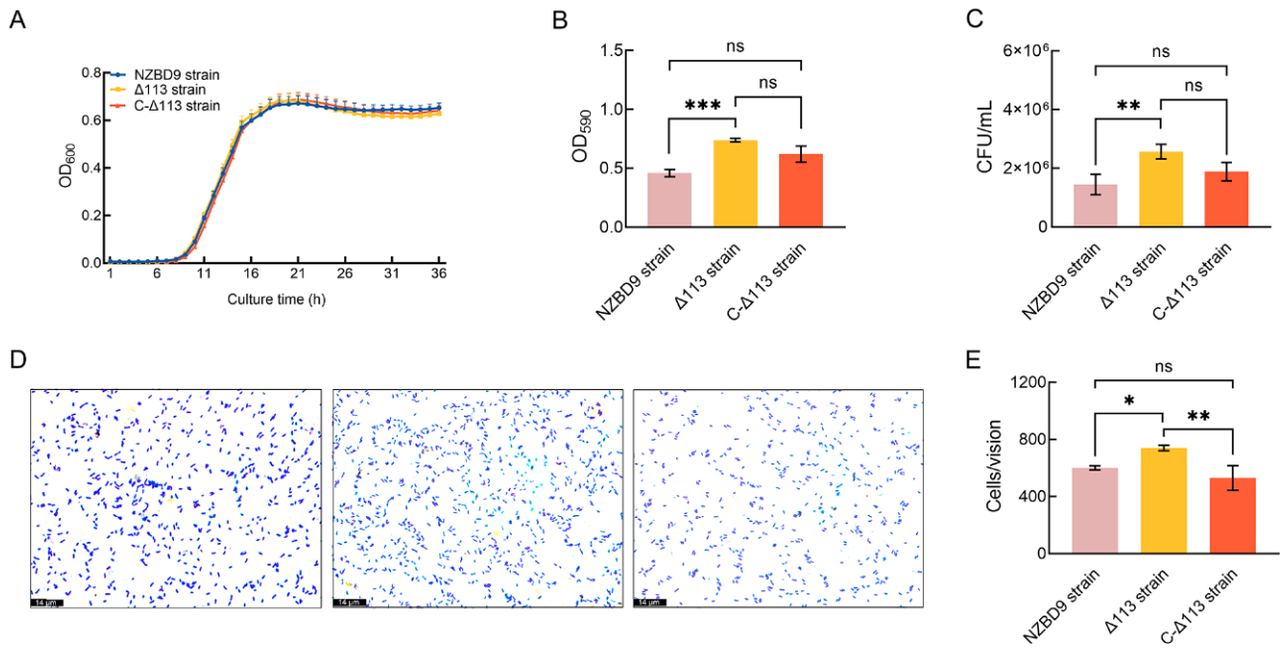


Figure 4 Effects of sRNA113 on biological characteristics of *Pseudomonas plecoglossicida*

A: Growth curves of NZBD9, Δ113, and C-Δ113 strains (n=8). B: Biofilm formation ability of NZBD9, Δ113, and C-Δ113 strains (n=6). C: Chemotactic ability of NZBD9, Δ113, and C-Δ113 strains (n=3). D: NZBD9, Δ113, and C-Δ113 strains adhered to slides. Scale bar: 7 μm. E: Adhesion ability of NZBD9, Δ113, and C-Δ113 strains (n=3). Error bars represent SD of the mean. ns: Not significant; *: P<0.05; **: P<0.01; ***: P<0.001.

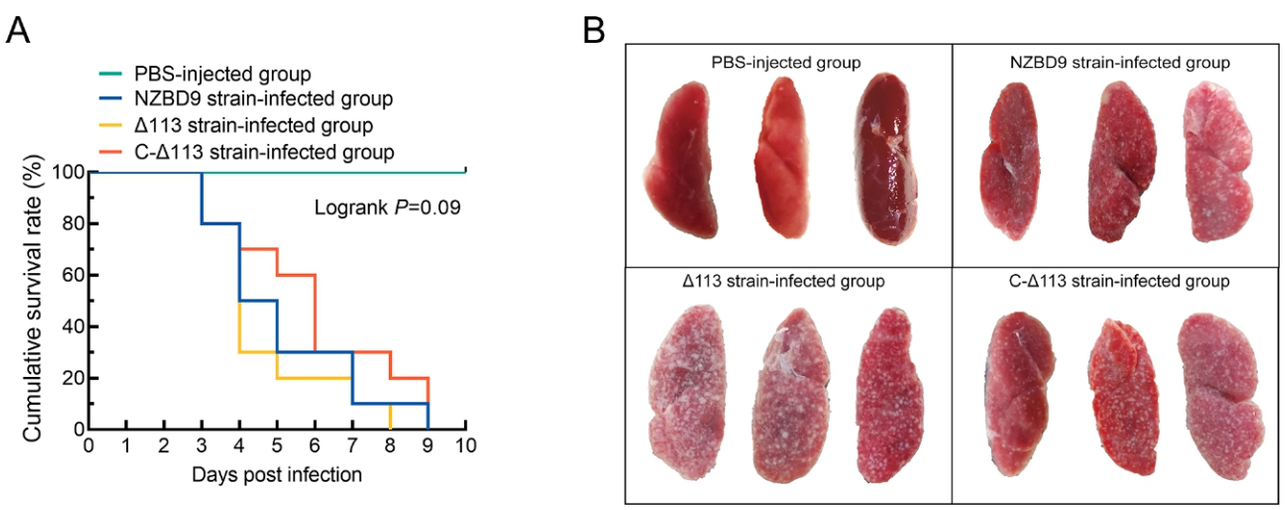


Figure 5 Comparative pathogenicity of NZBD9, Δ113, and C-Δ113 *Pseudomonas plecoglossicida* strains to pearl gentian grouper

A: Cumulative survival rate of pearl gentian groupers infected with NZBD9, Δ113, or C-Δ113 strains over a 10 day period. B: White nodules on spleen surface of pearl gentian groupers infected with NZBD9, Δ113, or C-Δ113 strains at 4 dpi.

declined to 0% at 8 dpi. In comparison, fish infected with the NZBD9 strain exhibited a 50% survival rate at 4 dpi, which declined to 0% at 9 dpi. However, statistical analysis indicated no significant differences in cumulative survival among the infection groups. Dissections conducted at 4 dpi revealed splenic symptoms in all infected groups. Fish infected with the NZBD9, Δ113, and C-Δ113 strains exhibited white nodules on the spleen surface, with the most pronounced symptoms observed in the Δ113-infected group (Figure 5B). These findings suggest that sRNA113 deletion enhances *P. plecoglossicida* pathogenicity.

Bacterial load analysis and histopathological observations in pearl gentian grouper

Given that *P. plecoglossicida* primarily targets immune organs in fish, bacterial load and histopathological changes were examined in the spleen, intestine, head kidney, and liver of pearl gentian groupers infected with the NZBD9 and Δ113 strains. Bacterial load analysis revealed that bacterial levels in the four tissues peaked at 4 dpi, with the Δ113 strain consistently exhibiting higher loads than the NZBD9 strain throughout the course of infection (Figure 6A). Histopathological observations (Figure 6B) showed that spleen structure in the PBS-injected fish remained intact, with distinct demarcation between red and white pulp. In contrast, infection with *P. plecoglossicida* induced evident lesions in the spleen, including granuloma formation and tissue necrosis, with more severe damage observed in the Δ113-infected group. The PBS-injected group displayed an intact serosal

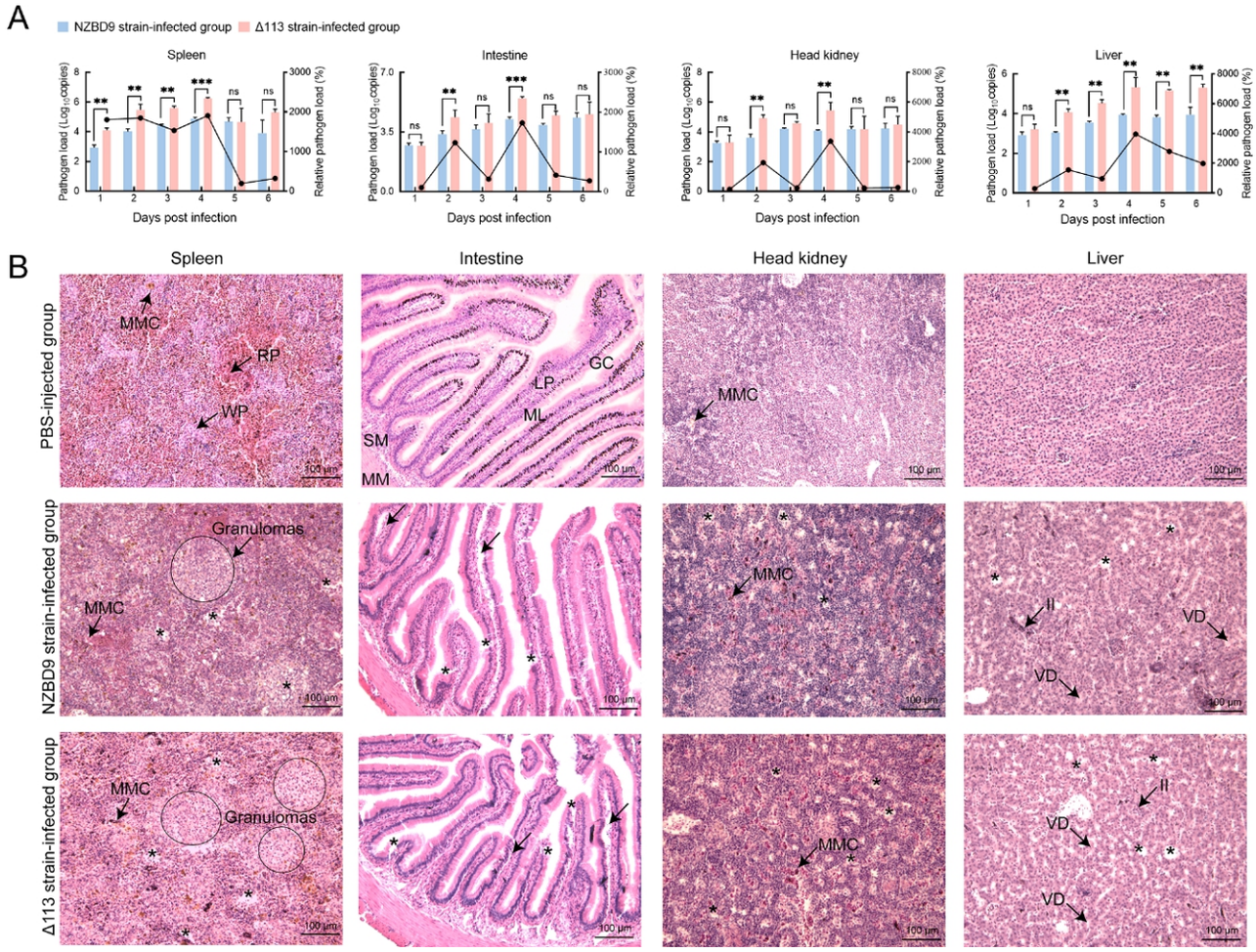


Figure 6 Bacterial load analysis and histopathological changes in pearl gentian grouper

A: Bacterial load analysis. Bar charts depict bacterial loads, while line charts represent percentage of pathogen load for the Δ113 strain relative to that of the NZBD9 strain. Error bars represent SD of the mean (n=3). ns: Not significant; *: P<0.05; **: P<0.01; ***: P<0.001. B: Histopathological changes in spleen, intestine, head kidney, and liver of pearl gentian grouper at 4 dpi after challenge with NZBD9 and Δ113 strains of *Pseudomonas plecoglossicida*. Spleen: Red pulp (RP), white pulp (WP), melanin macrophage center (MMC), tissue necrosis (⋆), circle indicates granuloma. Intestine: Serosa (S), muscularis mucosa (MM), submucosal (SM), mucosal layer (ML), lamina propria (LP), goblet cell (GC), tissue dissociation of mucosal layer and lamina propria (⟷), damaged mucosal layer (⋆). Head kidney: Tissue necrosis (⋆). Liver: Vacuolation degeneration (VD), inflammatory cell infiltration (II). Scale bar: 100 μm.

layer, muscularis mucosa, submucosa, mucosa, and lamina propria, as well as goblet cells of varying sizes. In contrast, the NZBD9 and Δ113 strain-infected groups exhibited extensive mucosal layer damage and detachment from the lamina propria. In the head kidney, infection caused diffuse hemorrhage and widespread necrosis. In the liver, hepatocytes exhibited regular arrangement in the PBS-injected group, while infected groups displayed sparse hepatocyte organization, increased necrotic foci, and local inflammatory cell infiltration.

Transcriptomic analysis of the effects of *P. plecoglossicida* sRNA113 on immune response of pearl gentian grouper

To further investigate the impact of *P. plecoglossicida* sRNA113 on the anti-infection immune response in pearl gentian grouper, transcriptomic analysis was employed to compare transcriptional differences in the spleen of fish infected with the NZBD9 or Δ113 strains. A total of six cDNA libraries were constructed, yielding clean data exceeding 6.94 Gb per sample, with a Q30 base percentage surpassing 95.70% (Supplementary Table S2). In total, 2 433 DEGs were identified in the Δ113 strain-infected group, including 1 061 up-regulated and 1 372 down-regulated DEGs compared to the NZBD9 strain-infected group (Figure 7A).

GO enrichment analysis provided insights into the functional roles of these DEGs in response to Δ113 infection compared to NZBD9 infection. Notably, significant enrichment was observed in 92 GO terms related to biological processes, including “leukocyte chemotaxis” (GO:0030595), “immune response” (GO:0006955), “inflammatory response” (GO:0006954), and “MHC class II protein complex” (GO:0042613); molecular functions, including “extracellular space” (GO:0005615), and “integral component of membrane” (GO:0016021); and cellular components, including “cytokine receptor binding” (GO:0005126), “signaling receptor binding” (GO:0005102), and “chemokine receptor binding” (GO:0042379) (Figure 7B). Most of the DEGs within these enriched GO terms were significantly downregulated, reflecting altered immune processes in response to the Δ113 strain infection (Figure 7B).

KEGG pathway enrichment analysis revealed 81 significantly enriched pathways (Figure 7C), categorized into immune system pathways, including “Antigen processing and

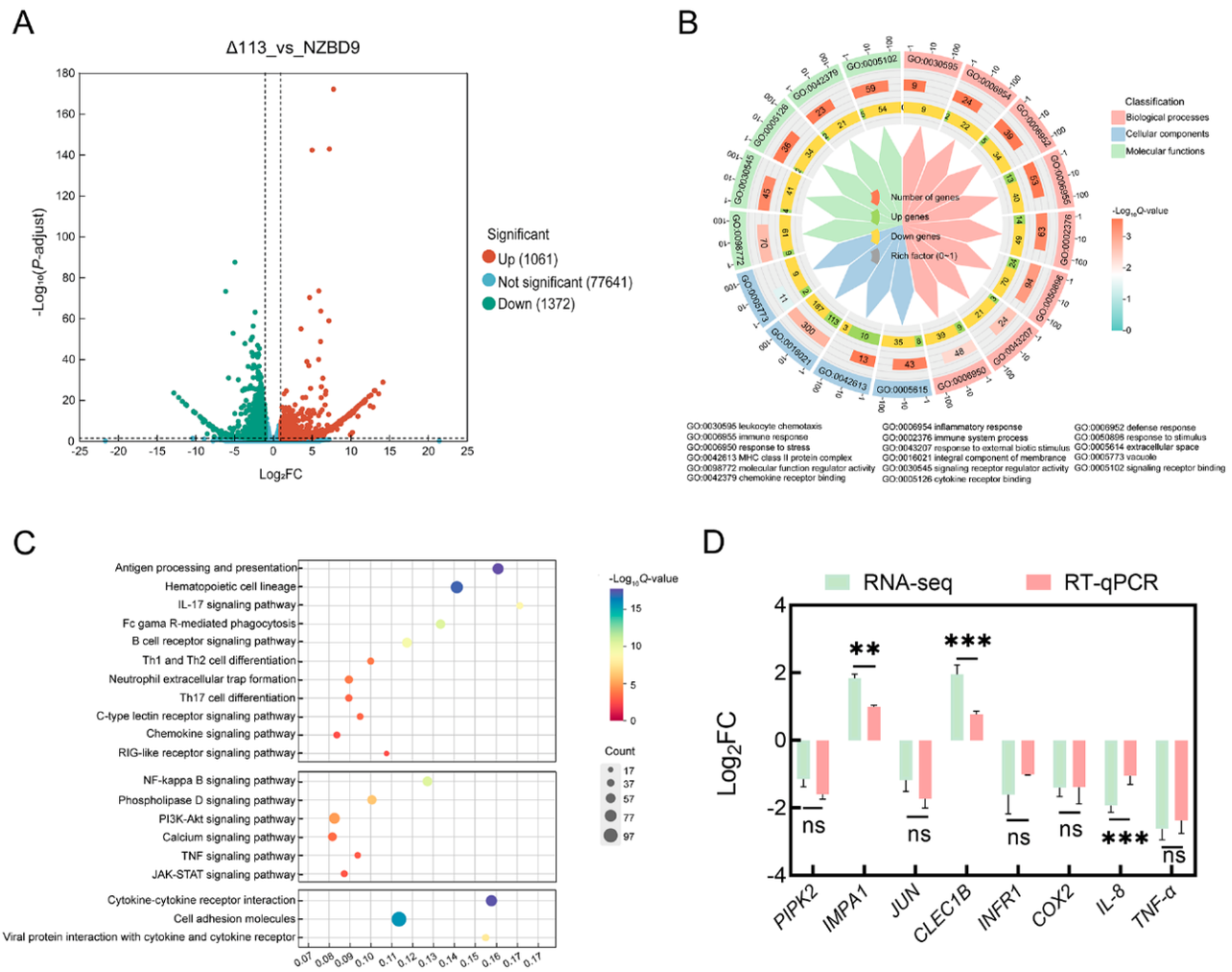


Figure 7 Transcriptomic analysis

A: Number of DEGs in spleen of grouper infected with NZBD9 and Δ113 strains of *Pseudomonas plecoglossicida*. B: GO enrichment analysis of DEGs. C: Bubble plot illustrating KEGG pathways enriched in DEGs, categorized into three secondary groups: immune system, signal transduction, and signaling molecules. D: Verification of DEGs by RT-qPCR. Error bars represent SD of the mean (n=3). ns: Not significant; *: P<0.05; **: P<0.01; ***: P<0.001.

presentation" (map04612), "Hematopoietic cell lineage" (map04640), and "Fc gamma R-mediated phagocytosis" (map04666); signal transduction pathways, including "NF-kappa B signaling pathway" (map04064), "Phospholipase D signaling pathway" (map04072), and "PI3K-Akt signaling pathway" (map04151); and signaling molecules and interaction pathways, including "Cytokine-cytokine receptor interaction" (map04060), "Cell adhesion molecules" (map04514), and "Viral protein interaction with cytokine and cytokine receptor" (map04061).

To validate the transcriptomic findings, eight genes (*PIPK2*, *IMPA1*, *JUN*, *CLEC1B*, *INFR1*, *COX2*, *IL-8*, and *TNF-α*) were selected for RT-qPCR analysis. Significant differences in the expression levels of *IMPA1*, *CLEC1B*, and *IL-8* were observed between the RT-qPCR and RNA-seq results, whereas no differences were found among the remaining genes. Overall, the expression patterns of these genes were consistent with the RNA-seq results (Figure 7D), confirming the reliability and accuracy of the RNA-seq data.

Effects of *P. plecoglossicida* sRNA113 on immune-related gene regulation in pearl gentian grouper and lateral flagella-related gene expression during infection

To investigate the role of *P. plecoglossicida* sRNA113 in modulating the immune response of pearl gentian grouper during infection, the transcriptional levels of inflammatory-related genes (*IL-6*, *IL-8*, *IL-12*, *TNFα*, *IL-10*, *CCL20*, and *COX2*) were assessed using RT-qPCR (Figure 8A). Compared to the NZBD9-infected group, the Δ113 strain-infected group exhibited a sustained decrease in the expression levels of *IL-6*, *IL-8*, *IL-12*, *TNFα*, and *IL-10* during most of the infection period, particularly during the later stages of infection (4–6 dpi). The expression of *CCL20* showed a significant decrease only at 6 dpi. In contrast, *COX2* showed a significant up-regulation at 3 dpi, followed by a marked down-regulation at 4–5 dpi.

To further explore the regulatory role of sRNA113 in modulating the expression of lateral flagellar type III secretion system-related genes and its influence on the immune response of pearl gentian grouper, RT-qPCR analysis was conducted to detect the expression of type III secretion system-related genes *flhABfliPQRMN* in the spleen of infected fish (Figure 8B). The Δ113 strain-infected group exhibited sustained and significant up-regulation of *fliP* expression throughout the infection period compared to the NZBD9-infected group. Similarly, *fliQ* and *fliN* showed consistent up-regulation during most of the infection period, while *flhA*, *flhB*,

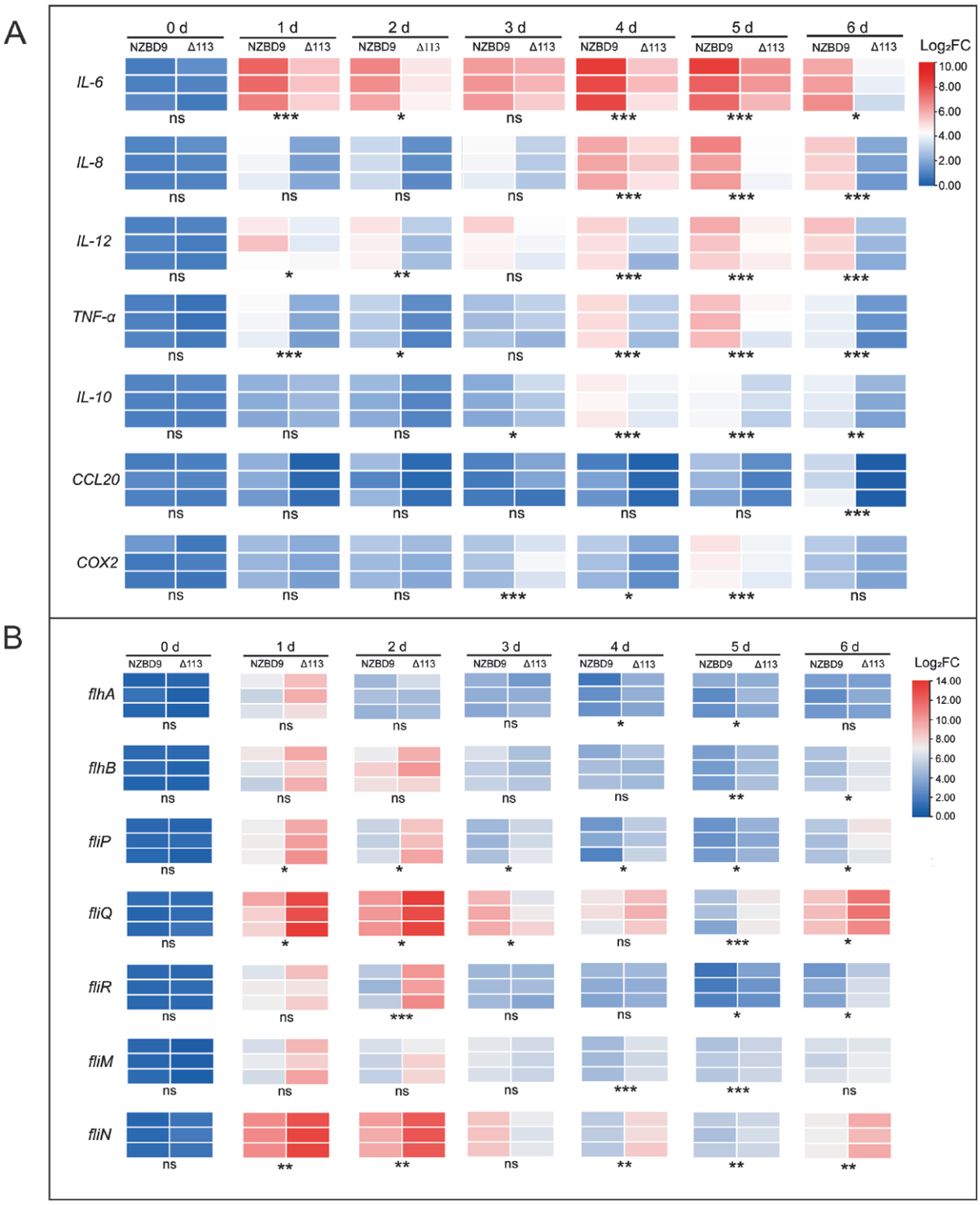


Figure 8 Heatmap analysis of relative expression levels of inflammatory-related genes in pearl gentian groupers and lateral flagella-related genes in *Pseudomonas plecoglossicida* during infection

A: Relative expression levels of inflammatory-related genes in the spleen of pearl gentian groupers at 0–6 dpi. B: Relative expression levels of lateral flagella-related genes in *P. plecoglossicida* at 0–6 dpi. Fold changes in all comparisons were assessed using the NZBD9-infected group at 0 dpi as the reference standard. Statistical analysis was conducted comparing the NZBD9-infected group (control) to the Δ113-infected group (experimental). ns: Not significant; *: P<0.05; **: P<0.01; ***: P<0.001.

fliR, and *fliM* were only significantly up-regulated in the late stage of infection.

DISCUSSION

The flagellar type III secretion system plays a pivotal role in bacterial flagellar assembly and is composed of a transmembrane export gate complex, including FlhA, FlhB, FliP, FliQ, and FliR, alongside a cytoplasmic ATPase ring complex comprising FliH, FliI, and FliJ (Halte & Erhardt, 2021). We previously identified *fliP* as a crucial virulence gene in *P. plecoglossicida* (He et al., 2023b). However, the molecular mechanisms by which *P. plecoglossicida* regulates *fliP* to

modulate bacterial virulence during infection and its impact on host immune response remain elusive. In this study, we identified a novel sRNA (sRNA113) with regulatory potential over the lateral flagellar type III secretion system of *P. plecoglossicida*, indicating significance in the modulation of bacterial virulence.

Bacteria with dual-flagellar systems, such as *P. plecoglossicida*, exclusively produce lateral flagella under certain conditions, such as on viscous media or solid substrates (McCarter, 2004). Swarming motility, a behavior associated with lateral flagella, varies significantly among bacterial species. For instance, *Vibrio parahaemolyticus* exhibits robust swarming motility on media with 0.5%–2.5% agar (Gode-Potratz et al., 2011), whereas certain α-proteobacteria display swarming behavior on surfaces with 0.4%–0.8% agar (McCarter, 2004). The regulation of flagella expression is often coordinated through operons, while sRNAs often act as post-transcriptional repressors, modulating the expression of operon-encoded mRNAs (Urban et al., 2007). Recent studies have identified several sRNAs that regulate genes within bacterial operons (Balasubramanian & Vanderpool, 2013). Therefore, the operon *flhABfliPQRMN* was considered in subsequent experiments. Notably, the expression of sRNA113 and *flhABfliPQRMN* in *P. plecoglossicida* was assessed under different culture conditions: liquid, semi-solid agar (0.5%), and solid agar (1.5%). The up-regulation of *flhABfliPQRMN* and down-regulation of sRNA113 on the semi-solid plate indicate a potential negative regulatory role of sRNA113 in modulating *flhABfliPQRMN* expression. Conversely, no significant differences in the expression of *flhABfliPQRMN* or sRNA113 were observed under liquid or solid culture conditions, suggesting that lateral flagellar expression in *P. plecoglossicida* is suppressed when grown on solid media. Therefore, a 0.5% agar plate was employed for the assessment of bacterial swarming motility in this investigation.

To evaluate the regulatory impact of sRNA113 on the swarming motility and virulence of *P. plecoglossicida*, a comparative analysis was conducted between the NZBD9 and mutant strains (Δ113 and C-Δ113). This included assessing swarming motility and the expression levels of lateral flagellar *flhABfliPQRMN* genes. The deletion of sRNA113 significantly increased swarming ability, accompanied by up-regulated expression of lateral flagella-associated genes. Additionally, sRNA113 deletion resulted in a marked increase in biofilm formation, adhesion, and chemotaxis, highlighting its role as a negative regulator of lateral flagellar genes and associated motility, biofilm, and virulence-related processes in *P. plecoglossicida*. Swarming motility, biofilm formation, and chemotaxis are well-documented contributors to bacterial pathogenicity (Tao et al., 2024a). The regulatory function of sRNA113 aligns with similar roles reported for motility- and biofilm-regulating sRNAs in other bacterial species. For instance, in *P. aeruginosa*, sRNAs such as AmrZ, RsmZ, RsmY, RsmW, PhrS, NrsZ, RgsA, and ErsA have been implicated in controlling motility, biofilm formation, and virulence (Liu et al., 2022). Likewise, *E. coli* sRNA FimR2 has been shown to regulate flagellar biosynthesis, biofilm development, and virulence (Raad et al., 2022). Although the expression of sRNA113 was up-regulated 8.9-fold, biofilm formation and adherence in the C-Δ113 strain failed to fully recover to levels observed in the NZBD9 strain, a phenomenon also observed in other bacterial species (Li et al., 2021b). One potential explanation is that flagellar assembly relies on the coordinated interaction of multiple flagella-related proteins, and elevated expression of certain flagella-related proteins may be insufficient to fully restore functional flagella or enhance biofilm formation.

Pseudomonas plecoglossicida is recognized for its predilection to infect visceral tissues, often leading to the development of granulomas in the spleen (Zhang et al., 2014). As granulomas mature, necrotic regions develop within the affected tissues, causing extensive damage and contributing to disease progression (Pagán & Ramakrishnan, 2018). Artificial infection experiments confirmed that the deletion of sRNA113 significantly enhanced the pathogenicity of *P. plecoglossicida*, as evidenced by the reduction in host survival, increased severity of spleen white nodules, increased bacterial loads in tissues, and aggravated histopathological damage. These findings suggest that sRNA113 may modulate lateral flagellar gene expression in *P. plecoglossicida*, thereby regulating critical processes such as swarming motility, biofilm formation, and chemotaxis. This regulatory mechanism ultimately increases bacterial virulence and the ability to damage host immune organs, including the spleen, intestine, liver, and head kidney, ultimately leading to necrosis and, in severe cases, host fatality.

Bacterial-host interactions represent a dynamic conflict wherein bacteria persist and proliferate by exploiting host resources, while the host mounts an immune response to counteract pathogenic invasion (Lin et al., 2023). To clarify the molecular mechanisms by which *P. plecoglossicida* sRNA113 influences host immune responses, transcriptomic analysis was conducted. Results showed that infection with the Δ113 strain led to differential expression of 2 433 genes compared to the NZBD9 strain, with 1 061 up-regulated and 1 392 down-regulated. GO and KEGG enrichment analyses revealed that Δ113 strain infection activated key signaling pathways, including PI3K-Akt and NF-κB. These pathways are central to modulating inflammatory responses and orchestrating cellular processes critical to host defense (Yu et al., 2022). The PI3K-Akt pathway is well-established for its role in recruiting and activating innate immune cells, particularly macrophages (He et al., 2022b). Similarly, the NF-κB pathway serves as a master regulator of inflammation (Capece et al., 2022; Li et al., 2024), stimulating immune cells to produce pro-inflammatory cytokines such as IL-1β, IL-6, IL-12, and TNF-α, or anti-inflammatory cytokines such as IL-10, thereby modulating the inflammatory response (Roe, 2021). Monocyte activation during infection also induces the production of crucial enzymes such as COX2, which further amplify inflammatory responses (Szlasa et al., 2023). Notably, this study observed a pronounced suppression of the host pro-inflammatory response during the late stages of Δ113 strain infection. This suppression may be attributed to severe spleen tissue damage and impaired pathogenic bacteria clearance during the late stage of infection. Additionally, the suppression of the anti-inflammatory cytokine *IL-10* suggests a potential immune response by the host to maintain the delicate balance between pro-inflammatory and anti-inflammatory reactions during infection (Hoffmann et al., 2000).

Further investigation into the expression of the lateral flagellar operon *flhABfliPQRMN* in the spleens of infected pearl gentian groupers revealed that sRNA113 acts as a negative regulator of these genes, thereby impacting bacterial virulence. Enhanced swarming motility of bacteria facilitates

colonization within the host, subsequently enhancing pathogenicity, leading to tissue damage and ultimately mortality (Rütschlin & Böttcher, 2020).

CONCLUSIONS

This study identified and elucidated the molecular mechanism by which sRNA113 negatively regulates the expression of lateral flagella to modulate *P. plecoglossicida* virulence. Deletion of sRNA113 significantly enhanced bacterial swarming, which, in turn, increased bacterial virulence, leading to severe tissue damage, disruption of host immune responses, and eventual mortality. These findings provide valuable insights into the functional role of sRNA113 in regulating bacterial virulence and its broader impact on host immune responses against infection. Moreover, this study deepens our understanding of the molecular mechanisms underlying virulence regulation in *P. plecoglossicida*.

DATA AVAILABILITY

The RNA-seq data can be downloaded from the NCBI (BioProjectID PRJNA1092597), China National Center for Bioinformation (PRJCA032388), and Science Data Bank databases (DOI: 10.57760/sciencedb.j00139.00118).

SUPPLEMENTARY DATA

Supplementary data to this article can be found online.

COMPETING INTERESTS

The authors declare that they have no competing interests.

AUTHORS' CONTRIBUTIONS

L.H. designed the experiments and drafted the paper. L.H., M.Q.M., L.M.Z., and Q.L. participated in the analysis of experimental results. H.G., J.N.Z., and J.L.Z. revised the paper for intellectual content. Q.P.Y. participated in literature searching and manuscript modification. All authors read and approved the final version of the manuscript.

ACKNOWLEDGMENTS

We are grateful to Dou Yang and Lian Shi (Fisheries College, Jimei University) for their assistance with fish rearing. We also thank Xi Wang, Xiao-Yu Chen, and Yu-Xin Yao (Fisheries College, Jimei University) for assisting with sample collection.

REFERENCES

Akayli T, Çanak Ö, Başaran B. 2011. A new *Pseudomonas* species observed in cultured young rainbow trout (*Oncorhynchus mykis* Walbaum, 1792): *Pseudomonas plecoglossicida*. *Bibad Biyoloji Bilimleri Araştırma Dergisi*, **4**(1): 107–111.

Bak G, Lee J, Suk S, et al. 2015. Identification of novel sRNAs involved in biofilm formation, motility and fimbriae formation in *Escherichia coli*. *Scientific Reports*, **5**: 15287.

Balasubramanian D, Vanderpool CK. 2013. New developments in post-transcriptional regulation of operons by small RNAs. *RNA Biology*, **10**(3): 337–341.

Capece D, Verzella D, Flati I, et al. 2022. NF-κB: blending metabolism, immunity, and inflammation. *Trends in Immunology*, **43**(9): 757–775.

Dutta T, Srivastava S. 2018. Small RNA-mediated regulation in bacteria: a growing palette of diverse mechanisms. *Gene*, **656**: 60–72.

Gill EE, Chan LS, Winsor GL, et al. 2018. High-throughput detection of RNA processing in bacteria. *BMC Genomics*, **19**(1): 223.

Gode-Potratz CJ, Kustusch RJ, Breheny PJ, et al. 2011. Surface sensing in *Vibrio parahaemolyticus* triggers a programme of gene expression that promotes colonization and virulence. *Molecular Microbiology*, **79**(1): 240–263.

Halte M, Erhardt M. 2021. Protein export via the type III secretion system of the bacterial flagellum. *Biomolecules*, **11**(2): 186.

He L, Zhao LM, Li Q, et al. 2023a. Flagellar gene *fliP* contributes to the virulence of *Pseudomonas plecoglossicida* by regulating its motility. *Aquaculture*, **576**: 739874.

He L, Zhao LM, Li Q, et al. 2023b. *Pseudomonas plecoglossicida fliP* gene affects the immune response of *Epinephelus fuscoguttatus* ♀ × *Epinephelus lanceolatus* ♂ to infection. *Fish & Shellfish Immunology*, **140**: 108971.

He LY, Kang JL, Chen XF, et al. 2024. Evaluation of immunogenicity and protective efficacy of the outer membrane porin F (OprF) against *Pseudomonas plecoglossicida* in large yellow croaker (*Larimichthys crocea*). *Fish & Shellfish Immunology*, **146**: 109427.

He LY, Li YS, Kang JL, et al. 2023c. Development and potential use of *Pseudomonas plecoglossicida* mutant Δ*OmpR*Δ*rpoS* as a live attenuated vaccine against visceral white nodules disease in large yellow croaker (*Larimichthys crocea*). *Aquaculture*, **574**: 739718.

He RC, Wang JJ, Lin MZ, et al. 2022a. Effect of ferredoxin receptor *FusA* on the virulence mechanism of *Pseudomonas plecoglossicida*. *Frontiers in Cellular and Infection Microbiology*, **12**: 808800.

He XG, Li Y, Deng B, et al. 2022b. The PI3K/AKT signalling pathway in inflammation, cell death and glial scar formation after traumatic spinal cord injury: mechanisms and therapeutic opportunities. *Cell Proliferation*, **55**(9): e13275.

Hofacker IL. 2003. Vienna RNA secondary structure server. *Nucleic Acids Research*, **31**(13): 3429–3431.

Hoffmann KF, Cheever AW, Wynn TA. 2000. IL-10 and the dangers of immune polarization: excessive type 1 and type 2 cytokine responses induce distinct forms of lethal immunopathology in murine schistosomiasis. *The Journal of Immunology*, **164**(12): 6406–6416.

Huang LX, Zhao LM, Su YQ, et al. 2018. Genome sequence of *Pseudomonas plecoglossicida* strain NZBD9. *Genome Announcements*, **6**(4): e01412–17.

Huang LX, Zuo YF, Qin YX, et al. 2021. The Zinc nutritional immunity of *Epinephelus coioides* contributes to the importance of *znuC* during *Pseudomonas plecoglossicida* infection. *Frontiers in Immunology*, **12**: 678699.

Izumi S, Yamamoto M, Suzuki K, et al. 2007. Identification and detection of *Pseudomonas plecoglossicida* isolates with PCR primers targeting the *gyrB* region. *Journal of Fish Diseases*, **30**(7): 391–397.

Jørgensen MG, Pettersen JS, Kallipolitis BH. 2020. sRNA-mediated control in bacteria: an increasing diversity of regulatory mechanisms. *Biochimica et Biophysica Acta (BBA) - Gene Regulatory Mechanisms*, **1863**(5): 194504.

Lau TTV, Puah SM, Tan JAMA, et al. 2021. Characterization of the relationship between polar and lateral flagellar genes in clinical *Aeromonas dhakensis*: phenotypic, genetic and biochemical analyses. *Brazilian Journal of Microbiology*, **52**(2): 517–529.

Li JP, Fan QY, Jin MY, et al. 2021a. Paeoniflorin reduce *luxS*/AI-2 system-controlled biofilm formation and virulence in *Streptococcus suis*. *Virulence*, **12**(1): 3062–3073.

Li Q, Jiang BJ, Zhang ZQ, et al. 2022. Involvement and characterization of NLRCs and pyroptosis-related genes in Nile tilapia (*Oreochromis niloticus*) immune response. *Fish & Shellfish Immunology*, **130**: 602–611.

Li RM, Tian JX, Shi QM, et al. 2021b. Cadaverine reverse transporter (CadA protein) contributes to the virulence of *Aeromonas veronii* TH0426. *Aquaculture Reports*, **21**: 100850.

Li ZM, Qin XW, Zhang Q, et al. 2024. Mandarin fish von Hippel-Lindau protein regulates the NF-κB signaling pathway via interaction with IκB to promote fish ranavirus replication. *Zoological Research*, **45**(5): 990–1000.

Lin YT, Xu T, Ip JCH, et al. 2023. Interactions among deep-sea mussels and their epibiotic and endosymbiotic chemoautotrophic bacteria: Insights

from multi-omics analysis. *Zoological Research*, **44**(1): 106–125.

Liu P, Yue CW, Liu LH, et al. 2022. The function of small RNA in *Pseudomonas aeruginosa*. *PeerJ*, **10**: e13738.

Luo G, Sun YJ, Huang LX, et al. 2020. Time-resolved dual RNA-seq of tissue uncovers *Pseudomonas plecoglossicida* key virulence genes in host-pathogen interaction with *Epinephelus coioides*. *Environmental Microbiology*, **22**(2): 677–693.

Mao ZJ, Li MF, Chen JG. 2013. Draft genome sequence of *Pseudomonas plecoglossicida* strain NB2011, the causative agent of white nodules in large yellow croaker (*Larimichthys crocea*). *Genome Announcements*, **1**(4): e00586–13.

Mao ZJ, Li SS, Li YY, et al. 2024. The bacterial pathogen *Pseudomonas plecoglossicida*, its epidemiology, virulence factors, vaccine development, and host-pathogen interactions. *Journal of Aquatic Animal Health*, **36**(2): 181–191.

McCarter LL. 2004. Dual flagellar systems enable motility under different circumstances. *Journal of Molecular Microbiology and Biotechnology*, **7**(1–2): 18–29.

Nedeljković M, Sastre DE, Sundberg EJ. 2021. Bacterial flagellar filament: a supramolecular multifunctional nanostructure. *International Journal of Molecular Sciences*, **22**(14): 7521.

Nishimori E, Kita-Tsukamoto K, Wakabayashi H. 2000. *Pseudomonas plecoglossicida* sp. nov. , the causative agent of bacterial haemorrhagic ascites of ayu, *Plecoglossus altivelis*. *International Journal of Systematic and Evolutionary Microbiology*, **50**(1): 83−89.

Pagán AJ, Ramakrishnan L. 2018. The formation and function of granulomas. *Annual Review of Immunology*, **36**: 639–665.

Raad N, Tandon D, Hapfelmeier S, et al. 2022. The stationary phase-specific sRNA FimR2 is a multifunctional regulator of bacterial motility, biofilm formation and virulence. *Nucleic Acids Research*, **50**(20): 11858–11875.

Reyes-Darias JA, García V, Rico-Jiménez M, et al. 2016. Identification and characterization of bacterial chemoreceptors using quantitative capillary and gradient plate chemotaxis assays. *Bio-Protocol*, **6**(8): e1789.

Roe K. 2021. An inflammation classification system using cytokine parameters. *Scandinavian Journal of Immunology*, **93**(2): e12970.

Rütschlin S, Böttcher T. 2020. Inhibitors of bacterial swarming behavior. *Chemistry – A European Journal*, **26**(5): 964–979.

Silva IJ, Barahona S, Eyraud A, et al. 2019. SraL sRNA interaction regulates the terminator by preventing premature transcription termination of *rho* mRNA. *Proceedings of the National Academy of Sciences of the United States of America*, **116**(8): 3042–3051.

Sun YJ, Zhu ZM, Weng SP, et al. 2020. Characterization of a highly lethal barramundi (*Lates calcarifer*) model of *Pseudomonas plecoglossicida* infection. *Microbial Pathogenesis*, **149**: 104516.

Szlasa W, Ślusarczyk S, Nawrot-Hadzik I, et al. 2023. Betulin and its derivatives reduce inflammation and COX-2 activity in macrophages. *Inflammation*, **46**(2): 573–583.

Tao LT, Wang L, Xiong J, et al. 2024a. *QseC* regulates chemotaxis, biofilm formation, motility, and virulence in *Aeromonas veronii* TH0426. *Aquaculture*, **588**: 740928.

Tao Z, Ye HD, Zhang CZ, et al. 2024b. PvgAS: A novel two-component system that controls type III and type VI secretion systems and virulence in the fish pathogen *Pseudomonas plecoglossicida*. *Aquaculture*, **578**: 740102.

Urban JH, Papenfort K, Thomsen J, et al. 2007. A conserved small RNA promotes discoordinate expression of the *glmUS* operon mRNA to activate GlmS synthesis. *Journal of Molecular Biology*, **373**(3): 521–528.

Wang JL, Ma WJ, Wang YZ, et al. 2018. Deletion of 76 genes relevant to flagella and pili formation to facilitate polyhydroxyalkanoate production in *Pseudomonas putida*. *Applied Microbiology and Biotechnology*, **102**(24): 10523–10539.

Wu XY, Xiong JB, Fei CJ, et al. 2022. Prior exposure to ciprofloxacin disrupts intestinal homeostasis and predisposes ayu (*Plecoglossus altivelis*) to subsequent *Pseudomonas plecoglossicida*-induced infection. *Zoological Research*, **43**(4): 648–665.

Xiong ZQ, Lv ZX, Song X, et al. 2021. Recent research advances in small regulatory RNAs in *Streptococcus*. *Current Microbiology*, **78**(6): 2231–2241.

Yang D, Zhao LM, Li Q, et al. 2023a. *flgC* gene is involved in the virulence regulation of *Pseudomonas plecoglossicida* and affects the immune response of *Epinephelus coioides*. *Fish & Shellfish Immunology*, **132**: 108512.

Yang D, Zhao LM, Li Q, et al. 2023b. The involvement of the T6SS *vgrG* gene in the pathogenicity of *Pseudomonas plecoglossicida*. *Journal of Fish Diseases*, **46**(10): 1097–1108.

Yu GL, Yu H, Yang QK, et al. 2022. *Vibrio harveyi* infections induce production of proinflammatory cytokines in murine peritoneal macrophages via activation of p38 MAPK and NF-κB pathways, but reversed by PI3K/AKT pathways. *Developmental & Comparative Immunology*, **127**: 104292.

Yuan B, Zhao LM, Zhuang ZX, et al. 2022. Transcriptomic and metabolomic insights into the role of the *flgK* gene in the pathogenicity of *Pseudomonas plecoglossicida* to orange-spotted grouper (*Epinephelus coioides*). *Zoological Research*, **43**(6): 952–965.

Zhang J, Wang Y, Guo H, et al. 2017. Identification and characterization of a phospholipase A1 activity type three secreted protein, PP_ExoU from *Pseudomonas plecoglossicida* NB2011, the causative agent of visceral granulomas disease in large yellow croaker (*Larimichthys crocea*). *Journal of Fish Diseases*, **40**(6): 831–840.

Zhang JT, Zhou SM, An SW, et al. 2014. Visceral granulomas in farmed large yellow croaker, *Larimichthys crocea* (Richardson), caused by a bacterial pathogen, *Pseudomonas plecoglossicida*. *Journal of Fish Diseases*, **37**(2): 113–121.

Zheng CK, Qiu J, Zhai YM, et al. 2023. ZrgA contributes to zinc acquisition in *Vibrio parahaemolyticus*. *Virulence*, **14**(1): 2156196.

Zhou SM, Wang Y, Shu FL, et al. 2023. Functional insights of a two-component system sensor kinase GacS in a fish pathogen, *Pseudomonas plecoglossicida*. *Aquaculture*, **562**: 738866.

Kwon et al. *Zool. Res.* 2025, 46(1): 165−176
https://doi.org/10.24272/j.issn.2095-8137.2024.277
https://cstr.cn/32248.14.zr.2024.277

ZR | Zoological Research

Article Open Access

Deciphering the toxic effects of polystyrene nanoparticles on erythropoiesis at single-cell resolution

Eun Jung Kwon[1,#], Hyeon Mi Sung[2,3,#], Hansong Lee[1], Soyul Ahn[2,3], Yejin Kim[2,3], Chae Rin Lee[2,3], Kihun Kim[4,5], Kyungjae Myung[6,7], Won Kyu Kim[8,9,10], Dokyoung Kim[11,12,13,14,15,16,17,18], Sanghwa Jeong[19,*], Chang-Kyu Oh[2,20,*], Yun Hak Kim[4,5,*]

[1] *Medical Research Institute*, *Pusan National University*, *Yangsan*, *Gyeongsangnam-do* 50612, *Republic of Korea*
[2] *Institute for Future Earth*, *Pusan National University*, *Busan* 46241, *Republic of Korea*
[3] *Department of Convergence Medical Sciences*, *School of Medicine*, *Pusan National University*, *Yangsan*, *Gyeongsangnam-do* 50612, *Republic of Korea*
[4] *Department of Biomedical Informatics*, *School of Medicine*, *Pusan National University*, *Yangsan*, *Gyeongsangnam-do* 50612, *Republic of Korea*
[5] *Department of Anatomy*, *School of Medicine*, *Pusan National University*, *Yangsan*, *Gyeongsangnam-do* 50612, *Republic of Korea*
[6] *Center for Genomic Integrity*, *Institute for Basic Science*, *Ulsan* 689-798, *Republic of Korea*
[7] *Department of Biomedical Engineering*, *College of Information-Bio Convergence Engineering*, *Ulsan National Institute of Science and Technology*, *Ulsan* 44919, *Republic of Korea*
[8] *Natural Product Research Center*, *Korea Institute of Science and Technology (KIST)*, *Gangneung*, *Gangwon-do* 25451, *Republic of Korea*
[9] *Department of Convergence Medicine*, *Yonsei University Wonju College of Medicine*, *Wonju*, *Gangwon-do* 26426, *Republic of Korea*
[10] *Natural Product Applied Science*, *KIST School*, *University of Science and Technology (UST)*, *Gangneung*, *Gangwon-do* 25451, *Republic of Korea*
[11] *Department of Biomedical Science*, *Graduate School*, *Kyung Hee University*, *Seoul* 02447, *Republic of Korea*
[12] *Department of Anatomy and Neurobiology*, *College of Medicine*, *Kyung Hee University*, *Seoul* 02447, *Republic of Korea*
[13] *Department of Precision Medicine*, *Graduate School*, *Kyung Hee University*, *Seoul* 02447, *Republic of Korea*
[14] *Center for Converging Humanities*, *Kyung Hee University*, *Seoul* 02447, *Republic of Korea*
[15] *KHU-KIST Department of Converging Science and Technology*, *Kyung Hee University*, *Seoul* 02447, *Republic of Korea*
[16] *UC San Diego Materials Research Science and Engineering Center*, 9500 *Gilman Drive*, *La Jolla*, *California* 92093, *USA*
[17] *Medical Research Center for Bioreaction to Reactive Oxygen Species and Biomedical Science Institute*, *Core Research Institute (CRI)*, *Kyung Hee University*, *Seoul* 02447, *Republic of Korea*
[18] *Center for Brain Technology*, *Brain Science Institute*, *Korea Institute of Science and Technology (KIST)*, *Seoul* 02792, *Republic of Korea*
[19] *School of Biomedical Convergence Engineering*, *Pusan National University*, *Yangsan*, *Gyeongsangnam-do* 50612, *Republic of Korea*
[20] *Department of Biochemistry*, *School of Medicine*, *Pusan National University*, *Yangsan*, *Gyeongsangnam-do* 50612, *Republic of Korea*

ABSTRACT

Polystyrene nanoparticles pose significant toxicological risks to aquatic ecosystems, yet their impact on zebrafish (*Danio rerio*) embryonic development, particularly erythropoiesis, remains underexplored. This study used single-cell RNA sequencing to comprehensively evaluate the effects of polystyrene nanoparticle exposure on erythropoiesis in zebrafish embryos. *In vivo* validation experiments corroborated the transcriptomic findings, revealing that polystyrene nanoparticle exposure disrupted erythrocyte differentiation, as evidenced by the decrease in mature erythrocytes and concomitant increase in immature erythrocytes. Additionally, impaired heme synthesis further contributed to the diminished erythrocyte population.

This is an open-access article distributed under the terms of the Creative Commons Attribution Non-Commercial License (http://creativecommons.org/licenses/by-nc/4.0/), which permits unrestricted non-commercial use, distribution, and reproduction in any medium, provided the original work is properly cited.

Copyright ©2025 Editorial Office of Zoological Research, Kunming Institute of Zoology, Chinese Academy of Sciences

Received: 27 August 2024; Accepted: 22 November 2024; Online: 23 November 2024

Foundation items: This work was supported by the Institute for Basic Science (IBS-R022-D1), Global Learning & Academic Research Institution for Master's/PhD students and Post-Doc Program of the National Research Foundation of Korea Grant funded by the Ministry of Education (RS-2023-00301938), and National Research Foundation of Korea Grant funded by the Korean government (RS-2024-00406152, MSIT). Additional financial support was provided by the 2024 Post-Doc Development Program of Pusan National University, Korea Medical Institute, and KREONET

[#]Authors contributed equally to this work

*Corresponding authors, E-mail: sanghwa.jeong@pusan.ac.kr; ck1988@pusan.ac.kr; yunhak10510@pusan.ac.kr

These findings underscore the toxic effects of polystyrene nanoparticles on hematopoietic processes, highlighting their potential to compromise organismal health in aquatic environments.

Keywords: Polystyrene nanoparticles; Zebrafish embryos; Single-cell RNA sequencing; Erythropoiesis

INTRODUCTION

Plastics, known for their versatility, long lifespan, cost-effectiveness, and ability to replace heavier substances, such as metals and glass, have become indispensable in modern industries and contemporary life (Andrady & Neal, 2009). Common plastics include polyethylene, polyethylene terephthalate, polypropylene, polyvinyl chloride, and polystyrene (Andrady, 2011). Among these, polyethylene and polypropylene are extensively used in the production of disposable bags, bottle caps, and packaging materials, contributing significantly to marine plastic pollution (Schwarz et al., 2019; Thushari & Senevirathna, 2020). Polystyrene, valued for its relatively low cost and lightweight nature, is widely used in disposable tableware and toys. However, its aromatic ring structure renders it more toxic than polyethylene or polyethylene terephthalate, amplifying its potential ecological impact (Alimi et al., 2022).

In the natural environment, most plastics degrade gradually under the influence of sunlight, wind, and wave action, lacking microbial decomposition (Ekvall et al., 2019; Kik et al., 2020). This gradual degradation generates microplastics —particles smaller than 5 mm —which can bypass sewage treatment plants and accumulate in aquatic ecosystems (Law & Thompson, 2014). Microplastics are generally classified as either primary or secondary. Primary microplastics are intentionally manufactured as small particles, commonly incorporated into products such as cosmetics and detergents, or directly released into the marine environment (Cole et al., 2013; Wang et al., 2019). In contrast, secondary microplastics originate from the breakdown of larger plastic items through natural processes (Duis & Coors, 2016; Ogonowski et al., 2016). Both forms pose serious ecological threats, adversely affecting aquatic ecosystems and marine life, as well as contributing to water pollution. Recognizing these impacts, extensive research has been conducted to understand the environmental and biological consequences of microplastics in aquatic environments (Ryan et al., 2009).

In addition to microplastics, nanoplastics, which range from 1 nm to 1 μm in size (Jambeck et al., 2015), have garnered increasing attention due to their profound impact on aquatic ecosystems and organismal health. Notably, nanoplastics can infiltrate biological systems with great efficiency, accumulating in aquatic species such as fish, crustaceans, and shellfish. These particles have been implicated in cellular damage, growth inhibition, and ecosystem disruption (Timilsina et al., 2023). Studies have indicated that nanoparticle size plays a critical role in their absorption and distribution within tissues, with smaller particles exhibiting enhanced bioavailability and organ penetration (Wang et al., 2023). For instance, in Nile tilapia (*Oreochromis niloticus*), 0.1 μm polystyrene nanoparticles accumulate in the gills at levels 3.4-fold higher than those of 0.5 μm polystyrene nanoparticles, with approximately 0.8 μg per gram detected in the gills (Wang et al., 2023). Similarly, smaller particles have been shown to intensify neutrophil aggregation and macrophage apoptosis in the abdomen of zebrafish (*Danio rerio*) larvae, leading to significant hepatic inflammation (Cheng et al., 2022). The nanoscale size of these plastics allows them to easily penetrate cellular membranes, thereby disrupting growth, development, and metabolic processes in exposed organisms (Pedersen et al., 2020; Shen et al., 2019). The implications of nanoplastics extend to critical physiological systems. Studies have demonstrated their ability to pass through the blood-brain barrier, accumulating in brain tissue and potentially impairing brain function (Sökmen et al., 2020). Additionally, polystyrene nanoplastics have been shown to alter immune and secretory cell populations in the intestinal tissue of zebrafish (Gu et al., 2020), further highlighting their systemic effects.

The molecular mechanisms through which microplastics and nanoplastics exert their toxic effects on aquatic life remain unclear, despite extensive research into their impacts at cellular and tissue levels. Notably, while the influence of polystyrene nanoparticles on immune cells such as neutrophils and macrophages has been documented (Jiang et al., 2024; Zhu et al., 2022), their potential effects on erythropoiesis remain largely unexplored. Given that polystyrene nanoparticles are likely to interact with red blood cells (RBCs) during circulation, these cells may also be vulnerable to polystyrene-induced toxicity. However, research on the direct effects of these particles on RBCs, either *in vitro* or *in vivo*, is scarce.

In the current study, we hypothesized that exposure to polystyrene nanoparticles would negatively impact erythropoiesis in zebrafish embryos. To ensure precise concentration control and eliminate inaccuracies caused by nanoparticle penetration of chorion pores prior to 72 h post-fertilization (hpf), fully hatched zebrafish embryos were exposed to 20 nm polystyrene nanoparticles (PS20 nm) at 72 hpf. The exposure concentrations, ranging from 0.1 to 10 μg/mL, were selected to ensure adequate exposure and reflect levels found in natural water and marine environments (Wang et al., 2023). To rigorously test this hypothesis, both *in silico* and *in vivo* experiments were conducted. These complementary methodologies not only provided robust validation of the results but also aligned with findings from existing studies.

MATERIALS AND METHODS

Characterization of polystyrene nanoparticles

The hydrodynamic (HD) size of the polystyrene nanoparticles was determined using dynamic light scattering (DLS) with a Zetasizer Nano ZSP (Malvern PANalytical, UK). Measurements were conducted at 20°C in 1×phosphate-buffered saline (PBS) at pH 7.4, employing a non-invasive back-scattering mode at an angle of 173° under 633 nm excitation. High-resolution transmission electron microscopy (HR-TEM) images were obtained using a JEM-2100 instrument (JEOL, Japan). For HR-TEM sample preparation, a suspension of nanoparticles in water was dropped onto a standard TEM grid and allowed to dry under ambient conditions. Fourier transform infrared spectroscopy (FTIR) analysis was used to investigate the chemical structure of the nanoparticles. FTIR spectra were collected using an iS50 spectrometer (Thermo Fisher Scientific, USA) at a wavelength range of 4 000–400 cm^{-1}, with a standard KBr beam splitter in transmittance mode. Sample preparation involved repeated

filtration of the microbead dispersion using a 30 kDa molecular weight cutoff (MWCO) centrifugal filter to remove residual surfactants and salts. The filtered nanoparticles were suspended in deionized water, vacuum-dried, and mixed with KBr powder.

Zebrafish and embryo maintenance and chemical treatment

Wild-type zebrafish and *gata1:*DsRed transgenic zebrafish (provided by IBS, CGI, South Korea) were maintained in a fully automated circulation aquarium system (Techniplast, Maggio, Italy) at 28.5°C under a 14 h light/10 h dark cycle (pH: 7.0, electrical conductivity: 1 000 μS/cm). All procedures followed the guidelines of the Institutional Animal Care and Use Committee (IACUC) from Pusan National University (PNU-2023-0359). Zebrafish embryos were collected at 0.5 hpf and incubated at 28±1°C with E3 solution (14.61 g NaCl, 0.63 g KCl, 1.83 g $CaCl_2{\cdot}2H_2O$, and 1.99 g $MgSO_4$ in 1 L of deionized water). Polystyrene nanoparticles (Sigma-Aldrich, USA) were diluted in the E3 solution for exposure studies, with treatments applied daily from 72 hpf.

Confocal imaging of nanoparticle accumulation

To evaluate the biodistribution of polystyrene nanoparticles in zebrafish embryos, polystyrene nanoparticles at concentrations of 0.1–10 μg/mL were prepared. Embryos were anesthetized with 2 g of tricaine (Sigma-Aldrich, USA) dissolved in 1 L of E-pure water and mounted in 3% methylcellulose on a glass-bottomed culture dish. Samples were observed and imaged using a confocal microscope (LSM880; Carl Zeiss, Germany).

Sampling for single-cell RNA sequencing

Zebrafish embryos were sacrificed at 120 hpf using 2 g of tricaine (Sigma-Aldrich, USA) dissolved in 1 L of E-pure water. Sacrificed embryos were incubated with 100 μg/mL of Liberase™ (Hoffman-La Roche, Switzerland) in PBS to facilitate disassembly into single cells. Mechanical dissociation was performed via pipetting, followed by incubation at 32°C for 40 min. The samples were then centrifuged at 300 r/min for 4 min at 4°C, and the cell pellet was resuspended in 2% fetal bovine serum (FBS) in PBS. The resuspended cells were filtered through a 40 μm nylon mesh filter and washed with 1 mL of PBS, then centrifuged at 300 ×*g* for 4 min and resuspended in 10% FBS and 1% PBS in Dulbecco's Modified Eagle Medium (DMEM) for sequencing.

Sample preparation

Cell suspensions were carefully resuspended in a cold, calcium- and magnesium-free solution containing 0.04% bovine serum albumin (BSA)/PBS. Cell counting was performed using a LUNA-FX7™ Automated Fluorescence Cell Counter (Logos Biosystems, South Korea) with acridine orange (AO) and propidium iodide (PI) staining (Logos Biosystems, South Korea, Cat# F23001). Following this, the cells were processed using a Dead Cells Removal Kit (Miltenyi Biotec, Germany, Cat# 130-090-101) and Magnetic-Activated Cell Sorting (MS) columns (Miltenyi Biotec, Germany, Cat# 130-042-201) in accordance with the manufacturer's guidelines.

Library construction and single-cell RNA sequencing

Single-cell RNA sequencing libraries were prepared using the 10x Chromium Single Cell 5' v2 platform (10x Genomics, USA, document number CG000331), 10x Chromium Controller, and Next Gem Single Cell 5' Reagent v2 kits (10x Genomics, USA, PN-1000244). In brief, the cell suspension, targeting a recovery of 10 000 cells, was combined with a reverse transcription master mix and loaded onto a Single Cell K Chip (10x Genomics, USA, PN-1000286) along with Single Cell 5′ Gel Beads and Partitioning Oil. This process generated Gel Bead-in-Emulsion (GEM) droplets, in which RNA transcripts from single cells were uniquely barcoded and reverse-transcribed. Following GEM formation, barcoded full-length cDNA was synthesized from mRNA during the GEM-RT reaction and subsequently enriched via polymerase chain reaction (PCR). For 5' gene expression library preparation, amplified cDNA underwent enzymatic fragmentation, end-repair, A-tailing, adapter ligation, and index PCR. The purified libraries were quantified using qPCR following the qPCR Quantification Protocol Guide (KAPA) and assessed for quality using the Agilent Technologies 4200 TapeStation (Agilent Technologies, USA). Library sequencing was performed using the HiSeq platform (Illumina, USA).

Single-cell RNA sequencing data processing

The raw sequencing data were processed and demultiplexed using the 10x Genomics Cell Ranger (v.6.0.0) pipeline. Baseline sequencing files were converted into FASTQ file format, after which the sequences were aligned to the *Danio rerio* genome (GRCz11) to generate single-cell feature counts.

All downstream bioinformatic analyses were conducted using the Seurat package (v.4.3.0) (Hao et al., 2021) in R, with default parameters used unless otherwise specified. The analytical approach was consistent with methodologies detailed in our previous studies (Lee et al., 2023a; Lee et al., 2023b; Lee et al., 2024). Quality control measures were implemented to exclude low-quality cells for subsequent analyses. The criteria for exclusion were: (1) Genes expressed in fewer than 12 cells (~0.1% of the data) and cells with fewer than 300 detected genes; (2) Cells expressing more than 3 300 or fewer than 300 unique genes; and (3) Cells with mitochondrial gene content exceeding 10%.

Normalization of raw read counts was performed using the log-normalization method. Highly variable features were identified by applying the "vst" method, selecting the top 2 000 features with the highest variability. To address batch effects and integrate data across samples, the canonical correlation analysis algorithm was used.

Clustering analysis and cell type identification

The integrated single-cell dataset was scaled and processed through principal component analysis (PCA) to reduce dimensionality. The top 22 principal components (PCs) were selected, where the rate of change between consecutive PCs was less than 0.1%. Using the selected PCs, a shared nearest-neighbor graph was constructed, and clustering was performed at a resolution of 0.4. The resulting cell clusters were visualized in two-dimensional (2D) space using Uniform Manifold Approximation and Projection (UMAP).

Cell type annotation was performed by verifying the expression of previously established marker genes using the Zebrafish Information Network (ZFIN, https://zfin.org/) (Bradford et al., 2022), resulting in the identification of 21 cell types: mesenchymal cells (*col6a2*, *col1a2*, and *col1a1b*), keratinocytes (*krt5*, *krtt1c19e*, and *epcam*), epithelial cells (*epcam*), pharynx cells (*cldne* and *dhrs13a.2*), nucleate erythrocytes (RBC) (*hbbe1.1*, *hbbe1.3*, and *hbae3*), fin cells (*and2*, *and1*, and *col1a1a*), radial glia (*fabp7a*, *glula*, *slc1a2b*,

and *atp1a1b*), notochord cells (*col2a1a* and *col9a2*), intestinal epithelial cells (*fabp2* and *epcam*), proliferating cells (*hmgn2*, *hmgb2b*, and *mki67*), myeloid cells (*lcp1*), oligodendrocytes (*mbpa* and *cldnk*), otic vesicle cells (*pax2a* and *stm*), xanthophores (*gch2* and *aox5*), ionocytes (Gill) (*atp1b1b*, *foxi3b*, and *epcam*), olfactory neurons (*pvalb5*, *fstl5*, *s100z*, and *elavl3*), corneal cells (*scinla*), hepatocytes (*apoa1b* and *apoa2*), muscle cells (*ckmb*, *tpma*, *tnnc2*, and *tnnt3b*), and pronephric duct cells (*cdh17* and *dab2*). The expression profiles of these marker genes used for cell type annotation are shown in Supplementary Figure S1.

After identifying the cell types, RBCs were isolated for further sub-cluster analysis. For the sub-clustering process, 22 PCs were used with a resolution of 0.5.

Differentially expressed genes (DEGs) and Gene Ontology (GO) analysis

Clusters constituting more than 5% of the total cell population were analyzed to assess alterations in cell proportions resulting from exposure to polystyrene nanoparticles. Clusters exhibiting the most significant changes were selected for further investigation. DEGs between the control and experimental groups were identified using the Wilcoxon rank-sum test, with criteria of $|\log_2 FC|>0.2$ and adjusted $P<0.05$. GO enrichment analysis was performed on the identified DEGs using ClusterProfiler (v.4.6.2) (Yu et al., 2012) and org.Dr.eg.db (v.3.16.0) (Carlson, 2022), with a cutoff of $P<0.05$ and $Q<0.01$. For analysis of RBC sub-clusters, DEGs were identified using a cutoff of $|\log_2 FC|>0.2$ and $P<0.05$ and subsequent GO analysis was performed with $P<0.05$ and $Q<0.05$.

Calculating gene set module scores

Verification of the GO terms derived from the enrichment analysis was performed by calculating gene set scores using the *AddModuleScore* function (v.2.2.0) (Andreatta & Carmona, 2021) in the Seurat package. Gene sets used for score computation consisted of genes associated with significant GO terms, with details provided in the Supplementary Files.

Inference of cell fate

Cell differentiation trajectories within the RBC cluster were analyzed using the Monocle3 package (v.1.3.1) (Cao et al., 2019). The Seurat object was converted into a Monocle3 cell_data_set object using the *as.cell_data_set* function. Subsequent clustering was performed employing the *cluster_cell* function. The primary graph was constructed in reduced-dimensional space using the *learn_graph* function. The pseudotime starting point was determined based on the expression levels of the *myb* gene, a known marker for hematopoietic stem cells (HSCs) in zebrafish erythropoiesis (Zhang et al., 2021).

***O*-Dianisidine staining**

Sacrificed embryos were stained with a solution containing *o*-dianisidine (0.6 mg/mL), 0.01 mol/L sodium acetate, 0.65% H_2O_2, and 40% (v/v) ethanol for 30 min in a dark environment. The stained embryos were washed in a mixture of ultrapure water and ethanol (6:4, v/v), fixed in 4% paraformaldehyde (PFA) for 1 h, maintained in 3% methylcellulose, and imaged under a microscope.

Reverse transcription-quantitative real-time polymerase chain reaction (RT-qPCR)

Total RNA was extracted from zebrafish embryos using TRIzol reagent (Invitrogen, USA). Chloroform was added to separate protein fractions, and RNA was precipitated using isopropanol. RNA was resuspended in diethyl pyrocarbonate (DEPC)-treated water and reverse-transcribed using SuperScript IV (Thermo Fisher Scientific, USA). RT-qPCR was performed using PowerUp SYBR Green Master Mix (Thermo Fisher Scientific, USA). The expression levels of the target genes were analyzed using the comparative threshold method, and the results were normalized to β- actin as an endogenous control.

Whole-mount *in situ* hybridization

Embryos were fixed in 4% PFA and subsequently dehydrated using methanol. The dehydrated samples were resolved with acetone and incubated at −20°C for one day, followed by thorough washing in acetone. The embryos were incubated in hybridization buffer (500 mL formamide (50%), 250 mL of 20×SSC (5X), 500 μg/mL torula (yeast) RNA, 50 μg/mL heparin, 0.1% 20% Tween-20, 9 mmol/L citric acid, and 225 mL of E-pure water) at 65°C for 2 h, then incubated with anti-DIG *gata1* probe diluted in hybridization buffer at 65°C for 2 days. After incubation, a series of washes were performed at 65°C, including once with hybridization buffer for 1 min, once with 2×SSC for 15 min, and twice with 0.2×SSC for 30 min. The embryos were subsequently incubated in blocking solution (2% heat-inactivated goat serum, 2 mg/mL BSA in PBT [1× PBS+0.1% Tween-20]) for 2 h at room temperature. To detect probe signaling, embryos were incubated overnight at 4°C with a diluted DIG-AP antibody (1:4 000) (Hoffman-La Roche, Switzerland) prepared in the blocking solution. The embryos were then washed with PBT for 15 min. Signal visualization was achieved using 5-bromo-4-chloro-3-indolyl phosphate/nitro blue tetrazolium (BCIP/NBT) dissolved in alkaline phosphatase (AP) buffer, with the samples covered with foil and incubated at room temperature for 4 h. To quench the staining reaction, the embryos were immersed in 1 mmol/L EDTA in 1 mL of 1×PBS and subsequently washed with a solution adjusted to pH 5.2. Excess signals were removed by cleaning the embryos in MeOH for 1 h. Finally, the embryos were imaged using a mounting medium containing 3% methylcellulose.

Fluorescence microscopy of transgenic zebrafish

The erythrocyte-specific marker *gata1*:DsRed was used to identify undifferentiated erythrocytes in transgenic zebrafish. Embryos were anesthetized using a solution of 2 g of tricaine (Sigma-Aldrich, USA) dissolved in 950 mL of E-pure water, with pH adjusted to 7.0 with 1 mol/L Tris. Embryos were imaged under a microscope (SteREO Discovery V8, Zeiss, Germany).

Metabolome extraction

Dechorionated zebrafish embryos, previously freeze-dried and stored at −80°C, were processed for metabolome extraction on the following day. In brief, 1 mL of 0.25% NH_4OH (Fluka, Switzerland) in water, supplemented with 100 ng/mL of an internal standard substance (Coproporphyrin I $^{15}N_4$) (Toronto Research Chemicals, Canada), was added to the prepared sample and vortexed for 1 h. Ultrasonication was subsequently performed for 5 min, followed by the addition of 3 mL of acetonitrile (Tedia, USA) with shaking on a shaker for 5 min. The mixture was then centrifuged at 2 500 ×*g* for 5 min at 4°C to separate the supernatant and protein pellet. The collected supernatant was lyophilized, re-constituted in 1 mL

of 2% formic acid (Sigma-Aldrich, USA) and 80% acetonitrile, and analyzed by liquid chromatography-tandem mass spectrometry (LC-MS/MS) for the quantification of four target analytes. The residual protein pellet was treated with 4 mL of 2% formic acid in 80% acetonitrile supplemented with 100 ng/mL of an internal standard. To enhance protein precipitation, 1 mL of a solution containing 0.1 g of sodium chloride (Merck, Germany) and supersaturated $MgSO_4$ (Junsei Chemical, Japan) was added and shaken on a shaker, followed by centrifugation at 2 500 ×*g* for 5 min at 4°C. A 1 mL aliquot of the organic solution from the upper layer was collected and subjected to LC-MS/TS analysis targeting a specific analyte. Calibration curves for the four analytes were established using diluted solvents consisting of 2% formic acid in 80% acetonitrile. An additional calibration curve was generated for one analyte using a diluted solvent of 2% formic acid in acetonitrile.

LC-MS/MS analysis

Simultaneous quantification of the five analytes was performed using a Shimadzu Nexera X3 LC system and Shimadzu LCMS-8050 triple quadrupole mass spectrometer. Separation was achieved on a Shim-pack GIST C18 Metal Free column (2.1×50 mm, 5 μm). The mobile phase consisted of acetonitrile (solvent A) and a gradient elution system for solvent B with the following program: 0.1% acetonitrile (0.0–0.5 min), 100% acetonitrile (2.7–3.2 min), and 1% acetonitrile (3.3–5.0 min). Electrospray ionization (ESI) was employed as the ionization technique for each target component.

Statistical analysis of data from zebrafish experiments

Statistical analyses of gene expression data were performed using the Student's *t*-test for pairwise comparisons. For experiments involving multiple comparisons, one-way analysis of variance (ANOVA) was used. All experiments were performed in triplicate. A *P*-value less than 0.05 was considered statistically significant.

RESULTS

Characterization of polystyrene nanoparticles

DLS analysis demonstrated that the polystyrene nanoparticles exhibited a uniform size distribution, with an average particle size of 16.7 nm (Figure 1A). The dispersion profiles confirmed the stability and homogeneity of the nanoparticles in the aqueous phase. FTIR spectroscopy further validated the chemical composition of the polystyrene nanoparticles o, revealing characteristic peaks associated with C-H stretching and aromatic rings (Figure 1B) (Hermán et al., 2015). The C-H stretching peaks appeared between 2 800–3 000 cm^{-1}, corresponding to the presence of aliphatic hydrocarbons in the polystyrene structure. Additionally, out-of-plane aromatic C-H vibrations were observed as peaks at approximately 700 cm^{-1}, consistent with the presence of phenyl groups. A distinct O-H stretching vibration peak at approximately 3 400 cm^{-1} suggested surface oxidation or adsorbed water on the nanoparticles . These spectral features collectively confirmed the structural integrity and chemical identity of the polystyrene nanoparticles. HR-TEM analysis of the polystyrene nanoparticles revealed well-defined, spherical nanoparticles with diameters ranging from 10 to 20 nm (average size=14.3 nm) (Figure 1C), consistent with the values obtained from DLS measurements.

Polystyrene nanoparticles impact zebrafish embryo development

Exposure to PS20 nm at a concentration of 10 μg/mL resulted in the highest accumulation within zebrafish embryos (Figure 2A). Despite this, no significant differences in survival rate, overall phenotype, and lateral body length were observed compared to the control (CTRL) group (Figure 2B–D). However, PS20 nm-treated embryos exhibited an increase eye distance in dorsal view (Figure 2E, F) and a significant increase in heart rate (Figure 2G), indicating subtle developmental changes.

Polystyrene nanoparticle exposure alters RBC translation in zebrafish embryos

Quality control analysis of single-cell RNA sequencing data using the Seurat package retained 20 159 cells, including 10 184 from the CTRL group and 9 975 from the PS20 nm-exposed group (Supplementary Figure S1A). Cell-type annotation using established markers identified 20 distinct cell types (Supplementary Figure S1B–D). Subsequent analyses focused on cell types representing over 5% of the total cell population (Supplementary Figure S1E), which included mesenchymal cells (*n*=5 439), keratinocytes (*n*=2 790), epithelial cells (*n*=2 052), pharynx cells (*n*=1 619), RBCs (*n*=1 475), fin cells (*n*=1 389), and notochord cells (*n*=1 061) (Figure 3A) (details regarding the cell types that did not meet these criteria are shown in Supplementary Figure S1). Notable shifts were observed in the pharynx and RBC clusters (Figure 3B; Supplementary Figure S1F, G), with an increased proportion of pharyngeal cells and a decreased proportion of RBCs in the PS20 nm-exposed group.

DEGs in the pharynx cluster were identified between the two groups (Supplementary Table S1). GO analysis of

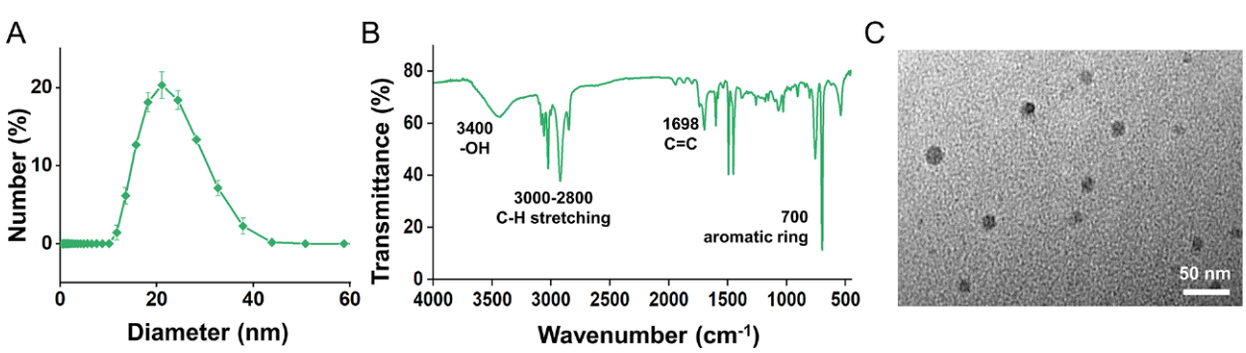


Figure 1 Characterization of polystyrene nanoparticles

A: Dynamic light scattering (DLS) spectra of polystyrene nanoparticles dispersion in water. B: Fourier transform infrared spectroscopy (FTIR) spectra of polystyrene nanoparticles. C: Transmission electron microscopy (TEM) image of polystyrene nanoparticles.

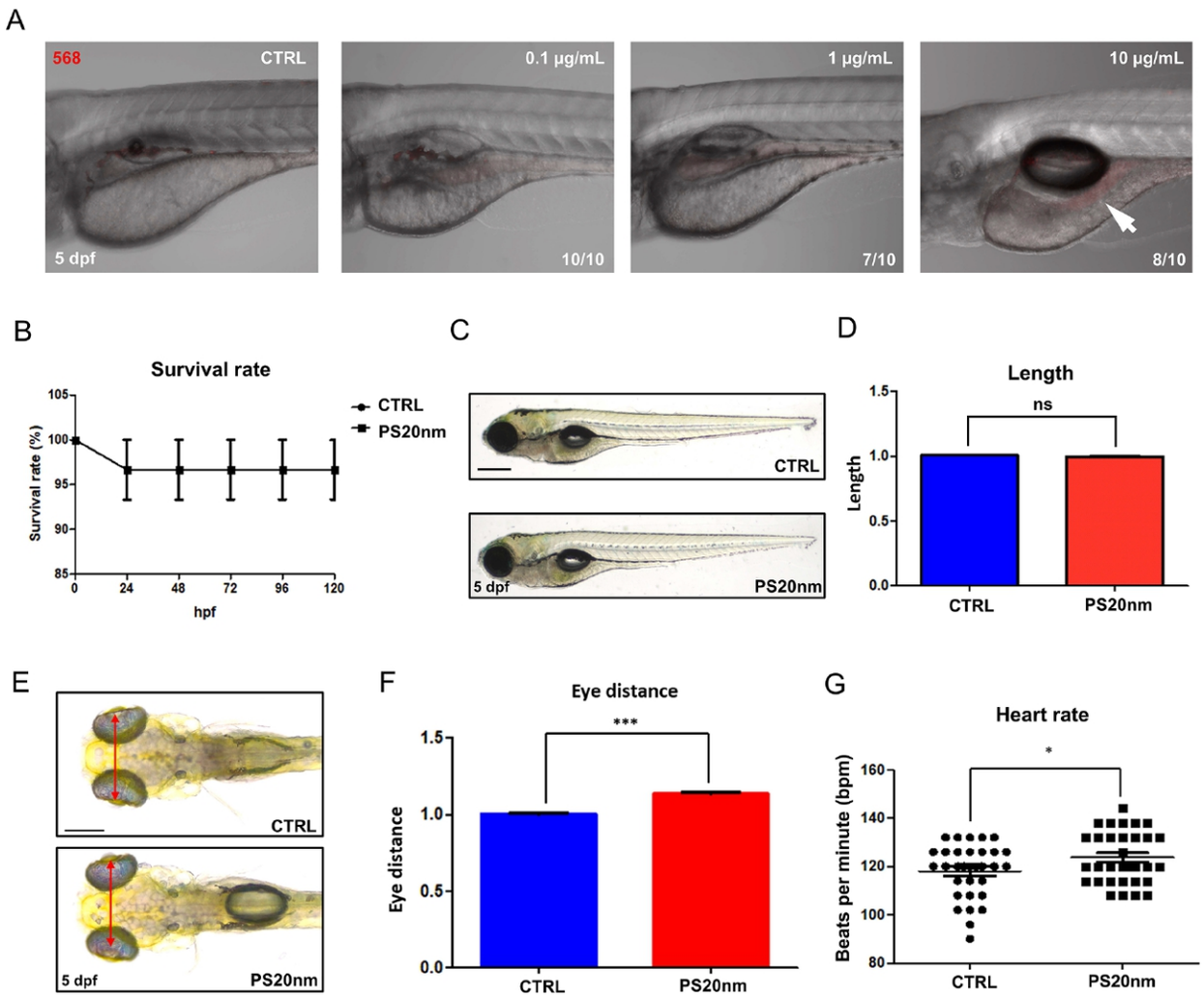


Figure 2 Effects of polystyrene nanoparticles on zebrafish embryo survival and morphology

A: Visualization of polystyrene nanoparticle accumulation in gastrointestinal tract at 0.1 μg/mL, 1 μg/mL, and 10 μg/mL concentrations. B: Effect of polystyrene nanoparticles on survival rate of zebrafish embryos at 5 days post-fertilization (dpf). Values are expressed as mean±SEM (n=30). C: Microscopic observation of zebrafish embryo phenotype following polystyrene nanoparticle treatment. Scale bars: 0.5 mm. D: Quantitative analysis of body length of zebrafish larvae between CTRL and PS20 nm-exposed groups. ns: Not significant. E: Eye distance in 5 dpf zebrafish larvae between CTRL and PS20 nm-exposed groups. Scale bars: 200 μm. F: Quantitative analysis of eye distance in zebrafish larvae, demonstrating a significant increase in the PS20 nm-exposed group compared to the CTRL. ***: P<0.001. G: Measurement of heart rate in zebrafish embryos at 5 dpf after polystyrene nanoparticle exposure. *: P<0.05.

biological processes (GO:BP) revealed an up-regulation of translation-related pathways in the PS20 nm-exposed group (Supplementary Figure S2A and Table S2). To assess the biological relevance of identified GO terms, a list of genes associated with each significant GO term was extracted from the Gene Ontology database (Supplementary Table S3). However, the module scores for the gene set related to translation did not differ significantly between the two groups (Supplementary Figure S2B).

Single-cell RNA sequencing revealed a significant reduction in RBCs upon PS20 nm exposure. This observation was validated using *o*-dianisidine staining, which confirmed a decrease in RBCs in zebrafish embryos following exposure to PS20 nm (Figure 3C). DEG analysis within the RBC cluster identified a global suppression of translation-related pathways and translation-related biological processes in the PS20 nm group (Supplementary Tables S4, S5; Figure 3D). Furthermore, the module scores for both translation and its positive regulation were significantly lower in the PS20 nm-exposed group (Supplementary Figure S2C). Among translation-associated genes, *rps7* demonstrated the most pronounced decrease in expression in the PS20 nm-treated group (Figure 3D, E).

To validate the single-cell RNA sequencing results, *rps7* knockdown experiments were conducted. Knockdown was confirmed by PCR (Figure 3F), and treated embryos exhibited facial malformations and pericardial edema (Figure 3G). In addition, o-dianisidine staining corroborated the reduction in RBCs observed in the PS20 nm-exposed group (Figure 3H).

Polystyrene nanoparticle exposure leads to the formation of immature RBCs

GO:BP analysis of the RBC cluster further revealed significant disruptions in RBC differentiation upon exposure to PS20 nm (Figure 4A; Supplementary Table S5). Based on these observations, we hypothesized that PS20 nm-exposed RBCs would demonstrate distinct differentiation patterns compared to CTRL RBCs. To investigate this, RBC sub-clustering and trajectory analysis were performed (Figure 4B; Supplementary

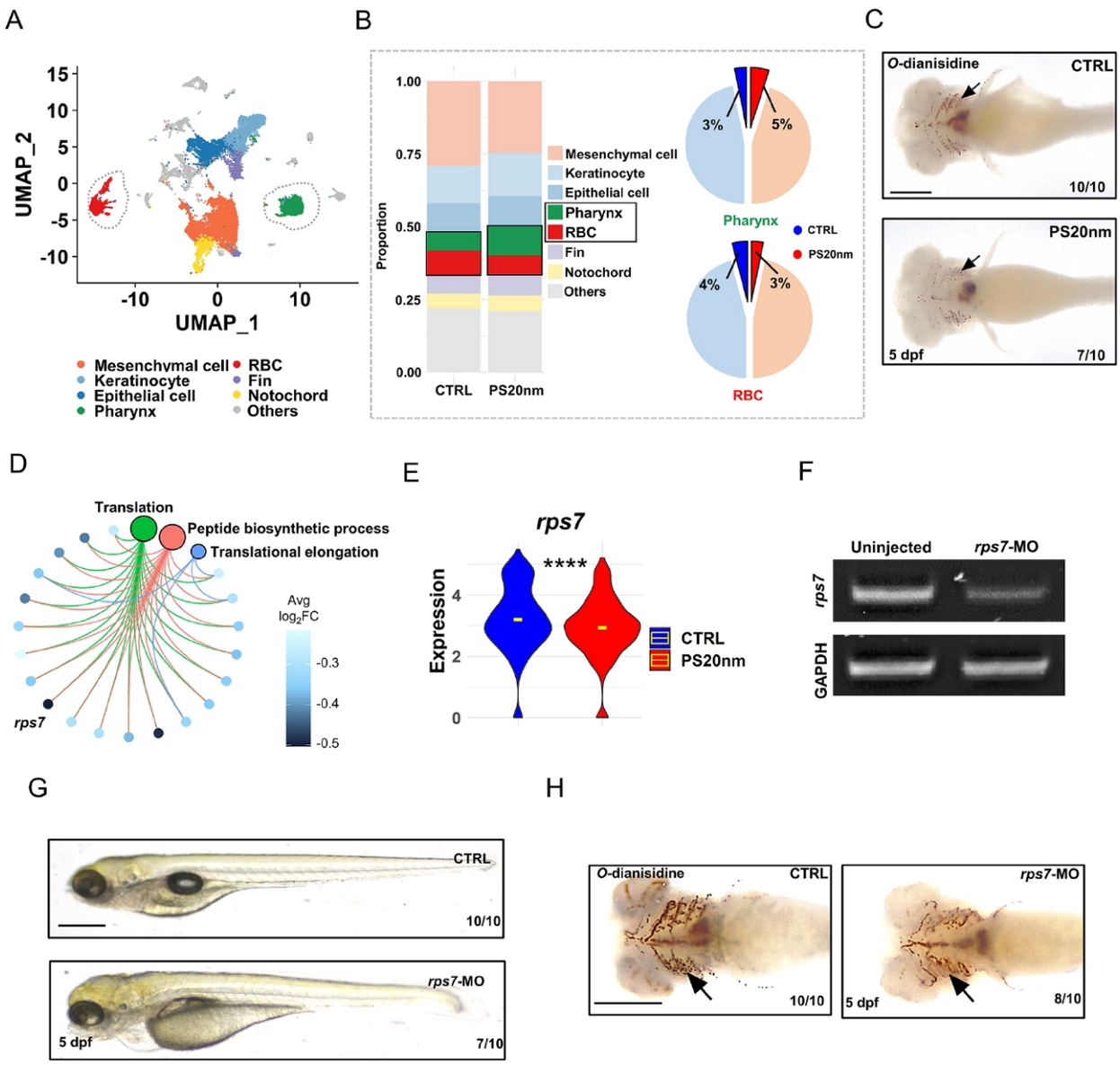


Figure 3 Single-cell RNA sequencing analysis of control and polystyrene nanoparticle-exposed zebrafish

A: UMAP visualization displaying seven cell types accounting for more than 5% of total cell population. B: Bar plots representing the proportion of the seven cell types (left) and pie charts showing notable changes in pharynx cell and RBC proportions between the CTRL and PS20 nm-treated groups (right). C: Examination of embryos from CTRL and PS20 nm-treated groups following o-dianisidine staining. Scale bar: 500 μm. D: Cnetplot showing translation-related terms from GO:BP analysis of RBC cluster. E: Violin plots showing expression levels of *rps7* (****: P<0.0001). F: RT-qPCR analysis of *rps7* and GAPDH in zebrafish embryos at 5 days post-fertilization (dpf). Total RNA was isolated from uninjected embryos and *rps7*-targeting morpholino-injected embryos (3.0 ng). G: Morphological comparison of embryos from uninjected CTRL group and *rps7*-injected group. Scale bars: 0.5 mm. H: Examination of embryos from uninjected CTRL and *rps7*-injected groups following o-dianisidine staining. Scale bar: 500 μm.

Figure S3A). Trajectory inference identified distinct stages of RBC differentiation, with the RBC1 cluster representing early differentiation and the RBC7 cluster representing final differentiation (Supplementary Figure S3A). Differentiation stages within each cluster were annotated using established markers (Figure 4C; Supplementary Figure S3B). Clusters RBC1–4 and 8 exhibited high expression of *myb* and *id1*, indicating HSC-like characteristics (Perry et al., 2007; Singh et al., 2018; Zhang et al., 2021). Clusters RBC5 and 6 were identified as resembling common myeloid progenitors (CMPs) based on the expression of *gata1a* (Zhang et al., 2021). Cluster RBC7, characterized by high expression of *band3* (*slc4a1a*), was determined to represent mature erythrocytes (Martin et al., 2011). A comparison of cell proportions between the CTRL and PS20 nm-exposed groups revealed a substantial increase in CMP-like cells in the PS20 nm-treated group, accompanied by a significant reduction in the proportion of mature erythrocytes (Figure 4D; Supplementary Figure S3C). Further analysis showed elevated expression of *gata1a* in the PS20 nm-exposed group, particularly in the RBC6 cluster, corresponding to CMP-like cells (Figure 4E). These findings suggest that exposure to polystyrene nanoparticles disrupts erythropoiesis in zebrafish, especially during the differentiation of CMP to mature erythrocytes. The expression of *gata1a*, a marker of CMP-like cells, was analyzed to validate the *in silico* findings. Exposure to PS20

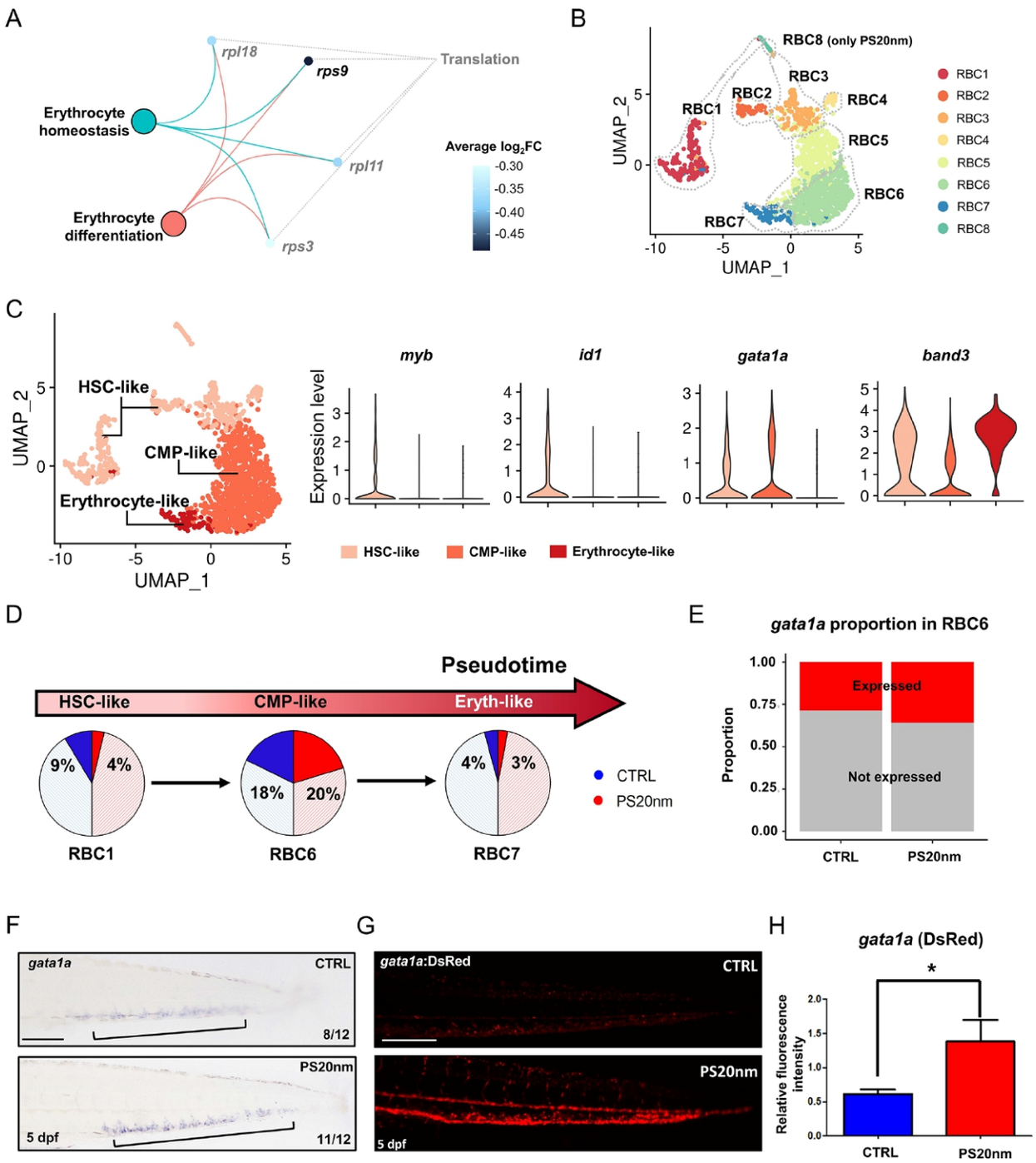


Figure 4 Impaired RBC differentiation in polystyrene nanoparticle-exposed zebrafish embryos identified through RBC sub-cluster analysis

A: Cnetplot illustrating erythropoiesis-related terms from GO:BP analysis of the RBC cluster. B: UMAP representation of RBC sub-clusters. C: Annotation of differentiation stages based on erythropoiesis stage-specific marker genes. D: Pie charts showing changes in cell proportion at each stage of differentiation. E: Bar plot showing proportion of *gata1a*-expressing cells identified in the RBC6 cluster. F: Whole-mount *in situ* hybridization of CTRL and PS20 nm-treated embryos at 5 dpf using erythrocyte marker *gata1a*. Scale bar: 200 μm. G, H: Fluorescence microscopy analysis of *gata1a*-expressing erythrocytes in transgenic zebrafish embryos at 5 dpf and quantification of *gata1a* expression using ImageJ (*: P<0.05). Scale bar: 200 μm.

nm significantly induced the expression of *gata1a* in caudal hematopoietic tissues (CHT), as demonstrated at both the mRNA (Figure 4F) and protein levels (Figure 4G).

Polystyrene nanoparticles impair heme synthesis in mature RBCs

GO:BP analysis of the RBC cluster identified a significant disruption in biological functions associated with heme synthesis following PS20 nm exposure (Figure 5A; Supplementary Table S5). Key genes involved in the heme biosynthesis pathway, including *cpox*, *urod*, and *hsbmb*, were significantly decreased in the PS20 nm-exposed group (Figure 5B; Supplementary Figure S4A). To gain deeper insight into the molecular disruptions, DEG and GO analyses were conducted across all RBC sub-clusters (Supplementary

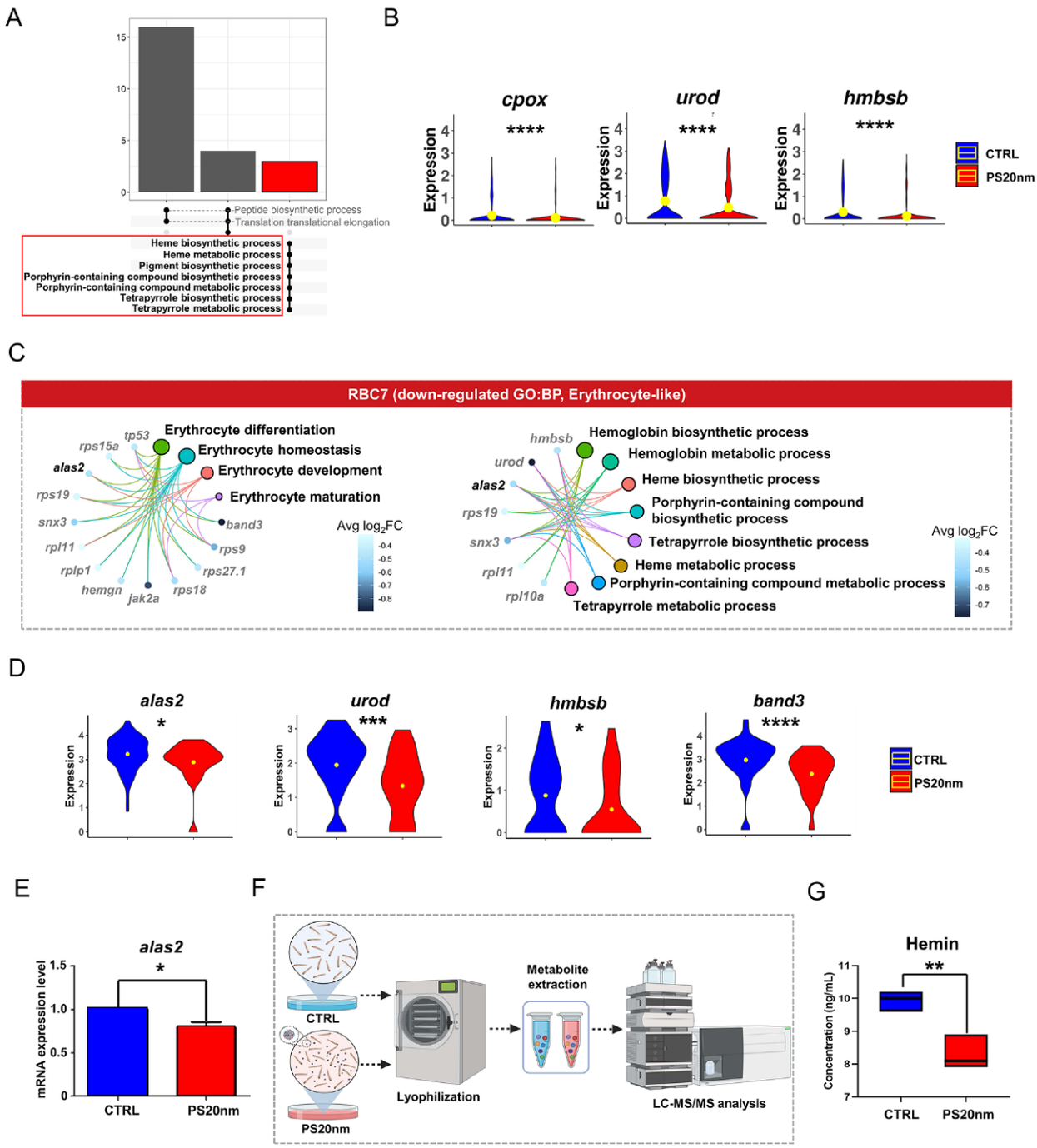


Figure 5 Inhibition of heme synthesis in zebrafish embryos exposed to polystyrene nanoparticles

A: GO:BP analysis highlighting heme synthesis-related terms within the RBC cluster. B: Violin plots showing expression levels of heme synthesis-related genes. ****: P<0.0001. C: Representative GO:BP analysis results for RBC7 cluster. D: Violin plots showing expression levels of heme synthesis-related genes in RBC7 cluster, inferred as the final stage of differentiation. E: RT-qPCR analysis of *alas2* expression in PS20 nm-treated embryos compared to untreated CTRL embryos. *: P<0.05. F, G: Measurement of hemin concentration in CTRL and PS20 nm-treated embryos using LC-MS/MS (*: P<0.01). F was created with BioRender.com.

Table S6). Down-regulation of pathways related to erythrocyte differentiation was observed in the RBC1, RBC6, and RBC7 clusters (Supplementary Figure S4B; Figure 5C). In the RBC1 cluster, *rps* genes associated with erythrocyte differentiation were down-regulated. Similarly, the RBC6 cluster showed down-regulation of genes related to erythrocyte differentiation, including *alas1*, which plays a critical role in the early stages of heme synthesis (Chiabrando et al., 2014). In the RBC7 cluster, pivotal heme synthesis genes, such as *alas2* and *urod*, were significantly down-regulated in the PS20 nm-treated group compared to the CTRL group, highlighting disruptions in erythropoiesis and heme biosynthesis (Chiabrando et al., 2014; Zhang et al., 2021) (Figure 5D).

The expression of *alas2*, a critical gatekeeper gene in heme biosynthesis, was validated in zebrafish embryos using RT-qPCR, confirming a significant reduction in its mRNA levels following PS20 nm exposure (Figure 5E). To further investigate the impact on heme biosynthesis, LC-MS/MS analysis was conducted (Figure 5F), revealing a marked decrease in hemin, the final metabolic product of heme

biosynthetic pathway, in PS20 nm-treated embryos (Figure 5G).

DISCUSSION

Polystyrene, a widely used plastic with a benzene ring structure, is highly reactive and frequently used in nanoplastic research. Nanoparticles with diameters of approximately 20 nm are particularly suitable for toxicity studies due to their ability to cross biological membranes and penetrate cells, enabling accurate assessment of their toxicological effects (Ding et al., 2024). Smaller nanoparticles exhibit a higher surface area-to-volume ratio, enhancing their chemical reactivity, biological interactions, cellular uptake, and tissue penetration (Jin et al., 2019; Shin et al., 2023; Teng et al., 2022). These properties make polystyrene nanoparticles especially valuable for exploring the relationship between toxicity and particle size (Chantho et al., 2024). Additionally, polystyrene is highly prevalent in environmental pollution, underscoring its relevance for toxicity studies. For example, extensive polystyrene microplastic contamination has been detected in river systems such as the Mulde and Elbe, primarily downstream of industrial sources (Laermanns et al., 2021). This environmental prevalence highlights the importance of studying the impact of polystyrene on ecological and biological health.

The concentrations of microplastics and nanoplastics in natural water and marine environments are typically reported to range from 6.35×10^{-3} to 6.94×10^{3} μg/L. However, laboratory studies often employ higher concentrations (1–100 mg/L) to assess the toxicological effects (Wang et al., 2023). In this study, a concentration range of 0.1 to 10 μg/mL was selected, reflecting more environmentally relevant exposure levels. This approach enhances the applicability of our findings and provides insights into potential environmental risks under natural conditions. Notably, zebrafish embryos exposed to a concentration of 10 μg/mL exhibited the highest accumulation of nanoparticles (Figure 2A). Although no severe morphological changes were observed, physiological alterations, including increased eye distance and elevated heart rate, were detected (Figure 2B–G). These findings suggest that polystyrene nanoparticles induce physiological stress responses, even in the absence of overt morphological defects, pointing to potential sub-lethal toxicity.

To assess the biological impacts of polystyrene nanoparticle exposure, zebrafish embryos exposed to 10 μg/mL polystyrene were analyzed using single-cell RNA sequencing (Figure 3A; Supplementary Figure S1). This high-resolution approach enabled precise identification of cellular reactions and gene expression alterations induced by nanoparticle exposure (Figure 3). While prior research has reported gut cell damage after prolonged exposure to 500 ng/mL polystyrene nanoparticles for 28 days (Deng et al., 2023), our study demonstrated significant effects on pharynx cells and RBCs within just 48 h of exposure (Figure 3B). Specifically, genes involved in translation in the RBC cluster showed marked down-regulation, correlating with reduced expression of genes crucial for erythropoiesis, such as *rps7* (Figure 3D–H). These results align with recent research demonstrating a reduction in erythrocyte production in zebrafish after treatment with silver nanoparticles (Cui et al., 2016). The single-cell RNA sequencing data indicated a widespread reduction in the expression of genes associated with translation (Supplementary Figure S2C), suggesting a pathological mechanism similar to that of Diamond-Blackfan anemia (DBA), a disorder associated with insufficient expression of ribosome-related genes, such as *rps19*, *rps24*, and *rps17* (Chen et al., 2020; Doherty et al., 2010). Interestingly, in PS20 nm-exposed zebrafish embryos, neither *p53* nor *TNF-α* expression was elevated (data not shown), which are hallmark mechanisms of DBA. However, facial deformities (Figure 2E, F) and a significant reduction in erythrocyte number (Figure 3B, C) were observed. These disruptions to erythropoiesis could lead to anemia-like symptoms, resulting in reduced physical performance, impaired feeding activity, and potential organ damage (Chiabrando et al., 2014).

Hematopoiesis in zebrafish embryos occurs in three distinct waves: primitive, transient, and definitive (Davidson & Zon, 2004). The primitive wave initiates the generation of blood cells to supply oxygen and establish the immune system (Davidson & Zon, 2004; Kulkeaw & Sugiyama, 2012). The transient wave serves as an intermediate stage, producing some blood cells and leading to the emergence of temporary blood components (Zhang et al., 2021). The definitive wave drives the formation of all blood cell types, establishing the complete hematopoietic system (Hu & Jing, 2023). This study focused on the hematopoietic process during the transient wave to investigate erythrocyte differentiation under polystyrene nanoparticle exposure. Representative gene expression levels, including *cmyb* (*myb*) and *gata1a*, were analyzed to track the erythropoietic process (Figure 4C). Results revealed that erythrocyte differentiation was arrested at the CMP stage (Figure 4D–H), resulting in the accumulation of immature erythrocytes and disrupted erythrocyte differentiation. Previous studies have examined the long-term effects of micro- and nanoplastics on hematopoiesis. For example, (Jing et al., 2022) investigated mammalian models exposed to micro-/nanoplastics for 42 days, identifying erythrocyte reductions linked to changes in HSCs mediated by interactions with gut microbiota and cytokines. In contrast, our zebrafish embryonic model with a shorter exposure duration (48 h) did not show alterations in HSCs within the CHT (Supplementary Figure S5A). Instead, polystyrene nanoparticles directly impacted translation-related pathways and RBC differentiation. These findings provide insights into how polystyrene nanoparticles disrupt erythrocyte differentiation, leading to a reduction in erythrocytes, and emphasize the importance of examining the effects of nanoplastic exposure on erythrocyte differentiation under varied conditions.

Single-cell RNA sequencing indicated a general decline in the expression of genes associated with translation and heme synthesis (Figure 5A). GO analysis further highlighted a marked decrease in the expression of key genes involved in heme synthesis, including *cpox*, *urod*, and *hmbsb*, implying a reduction in the availability of heme metabolites required for erythropoiesis (Figure 5B). Notably, the expression of *alas2*, a critical regulator in the heme biosynthesis pathway, was significantly reduced at the mRNA level (Figure 5D, E). Due to the low abundance of heme in zebrafish embryos and the limitations of traditional quantification methods, LC-MS/MS was employed to measure heme metabolites (Figure 5F), a technique previously used to quantify linezolid and heme concentrations in infected individuals and their relationship (Feng et al., 2022). In this study, LC-MS/MS analysis confirmed a notable reduction in heme metabolites in zebrafish embryos following the administration of polystyrene

nanoparticles (Figure 5G). These findings provide compelling evidence that polystyrene nanoparticles inhibit heme biosynthesis, leading to impaired erythropoiesis.

Extensive research has investigated the toxic effects of polystyrene nanoparticles on aquatic organisms, primarily focusing on oxidative stress and inflammation (Feng et al., 2022; Pei et al., 2022; Wu et al., 2022). However, the impact of polystyrene nanoparticles on erythropoiesis remains poorly understood. This study validated results from single-cell RNA sequencing through *in vivo* analysis, confirming disruptions at the mRNA level. Despite these insights, additional validation via proteomic approaches and comprehensive investigation into the entire hematopoietic process are necessary to fully elucidate the toxicological mechanisms. Nonetheless, this study revealed that exposure to polystyrene nanoparticles inhibits translation and heme synthesis, leading to the formation of immature erythrocytes. These findings highlight the toxic effects of polystyrene nanoparticles on erythropoiesis and underscore the importance of investigating diverse biological responses to nanoparticle exposure, which should contribute to a broader understanding of hematological impacts on aquatic organisms.

The observed reduction in RBCs and development of anemia resulting from exposure to polystyrene nanoparticles can pose significant risks to both animal populations and ecosystems. Reduced RBC levels impair oxygen transport, leading to diminished physical capabilities, impaired feeding behaviors, increased organ damage, and compromised immune systems (Canny et al., 2023; Ekiz et al., 2005). These physiological impairments may cascade into reduced reproduction and survival rates, disrupting population dynamics and ecosystem balance. As a result, the hematological disruptions induced by polystyrene nanoparticles may have far-reaching consequences that extend beyond individual organisms, impacting the ecosystem as a whole.

This study is the first to specifically investigate the effects of nanoparticles on RBCs, serving as a foundational pilot study for future research on how various nanoparticles influence erythropoiesis. Our findings demonstrated that exposure to polystyrene nanoparticles at a concentration of 10 μg/mL significantly disrupted erythropoiesis in zebrafish embryos. By interfering with translation and heme synthesis pathways, these nanoparticles caused an accumulation of immature erythrocytes. Importantly, the selected concentration reflects realistic environmental levels, accounting for regional and ecological variability. The significant disruption of erythropoiesis observed in this study underscores the potential risks posed by nanoparticle pollution in aquatic ecosystems. These findings highlight the urgent need for further research to explore the full extent of environmental and biological impacts of polystyrene nanoparticles, particularly regarding their implications for organismal health and ecosystem stability.

DATA AVAILABILITY

All single-cell RNA sequencing data used for this study are available at Gene Expression Omnibus (GEO, https://www.ncbi.nlm.nih.gov/geo/) under accession number GSE270075.

SUPPLEMENTARY DATA

Supplementary data to this article can be found online.

COMPETING INTERESTS

The authors declare that they have no competing interests.

AUTHORS' CONTRIBUTIONS

Conceptualization: C.-K.O. and Y.H.K.; Characterization of polystyrene nanoparticles: S.J.; *In silico* experiments: E.J.K. and H.L.; *In vivo* experiments: H.M.S., S.A., Y.K., and C.R.L.; Funding acquisition: E.J.K., K.M., C.-K.O., and Y.H.K.; Writing the manuscript: E.J.K. and H.M.S.; Reviewing the manuscript: K.M., K.K., W.K.K., and D.K., Supervising the research: C.-K.O., S.J., and Y.H.K. All authors read and approved the final version of the manuscript.

ACKNOWLEDGMENTS

We would like to thank Nuri Lim and Youngmin Hong from the Shimadzu Corporation for their assistance with LC-MS/MS analysis of heme metabolites. The authors thank all members of DecodeCell Inc. and Macrogen Inc. for helpful comments and discussions.

REFERENCES

Alimi OS, Claveau-Mallet D, Kurusu RS, et al. 2022. Weathering pathways and protocols for environmentally relevant microplastics and nanoplastics: what are we missing?. *Journal of Hazardous Materials*, **423**: 126955.

Andrady AL. 2011. Microplastics in the marine environment. *Marine Pollution Bulletin*, **62**(8): 1596–1605.

Andrady AL, Neal MA. 2009. Applications and societal benefits of plastics. *Philosophical Transactions of the Royal Society B Biological Sciences*, **364**(1526): 1977–1984.

Andreatta M, Carmona SJ. 2021. UCell: Robust and scalable single-cell gene signature scoring. *Computational and Structural Biotechnology Journal*, **19**: 3796–3798.

Bradford YM, Van Slyke CE, Ruzicka L, et al. 2022. Zebrafish information network, the knowledgebase for *Danio rerio* research. *Genetics*, **220**(4): iyac016.

Canny SP, Orozco SL, Thulin NK, et al. 2023. Immune mechanisms in inflammatory anemia. *Annual Review of Immunology*, **41**: 405–429.

Cao JY, Spielmann M, Qiu XJ, et al. 2019. The single-cell transcriptional landscape of mammalian organogenesis. *Nature*, **566**(7745): 496–502.

Carlson M. 2022. org. Dr. eg. db: Genome wide annotation for Zebrafish. https://bioconductor.org/packages/release/data/annotation/html/org.Dr.eg.db.html.

Chantho V, Sillapaprayoon S, Saenmuangchin R, et al. 2024. Effects of polystyrene nanoplastic size on zebrafish embryo development. *Toxicology in Vitro*, **99**: 105868.

Chen C, Lu MJ, Lin S, et al. 2020. The nuclear gene *rpl18* regulates erythroid maturation via JAK2-STAT3 signaling in zebrafish model of diamond-blackfan anemia. *Cell Death & Disease*, **11**(2): 135.

Cheng HD, Duan ZH, Wu YH, et al. 2022. Immunotoxicity responses to polystyrene nanoplastics and their related mechanisms in the liver of zebrafish (*Danio rerio*) larvae. *Environment International*, **161**: 107128.

Chiabrando D, Mercurio S, Tolosano E. 2014. Heme and erythropoieis: more than a structural role. *Haematologica*, **99**(6): 973–983.

Cole M, Lindeque P, Fileman E, et al. 2013. Microplastic ingestion by zooplankton. *Environmental Science & Technology*, **47**(12): 6646–6655.

Cui B, Ren L, Xu QH, et al. 2016. Silver_ nanoparticles inhibited erythrogenesis during zebrafish embryogenesis. *Aquatic Toxicology*, **177**: 295–305.

Davidson AJ, Zon LI. 2004. The 'definitive' (and 'primitive') guide to zebrafish hematopoiesis. *Oncogene*, **23**(43): 7233–7246.

Deng JW, Zeng XL, Li JJ, et al. 2023. Single-cell transcriptomic analysis reveals heterogeneity of the patterns of responsive genes and cell communications in liver cell populations of zebrafish exposed to polystyrene nanoplastics. *Science of the Total Environment*, **889**: 164082.

Ding RY, Chen YY, Shi XM, et al. 2024. Size-dependent toxicity of polystyrene microplastics on the gastrointestinal tract: Oxidative stress

related-DNA damage and potential carcinogenicity. *Science of the Total Environment*, **912**: 169514.

Doherty L, Sheen MR, Vlachos A, et al. 2010. Ribosomal protein genes RPS10 and RPS26 are commonly mutated in diamond-blackfan anemia. *The American Journal of Human Genetics*, **86**(2): 222–228.

Duis K, Coors A. 2016. Microplastics in the aquatic and terrestrial environment: sources (with a specific focus on personal care products), fate and effects. *Environmental Sciences Europe*, **28**(1): 2.

Ekiz C, Agaoglu L, Karakas Z, et al. 2005. The effect of iron deficiency anemia on the function of the immune system. *The Hematology Journal*, **5**(7): 579–583.

Ekvall MT, Lundqvist M, Kelpsiene E, et al. 2019. Nanoplastics formed during the mechanical breakdown of daily-use polystyrene products. *Nanoscale Advances*, **1**(3): 1055–1061.

Feng ML, Luo JJ, Wan YP, et al. 2022. Polystyrene nanoplastic exposure induces developmental toxicity by activating the oxidative stress response and base excision repair pathway in zebrafish (*Danio rerio*). *ACS Omega*, **7**(36): 32153–32163.

Gu WQ, Liu S, Chen L, et al. 2020. Single-cell RNA sequencing reveals size-dependent effects of polystyrene microplastics on immune and secretory cell populations from zebrafish intestines. *Environmental Science & Technology*, **54**(6): 3417–3427.

Hao YH, Hao S, Andersen-Nissen E, et al. 2021. Integrated analysis of multimodal single-cell data. *Cell*, **184**(13): 3573–3587. e29.

Hermán V, Takacs H, Duclairoir F, et al. 2015. Core double–shell cobalt/graphene/polystyrene magnetic nanocomposites synthesized by *in situ* sonochemical polymerization. *RSC Advances*, **5**(63): 51371–51381.

Hu YX, Jing Q. 2023. Zebrafish: a convenient tool for myelopoiesis research. *Cell Regeneration*, **12**(1): 2.

Jambeck JR, Geyer R, Wilcox C, et al. 2015. Plastic waste inputs from land into the ocean. *Science*, **347**(6223): 768–771.

Jiang WL, Liu YL, Wu YQ, et al. 2024. Polystyrene nanoplastics of different particle sizes regulate the polarization of pro-inflammatory macrophages. *Scientific Reports*, **14**(1): 16329.

Jin YX, Lu L, Tu WQ, et al. 2019. Impacts of polystyrene microplastic on the gut barrier, microbiota and metabolism of mice. *Science of the Total Environment*, **649**: 308–317.

Jing JR, Zhang L, Han L, et al. 2022. Polystyrene micro-/nanoplastics induced hematopoietic damages via the crosstalk of gut microbiota, metabolites, and cytokines. *Environment International*, **161**: 107131.

Kik K, Bukowska B, Sicińska P. 2020. Polystyrene nanoparticles: sources, occurrence in the environment, distribution in tissues, accumulation and toxicity to various organisms. *Environmental Pollution*, **262**: 114297.

Kulkeaw K, Sugiyama D. 2012. Zebrafish erythropoiesis and the utility of fish as models of anemia. *Stem Cell Research & Therapy*, **3**(6): 55.

Laermanns H, Reifferscheid G, Kruse J, et al. 2021. Microplastic in water and sediments at the confluence of the elbe and mulde rivers in Germany. *Frontiers in Environmental Science*, **9**: 794895.

Law KL, Thompson RC. 2014. Microplastics in the seas. *Science*, **345**(6193): 144–145.

Lee H, Joo JY, Kang J, et al. 2023a. Single-cell analysis of platelets from patients with periodontitis and diabetes. *Research and Practice in Thrombosis and Haemostasis*, **7**(2): 100099.

Lee H, Joo JY, Song JM, et al. 2023b. Immunological link between periodontitis and type 2 diabetes deciphered by single-cell RNA analysis. *Clinical and Translational Medicine*, **13**(12): e1503.

Lee H, Park S, Yun JH, et al. 2024. Deciphering head and neck cancer microenvironment: single-cell and spatial transcriptomics reveals human papillomavirus-associated differences. *Journal of Medical Virology*, **96**(1): e29386.

Martin CS, Moriyama A, Zon LI. 2011. Hematopoietic stem cells, hematopoiesis and disease: lessons from the zebrafish model. *Genome Medicine*, **3**(12): 83.

Ogonowski M, Schür C, Jarsén Å, et al. 2016. The effects of natural and anthropogenic microparticles on individual fitness in daphnia magna. *PLoS One*, **11**(5): e0155063.

Pedersen AF, Meyer DN, Petriv AMV, et al. 2020. Nanoplastics impact the zebrafish (*Danio rerio*) transcriptome: associated developmental and neurobehavioral consequences. *Environmental Pollution*, **266**: 115090.

Pei X, Heng X, Chu WH. 2022. Polystyrene nano/microplastics induce microbiota dysbiosis, oxidative damage, and innate immune disruption in zebrafish. *Microbial Pathogenesis*, **163**: 105387.

Perry SS, Zhao Y, Nie L, et al. 2007. Id1, but not Id3, directs long-term repopulating hematopoietic stem-cell maintenance. *Blood*, **110**(7): 2351–2360.

Ryan PG, Moore CJ, Van Franeker JA, et al. 2009. Monitoring the abundance of plastic debris in the marine environment. *Philosophical Transactions of the Royal Society B Biological Sciences*, **364**(1526): 1999–2012.

Schwarz AE, Ligthart TN, Boukris E, et al. 2019. Sources, transport, and accumulation of different types of plastic litter in aquatic environments: a review study. *Marine Pollution Bulletin*, **143**: 92–100.

Shen M C, Zhang Y X, Zhu Y, et al. 2019. Recent advances in toxicological research of nanoplastics in the environment: a review. *Environmental Pollution*, **252**: 511–521.

Shin HS, Lee SH, Moon HJ, et al. 2023. Exposure to polystyrene particles causes anxiety-, depression-like behavior and abnormal social behavior in mice. *Journal of Hazardous Materials*, **454**: 131465.

Singh SK, Singh S, Gadomski S, et al. 2018. Id1 ablation protects hematopoietic stem cells from stress-induced exhaustion and aging. *Cell Stem Cell*, **23**(2): 252–265. e8.

Sökmen TÖ, Sulukan E, Türkoğlu M, et al. 2020. Polystyrene nanoplastics (20 nm) are able to bioaccumulate and cause oxidative DNA damages in the brain tissue of zebrafish embryo (Danio rerio). *Neurotoxicology*, **77**: 51–59.

Teng MM, Zhao XL, Wang CJ, et al. 2022. Polystyrene nanoplastics toxicity to zebrafish: dysregulation of the brain-intestine-microbiota axis. *ACS Nano*, **16**(5): 8190–8204.

Thushari GGN, Senevirathna JDM. 2020. Plastic pollution in the marine environment. *Heliyon*, **6**(8): e04709.

Timilsina A, Adhikari K, Yadav AK, et al. 2023. Effects of microplastics and nanoplastics in shrimp: Mechanisms of plastic particle and contaminant distribution and subsequent effects after uptake. *Science of the Total Environment*, **894**: 164999.

Wang T, Li BJ, Zou XQ, et al. 2019. Emission of primary microplastics in mainland China: invisible but not negligible. *Water Research*, **162**: 214–224.

Wang WY, Mao X, Zhang R, et al. 2023. Nanoplastic exposure at environmental concentrations disrupts hepatic lipid metabolism through oxidative stress induction and endoplasmic reticulum homeostasis perturbation. *Environmental Science & Technology*, **57**(38): 14127–14137.

Wu H, Guo JM, Yao YJ, et al. 2022. Polystyrene nanoplastics induced cardiomyocyte apoptosis and myocardial inflammation in carp by promoting ROS production. *Fish & Shellfish Immunology*, **125**: 1–8.

Yu GC, Wang LG, Han YY, et al. 2012. clusterProfiler: an R package for comparing biological themes among gene clusters. *OMICS: A Journal of Integrative Biology*, **16**(5): 284–287.

Zhang YH, Chen MY, Chen CY. 2021. Using the zebrafish as a genetic model to study erythropoiesis. *International Journal of Molecular Sciences*, **22**(19): 10475.

Zhu XY, Peng L, Song EQ, et al. 2022. Polystyrene nanoplastics induce neutrophil extracellular traps in mice neutrophils. *Chemical Research in Toxicology*, **35**(3): 378–382.

Li et al. *Zool. Res.* 2025, 46(1): 177−192
https://doi.org/10.24272/j.issn.2095-8137.2024.223
https://cstr.cn/32248.14.zr.2024.223

ZR | Zoological Research

Article Open Access

Multi-omics analysis and experimental verification reveal testicular fatty acid metabolism disorder in non-obstructive azoospermia

Zhou Li[1,#], Yi-Jian Xiang[2,#], Zhi-Chuan Zou[1], Yu-Ming Feng[1], Hui Wang[1], Wei-Qing Chen[1], Xie Ge[1], Jin-Zhao Ma[1,*], Jun Jing[1,2,*], Bing Yao[1,2,*]

[1] *Department of Reproductive Medicine*, *Jinling Hospital*, *Affiliated Hospital of Medical School*, *Nanjing University*, *Nanjing*, *Jiangsu* 210000, *China*

[2] *State Key Laboratory of Reproductive Medicine and Offspring Health*, *Nanjing Medicine University*, *Nanjing*, *Jiangsu* 211166, *China*

ABSTRACT

Increasing evidence implicates disruptions in testicular fatty acid metabolism as a contributing factor in non-obstructive azoospermia (NOA), a severe form of male infertility. However, the precise mechanisms linking fatty acid metabolism to NOA pathogenesis have not yet been fully elucidated. Multi-omics analyses, including microarray analysis, single-cell RNA sequencing (scRNA-seq), and metabolomics, were utilized to investigate disruptions in fatty acid metabolism associated with NOA using data from public databases. Results identified *ACSL6*, *ACSBG2*, and *OLAH* as key genes linked to fatty acid metabolism dysregulation, suggesting their potential causative roles in NOA. A marked reduction in omega-3 polyunsaturated fatty acids, especially docosahexaenoic acid (DHA), was observed, potentially contributing to the pathological process of NOA. Sertoli cells in NOA patients exhibited apparent fatty acid metabolic dysfunction, with PPARG identified as a key transcription factor (TF) regulating this process. Functional analyses demonstrated that PPARG is crucial for maintaining blood-testis barrier (BTB) integrity and promoting spermatogenesis via regulation of fatty acid metabolism. These findings reveal the pivotal role of fatty acid metabolism in NOA and identify PPARG as a potential therapeutic target.

Keywords: Non-obstructive azoospermia; Fatty acid metabolism; Sertoli cell; Multi-omics; Single-cell RNA sequencing

INTRODUCTION

Non-obstructive azoospermia (NOA), the most severe form of male infertility, is characterized as impaired spermatogenesis and the complete absence of sperm in the ejaculate. Affecting 0.4%–2.0% of the male population (Itoh et al., 2001; Jarow et al., 1989; Willott, 1982) and 10%–15% of infertile males (Piechka et al., 2024), NOA arises from a complex interplay of genetic and environmental factors. While considerable research has focused on genetic contributions to NOA (Nagirnaja et al., 2022), the role of metabolic dysfunction (Aaronson et al., 2010), particularly fatty acid metabolism, remains to be fully elucidated.

Emerging evidence suggests a strong association between fatty acid metabolism disorders and male infertility. Fatty acids (FAs) are categorized based on carbon chain length into short-, medium-, and long-chain fatty acids (LCFAs). Long-chain polyunsaturated fatty acids (LCPUFAs), which possess at least one double bond, can be further categorized into omega-6 and omega-3 polyunsaturated fatty acids (ω-6 and ω-3 PUFAs, respectively) (Duan et al., 2023). LCFAs primarily produce adenosine triphosphate (ATP) upon activation to fatty acyl-CoA esters by acyl-CoA synthases (Wu et al., 2022). Beyond energy production, certain LCFAs, such as docosahexaenoic acid (DHA) and arachidonic acid (AA), function as signaling mediators and structural lipids (Jeon et al., 2023). The male reproductive system, including the testes, epididymis, and sperm, possesses a unique fatty acid profile that is vital for spermatogenesis (Gautier & Aurich, 2022). The importance of fatty acid metabolism in male reproduction has been demonstrated in studies using gene knockout models targeting fatty acid synthesis-related pathways (Iizuka-Hishikawa et al., 2017; Komljenovic et al.,

This is an open-access article distributed under the terms of the Creative Commons Attribution Non-Commercial License (http://creativecommons.org/licenses/by-nc/4.0/), which permits unrestricted non-commercial use, distribution, and reproduction in any medium, provided the original work is properly cited.

Copyright ©2025 Editorial Office of Zoological Research, Kunming Institute of Zoology, Chinese Academy of Sciences

Received: 13 October 2024; Accepted: 22 November 2024; Online: 23 November 2024

Foundation items: This work was supported by the National Natural Science Foundation of China (U22A20277, 81971373), Jiangsu Provincial Medical Key Discipline Cultivation Unit (JSDW202215), 333 High-level Personnel Training Project of Jiangsu Province (BRA2019109), and Postgraduate Research & Practice Innovation Program of Jiangsu Province (KYCX22_1826)

#Authors contributed equally to this work

*Corresponding authors, E-mail: majinzhao07@163.com; jingjun36@163.com; yaobing@nju.edu.cn

2009; Shishikura et al., 2019; Stoffel et al., 2008; Zadravec et al., 2011). Recent studies have reported that dysregulated fatty acid metabolism contributes to reproductive dysfunction in NOA. Notably, using metabolomics in seminal plasma, (Jing et al., 2023) found that patients with NOA exhibit reduced ω-3/ω-6 PUFA ratios and decreased DHA and docosapentaenoic acid (DPA) levels compared to patients with obstructive azoospermia (OA). Furthermore, (Zhang et al., 2017) reported that palmitic acid, oleic acid, and gaidic acid are down-regulated in the plasma of NOA patients relative to men with normal spermatogenesis. Conversely, (Ma et al., 2019) determined that glycerol monostearate, glyceryl palmitate, and pelargonic acid are up-regulated in the plasma of NOA patients. Despite these insights, critical gaps remain in our understanding of the role of testicular cell fatty acid metabolism in NOA pathogenesis. Unresolved challenges include the lack of identified causal genes linked to NOA, insufficient exploration of testicular cell heterogeneity in relation to fatty acid metabolism, and the incomplete characterization of transcription factors (TFs) governing fatty acid metabolism-related genes in testicular cells affected by NOA.

Advancements in high-throughput sequencing technologies have significantly impacted the study of NOA in recent years. Bulk RNA sequencing has led to the identification of several NOA-associated genes, including ART3 (Okada et al., 2008), AKAP4 (Malcher et al., 2013), and CYP11A1 (Hodžić et al., 2023). Furthermore, single-cell RNA sequencing (scRNA-seq) has provided a transformative approach for analyzing the cellular heterogeneity of NOA-affected testes. For instance, (Zhao et al., 2020) classified Sertoli cells into three distinct types based on metabolic states, noting that Sertoli cells from NOA patients exhibited reduced glycolytic activity. Similarly, metabolomics has emerged as a powerful tool for identifying noninvasive biomarkers predictive of sperm retrieval success, such as fructose, inhibin B (INHB), and anti-Müllerian hormone (AMH) (Li et al., 2023). Despite these breakthroughs, each technique presents limitations. Bulk RNA-seq fails to capture cellular heterogeneity, scRNA-seq is constrained by limited sample size, and metabolomics faces challenges in uncovering underlying mechanisms (Wagner et al., 2023).

This study integrated multiple high-throughput sequencing datasets, including bulk RNA-seq, scRNA-seq, and metabolomics, sourced from public databases, to investigate disruptions in fatty acid metabolism associated with NOA. Our analysis identified DHA as a potential causal metabolite for NOA. Additionally, decreased expression of *ACSL6*, *ACSBG2*, and *OLAH* in Sertoli cells was linked to impaired fatty acid metabolism and proposed as potential genetic contributors to NOA. Furthermore, PPARG was shown to regulate the expression of fatty acid-related genes, with its inhibition leading to impaired blood-testis barrier (BTB) integrity and defective spermatogenesis. Overall, this study provides novel insights into the role of fatty acid metabolism in testicular cells and highlights PPARG as a potential therapeutic target for NOA.

MATERIALS AND METHODS

Sample collection and ethics approval

Seminal plasma samples from adult males in the control group (CTL, *n*=25) and the NOA group (*n*=21) were collected during routine semen analysis at our clinical laboratory. All samples were confirmed to have normal chromosomal karyotypes and no deletions in the azoospermia factor (AZF) region. Detailed information on these samples has been described in our previous study (Jing et al., 2023).

For immunofluorescence experiments, testicular tissue samples were obtained from three OA and nine NOA patients undergoing micro-dissection testicular sperm extraction (microTESE) or testicular sperm extraction (TESE). Donors were aged between 20 and 44 years and were diagnosed with azoospermia based on the absence of spermatozoa in semen analysis. OA cases (*n*=3) were defined by the presence of motile or mature spermatozoa retrieved through microTESE or TESE procedures. Patients with azoospermia resulting from varicocele, ejaculatory dysfunction, endocrinopathy, or histologically confirmed OA were excluded from the study. NOA cases were defined as hypospermatogenesis (*n*=3), maturation arrest (*n*=3), and Sertoli cell only syndrome (*n*=3) according to the histological patterns of spermatogenesis (Dohle et al., 2012). Individuals with chromosomal abnormalities, AZF region deletions (assessed via spectral karyotyping and RNA extraction and reverse transcription-quantitative polymerase chain reaction (RT-qPCR)), or histological evidence inconsistent with NOA were excluded. Signed informed consent was obtained from all donors, who voluntarily donated testicular tissue for this study. All study protocols and treatments involving humans were approved by the Research Ethics Committee of Jinling Hospital (2015NZKY-017-02).

Animals

Six-week-old C57BL/6 and 20-day-old ICR mice were obtained from Junke Biological Co., Ltd. (China). The mice were housed at 20–26°C under a 12/12-h light/dark cycle with free access to food and water. All experimental procedures involving animals were conducted according to the NIH Guide for the Care and Use of Laboratory Animals and performed with approval from the Ethics Committee of Nanjing Jinling Hospital (2023JLHGZRDWLS-000128). All C57BL/6 mice were randomly divided into two groups: (1) GW9662 group (*n*=6), intraperitoneally injected with 2 mg/kg body weight GW9662 (Selleck, S2915, USA) every two days for 35 days (Zhang et al., 2020); and (2) control group (CTL, *n*=6), intraperitoneally administered the same volume of phosphate-buffered saline (PBS) over the same period.

Sperm parameter testing

Sperm concentration and motility were assessed following previously described protocols (Ge et al., 2022). Briefly, sperm collected from the mouse epididymis was suspended in 0.4 mL of HTF medium (AibeiBio, China) and incubated for 5 min in a 37°C water bath. Sperm parameters were evaluated using a hemocytometer (Qiujing, China) under a light microscope (Olympus, Japan).

Protein extraction and western blot analysis

Tissue and cell samples were lysed in radioimmunoprecipitation assay buffer (Beyotime, P0013B, China) for 30 min at 4°C. Lysates were centrifuged at 12 000 r/min at 4°C for 10 min, and the supernatant was mixed with 5×loading buffer before being boiled at 98°C for 10 min. Protein concentrations were determined using a bicinchoninic acid protein assay kit (P0012, Beyotime, China). For electrophoresis, 10–20 μg of protein was loaded onto a polyacrylamide gel and subsequently transferred to a

polyvinylidene fluoride (PVDF) membrane (Merck Millipore, USA) and blocked with 5% bovine serum albumin (Biofroxx, China) for 1 h. The membranes were then exposed to primary antibodies overnight at 4°C, including β-actin (Cell Signaling Technology, 8H10D10, 1:1 000, USA), PPARG (Proteintech, 16643-1-AP, 1:1 000, China), ZO-1 (Proteintech, 21773-1-AP, 1:5 000, China), and occludin (Proteintech, 13409-1-AP, 1:2 000, China), followed by incubation with anti-rabbit or anti-mouse immunoglobulin G secondary antibodies at room temperature for 1 h. Protein levels were quantified using ImageJ software (v.1.8.0).

Histopathological examinations and immunofluorescent staining

Following euthanasia, testicular and epididymal tissues were fixed in 4% paraformaldehyde (Biohao, China) for 24 h. Tissues were dehydrated through various concentrations of ethanol (70%, 90%, and 100%) and embedded in paraffin. Paraffin blocks were sectioned at 5 μm and rehydrated by immersion in xylene for 30 min, followed by 5 min washes in 100%, 85%, and 75% ethanol. The sections were then stained in hematoxylin and eosin (H&E) solution for analysis. For immunofluorescent staining, tissue sections were first permeabilized with 0.1% (v/v) Tween-20 (Sigma, USA) and blocked with 1% bovine serum albumin at room temperature for 1 h. Sections were incubated overnight at 4°C with primary antibodies, including PPARG (Proteintech, C16643-1-AP, 1:100, China), SOX9 (Merck, ab5535, 1:750, USA), RXRA (Proteintech, 21218-1-AP, 1:100, China), LIN28 (Abcam, ab279647, 1:500, USA), STRA8 (Abcam, ab49602, 1:1 000, USA), SYCP3 (Proteintech, 23024-1-AP, 1:1 000, China), TNP1 (Proteintech, 17178-1-AP, 1:200, China), DDX4 (Abcam, ab13840, 1:1 000, USA), and Hoechst (Invitrogen, H1399, 1:2 000, USA). The sections were subsequently incubated with anti-rabbit immunoglobulin secondary antibodies at room temperature for 1 h and counterstained with 4',6-diamidino-2-phenylindole (DAPI, Solarbio, D8200, 1:1 000, China) for 5 min at room temperature. Finally, the sections were stained with hematoxylin. All images were captured using a confocal microscope (Olympus, Japan). Fluorescence quantification was performed using ImageJ (v.1.8.0). Fluorescence intensities of LIN28+, STRA8+, SYCP3+, TNP1+, DDX4+, and SOX9+ cells were measured in five randomly selected fields per testis cross-section. Analyses were conducted on three sections per group, with each section derived from separate experiments.

C/C score

The C/C score, defined as the ratio of the total number of cells to the lumen circumference, was calculated with reference to previous studies (Deng et al., 2024). Testicular tissues from CTL and GW9662-treated mice (n=6) were stained with DAPI (Solarbio, D8200, 1:1 000, China). The total number of DAPI-positive cells and the perimeter of the seminiferous tubules were measured using ImageJ (v.1.8.0) and the C/C score was derived as the ratio of these two values. For quantification, three independent experiments were conducted for each group. A total of 15 complete seminiferous tubules were analyzed across at least three sections per group.

Isolation and purity assessment of primary mouse Sertoli cells

Primary Sertoli cells were isolated from the testes from 20-day-old ICR mice, as described previously (Mruk & Cheng, 2011). The testes from five mice were decapsulated and enzymatically digested with 0.25% trypsin (Millipore Sigma, USA) and centrifuged at 100 r/min for 5 min at 37 °C. After removing the supernatant, the remaining tissue was washed with PBS. The seminiferous tubules were then incubated with 0.5 mg/mL collagenase type I (Millipore Sigma, USA) and centrifuged at 200 r/min for 6 min at 37°C to obtain primary Sertoli cells. The primary Sertoli cells were cultured in Dulbecco's Modified Eagle Medium/Nutrient Mixture F-12 (DMEM/ F12, Thermo Fisher Scientific, USA) with 1% penicillin-streptomycin (Life Technologies, USA) and 10% fetal bovine serum (Gibco, USA) for subsequent experiments. After one week of culture, the purity of the Sertoli cells was assessed via immunofluorescent co-staining with SOX9 and Hoechst (Invitrogen, H1399, 1:2 000, USA). Co-localization of SOX9 with DAPI indicated the presence of Sertoli cells. The percentage of SOX9-positive cells among DAPI-stained nuclei reached 93.4%.

Transfection of small interfering RNA (siRNA)

Both siRNAs targeting *PPARG* and a non-specific siRNA (negative control, NC) were designed and synthesized by GenePharma (China). Primary Sertoli cells were transfected with siRNAs using Lipofectamine 3000 reagent (Thermo Fisher Scientific, USA) according to the manufacturer's instructions.

CCK-8 cell viability analysis

After interfering with PPARG expression in primary Sertoli cells for 24 h, the cells were seeded in 96-well plates at a density of 5×10^3 cells/well. Cell viabilities were then analyzed using the Cell Counting Kit-8 (Beyotime, China).

Transepithelial resistance (TER) measurements

After interfering with PPARG expression in primary Sertoli cells for 24 h, the cells were plated on Millicell Hanging Cell Culture Inserts (PET 0.4 μm, Merck Millipore, USA) at a density of 0.5×10^6 cells/cm^2 and cultured for 7 days to allow cell barrier formation. Each day, TER was monitored using a Millicell Electrical Resistance System (Merck Millipore, USA).

RT-qPCR

Total RNA was extracted from primary Sertoli cells using a Total RNA Isolation Kit (BEI-BEI Biotech, China). Subsequently, cDNA synthesis was performed using PrimeScript® RT Master Mix (TaKaRa, Japan), with the resulting cDNA used for qPCR using the Roche Light Cycler 96 real-time PCR system (Roche Diagnostics, Switzerland) and SYBR Green Premix Pro Taq HS qPCR Tracking Kit (Accurate Biotechnology Company, AG11733, China). Relative gene expression was calculated using the ΔΔCt method, with β-actin serving as the internal control.

Metabolic data analysis

Metabolic data from 25 CTL and 21 NOA seminal plasma samples were obtained from our previous study (Jing et al., 2023). The data were analyzed using MetaboAnalyst (v.6.0) (https://www.metaboanalyst.ca). Statistical analysis was performed to generate a partial least squares discriminant analysis (PLS-DA) plot with default settings. Key pathogenic metabolites were identified using the Support Vector Machine (SVM) in the Biomarker Analysis module. Receiver operating characteristic (ROC) curves were generated based on cross-validation (CV) performance, and Model 2 (Features 10) was selected as the optimal SVM model. Functional enrichment

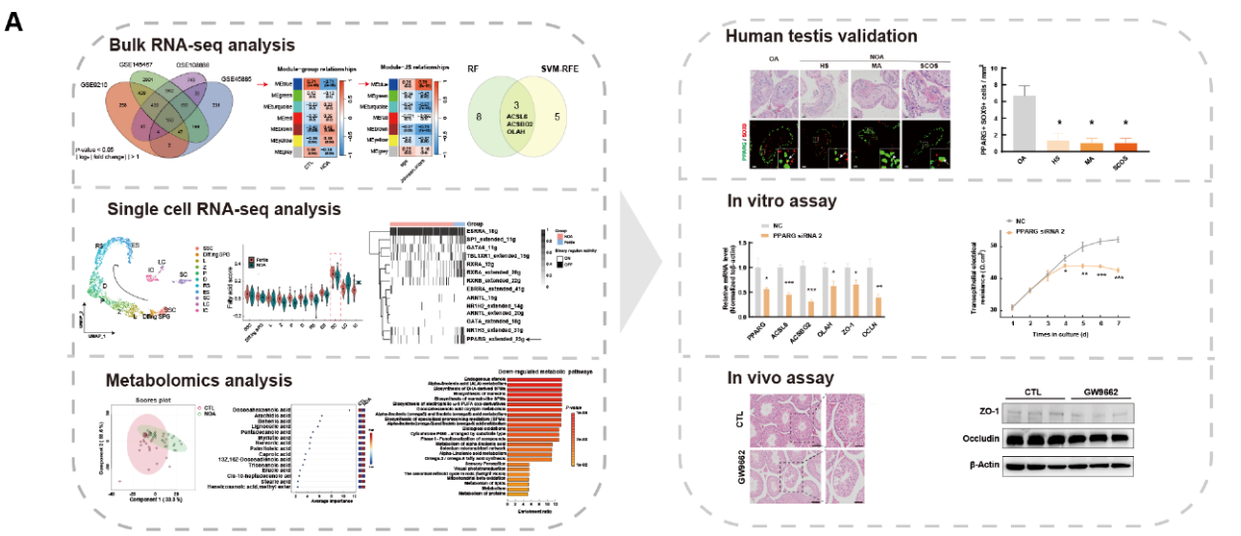
analysis of metabolic pathways was performed using the RaMP database (https://rampdb.nih.gov/).

Transcriptomic data collection and preparation

Transcriptomic datasets were sourced from the Gene Expression Omnibus (GEO) database, including microarray data (GSE45885, GSE9210, GSE108886, and GSE145467) and scRNA-seq data (GSE157421 (Wang et al., 2021) and GSE106487 (Wang et al., 2018)). Detailed information regarding these datasets is presented in Figure 1B. For microarray data preparation, the "GEOquery" R package (v.2.66.0) was used to retrieve raw microarray data and assign gene and group information. For scRNA-seq data, standard procedures and default parameters were followed, as outlined in the Seurat documentation (https://satijalab.org/seurat/articles/get_started.html). Analysis was performed using the Seurat R package (v.4.3.0), which involved reading the raw matrix, filtering out low-quality cells (maximum mitochondrial RNA content of 10% and minimum feature count of 200), conducting principal component analysis (PCA) with 20 principal components (PCs), identifying 2 000 highly variable genes, and removing batch effects using canonical correlation analysis (CCA) with 20 dimensions. Finally, dimensionality reduction was performed using uniform manifold approximation and projection (UMAP). Cell type identification was then carried out using known markers.

Differentially expressed gene (DEG) analysis

The R package "limma" (v.3.54.2) was used to identify DEGs between the CTL and NOA groups from the microarray data. Significant DEGs between groups were identified using the criteria $|\log_2(\text{fold change})|>1$ and $P<0.05$. The R packages "ggplot2" (v.3.5.0) and "pheatmap" (v.1.0.12) were used to construct volcano and Venn plots.



B

1. Bulk RNA sequencing data

GEO ID	Group	
	Control (n=27)	Non-obstructive azoospermia (n=92)
GSE45885	3	27
GSE9210	10	47
GSE108886	4	8
GSE145467	10	10

2. Single-cell RNA sequencing data

GEO ID	Group	
	Fertile (n=9)	Non-obstructive azoospermia (n=2)
GSE157421		1
GSE106487	9	1

3. Metabolomics data

ScienceDB DOI	Group	
	Control	Non-obstructive azoospermia
10.57760/sciencedb.17029	25	21

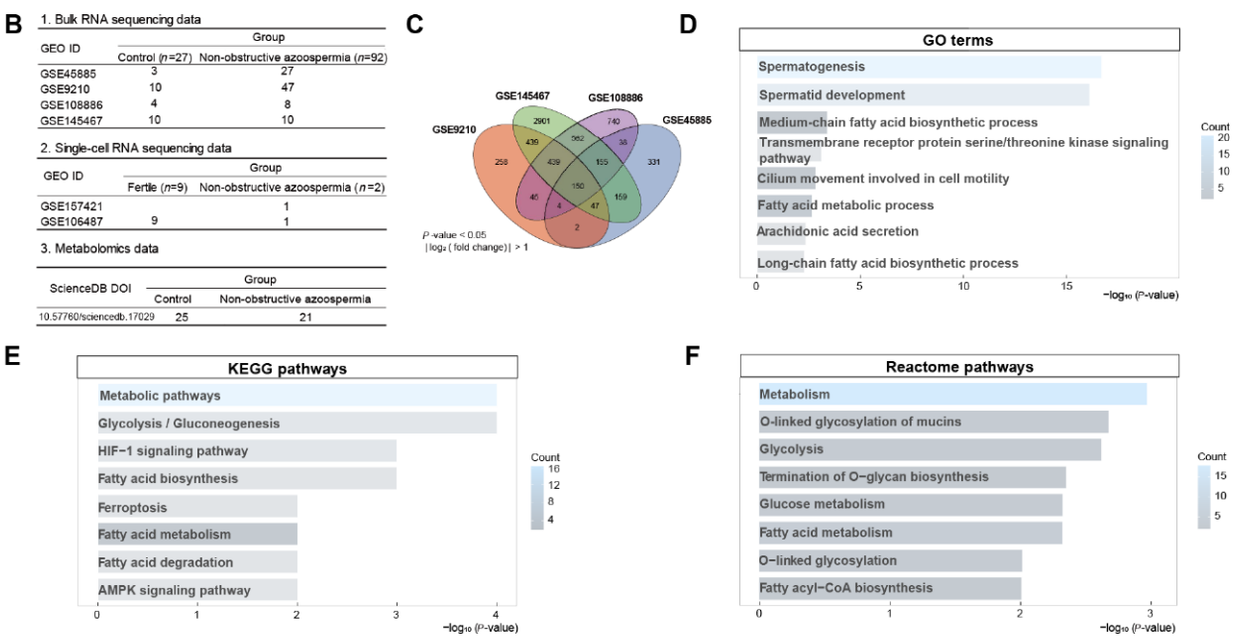


Figure 1 Differentially expressed genes (DEGs) and functional enrichment analysis of NOA testicular microarray data

A: Schematic representation of the study design. Various data types and key findings were integrated to establish a network linking fatty acid metabolism and spermatogenesis in NOA. B: Summary of datasets utilized in this study. C: Venn diagram showing intersecting DEGs identified across GSE9210, GSE145467, GSE108886, and GSE45885 datasets. D–F: Bar chart showing eight representative functional enrichment terms derived from 150 intersecting DEGs based on GO, KEGG, and Reactome analyses. Line at bottom represents -$\log_{10}$(P-value), while blue bars represent terms with a higher gene count and white bars represent those with a lower count.

Functional enrichment analysis

Functional enrichment analysis was conducted using KOBAS(http://bioinfo.org/kobas) based on the Gene Ontology (GO), Kyoto Encyclopedia of Genes and Genomes (KEGG), and Reactome databases. A threshold of $P<0.05$ was applied for significant enrichment in all analyses.

Weighted gene co-expression network analysis (WGCNA)

The R package “WGCNA” (v.1.72-5) was used to identify key gene modules associated with fatty acid metabolism. A total of 210 fatty acid metabolism-related genes were input into R (v.4.2.2) for comparative analysis between the CTL and NOA groups. Hierarchical clustering was performed using the “plotDendroAndColors” function of WGCNA (β=16), resulting in the identification of seven modules. To determine the module most closely associated with NOA phenotypes and Johnsen scores, the “Bicor” function was applied. The MEblue module, comprising 30 genes, was identified as the most relevant gene set for these parameters.

Identification of key candidate NOA pathogenic genes

To identify potential causal genes for NOA, random forest (RF) (Rigatti, 2017) and support vector machine recursive feature elimination (SVM-RFE) (Sanz et al., 2018) were applied.

Based on GSE45885 data, 30 genes were first input into R and an RF model was constructed using the “glm” function in R with default settings. The RF model was implemented in the randomForest package with the following parameters: ntree=500, mtry=4, importance=True. Genes were then filtered and sorted based on their importance, yielding the top 15 genes. The same 30 genes were further analyzed using the SVM-RFE model, implemented via “e1071” in R (v.1.7-14). Ten-fold cross-validation errors were calculated, and genes were sorted using MeanDecreaseGini. The top eight gene candidates identified by SVM-RFE were selected as key candidates. By overlapping the results of the RF and SVM-RFE analyses, *ACSL6*, *ACSBG2*, and *OLAH* were identified as key genes. For area under the curve (AUC) calculations, R package “pROC” (v.1.15.0) was used. Six combinations of *ACSL6*, *ACSBG2*, and *OLAH* were generated, and AUC values were calculated using the “roc” function of pROC. The R package “ggplot2” (v.3.5.0) was used to construct the bar plot.

Fatty acid metabolism score analysis

Preparation of scRNA-seq data followed previously described methods. A total of 210 fatty acid-related genes were identified from the GO and KEGG databases using the keyword ‘fatty acid’. These genes were scored based on scRNA-seq data using the AddModuleScore function in the R package “Seurat” and loaded into the meta.data of the Seurat file. The scoring involved calculating the average expression levels of fatty acid-related genes at the single-cell level, adjusted by subtracting the aggregated expression of control feature sets. All analyzed features were binned based on their average expression, and control features were randomly selected from each bin. A violin plot visualizing the fatty acid metabolism scores was generated using the "VlnPlot" function in Seurat.

Transcription factor prediction

After integrating scRNA-seq data from fertile and NOA samples into Seurat, the Sertoli cells cluster was isolated for further analysis. Standard scRNA-seq data processing was applied, and batch effects were removed (ndim=20) via CCA. To predict TFs potentially regulating Sertoli cells, the R package “SCENIC” (v1.2.4) (Aibar et al., 2017) was employed. Regulatory networks were constructed using the GENIE3 algorithm, while gene regulators and motifs were identified using the RcisTarget package. TF activity was assessed for the fertile and NOA groups, resulting in the identification of 10 TFs. All procedures were run with default settings. Additionally, TFs associated with *ACSL6*, *ACSBG2*, and *OLAH* were predicted using the Gene Transcription Regulation Database (GTRD) (Kolmykov et al., 2021). The intersection of TFs identified across the different databases was then determined.

Statistical analysis

All statistical analyses were conducted using R (v.4.2.2) or GraphPad Prism software (v.8.0.1). The assessment of statistical significance was performed using Student’s *t*-test or Wilcoxon test for comparisons between two groups. Analysis of variance (ANOVA) was used to determine significance among three or more groups. Correlation coefficients were computed using Pearson's correlation. Data are shown as mean±standard error of the mean (SEM), unless otherwise specified. Associated *P*-values are indicated as follows: ns: Not significant; *: $P<0.05$; **: $P<0.01$; ***: $P<0.001$.

RESULTS

Disorders of fatty acid metabolism occur in NOA testes

The schematic workflow of the study is presented in Figure 1A. To characterize the homogeneity of testicular changes between CTL and NOA patients, four microarray datasets from the GEO database were separately analyzed (Figure 1B; Supplementary Figure S1A–D). Differential gene expression analysis, applying a threshold of $|\log_2(\text{fold change})|>1$ and $P<0.05$, identified 150 DEGs (Figure 1C). These genes were subjected to functional enrichment analysis using KOBAS (http://bioinfo.org/kobas/download/) (Bu et al., 2021). Results from the GO, KEGG, and Reactome databases consistently highlighted significant functional terms related to fatty acid metabolism, including “medium-chain fatty acid biosynthetic process”, “fatty acid metabolic process”, and “long-chain fatty acid biosynthetic process” (Figure 1D, F). These findings indicate that fatty acid metabolism undergoes substantial dysregulation in the testes of NOA patients.

Fatty acid metabolism in the seminal plasma of NOA patients

To further explore the metabolomic alterations associated with NOA, metabolomics data from seminal plasma samples of 25 CTL and 21 NOA participants were reanalyzed. PLS-DA revealed a clear separation between CTL and NOA groups based on their fatty acid metabolite profiles (Figure 2A). Key metabolites contributing to this distinction were identified using SVM algorithms (Pang et al., 2022), enabling precise identification of valuable metabolites. Notably, DHA emerged as the metabolite with the highest average importance, showing significant down-regulation in the NOA group. Arachidonic acid (AA) and behenic acid (BA) were the second and third most important metabolites, respectively, and both were similarly down-regulated in the NOA group (Figure 2B, C). Functional enrichment analysis revealed distinct metabolic pathway alterations. Up-regulated pathways were primarily enriched in “linoleic acid (LA) metabolism” and “cellular responses to stress”, while down-regulated pathways were

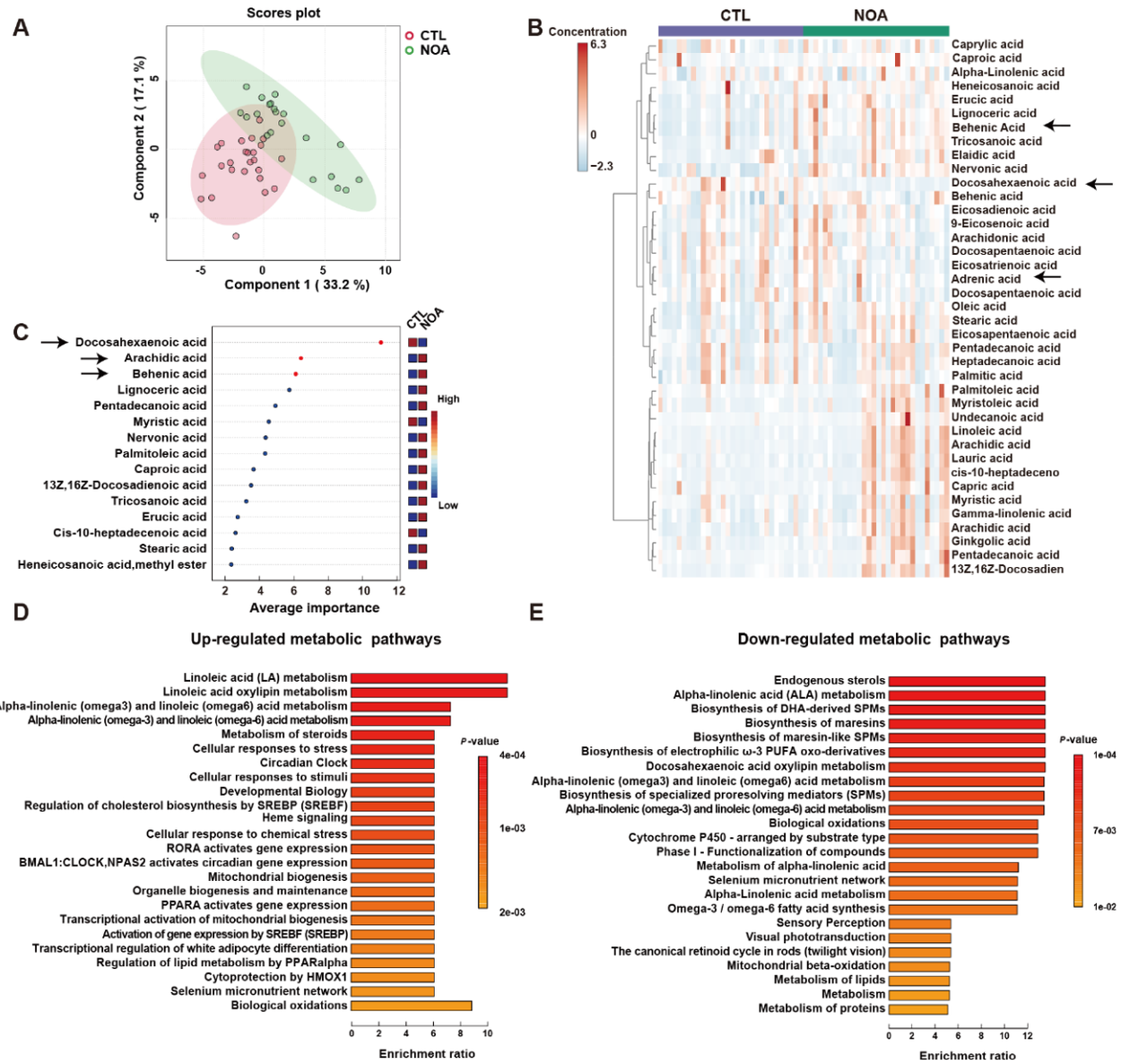


Figure 2 Metabolomic analysis of NOA semen

A: Partial least squares discriminant analysis (PLS-DA) illustrating the clustering of semen metabolomic data between CTL (control, *n*=25) and NOA (*n*=21) samples. B: Heatmap showing concentration of seminal metabolites in CTL and NOA groups. C: Plot showing top 15 key metabolites identified through support vector machine (SVM) analysis, with higher average importance indicating greater predictive power for NOA. D, E: Bar chart showing top 24 up-regulated and down-regulated metabolic pathways in the NOA group.

primarily enriched in PUFA-related metabolism, such as "alpha-linolenic acid (ALA) metabolism" and "biosynthesis of DHA-derived SPMs" (Figure 2D, E). These findings demonstrate significant differences in the fatty acid profiles of seminal plasma between the CTL and NOA groups. Notably, DHA, AA, and BA were identified as potential lipid biomarkers for the diagnosis of NOA.

Distinct gene modules associated with fatty acid metabolism in NOA

To characterize the fatty acid metabolism gene modules involved in spermatogenesis and the pathogenesis of NOA, WGCNA was applied to 210 fatty acid metabolism-related genes from the GSE44885 dataset. Hierarchical clustering of samples effectively distinguished between the CTL and NOA groups (Figure 3A), suggesting significant heterogeneity in fatty acid metabolism gene expression profiles between these two groups. Additionally, gene module clustering identified seven distinct gene modules associated with fatty acid metabolism (Figure 3B). Among these, the MEblue module exhibited a strong negative correlation with NOA (Figure 3C) and a positive correlation with Johnsen scores (Figure 3D). Functional enrichment analysis of the 30 genes within the MEblue module revealed involvement in "fatty acid metabolism", "PPAR signaling pathways", and "adipocytokine signaling pathways" (Figure 3E). These results suggest that the MEblue module may represent a key gene set associated with fatty acid metabolism and the pathogenesis of NOA.

Identification of candidate NOA pathogenic genes

To identify critical genes involved in fatty acid metabolism in the testes of NOA patients, two machine learning algorithms were applied to the expression matrix of GSE44885, focusing on genes from the MEblue module. An RF classifier was constructed with the parameters: mtry=5 and ntree=500, achieving an out-of-bag (OOB) error rate of 0.164 (Figure 4A,

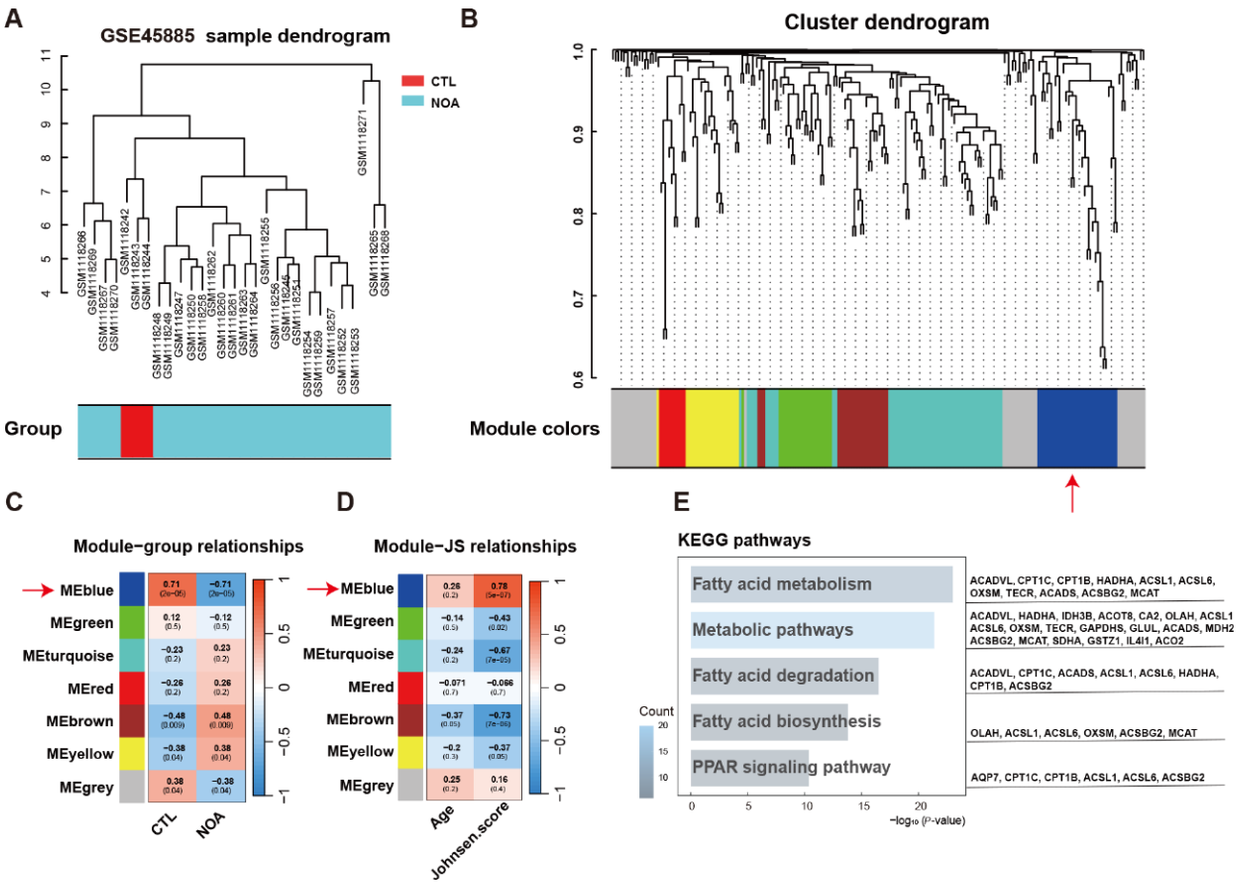


Figure 3 Identification of fatty acid metabolism gene modules in NOA

A: Hierarchical clustering dendrograms of control (CTL) and NOA groups based on 210 fatty acid metabolism-related genes. Red bar represents CTL (*n*=3) and blue bar represents NOA (*n*=27). B: Module clustering of 210 fatty acid metabolism-related genes between CTL and NOA groups. Different colors represent different gene modules, with gray representing unclassified genes. C, D: Heatmaps showing Pearson correlation analysis of gene modules with clinical phenotypes and disease classification in CTL and NOA groups. Right red bars represent high Pearson correlation coefficients, while blue bars indicate low correlations. E: Bar chart showing functional enrichment analysis of 30 genes from the MEblue module in Figure 3B.

B). Genes with a MeanDecreaseGini below 0.5 were excluded, resulting in the identification of eight key genes according to their importance (Figure 4A). As applied in previous research (Sanz et al., 2018), the SVM-RFE model was established to identify key genes with the following parameters: method="CV", repeats="5", nfolds=10 (Figure 4B). By overlapping the genes identified through RF and SVM-RFE, *ACSL6*, *ACSBG2*, and *OLAH* were identified as potential fatty acid-related pathogenic genes (Figure 4C). The AUC values of the key genes in the GSE45885 dataset were calculated, revealing high diagnostic performance for all three genes (AUC>0.8). Notably, when the three genes (*ACSL6*, *ACSBG2*, and *OLAH*) were combined, their predictive ability reached the highest AUC value of 0.9537 (Figure 4D). Additionally, gene expression analysis across multiple datasets (GSE45885, GSE9210, GSE108886, and GSE145467) showed that *ACSL6*, *ACSBG2*, and *OLAH* were significantly down-regulated in the NOA group compared to the CTL group (Figure 4E, H). These results suggest that *ACSL6*, *ACSBGC2*, and *OLAH* are potential pathogenic genes contributing to fatty acid metabolism disorders in the testes of NOA patients.

Fatty acid metabolism patterns in Sertoli cells in NOA

While the microarray data provided insights into gene expression at the whole-tissue level, it failed to capture the cellular heterogeneity in fatty acid metabolism between fertile and NOA testicular cells. Therefore, the GSE157421 and GSE106487 scRNA-seq datasets were integrated for further analysis (Wang et al., 2018; Wang et al., 2021). After quality control, normalization, and removal of batch effects, 3 472 cells from the CTL and fertile groups were obtained. Using established markers, 11 cell types were identified, including spermatogonial stem cells (SSCs), differentiating spermatogonia (Diff. SPG), leptotene cells (L), zygotene cells (Z), pachytene cells (P), diplotene cells (D), round spermatids (RSs), elongated spermatids (ESs), Sertoli cells (SCs), Leydig cells (LCs), and immune cells (ICs) (Figure 5A, B). Fatty acid scores were calculated to compare the degree of active fatty acid metabolism in the different cell types. Across multiple testicular cell types, fatty acid scores were reduced in NOA samples compared to fertile controls, including SSCs, Diff. SP, L, Z, P, D, RS, ES, SCs, LCs, and ICs. Specifically, Sertoli cells exhibited the highest fatty acid scores among all cell types, highlighting active fatty acid metabolism. However, in NOA samples, fatty acid scores in Sertoli cells were markedly reduced, indicating a profound disruption in their fatty acid metabolic processes (Figure 5C). To understand the functional changes in Sertoli cells, GO enrichment analysis was performed on DEGs between the fertile and NOA groups. Consistent with previous research (Alfano et al., 2021), our

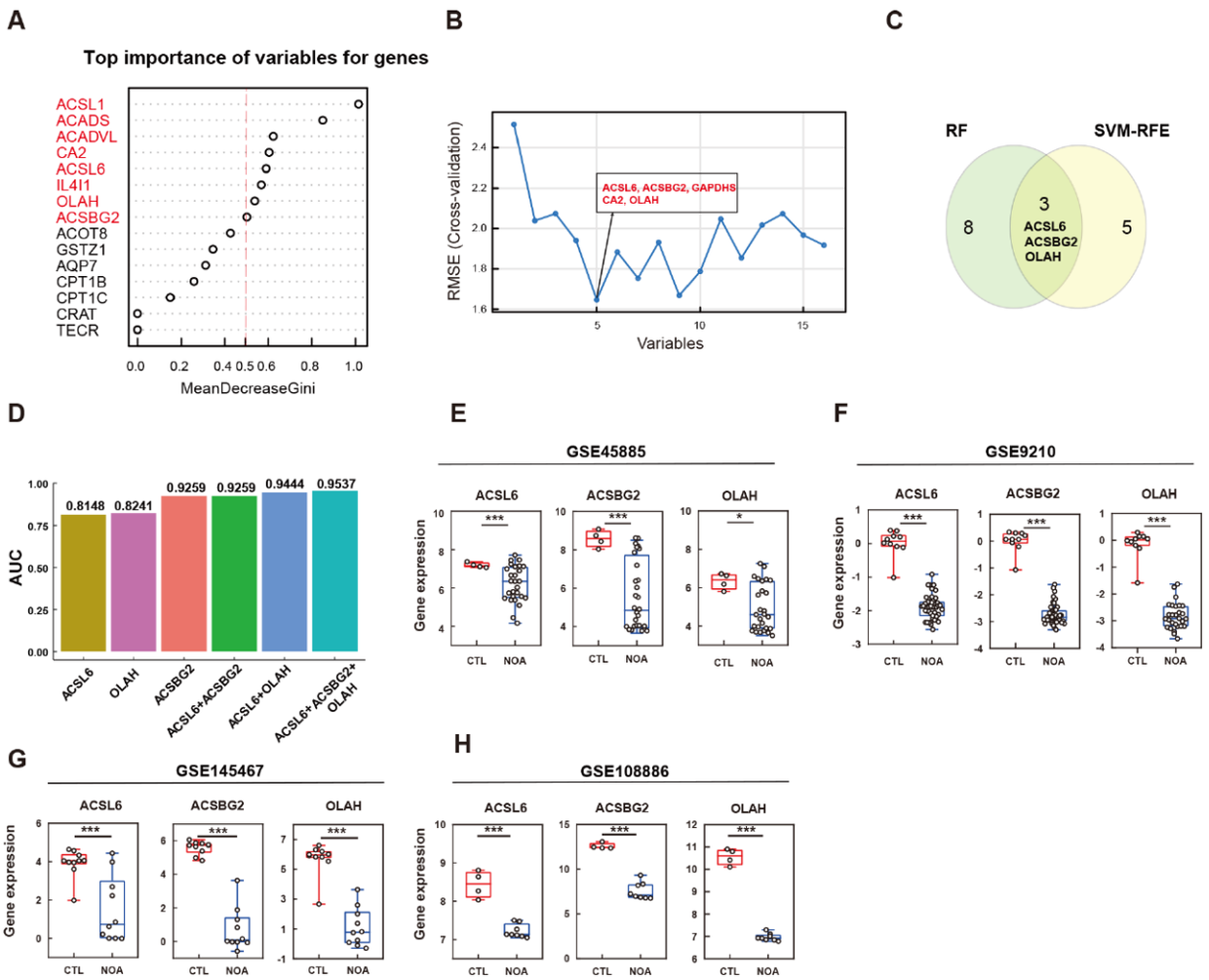


Figure 4 Identification of *ACSL6*, *ACSBG2*, and *OLAH* as key candidate causal genes for NOA

A: Top 15 fatty acid metabolism-related genes identified using the Gini coefficient method based on a random forest (RF) classifier. A higher Gini coefficient represents greater predictive power for NOA. B: Five key genes were selected using the support vector machines-recursive feature elimination (SVM-RFE) with ten-fold cross-validation. C: Venn diagram showing overlap of RF- and SVM-RFE-selected genes. D: Bar chart showing different combinations of key genes sorted by their area under the curve (AUC) values. AUC closer to 1 represents a higher probability diagnosis for NOA. E–H: Expression levels of *ACSL6*, *ACSBG2*, and *OLAH* between CTL and NOA groups in GSE45885, GSE9210, GSE145467, and GSE108886 datasets. Data are presented as mean±SEM. Student's *t*-test was used to calculate *P* values. ns: Not significant; *: $P<0.05$; ***: $P<0.001$.

results showed significant enrichment in inflammation-related pathways, such as the "interleukin-1-mediated signaling pathway", "apoptotic process", "NIK/NF-kappa B signaling", and "response to oxidative stress", underscoring the inflammatory and oxidative stress status of NOA Sertoli cells. In contrast, significantly down-regulated DEGs were enriched in terms such as "spermatogenesis", "ATP binding", "cell-cell adhesion", and "cell-cell junction", suggesting potential impairment of the BTB in NOA testes (Figure 5D). Further analysis revealed that the mRNA expression of genes involved in PUFA synthesis, such as DEGS1, ELOVL2, ELOVL5, ELOVL6, FADS1, FADS2, LPL, and SCD, was downregulated in NOA Sertoli cells (Figure 5E). Similarly, genes related to PUFA activation, such as *ACSL1*, *ACSL3*, *ACSL4*, *ACSL5*, *ACSL6*, and *ACSBG2*, also showed decreased expression (Figure 5F). Overall, Sertoli cells in NOA exhibit significant disruptions in fatty acid metabolism, characterized by impaired synthesis and activation of PUFAs, dysfunction in cellular connections, and reduced energy production. These findings highlight the critical role of Sertoli cell metabolic dysfunction in the pathogenesis of NOA.

PPARG as a potential regulator of fatty acid metabolism

TFs play a pivotal role in modulating gene expression by binding to specific DNA motifs, thereby activating or repressing target genes (Lambert et al., 2018). To identify key TFs involved in fatty acid metabolism dysregulation in Sertoli cells of NOA patients, the computational framework SCENIC (Single-Cell Regulatory Network Inference and Clustering) was applied. SCENIC simultaneously reconstructs gene regulatory networks and identifies cell states using scRNA-seq data (Aibar et al., 2017). Analysis revealed that Sertoli cells in NOA exhibited altered regulon activity compared to the controls. In the CTL group, TFs such as SP1, GATA6, TBL1, XR1, RXRA, RXRB, NRNTL1, and PPARG were identified as regulators. However, their regulon activity in NOA Sertoli cells was markedly diminished (Figure 6A). To refine the identification of TFs specifically regulating *ACSL6*, *ACSBG2*, and *OLAH*, the GTRD was used to predict TFs. By integrating TF predictions from multiple sources, PPARG emerged as the key transcription factor (Figure 6B). The predicted schematic

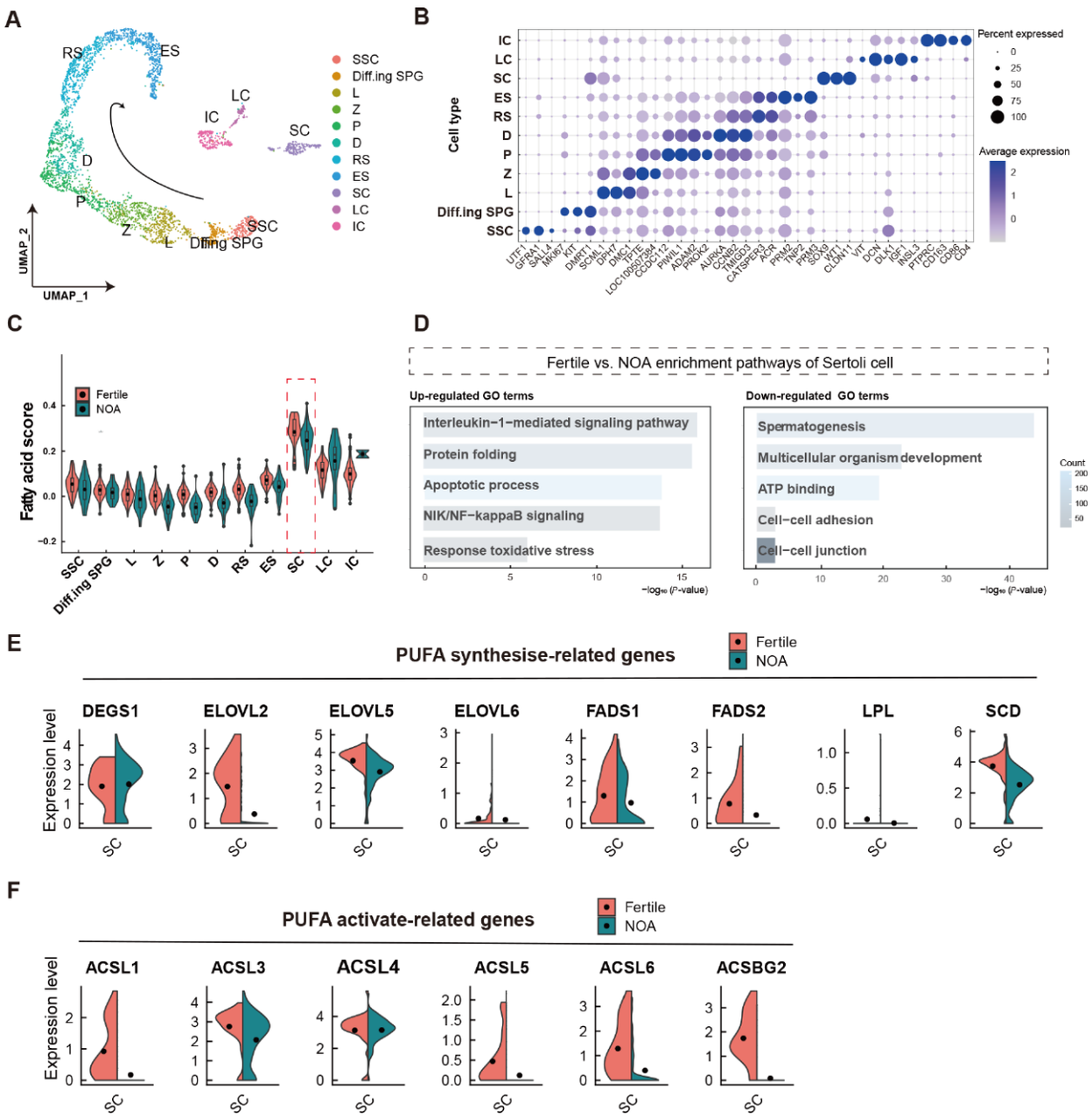


Figure 5 ScRNA-seq analysis of fatty acid metabolism and gene expression patterns in Sertoli cells between fertile and NOA patients

A: UMAP plot showing integration of scRNA-seq data with GSE157421 and GSE106487. B: Dot plot showing expression patterns of selected markers in spermatogonial stem cells (SSC), differentiating spermatogonia (Diff. SPG), leptotene cells (L), zygotene cells (Z), pachytene cells (P), diplotene cells (D), round spermatids (RS), elongated spermatids (ES), Sertoli cells (SC), Leydig cells (LC), and immune cells (IC). Blue dots represent high average gene expression, white dots represent low average gene expression. Larger dots represent a higher percentage of cells expressing the marker. C: Violin plots showing fatty acid score between fertile and NOA groups. Dot in the middle of each violin plot represents average expression of one gene. D: Bar chart showing top five GO terms in up-regulated and down-regulated Sertoli DEGs between fertile and NOA groups. Line on the bottom represents –$\log_{10}$(*P*-value). E, F: Violin plot showing expression of fatty acid synthesis-related genes and fatty acid activation-related genes in Sertoli cells between fertile and NOA groups. Black dots represent mean expression levels.

motif diagram generated via SCENIC is shown in Figure 6C. Functionally, PPARG translocates to the nucleus to regulate gene expression (Yu et al., 2024). Immunofluorescence analysis showed reduced nuclear expression of PPARG in NOA Sertoli cells (PPARG+ SOX9+ cells) compared to those in OA patients (Figure 6D, E). Consistent with this, scRNA-seq data revealed significantly lower expression levels of the PPARG gene in NOA Sertoli cells (Figure 6F). These findings suggest that PPARG plays a crucial role in regulating fatty acid metabolism-related genes in Sertoli cells and that its activity is inhibited in NOA.

Inhibition of PPARG impairs cell-cell junction and barrier function in Sertoli cells

To further explore the functional role of PPARG in Sertoli cells, primary mouse Sertoli cells were extracted and cultured, achieving a purity of 93.4% (Figure 7A, B). Among three siRNA duplexes targeting PPARG siRNA 2 demonstrated the most effective silencing at both the mRNA and protein levels (Figure 7C, D) and was selected for subsequent experiments.

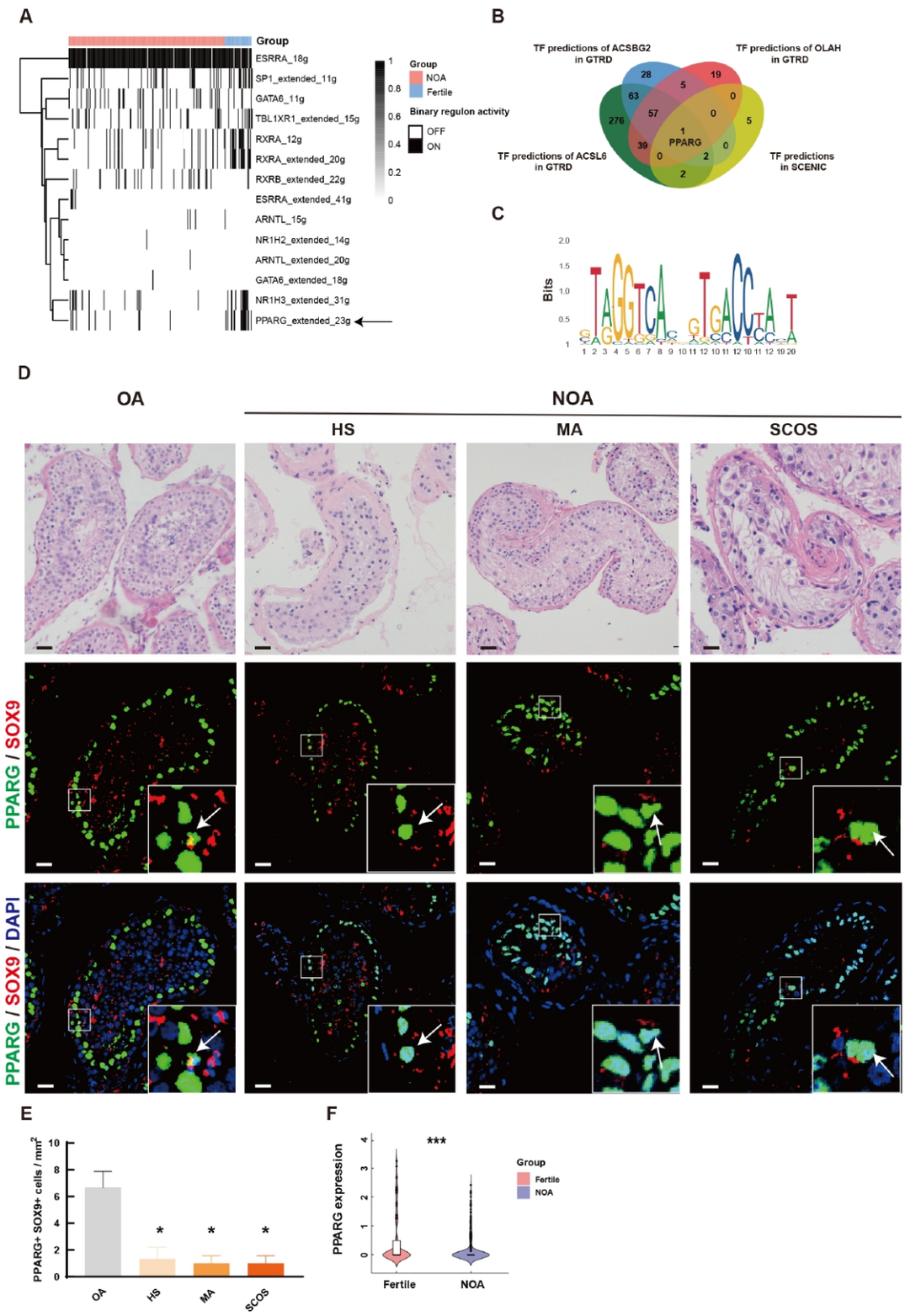


Figure 6 Identification of potential transcription factors (TFs) regulating key genes

A: Heatmap of active regulons in Sertoli cells constructed using SCENIC analysis. Binary activity scores are shown, with white indicating "OFF/active" and black indicating "ON/inactive". B: Venn diagram showing overlap of TF predictions for *ACSL6*, *ACSBG2*, and *OLAH* based on Gene Transcription Regulation Database (GTRD) and SCENIC predictions. C: Schematic representation of predicted PPARG binding motifs generated through SCENIC analysis. Larger bases indicate higher predicted binding likelihood. D: H&E and immunofluorescence staining of PPARG (red) and SOX9 (green) in testicular tissue from patients with obstructive azoospermia (OA, n=3), hypospermatogenesis (HS, n=3), maturation arrest (MA, n=3), and Sertoli cell-only syndrome (SCOS, n=3) subtypes of NOA. Arrows indicate positive staining. Scale bar: 20 μm. E: Boxplot showing cell count of co-positive signaling of PPARG and SOX9 in Figure 6D. Data are expressed as mean±SEM. Student's t-test was used to calculate P values of HS, MA, and SCOS groups in comparison to OA group. ns: Not significant; *: P<0.05. F: Violin plot showing PPARG expression in Sertoli cells between fertile and NOA groups based on scRNA-seq data. Wilcoxon test was used to calculate P values, ***: P<0.001.

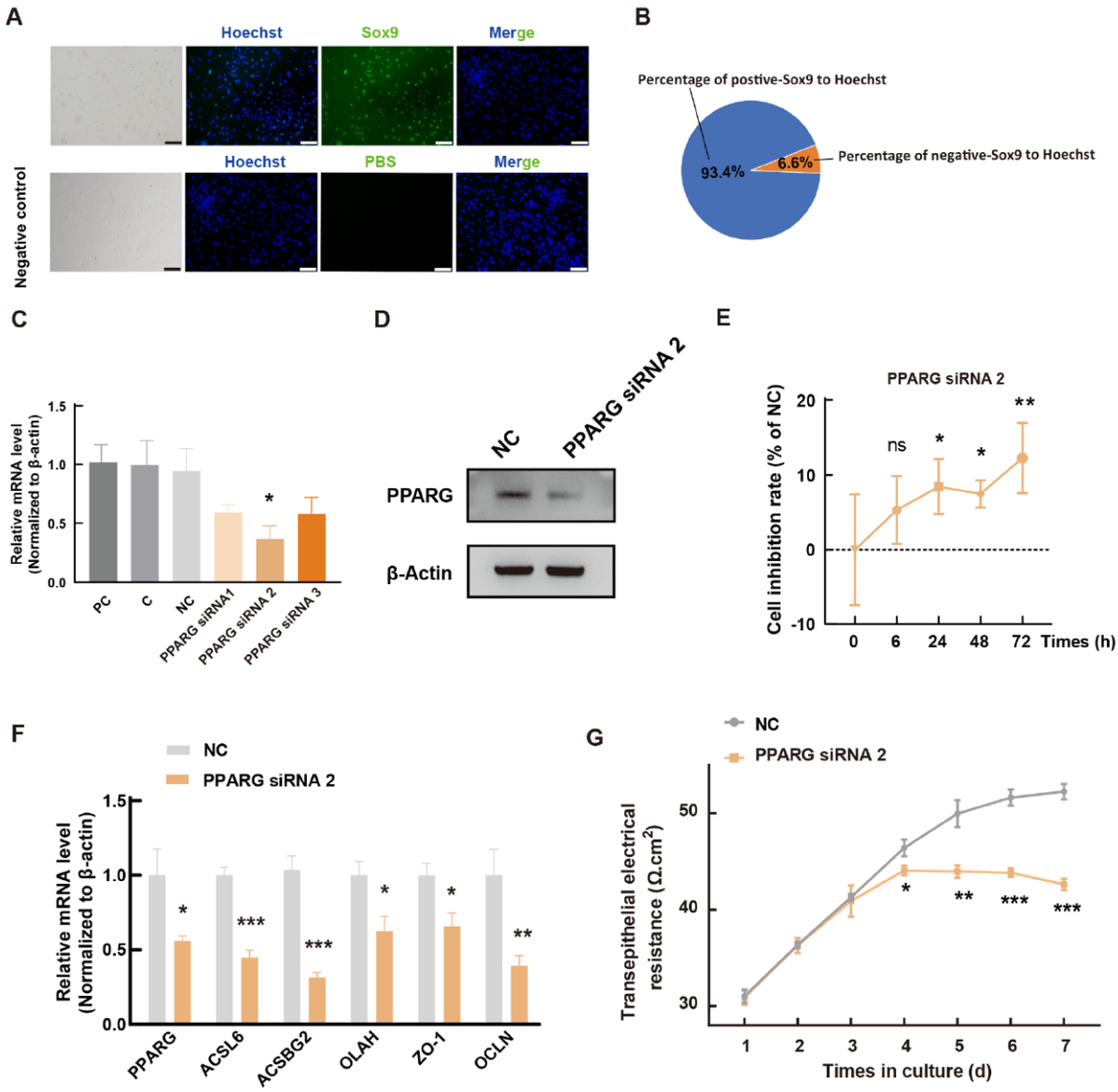


Figure 7 Reduced PPARG expression impairs Sertoli cell function

A: Immunofluorescence staining of SOX9 or PBS (negative control) in mouse primary Sertoli cells cultured for one week. Co-localization of SOX9 and Hoechst cells confirmed identity of Sertoli cells. Scale bars: 50 μm. B: Pie plot showing purity of primary Sertoli cells (93.4%), with other cells reaching 6.6%. C, D: Primary Sertoli cells were transfected with PPARG siRNA 1, PPARG siRNA 2, PPARG siRNA 3, scrambled siRNA (negative control, NC), or with blank control for 24 h. mRNA expression of *PPARG* was detected by RT-qPCR and western blotting. E: CCK8 assay evaluating Sertoli cell viability at 0 h, 6 h, 24 h, 48 h, and 72 h after PPARG knockdown. F: Gene expression levels of *PPARG*, *ACSL6*, *ACSBG2*, and *OLAH* after PPARG knockdown. G: Transepithelial electrical resistance (TER) detection of primary Sertoli cell barriers. Data are expressed as mean±SEM. Student's *t*-test was used to calculate *P* values. ns: Not significant; *: $P<0.05$; **: $P<0.01$; ***: $P<0.001$.

Knockdown of *PPARG* impaired cell viability after 24 h (Figure 7E). The expression levels of fatty acid metabolism-related genes *PPARG*, *ACSL6*, *ACSBG2*, and *OLAH* were markedly down-regulated following *PPARG* inhibition (Figure 7C), confirming the regulatory role of PPARG in activating these genes. In addition to its impact on fatty acid metabolism, *PPARG* inhibition disrupted cell-cell junctions, significantly reducing the mRNA levels of tight junction markers ZO-1 and occludin (Figure 7F). To evaluate the functional integrity of the Sertoli cell barrier, transepithelial/transendothelial resistance (TER) was measured after 4 days of *PPARG* knockdown. Sertoli cells typically form a stable cell barrier after 3 days of culture (Ge et al., 2022). However, *PPARG* inhibition caused a significant decline in TER, indicating compromised cell barrier function (Figure 7G). These findings demonstrate that PPARG plays a crucial role in maintaining Sertoli cell viability, regulating fatty acid metabolism-related genes, and preserving cell-cell junction integrity. Its inhibition induces profound disruptions in fatty acid gene expression, reduces cell viability, and impairs the structural and functional integrity of the Sertoli cell barrier.

Inhibition of PPARG impairs the BTB and disrupts spermatogenesis

To explore the role of PPARG in spermatogenesis, GW9662, a selective PPARG inhibitor, was administered to mice for 35 days (Figure 8A). Histological analysis revealed a marked

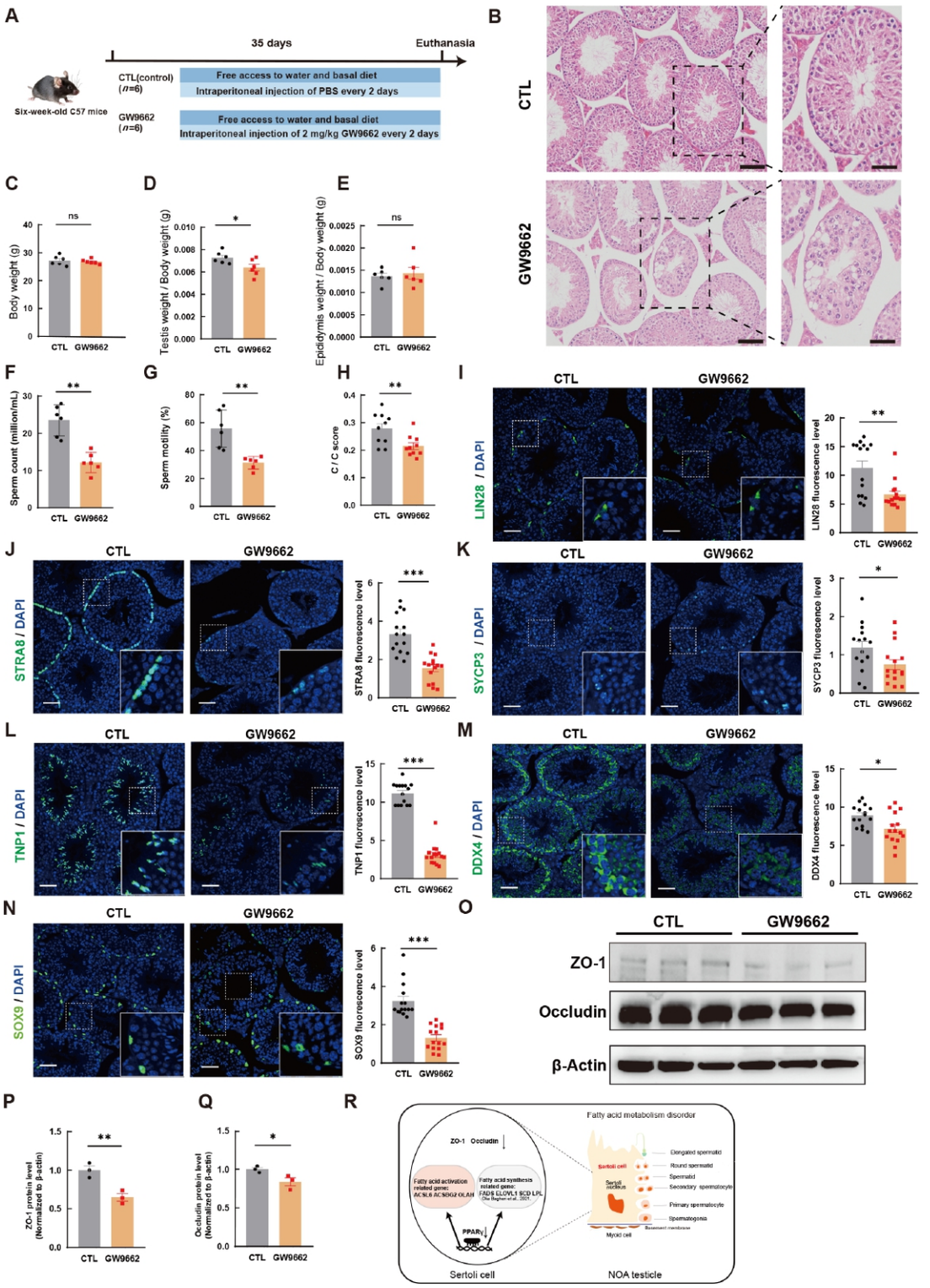


Figure 8 GW9662 treatment impaired BTB and spermatogenesis

A: Experimental design schematic of PPARG inhibition. B: H&E-stained sections of seminiferous tubules and epididymis (C) from CTL (control) and GW9662 (GW9662-induced) mice. Scale bar: 50 μm (5 μm in enlarged panels). C–E: Comparison of body weight, testicular organ index (testis/body weight), epididymal organ index (epididymis/body weight) between CTL and GW9662-treated groups (n=6 per group). F,G: Sperm count (million/mL) and sperm motility (%) in CTL and GW9662-treated groups (n=6 per group). Data are displayed as mean±SEM. Student's t-test was used to calculate P values. **: P<0.01. H: Comparison of C/C scores between CTL and GW9662-treated groups (n=6). I–N: Immunofluorescence analysis of germ cell (LIN28, STRA8, SYCP3, TNP1, DDX4) and Sertoli cell (SOX9) markers in testes of CTL and GW9662-treated groups (n=6). Scale bar: 20 μm (5 μm in enlarged panels). Data are displayed as mean±SEM. Student's t-test was used to calculate P values. ns: Not significant; *: P<0.05; **: P<0.01; ***: P<0.001. O: Western blot analysis of BTB markers ZO-1 and occludin in each group (n=3 per group) compared to control mice. P, Q: Quantification of ZO-1 and occludin was performed by normalizing protein levels to internal control β-actin (n=3). R: Schematic showing role of PPARG in testes of patients with NOA.

reduction in the diameter of seminiferous tubules, disorganization of germ cells, and a sparse mesenchymal transition in treated mice (Figure 8B). The impact of PPARG inhibition on spermatogenic cells was quantified using the C/C score, defined as the total number of testicular cells (C) divided by the circumference of seminiferous tubules (Deng et al., 2024). The GW9662-treated group exhibited significantly lower C/C scores compared to the controls, suggesting that PPARG inhibition induces spermatogenic disorder (Figure 8H). Additionally, the testicular organ index (testis weight/body weight) was significantly reduced in the GW9662 group (Figure 8D). Sperm analysis further demonstrated that GW9662 treatment led to a significant decrease in both sperm count and motility (Figure 8F, G), highlighting a significant loss of germ cells and impaired sperm maturation. Notably, no significant changes were observed in body or epididymis weight relative to body weight (Figure 8C).

To assess the impact of PPARG inhibition on specific germ cell populations, markers for various stages of spermatogenesis were analyzed, including LIN28 (spermatogonia), STRA8 (initiation of meiosis), SYCP3 (spermatocytes), TNP1 (spermatids), DDX4 (pan-germ cells), and SOX9 (Sertoli cells). These germ cell types showed a decline in GW9662 compared to the CTL group (Figure 8I–N). Interestingly, SOX9 fluorescence levels were also markedly decreased in the GW9662 group compared to the CTL group. Analysis of blood-testis barrier (BTB) integrity revealed a decline in the protein levels of BTB markers ZO-1 and occludin in the GW9662 group, indicating structural impairment of the BTB (Figure 8O-Q). These findings demonstrate that PPARG plays a crucial role in maintaining the integrity of the blood-testis barrier, supporting spermatogenesis, and ensuring sperm quality. Inhibition of PPARG leads to BTB dysfunction, disorganized germ cells, impaired sperm maturation, and a decline in overall sperm quality, underscoring its significance in male fertility.

DISCUSSION

Disruptions in fatty acid metabolism have been implicated in male infertility, but their specific impact on spermatogenesis in NOA remains unclear. This study employed multi-omics analyses and experimental validation to better understand the landscape of fatty acid metabolism in NOA. Our findings revealed significant fatty acid metabolism disorders in the testicular cells of NOA patients, especially in Sertoli cells. Furthermore, *ACSL6*, *ACSBG2*, and *OLAH* were identified as potential candidate pathogenic genes, while PPARG emerged as a key regulator of fatty acid metabolism and spermatogenesis (Figure 8R). These findings provide novel insights into the molecular mechanisms underlying NOA and propose potential therapeutic targets.

Differential gene expression and functional enrichment analyses of testicular microarray data confirmed significant disruptions in fatty acid metabolism in NOA testicles (Figure 1D, F). These findings were corroborated by metabolomic analyses of seminal plasma (Figure 3B), which revealed widespread changes in ω-3 and ω-6 PUFA-related metabolites and pathways (Figure 2D, E), consistent with our previous study (Jing et al., 2023). Decreased levels of DHA were observed in the NOA group compared to the CTL group. DHA is essential for sperm function due to its role in cell membrane composition. In the sperm tail, DHA ensures motility through its contribution to membrane fluidity and flexibility, while the sperm relies on DHA for processes such as acrosome reaction and membrane fusion (Argov-Argaman et al., 2013a). In non-human primates, almost all DHA in sperm is located in the tail, directly influencing movement (Connor et al., 1998). In humans and bulls, higher concentrations of ω-3 PUFAs, especially DHA, are found in the sperm head compared to the tail (Argov-Argaman et al., 2013b). Deficiency of DHA has profound effects on spermatogenesis. Notably, mice fed a DHA-deficient diet show an impaired acrosomal reaction (Roqueta-Rivera et al., 2011). Furthermore, ω-3 PUFA derivatives, such as 12-HEPE, promote spermatogonial self-renewal and differentiation by regulating the BMP4 protein in Sertoli cells, enhancing spermatogenesis (Jing et al., 2023). Clinically, DHA levels in seminal plasma correlate positively with sperm concentration, total sperm count, and normal sperm morphology in humans (Huang et al., 2019). Supplementation with DHA has been shown to increase the total antioxidant capacity (TAC) of seminal plasma, reduce apoptotic sperm, and improve the number of forward-moving sperm (Martínez-Soto et al., 2016).

The relationship between fatty acid metabolism and male infertility suggests that disruptions in specific fatty acid pathways contribute to spermatogenesis disorders. In this study, AA and BA levels were increased in the NOA group compared to the CTL group (Figure 2B, C). As an ω-6 PUFA, AA has been shown to activate the p38 MAPK pathway through the LOX, cytochrome P450, and COX metabolic pathways, resulting in reduced sperm motility (Yu et al., 2019). These findings suggest that DHA, AA, and BA may serve as potential biomarkers for diagnosing NOA, although further research is needed to elucidate their roles and precise mechanisms.

Using WGCNA and machine learning analysis of the GSE45885 dataset, *ACSL6*, *ACSBG2*, and *OLAH* were identified as potential candidate genes associated with fatty acid metabolism disorders in NOA. *ACSL6* and *ACSBG2* belong to the acyl-CoA synthetase (ACS) family, which catalyzes the activation of fatty acids by linking them to CoA, an ATP-dependent process critical for their participation in various metabolic pathways, including triacylglycerol synthesis, β-oxidation, and phospholipid production (Coleman et al., 2002; Watkins & Ellis, 2012). Failure of this activation may impair spermatogenesis. In mice, *ACSL6* expression is highest in the brain and testes (Fernandez et al., 2018; Grevengoed et al., 2014), with knockout studies demonstrating that its loss results in reduced germ cell count and impaired sperm motility (Hale et al., 2019). The apparent loss of *ACSL6* in NOA Sertoli cells (Figure 5E) may disrupt the ATP-dependent binding of CoA to fatty acids and disturb DHA enrichment in phospholipids, thereby disrupting BTB and spermatogenesis. Similarly, *ACSBG2*, highly expressed in the brain and testis (Pei et al., 2006), is involved in the transformation of medium- to long-chain fatty acids (C14 to C24) and plays an important role in lipid synthesis and deposition (Pei et al., 2006; Xing et al., 2021). The reduced mRNA expression of *ACSBG2* in NOA Sertoli cells suggests impaired lipid synthesis or deposition (Figure 5E), with the combined loss of *ACSL6* and *ACSBG2* in Sertoli cells potentially exacerbating PUFA activation failure. However, the precise role of ACSBG2 in the testis remains unclear and

further studies are needed.

OLAH, in cooperation with fatty acid synthase, preferentially facilitates the production of medium-chain fatty acids (Ritchie et al., 2016). Silencing of *OLAH* in cytotrophoblast cells has been shown to down-regulate BCL2 (De Alwis et al., 2022), leading to an imbalance in apoptosis. Consistent with this, our results demonstrated a significant reduction in *OLAH* mRNA expression in Sertoli cells and at the whole testicular tissue level in NOA patients, suggesting that loss of *OLAH* may induce BCL2-dependent apoptosis in testicular cells and contribute to cellular dysfunction (Figure 5E). On the other hand, the mRNA levels of PUFA-synthesizing enzyme-related genes, including elongation of very-long-chain fatty acids-like 2 (ELOVL2), fatty acid desaturase 2 (FADS2), lipoprotein lipase (LPL), and stearoyl-CoA desaturase (SCD), were significantly reduced in NOA testicular tissue compared to OA patients (Olia Bagheri et al., 2021). These results highlight a dual disruption in PUFA metabolism in NOA, with impairments in both synthesis and activation of PUFAs contributing to Sertoli cell dysfunction (Figure 5E, F). These findings suggest that testicular cells in NOA patients may suffer from both impaired PUFA synthesis and failure to activate fatty acids, which are essential for maintaining testicular cell function.

The combined loss of *ACSL6*, *ACSBG2*, and *OLAH* may represent a key pathogenic mechanism in NOA. However, the roles of these genes in the male reproductive system remain poorly elucidated, and their exact contributions to spermatogenesis are unclear. Additionally, germ cell dysfunction was observed following treatment with the PPARG inhibitor GW9662 (Figure 8J–O). However, it remains uncertain whether the spermatogenesis disorder observed in the GW9662 group is caused by Sertoli or germ cell dysfunction. Further research is needed to clarify the role of PPARG in other testicular cell types and its broader impact on testicular function.

PPARG emerged as a key regulator of fatty acid metabolism-related genes in Sertoli cells, identified through the SCENIC method and CTRD database. PPAR belongs to the nuclear receptor family and regulates cellular processes by binding ligands and interacting with specific gene promoters (Brunmeir & Xu, 2018). It has three isoforms —PPARα, PPARβ, and PPARγ —expressed in the hypothalamus-pituitary-testis axis (Santoro et al., 2020), especially in the nuclear region of Sertoli cells (Wang et al., 2020), consistent with our results (Figure 6C–E). Upon binding to its ligand, PPARG forms a heterodimer with the retinoid X-like receptor (RXR) and interacts with PPAR response elements in target genes in the nucleus (Varga et al., 2011). PPARG is involved in critical processes, such as lipid accumulation (Ge et al., 2018), lactate production (Gorga et al., 2017), steroidogenesis (Wang et al., 2020), and PUFA synthesis (Olia Bagheri et al., 2021). In freshwater carp, PPARG activation enhances *ACSL6* expression (Xie et al, 2020). In human NOA testis samples, fatty acid synthesis-related genes, such as *FADS*, *ELOVL1*, *SCD*, and *LPL*, show reduced expression compared to OA samples, alongside reduced PPARG chromatin admixture in their promoter regions (Olia Bagheri et al., 2021). Consistent with these findings, our study demonstrated that PPARG regulon activity was diminished in NOA Sertoli cells (Figure 6A), exhibiting decreased mRNA and protein expression. Immunohistochemical analysis further confirmed reduced nuclear expression of PPARG in NOA Sertoli cells compared to the OA group, suggesting impaired transcriptional activity (Figure 6D). Functionally, this diminished activity may underlie the reduced expression of genes related to fatty acids, such as *ACSL6* and *ACSBG2*, after inhibiting PPARG in primary Sertoli cells, confirming its critical role as a critical TF for fatty acid metabolism (Figure 7C).

Sertoli cells, highly metabolically active, are essential for germ cell development, forming the BTB, maintaining immune privilege, and secreting nutrients and regulatory factors (França et al., 2016). These cells rely on glucose and fatty acids for energy production, with fatty acid β-oxidation being a major pathway. PPARG promotes fatty acid β-oxidation and enhances lactate production, an essential energy source for germ cells (Gorga et al., 2017). Disruptions in fatty acid metabolism in Sertoli cells, such as impaired β-oxidation, can lead to apoptosis and BTB dysfunction (Rindone et al., 2024; Xu et al., 2022). Our results indicated that inhibition of PPARG in primary mouse Sertoli cells reduced cell viability, disrupted cell barriers and cell junctions, and impaired β-oxidation (Figure 7D). To evaluate these effects *in vivo*, GW9662, PPARG inhibitor (Zhang et al., 2020), was intraperitoneally administered to mice for 35 days. Loss of PPARG led to BTB disruption, impaired spermatogenesis, and reduced sperm quality (Figure 8A–H). These findings suggest a critical role for PPARG in maintaining Sertoli cell function and testicular homeostasis. Notably, pharmacological activation of PPARG holds potential therapeutic value for male infertility in animals and humans. Selective PPARγ agonists, such as 15-deoxy-12,14-prostaglandin J2 (PGJ2) and rosiglitazone (BRL), have been shown to improve sperm capacitation, acrosome reaction and motility in humans (Aquila et al., 2006). These results highlight PPARG as a promising target for the treatment of NOA. However, while this study observed decreased expression of genes involved in PUFA synthesis and activation in the testes of NOA patients, the specific relationship between PPARG and fatty acid regulation remains unclear. Further research is needed to elucidate the role of PPARG activation in addressing male infertility.

This study conducted a comprehensive analysis of fatty acid gene expression profiles at both the whole-tissue and single-cell level in NOA. Our findings revealed a strong association between fatty acid metabolism and dysfunctional spermatogenesis in NOA. Key candidate genes, including *ACSL6*, *ACSBG2*, and *OLAH*, were identified as potential contributors to NOA pathogenesis. Additionally, the pivotal role of *PPARG* in regulating spermatogenesis was elucidated via both *in vivo* and *in vitro* experiments. Overall, this study provides novel insights into the molecular mechanisms underlying NOA and identifies promising targets for therapeutic intervention, advancing both our understanding and potential treatment of this complex condition.

DATA AVAILABILITY

All scRNA-seq and microarray data mentioned in this article were obtained from the GEO public database (see corresponding citations for GEO IDs). The human seminal plasma metabolic data were obtained from our previous work (Jing et al., 2023), available in the Science Data Bank database (10.57760/sciencedb.17029).

SUPPLEMENTARY DATA

Supplementary data to this article can be found online.

COMPETING INTERESTS

The authors declare that they have no competing interests.

AUTHORS' CONTRIBUTIONS

B.Y., J.J., J.Z.M., and Z.L. contributed to the concept and design of the original research. Z.L. participated in the single-cell RNA, bulk RNA, and metabolomic analyses. Z.L and Y.J.X. prepared the primary Sertoli cells and conducted *in vitro* and *in vivo* experiments. Z.C.Z., Y.M.F., H.W., W.Q.C., and X.G. collected human testicular tissues. Z.L., Y.J.X., J.Z.M., and J.J. wrote the manuscript. All authors read and approved the final version of the manuscript.

ACKNOWLEDGMENTS

We thank Dr. Jian-Ming Zeng (University of Macau) and all members of the bioinformatics team at Biotrainee for generously sharing their experience and codes.

REFERENCES

Aaronson DS, Iman R, Walsh TJ, et al. 2010. A novel application of ^{1}H magnetic resonance spectroscopy: non-invasive identification of spermatogenesis in men with non-obstructive azoospermia. *Human Reproduction*, **25**(4): 847–852.

Aibar S, González-Blas CB, Moerman T, et al. 2017. SCENIC: single-cell regulatory network inference and clustering. *Nature Methods*, **14**(11): 1083–1086.

Alfano M, Tascini AS, Pederzoli F, et al. 2021. Aging, inflammation and DNA damage in the somatic testicular niche with idiopathic germ cell aplasia. *Nature Communications*, **12**(1): 5205.

Aquila S, Bonofiglio D, Gentile M, et al. 2006. Peroxisome proliferator-activated receptor (PPAR)γ is expressed by human spermatozoa: its potential role on the sperm physiology. *Journal of Cellular Physiology*, **209**(3): 977–986.

Argov-Argaman N, Mahgrefthe K, Zeron Y, et al. 2013a. Season-induced variation in lipid composition is associated with semen quality in Holstein bulls. *Reproduction*, **145**(5): 479–489.

Argov-Argaman N, Mahgrefthe K, Zeron Y, et al. 2013b. Variation in lipid profiles within semen compartments —the bovine model of aging. *Theriogenology*, **80**(7): 712–721.

Brunmeir R, Xu F. 2018. Functional regulation of PPARs through post-translational modifications. *International Journal of Molecular Sciences*, **19**(6): 1738.

Bu DC, Luo HT, Huo PP, et al. 2021. KOBAS-i: intelligent prioritization and exploratory visualization of biological functions for gene enrichment analysis. *Nucleic Acids Research*, **49**(W1): W317–W325.

Coleman RA, Lewin TM, Van Horn CG, et al. 2002. Do long-chain acyl-CoA synthetases regulate fatty acid entry into synthetic versus degradative pathways?. *The Journal of Nutrition*, **132**(8): 2123–2126.

Connor WE, Lin DS, Wolf DP, et al. 1998. Uneven distribution of desmosterol and docosahexaenoic acid in the heads and tails of monkey sperm. *Journal of Lipid Research*, **39**(7): 1404–1411.

De Alwis N, Beard S, Binder NK, et al. 2022. Placental OLAH levels are altered in fetal growth restriction, preeclampsia and models of placental dysfunction. *Antioxidants*, **11**(9): 1677.

Deng ZW, Zhao LY, Li S, et al. 2024. Targeting dysregulated phago-/auto-lysosomes in Sertoli cells to ameliorate late-onset hypogonadism. *Nature Aging*, **4**(5): 647–663.

Dohle GR, Elzanaty S, Van Casteren NJ. 2012. Testicular biopsy: clinical practice and interpretation. *Asian Journal of Andrology*, **14**(1): 88–93.

Duan H, Song W, Zhao J, et al. 2023. Polyunsaturated fatty acids (PUFAs): sources, digestion, absorption, application and their potential adjunctive effects on visual fatigue. *Nutrients*, **15**(11): 2633.

Fernandez RF, Kim SQ, Zhao YW, et al. 2018. Acyl-CoA synthetase 6 enriches the neuroprotective omega-3 fatty acid DHA in the brain. *Proceedings of the National Academy of Sciences of the United States of America*, **115**(49): 12525–12530.

França LR, Hess RA, Dufour JM, et al. 2016. The Sertoli cell: one hundred fifty years of beauty and plasticity. *Andrology*, **4**(2): 189–212.

Gautier C, Aurich C. 2022. "Fine feathers make fine birds" - The mammalian sperm plasma membrane lipid composition and effects on assisted reproduction. *Animal Reproduction Science*, **246**: 106884.

Ge X, He ZWY, Cao C, et al. 2022. Protein palmitoylation-mediated palmitic acid sensing causes blood-testis barrier damage via inducing ER stress. *Redox Biology*, **54**: 102380.

Ge X, Pan P, Jing J, et al. 2018. Rosiglitazone ameliorates palmitic acid-induced cytotoxicity in TM4 Sertoli cells. *Reproductive Biology and Endocrinology*, **16**(1): 98.

Gorga A, Rindone GM, Regueira M, et al. 2017. PPARγ activation regulates lipid droplet formation and lactate production in rat Sertoli cells. *Cell and Tissue Research*, **369**(3): 611–624.

Grevengoed TJ, Klett EL, Coleman RA. 2014. Acyl-CoA metabolism and partitioning. *Annual Review of Nutrition*, **34**: 1–30.

Hale BJ, Fernandez RF, Kim SQ, et al. 2019. Acyl-CoA synthetase 6 enriches seminiferous tubules with the ω-3 fatty acid docosahexaenoic acid and is required for male fertility in the mouse. *Journal of Biological Chemistry*, **294**(39): 14394–14405.

Hodžić A, Maver A, Zorn B, et al. 2023. Transcriptomic signatures for human male infertility. *Frontiers in Molecular Biosciences*, **10**: 1226829.

Huang QY, Liu LP, Wu Y, et al. 2019. Seminal plasma metabolites mediate the associations of multiple environmental pollutants with semen quality in Chinese men. *Environment International*, **132**: 105066.

Iizuka-Hishikawa Y, Hishikawa D, Sasaki J, et al. 2017. Lysophosphatidic acid acyltransferase 3 tunes the membrane status of germ cells by incorporating docosahexaenoic acid during spermatogenesis. *Journal of Biological Chemistry*, **292**(29): 12065–12076.

Itoh N, Kayama F, Tatsuki TJ, et al. 2001. Have sperm counts deteriorated over the past 20 years in healthy, young Japanese men? Results from the Sapporo area. *Journal of Andrology*, **22**(1): 40–44.

Jarow JP, Espeland MA, Lipshultz LI. 1989. Evaluation of the azoospermic patient. *The Journal of Urology*, **142**(1): 62–65.

Jeon YG, Kim YY, Lee G, et al. 2023. Physiological and pathological roles of lipogenesis. *Nature Metabolism*, **5**(5): 735–759.

Jing J, Ouyang L, Zhang H, et al. 2023. Omega-3 polyunsaturated fatty acids and its metabolite 12-HEPE rescue busulfan disrupted spermatogenesis via target to GPR120. *Cell Proliferation*, **57**(2): e13551.

Kolmykov S, Yevshin I, Kulyashov M, et al. 2021. GTRD: an integrated view of transcription regulation. *Nucleic Acids Research*, **49**(D1): D104–D111.

Komljenovic D, Sandhoff R, Teigler A, et al. 2009. Disruption of blood-testis barrier dynamics in ether-lipid-deficient mice. *Cell and Tissue Research*, **337**(2): 281–299.

Lambert SA, Jolma A, Campitelli LF, et al. 2018. The human transcription factors. *Cell*, **172**(4): 650–665.

Li JJ, Yang F, Dong L, et al. 2023. Seminal plasma biomarkers for predicting successful sperm retrieval in patients with nonobstructive azoospermia: a narrative review of human studies. *Basic and Clinical Andrology*, **33**(1): 9.

Ma P, Zhang ZM, Zhou XY, et al. 2019. Characterizing semen abnormality male infertility using non-targeted blood plasma metabolomics. *PLoS One*, **14**(7): e0219179.

Malcher A, Rozwadowska N, Stokowy T, et al. 2013. Potential biomarkers of nonobstructive azoospermia identified in microarray gene expression analysis. *Fertility and Sterility*, **100**(6): 1686–1694. e7.

Martínez-Soto JC, Domingo JC, Cordobilla B, et al. 2016. Dietary supplementation with docosahexaenoic acid (DHA) improves seminal

antioxidant status and decreases sperm DNA fragmentation. *Systems Biology in Reproductive Medicine*, **62**(6): 387–395

Mruk DD, Cheng CY. 2011. An in vitro system to study Sertoli cell blood-testis barrier dynamics. *Methods in Molecular Biology*, **763**: 237–252

Nagirnaja L, Lopes AM, Charng WL, et al. 2022. Diverse monogenic subforms of human spermatogenic failure. *Nature Communications*, **13**(1): 7953.

Okada H, Tajima A, Shichiri K, et al. 2008. Genome-wide expression of azoospermia testes demonstrates a specific profile and implicates *ART3* in genetic susceptibility. *PLoS Genetics*, **4**(2): e26.

Olia Bagheri F, Alizadeh A, Sadighi Gilani MA, et al. 2021. Role of peroxisome proliferator-activated receptor gamma (PPARγ) in the regulation of fatty acid metabolism related gene expressions in testis of men with impaired spermatogenesis. *Reproductive Biology*, **21**(4): 100543.

Pang ZQ, Zhou GY, Ewald J, et al. 2022. Using MetaboAnalyst 5.0 for LC-HRMS spectra processing, multi-omics integration and covariate adjustment of global metabolomics data. *Nature Protocols*, **17**(8): 1735–1761.

Pei ZT, Jia ZZ, Watkins PA. 2006. The second member of the human and murine “bubblegum” family is a testis- and brainstem-specific acyl-CoA synthetase. *Journal of Biological Chemistry*, **281**(10): 6632–6641.

Piechka A, Sparanese S, Witherspoon L, et al. 2024. Molecular mechanisms of cellular dysfunction in testes from men with non-obstructive azoospermia. *Nature Reviews Urology*, **21**(2): 67–90.

Rigatti SJ. 2017. Random forest. *Journal of Insurance Medicine*, **47**(1): 31–39.

Rindone GM, Dasso ME, Centola CL, et al. 2024. Effect of metformin on sertoli cell fatty acid metabolism and blood-testis barrier formation. *Biology*, **13**(5): 330.

Ritchie MK, Johnson LC, Clodfelter JE, et al. 2016. Crystal structure and substrate specificity of human thioesterase 2: insights into the molecular basis for the modulation of fatty acid synthase. *Journal of Biological Chemistry*, **291**(7): 3520–3530.

Roqueta-Rivera M, Abbott TL, Sivaguru M, et al. 2011. Deficiency in the omega-3 fatty acid pathway results in failure of acrosome biogenesis in mice. *Biology of Reproduction*, **85**(4): 721–732.

Santoro M, De Amicis F, Aquila S, et al. 2020. Peroxisome proliferator-activated receptor gamma expression along the male genital system and its role in male fertility. *Human Reproduction*, **35**(9): 2072–2085.

Sanz H, Valim C, Vegas E, et al. 2018. SVM-RFE: selection and visualization of the most relevant features through non-linear kernels. *BMC Bioinformatics*, **19**(1): 432.

Shishikura K, Kuroha S, Matsueda S, et al. 2019. Acyl-CoA synthetase 6 regulates long-chain polyunsaturated fatty acid composition of membrane phospholipids in spermatids and supports normal spermatogenic processes in mice. *The FASEB Journal*, **33**(12): 14194–14203.

Stoffel W, Holz B, Jenke B, et al. 2008. Δ6-desaturase (FADS2) deficiency unveils the role of ω3- and ω6-polyunsaturated fatty acids. *The EMBO Journal*, **27**(17): 2281–2292.

Varga T, Czimmerer Z, Nagy L. 2011. PPARs are a unique set of fatty acid regulated transcription factors controlling both lipid metabolism and inflammation. *Biochimica et Biophysica Acta (BBA) - Molecular Basis of Disease*, **1812**(8): 1007–1022.

Wagner AO, Turk A, Kunej T. 2023. Towards a multi-omics of male infertility. *The World Journal of Men's Health*, **41**(2): 272–288.

Wang G, Cheng ST, Zhang SS, et al. 2020. LPS impairs steroidogenesis and ROS metabolism and induces PPAR transcriptional activity to disturb estrogen/androgen receptor expression in testicular cells. *Molecular Biology Reports*, **47**(2): 1045–1056.

Wang M, Liu XX, Chang G, et al. 2018. Single-cell RNA sequencing analysis reveals sequential cell fate transition during human spermatogenesis. *Cell Stem Cell*, **23**(4): 599–614. e4.

Wang M, Xu YW, Zhang YC, et al. 2021. Deciphering the autophagy regulatory network via single-cell transcriptome analysis reveals a requirement for autophagy homeostasis in spermatogenesis. *Theranostics*, **11**(10): 5010–5027.

Watkins PA, Ellis JM. 2012. Peroxisomal acyl-CoA synthetases. *Biochimica et Biophysica Acta (BBA) - Molecular Basis of Disease*, **1822**(9): 1411–1420.

Willott GM. 1982. Frequency of azoospermia. *Forensic Science International*, **20**(1): 9–10.

Wu ZM, Sun J, Liao Z, et al. 2022. An update on the therapeutic implications of long-chain acyl-coenzyme A synthetases in nervous system diseases. *Frontiers in Neuroscience*, **16**: 1030512.

Xie D, He Z, Dong Y, et al. 2020. Molecular cloning, characterization, and expression regulation of acyl-CoA synthetase 6 gene and promoter in common carp *Cyprinus carpio*. *International Journal of Molecular Sciences*, **21**(13): 4736

Xing SY, Liu RR, Zhao GP, et al. 2021. Time course transcriptomic study reveals the gene regulation during liver development and the correlation with abdominal fat weight in chicken. *Frontiers in Genetics*, **12**: 723519.

Xu XQ, Luo DD, Xuan QH, et al. 2022. Atlas of metabolism reveals palmitic acid results in mitochondrial dysfunction and cell apoptosis by inhibiting fatty acid β-oxidation in Sertoli cells. *Frontiers in Endocrinology*, **13**: 1021263.

Yu LS, Yang XJ, Ma B, et al. 2019. Abnormal arachidonic acid metabolic network may reduce sperm motility via P38 MAPK. *Open Biology*, **9**(4): 180091.

Yu YX, Farooq MS, Eberhart Meessen S, et al. 2024. Nuclear pore protein POM121 regulates subcellular localization and transcriptional activity of PPARγ. *Cell Death & Disease*, **15**(1): 7.

Zadravec D, Tvrdik P, Guillou H, et al. 2011. ELOVL2 controls the level of n-6 28: 5 and 30: 5 fatty acids in testis, a prerequisite for male fertility and sperm maturation in mice. *Journal of Lipid Research*, **52**(2): 245–255.

Zhang Y, Yang X, Yan WC, et al. 2020. Thymopentin improves the survival of septic mice by promoting the production of 15-deoxy-prostaglandin J2 and activating the PPARγ signaling pathway. *The FASEB Journal*, **34**(9): 11772–11785.

Zhang Z, Zhang YW, Liu CJ, et al. 2017. Serum metabolomic profiling identifies characterization of non-obstructive azoospermic men. *International Journal of Molecular Sciences*, **18**(2): 238.

Zhao LY, Yao CC, Xing XY, et al. 2020. Single-cell analysis of developing and azoospermia human testicles reveals central role of Sertoli cells. *Nature Communications*, **11**(1): 5683.

Huang et al. *Zool. Res.* 2025, 46(1): 193−208
https://doi.org/10.24272/j.issn.2095-8137.2024.102
https://cstr.cn/32248.14.zr.2024.102

ZR | Zoological Research

Article Open Access

Cross-species single-cell transcriptomics reveals neuronal similarities and heterogeneity in amniote pallium

Fu-Bao-Qian Huang[1,2,#], Kuo Liao[1,2,#], Yu-Nong Sun[1,2], Zi-Hao Li[1,2], Yan-Ru Zhang[1], Ping-Fang Liao[2,3], Si-Yuan Jiang[2,3], Zhi-Yong Zhu[2,3], Duo-Yuan Chen[2,4], Ying Lei[2,4], Shi-Ping Liu[2,4], You-Ning Lin[2,4,*], Zhen-Kun Zhuang[2,4,*]

[1] *School of Biology and Biological Engineering*, *South China University of Technology*, *Guangzhou*, *Guangdong* 510006, *China*

[2] *BGI Research*, *Hangzhou*, *Zhejiang* 310030, *China*

[3] *College of Life Sciences*, *University of Chinese Academy of Sciences*, *Beijing* 100049, *China*

[4] *BGI Research*, *Shenzhen*, *Guangdong* 518083, *China*

ABSTRACT

The amniote pallium, a vital component of the forebrain, exhibits considerable evolutionary divergence across species and mediates diverse functions, including sensory processing, memory formation, and learning. However, the relationships among pallial subregions in different species remain poorly characterized, particularly regarding the identification of homologous neurons and their transcriptional signatures. In this study, we utilized single-nucleus RNA sequencing to examine over 130 000 nuclei from the macaque (*Macaca fascicularis*) neocortex, complemented by datasets from humans (*Homo sapiens*), mice (*Mus musculus*), zebra finches (*Taeniopygia guttata*), turtles (*Chrysemys picta bellii*), and lizards (*Pogona vitticeps*), enabling comprehensive cross-species comparison. Results revealed transcriptomic conservation and species-specific distinctions within the amniote pallium. Notable similarities were observed among cell subtypes, particularly within *PVALB*$^{+}$ inhibitory neurons, which exhibited species-preferred subtypes. Furthermore, correlations between pallial subregions and several transcription factor candidates were identified, including *RARB*, *DLX2*, *STAT6*, *NR3C1*, and *THRB*, with potential regulatory roles in gene expression in mammalian pallial neurons compared to their avian and reptilian counterparts. These results highlight the conserved nature of inhibitory neurons, remarkable regional divergence of excitatory neurons, and species-specific gene expression and regulation in amniote pallial neurons. Collectively, these findings provide valuable insights into the evolutionary dynamics of the amniote pallium.

Keywords: Amniote; Pallium evolution; Cross-species comparison; Comparative transcriptomics; Single-nucleus RNA sequencing

This is an open-access article distributed under the terms of the Creative Commons Attribution Non-Commercial License (http://creativecommons.org/licenses/by-nc/4.0/), which permits unrestricted non-commercial use, distribution, and reproduction in any medium, provided the original work is properly cited.

Copyright ©2025 Editorial Office of Zoological Research, Kunming Institute of Zoology, Chinese Academy of Sciences

INTRODUCTION

Deciphering the conservation and innovation of the vertebrate brain throughout evolution can offer crucial insights into the origin of cognition. Approximately 320 million years ago, the amniote ancestor diverged into two main lineages: mammals and sauropsids (reptiles and birds) (Benton & Donoghue, 2007; Woych et al., 2022). Despite this extensive period of evolutionary divergence, the fundamental brain architecture of developing amniotes retains strong similarities to that of their shared ancestor, comprising four principal regions: the telencephalon, diencephalon, mesencephalon (or midbrain), and rhombencephalon (or hindbrain) (Pessoa et al., 2019). While this basic structure of the amniote brain is highly conserved, the telencephalon, especially the pallium, has undergone distinct evolutionary expansions in different lineages (Butler, 1994; Kverková et al., 2022; Puelles, 2001). For instance, the mammalian neocortex evolved into a highly expanded, six-layered structure, while the dorsal ventricular ridge (DVR) evolved in the pallium of birds and reptiles, with both serving as neural centers for processing sensory information and supporting advanced cognitive functions (Güntürkün, 2012; Jarvis et al., 2005; Nieder et al., 2020; Roth, 2015). Moreover, the dorsal cortex (DC) of reptiles shares developmental homology with the mammalian neocortex, further underscoring the evolutionary relationships between these pallial structures (Butler et al., 2011; Karten, 2015). Although substantial evidence supports the embryonic homology between the pallium of mammals and sauropsids, the precise relationships among cell types and subregions

Received: 14 August 2024; Accepted: 11 October 2024; Online: 12 October 2024

Foundation items: This work was supported by the National Key Research and Development Program (2022YEF0203200), National Science and Technology Innovation 2030 Major Program (STI2030-2021ZD0200100), and National Key Research and Development Program (2018YFA0801400, 2021YFA0805100)

[#]Authors contributed equally to this work

*Corresponding authors, E-mail: linyouning@genomics.cn; zhuangzhenkun@genomics.cn

within the amniote pallium remain to be fully elucidated (Cárdenas & Borrell, 2020; Liao et al., 2024; Montiel & Aboitiz, 2018; Nomura et al., 2014; Puelles et al., 2000). Additionally, the molecular mechanisms underlying the differential expansion of the pallium and the functional convergence observed in amniote brain evolution are not yet well understood (Aboitiz, 2011; Cárdenas & Borrell, 2020; Tosches & Laurent, 2019).

Recent advances in high-resolution cellular technologies, such as single-cell/single-nucleus RNA sequencing (scRNA-seq/snRNA-seq), have significantly enhanced our understanding of the brain across various species (Colquitt et al., 2021; Svensson et al., 2018; Tang et al., 2009; Tosches et al., 2018). These studies have highlighted the conservation of cellular composition in amniote brains and identified species-specific neuronal subtypes (Hain et al., 2022; Han et al., 2022; Hodge et al., 2019; Li et al., 2023). However, most studies have been limited to one or two species, lacking a systematic cellular comparison across a broader range of taxa. Given the distinct evolutionary rates of different cell types (Chen et al., 2023; Jorstad et al., 2023; Tasic et al., 2018), expanding the scope of species included in such analyses is crucial. Furthermore, when analyzing correlations among certain cell types or brain subregions, it is essential to distinguish between the roles of transcription factors (TFs) and non-TFs (effector genes). TFs typically define cell identity, whereas non-TFs directly mediate cellular functions (Arendt et al., 2016; Wagner, 2014). However, previous research has often failed to make this distinction, resulting in inconsistent findings (Colquitt et al., 2021; Liang et al., 2018). Consequently, the homologous signatures of pallial cell types and subregions between mammals and sauropsids remain unresolved.

In this study, we employed snRNA-seq to construct a cellular atlas of the macaque pallium. Integrating these data with human, mouse, zebra finch, turtle, and lizard datasets, we conducted a cross-species comparative analysis to investigate gene expression patterns and regulatory networks at the cellular level. Our approach focused on identifying both conserved and species-specific characteristics within the pallium of amniotes, shedding light on the evolutionary dynamics of this critical brain region.

MATERIALS AND METHODS

Ethics statement and sample collection

This project was carried out in strict compliance with animal research regulations and was approved by the Institutional Animal Care and Use Committee of Yunnan Key Laboratory of Primate Biomedical Research, Institutional Animal Care and Use Committee of Huazhen Bioscience (permit HZ2019027), and Institutional Review Board of the BGI Ethics Committee (permit BGI-IRB A21025-T1).

Tissue samples were isolated from the prefrontal cortex of two 72-month-old female cynomolgus macaques (*Macaca fascicularis*) and immediately frozen in liquid nitrogen. The dorsal and ventral prefrontal cortex samples were collected in both macaques and subsequently utilized for snRNA-seq analysis.

Isolation and purification of nuclei

Frozen macaque tissue blocks were homogenized in 1 mL of pre-chilled Dounce homogenization buffer using a Dounce homogenizer, applying 10 loose and 10 tight strokes, with the samples immersed in ice throughout. Following homogenization, 2 mL of additional buffer was added, and the homogenate was filtered through a 40 μm cell strainer (Miltenyi Biotec, Germany) into a 15 mL conical tube and centrifuged at 900 ×*g* for 10 min to pellet the cell nuclei at 4°C. Fluorescence microscopy was used to estimate the quality and quantity of the extracted nuclei.

Library preparation and sequencing for snRNA-seq

The snRNA-seq library was prepared using the DNBelab C Series Single-Cell Library Preparation Kit (MGI, #1000021082, China) for DNBelab C4 RNA-seq analysis based on droplet technology. The single-cell nuclear suspension, obtained from the previously prepared snRNA samples, was washed twice with phosphate-buffered saline (PBS) containing 0.04% bovine serum albumin (BSA). The nuclear suspension was resuspended, filtered through a 40 μm cell strainer, and the cell suspension and nuclear concentrations were measured and recorded. Droplets were prepared using the DNBelab C Series Single-Cell Library Preparation Kit (MGI, #1000021082, China), and cell lysis and mRNA capture were performed with magnetic beads within the droplets. The single-cell magnetic beads were then recovered using a lysis reagent recovery system with a vacuum pump, and the captured mRNA was reverse transcribed into cDNA. Following synthesis, the double-stranded cDNA and Oligo products were amplified and screened. The Oligo products were barcoded using polymerase chain reaction (PCR) for subsequent preparation into Oligo loaded-into-machine libraries. Finally, the cDNA product was fragmented, end repaired, ligated, PCR amplified, denatured, circularized, and digested to prepare a single-stranded DNA library. After library preparation, sequencing was performed using the DIPSEQ T1 sequencing platform at the China National Gene Bank (Shenzhen).

Processing macaque snRNA-seq data

PISA (v.0.7) was employed to filter and demultiplex the raw sequencing reads generated by DNBelab C4 RNA-seq, while STAR (v.2.6.1a) was used to align these reads. For alignment, a modified GTF file of the Macaca_fascicularis_5.0 genome was used, which included both intronic and exonic regions. The aligned sequences were then sorted with Sambamba (v.0.7), and a Unique Molecular Identifier (UMI) counts matrix mapping individual cells to genes was generated.

Quality control, dimensionality reduction, and cell clustering were performed using the R package Seurat (v.4.0.3) (Butler et al., 2018). Low-quality cells were removed by excluding those with fewer than 500 or more than 6 000 detected genes, or a percentage of mitochondrial gene expression exceeding 5%. To identify and eliminate potential doublets within the snRNA-seq data, DoubletFinder (v.2.0.3) (McGinnis et al., 2019) was applied.

Following strict quality control, a total of 135 986 nuclei were retained, with a median of 4 260 UMIs and 1 670 genes per cell. The datasets were then split by individual macaque using the SplitObject function, and each subset was normalized using SCTransform, with the parameter vars.to.regress set to “percent.mt”. Batch correction was subsequently performed by implementing PrepSCTIntegration, FindIntegrationAnchors, and IntegrateData, using 3 000 features identified through SelectIntegrationFeatures. Additionally, RunPCA, RunUMAP, FindNeighbors, and FindClusters were employed for dimensionality reduction and clustering analysis, with 30 principal components (PCs) utilized for principal component

analysis (PCA). Differentially expressed genes (DEGs) were identified using FindAllMarkers with the criteria fold-change>1.5 and adjusted *P*<0.05.

Cell subtype prediction for macaque datasets

Cell subtype annotation for the macaque datasets was performed using Seurat (v.4.0.3) according to previous study (Lei et al., 2022). Macaque cells were mapped to human subtypes by identifying anchors with FindIntegrationAnchors (dimension set to 30) using SCT assays. The TransferData function was then applied to classify macaque cells based on human subtypes, and the predicted labels were used to define macaque cell subtypes. Subsequently, these annotations were verified by assessing the expression of classical marker genes.

Hierarchical clustering analysis

Cell group dendrograms were constructed based on hierarchical clustering across cell types, subtypes, and clusters and visualized using ape (v.5.6.2) and ggtree (v.3.4.4) (Yu et al., 2017). Highly variable genes (HVGs) were identified using FindVariableFeatures, and the average expression of 3 000 HVGs was calculated for each cell group. Hierarchical clustering was performed using the dist and hclust functions in R. The dendrogram branches were adjusted manually without changing the tree structure.

DEG expression analysis across species

DEGs were identified for each cell type in each specie using the FindAllMarkers function, retaining only genes with a fold-change>2. Additionally, DEG intersections were calculated using five pseudobulk methods implemented in Libra (v.1.0.0) (Squair et al., 2021). UpSet plots, generated with UpSetR (v.1.4.0), were used to display intersection counts of DEGs for excitatory neurons (EXs), inhibitory neurons (INs), and non-neuronal cells. Conserved genes for cluster C0 were identified using the FindConservedMarkers function with default parameters.

Cross-species pairwise cluster correlations

Correlation analysis among cell subtypes from two species was conducted using one-to-one orthologs (provided in Supplementary Table S1), as previously reported (Tosches et al., 2018). Analysis involved four main steps: (1) Two gene sets were selected for comparison: (i) shared TFs in both datasets and (ii) the union of 3 000 HVGs from both datasets, excluding TFs; (2) Average expression levels of the selected gene sets in each cell group were calculated using the AverageExpression function in Seurat; (3) Resulting "gene set×group type" matrices were transformed into gene specificity matrices; (4) Spearman rank correlations and associated *P*-values of gene specificities between all pairs of group types across the two datasets were calculated based on scripts provided by Tosches et al. (2018). To enhance the robustness of our findings, additional correlations were calculated using HVGs, excluding TFs, matched in count to the number of TFs (sHVGs). Results were visualized as heatmaps using pheatmap (v.1.0.12) and gene set expression levels were calculated using UCell (v.1.1.0). The accuracy of the macaque data in this study was validated using the macaque dataset from Chen et al. (2023) and human dataset from Nagy et al. (2020).

Gene Ontology (GO) enrichment analysis

GO enrichment analysis was performed using the R package clusterProfiler (v.3.18.0) (Yu et al., 2012) with the org.Hs.eg.db (v.3.12.0) annotation as the background. Results were visualized using the R package enrichplot (v.1.10.1).

Integration of neurons across species

Integration followed the procedures outlined in "Processing macaque snRNA-seq data", with slight modifications. To address significant differences in the number of EXs and INs across species, down-sampling was applied prior to integration. Approximately 9 000 EXs and 4 000 INs were down-sampled from human, macaque, and mouse datasets. Only one-to-one homologous genes were retained for subsequent analyses. Using the human atlas as a reference for cross-species comparison, one-to-one orthologous gene lists for macaque, mouse, and zebra finch were acquired using biomaRt (v.2.46.0), while those for lizards and turtles were provided by Tosches et al. (2018). Additionally, the FindClusters function was used at a resolution of 0.3 in both EXs and INs groups.

Partition-based graph abstraction (PAGA) trajectory analysis

PAGA analysis was conducted on PVALB$^+$ cell clusters using Scanpy (v.1.9.1) (Wolf et al., 2018). The PAGA graph was computed with the top 5 000 genes, and positions were visualized by setting the parameter threshold to 0.03.

Sauropsid single-cell and mouse *in situ* hybridization (ISH) comparison

Interspecies correlations were calculated using scripts from Colquitt et al. (2021) and the R package cocoframer (v.0.1.1). For the comparison, shared TFs or 6 000 HVGs excluding TFs were selected. Analysis highlighted the neocortex and other telencephalic compartments, including the pallial amygdala and endopiriform.

Neocortex ISH of mice and humans

ISH images were downloaded from the Allen Brain Atlas and BrainSpan platforms, and images were cropped for optimal visualization. Mouse ISH images were downloaded from various websites (Lein et al., 2007) (https://mouse.brain-map.org/): *Bdnf*: https://mouse.brain-map.org/experiment/siv?id=79587720&imageId=79593146&initImage=ish&contrast=0.5,0.5,0,255,4; *Gfra1*: https://mouse.brain-map.org/experiment/siv?id=71064217&imageId=71054294&initImage=ish&contrast=0.5,0.5,0,255,4; *Dlx2*: https://mouse.brain-map.org/experiment/siv?id=1482&imageId=101313722&initImage=ish&contrast=0.5,0.5,0,255,4; *Rarb*: https://mouse.brain-map.org/experiment/siv?id=75038442&imageId=74930054&initImage=ish&contrast=0.5,0.5,0,255,4; *Stat6*: https://mouse.brain-map.org/experiment/siv?id=69290549&imageId=69253420&initImage=ish&contrast=0.5,0.5,0,255,4; *Nr3c1*: https://mouse.brain-map.org/experiment/siv?id=727&imageId=101309852&initImage=ish&contrast=0.5,0.5,0,255,4; *Thrb*: https://mouse.brain-map.org/experiment/siv?id=71249069&imageId=71109047&initImage=ish&contrast=0.5,0.5,0,255,4.

Human images were also downloaded from two websites (Miller et al., 2014) (https://www.brainspan.org/): *BDNF*: https://www.brainspan.org/ish/experiment/dual_view?id=100125098&imageId=101712779&imageType=ish,expression,nissl&initImage=ish&z=-1; *GFRA1*: https://www.brainspan.org/ish/experiment/dual_view?id=100101516&imageId=101633475&imageType=ish,expression,nissl&initImage=ish&z=-1.

Soft clustering of TF expression

Soft clustering of TF expression in mammalian EXs subtypes

was performed using Mfuzz (v.2.50.0). Only gene sets exhibiting layer-biased expression were retained.

Gene regulatory network analysis

SCENIC (v.1.3.1) (Aibar et al., 2017) and pySCENIC (v.0.12.1) were used to analyze activated regulons in each cell group following the official tutorial (https://scenic.aertslab.org/). Initially, differentially activated regulons were identified across all EXs in each species. The top 10 activated regulons for EX subclasses were visualized. Subsequently, a more comprehensive analysis was performed for EX subclasses within each species to generate a complete regulon list. The intersections of key TFs across species-specific subclasses were visualized using Venn diagrams with the R package VennDiagram (v.1.6.20).

Co-expression network analysis

Co-expression analysis was performed using the R package WGCNA (v.1.71). To avoid computational memory issues, pseudo-cells were condensed into groups of 100 cells. Gene modules were calculated separately for each dataset, with soft power thresholds determined using the pickSoftThreshold function. Only representative gene modules were retained.

Protein sequence alignment

Cross-species TF protein sequences were aligned using UniProt (https://www.uniprot.org/) with three iterations. Four mammals (*Homo sapiens* (human), *Macaca fascicularis* (cynomolgus monkey), *Callithrix jacchus* (white-tufted-ear marmoset), and *Mus musculus* (mouse)), three reptiles (*Chrysemys picta bellii* (western painted turtle), *Pogona vitticep*s (central bearded dragon), and *Crocodylus porosus* (saltwater crocodile)), three birds (*Taeniopygia guttata* (zebra finch), *Columba livia* (rock dove), and *Gallus gallus* (chicken)), *Ornithorhynchus anatinus* (duckbill platypus), and two amphibians (*Xenopus laevis* (African clawed frog) and *Xenopus tropicalis* (western clawed frog)) were used for comparison. Percent identity matrices are provided in Supplementary Table S2.

Validation using spatial transcriptomics

Spatial transcriptomic validation was performed using the macaque and teleost datasets from Chen et al. (2023) and Hegarty et al. (2024), respectively. Selected gene expression levels were visualized using Seurat, and spatial transcriptomic figures for zebra finch, mouse, and Chinese softshell turtle were obtained from the Spatial Transcript Omics Database (https://db.cngb.org/stomics/datasets/STDS0000241).

RESULTS

Cell transcriptomic atlas of the amniote pallium

Using snRNA-seq, we generated a high-quality dataset comprising 135 986 nuclei from the prefrontal cortex (PFC), a region of the neocortex, dissected from two female adult macaques (Figure 1A, B). To identify cell subtypes, nuclei from the macaque dataset were matched against human cell subtype expression patterns using a reference transcriptomic atlas of human. These annotations were validated based on the expression of classical marker genes (Figure 1C–E; Supplementary Figure S1A) and correlations with reliable external datasets (Supplementary Figure S2A, B), and included 85 868 excitatory neurons (EXs: *SLC17A7*, *SLC17A6*), 27 397 inhibitory neurons (INs: *GAD1*, *GAD2*), and 22 721 non-neuronal cells (astrocytes (ASTs): *SLC1A2*, *GFAP*; oligodendrocytes (OLIs): *MOG*, *OPALIN*; oligodendrocyte progenitor cells (OPCs): *PDGFRA*, *PCDH15*; microglial cells (MICs): *APBB1IP*, *CTSS*; pericytes (PERIs): *PDGFRB*; and endothelial cells (ENDOs): *FLT1*). Additionally, we downloaded five amniote datasets (Figure 1F; Supplementary Figure S1C), including 26 583 nuclei from the human neocortical regions (primary motor cortex, M1; primary visual cortex, V1; middle temporal gyrus, MTG), 34 331 nuclei from the mouse neocortex (frontal cortex, FC), 25 392 nuclei from the zebra finch DVR (HVC proper name (HVC), robust nucleus of the arcopallium (RA)), 18 537 nuclei from the turtle pallium (PL) (including DC and DVR), and 20 257 nuclei from the lizard PL (including DC and DVR).

Marker gene expression patterns were compared across the six species. Consistent with previous reports (Colquitt et al., 2021; Tosches et al., 2018), INs exhibited conserved expression of *GAD1* and *GAD2* across all species (Figure 1G). In contrast, EXs and certain non-neuronal cells, such as oligodendrocytes and astrocytes, displayed species-specific expression patterns, reflecting potential divergence. However, other non-neuronal cell types, such as microglial and endothelial cells, showed conserved expression of classical marker genes. Cell type proportions across species are presented in Supplementary Figure S1B; however, these proportions were not comparable due to experimental bias. For example, the mouse dataset was experimentally enriched for neuronal populations, resulting in a reduced representation of non-neuronal cells (Yao et al., 2021).

Conservation and divergence of cell types across species

To investigate the conservation and divergence of cell types across species, we conducted a series of comparative analyses using six datasets. Initially, hierarchical clustering was performed on neurons and glial cells. INs from different species were clustered together (Figure 2A), while other cell types were more dispersed. Next, we identified DEGs for each cell type using six methods across the species (Figure 2B) and analyzed their intersections. Most DEGs were species-specific, with only a small number shared among the six species across the three cell types, including four in EXs, one in INs, and several in non-neuronal cells. This pattern suggests that divergence among cell types across species may be driven by species-specific DEGs, while shared DEGs likely preserve fundamental cell type identities. Notably, INs displayed fewer species-specific DEGs, highlighting their conserved nature, whereas non-neuronal cells demonstrated a higher proportion of species-specific DEGs (Supplementary Table S3). Nonetheless, non-neuronal cells also shared several genes, indicating a balance between conservation and divergence. These findings reflect the conservation of INs, while supporting the hypothesis that non-neuronal cells are more divergent across the amniote pallium (Hodge et al., 2019; Ma et al., 2022).

Gene regulatory networks governed by TFs are typically conserved, while downstream effector genes exhibit greater flexibility (Wagner, 2014). Mutations or deletions in TFs can disrupt entire regulatory networks, potentially altering cell types (Arendt et al., 2016). In contrast, changes in effector genes are less likely to cause significant disruptions as they are often functionally replaceable. Consequently, the expression patterns of TFs and effector genes convey different biological significance. TFs reflect regulatory programs that preserve regional or cell type identity, whereas

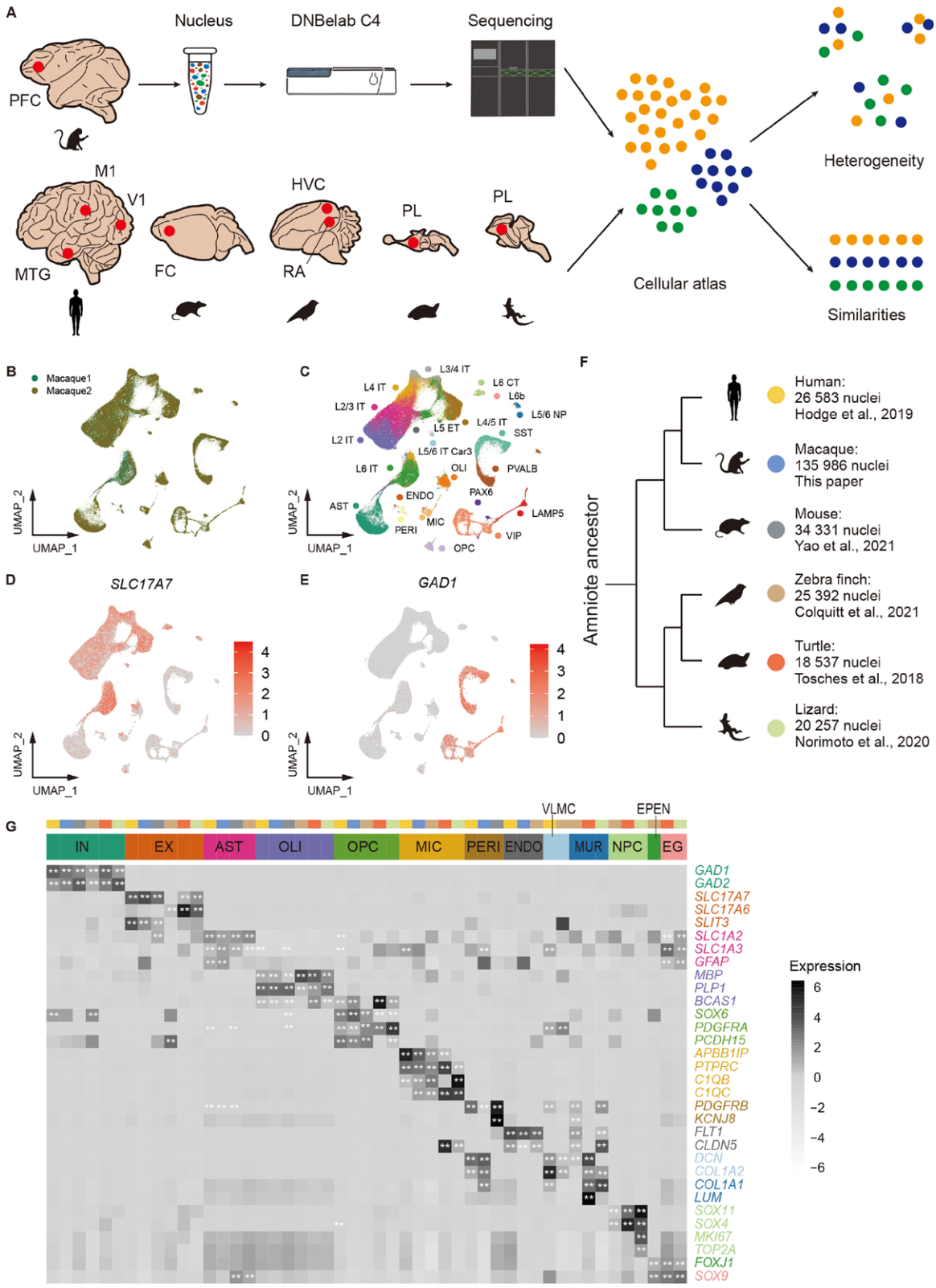


Figure 1 Single-cell atlas of amniote pallium

A: Schematic exhibiting overall study design. PFC, prefrontal cortex; M1, primary motor cortex; V1, primary visual cortex; MTG, middle temporal gyrus; FC, frontal cortex; HVC, HVC proper name; RA, robust nucleus of the arcopallium; PL, pallium. B, C: UMAP representation of 135 986 macaque (*Macaca fascicularis*) nuclei colored by sample (B) and cell type (C). AST, astrocyte; ENDO, endothelial cell; IT, intra-telencephalic-projecting neuron; ET, extra-telencephalic-projecting neuron; NP, near-projecting neuron; CT, corticothalamic neuron; L1–L6, layer 1 to layer 6; MIC, microglia; OLI, oligodendrocyte; OPC, oligodendrocyte precursor cell; EPEN, ependymal cell; PERI, pericyte; LAMP5, PAX6, PVALB, SST and VIP are inhibitory neuron subtypes; IN, inhibitory neuron; EX, excitatory neuron. D, E: Expression of EX marker gene *SLC17A7* (D) and IN marker gene *GAD1* (E) in macaque dataset. F: Phylogenetic tree of six species. G: Heatmap of classical marker genes in all cell types across species. MUR, mural cell; EG, ependymoglial cell; VLMC, vascular and leptomeningeal cell; NPC, neuronal progenitor cell. **: P<0.01.

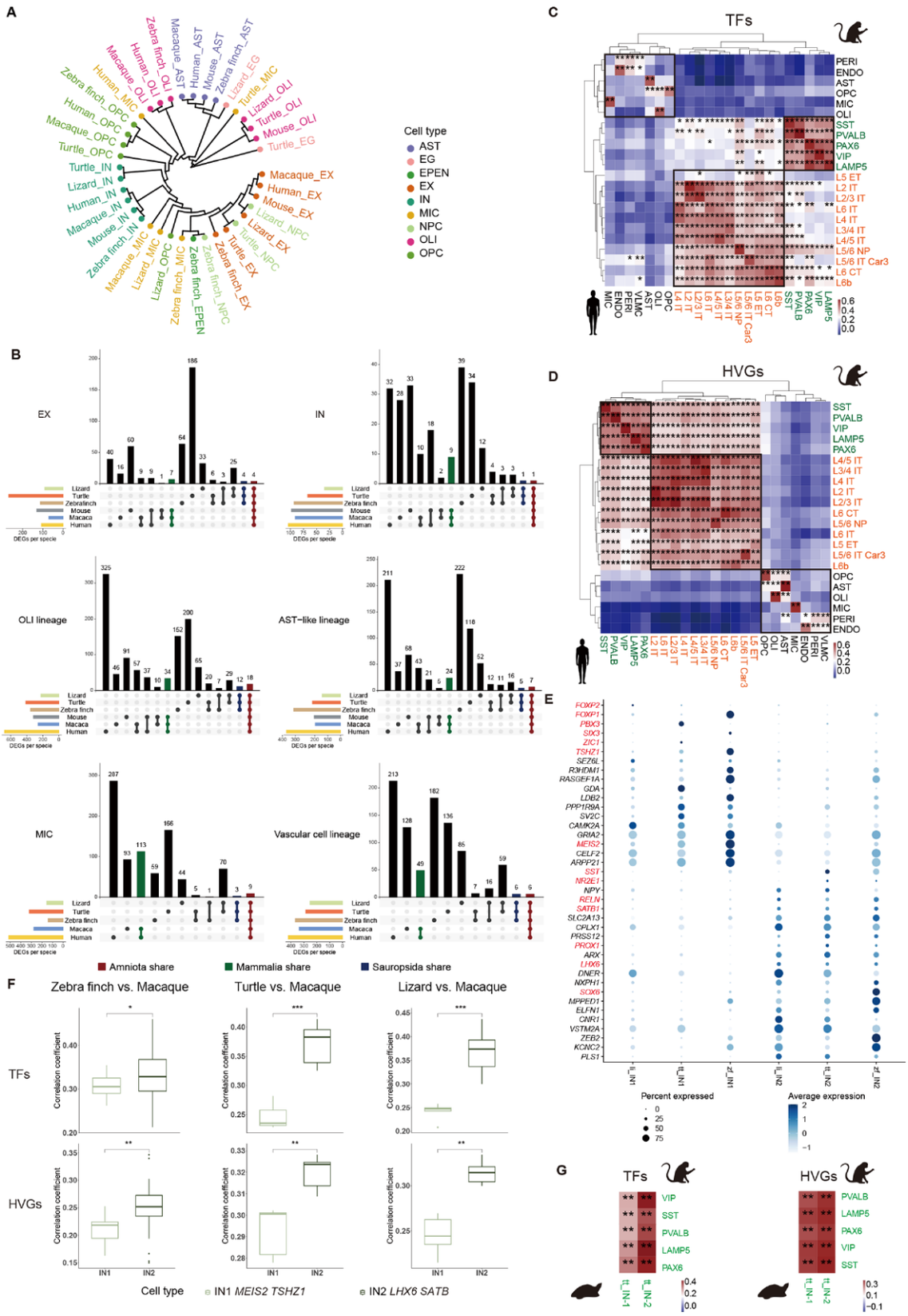


Figure 2 Comparison across cell types in amniote pallium

A: Hierarchical clustering of cell types using average expression profiles. B: UpSet plots exhibiting DEG counts of EXs, INs, and non-neuronal cells across species. OLI lineage includes OLI and OPC; AST-like lineage includes AST, EG, and EPEN; vascular cell lineage includes ENDO, PERI, VLMC, and MUR. C, D: Correlation heatmap between humans and macaques using TF profiles (C) and HVG profiles (D). Asterisks represent significance, ns: Not significant; *: P<0.05; **: P<0.01; ***: P<0.001; ****: P<0.0001. E: Bubble plot showing expression levels of differentially expressed markers for IN1 and IN2 in sauropsids. F: Box plots comparing correlation coefficients between IN1 and IN2. G: Section of correlation heatmap for INs between macaques and turtles using TF profiles (left) and HVG profiles (right).

non-TFs/effector genes are more flexible and directly linked to neuronal functions (Colquitt et al., 2021; Wagner, 2014). To compare cell subtype signatures across species, we calculated pairwise correlations between cell groups using TF expression profiles and HVGs excluding TFs (representing non-TFs/effector genes). In mammals, nearly all macaque cell subtypes exhibited one-to-one orthologous relationships with human or mouse subtypes based on both TF and HVG profiles (Figure 2C, D; Supplementary Figure S3A, B). However, when compared to sauropsids, macaque EX and IN subtypes showed broad similarities with most neuronal subtypes and even some non-neuronal subtypes (Supplementary Figure S3C–H), consistent with previously reported homologies (Colquitt et al., 2021; Hodge et al., 2019; Norimoto et al., 2020; Tosches et al., 2018). These results reveal conserved correlations among pallial cell subtypes from closely related mammals and broad similarities among major cell types in distantly related amniotes.

When analyzing datasets from closely related species or the same species, the correlation coefficients derived from TF expression profiles were comparable to those obtained using HVGs, with the latter often being higher. This indicates that non-TFs may contribute more significantly to pallial similarities among closely related species than TFs (Figure 2C, D; Supplementary Figure S2A–C). Conversely, for distantly related species, correlation coefficients based on TF expression profiles were consistently higher than those obtained using HVGs (Supplementary Figure S3A–H), supporting the conserved nature of TF expression, as previously reported (Colquitt et al., 2021; Tosches et al., 2018). Additional analyses using HVGs matched in number to TFs (sHVGs) confirmed that these observations were not influenced by unequal gene set sizes or varying expression levels (Supplementary Figure S4A–E).

Intriguingly, we identified two IN subtypes in sauropsids, distinguished by their correlation patterns: IN1, marked by lateral ganglionic eminence (LGE)-derived IN markers (*MEIS2*$^+$, *TSHZ1*$^+$), exhibited weaker correlations with macaque INs; IN2, characterized by medical/caudal ganglionic eminence (MGE/CGE)-derived IN markers (*LHX6*$^+$, *SATB1*$^+$) (Colquitt et al., 2021), exhibited stronger correlation with macaque INs (Figure 2E–G; Supplementary Figures S3K, S2F). Notably, mammalian cerebral cortex INs are predominantly composed of MGE/CGE neurons (Su-Feher et al., 2022; Torigoe et al., 2016; Tosches & Laurent, 2019). Based on these markers, we defined IN1 *MEIS2 TSHZ1* as LGE-derived INs and IN2 *LHX6 SATB1* as MGE/CGE-derived INs. Analysis of DEGs revealed that IN2 shared more DEGs across the three species than IN1 (Supplementary Figure S3I). These findings imply that IN2 is more conserved and involved in pathways related to pallium formation (Supplementary Figure S3J and Table S4), indicating functional similarities between mammalian INs and sauropsid IN2.

Our comparative analysis across six amniote species highlighted transcriptomic conservation of INs and heterogeneity among major cell types. Cell subtype homology became ambiguous with increasing phylogenetic distance between species. Notably, INs displayed fewer species-specific DEGs, while non-neuronal cells exhibited a higher degree of species-specific divergence. Correlation coefficients from TF expression profiles were higher than those from non-TFs in distantly related amniotes, whereas the reverse was true for closely related species, highlighting the conserved nature of TF expression. Additionally, the identification of two IN subtypes in sauropsids, based on their correlations with macaque INs, implies that MGE/CGE-derived INs are more conserved than LGE-derived INs within the amniote pallium.

Shared and distinct signatures of INs in amniote pallium

Building on our findings regarding marker gene expression and subtype correlations of INs across the amniote pallium, we further investigated their defining signatures. By integrating INs from six species and performing unsupervised clustering, 10 distinct cell clusters were identified (Figure 3A, B). These clusters were identified based on marker expression: C5 *PROX1 NR2E1* and C6 *VIP PROX1* as CGE-derived INs (*VIP*$^+$, *PROX1*$^+$, *NR2E1*$^+$), C0 *VIP MEIS2* as a CGE/LGE-derived mixed INs (*VIP*$^+$, *MEIS2*$^+$, *TSHZ1*$^+$), and the remaining INs as MGE-derived INs (*SOX6*$^+$, *LHX6*$^+$, *SATB1*$^+$) (Figure 3B; Supplementary Figure S5A, B).

Most clusters were evenly distributed across the six datasets, except for C7 *RELN NR2E1*, C8 *PVALB NR2E1*, and C9 *PVALB LHX6* (Figure 3C; Supplementary Figure S5C, D). Notably, C7 and C9 predominantly consisted of mammalian INs, while C8 was primarily composed of sauropsid INs, suggesting species-specific IN subtypes in the mammalian and sauropsid pallium. C7 *RELN NR2E1* was inferred to represent an MGE-derived IN subtype with DEGs enriched in telencephalon formation pathways (Figure 3D, E; Supplementary Figure S5E). C8 *PVALB NR2E1* and C9 *PVALB LHX6* were identified as *PVALB*$^+$ IN subtypes involved in neuronal signal transmission in the sauropsid and mammalian pallium, respectively. Additionally, PVALB$^+$ cluster C2 (*PVALB*, *SOX6*) was analyzed alongside these subtypes. Trajectory analysis revealed that C2 extended into two distinct branches connecting to C8 and C9, with numerous genes such as *PVALB*, *DAAM2*, and *NR2E1* showing dynamic expression along the trajectory (Figure 3F; Supplementary Figure S5F). These results indicate that C2 represents a conserved *PVALB*$^+$ IN subtype, whereas C8 and C9 may be evolutionarily novel subtypes with significant changes in gene expression. Prior research has reported high *PVALB* expression in specific layers of the mammalian neocortex and the song motor pathway of birds (Glezer et al., 1993; Hara et al., 2012; Sherwood et al., 2010), hinting at potential divergence in *PVALB*$^+$ IN subtypes across the amniote pallium. Further experimental verification is required to confirm these evolutionary patterns and functional implications.

Previous studies have reported that LGE-derived INs share greater transcriptomic similarity with CGE-derived INs than MGE-derived INs (Su-Feher et al., 2022), and that *VIP*$^+$ INs are absent from the reptilian pallium (Briscoe et al., 2018; Tosches et al., 2018). Consistent with these findings, our data showed that C0 *VIP MEIS2* was highly expressed in both LGE-derived and CGE-derived IN marker genes and was predominantly composed of mammalian *VIP*$^+$ INs and sauropsid LGE-derived INs (Figure 3D; Supplementary Figure S5C, D). Based on its composition and gene expression patterns, C0 was deduced to represent a mixture of INs and was enriched in pathways related to axonogenesis (Figure 3G–H). Further analysis revealed that C0 could be divided into high and low *VIP*$^+$ C0 subclusters, similar to the CGE-derived clusters C5 *PROX1 NR2E1* and C6 *VIP PROX1*, respectively (Supplementary Figure S6A–D), highlighting the close relationship between LGE- and CGE-derived INs (Su-

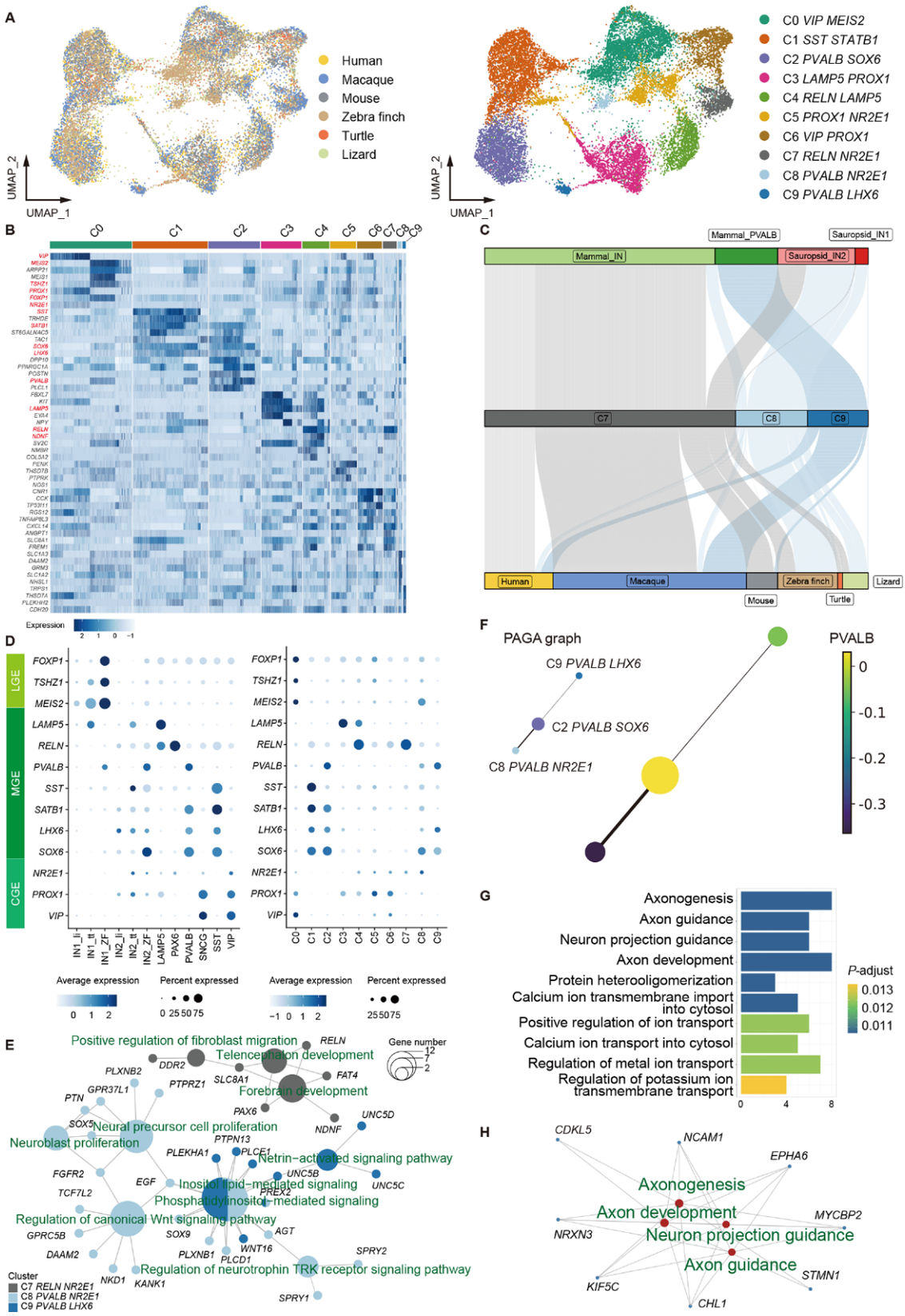


Figure 3 Inhibitory neurons (INs) in amniote pallium

A: UMAP plots of sampled INs, colored by species (left) and unsupervised clustering cell clusters (right). B: Heatmap of DEG expression across IN cell clusters. C: Sankey diagram showing cellular compositional makeup of species and cell subtypes in species-biased cell clusters. D: Bubble plot showing expression of differentially expressed markers for IN subtypes and cell clusters. E: Network of key genes and pathways in species-biased clusters. F: PAGA analysis of PVALB clusters. Left, PAGA positions of three clusters; right, expression of PVALB in PAGA positions. Edge weights represent confidence in the presence of connections. G: Bar plot showing representative GO enrichment pathways of C0. H: Network exhibiting key genes and pathways in (G).

Feher et al., 2022). These findings suggest that C0 may represent an intermediate population reflecting shared features between LGE- and CGE-derived INs within the amniote pallium. Furthermore, some reptilian LGE-derived INs may share similar functions with mammalian *VIP*$^+$ INs, given their high expression of conserved genes within C0 (Supplementary Figure S5G).

In conclusion, we observed homologous IN subtypes across amniotes and notable interspecies variability. For example, we identified *PVALB*$^+$ IN subtypes with evident differences between mammals and sauropsids, as well as a mixed cell cluster of LGE- and CGE-derived INs (C0 *VIP MEIS2*). These findings provide evidence for divergent evolutionary pathways in neuronal diversification and offer insights into the absence of *VIP*$^+$ INs in the reptilian pallium.

Transcriptomic heterogeneity among EXs in the mammalian neocortex and avian DVR

EXs exhibit diversity and abundance within the mammalian pallium (Hodge et al., 2019; Ma et al., 2022; Yao et al., 2021). To explore whether homologous EX subtypes exist across amniotes, we co-clustered EX subtypes from six species, resulting in 15 distinct clusters. These clusters were then classified as resembling upper layer (UL)-like EXs (*RFX3*$^+$, *RORB*$^+$, *UNC5D*$^+$), deeper layer (DL)-like EXs (*CRYM*$^+$, *CDH13*$^+$, *NR4A2*+), mixture populations, or species-specific subtypes (Figure 4A, B; Supplementary Figure S7A, B). However, consistent with prior correlation analyses, identifying one-to-one homologous EX subtypes was challenging due to widespread co-expression of UL and DL marker genes across clusters. Five species-biased clusters were distinguished, with C0 *TAC1 NR2F2* cells being present across all amniotes except humans, while the C9 *PENK PROX1* cluster was primarily found in sauropsids, the C10 *CDH13 SOX5* cluster predominantly in mammals, the C11 *RORB UNC5D* cluster mostly in primates, and the C14 *RORB CPNE4* cluster uniquely in humans. Further analysis indicated that C0 likely represented a low-quality cluster (Supplementary Figure S6E), while C14 was validated using other integration methods (Supplementary Figure S6F, G). These findings imply that while transcriptomic homology exists among amniote EXs, the evolution of more specialized cell subtypes in higher vertebrates, such as primates and humans, has contributed to significant diversification (Lamanna et al., 2023; Musser et al., 2021; Naumann & Laurent, 2020; Norimoto et al., 2020). This evolutionary divergence likely explains the difficulty in identifying homologous EX subtypes across all amniotes.

The mammalian neocortex and reptilian DC are derived from the dorsal pallium, while the sauropsid DVR originates from the ventral pallium (Güntürkün et al., 2020; Naumann & Laurent, 2020; Puelles et al., 2017). Earlier research noted significant correlations among these regions, yet their complex interrelationships remain poorly understood (Norimoto et al., 2020; Tosches et al., 2018). To address this, we first performed correlation analysis of mammalian and avian EX subtypes to identify distinctions and homologies. According to the “nucleus-to-layer” model l(Dugas-Ford et al., 2012; Jarvis et al., 2005; Karten, 1991), HVC was homologous to the neocortical layer 2/3, and RA was homologous to layer 5 (L5) (Figure 4C). In our macaque data, RA EXs exhibited strong similarities to L5 neurons as well as correlations with other DL neurons (Supplementary Figure S7C, D), consistent with earlier studies (Colquitt et al., 2021). Similarly, HVC EXs resembled macaque DL neurons, mirroring previous research comparing mouse DL profiles (Colquitt et al., 2021). However, no correlations were found between HVC EXs and UL neurons, potentially due to divergence between primate and rodent UL neurons (Fame et al., 2017; Huang et al., 2023; Loomba et al., 2022). Further insights were obtained by mapping zebra finch EX data onto ISH profiles from the mouse pallium. RA EXs exhibited stronger correlations with entorhinal DL neurons using TF expression profiles, whereas HVG-based analysis revealed greater similarity to non-entorhinal DLs (Figure 4D, E), consistent with prior studies (Colquitt et al., 2021; Wagner, 2014). HVC EXs, in contrast, demonstrated significant similarities to both UL and DL neurons based on HVGs and to DL neurons using TF profiles. Verification with ISH data for *BDNF* and *GFRA1* in mouse and human pallia showed high expression of these HVC marker genes in DLs (Supplementary Figure S7J, S8A, B). Overall, these results indicate that both avian RA and HVC EXs may be more akin to mammalian DL neurons than to UL neurons, with TF profiles providing stronger correlations. While the "nucleus-to-layer" model offers valuable insights, our findings indicate that this framework may oversimplify these relationships and requires further refinement and additional confirmatory evidence.

We speculated that the observed similarities between the avian DVR and mammalian DLs may be driven by key TFs. To explore this, we first conducted soft clustering of all TFs using the primate expression matrix and identified four distinct gene sets: GS1, GS3, and GS4 associated with ULs and GS2 associated with DLs). These gene sets were enriched in pattern formation and regionalization of the amniote pallium (Figure 4F, G; Supplementary Figure S7E–G and Table S2). Next, we performed gene regulatory network analysis on EXs from both mammals and zebra finch (Figure 4H–J; Supplementary Figure S7H, I). This analysis identified two TFs, *RARB* and *DLX2*, as pivotal regulators. Both TFs are vital for avian brain regionalization (Koszinowski et al., 2015; Marcucio et al., 2005) and were extensively expressed in the macaque pallium (Supplementary Figure S6H, S8C). *RARB*, a member of GS1, emerged as a key TF in the regulon intersections across four EX classes. This TF is involved in eye development, cognitive function, and synapse formation (Srour et al., 2016), aligning with GS1 enrichment analysis (Figure 4K, L). In contrast, *DLX2* was associated with GS2 and identified as a key TF in the regulon intersections of most EX classes, except for mammalian ULs. This TF is critical for forebrain morphogenesis, retina formation, and ganglion cell development (Tan & Testa, 2021), consistent with the enrichment results. In addition, the nuclear factor I gene family, implicated in brain development and intelligence (Zenker et al., 2019), was active across the four EX classes, with *NFIX*, *NFIA*, and *NFIB* known to play vital roles in the regulatory network of salamander cortical neurons (Lust et al., 2022; Wei et al., 2022). These findings underscore the pivotal role of TFs in amniote pallial formation and regulation, potentially driving the similarities between the avian DVR and mammalian neocortex. Such regulatory mechanisms provide further evidence supporting the convergent evolution of these brain regions in avians and mammals (Hintermann et al., 2022; Yokoyama & Pollock, 2012).

This study highlighted both the heterogeneity and shared characteristics of EXs across mammals and sauropsids. We distinguished species-specific EX subtypes, including human-

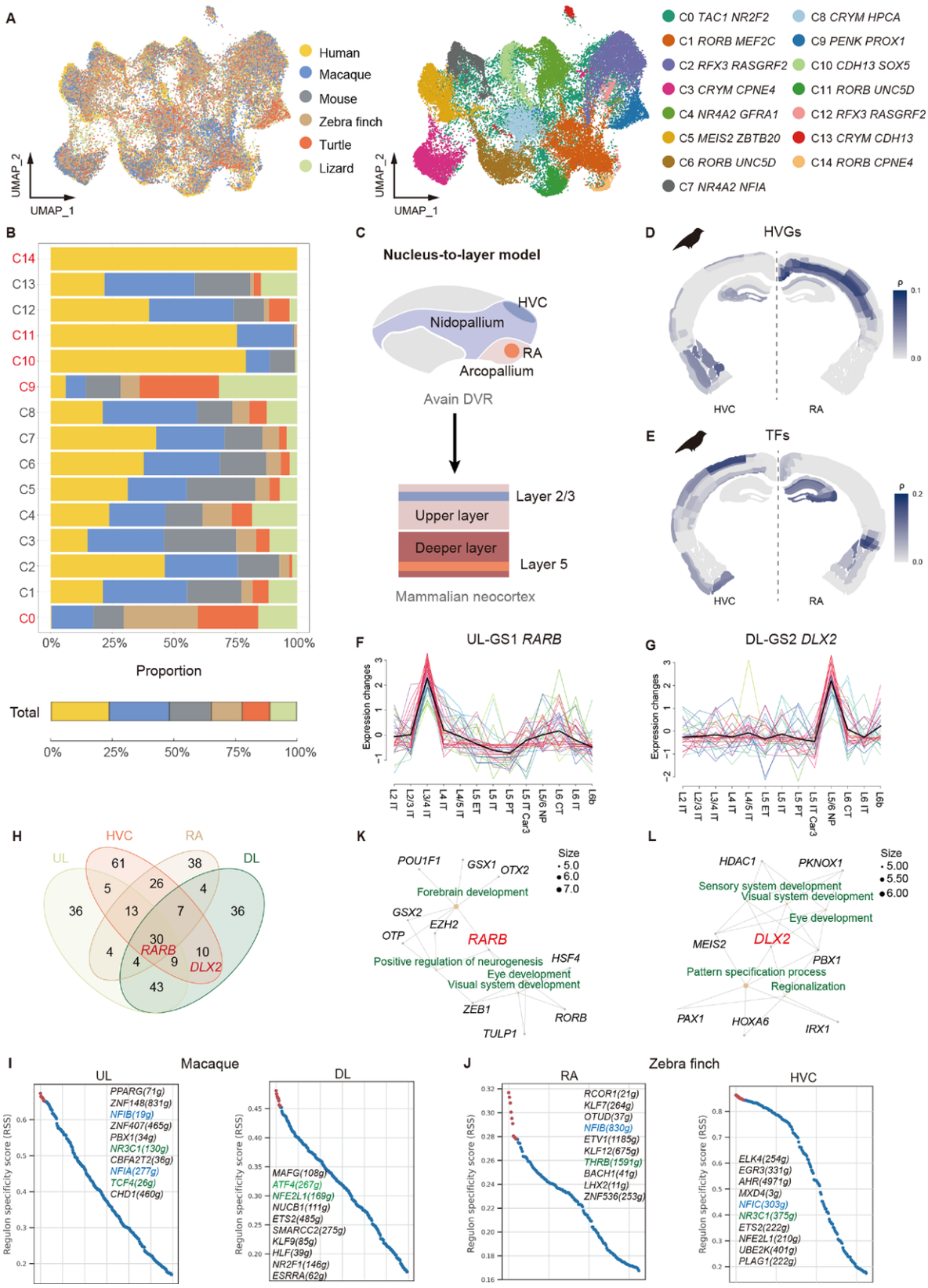


Figure 4 Heterogeneity among mammalian neocortex and avian DVR

A: UMAP plots of sampled EXs colored by species (left) and unsupervised clustering cell clusters (right). B: Bar plots showing distribution of cell clusters across species. C: Schematic illustrating nucleus-to-layer model (Colquitt et al., 2021; Karten, 1991). D, E: Spearman correlations between zebra finch EXs (HVC and RA) and mouse pallium, mapped onto coronal sections from the Adult Mouse Atlas (ABA) (Lein et al., 2007). F, G: Soft clustering gene sets of TFs in UL and DL EXs. H: Venn diagram showing intersections of active TFs between mammalian and avian EXs. I, J: Top 10 active regulons in EXs in macaques (UL and DL) and zebra finches (RA and HVC). Conserved TFs are labeled in green, while NFI gene family is labeled in blue. K, L: Network showing representative GO enrichment pathways of groups in F (UL-GS1 *RARB*) and G (DL-GS2 *DLX2*).

absent C0, sauropsid-preferred C9, mammal-preferred C10, primate-preferred C11, and human-exclusive C14, suggesting the emergence of novel subtypes as species complexity increases. Our findings showed that avian RA EXs exhibit strong similarity to macaque DL EXs, while HVC EXs resemble both DLs and ULs, challenging the "nucleus-to-layer" model (Colquitt et al., 2021) and reflecting the likeness of HVCs to primate DLs. Furthermore, we identified key TFs, especially *RARB* and *DLX2*, as crucial to these similarities, potentially reflecting convergent evolution in the avian and mammalian pallium (Hintermann et al., 2022; Yokoyama & Pollock, 2012). These findings indicate that while ancestral TFs are conserved across amniotes, their regulatory networks may have undergone distinct evolutionary adaptations, a hypothesis requiring further verification.

Transcriptomic heterogeneity among EXs in the mammalian neocortex and reptilian DVR and DC

To elucidate the relationship between mammalian and reptilian pallial EXs, we analyzed their gene expression signatures. Turtle DC EXs exhibited stronger similarities to mouse neocortex ISH data when TF profiles were used, whereas DVR EXs aligned more closely with the neocortex when HVG profiles were used (Figure 5A, B). Comparable trends were observed when using macaque and lizard datasets, although the results were less pronounced due to fewer cells and poorer quality (Supplementary Figure S9A–D). Likewise, turtle DVR EXs were correlated with macaque L6b neurons based on HVGs and with L4 IT based on TFs, while DC EXs were only correlated with L5/6 NP neurons based on TFs (Figure 5C). DC EXs showed no significant similarity to human neocortex EXs using HVGs but exhibited similarities to DL EXs using TFs (Supplementary Figure S9A). Comparatively, lizard DVR EXs were correlated with both DL and UL neurons based on HVGs but only with DL neurons when using TFs, while DC EXs were similar to DL neurons for both gene sets (Supplementary Figure S9B). These findings highlight that TFs and non-TFs convey distinct biological insights. The reptilian DC appears to resemble the neocortex in cellular or regional identity, likely due to a common developmental origin (Güntürkün et al., 2020; Naumann & Laurent, 2020; Puelles et al., 2017), whereas the DVR may parallel neocortical functionality, reflecting evolutionary adaptations inherited from shared ancestors. Our results further underscore significant differences in TF- and HVG-based profiles in comparative analyses across amniote pallial EXs (Figure 5D). These observations support the hypothesis that reptilian DC may be homologous to mammalian DL neurons (Briscoe & Ragsdale, 2018; Güntürkün et al., 2020; Luzzati, 2015), while the DVR may perform functions analogous to the neocortex (Briscoe et al., 2018; Yamashita & Nomura, 2017).

Despite distinct signatures between the reptilian DC and DVR, their EXs shared numerous active TFs with those in the mammalian neocortex (Figure 5E–H). Among these, three representative TFs (*STAT6*, *THRB*, and *NR3C1*) were identified as key regulators due to their essential roles in neural pathways. Notably, *STAT6* was inactive in zebra finch EXs, while *THRB* and *NR3C1* were members of the intersection of active TFs across all six species, alongside *BACH2*, *BCLAF1*, *EP300*, *GABPA*, *NFE2L1*, and *SREBF2*. The conservation of these TFs was validated by their widespread expression in both the macaque and teleost pallium (Supplementary Figure S8D, S9H, I). *STAT6* is involved in the neuroimmunological response, including maintaining homeostatic microglia and regulating inflammatory mediators (olde Heuvel et al., 2019). Protein sequence alignment of *STAT6* across 12 species revealed high conservation among mammals, with the platypus exhibiting greater sequence similarity to other mammals than to avians, lizards, crocodiles, turtles, and frogs (internally conservative) (Figure 5I). These findings suggest that while amniotes share conserved TFs regulating neuroimmunological responses, different evolutionary branches may employ orthologous TFs in divergent neuroimmune pathways, which warrants additional verification.

In contrast, *NR3C1* and *THRB* protein sequences demonstrated high percent identity across amniotes (Figure 5J), with *THRB* also showing high scores in frogs (Supplementary Figure S9F). Both TFs are crucial for maintaining nervous system homeostasis. For example, *NR3C1* expression is reduced in individuals with histories of child abuse, schizophrenia, depression, and suicide, as well as in alcohol-dependent animal models (Gatta et al., 2021; Holmes et al., 2019). *THRB* plays critical physiological roles in the biological activity of thyroid hormones, development, growth, and metabolism (Liu et al., 2021; Liu & Brent, 2018). In brief, our findings imply that *NR3C1* function may be conserved in amniotes, while *THRB* function may be conserved in both amniotes and amphibians, indicating that homologous TFs may show varied transcriptomic conservation due to differences in protein sequences or regulatory networks.

To further investigate the role of TFs in shaping gene regulatory networks across amniotes, we analyzed gene modules containing at least one of the identified TFs in EXs from distinct cell classes (Figure 5K, L). Gene modules obtained from mammalian neocortex EXs, such as UL_STAT6_THRB and DL_STAT6_NR3C1, exhibited higher expression levels in mammalian and zebra finch cells compared to reptilian cells, whereas gene modules obtained from reptilian DC EXs, such as DC_STAT6, DC_THRB and DC_NR3C1, displayed similar expression across species. These findings signify that novel gene regulatory networks involving TFs have evolved in the mammalian and avian pallium, while ancestral regulatory networks existing in reptiles have been retained in other modern amniotes.

Further analysis of active regulons in reptilian pallial EXs and sauropsid DVR EXs identified 25 shared key TFs (Supplementary Figure S9E). From these, we discerned three gene modules, each containing at least one of these TFs. The HVC_GFRA1 gene module was highly expressed in both zebra finch DVR and mammalian neocortex EXs, RA_ELK4 was exclusively expressed in zebra finch EXs, and DVR_BCLAF1 was solely expressed in reptilian EXs (Supplementary Figure S9G). These results indicate that orthologous TFs may regulate different gene networks in pallial EXs across amniotes (Berto & Nowick, 2018; Wang et al., 2016), potentially contributing to the observed heterogeneity.

Building on earlier research (Colquitt et al., 2021; Norimoto et al., 2020; Tosches et al., 2018), our findings further elucidated the divergent and conserved signatures of EXs across the mammalian and reptilian pallium. TF expression patterns of reptilian DC EXs displayed greater similarity to those of mammalian neocortical EXs, while DVR EXs were

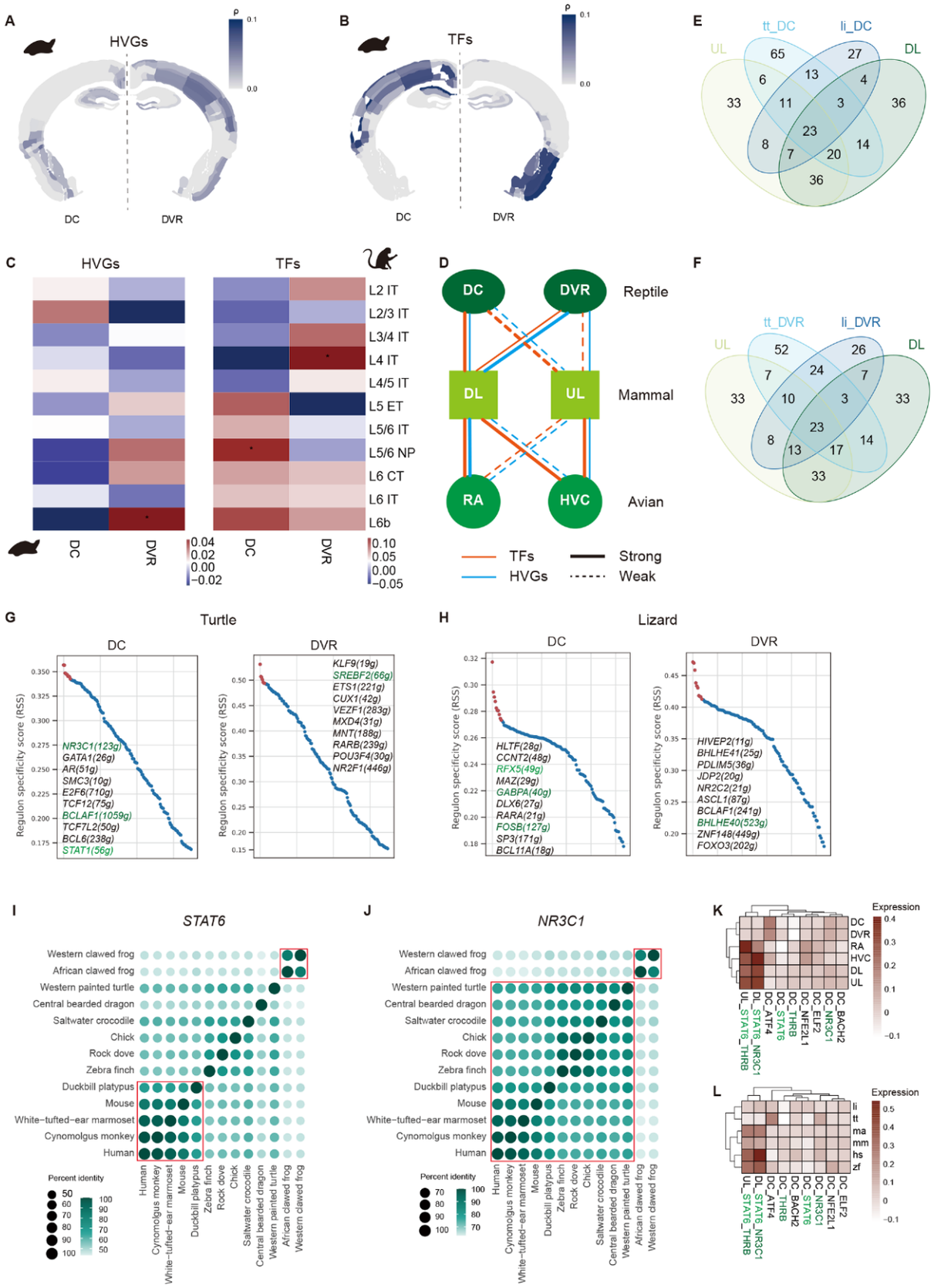


Figure 5 Heterogeneity among mammalian neocortex and reptilian DVR and DC

A, B: Spearman correlations between zebra finch EXs (DC and DVR) and mouse pallium, mapped onto coronal sections from ABA (Lein et al., 2007). C: Heatmap reflecting correlations between macaque EX subtypes and turtle DVR EX subtypes using TFs or HVGs (excluding TFs). D: Overview of correlations among amniote regional EXs. E, F: Venn diagram showing intersections of active TFs between mammalian neocortex, reptilian DC (E) and DVR (F) EXs. G, H: Top 10 active regulons in EXs in turtles (G) and lizards (H). I, J: Heatmap of *STAT6* (I) and *NR3C1* (J) protein sequence percent identity among amniotes and amphibians. K, L: Heatmap of gene module expression levels in amniote pallial EXs.

significantly correlated with mammalian EXs when non-TFs were analyzed. These observations suggest developmental homology between the reptilian DC and mammalian neocortex, alongside an ancestral evolutionary connection between the DVR and neocortex. Additionally, three TF candidates (*STAT6*, *NR3C1*, and *THRB*) were identified as shared between reptilian and mammalian pallial EXs. These TFs demonstrated varying levels of protein sequence conservation and were associated with distinct gene co-expression networks, indicating significant evolutionary divergence in their regulatory mechanisms. Notably, reptilian pallial EXs exhibited closer homology to mammalian DL neurons than to UL neurons, supporting the hypothesis that ULs may have originated from DLs (Naumann & Laurent, 2020).

DISCUSSION

The amniote pallium, essential for a range of functions, such as sensation, sleep, movement, and learning, has undergone remarkable structural and functional diversification throughout evolution (Güntürkün et al., 2020; Naumann & Laurent, 2020; Puelles et al., 2017; Roth, 2015), leading to the emergence of unique structures such as the mammalian neocortex and sauropsid DVR. In this study, we constructed a single-cell transcriptomic atlas of the macaque pallium and incorporated datasets from humans, mice, zebra finches, turtles, and lizards for cross-species comparison. Our analysis revealed both conserved and divergent gene expression and regulatory patterns among pallial neurons across amniotes.

Our findings highlighted conservation of INs across species, as evidenced by fewer species-specific DEGs in these populations, but evident divergence in species-preferred *PVALB*$^{+}$ IN subtypes. Among INs, MGE/CGE-derived INs exhibited greater conservation than LGE-derived INs, although LGE-derived INs showed notable similarities to CGE-derived INs. In contrast, EXs exhibited greater transcriptomic heterogeneity, with distinct species-preferred subtypes correlating with increasing organismal complexity (Lamanna et al., 2023; Musser et al., 2021; Naumann & Laurent, 2020; Norimoto et al., 2020). Mammalian and sauropsid EXs shared many transcriptomic commonalities, but also distinct differences, pointing to shared developmental origins and potential convergent or parallel evolution (Colquitt et al., 2021; Güntürkün, 2012; Hintermann et al., 2022; Roth, 2015; Yokoyama & Pollock, 2012). In addition, TFs, such as *DLX2*, *RARB*, *STAT6*, *NR3C1*, and *THRB*, emerged as key conserved regulators among pallial neurons across distantly related amniotes. Conversely, non-TFs appeared to play a pivotal role in maintaining homology among pallial neurons of closely related species. These findings enhance our understanding of the evolutionary signatures of the amniote pallium and provide the foundation for future explorations into the molecular features of brain complexity.

This study explored the conserved and divergent aspects of gene expression and regulation in pallial neurons, shedding light on the evolutionary characteristics and trajectories of the amniote pallium. The evolution of neuronal cell types has become a focal area of research in recent years (Briscoe et al., 2018; Dugas-Ford et al., 2012; Hodge et al., 2019; Musser et al., 2021; Tosches, 2021), presenting challenges in defining homologous cell types —a task that demands consideration of developmental origins, function, multi-omics features, and morphology. Advances in single-cell technologies have alleviated some difficulties, allowing for more precise classification of homologous cell types across species (Colquitt et al., 2021; Ma et al., 2022; Norimoto et al., 2020; Tosches et al., 2018). For example, while the conserved expression patterns of INs allow for their classification into homologous subtypes across species, rapidly evolving cell types, like EXs, pose greater complexity due to their divergent transcriptomic profiles and phenotypic diversity. TFs have emerged as relatively conserved regulators across amniotes (Colquitt et al., 2021; Tosches, 2021; Tosches et al., 2018), providing a foundation for understanding homology. However, significant evolutionary modifications in their sequences or structures may lead to shifts in regulatory networks, cellular morphology, and function. This poses a conundrum: should cells with pronounced phenotypic divergence but shared ancestry be considered homologous, or do they represent entirely novel cell types? Moreover, heavy reliance on model species for gene function studies introduces uncertainties about the applicability of findings to non-model species. Variability in the availability and quality of spatial and molecular data across species, particularly between well-studied mammals and less-studied groups like birds and reptiles, further complicates the accurate identification of certain subpopulations. For example, both prior studies and our results reveal substantial differences between mammalian UL EXs and those in sauropsids, indicating that UL EXs may represent an entirely new subtype (Naumann & Laurent, 2020; Tosches & Laurent, 2019). Future research should aim to standardize criteria for identifying homologous cell types and expand foundational studies to non-model organisms at pivotal evolutionary junctures to clarify the evolutionary paths of the brain, pallium, and neurons. Key approaches could include fine mapping of brain regions in non-model organisms through ISH, exploration of neural pathways via connectomics, application of spatial transcriptomics to elucidate gene expression characteristics in different brain regions, and integration of behavioral and electrophysiological techniques to validate the biological functions of various brain regions.

Mammals, reptiles, and avians share a common ancestor and possess pallial frameworks that largely adhere to the tetrapartite model (Cárdenas & Borrell, 2020; Puelles et al., 2017). Despite this shared blueprint, these taxa exhibit significant interspecies variations in structural organization, cellular composition, and molecular profiles. In mammals, the neocortex dominates the pallium and serves as the primary center for advanced cognitive functions, while in birds, the DVR occupies a similar role, functioning as a hub for complex behaviors and intelligence (Güntürkün, 2012; Hara et al., 2012; Roth, 2015). In contrast, the reptilian pallium, containing regions developmentally homologous to both the mammalian neocortex and avian DVR, is often regarded as the “original version” of the amniote pallium (Güntürkün et al., 2020; Karten, 2015; Naumann & Laurent, 2020; Puelles et al., 2017). Our results indicated that EXs in the reptilian DC resembled DL neurons in the mammalian neocortex, while INs in both reptilian and zebra finch DVRs shared lineage markers characteristic of LGE-derived INs. However, significant differences were also observed, consistent with previous studies (Colquitt et al., 2021; Tosches et al., 2018). For instance, species-specific cell clusters were identified in the mammalian neocortex, while the gene expression profiles of EXs in the avian DVR exhibited significant divergence from their reptilian counterparts. Additionally, similarities between

the mammalian neocortex and avian DVR, such as divergent *PVALB*$^{+}$ IN subtypes and analogous gene expression patterns observed in zebra finch RA and HVC nuclei with mammalian cortical layers, may signify convergent evolution (Hintermann et al., 2022; Yokoyama & Pollock, 2012). The evolutionary trajectories of amniote pallial structures may be shaped by variations in TFs (Arendt et al., 2016), as we distinguished key TFs with varying degrees of conservation that exhibited species-restricted similarities in protein sequences and co-expression networks. Although development and evolution are distinct processes —development representing an orderly progression based on the genomic blueprint, and evolution reflecting the long-term accumulation of adaptive traits —development often mirrors certain aspects of evolutionary history (Kuratani et al., 2022). This interplay is especially important when defining homologous brain regions or cell types. Future investigations should prioritize studies on pivotal species, such as reptiles and oviparous mammals, as well as the role of TFs in shaping regional and cellular identities. Integrating developmental studies with evolutionary research will be crucial for clarifying the complex evolutionary history of the amniote pallium.

Our study has several areas that could be enhanced and refined. While the pallium encompasses a vast region, our analysis were restricted to specific regions within each species. This limitation raises the possibility that some observed differences may arise from variability across pallial regions rather than true interspecies divergence. Nevertheless, we believe that interspecies differences are more significant than intraspecies regional differences within the pallium. The patterns of conservation and divergence identified in our study are supported by previous research, providing confidence in the robustness of these findings. Comparative transcriptomic analyses offer valuable insights into the molecular underpinnings of evolutionary processes, such as the development of regulatory networks and evolution of cell type-specific characteristics. However, to achieve a more comprehensive understanding of these processes, it is essential to integrate transcriptomic data with other omics datasets. For example, combining transcriptomics with genomics, proteomics, and phenotype-related studies could elucidate the fundamental drivers of transcriptomic changes during evolution and their impact on related pathways and phenotypes. Additionally, combining transcriptomic and phenotypic data through comparative morphology, physiology, behavior, and functional genomics would provide a deeper understanding of the biological significance of observed transcriptomic patterns. A persistent challenge in evolutionary studies, including our own, is the limited number of species available for comparison. While our study included a broader range of species and provided a more comprehensive analysis than many prior efforts, this remains a critical area for improvement. Expanding the scope of future studies to include a wider array of species and a more detailed examination of diverse pallial regions will likely yield more robust and reliable results, further advancing our understanding of the evolutionary dynamics of the amniote pallium.

DATA AVAILABILITY

The raw sequencing data generated in this study were deposited in the CNGB Nucleotide Sequence Archive (CNSA: https://db.cngb.org/cnsa) under accession code CNP0003026. Sample numbers include MK-002-1L-10, MK-002-2L-44, MK-002-2L-45, MK-003-1L-10, MK-003-1L-9, MK-003-2L-44, and MK-003-2L-45. The macaque expression matrix is available under accession code CSE0000427. The code can be found at: https://github.com/FupaulHuang/AmniotePalliumTranscriptome. Datasets generated in this study were also deposited in the Genome Sequence Archive (GSA) database (https://ngdc.cncb.ac.cn/gsa/) (accession number PRJCA031422), Science Data Bank (doi: 10.57760/sciencedb.17214), and NCBI database (BioProjectID PRJNA1175883).

SUPPLEMENTARY DATA

Supplementary data to this article can be found online.

COMPETING INTERESTS

The authors declare that they have no competing interests.

AUTHORS' CONTRIBUTIONS

Z.K.Z., S.P.L., and F.B.Q.H. conceived and designed the study. F.B.Q.H. and K.L. wrote the manuscript and Z.K.Z., Y.N.L., D.Y.C., S.P.L., K.L., and F.B.Q.H. contributed to the discussion and revision of the manuscript. Y.L., S.Y.J., Z.H.L., and. Y.N.S contributed to sample collection. Z.K.Z, S.P.L., Y.N.L., and F.B.Q.H. participated in guiding and providing suggestions for the study. F.B.Q.H., K.L., P.F.L., Y.R.Z., and Z.Y.Z. provided technical support and conducted data analysis. All authors read and approved the final version of the manuscript.

ACKNOWLEDGMENTS

We thank China National GeneBank for providing technical support.

REFERENCES

Aboitiz F. 2011. Genetic and developmental homology in amniote brains. Toward conciliating radical views of brain evolution. *Brain Research Bulletin*, **84**(2): 125–136.

Aibar S, González-Blas CB, Moerman T, et al. 2017. SCENIC: single-cell regulatory network inference and clustering. *Nature Methods*, **14**(11): 1083–1086.

Arendt D, Musser JM, Baker CVH, et al. 2016. The origin and evolution of cell types. *Nature Reviews Genetics*, **17**(12): 744–757.

Benton M J, Donoghue P C. 2007. Paleontological evidence to date the tree of life. *Molecular Biology and Evolution*, **24**(1): 26–53.

Berto S, Nowick K. 2018. Species-specific changes in a primate transcription factor network provide insights into the molecular evolution of the primate prefrontal cortex. *Genome Biology and Evolution*, **10**(8): 2023–2036.

Briscoe SD, Albertin CB, Rowell JJ, et al. 2018. Neocortical association cell types in the forebrain of birds and alligators. *Current Biology*, **28**(5): 686–696. e6.

Briscoe SD, Ragsdale CW. 2018. Molecular anatomy of the alligator dorsal telencephalon. *Journal of Comparative Neurology*, **526**(10): 1613–1646.

Butler A, Hoffman P, Smibert P, et al. 2018. Integrating single-cell transcriptomic data across different conditions, technologies, and species. *Nature Biotechnology*, **36**(5): 411–420.

Butler AB. 1994. The evolution of the dorsal pallium in the telencephalon of amniotes: cladistic analysis and a new hypothesis. *Brain Research Reviews*, **19**(1): 66–101.

Butler AB, Reiner A, Karten HJ. 2011. Evolution of the amniote pallium and the origins of mammalian neocortex. *Annals of the New York Academy of Sciences*, **1225**: 14–27.

Cárdenas A, Borrell V. 2020. Molecular and cellular evolution of corticogenesis in amniotes. *Cellular and Molecular Life Sciences*, **77**(8): 1435–1460.

Chen A, Sun YD, Lei Y, et al. 2023. Single-cell spatial transcriptome reveals cell-type organization in the macaque cortex. *Cell*, **186**(17): 3726–3743. e24.

Colquitt BM, Merullo DP, Konopka G, et al. 2021. Cellular transcriptomics reveals evolutionary identities of songbird vocal circuits. *Science*, **371**(6530): eabd9704.

Dugas-Ford J, Rowell JJ, Ragsdale CW. 2012. Cell-type homologies and the origins of the neocortex. *Proceedings of the National Academy of Sciences of the United States of America*, **109**(42): 16974–16979.

Fame RM, Dehay C, Kennedy H, et al. 2017. Subtype-specific genes that characterize subpopulations of callosal projection neurons in mouse identify molecularly homologous populations in macaque cortex. *Cerebral Cortex*, **27**(3): 1817–1830.

Gatta E, Grayson DR, Auta J, et al. 2021. Genome-wide methylation in alcohol use disorder subjects: implications for an epigenetic regulation of the cortico-limbic glucocorticoid receptors (NR3C1). *Molecular Psychiatry*, **26**(3): 1029–1041.

Glezer II, Hof PR, Leranth C, et al. 1993. Calcium-binding protein-containing neuronal populations in mammalian visual cortex: a comparative study in whales, insectivores, bats, rodents, and primates. *Cerebral Cortex*, **3**(3): 249–272.

Güntürkün O. 2012. The convergent evolution of neural substrates for cognition. *Psychological Research*, **76**(2): 212–219.

Güntürkün O, Stacho M, Ströckens F. 2020. The brains of reptiles and birds. *In*: Kaas JK. Evolutionary Neuroscience. 2nd ed. London: Academic Press, 159–212.

Hain D, Gallego-Flores T, Klinkmann M, et al. 2022. Molecular diversity and evolution of neuron types in the amniote brain. *Science*, **377**(6610): eabp8202.

Han L, Wei XY, Liu CY, et al. 2022. Cell transcriptomic atlas of the non-human primate *Macaca fascicularis*. *Nature*, **604**(7907): 723–731.

Hara E, Rivas MV, Ward JM, et al. 2012. Convergent differential regulation of parvalbumin in the brains of vocal learners. *PLoS One*, **7**(1): e29457.

Hegarty BE, Gruenhagen GW, Johnson ZV, et al. 2024. Spatially resolved cell atlas of the teleost telencephalon and deep homology of the vertebrate forebrain. *Communications Biology*, **7**(1): 612.

Hintermann A, Guerreiro I, Lopez-Delisle L, et al. 2022. Developmental and evolutionary comparative analysis of a regulatory landscape in mouse and chicken. *Development*, **149**(12): dev200594.

Hodge RD, Bakken TE, Miller JA, et al. 2019. Conserved cell types with divergent features in human versus mouse cortex. *Nature*, **573**(7772): 61–68.

Holmes Jr L, Shutman E, Chinaka C, et al. 2019. Aberrant epigenomic modulation of glucocorticoid receptor gene (NR3C1) in early life stress and major depressive disorder correlation: systematic review and quantitative evidence synthesis. *International Journal of Environmental Research and Public Health*, **16**(21): 4280.

Huang LW, Ma ZY, Yu LT, et al. 2023. Deep spiking neural networks with high representation similarity model visual pathways of macaque and mouse. *Proceedings of the AAAI Conference on Artificial Intelligence*, **37**(1): 31–39.

Jarvis ED, Güntürkün O, Bruce L, et al. 2005. Avian brains and a new understanding of vertebrate brain evolution. *Nature Reviews Neuroscience*, **6**(2): 151–159.

Jorstad NL, Song JHT, Exposito-Alonso D, et al. 2023. Comparative transcriptomics reveals human-specific cortical features. *Science*, **382**(6667): eade9516.

Karten HJ. 1991. Homology and evolutionary origins of the 'neocortex'. *Brain, Behavior and Evolution*, **38**(4–5): 264–272.

Karten HJ. 2015. Vertebrate brains and evolutionary connectomics: on the origins of the mammalian 'neocortex'. *Philosophical Transactions of the Royal Society B: Biological Sciences*, **370**(1684): 20150060.

Koszinowski S, Boerries M, Busch H, et al. 2015. RARβ regulates neuronal cell death and differentiation in the avian ciliary ganglion. *Developmental Neurobiology*, **75**(11): 1204–1218.

Kuratani S, Uesaka M, Irie N. 2022. How can recapitulation be reconciled with modern concepts of evolution?. *Journal of Experimental Zoology Part B: Molecular and Developmental Evolution*, **338**(1–2): 28–35.

Kverková K, Marhounová L, Polonyiová A, et al. 2022. The evolution of brain neuron numbers in amniotes. *Proceedings of the National Academy of Sciences of the United States of America*, **119**(11): e2121624119.

Lamanna F, Hervas-Sotomayor F, Oel AP, et al. 2023. A lamprey neural cell type atlas illuminates the origins of the vertebrate brain. *Nature Ecology & Evolution*, **7**(10): 1714–1728.

Lei Y, Cheng MN, Li ZH, et al. 2022. Spatially resolved gene regulatory and disease-related vulnerability map of the adult Macaque cortex. *Nature Communications*, **13**(1): 6747.

Lein ES, Hawrylycz MJ, Ao N, et al. 2007. Genome-wide atlas of gene expression in the adult mouse brain. *Nature*, **445**(7124): 168–176.

Li Z, Sun Y, Ding L, et al. 2023. Deciphering the distinct transcriptomic and gene regulatory map in adult macaque basal ganglia cells. *GigaScience*, **12**: giad095.

Liang C, Musser JM, Cloutier A, et al. 2018. Pervasive correlated evolution in gene expression shapes cell and tissue type transcriptomes. *Genome Biology and Evolution*, **10**(2): 538–552.

Liao K, Xiang Y, Huang FBQ, et al. 2024. Spatial and single-nucleus transcriptomics decoding the molecular landscape and cellular organization of avian optic tectum. *Iscience*, **27**(2): 109009.

Liu M, Zhang XD, Wang Y. 2021. Curcumin alleviates $A\beta_{42}$-induced neuronal metabolic dysfunction via the Thrb/SIRT3 Axis and improves cognition in APP_{TG} mice. *Neurochemical Research*, **46**(12): 3166–3178.

Liu YY, Brent GA. 2018. Thyroid hormone and the brain: mechanisms of action in development and role in protection and promotion of recovery after brain injury. *Pharmacology & Therapeutics*, **186**: 176–185.

Loomba S, Straehle J, Gangadharan V, et al. 2022. Connectomic comparison of mouse and human cortex. *Science*, **377**(6602): eabo0924.

Lust K, Maynard A, Gomes T, et al. 2022. Single-cell analyses of axolotl telencephalon organization, neurogenesis, and regeneration. *Science*, **377**(6610): eabp9262.

Luzzati F. 2015. A hypothesis for the evolution of the upper layers of the neocortex through co-option of the olfactory cortex developmental program. *Frontiers in Neuroscience*, **9**: 162.

Ma SJ, Skarica M, Li Q, et al. 2022. Molecular and cellular evolution of the primate dorsolateral prefrontal cortex. *Science*, **377**(6614): eabo7257.

Marcucio RS, Cordero DR, Hu DN, et al. 2005. Molecular interactions coordinating the development of the forebrain and face. *Developmental Biology*, **284**(1): 48–61.

McGinnis CS, Murrow LM, Gartner ZJ. 2019. DoubletFinder: doublet detection in single-cell RNA sequencing data using artificial nearest neighbors. *Cell Systems*, **8**(4): 329–337. e4.

Miller JA, Ding SL, Sunkin SM, et al. 2014. Transcriptional landscape of the prenatal human brain. *Nature*, **508**(7495): 199–206.

Montiel JF, Aboitiz F. 2018. Homology in amniote brain evolution: the rise of molecular evidence. *Brain Behavior and Evolution*, **91**(2): 59–64.

Musser JM, Schippers KJ, Nickel M, et al. 2021. Profiling cellular diversity in sponges informs animal cell type and nervous system evolution. *Science*, **374**(6568): 717–723.

Nagy C, Maitra M, Tanti A, et al. 2020. Single-nucleus transcriptomics of the prefrontal cortex in major depressive disorder implicates oligodendrocyte precursor cells and excitatory neurons. *Nature Neuroscience*, **23**(6): 771–781.

Naumann R, Laurent G. 2020. Function and evolution of the reptilian cerebral cortex. *In*: Kaas JK. Evolutionary Neuroscience. 2nd ed. London: Academic Press, 213–245.

Nieder A, Wagener L, Rinnert P. 2020. A neural correlate of sensory

consciousness in a corvid bird. *Science*, **369**(6511): 1626–1629.
Nomura T, Murakami Y, Gotoh H, et al. 2014. Reconstruction of ancestral brains: exploring the evolutionary process of encephalization in amniotes. *Neuroscience Research*, **86**: 25–36.
Norimoto H, Fenk LA, Li HH, et al. 2020. A claustrum in reptiles and its role in slow-wave sleep. *Nature*, **578**(7795): 413–418.
olde Heuvel F, Holl S, Chandrasekar A, et al. 2019. STAT6 mediates the effect of ethanol on neuroinflammatory response in TBI. *Brain, Behavior, and Immunity*, **81**: 228–246.
Pessoa L, Medina L, Hof PR, et al. 2019. Neural architecture of the vertebrate brain: implications for the interaction between emotion and cognition. *Neuroscience & Biobehavioral Reviews*, **107**: 296–312.
Puelles L. 2001. Brain segmentation and forebrain development in amniotes. *Brain Research Bulletin*, **55**(6): 695–710.
Puelles L, Kuwana E, Puelles E, et al. 2000. Pallial and subpallial derivatives in the embryonic chick and mouse telencephalon, traced by the expression of the genes Dlx‐2, Emx‐1, Nkx‐2.1, Pax‐6, and Tbr‐1. *Journal of Comparative Neurology*, **424**(3): 409–438.
Puelles L, Sandoval JE, Ayad A, et al. 2017. The pallium in reptiles and birds in the light of the updated tetrapartite pallium model. *In*: Kaas J. Evolution of Nervous Systems. 2nd ed. Oxford: Amsterdam, Boston: Academic Press, 519–555.
Roth G. 2015. Convergent evolution of complex brains and high intelligence. *Philosophical Transactions of the Royal Society B: Biological Sciences*, **370**(1684): 20150049.
Sherwood CC, Raghanti MA, Stimpson CD, et al. 2010. Inhibitory interneurons of the human prefrontal cortex display conserved evolution of the phenotype and related genes. *Proceedings of the Royal Society B: Biological Sciences*, **277**(1684): 1011–1020.
Squair JW, Gautier M, Kathe C, et al. 2021. Confronting false discoveries in single-cell differential expression. *Nature Communications*, **12**(1): 5692.
Srour M, Caron V, Pearson T, et al. 2016. Gain‐of‐function mutations in *RARB* cause intellectual disability with progressive motor impairment. *Human Mutation*, **37**(8): 786–793.
Su-Feher L, Rubin AN, Silberberg SN, et al. 2022. Single cell enhancer activity distinguishes GABAergic and cholinergic lineages in embryonic mouse basal ganglia. *Proceedings of the National Academy of Sciences of the United States of America*, **119**(15): e2108760119.
Svensson V, Vento-Tormo R, Teichmann SA. 2018. Exponential scaling of single-cell RNA-seq in the past decade. *Nature Protocols*, **13**(4): 599–604.
Tan YF, Testa JR. 2021. DLX genes: roles in development and cancer. *Cancers*, **13**(12): 3005.
Tang FC, Barbacioru C, Wang YZ, et al. 2009. mRNA-Seq whole-transcriptome analysis of a single cell. *Nature Methods*, **6**(5): 377–382.
Tasic B, Yao ZZ, Graybuck LT, et al. 2018. Shared and distinct transcriptomic cell types across neocortical areas. *Nature*, **563**(7729): 72–78.
Torigoe M, Yamauchi K, Kimura T, et al. 2016. Evidence that the laminar fate of LGE/CGE-derived neocortical interneurons is dependent on their progenitor domains. *Journal of Neuroscience*, **36**(6): 2044–2056.
Tosches MA. 2021. From cell types to an integrated understanding of brain evolution: the case of the cerebral cortex. *Annual Review of Cell and Developmental Biology*, **37**: 495–517.
Tosches MA, Laurent G. 2019. Evolution of neuronal identity in the cerebral cortex. *Current Opinion in Neurobiology*, **56**: 199–208.
Tosches MA, Yamawaki TM, Naumann RK, et al. 2018. Evolution of pallium, hippocampus, and cortical cell types revealed by single-cell transcriptomics in reptiles. *Science*, **360**(6391): 881–888.
Wagner GP. 2014. Homology, Genes, and Evolutionary Innovation. Princeton, Oxford: Princeton University Press.
Wang P, Zhao DJ, Rockowitz S, et al. 2016. Divergence and rewiring of regulatory networks for neural development between human and other species. *Neurogenesis*, **3**(1): e1231495.
Wei XY, Fu SL, Li HB, et al. 2022. Single-cell Stereo-seq reveals induced progenitor cells involved in axolotl brain regeneration. *Science*, **377**(6610): eabp9444.
Wolf FA, Angerer P, Theis FJ. 2018. SCANPY: large-scale single-cell gene expression data analysis. *Genome Biology*, **19**(1): 15.
Woych J, Ortega Gurrola A, Deryckere A, et al. 2022. Cell-type profiling in salamanders identifies innovations in vertebrate forebrain evolution. *Science*, **377**(6610): eabp9186.
Yamashita W, Nomura T. 2017. The neocortex and dorsal ventricular ridge: functional convergence and underlying developmental mechanisms. *In*: Shigeno S, Murakami Y, Nomura T. Brain Evolution by Design: from Neural Origin to Cognitive Architecture. Tokyo: Springer, 291–309.
Yao ZZ, van Velthoven CTJ, Nguyen TN, et al. 2021. A taxonomy of transcriptomic cell types across the isocortex and hippocampal formation. *Cell*, **184**(12): 3222–3241. e26.
Yokoyama KD, Pollock DD. 2012. SP transcription factor paralogs and DNA-binding sites coevolve and adaptively converge in mammals and birds. *Genome Biology and Evolution*, **4**(11): 1102–1117.
Yu GC, Smith DK, Zhu HC, et al. 2017. GGTREE: an R package for visualization and annotation of phylogenetic trees with their covariates and other associated data. *Methods in Ecology and Evolution*, **8**(1): 28–36.
Yu GC, Wang LG, Han YY, et al. 2012. clusterProfiler: an R package for comparing biological themes among gene clusters. *OMICS: A Journal of Integrative Biology*, **16**(5): 284–287.
Zenker M, Bunt J, Schanze I, et al. 2019. Variants in nuclear factor I genes influence growth and development. *American Journal of Medical Genetics Part C: Seminars in Medical Genetics*, **181**(4): 611–626.

Mi et al. *Zool. Res.* 2025, 46(1): 209−224
https://doi.org/10.24272/j.issn.2095-8137.2024.240
https://cstr.cn/32248.14.zr.2024.240

ZR | Zoological Research

Article Open Access

Intranasal iron administration induces iron deposition, immunoactivation, and cell-specific vulnerability in the olfactory bulb of C57BL/6 mice

Xiao-Qing Mi[1,#], Bao-Chen Liu[1,#], Le Qu[1], Yu Yuan[1,2], Hui Li[1], Ao-Yang Xu[1], Yu-Lin Zhang[1], Jun-Xia Xie[1,*], Ning Song[1,*]

[1] *School of Basic Medicine*, *Institute of Brain Science and Disease*, *Shandong Provincial Key Laboratory of Pathogenesis and Prevention of Brain Diseases*, *Qingdao University*, *Qingdao*, *Shandong*, 266071, *China*

[2] *School of Life Science and Technology*, *ShanghaiTech University*, *Shanghai* 201210, *China*

ABSTRACT

Iron is the most abundant transition metal in the brain and is essential for brain development and neuronal function; however, its abnormal accumulation is also implicated in various neurological disorders. The olfactory bulb (OB), an early target in neurodegenerative diseases, acts as a gateway for environmental toxins and contains diverse neuronal populations with distinct roles. This study explored the cell-specific vulnerability to iron in the OB using a mouse model of intranasal administration of ferric ammonium citrate (FAC). Olfactory function was assessed through olfactory discrimination tests, while iron levels in OB tissues, cerebrospinal fluid (CSF), and serum were quantified using inductively coupled plasma mass spectrometry (ICP-MS), immunohistochemical staining, and iron assays. Transcriptomic changes and immune responses were assessed using RNA sequencing and immune cell infiltration analysis. Results showed that intranasal FAC administration impaired olfactory function, accompanied by iron deposition in the olfactory mucosa and OB, as well as damage to olfactory sensory neurons. Notably, these effects occurred without elevations in CSF or serum iron levels. OB iron accumulation activated multiple immune cells, including microglia and astrocytes, but did not trigger ferroptosis. Spatial transcriptomic sequencing of healthy adult mouse OBs revealed significant cellular heterogeneity, with an abundance of neuroglia and neurons. Among neurons, GABAergic neurons were the most prevalent, followed by glutamatergic and dopaminergic neurons, while cholinergic and serotonergic neurons were sparsely distributed. Under iron-stressed conditions, oligodendrocytes, dopaminergic neurons, and glutamatergic neurons exhibited significant damage, while GABAergic neurons remained unaffected. These findings highlight the selective vulnerability of neuronal and glial populations to iron-induced stress, offering novel insights into the loss of specific cell types in the OB during iron dysregulation.

Keywords: Intranasal administration; Olfactory bulb; Iron; Ferroptosis; Immune response

INTRODUCTION

Iron, the most abundant transition metal in the brain, is essential for brain development and central nervous system (CNS) function (Lotan et al., 2023), playing a crucial role in myelin and neurotransmitter synthesis, metabolism, and neuronal function (Möller et al., 2019; Ward et al., 2014). Despite its essential roles, abnormal iron deposition has been implicated in various CNS disorders, including Parkinson's disease (PD), Alzheimer's disease (AD), amyotrophic lateral sclerosis, multiple sclerosis, depression, and migraines (Ward et al., 2014; Wu et al., 2023; Zhou et al., 2020).

Pathological accumulation of iron in tissues serves as a catalyst for the Fenton reaction, exacerbating reactive oxygen species (ROS) production, leading to oxidative stress and distinct forms of cell death, such as ferroptosis, apoptosis, necroptosis, and pyroptosis (Galaris & Pantopoulos, 2008; Puntarulo, 2005; Zhou et al., 2018). Ferroptosis, an iron-dependent and lipid peroxidation-driven form of non-apoptotic cell death, is a prominent mechanism underlying iron toxicity in the brain (Dang et al., 2022; Tan et al., 2021; Tang et al., 2021; Ward et al., 2014; Yan et al., 2021). Iron and dopamine are considered a toxic couple, with iron promoting the dopamine metabolic pathway, leading to the production of neurotoxic species that promote neuronal death (Hare & Double, 2016), rendering dopaminergic neurons particularly vulnerable. Brain imaging and neuropathological studies have

This is an open-access article distributed under the terms of the Creative Commons Attribution Non-Commercial License (http://creativecommons.org/licenses/by-nc/4.0/), which permits unrestricted non-commercial use, distribution, and reproduction in any medium, provided the original work is properly cited.

Copyright ©2025 Editorial Office of Zoological Research, Kunming Institute of Zoology, Chinese Academy of Sciences

Received: 18 September 2024; Accepted: 14 October 2024; Online: 15 October 2024

Foundation items: This work was supported by the National Natural Science Foundation of China (32471188, 32170984, 82301787)

[#]Authors contributed equally to this work

*Corresponding authors, E-mail: jxiaxie@public.qd.sd.cn; ningsong@qdu.edu.cn

consistently demonstrated a correlation between iron deposition in the substantia nigra (SN) pars compacta and dopaminergic neuronal loss in PD (Biondetti et al., 2021; Depierreux et al., 2021). Single-cell RNA sequencing (scRNA-seq) of zebrafish brains exposed to manganese recently identified dopaminergic neurons as the most sensitive to manganese-related neurotoxicity (Zhang et al., 2023). However, understanding of the differential vulnerability of neuronal subtypes to iron toxicity remains limited.

Unlike other brain regions, the olfactory bulb (OB) directly receives inputs from the olfactory epithelium (OE) in the nasal cavity, a key component of the olfactory mucosa (OM), where olfactory sensory neurons (OSN) project their axons to the OB (Lochhead & Thorne, 2012; Mori et al., 2000; Sobiesk & Munakomi, 2023). This unique anatomical connection facilitates rapid access to the CNS via intranasal administration, enabling substances and proteins to traverse intracellular pathways through receptor-mediated endocytosis or paracellular pathways via intercellular junctions (Crowe et al., 2018; Zhang et al., 2021). Studies have demonstrated that intranasally administered gold nanorods reach the OB within minutes and subsequently distribute to other brain regions over time (Han et al., 2023). Intranasal delivery has also proven effective for transporting drugs and stem cells to the OB and other brain regions (Itokazu et al., 2021; Yu-Taeger et al., 2019). The OB is characterized by a heterogeneous neuronal composition, containing populations with distinct functions and properties (Li et al., 2020; Nagayama et al., 2014; Zhou et al., 2023). Each hemisphere of the mouse OB contains approximately 500 000 neurons (Zeppilli et al., 2021), making it a valuable model for studying neuronal diversity and cell-specific processes.

In the present study, we explored cell-specific vulnerability to iron in the OB using a mouse model of intranasal administration of ferric ammonium citrate (FAC). Repeated FAC administration every other day induced olfactory dysfunction, OM iron deposition, and OSN damage. While significant OB iron deposition was observed, along with a pronounced immune response involving microglia and astrocytes, ferroptosis was notably absent. Iron deposition in the OB resulted in damage to oligodendrocytes, glutamatergic neurons, and dopaminergic neurons, while GABAergic neurons remained unaffected. These findings provide insight into the differential susceptibility of neuronal and glial populations to iron toxicity and offer a foundation for understanding the specific patterns of cell loss in CNS disorders associated with iron accumulation.

MATERIALS AND METHODS

Mice and treatment

Eight-week-old male C57BL/6 mice were purchased from the Jiangsu GemPharmatech Company (China). The mice were housed in a clean facility with unrestricted access to water and food, maintained under a 12 h light/dark circadian cycle at a temperature of 19±2℃ and relative humidity of 50%±5%. The mice were randomly assigned to either a control group or FAC-treated group. Mice in the FAC-treated group received intranasal administration of FAC at a dose of 200 mg/kg (250 mg/mL) twice every other day. Control mice were administered an equivalent volume of saline intranasally. All animal experiments were conducted in accordance with the NIH Guide for the Care and Use of Laboratory Animals and were approved by the Institutional Animal Care and Use Committee at Qingdao University (QDU-AEC-2022116, 1 March 2022). Furthermore, the study was conducted according to the principles outlined in the Declaration of Helsinki.

Olfactory discrimination tests

Mice were fasted for 24 h prior to the olfactory experiments. In the olfactory preference test, a customized test box (45 cm length×35 cm width×25 cm height) was divided into two identical compartments connected by a central joint. One compartment contained 1 g of peanut butter as the preferred odor, while the other contained 50 μL of paraffin oil as a neutral odor. During the test, each mouse was placed in the central joint and allowed to move freely for 5 min. The EthoVision XT7 system recorded cumulative time spent in each compartment.

For the buried food-seeking test, mice were acclimated to a cage (15 cm length×25 cm width×10 cm height) for 10 min before the experiment. After acclimation, each mouse was removed, and a 2 g food pellet was buried approximately 0.5 cm beneath the surface of a 3.0 cm thick bedding layer. The mouse was then returned to the cage, and the time taken to locate the food pellet using its front paw or nose was recorded. If a mouse failed to find the food pellet within 5 min, the test was terminated, and latency was recorded as 300 s.

Perl's-diaminobenzidine (DAB) /immunohistochemical (IHC) staining

Mice were anesthetized and underwent cardiac perfusion with saline. The nasal cavity was decalcified by immersion in 0.01 mol/L phosphate-buffered saline (PBS) containing 10% EDTA (pH=7.6) for 2 weeks, while the brain was fixed in 4% paraformaldehyde (PFA) for 24 h, followed by replacement with 30% sucrose solution for 48 h. The OM or OB was sliced into 20 μm thick sections using a freezing microtome (CM1950, Leica, Germany). For Perl's-DAB staining, sections were soaked in 4% PFA for 5 min, rinsed in ddH_2O for 1 min, and incubated for 30 min at room temperature in a 1:1 solution of 2% potassium ferricyanide (P3289, Sigma, Germany) and 2% hydrochloric acid. The sections were then washed twice with 0.01 mol/L PBS, with each wash lasting 10 min, followed by incubation in 3% hydrogen peroxide of methanol for 20 min at room temperature. After two additional washes in 0.01 mol/L PBS, the sections were stained with DAB (ZLI-9019, ZSGB-BIO, China) for 10 min at room temperature, and the reaction was terminated by rinsing in ddH_2O.

For IHC staining, the sections were soaked in 4% PFA for 10 min, washed three times in 0.01 mol/L PBS, and soaked in 0.01 mol/L PBS containing 0.3% Triton X-100 (BS084, Biosharp, China) and 5% donkey serum (017-000-001, Jackson ImmunoResearch, USA) for 1 h at room temperature. The sections were then incubated overnight at 4℃ with primary antibodies, including olfactory marker protein (OMP; ab183947, Abcam, UK; 1:500), neuronal nuclei (NeuN; MAB377, ZooMAB, USA; 1:500), Iba-1 (17198, CST, USK; 1:200), glial fibrillary acidic protein (GFAP; 3670SS, CST, USA; 1:300), Olig2 (AF2418, R&D Systems, USA; 1:500), and tyrosine hydroxylase (TH; AB152, Millipore, USA; 1:3 000). The following day, the sections were washed three times with 0.01 mol/L PB, incubated with 3% hydrogen peroxide in methanol for 20 min at room temperature, washed twice with 0.01 mol/L PBS, and incubated with secondary antibodies, including goat anti-rabbit IgG-horseradish peroxidase (HRP)

(abs20002, Absin, China; 1:500), goat anti-Mouse IgG-HRP (abs20001, Absin, China; 1:500), and rabbit anti-goat IgG-HRP (abs20005, Absin, China; 1:500) for 2 h at room temperature. Staining was developed using DAB (ZLI-9019, ZSGB-BIO, China) for 10 min, and terminated in ddH_2O.

For Perl's-DAB and IHC double labeling, sections were washed twice with 0.01 mol/L PBS following Perl's-DAB staining and incubated in 0.01–0.02 mol/L NaOH for 10 min at room temperature. After washing three times with 0.01 mol/L PBS, IHC staining was performed and developed using blue DAB (36303ES01, Yeasen Biotechnology, China). Finally, the sections were mounted on glycerin-coated slides, sealed with neutral balsam, and scanned under a microscope (VS120, Olympus, Japan).

Inductively coupled plasma mass spectrometry (ICP-MS) analysis

The mouse OB was placed in a beaker with 1 mL of 65.0%–68.0% HNO_3 (10014508, Hushi, China). The beaker was covered with a watch glass and heated at 150℃ until the tissue was completely dissolved. The watch glass was then removed, with heating continued until only 100 μL of HNO_3 remained. The solution was diluted in ddH_2O to 1 mL. The concentrations of ^{54}Fe, ^{56}Fe, and ^{57}Fe were detected by ICP-MS.

Quantification of serum and cerebrospinal fluid (CSF) iron

Iron concentrations in serum and CSF were measured using an iron assay kit (ab83366, Abcam, UK). Blood was collected from mice following enucleation of the eyeballs and allowed to stand for 13–30 min until it clotted. The serum was obtained by centrifugation at 8 000 ×*g* for 15 min at room temperature. Glass electrodes were used to extract CSF from the cerebellar medulla cistern.

RNA-seq and data analysis

RNA-seq was performed by the Beijing Genomics Institute (BGI). Total RNA was extracted from the mouse OB using TRIzol reagent according to the provided instructions. Subsequently, 25–100 μL of diethyl pyrocarbonate (DEPC)-treated water was added to dissolve the RNA. Total RNA was qualified and quantified using a NanoDrop and Agilent 2100 Bioanalyzer (Thermo Fisher, USA). Oligo (dT)-attached magnetic beads were used to purify mRNA. The cDNA fragments obtained from the previous step were amplified by PCR, and the products were purified using AMPure XP Beads before being dissolved in EB solution. The final library was amplified using phi29 to produce DNA nanoballs, each containing over 300 copies of a single molecule. These nanoballs were loaded onto the patterned nanoarray, and single-end 50-bases reads were generated using the BGIseq500 platform.

Gene expression levels were quantified as fragments per kilobase transcriptome per million mapped reads (FPKM). Differentially expressed genes (DEGs) were identified with a *Q*-value<0.05 and absolute $\log_2$ fold-change (FC)>1. Correlation analysis, principal component analysis (PCA), and Gene Ontology (GO) pathway enrichment analysis were conducted using the BGI cloud platform.

Immune infiltration analysis

The Immune Cell Abundance Identifier (ImmuCellAI) was employed to estimate the abundance of 24 immune cell types, including 18 T-cell subtypes and six additional immune cell types (B cells, natural killer (NK) cells, monocytes, macrophages, neutrophils, and dendritic cells), based on the gene expression dataset. ImmuCellAI (https://guolab.wchscu.cn/ImmuCellAI) was used to quantify immune cell infiltration levels in the mouse OB RNA-seq data.

Quantitative real-time polymerase chain reaction (qPCR)

RNA was extracted from mouse OB samples using an RNA Easy Fast Tissue/Cell Kit (DP451, Tiangen, China), and its concentration was measured using a spectrophotometer. Synthesis of cDNA was performed using a RevertAid First Strand cDNA Synthesis Kit (K1622, Thermo Fisher, USA). A SYBR Green Kit (Q711-02, Vazyme, China) was used for qPCR, with GAPDH serving as the internal control for normalization. Specific primer sequences, synthesized by the Takara Company, are listed in Supplementary Table S1.

Western blotting

Protein extraction from mouse OB tissues was performed using RIPA lysis buffer (P0013B, Beyotime, China) containing a protease inhibitor (04693132001, Roche, SUI) and phosphoprotease inhibitor (04906837001, Roche, SUI). Protein concentrations were determined using a BCA Protein Assay Kit (CW0014, CWBIO, China). Equal amounts of protein were separated by electrophoresis on a 10% sodium dodecyl sulfate-polyacrylamide gel and transferred to a polyvinylidene difluoride membrane (ISEQ00010, Millipore, USA) for incubation with antibodies. Imaging was performed using a chemiluminescence imaging system (Fusion FX, Vilber, France). The antibodies used in this study were: L-ferritin (ab69090, Abcam, UK; 1:1 000), CD68 (ab125212, Abcam, UK; 1:100), glutathione peroxidase 4 (ab125066, GPX4, Abcam, UK; 1:10 000), NADPH oxidase 2 (NOX2; sc-130543, Santa Cruz, USA; 1:200), Acyl-CoA synthetase long chain family member 4 (ab155282ACSL4; Abcam, UK; 1:2 500), NeuN (MAB377, ZooMAB, USA; 1:500), vesicular glutamate transporter 1 (VGLUT1; R382310, ZenBio, China; 1:1 000), glutamate decarboxylase 1 (GAD1; ab26116, Abcam, UK; 1:5 000), choline acetyltransferase (ChAT; AB144P, Millipore, USA; 1:1 000), TH (AB152, Millipore, USA; 1:10 000), β-actin (Abs100532, Absin, China; 1:10 000), GAPDH (Abs132004, Absin, China), goat anti-rabbit IgG-HRP (abs20002, Absin, China; 1:10 000), goat anti-mouse IgG-HRP antibody (abs20001, Absin, China; 1:10 000), and rabbit anti-goat IgG-HRP antibody (abs20005, Absin, China; 1:10 000). Band intensities were normalized to those of β-actin or GAPDH.

Spatial transcriptome dataset

Spatial gene expression profiles of the OB were obtained from 10x Genomics Datasets (https://www.10xgenomics.com). The Visium gene expression library was prepared as described in the User's Guide for the Visium Spatial Reagent Kits (CG000239 Rev D). The sequencing data were processed using Space Ranger, and the downloaded dataset was utilized to visualize marker genes for various types of neurons with RStudio.

Statistical analysis

Statistical analyses were conducted using GraphPad Prism v.9.0. Data were represented as mean±standard error of the mean (SEM) and analyzed by two-tailed Student's unpaired *t*-test. Statistical significance was considered at $P<0.05$.

RESULTS

Intranasal FAC administration impairs olfactory function

To investigate the impact of iron on neuronal vulnerability, a mouse model of OB iron deposition was established using intranasal administration of FAC twice every other day. This approach avoided potential tissue damage associated with direct injection. Olfactory discrimination tests were conducted at the end of FAC administration, following 24 h of food deprivation prior to euthanasia (Figure 1A). Compared to the control mice, FAC-treated mice spent significantly less time in the peanut butter area during the preference test (Figure 1B–D), and spent significantly more time searching for buried food during the buried food-seeking test (Figure 1F), suggesting impaired olfactory function.

Intranasal FAC administration induces OM and OB iron deposition and OSN damage

Intranasal administration of FAC resulted in substantial OM and OB iron deposition and significant OSN damage. Compared with control mice, FAC-treated mice exhibited a marked increase in the number of iron-positive cells in the OM (Figure 2A), indicating significant iron deposition. The levels of OMP, a marker for mature OSNs essential for OSN signaling and odor recognition (Albeanu et al., 2018), were significantly reduced in the OM of FAC-treated mice (Figure 2B), likely contributing to the observed olfactory dysfunction in these mice. Iron deposited in the OM can be transported to the OB along the olfactory nerve via intracellular or paracellular pathways (Crowe et al., 2018; Lochhead & Thorne, 2012; Zhang et al., 2021). Consistent with this, mRNA levels of L-ferritin in the OB of FAC-treated mice increased by 70.38% (Figure 2C), while protein expression levels increased by 54.52% (Figure 2D). L-ferritin, a hollow iron storage protein critical for maintaining iron homeostasis (Zhang et al., 2022), was up-regulated, reflecting an increased requirement for iron storage.

OB iron deposition was further confirmed through ICP-MS analysis. FAC-treated mice showed a 59.66% increase in ^{56}Fe and a 56.52% increase in ^{57}Fe, along with a marginal elevation in ^{54}Fe concentrations (Figure 2E). Perl's-DAB staining revealed a 149.82% increase in iron-positive staining in the OB of FAC-treated mice (Figure 2F, G). These mice also exhibited a reduction in OB weight (Figure 1F), further demonstrating significant OB iron deposition as a consequence of FAC administration.

In addition to the olfactory nerves, iron can also enter the CNS through the blood-brain barrier and blood-CSF barrier (Qian & Ke, 2019). To evaluate alternative routes of iron entry, iron concentrations in serum and CSF were measured. Intranasal FAC administration did not alter serum iron concentrations (Figure 2H), and iron levels in the CSF were undetectable in all mice. These findings suggest that blood and CSF are not contributing sources of OB iron deposition, reinforcing the role of direct transport along the olfactory nerve.

Iron deposition elicits a strong immune response in the OB

To investigate the impact of iron deposition, RNA-seq analysis was performed on OB tissues isolated from FAC-treated and control mice, revealing significant transcriptomic alterations.

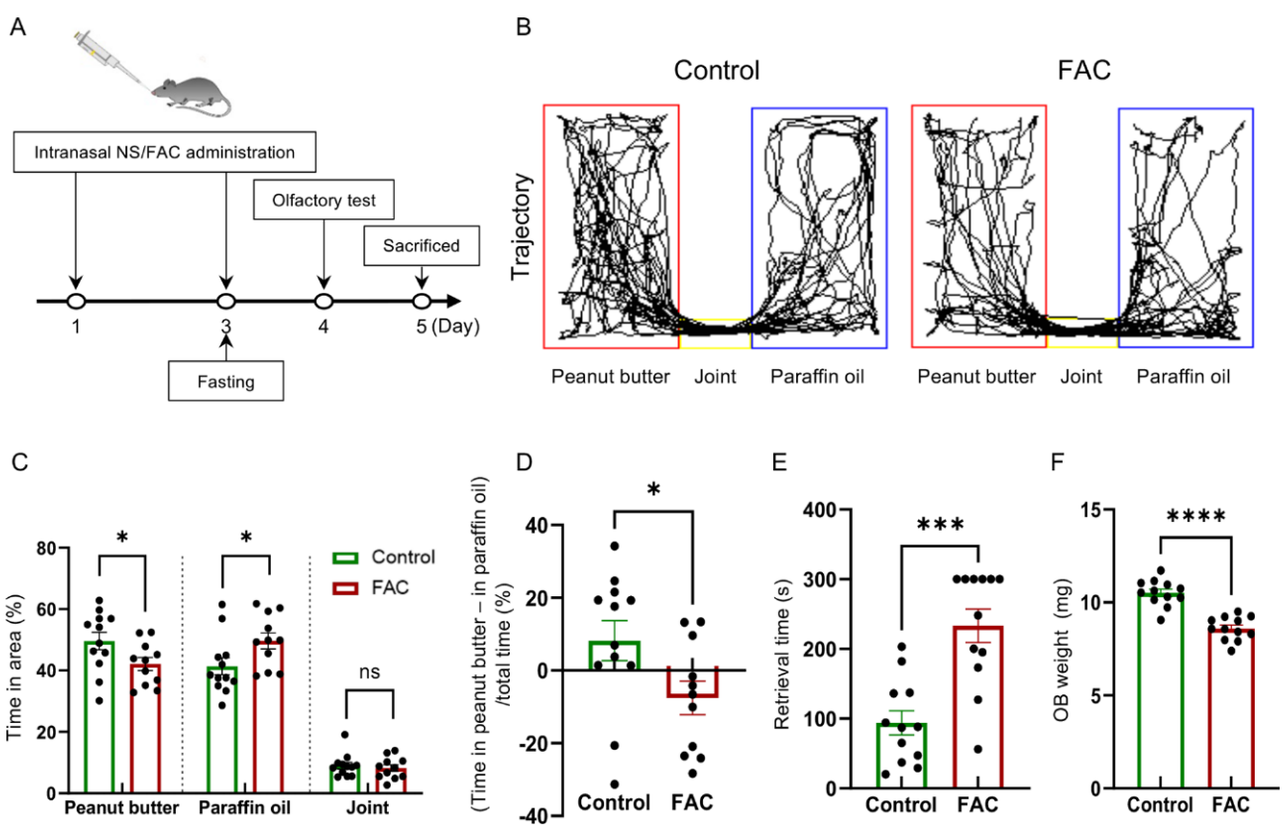


Figure 1 Effects of intranasal FAC administration on olfactory function

A: Schematic of experiment. B: Representative images of track visualization in the preference test. C: Accumulation time in peanut butter, paraffin oil, and joint areas. D: Preference index in the peanut butter area. E: Time to find buried food. F: Weight of OB. Data are presented as mean±SEM, n=12. ns: No significance; *: P<0.05; ***: P<0.001; ****: P<0.0001.

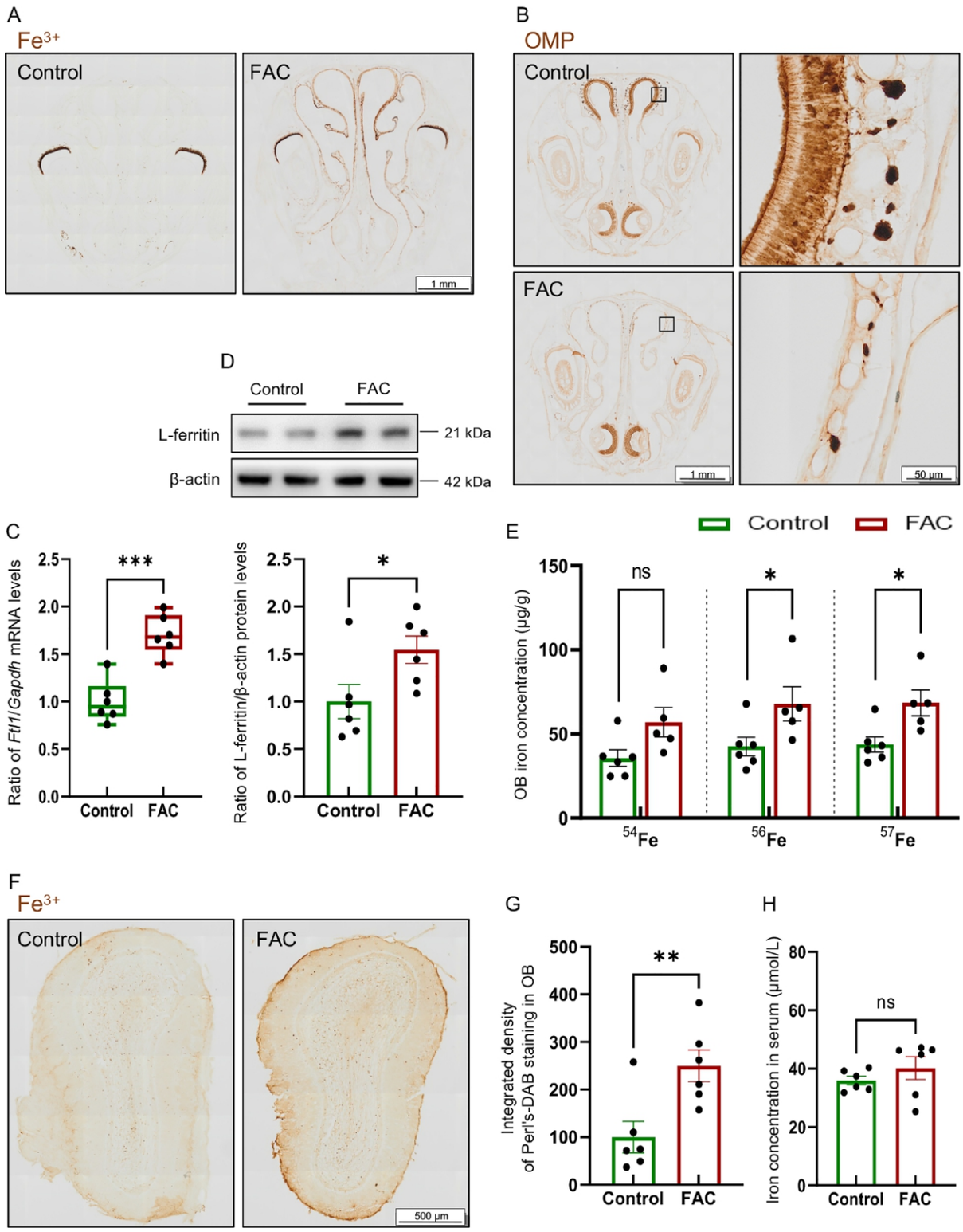


Figure 2 Effects of intranasal FAC administration on iron levels in the OM, OB and serum

A: Representative Perl's-DAB-stained images in the OM. B: Representative IHC staining images of OMP in the OM. C: OB *Ftl1* mRNA expression levels. D: OB L-ferritin protein expression levels. E: ^{54}Fe, ^{56}Fe, and ^{57}Fe concentrations in OB. F: Representative Perl's-DAB-stained images in OB. G: Average integrated density of Perl's-DAB staining in the OB. H: Iron concentration of serum. Data are presented as mean±SEM, n=5–6. OMP: Olfactory marker protein. ns: No significance; *: P<0.05; ***: P<0.001.

The gene expression boxplot confirmed high-quality transcriptomic data (Figure 3A). PCA and correlation analysis distinguished clear phenotypic differences between the control and FAC-treated mice (Figure 3B, C). Based on the $|\text{Log}_2(\text{FC})|>1$ and Q-value<0.05 thresholds, 771 DEGs were identified, including 535 up-regulated and 236 down-regulated genes in the FAC-treated group (Figure 3D; Supplementary Table S2). The distribution of these DEGs was visualized using a volcano plot and heatmap, highlighting distinct patterns of gene regulation (Figure 3E, F).

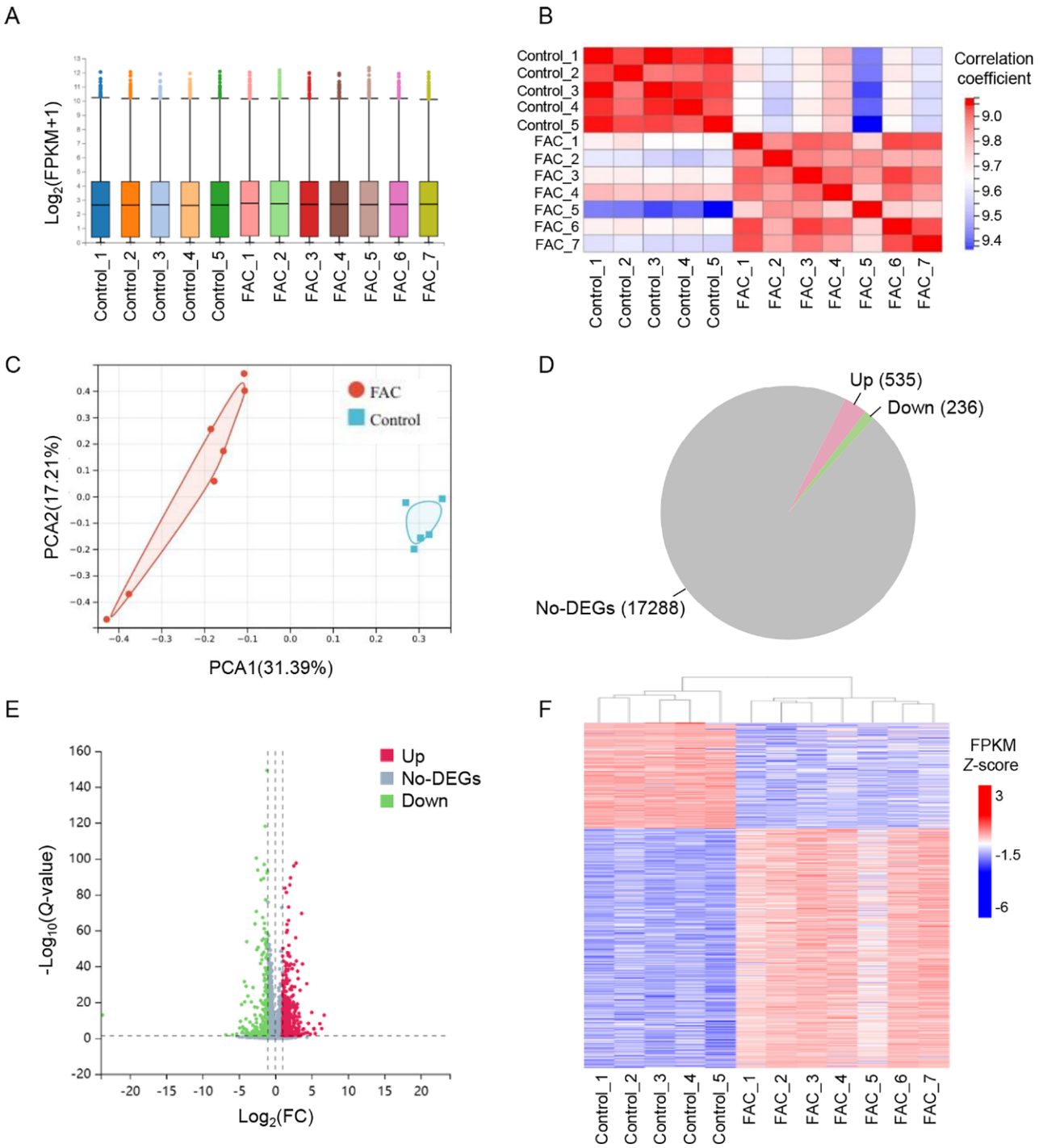


Figure 3 Effects of intranasal FAC administration on OB transcriptome

A: Box plots of gene expression data of individual OB tissues. B: Correlation analysis of individual OB tissues. C: PCA of individual OB tissues. D: Number of up- and down-regulated genes in OB after intranasal FAC administration. E: Volcano plot of up- and down-regulated genes in OB after intranasal FAC administration. F: Heatmap of up- and down-regulated genes in OB after intranasal FAC administration (adjusted|Log_2(FC)|>1 and *Q*-value<0.05). *n*=5–7. FPKM: Fragments per kilobase transcriptome per million mapped reads; PCA: Principal component analysis; FC: Fold-change.

GO analysis of up-regulated DEGs revealed significant enrichment in several biological processes, including “innate immune response”, “positive regulation of immune response” and “positive regulation of cytokine production” (Figure 4A). Notably, all top 10 enriched processes were related to immunity. Similarly, cellular component analysis demonstrated significant enrichment in immunomodulatory structures, including the NADPH oxidase complex and phagocytic vesicles, indicating that iron deposition promotes the synthesis of these components (Figure 4B).

While immune cell infiltration has been extensively studied in oncology, its role in neurological diseases has gained increasing attention (Rodríguez Murúa et al., 2022; Salvador et al., 2021; Tan et al., 2020). Using ImmuCellAI, a widely utilized tool for estimating the abundance of 24 immune cell types, we observed significantly increased immune cell

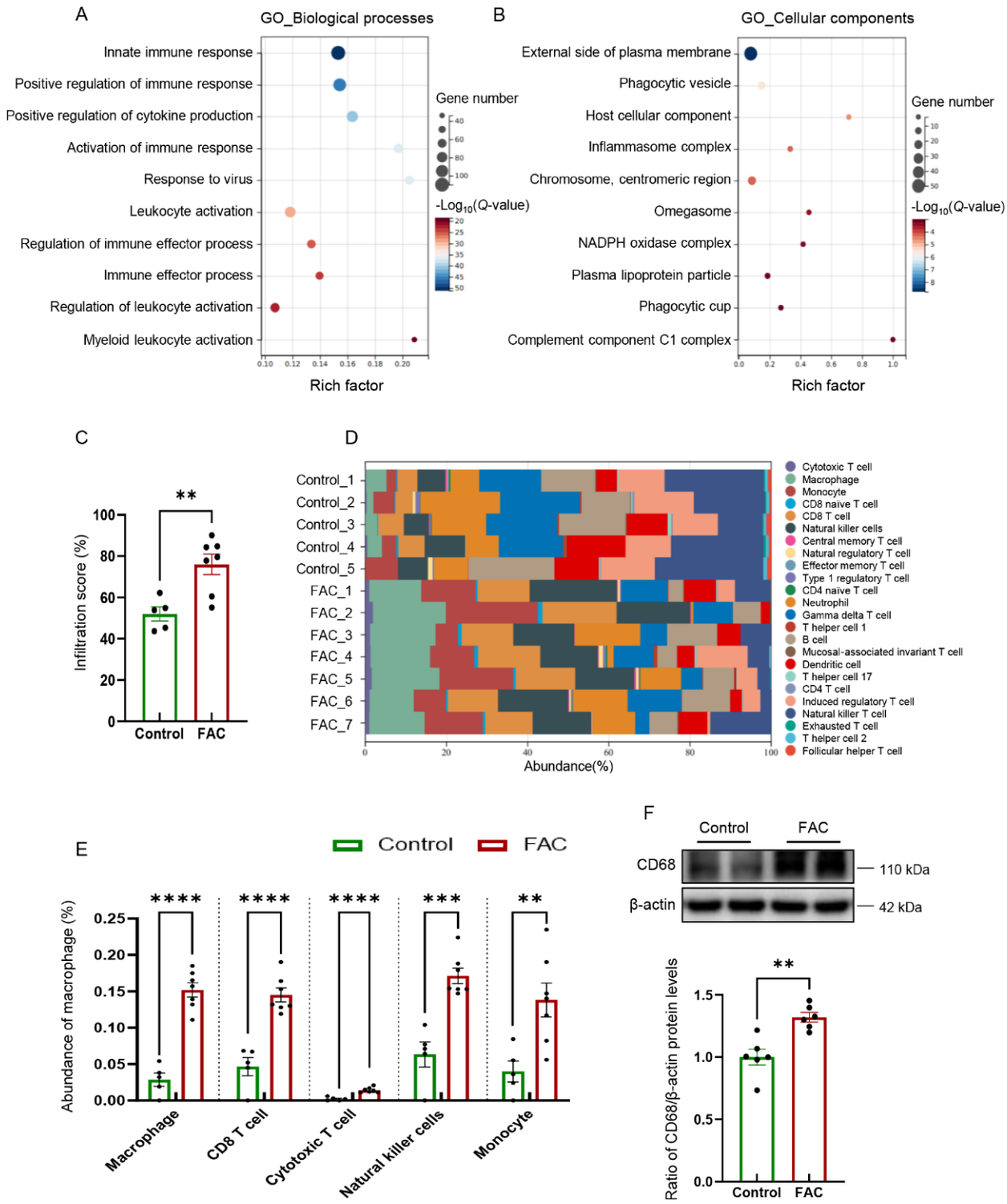


Figure 4 Effects of intranasal FAC administration on OB immune response

A: GO enrichment analysis of biological processes in up-regulated genes. B: GO enrichment analysis of cellular components in up-regulated genes. C: Infiltration of OB immune cells. D: Abundance of 24 immune cell types in OB. E: Abundance of macrophages, CD8+ T cells, cytotoxic T cells, natural killer cells, and monocytes in OB. F: OB CD68 protein expression levels. Data are presented as mean±SEM, n=5–7. **: P<0.01; ***: P<0.001; ****: P<0.0001.

infiltration in the OB of FAC-treated mice compared to control mice (Figure 4C). Specifically, the abundance of several immune cell populations, including macrophages, CD8+ T cells, cytotoxic T cells, NK cells, and monocytes, was significantly increased in FAC-treated mice (Figure 4D, E). Additionally, protein levels of the macrophage marker CD68 were elevated in OB of FAC-treated mice (Figure 4F), further confirming macrophage activation. These results provide strong evidence that iron deposition in the OB elicits a pronounced immune response.

Iron deposition in the OB does not induce ferroptosis

To further explore whether iron deposition triggers ferroptosis

in the OB of FAC-treated mice, RNA-seq analysis was performed. Results revealed that the expression levels of several key anti-ferroptotic genes, including *Gpx4*, *Cbs*, *GSS*, *Gclc*, *Gsta4*, *Gstm1*, *Gstm4*, *Gstm5*, *Gstm6*, *Gstp1*, *Gstt2*, *Slc3a2*, and *Slc7a11* (Rothammer et al., 2022), remained unchanged between FAC-treated and control mice (Figure 5A). These findings were verified by consistent GPX4 mRNA levels, protein levels, and GPX4-positive cell counts in the OB regardless of iron deposition (Figure 5C, G, J). Gene set enrichment analysis (GSEA) further validated the absence of a relationship between OB iron deposition and ferroptosis (Figure 5B). These results suggest that iron deposition in the OB does not necessarily induce ferroptosis.

ACSL4, a key regulator of ferroptosis sensitivity, modulates cellular lipid composition by catalyzing several polyunsaturated fatty acids. Elevated ACSL4 expression increases ferroptosis sensitivity, while pharmacological inhibition of ACSL4 protects against ferroptosis (Doll et al., 2017). In the OB of FAC-treated mice, both mRNA and protein levels of ACSL4 were significantly reduced (Figure 5D, E, H). Similarly, NOX2 protein levels were also decreased (Figure 5I), despite an observed increase in mRNA levels of *cybb*, which encodes NOX2 (Figure 5F). As the catalytic subunit of the NADPH oxidase complex, NOX2 catalyzes the production of ROS (Liu et al., 2022; Ogboo et al., 2022), which can promote cellular ferroptosis (Chen et al., 2021; Stockwell, 2022). We speculate that the reduced expression of both ACSL4 and NOX2 in the presence of iron deposition may be an adaptive response aimed at mitigating oxidative damage and preventing ferroptosis in the OB.

Iron vulnerability varies among neuronal types

To explore neuron-type-specific vulnerability to iron deposition, spatial transcriptomic analysis of OB tissue from healthy mice was conducted using datasets from 10x Genomics to visualize the expression of relevant genes. Gene expression analysis revealed a high abundance of neurons in the OB, as indicated by robust expression of neuronal markers *Rbfox3* and *Map2*. Among neuronal subtypes, GABAergic neurons (*Gad1* and *Gad2*) were the most abundant, followed by glutamatergic neurons (*Slc17a7* and *Slc17a6*) and dopaminergic neurons (*Th* and *Slc6a3*). In contrast, cholinergic neurons (*Tph1* and *Tph2*) and serotonergic neurons (*Chat* and *Slc18a3*) exhibited minimal expression, indicating sparse populations in the OB (Figure 6A). Analysis of glial cell markers revealed widespread distribution of astrocytes (*Gfap* and *S100b*), microglia (*Aif1* and *Tmem119*), and oligodendrocytes (*Olig1* and *Olig2*) in the OB (Figure 6B).

To identify the cell types associated with iron deposition, iron-positive cells were double-labeled with markers for microglia, astrocytes, oligodendrocytes, and neurons in the glomerular layer (GL) and granule cell layer (GCL). Iron-positive staining was detected in both neurons and glial cells, regardless of FAC administration (Figure 7A). Robust expression of Iba1 and GFAP in the GL and GCL, consistent with the RNA-seq results showing increased *Aif1* (encoding Iba-1) and *Gfap* (encoding GFAP), suggested significant activation of microglia and astrocytes in response to OB iron deposition (Figure 7A–C). In contrast, the boundaries of Olig2-positive cells in the iron-deposited OB were indistinct, and RNA-seq indicated a decrease in *Olig2* expression (Figure 7A, D), suggesting potential oligodendrocyte damage.

For neurons, iron deposition in the OB resulted in a pronounced decrease in NeuN-positive cells of the GL (Figure 7A), a region densely populated by dopaminergic neurons (Li et al., 2024). This was further corroborated by a significant reduction in TH-positive cells in the GL (Figure 8A) and decreased TH mRNA and protein expression levels in the OB (Figure 8E–G), suggesting a remarkable loss of dopaminergic neurons in the OB of FAC-treated mice. Considering that dopaminergic neurons represent only 5% of the total neuronal population in the OB (Paß et al., 2020), this explains why the overall *Rbfox3* (encoding NeuN) mRNA levels and NeuN protein levels remained unchanged (Figures 7E; 8E–G).

The vulnerability of other neuronal subtypes to iron deposition in the OB was also assessed by examining the expression of neuronal marker genes. RNA-seq analysis, based on $|\mathrm{Log_2(FC)}|>0.4$ and Q-value<0.05 thresholds, revealed reduced expression of glutamatergic neuronal markers (*Slc17a7* and *Slc17a6*) and dopaminergic neuronal markers (*Th* and *Slc6a3*) (Figure 8C, D) in FAC-treated mice. These findings were verified by qPCR (Figure 8E). Protein levels of VGLUT1, encoded by *Slc17a7*, were also decreased (Figure 8F, G), indicating damage to glutamatergic neurons. Similarly, qPCR and western blot analyses showed reduced *Chat* mRNA and ChAT protein levels (Figure 8E–G), although RNA-seq analysis indicated no significant differences in cholinergic neuronal markers (*Chat* and *Slc18a3*) between the two groups (Figure 8C, D). The presence of intrinsic cholinergic neurons in the OB remains controversial, despite the well-established cholinergic inputs from the basal forebrain (De Saint Jan, 2022). The discrepancy in the data may be due to the low expression of the neuronal marker gene *Chat*, consistent with the absence of detectable cholinergic neurons in the OB, as shown in Figure 6A.

For other neuronal types, RNA-seq results showed no significant differences in the expression of GABAergic markers (*Gad1* and *Gad2*), serotonergic markers (*Tph1* and *Tph2*), or universal neuronal markers (*Rbfox3* and *Map2*) between the two groups of mice (Figure 8C, D). These findings were verified by qPCR analysis (Figure 8E) and consistent protein levels of GAD1 (encoded by *Gad1*), as well as the unchanged number of GAD1-positive cells (Figure 8F, G, B). Additionally, NeuN-positive cells in the GCL, predominantly composed of GABAergic neurons (Li et al., 2024), remained unaffected by iron deposition (Figure 7A). These results suggest that GABAergic neurons, the predominant neuronal subtype in the OB, are resilient to iron-induced damage, preserving the overall neuronal population. Whether serotonergic neurons are resistant to iron remains uncertain due to their sparse distribution in the OB (Figure 6A).

DISCUSSION

Intranasal delivery has gained recognition as an effective and non-invasive strategy for bypassing the blood-brain barrier, enabling rapid transport of substances from the nasal cavity to the brain. This approach offers superior bioavailability and faster delivery compared to oral or intravenous routes, while avoiding the potential risks and damage associated with invasive techniques such as intracerebral or intraventricular injections (Agrawal et al., 2018; Zhang et al., 2021). In this study, a mouse model of OB iron deposition was established by intranasal iron administration to evaluate the effects of iron on cellular vulnerability.

Iron deposited in the OM can be transported to the OB

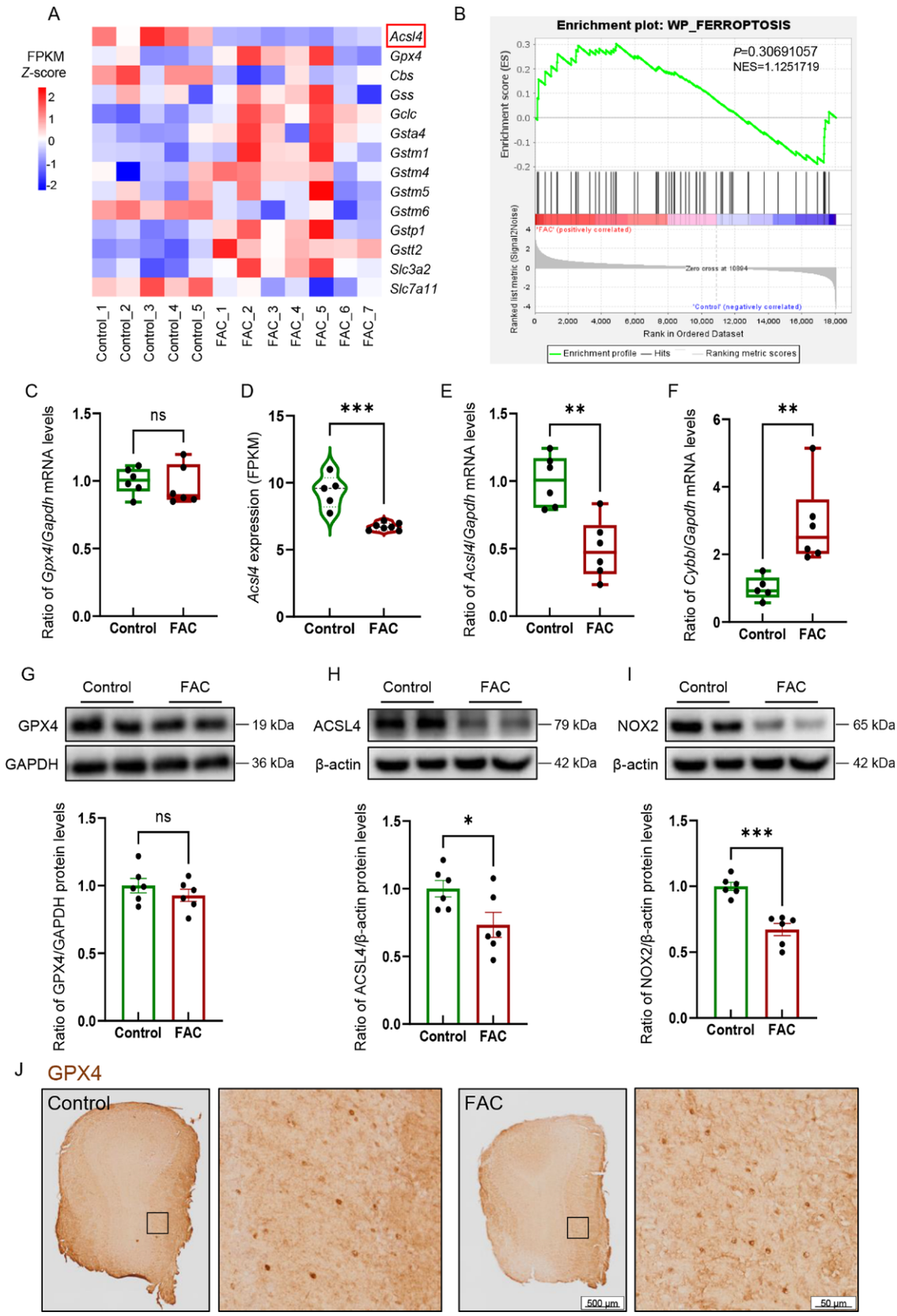


Figure 5 Figure 5 Effects of intranasal FAC administration on OB ferroptosis

A: Heatmap of ferroptosis-associated genes in the OB. B: GSEA between intranasal FAC administration and ferroptosis. C: OB *Gpx4* mRNA expression levels. D: FPKM values of OB *Acsl4* gene. E: OB *Acsl4* mRNA expression levels. F: OB *Cybb* mRNA expression levels. G: OB GPX4 protein expression levels. H: OB ACSL4 protein expression levels. I: OB NOX2 protein expression levels. J: Representative IHC-stained images of GPX4 in the OB. Data are presented as mean±SEM, n=5–7. FPKM: Fragments per kilobase transcriptome per million mapped reads; GPX4: Glutathione peroxidase 4; ACSL4: Acyl-CoA synthetase long chain family member 4; NOX2: NADPH oxidase 2. ns: No significance; *: P<0.05; **: P<0.01; ***: P<0.001.

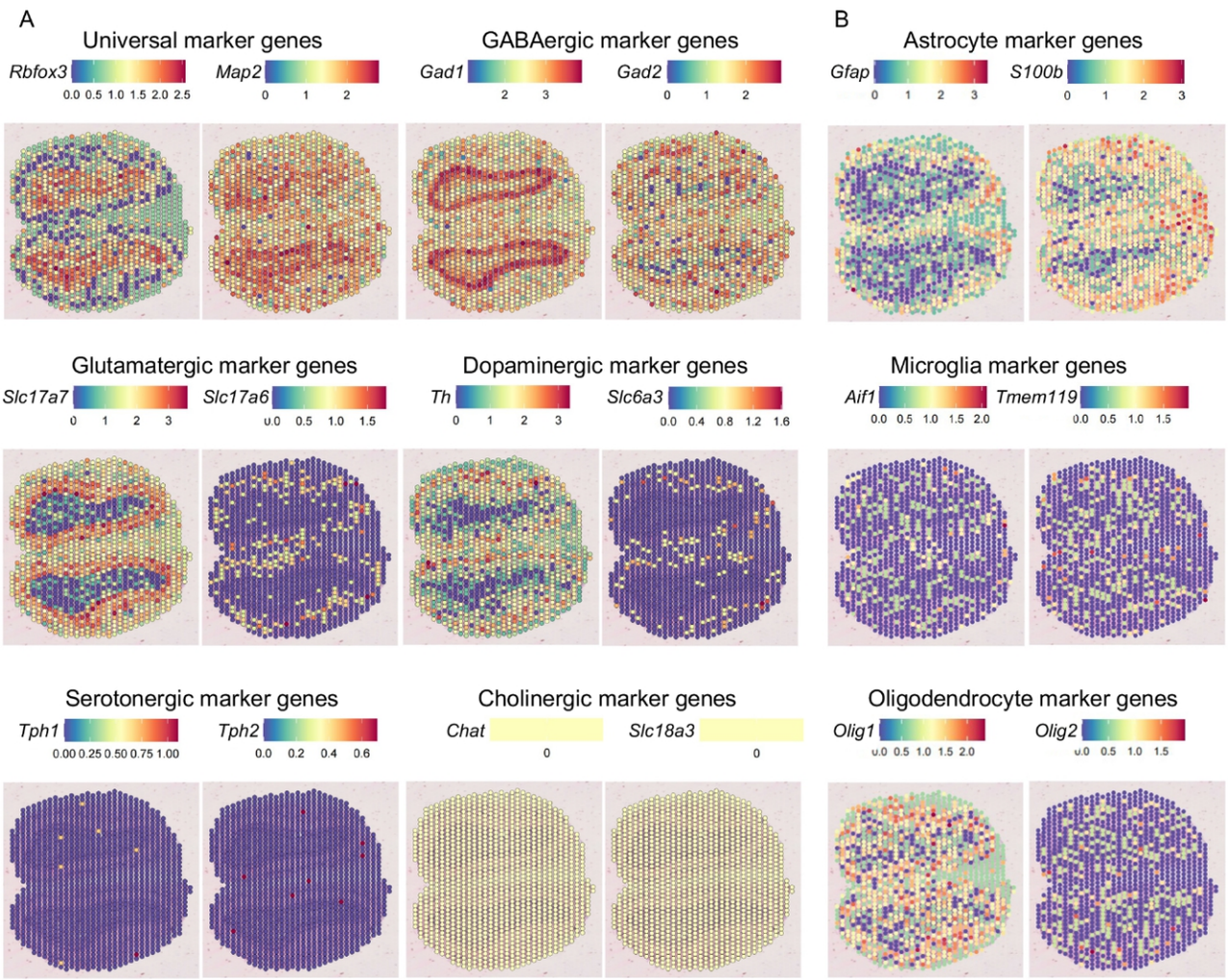


Figure 6 Spatial feature plots of neuronal and glial marker genes in healthy adult mouse OB tissues

A: Images of universal, GABAergic, glutamatergic, dopaminergic, serotonergic, and cholinergic marker gene expression in spatial transcriptome dataset. B: Images of astrocyte, microglia, and oligodendrocyte marker gene expression in spatial transcriptome dataset.

either intracellularly or paracellularly. The intracellular pathway involves receptor-mediated endocytosis of substances into OSNs, where vesicles are transported along axons to nerve endings and released into the OB via exocytosis (Crowe et al., 2018; Zhang et al., 2021). However, our observation of marked OSN loss in response to intranasal iron administration suggests that this pathway is unlikely to play a major role in OM-to-OB iron transport under these conditions. The paracellular pathway provides an alternative mechanism for iron transport to the OB and CNS. In this pathway, substances infiltrate intercellular junctional structures, including the perineural and perivascular pathways (Crowe et al., 2018; Zhang et al., 2021). The continuous renewal of neurons and basal cells in the nasal cavity contributes to the permeability of intercellular connections, facilitating the transport of substances. Within the CNS, the perineural pathway relies on the perineuronal space, the extracellular region between the neuron and myelin sheath formed by oligodendrocytes (Zhang et al., 2021). Our findings revealed oligodendrocyte damage in the OB of FAC-treated mice, supporting the hypothesis that iron transport to the OB occurs through the paracellular pathway.

Olfactory dysfunction is widely recognized as an early biomarker of neurodegenerative diseases, affecting approximately 90% of patients with early PD and 85% of patients with early AD (Dan et al., 2021). In PD, olfactory dysfunction is one of the most prevalent and well-characterized non-motor symptoms, often preceding the onset of classical motor deficits by at least 4 years (Ross et al., 2008). Despite its diagnostic potential, the mechanisms underlying olfactory dysfunction have not been clearly elucidated. Several studies have implicated α-synuclein inclusions (Lewy bodies and Lewy neurites), neuroinflammation in olfactory regions, and disruptions in neurotransmitter systems as contributors to PD-related olfactory dysfunction (Dan et al., 2021; Rey et al., 2018). Additionally, region-specific iron deposition has been observed in various neurological disorders, including the SN in PD, amyloid-beta (Aβ) deposition sites in AD, and prefrontal cortex in depression (Ward et al., 2014; Wu et al., 2023; Zhou et al., 2020). In PD patients, iron accumulation has also been detected in the OB, a phenomenon potentially linked to olfactory dysfunction (Gardner et al., 2017). We previously demonstrated both OB iron deposition and olfactory dysfunction in rotenone-induced PD mice (Yuan et al., 2023), although the relationship between these events remained unclear. In the present study, significant OSN injury and OB iron deposition were observed in FAC-treated mice, suggesting that both factors may contribute to the observed olfactory dysfunction.

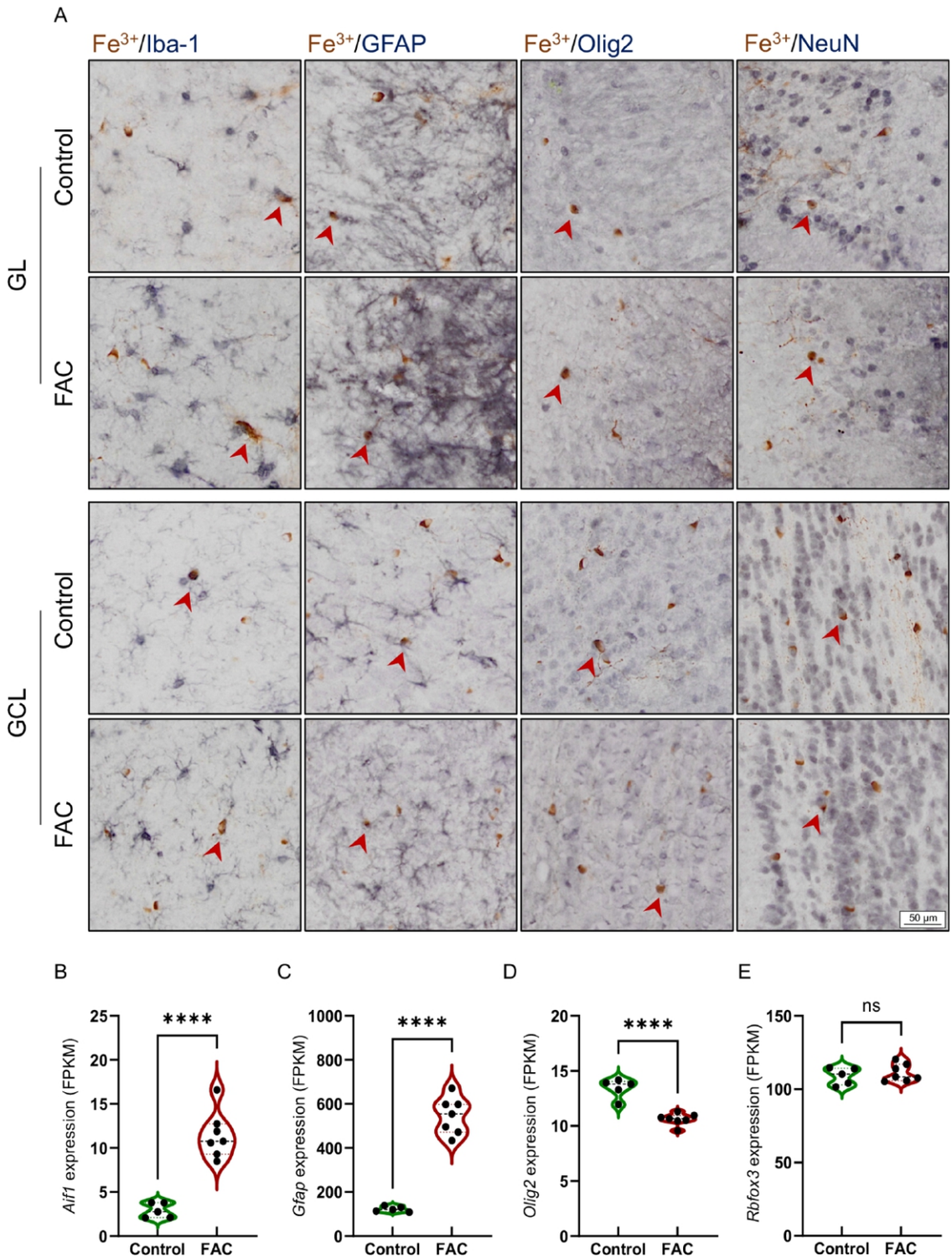


Figure 7 Effects of intranasal FAC administration on OB neurons and glial cells

A: Perl's-DAB staining of iron-positive cells (dark brown) and IHC staining of Iba-1, GFAP, olig2, or NeuN (blue) double-labeled cells. B: FPKM values of OB *Aif1* gene. C: FPKM values of OB *Gfap* gene. D: FPKM values of OB *Olig2* gene. E: FPKM values of OB *Rbfox3* gene. Data are presented as mean±SEM, n=5–7. GL: Glomerular layer; GCL: Granule cell layer; GFAP: Glial fibrillary acidic protein; NeuN: Neuronal nuclei. ns: No significance; ****: P<0.0001.

Our results also demonstrated that the OB of FAC-treated mice exhibited significant loss of both glutamatergic and dopaminergic neurons. Previous studies have linked performance in olfactory tests to dopamine transporter activity in the SN and striatum of PD patients (Bohnen et al., 2007; Deeb et al., 2010). However, whether dopaminergic neurons in the OB are associated with olfactory dysfunction remains unclear. Dopaminergic neurons, which constitute approximately 5% of the total neuronal population in the OB, are essential for odor discrimination (Paß et al., 2020). Interestingly, studies have reported contradictory findings regarding the number of OB dopaminergic neurons in neurodegenerative diseases, While some studies have observed an increase in dopaminergic neurons in the OB of

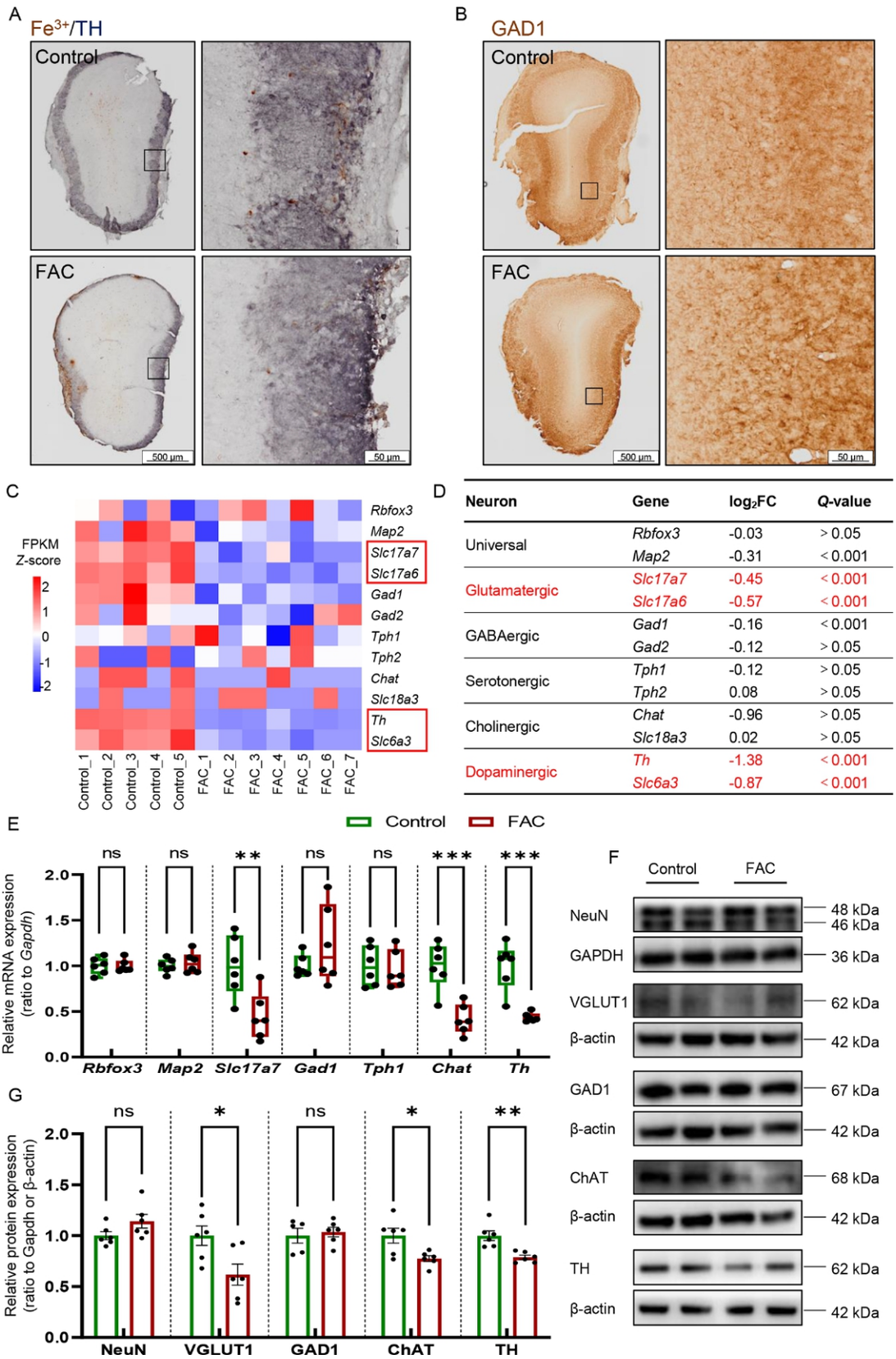


Figure 8 Effects of intranasal FAC administration on neuronal marker genes and protein levels in the OB

A: Perl's-DAB staining of iron-positive cells (dark brown) and IHC staining of TH (blue) double-labeled cells. B: Representative IHC-stained images of GAD1 in the OB. C: Heatmap of neuronal marker genes in OB. D: Generalization of neuronal marker genes in OB. E: OB mRNA expression levels of neuronal marker genes. F: Western blots showing OB expression of neuronal marker proteins. G: OB protein expression levels of neuronal marker proteins. Data are presented as mean±SEM, n=5–7. TH: Tyrosine hydroxylase; GAD1: Glutamate decarboxylase 1; FPKM: Fragments per kilobase transcriptome per million mapped reads; FC: Fold-change; NeuN: Neuronal nuclei; VGLUT1: Vesicular glutamate transporter 1; GAD1: Glutamate decarboxylase 1; ChAT: Choline acetyltransferase. ns: No significance; *: P<0.05; **: P<0.01.

PD and AD patients (Huisman et al., 2004; Mundiñano et al., 2011), potentially reflecting the plasticity of the olfactory system (Höglinger et al., 2004; Marin et al., 2017), others have reported no significant differences between PD patients and healthy individuals (Cave et al., 2016; Huisman et al., 2008). More intriguingly, lesions of OB dopaminergic neurons induced by 6-OHDA result in olfactory dysfunction in mice but paradoxically prevent the development of hyposmia when 6-OHDA lesions are introduced in the SN (Ilkiw et al., 2019). These findings highlight the complexity and uncertainty surrounding the relationship between OB dopaminergic neurons and olfactory function.

In addition to dopaminergic neurons, glutamatergic neurons in the OB appear to play a critical role in olfactory processing. Recent RNA-seq analyses revealed significant down-regulation of excitatory neuron-related genes, particularly glutamatergic *Slc17A7*, in the OB of normal and PD subjects, suggesting a strong association with olfactory dysfunction (Tremblay et al., 2024). Similarly, in the present study, *Slc17A7* was down-regulated in the OB of FAC-treated mice. Glutamatergic excitatory mitral and tufted cells, as principal output neurons of the OB, play crucial roles in odor discrimination and olfactory learning (Liu et al., 2020; Murphy et al., 2005). Additionally, glutamatergic neurons expressing vesicular glutamate transporter 3 regulate the transmission of olfactory signals from sensory neurons to the cortex (Tatti et al., 2014). Specific ablation of the OB glutamatergic neurons in mice has been shown to result in olfactory-related behavioral abnormalities, including depression and sleep disturbance (Yuan et al., 2020). These observations suggest that glutamatergic neuronal damage may play an important role in olfactory dysfunction induced by intranasal iron administration.

Environmental insults, such as those from bacteria, viruses, mold, dust, and chemicals, have the potential to enter the nasal cavity and act as allergens, triggering inflammation and immunoactivation within the olfactory system (Ahmad & Zacharek, 2008; Imamura & Hasegawa-Ishii, 2016). In this study, significant immune cell infiltration was observed in the OB of FAC-treated mice, a key hallmark of tissue inflammation (Sun et al., 2020). This finding suggests that intranasal iron administration induces a robust inflammatory and immune response in the OB. Although the brain was once considered “immune-privileged”, it is now clear that nearly all neurological diseases involve immune responses (Peng et al., 2024). In early-stage PD, elevated levels of the chemokine prokineticin-2 have been detected in OSNs (Schirinzi et al., 2023), indicating inflammation in the nasal mucosa. Transcriptomic analysis of the OB in PD patients has also shown up-regulation of genes associated with neuroinflammation, immune activation, and inflammatory pathways, as well as in microglia and astrocytes (Tremblay et al., 2024). In mouse models of tauopathy and multiple sclerosis, T cell infiltration has been implicated in promoting neuroinflammation through both independent mechanisms and interactions with activated microglia and macrophages via cell-to-cell contact and cytokine-mediated signaling (Dong & Yong, 2019; Laurent et al., 2017). Neuroinflammation has also been shown to propagate through axonal projections in the CNS, spreading anterogradely or retrogradely to trigger remote neuroimmune activation (Cooper & Clark, 2013; Peng et al., 2024). These observations highlight the potential role of inflammation and immunoactivation in the OB as contributors to the development and progression of neurodegenerative and neurological diseases.

Our findings revealed significant iron deposition in the OB of mice following intranasal FAC administration. Surprisingly, this iron accumulation did not appear to induce ferroptosis. Our previous study using a mouse model with continuous intraperitoneal injection of iron dextran demonstrated substantial iron overload in the liver and spleen without changes in ACSL4 and GPX4 protein levels over 4 weeks (Liang et al., 2023). These findings suggest that iron deposition alone does not necessarily trigger ferroptosis in peripheral organs.

In the brain, ferroptosis has been reported in PD, AD, Huntington’s disease, amyotrophic lateral sclerosis, multiple sclerosis, and Friedreich’s ataxia (Costa et al., 2023). As an iron- and ROS-dependent form of cell death, ferroptosis is characterized by iron accumulation and lipid peroxidation (Tang et al., 2021), which drive the lethal accumulation of ROS. The process is tightly regulated by ACSL4 and GPX4, which act as positive and negative regulators, respectively (Sha et al., 2021). ACSL4, an enzyme involved in fatty acid metabolism, is a specific biomarker and a key driver of ferroptosis. Up-regulation of ACSL4 enhances polyunsaturated fatty acid content in phospholipids, increasing their susceptibility to oxidative damage, thereby promoting ferroptosis (Tang et al., 2021). Notably, ACSL4 knockout can resist ferroptosis induced by RSL3, erastin, and BSO, and additionally, GPX4-ACSL4 double knockout exhibits unprecedented resistance to ferroptosis induced by GPX4 knockout in cells (Doll et al., 2017). In mouse models of cerebral ischemia/reperfusion, ACSL4 has been shown to mediate thrombin-induced ferroptosis and neurotoxicity, even in the absence of iron accumulation. Furthermore, genetic inhibition of ACSL4 effectively mitigates thrombin-induced ferroptosis, highlighting its pivotal role in this pathway (Tuo et al., 2022). Similarly, NOX2, a catalytic component of the NADPH oxidase complex, is involved in promoting ROS production and initiating ferroptosis through lipid peroxidation (Kuang et al., 2020). NOX2 knockdown can reverse hypoxia and RSL3-induced ferroptosis, reduce cellular ROS and lipid peroxidation, and inhibit mitochondrial dysfunction (Xu et al., 2024). Together, ACSL4 and NOX2 act as key regulators of ferroptosis by modulating ROS and lipid peroxidation. In this study, reduced expression of ACSL4 and NOX2 in the OB of FAC-treated mice may explain the absence of ferroptosis despite substantial iron deposition.

Susceptibility to iron overload and ferroptosis differs markedly among cell types, with microglia being the most vulnerable and neurons showing relative resistance (Jiao et al., 2022). This pattern has also been demonstrated in a tri-culture system derived from human-induced pluripotent stem cells, consisting of approximately 15% microglia, 25% neurons, and 60% astrocytes, where microglia exhibited the highest iron reactivity and the greatest degree of cell death (Ryan et al., 2023). However, whether iron sensitivity differs among neuronal subtypes remains largely unexplored.

Our findings revealed that iron deposition in the OB selectively damaged glutamatergic and dopaminergic neurons while sparing GABAergic neurons. Previous research has shown that Fe-NTA, an iron complex that increases neuronal iron levels, impairs glutamatergic synaptic transmission and plasticity in rat hippocampal CA1 cultures (De La Fuente-Ortega et al., 2019). Additionally, the interplay between iron

and dopamine, often referred to as a “toxic couple, has been reported to exacerbate neurotoxicity (Hare & Double, 2016). Consistent with these observations, our previous study demonstrated a time-dependent reduction in TH protein levels following intranasal iron administration, with decreases of 21.23% at 3.5 days, 63.05% at 3 weeks, and 86.97% at 6 weeks, while GAD1 protein levels remained stable (Yuan et al., 2023). Interestingly, similar cell-type-specific vulnerability has been reported in zebrafish, where exposure to manganese selectively damages dopaminergic neurons while sparing GABAergic neurons, resulting in a shift in the dominant cell type from dopaminergic to GABAergic neurons (Zhang et al., 2023). These findings suggest that GABAergic neurons are inherently more resistant to iron and iron-induced toxicity. It is worth noting that dopaminergic periglomerular neurons, a subset of GABAergic neurons that utilize dopamine as a secondary neurotransmitter (Angelova et al., 2023; Nieto-Estévez et al., 2022; Schmitz et al., 2022), exhibited heightened vulnerability to iron due to their dopaminergic properties.

Our results further indicated that iron deposition in the OB was associated with significant activation of microglia and astrocytes and damage to oligodendrocytes, highlighting potential mechanisms of neuronal vulnerability. Astrocyte and microglial activation has been linked to dopaminergic neuron degeneration in the nigrostriatal pathway (Szego et al., 2022), and may play a comparable role in the OB. The paracellular transport of iron into the OB likely exacerbates oligodendrocyte susceptibility, as these cells contain the highest iron levels in the CNS (Friedrich et al., 2021) and are critical for protecting neurons against iron-induced cytotoxicity through H-ferritin secretion (Mukherjee et al., 2020). Evidence from a cuprizone-induced model of multiple sclerosis suggests that ferritin-bound iron mobilization leads to oligodendrocyte loss and demyelination, releasing iron that can further harm neurons (Jhelum et al., 2020). Similarly, in the OB, the interplay between glial activation, oligodendrocyte damage, and neuronal loss likely contributes to the observed depletion of glutamatergic and dopaminergic neurons. This combined loss of glial and neuronal populations may also underlie the reduction in OB weight under iron overload conditions.

In conclusion, this study established a model of OB iron deposition through intranasal administration of FAC. Results demonstrated that iron accumulation in the OB elicited immune and inflammatory responses and significant glutamatergic and dopaminergic neuronal loss, while GABAergic neurons remained relatively unaffected. These findings provide new insights into the selective vulnerability of neuronal populations under iron-induced stress, advancing our understanding of the mechanisms underlying iron-related neurological diseases.

DATA AVAILABILITY

The raw RNA-seq data analyzed in this study are available from the NCBI database (BioProjectID PRJNA1162233), China National Center for Bioinformation database of Genome Sequence Archive (GSA) (PRJCA031055), and Science Data Bank database (DOI:10.57760/sciencedb.j00139.00105).

SUPPLEMENTARY DATA

Supplementary data to this article can be found online.

COMPETING INTERESTS

The authors declare that they have no competing interests.

AUTHORS’ CONTRIBUTIONS

X.Q.M. performed the experiments and composed the first draft. B.C.L., L.Q., Y.Y., H.L., A.Y.X., and Y.L.Z. performed the experiments. J.X.X. and N.S. guided the experiment, polished and finalized the article, conceived and directed the project. All authors read and approved the final version of the manuscript.

REFERENCES

Agrawal M, Saraf S, Saraf S, et al. 2018. Nose-to-brain drug delivery: an update on clinical challenges and progress towards approval of anti-Alzheimer drugs. *Journal of Controlled Release*, **281**: 139–177.

Ahmad N, Zacharek MA. 2008. Allergic rhinitis and rhinosinusitis. *Otolaryngologic Clinics of North America*, **41**(2): 267–281.

Albeanu DF, Provost AC, Agarwal P, et al. 2018. Olfactory marker protein (OMP) regulates formation and refinement of the olfactory glomerular map. *Nature Communications*, **9**(1): 5073.

Angelova A, Tiveron MC, Loizeau MD, et al. 2023. Effects of sensory deprivation on glomerular interneurons in the mouse olfactory bulb: differences in mortality and phenotypic adjustment of dopaminergic neurons. *Frontiers in Cellular Neuroscience*, **17**: 1170170.

Biondetti E, Santin MD, Valabrègue R, et al. 2021. The spatiotemporal changes in dopamine, neuromelanin and iron characterizing Parkinson's disease. *Brain*, **144**(10): 3114–3125.

Bohnen NI, Gedela S, Kuwabara H, et al. 2007. Selective hyposmia and nigrostriatal dopaminergic denervation in Parkinson's disease. *Journal of Neurology*, **254**(1): 84–90.

Cave JW, Fujiwara N, Weibman AR, et al. 2016. Cytoarchitectural changes in the olfactory bulb of Parkinson's disease patients. *npj Parkinson's Disease*, **2**: 16011.

Chen X, Kang R, Kroemer G, et al. 2021. Targeting ferroptosis in pancreatic cancer: a double-edged sword. *Trends in Cancer*, **7**(10): 891–901.

Cooper MS, Clark VP. 2013. Neuroinflammation, neuroautoimmunity, and the co-morbidities of complex regional pain syndrome. *Journal of Neuroimmune Pharmacology*, **8**(3): 452–469.

Costa I, Barbosa DJ, Benfeito S, et al. 2023. Molecular mechanisms of ferroptosis and their involvement in brain diseases. *Pharmacology & Therapeutics*, **244**: 108373.

Crowe TP, Greenlee MHW, Kanthasamy AG, et al. 2018. Mechanism of intranasal drug delivery directly to the brain. *Life Sciences*, **195**: 44–52.

Dan XL, Wechter N, Gray S, et al. 2021. Olfactory dysfunction in aging and neurodegenerative diseases. *Ageing Research Reviews*, **70**: 101416.

Dang XT, Huan XJ, Du XX, et al. 2022. Correlation of ferroptosis and other types of cell death in neurodegenerative diseases. *Neuroscience Bulletin*, **38**(8): 938–952.

De La Fuente-Ortega E, Plaza-Briceño W, Vargas-Robert S, et al. 2019. Prenatal ethanol exposure misregulates genes involved in iron homeostasis promoting a maladaptation of iron dependent hippocampal synaptic transmission and plasticity. *Frontiers in Pharmacology*, **10**: 1312.

De Saint Jan D. 2022. Target-specific control of olfactory bulb periglomerular cells by GABAergic and cholinergic basal forebrain inputs. *eLife*, **11**: e71965.

Deeb J, Shah M, Muhammed N, et al. 2010. A basic smell test is as sensitive as a dopamine transporter scan: comparison of olfaction, taste and DaTSCAN in the diagnosis of Parkinson's disease. *QJM: An International Journal of Medicine*, **103**(12): 941–952.

Depierreux F, Parmentier E, Mackels L, et al. 2021. Parkinson's disease multimodal imaging: F-DOPA PET, neuromelanin-sensitive and quantitative iron-sensitive MRI. *npj Parkinson's Disease*, **7**(1): 57.

Doll S, Proneth B, Tyurina YY, et al. 2017. ACSL4 dictates ferroptosis sensitivity by shaping cellular lipid composition. *Nature Chemical Biology*, **13**(1): 91–98.

Dong YF, Yong VW. 2019. When encephalitogenic T cells collaborate with microglia in multiple sclerosis. *Nature Reviews Neurology*, **15**(12): 704–717.

Friedrich I, Reimann K, Jankuhn S, et al. 2021. Cell specific quantitative iron mapping on brain slices by immuno-μPIXE in healthy elderly and Parkinson's disease. *Acta Neuropathologica Communications*, **9**(1): 47.

Galaris D, Pantopoulos K. 2008. Oxidative stress and iron homeostasis: mechanistic and health aspects. *Critical Reviews in Clinical Laboratory Sciences*, **45**(1): 1–23.

Gardner B, Dieriks BV, Cameron S, et al. 2017. Metal concentrations and distributions in the human olfactory bulb in Parkinson's disease. *Scientific Reports*, **7**(1): 10454.

Han SP, Wang JTW, Yavuz E, et al. 2023. Spatiotemporal tracking of gold nanorods after intranasal administration for brain targeting. *Journal of Controlled Release*, **357**: 606–619.

Hare DJ, Double KL. 2016. Iron and dopamine: a toxic couple. *Brain*, **139**(4): 1026–1035.

Höglinger GU, Rizk P, Muriel MP, et al. 2004. Dopamine depletion impairs precursor cell proliferation in Parkinson disease. *Nature Neuroscience*, **7**(7): 726–735.

Huisman E, Uylings HBM, Hoogland PV. 2004. A 100% increase of dopaminergic cells in the olfactory bulb may explain hyposmia in Parkinson's disease. *Movement Disorders*, **19**(6): 687–692.

Huisman E, Uylings HBM, Hoogland PV. 2008. Gender-related changes in increase of dopaminergic neurons in the olfactory bulb of Parkinson's disease patients. *Movement Disorders*, **23**(10): 1407–1413.

Ilkiw JL, Kmita LC, Targa ADS, et al. 2019. Dopaminergic lesion in the olfactory bulb restores olfaction and induces depressive-like behaviors in a 6-OHDA model of Parkinson's disease. *Molecular Neurobiology*, **56**(2): 1082–1095.

Imamura F, Hasegawa-Ishii S. 2016. Environmental toxicants-induced immune responses in the olfactory mucosa. *Frontiers in Immunology*, **7**: 475.

Itokazu Y, Fuchigami T, Morgan JC, et al. 2021. Intranasal infusion of GD3 and GM1 gangliosides downregulates alpha-synuclein and controls tyrosine hydroxylase gene in a PD model mouse. *Molecular Therapy*, **29**(10): 3059–3071.

Jhelum P, Santos-Nogueira E, Teo W, et al. 2020. Ferroptosis mediates cuprizone-induced loss of oligodendrocytes and demyelination. *The Journal of Neuroscience*, **40**(48): 9327–9341.

Jiao LL, Li XL, Luo YX, et al. 2022. Iron metabolism mediates microglia susceptibility in ferroptosis. *Frontiers in Cellular Neuroscience*, **16**: 995084.

Kuang FM, Liu J, Tang DL, et al. 2020. Oxidative damage and antioxidant defense in ferroptosis. *Frontiers in Cell and Developmental Biology*, **8**: 586578.

Laurent C, Dorothée G, Hunot S, et al. 2017. Hippocampal T cell infiltration promotes neuroinflammation and cognitive decline in a mouse model of tauopathy. *Brain*, **140**(1): 184–200.

Li AN, Rao XP, Zhou Y, et al. 2020. Complex neural representation of odour information in the olfactory bulb. *Acta Physiologica*, **228**(1): e13333.

Li H, Qian JL, Wang YC, et al. 2024. Potential convergence of olfactory dysfunction in Parkinson's disease and COVID-19: the role of neuroinflammation. *Ageing Research Reviews*, **97**: 102288.

Liang MY, Chen L, He Q, et al. 2023. Intraperitoneal injection of iron dextran induces peripheral iron overload and mild neurodegeneration in the nigrostriatal system in C57BL/6 mice. *Life Sciences*, **320**: 121508.

Liu PL, Cao TT, Xu JS, et al. 2020. Plasticity of sniffing pattern and neural activity in the olfactory bulb of behaving mice during odor sampling, anticipation, and reward. *Neuroscience Bulletin*, **36**(6): 598–610.

Liu R, Song KC, Wu JX, et al. 2022. Structure of human phagocyte NADPH oxidase in the resting state. *eLife*, **11**: e83743.

Lochhead JJ, Thorne RG. 2012. Intranasal delivery of biologics to the central nervous system. *Advanced Drug Delivery Reviews*, **64**(7): 614–628.

Lotan A, Luza S, Opazo CM, et al. 2023. Perturbed iron biology in the prefrontal cortex of people with schizophrenia. *Molecular Psychiatry*, **28**(5): 2058–2070.

Marin C, Laxe S, Langdon C, et al. 2017. Olfactory function in an excitotoxic model for secondary neuronal degeneration: role of dopaminergic interneurons. *Neuroscience*, **364**: 28–44.

Möller HE, Bossoni L, Connor JR, et al. 2019. Iron, myelin, and the brain: neuroimaging meets neurobiology. *Trends in Neurosciences*, **42**(6): 384–401.

Mori K, von Campenhausen H, Yoshihara Y. 2000. Zonal organization of the mammalian main and accessory olfactory systems. *Philosophical Transactions of the Royal Society B: Biological Sciences*, **355**(1404): 1801–1812.

Mukherjee C, Kling T, Russo B, et al. 2020. Oligodendrocytes provide antioxidant defense function for neurons by secreting ferritin heavy Chain. *Cell Metabolism*, **32**(2): 259–272. e10.

Mundiñano IC, Caballero MC, Ordóñez C, et al. 2011. Increased dopaminergic cells and protein aggregates in the olfactory bulb of patients with neurodegenerative disorders. *Acta Neuropathologica*, **122**(1): 61–74.

Murphy GJ, Darcy DP, Isaacson JS. 2005. Intraglomerular inhibition: signaling mechanisms of an olfactory microcircuit. *Nature Neuroscience*, **8**(3): 354–364.

Nagayama S, Homma R, Imamura F. 2014. Neuronal organization of olfactory bulb circuits. *Frontiers in Neural Circuits*, **8**: 98.

Nieto-Estévez V, Defterali Ç, Vicario C. 2022. Distinct effects of BDNF and NT-3 on the dendrites and presynaptic boutons of developing olfactory bulb GABAergic interneurons in vitro. *Cellular and Molecular Neurobiology*, **42**(5): 1399–1417.

Ogboo BC, Grabovyy UV, Maini A, et al. 2022. Architecture of the NADPH oxidase family of enzymes. *Redox Biology*, **52**: 102298.

Paß T, Aßfalg M, Tolve M, et al. 2020. The impact of mitochondrial dysfunction on dopaminergic neurons in the olfactory bulb and odor detection. *Molecular Neurobiology*, **57**(9): 3646–3657.

Peng B, Rao YX, Wang Y, et al. 2024. Immunology reshapes neuroscience, and neuroscience reshapes immunology. *Fundamental Research*, **4**(2): 199–200.

Puntarulo S. 2005. Iron, oxidative stress and human health. *Molecular Aspects of Medicine*, **26**(4-5): 299–312.

Qian ZM, Ke Y. 2019. Brain iron transport. *Biological Reviews*, **94**(5): 1672–1684.

Rey NL, Wesson DW, Brundin P. 2018. The olfactory bulb as the entry site for prion-like propagation in neurodegenerative diseases. *Neurobiology of Disease*, **109**: 226–248.

Rodríguez Murúa S, Farez MF, Quintana FJ. 2022. The immune response in multiple sclerosis. *Annual Review of Pathology: Mechanisms of Disease*, **17**: 121–139.

Ross GW, Petrovitch H, Abbott RD, et al. 2008. Association of olfactory dysfunction with risk for future Parkinson's disease. *Annals of Neurology*, **63**(2): 167–173.

Rothammer N, Woo MS, Bauer S, et al. 2022. G9a dictates neuronal vulnerability to inflammatory stress via transcriptional control of ferroptosis. *Science Advances*, **8**(31): eabm5500.

Ryan SK, Zelic M, Han YN, et al. 2023. Microglia ferroptosis is regulated by SEC24B and contributes to neurodegeneration. *Nature Neuroscience*, **26**(1): 12–26.

Salvador AF, De Lima KA, Kipnis J. 2021. Neuromodulation by the immune system: a focus on cytokines. *Nature Reviews Immunology*, **21**(8): 526–541.

Schirinzi T, Maftei D, Passali FM, et al. 2023. Olfactory neuron prokineticin-2 as a potential target in Parkinson's disease. *Annals of Neurology*, **93**(1):

196–204.
Schmitz MT, Sandoval K, Chen CP, et al. 2022. The development and evolution of inhibitory neurons in primate cerebrum. *Nature*, **603**(7903): 871–877.
Sha R, Xu YQ, Yuan CW, et al. 2021. Predictive and prognostic impact of ferroptosis-related genes ACSL4 and GPX4 on breast cancer treated with neoadjuvant chemotherapy. *eBioMedicine*, **71**: 103560.
Sobiesk JL, Munakomi S. 2023. Anatomy, head and neck, nasal cavity. *In*: StatPearls [Internet]. Treasure Island (FL): StatPearls Publishing.
Stockwell BR. 2022. Ferroptosis turns 10: emerging mechanisms, physiological functions, and therapeutic applications. *Cell*, **185**(14): 2401–2421.
Sun LZ, Wang XW, Saredy J, et al. 2020. Innate-adaptive immunity interplay and redox regulation in immune response. *Redox Biology*, **37**: 101759.
Szego EM, Malz L, Bernhardt N, et al. 2022. Constitutively active STING causes neuroinflammation and degeneration of dopaminergic neurons in mice. *eLife*, **11**: e81943.
Tan EK, Chao YX, West A, et al. 2020. Parkinson disease and the immune system-associations, mechanisms and therapeutics. *Nature Reviews Neurology*, **16**(6): 303–318.
Tan QY, Fang YY, Gu Q. 2021. Mechanisms of modulation of ferroptosis and its role in central nervous system diseases. *Frontiers in Pharmacology*, **12**: 657033.
Tang DL, Chen X, Kang R, et al. 2021. Ferroptosis: molecular mechanisms and health implications. *Cell Research*, **31**(2): 107–125.
Tatti R, Bhaukaurally K, Gschwend O, et al. 2014. A population of glomerular glutamatergic neurons controls sensory information transfer in the mouse olfactory bulb. *Nature Communications*, **5**: 3791.
Tremblay C, Aslam S, Walker JE, et al. 2024. RNA sequencing of olfactory bulb in Parkinson's disease reveals gene alterations associated with olfactory dysfunction. *Neurobiology of Disease*, **196**: 106514.
Tuo QZ, Liu Y, Xiang Z, et al. 2022. Thrombin induces ACSL4-dependent ferroptosis during cerebral ischemia/reperfusion. *Signal Transduction and Targeted Therapy*, **7**(1): 59.
Ward RJ, Zucca FA, Duyn JH, et al. 2014. The role of iron in brain ageing and neurodegenerative disorders. *The Lancet Neurology*, **13**(10): 1045–1060.
Wu YT, Torabi SF, Lake RJ, et al. 2023. Simultaneous Fe^{2+}/Fe^{3+} imaging shows Fe^{3+} over Fe^{2+} enrichment in Alzheimer's disease mouse brain. *Science Advances*, **9**(16): eade7622.
Xu X, Zhu MW, Zu YZ, et al. 2024. Nox2 inhibition reduces trophoblast ferroptosis in preeclampsia via the STAT3/GPX4 pathway. *Life Sciences*, **343**: 122555.
Yan HF, Zou T, Tuo QZ, et al. 2021. Ferroptosis: mechanisms and links with diseases. *Signal Transduction and Targeted Therapy*, **6**(1): 49.
Yu-Taeger L, Stricker-Shaver J, Arnold K, et al. 2019. Intranasal administration of mesenchymal stem cells ameliorates the abnormal dopamine transmission system and inflammatory reaction in the R6/2 mouse model of Huntington disease. *Cells*, **8**(6): 595.
Yuan MY, Chen ZK, Ni J, et al. 2020. Ablation of olfactory bulb glutamatergic neurons induces depressive-like behaviors and sleep disturbances in mice. *Psychopharmacology*, **237**(8): 2517–2530.
Yuan Y, Ma XZ, Mi XQ, et al. 2023. Dopaminergic neurodegeneration in the substantia nigra is associated with olfactory dysfunction in mice models of Parkinson's disease. *Cell Death Discovery*, **9**(1): 388.
Zeppilli S, Ackels T, Attey R, et al. 2021. Molecular characterization of projection neuron subtypes in the mouse olfactory bulb. *eLife*, **10**: e65445.
Zhang N, Yu XQ, Song LM, et al. 2022. Ferritin confers protection against iron-mediated neurotoxicity and ferroptosis through iron chelating mechanisms in MPP^+-induced MES23.5 dopaminergic cells. *Free Radical Biology and Medicine*, **193**: 751–763.
Zhang SX, Wu LL, Zhang JR, et al. 2023. Multi-omics analysis reveals Mn exposure affects ferroptosis pathway in zebrafish brain. *Ecotoxicology and Environmental Safety*, **253**: 114616.
Zhang YT, He KJ, Zhang JB, et al. 2021. Advances in intranasal application of stem cells in the treatment of central nervous system diseases. *Stem Cell Research & Therapy*, **12**(1): 210.
Zhou B, Zhang JY, Liu XS, et al. 2018. Tom20 senses iron-activated ROS signaling to promote melanoma cell pyroptosis. *Cell Research*, **28**(12): 1171–1185.
Zhou FW, Hook C, Puche AC. 2023. Frequency-dependent centrifugal modulation of the activity of different classes of mitral and tufted cells in olfactory bulb. *Journal of Neurophysiology*, **129**(6): 1515–1533.
Zhou RP, Chen Y, Wei X, et al. 2020. Novel insights into ferroptosis: implications for age-related diseases. *Theranostics*, **10**(26): 11976–11997.

Ma et al. *Zool. Res.* 2025, 46(1): 225−235
https://doi.org/10.24272/j.issn.2095-8137.2024.228
https://cstr.cn/32248.14.zr.2024.228

ZR | Zoological Research

Article Open Access

Elevated CXCL1 triggers dopaminergic neuronal loss in the substantia nigra of C57BL/6J mice: Evaluation of a novel Parkinsonian mouse model

Xi-Zhen Ma[1,2,#], Guo-Rui Jia[1,#], Meng-Yu Li[1], Sheng-Han Zhang[1], Zhao-Xin Wang[1], Ning Song[1], Ying-Juan Liu[1,*], Jun-Xia Xie[1,*]

[1] *Institute of Brain Science and Disease*, *School of Basic Medicine*, *Shandong Provincial Key Laboratory of Pathogenesis and Prevention of Neurological Disorders*, *Qingdao University*, *Qingdao*, *Shandong* 266071, *China*

[2] *College of Life Sciences and Health*, *University of Health and Rehabilitation Science*, *Qingdao*, *Shandong* 266113, *China*

ABSTRACT

Substantial evidence points to the early onset of peripheral inflammation in the development of Parkinson's disease (PD), supporting the “body-first” hypothesis. However, there remains a notable absence of PD-specific animal models induced by inflammatory cytokines. This study introduces a novel mouse model of PD driven by the proinflammatory cytokine CXCL1, identified in our previous research. The involvement of CXCL1 in PD pathogenesis was validated using subacute and chronic MPTP-induced mouse models. Based on these findings, 2-month-old C57BL/6J mice were intravenously administered CXCL1 (20 ng/kg/day) for 2 weeks (5 days per week), successfully replicating motor deficits and pathological alterations in the substantia nigra observed in the chronic MPTP model. These results demonstrate the potential of CXCL1-induced inflammation as a mechanism for PD modeling. The model revealed activation of the PPAR signaling pathway in CXCL1-mediated neuronal damage by CXCL1. Linoleic acid, a PPAR-γ activator, significantly mitigated MPTP- and CXCL1-induced toxicity and reduced serum CXCL1 levels. In addition, the CXCL1-injected mouse model shortened the timeline for developing chronic PD mouse model to 2 weeks, offering an efficient platform for studying inflammation-driven processes in PD. The findings provide critical insights into the inflammatory mechanisms underlying PD and identify promising therapeutic targets for intervention.

Keywords: Parkinson’s disease; Mouse model; CXCL1; Inflammation; PPAR signaling pathway

This is an open-access article distributed under the terms of the Creative Commons Attribution Non-Commercial License (http://creativecommons.org/licenses/by-nc/4.0/), which permits unrestricted non-commercial use, distribution, and reproduction in any medium, provided the original work is properly cited.

Copyright ©2025 Editorial Office of Zoological Research, Kunming Institute of Zoology, Chinese Academy of Sciences

INTRODUCTION

Extensive evidence from studies of serum and cerebrospinal fluid samples in Parkinson’s disease (PD) patients, as well as neuropathological research in animal models, suggests that inflammation affects both the peripheral and central nervous systems in PD (Harms et al., 2021; Williams et al., 2022). Recent research has increasingly focused on the interplay between peripheral inflammation and neuroinflammation, corresponding to the two main hypotheses regarding the origin of PD: the “brain-first” (top-down) and “body-first” (bottom-up) pathways (Horsager et al., 2020). The body-first hypothesis, which posits that peripheral inflammation initiates early pathological changes that progress to the brain, has attracted significant attention due to its implications for disease mechanisms and potential therapeutic targets. Despite growing interest in the contribution of peripheral inflammation to PD pathology, the complexity of inflammatory pathways and the protective role of the blood-brain barrier (BBB) have hindered detailed investigation into the molecular mechanisms by which specific peripheral inflammatory factors mediate central neurodegeneration. Furthermore, the development of suitable animal models specifically induced by inflammatory cytokines remains limited, leaving a critical gap in the ability to accurately replicate the role of peripheral inflammation in PD pathogenesis.

Over the past several decades, a wide range of animal models has been developed to investigate the pathophysiology of PD. Although none of these models precisely recapitulates the pathology of PD, they have significantly advanced our understanding of the disease and highlighted limitations in current treatment options. Existing *in vivo* models are primarily induced through neurotoxins, pesticides, genetic alterations, α-synuclein inoculation, or viral

Received: 23 October 2024; Accepted: 22 November 2024; Online: 23 November 2024

Foundation items: This work was supported by the National Natural Science Foundation of China (32471049, 32170984, 32471188, 32200802) and Natural Science Foundation of Shandong Province (ZR2023QH110)

[#]Authors contributed equally to this work

*Corresponding authors, E-mail: jxiaxie@public.qd.sd.cn; liuyingjuan829@163.com

vector delivery. Neurotoxin-based models, such as those employing rotenone, 1-methyl-4-phenyl-1,2,3,6-tetrahydropyridine (MPTP), or 6-hydroxydopamine (6-OHDA), have been instrumental in elucidating the molecular cascades underlying dopaminergic neuronal death (Chia et al., 2020). While each neurotoxin model recapitulates certain aspects of PD pathology, neuroinflammation consistently emerges as a shared pathological feature. However, mature animal models specifically induced by inflammatory factors remain undeveloped. Single intraperitoneal injections of lipopolysaccharide (LPS) or tumor necrosis factor-α (TNF-α) in adult wild-type mice have demonstrated the capacity to induce chronic neuroinflammation. For example, a single injection of LPS at a dose of 5 mg/kg has been shown to reduce dopaminergic neurons in the substantia nigra (SN) by 23% at 7 months post-treatment (Qin et al., 2007). However, the prolonged timeline required for such models limits their practicality for PD research.

In our previous studies using rotenone-induced aged mouse models of PD, we similarly detected up-regulation of C-X-C motif chemokine ligand-1 (CXCL1) in both the peripheral and central nervous systems (Ma et al., 2024). CXCL1, the murine ortholog of CXCL8 (IL-8) in primates, exhibits functional similarities to IL-8 and acts as a neutrophil chemoattractant. It is expressed by neurons, astrocytes, microglia, and peripheral mononuclear macrophages. CXCL1 derived from astrocytes and neurons facilitates neutrophil transmigration across the BBB (Michael et al., 2020), triggering a cascade of inflammatory responses. Elevated IL-8 (CXCL1) levels have been detected in both cerebrospinal fluid and serum of PD patients (Calvani et al., 2020; Wijeyekoon et al., 2020), highlighting the potential role of CXCL1 in early PD pathology.

Emerging evidence suggests that CXCL1 may be involved in neuroimmune regulation associated with PD (Qian et al., 2021). Notably, safinamide, a clinically approved drug for PD, inhibits CXCL1 production by targeting the TLR4/NF-κB signaling pathway, thereby preventing leukocyte migration (Qian et al., 2021). Sustained CXCL1 elevation in the bloodstream has been shown to induce pathological injuries, including microglial activation, iron deposition, and dopaminergic neuronal loss in the SN of aging mice (Ma et al., 2024). Despite these findings, literature on the involvement of CXCL1 in PD remains limited.

Given this background, CXCL1 may represent a key inflammatory factor for developing novel PD mouse models. To address the challenges of using aged mice, experiments were conducted with 2-month-old C57BL/6J male mice to investigate the role of CXCL1 in PD pathology. Both MPTP-induced PD models and mice subjected to intravenous injection of CXCL1 were employed. Preliminary findings suggested that intravenous CXCL1 injection could serve as a novel approach for PD modeling, offering an efficient alternative for studying inflammation-driven mechanisms in PD. These results expand the range of available PD models and provide a valuable tool for future research in the field.

MATERIALS AND METHODS

Materials

1-Methyl-4-phenyl-1,2,3,6-tetrahydropyridine (MPTP, Cas No. 23007-85-4) was purchased from Sigma-Aldrich (USA). Mouse CXCL1 (GRO-α) and linoleic acid were purchased from MedChemExpress (USA). Information on the primary and secondary antibodies is shown in Supplementary Table S1. Blocking solution (normal donkey serum) was provided by Jackson ImmunoResearch (USA). All other chemicals were purchased from domestic reagent companies in China.

Animals

Eight-week male C57BL/6J mice were purchased from GemPharmatech Co., Ltd. (Jiangsu, China). Mice were acclimated to and maintained at 23±2°C under a 12 h light/dark cycle with 50% air humidity. Standard laboratory cages were used to house the mice (five mice per cage), with food and water provided freely. The study was conducted according to the guidelines of the Declaration of Helsinki and was approved by the Ethics Committee of the Medical College of Qingdao University (QDU-AEC-2022454, 30 November 2022).

In the MPTP-induced chronic PD mouse model, 8-week-old male C57BL/6J mice received intraperitoneal injections of MPTP at a dose of 18 mg/kg/day, administered twice per week for 5 weeks. For the MPTP-induced subacute PD mouse model, 8-week-old male C57BL/6J mice received intraperitoneal injections of MPTP at a dose of 30 mg/kg/day for five consecutive days. Sterilized normal saline was administered to the control groups.

In the CXCL1 intravenous injection model, 8-week-old male mice were divided into two groups: the CXCL1 treatment group and the vehicle group. CXCL1 was prepared as a stock solution of 10 μg/mL in normal saline, aliquoted, and stored at −20°C. Prior to administration, it was diluted to 2 ng/mL in normal saline. Mice in the CXCL1 group received tail vein injections at a dose of 20 ng/kg/day for 2 weeks (5 days per week). The control group received an equal volume of normal saline.

For linoleic acid treatment, mice were intragastrically administered linoleic acid at a dose of 60 mg/kg/day. A pre-protective regimen of linoleic acid was provided for 3 days, followed by continuous daily gavage throughout the MPTP or CXCL1 treatment period.

At the end of each experiment, mice were anesthetized with sodium pentobarbital prior to sacrifice for sample collection. Serum, SN, and striatum samples were collected for subsequent analyses.

Enzyme-linked immunosorbent assay (ELISA)

Serum samples were subjected to CXCL1 ELISA testing following the protocols outlined in the manufacturer's instructions. Detailed information regarding the ELISA kits is shown in Supplementary Table S1.

Motor behavior test

Motor coordination in mice was assessed using the classical pole test. A metallic pole, 50 cm in height and 0.5 cm in diameter, was wrapped with medical tape to prevent slipping. The pole was positioned vertically in a cage (40 cm×60 cm), with the base covered with corn cob granules to minimize the risk of injury. A rubber ball wrapped in tape was affixed to the top of the pole. Prior to testing, mice were acclimated and pre-trained three times on the day before the pole test. During the test, the time taken for the mice to turn around and descend from the top to the bottom of the pole was recorded. Motor coordination changes were primarily reflected in the turning time, which served as a key indicator.

Olfactory discrimination test

Olfactory function was evaluated based on the preference of

mice to remain in a familiar environment. The test was conducted in a transparent acrylic box (30cm length×20cm width×20cm height) divided into two equal compartments connected by an arched passage, allowing the mice to move freely between them. Mice were habituated to the setup for 2 min prior to testing. Clean bedding was placed in the non-familiar compartment, while bedding collected from the home cage of the mouse, used for 3 days before testing, was placed on the other side of the box (familiar compartment). Each mouse was positioned in the center of the arched passage, and the accumulated time spent in each compartment was recorded for 3 min using the EthoVision XT7 system.

Perl's-DAB and immunofluorescence staining

Mice were deeply anesthetized and transcardially perfused with normal saline. Brains were postfixed in 4% paraformaldehyde prepared in 0.1 mol/L phosphate-buffered saline (PBS) overnight and subsequently stored in 30% sucrose (dissolved in 0.1 mol/L PBS) in 4°C. Coronal brain sections (20 μm thick) were obtained at three-section intervals along the coronal plane after embedding in Tissue-Tek OCT (Sakura Finetek, USA). The SN was identified and collected based on the mouse brain atlas (*The Mouse Brain in Stereotaxic Coordinates Third Edition*, 2007).

Perl's iron staining combined with 3,3'-diaminobenzidine (DAB) enhancement was performed to detect iron-positive cells (Wang et al., 2019b). For immunofluorescence staining, brain sections were incubated with 5% donkey serum to block non-specific binding sites. Primary antibodies were added for overnight incubation at 4°C. The sections were washed three times, then incubated in secondary antibodies for 2 h at room temperature. 4',6-Diamidino-2-phenylindole (DAPI) was added to the secondary antibody solution 5 min prior to the end of incubation to counterstain nuclei. Details, including antibody dilution ratios, are provided Supplementary Table S1.

Images were captured using a digital pathology scanning system (OLYMPUS, Japan, VS120). The total number of tyrosine hydroxylase (TH)-positive cells in the SN and the average numbers of other indicators were quantified to assess expression levels. An unbiased stereological protocol was employed for cell counting, with the number of positive cells counted by an experimenter blinded to group assignments.

High-performance liquid chromatography (HPLC)

The striatum was rapidly dissected immediately after removing the mouse brain from the skull. After weighing, the striatum was homogenized in 120 μL of liquid A (0.4 mol/L $HClO_4$), with the homogenized tissue left on ice for 1 h, followed by centrifugation at 4°C and 12 000 r/min for 30 min. The resulting supernatant (80 μL) was added to 40 μL of liquid B (1.6 g of $C_6H_5K_3O_7$, 13.06 g of K_2HPO_4, and 0.185 g of EDTA·2Na dissolved in 250 mL of double distilled water). After thorough mixing, the samples were incubated on ice for 1 h and centrifuged again under the same conditions. The resulting supernatant was filtered through a nylon membrane and analyzed using HPLC (Thermo Scientific, UltiMate 3000, USA). Dopamine hydrochloride (DA, PHR1090-1G), homovanillic acid (HVA, 69673-25MG) and 3,4-dihydroxyphenylacetic acid (DOPAC, 11569-25MG) standards were purchased from Sigma (USA).

CY3 fluorescence signal tracing

To trace CXCL1 distribution, a CY3-labeled CXCL1 fluorophore (CY3-CXCL1, HY-D0822) was customized by MedChemExpress (USA). Mice received intravenous tail vein injections of CY3-CXCL1 with a red fluorescence signal at a dose of 20 ng/kg/day for five consecutive days. Following the final injection, mice were deeply anesthetized and transcardially perfused with normal saline. Brains were postfixed in 4% paraformaldehyde prepared in 0.1 mol/L PBS overnight and subsequently dehydrated in 30% sucrose (dissolved in 0.1 mol/L PBS). Coronal brain sections (20 μm thick) were prepared to observe the presence of CY3 red fluorescence signals. To confirm the distribution of CY3-labeled CXCL1, sections were co-stained with TH and DAPI for immunofluorescence.

Western blotting

The SN was carefully dissected from mouse brains immediately after extraction, following the guidelines of the mouse brain atlas. Tissues were lysed, and the protein supernatant was isolated through centrifugation at 4°C and 12 000 r/min for 30 min. Protein concentrations were ascertained using a bicinchoninic acid (BCA) protein assay kit to ensure accurate quantification. Equal quantities of soluble protein (10 μg) were subjected to sodium dodecyl sulfate–polyacrylamide gel electrophoresis (SDS-PAGE), with the subsequent blots developed using an ultrasensitive multichemiluminescence system (Fusion FX. EDGE, Vilber Lourmat, France) for enhanced detection sensitivity. Details regarding the primary and secondary antibodies employed are provided in Supplementary Table S1. Quantitative densitometric analyses were conducted on digitized images of the immunoblots using the NIH ImageJ program, with band densities normalized relative to β-actin to account for loading variability.

Statistical analysis

All results are expressed as the mean±standard error of the mean (SEM) and were analysed using SPSS v.23.0 software. Comparisons between two groups were performed using student's *t*-test, while comparisons among multiple groups were analyzed via one-way analysis of variance (ANOVA) followed by Newman-Keuls multiple-comparison test. Pearson correlation coefficients were used to analyze the relationships between variables. Statistical significance was defined as $P<0.05$.

RESULTS

Crucial role of CXCL1 in MPTP-induced PD model

In our prior research, we observed elevated serum CXCL1 levels in rotenone-induced Parkinsonian mice, concurrent with pathological changes in the brain. To further investigate the role of CXCL1 in PD, its involvement was evaluated in MPTP-induced PD mouse models. ELISA results revealed significantly increased serum CXCL1 levels in both the subacute (Figure 1A) and chronic (Figure 1B) phases of MPTP-induced PD mouse models, indicating that elevated CXCL1 levels may represent a common feature across PD mouse models.

MPTP administration also induced a series of pathological changes in the SN of mice, including activation of microglia (Figure 1G, H) and astrocytes (Figure 1I, J), abnormal iron deposition (Figure 2A, B), aggregation of phosphorylated α-synuclein within dopaminergic neurons, and dopaminergic neuronal loss (Figure 2C–F). In addition, dopamine (DA) levels in the striatum were significantly reduced (Figure 2G),

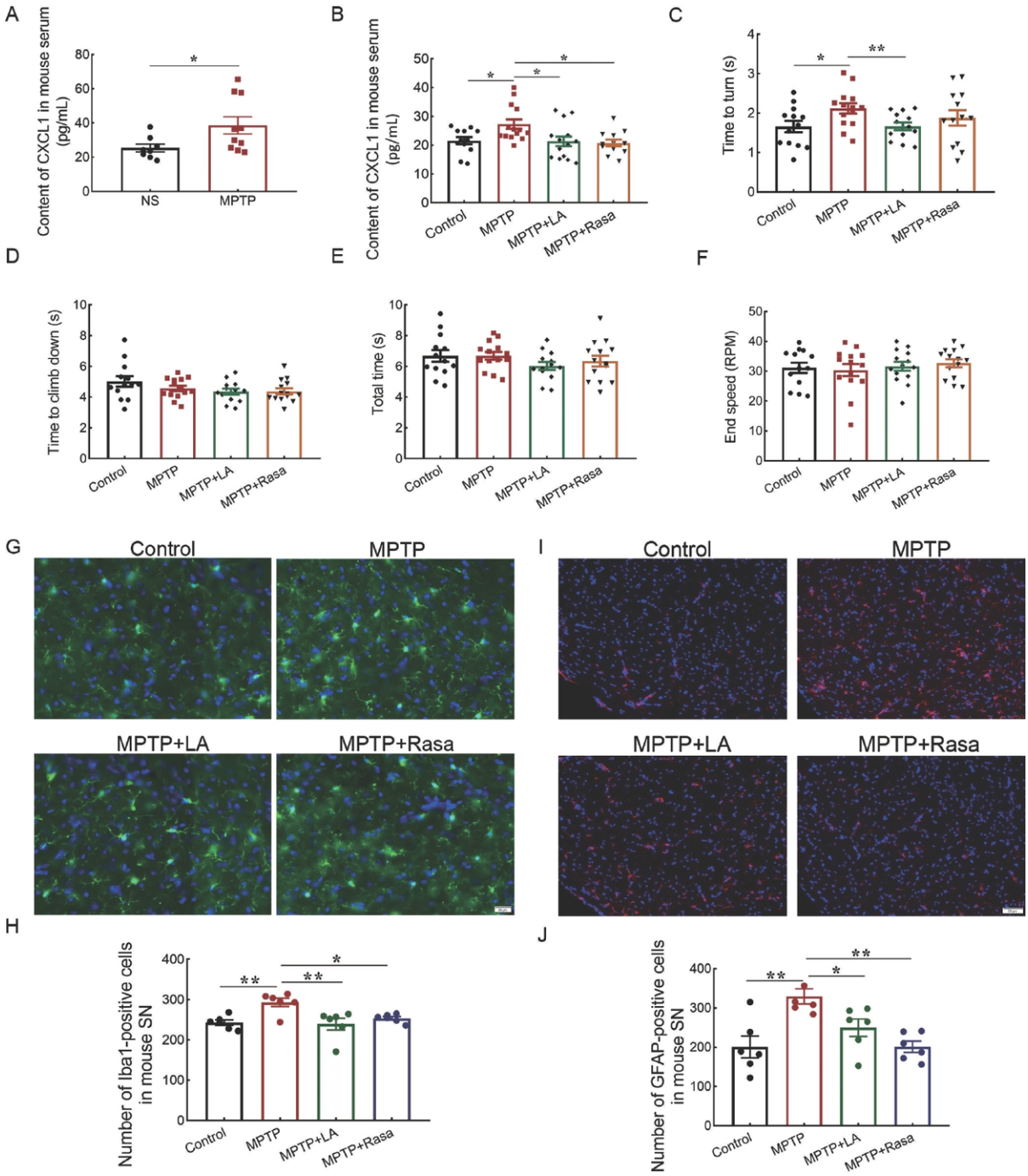


Figure 1 Linoleic acid (LA) and rasagiline (Rasa) inhibit CXCL1 elevation, movement disorders, and neuroinflammation induced by MPTP

A: ELISA analysis of CXCL1 levels in the serum of mice in the MPTP-induced subacute model (n=8, 10; P<0.05, Student's t-test). B: ELISA analysis of CXCL1 levels in the serum of MPTP-induced chronic model mice pre-treated with LA and Rasa (n=13, 15, 13, 14). C–F: Motor behavior assessment using the pole (C–E) and rotarod tests (F) in MPTP-treated mice with LA or Rasa pre-treatment (n=13, 15, 13, 14). G–J: Immunohistochemical staining for Iba1 (G, H; scale bar: 20 μm) and GFAP (I, J; scale bar: 50 μm) in the SN (n=6). *: P<0.05; **: P<0.01, one-way ANOVA with Newman-Keuls multiple-comparison test. Data are presented as mean±SEM.

and mice exhibited impaired motor coordination, reflected by prolonged turning times in the pole test (Figure 1C). To explore the relationship between CXCL1 concentration and neuroinflammation in the SN, Pearson correlation analysis was performed. A significant positive correlation was identified between serum CXCL1 levels and the number of activated microglia in the SN (r=0.6610, P<0.05, Figure 3A). The findings indicate that CXCL1 plays a pivotal role in the pathogenesis of PD.

Linoleic acid inhibits CXCL1 elevation and PD-like pathology induced by MPTP

The ELISA results showed that linoleic acid effectively prevented the increase in serum CXCL1 observed in the MPTP-induced chronic PD mouse model (Figure 1B). Furthermore, linoleic acid also inhibited MPTP-induced PD-like pathological changes in the SN of mice. Behavioral analyses indicated that linoleic acid preserved motor coordination, as shown by improved performance in the pole

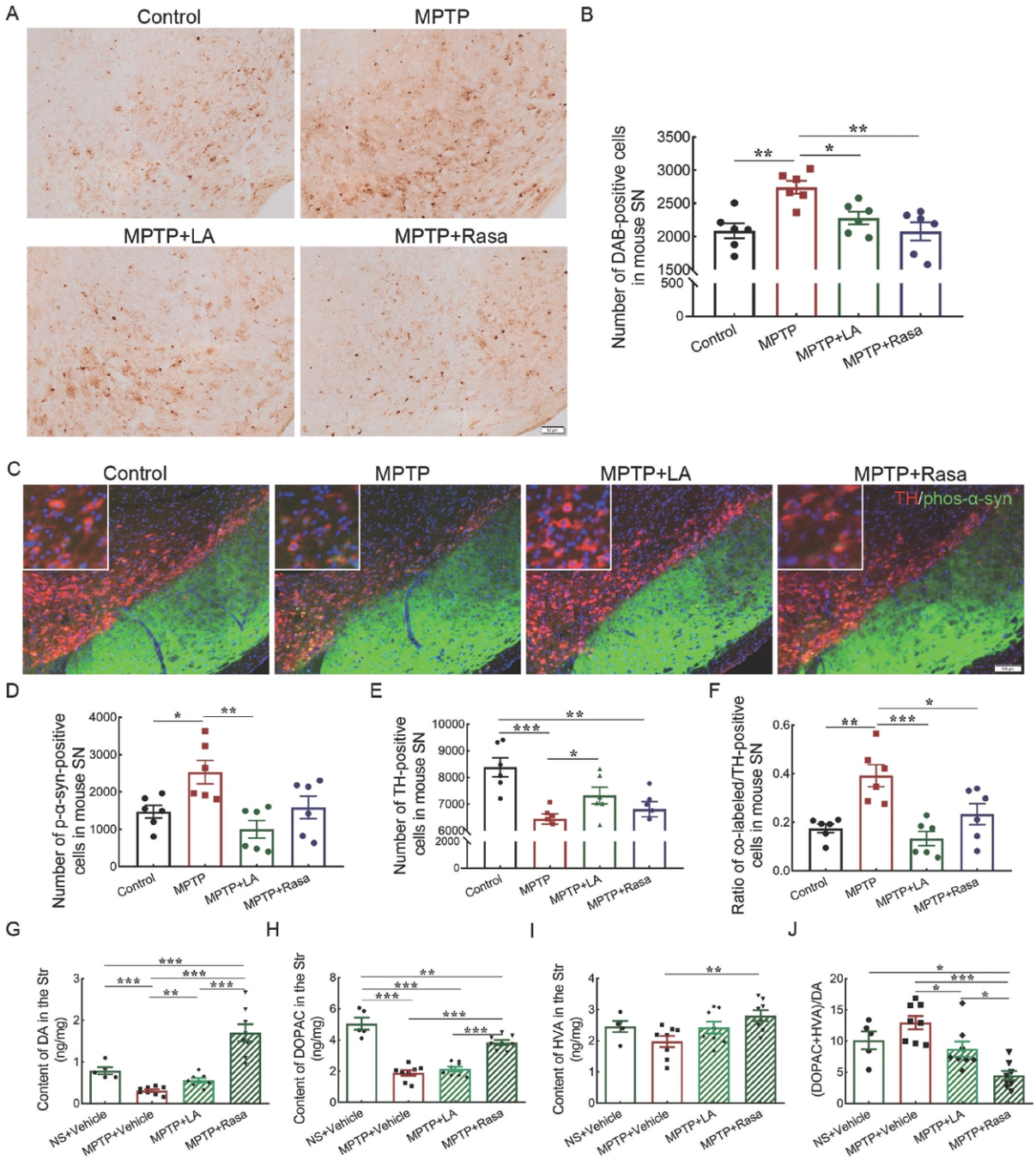


Figure 2 Linoleic acid (LA) inhibits iron deposition, p-α-syn aggregation, dopaminergic neuronal loss, and dopamine metabolism disorder induced by MPTP

MPTP-induced chronic mice with LA and Rasa pre-administered, A, B: Perls'-DAB staining of iron in mouse SN (*n*=6, scale bar: 50 μm); C–E: Immunohistochemistry staining of p-α-syn (green) and TH (red) positive cells in mouse SN (*n*=6, scale bar: 100 μm); F: The ratio of p-α-syn positive dopaminergic neurons in total dopaminergic neurons in the SN (*n*=6); G–J: HPLC analysis of dopamine (DA, G), 3,4-Dihydroxyphenylacetic acid (DOPAC, H), homovanillic acid (HVA, I) and dopamine turnover rate ((DOPAC+HVA)/DA, J) in the striatum (*n*=5, 8, 8, 8). *: $P<0.05$; **: $P<0.01$; ***: $P<0.001$, one-way ANOVA with Newman-Keuls multiple-comparison test was applied, data was presented as mean±SEM.

test (Figure 1C–F). Specifically, the time taken to turn remained at control levels in the linoleic acid group (Figure 1C), and the protective effect was pronounced than that observed with rasagiline treatment. Immunohistochemical analysis further supported the protective effects of linoleic acid. Both microglial (Figure 1G, H) and astrocyte activation (Figure 1I, J) in the SN, which were up-regulated in the MPTP group of mice, were counteracted in the MPTP+linoleic acid and MPTP+rasagiline groups, maintaining levels comparable to controls.

Perls'-DAB staining revealed that linoleic acid and rasagiline also reduced abnormal iron deposition in the SN of MPTP-treated mice (Figure 2A, B). Double-labeling immunofluorescence for phosphorylated alpha-synuclein (p-α-syn) and TH demonstrated a significant increase in p-α-syn-positive cells in the SN pars compacta of the MPTP-treated group. However, linoleic acid effectively reduced this increase, exhibiting a protective effect comparable to rasagiline

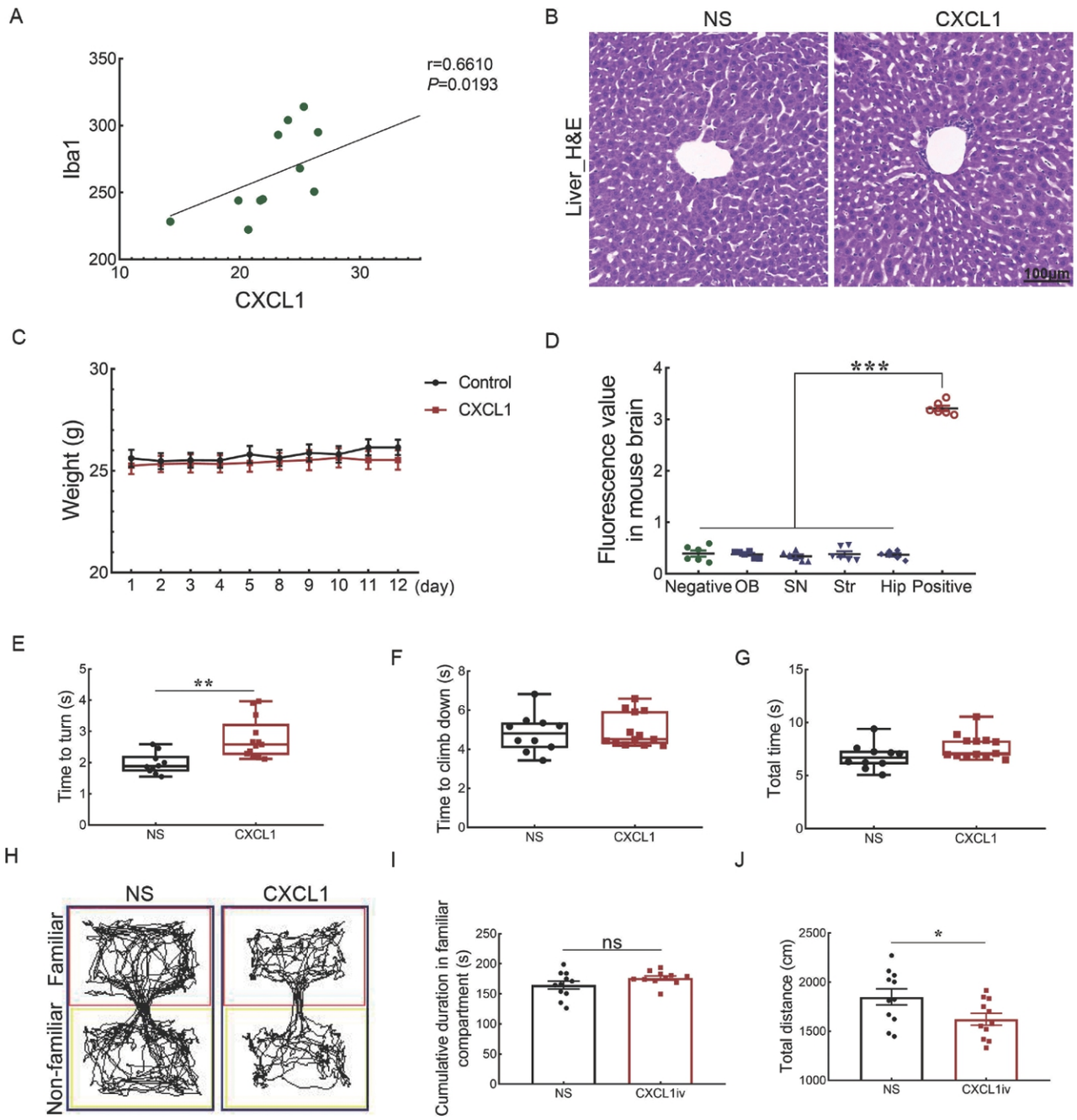


Figure 3 CXCL1 induces systemic inflammation in the liver and movement disorders without blood-brain barrier (BBB) injury

A: Correlation analysis between serum CXCL1 levels and the number of Iba-1 positive cells in the SN of MPTP-induced chronic model mice (r=0.6610, P<0.05, Pearson correlation test). Two-month-old C57BL/6J male mice received intravenous CXCL1 injections for 2 weeks. B: H&E staining of liver tissue (Scale bar: 100 μm). C: Body weight of mice. D: Fluorescence intensity in mouse brain tissue following intravenous injection of fluorochrome to assess BBB function (n=6, ***: P<0.001, one-way ANOVA with Newman-Keuls multiple-comparison test). Data are presented as mean±SEM. E–G: Pole test assessing motor behavior in mice (n=10, 13). H: Representative track visualization images from olfactory discrimination test. I, J: Quantification of accumulated duration in the familiar compartment (I) and total movement distance (J) in the olfactory discrimination test (n=11). ns: Not significant; *: P<0.05; **: P<0.01, student's t-test. Data are presented as mean±SEM.

(Figure 2C, D). Moreover, linoleic acid protected dopaminergic neurons from MPTP-induced damage, reducing dopaminergic neuronal loss (23.1%) in the SN, an effect not observed with rasagiline (Figure 2C, E). The proportion of p-α-syn-positive dopaminergic neurons in total dopaminergic neurons (Figure 2C, F) followed the same trend, indicating that MPTP increased the accumulation of p-α-syn in dopaminergic neurons.

HPLC analysis of striatal DA metabolism revealed that MPTP significantly reduced DA and its metabolites, DOPAC and HVA, in the striatum of mice (Figure 2G, H). Linoleic acid blocked the down-regulation of DA levels, whereas rasagiline, as a monoamine oxidase B (MAO-B) inhibitor, significantly increased DA content compared to both the control and MPTP-treated groups. Rasagiline also significantly up-regulated DOPAC and HVA levels compared to the MPTP-treated group, a distinct effect compared to linoleic acid (Figure 2H, I). The DA turnover rate ((DOPAC+HVA)/DA) in

the MPTP group was normalized by linoleic acid, with an even greater reduction observed in the MPTP+rasagiline group (Figure 2J). These findings suggest that the protective mechanism of linoleic acid operates upstream of the target of rasagiline within dopaminergic neurons. Notably, no significant increase in cytokines, including CXCL1, was detected in the SN of MPTP-treated mice (Supplementary Figure S1).

In conclusion, linoleic acid, a PPAR signaling pathway activator, inhibited PD-like pathological changes in the SN and prevented serum CXCL1 elevation in MPTP-induced PD models. However, it remains unclear whether the pathological changes in the SN are directly related to serum CXCL1 levels, warranting further investigation into this potential connection.

CXCL1 elevation in serum triggers PD-like pathological changes via BBB penetration, establishing a potential novel PD mouse model

To investigate the causal relationship between elevated CXCL1 in serum and pathological changes in the SN, 2-month-old C57BL/6J male mice were intravenously injected with CXCL1 (20 ng/kg/day). The H&E staining results revealed significant inflammatory cell infiltration in the liver of CXCL1-treated mice compared to the normal saline group, indicating systemic inflammation (Figure 3B). No significant pathological changes were observed in the spleen (Supplementary Figure S2A). Body weight remained consistent between the CXCL1 and control groups (Figure 3C). BBB integrity was confirmed by a fluorescent dye exclusion assay, as brain fluorescence levels in CXCL1-injected mice were comparable to negative controls, suggesting the BBB was intact (Figure 3D). Furthermore, DA metabolism showed no significant alterations, although this finding was based on a small sample size (n=5, Supplementary Figure S3A–D).

Motor coordination deficits were assessed using the pole (Figure 3E–G) and rotarod tests (Supplementary Figure S3E, F). Prolonged turning times in the pole test indicated impaired motor function following intravenous CXCL1 injection. However, no significant changes in olfactory function were detected in olfactory discrimination test (Figure 3H, I). Spontaneous activity, measured by cumulative movement distance, was reduced in CXCL1-treated mice (Figure 3H, J), further supporting movement-related impairments associated with elevated CXCL1 levels.

To determine whether CXCL1 directly crosses the BBB, CXCL1 labeled with CY3 fluorescence (CY3-CXCL1) was intravenously administered (20 ng/kg/day) for 5 days. Notably, CY3 fluorescence signals (red) were extensively observed in brains of mice, indicating BBB penetration (Figure 4A). Immunofluorescence analysis revealed increased expression of the CXCL1 receptor, CXCR2, in the SN of mice 2 weeks after caudal vein injection of CXCL1 (Figure 4B, C). These results suggest that CXCL1 crosses the BBB and interacts with CXCR2 to exert central effects, without brain region specificity. CXCL1 administration resulted in a marked increase in microglial activation, as indicated by Iba1-positive cells in the SN, while dopaminergic neurons decreased by 19.7% (Figure 4D, E, L, M). These effects were not observed in the ventral tegmental area (VTA) or temporal association area (TeA) (Supplementary Figure S2B–E). NeuN-positive cells in the SN and TeA also showed no significant changes (Supplementary Figure S2F–I). The number of iron-positive cells (Figure 4F, G) and fluorescence intensity of filamentous α-synuclein (fila-α-syn) (Figure 4H, I) increased in the SN. Immunofluorescence of PPARγ revealed that CXCL1 inhibited the PPAR signaling pathway, consistent with the protective effects of linoleic acid as a PPAR agonist (Figure 4J, K). Notably, no significant changes were detected in the ferroptosis markers ACSL4 and GPX4 (Supplementary Figure S4), indicating that ferroptosis was not replicated in this model.

Linoleic acid inhibits PD-like pathological changes induced by CXCL1

In the pole test, linoleic acid effectively preserved motor coordination, maintaining both the turning time and total descent time at levels comparable to the control group (Figure 5A–C). Immunohistochemical analysis further confirmed the protective effects of linoleic acid in the SN. Notably, linoleic acid mitigated the CXCL1-induced loss of dopaminergic neurons, maintaining their numbers near control levels (Figure 5D, E), and significantly reduced microglial activation in the SN (Figure 5F, G), counteracting the inflammatory response triggered by CXCL1.

These findings indicate that elevated CXCL1 in the blood of 2-month-old C57BL/6J mice crosses the BBB, leading to PD-like lesions in the SN, highlighting the utility of this model as a promising tool for studying PD pathogenesis.

DISCUSSION

Mouse CXCL1 (GRO-α), the murine ortholog of CXCL8 (IL-8), shares similar but not identical biological activities with its primate counterpart. Alpha-chemokines, including CXCL1, CXCL6, and CXCL8, have been implicated in the development of TH-positive neurons in ventral midbrain, suggesting their potential relevance to PD therapy (Edman et al., 2008). Conversely, safinamide, a clinically approved drug for PD treatment, has been shown to suppress CXCL1 production by inhibiting the TLR4/NF-κB signaling pathway (Qian et al., 2021). These observations underscore the dual role of CXCL1 in PD, acting as both a modulator of neuronal development and a contributor to neuroinflammation.

In this study, significant elevations in serum CXCL1 were observed in 2-month-old mice subjected to MPTP treatment, both in subacute and chronic PD models. This finding is consistent with previous research in aging rotenone-induced models (Ma et al., 2024), indicating that elevated CXCL1 is a relatively common phenomenon across PD mouse models. In addition, at early stages (2 weeks), a moderate positive correlation was identified between serum CXCL1 levels and microglial activation in the SN, suggesting a link between peripheral CXCL1 elevation and central neuroinflammation. Behavioral assessments of CXCL1-injected mice revealed motor deficits comparable to those in MPTP-induced PD models, with significantly impaired motor coordination observed in the pole test within just 2 weeks of intravenous CXCL1 administration. Pathological analyses showed that elevated CXCL1 in serum triggered neuroinflammation, iron accumulation, and dopaminergic neuronal loss (19.7%) in the SN. Notably, this neuronal loss was similar to that observed in chronic MPTP models (23.1%). These findings highlight the successful establishment of a novel PD mouse model through intravenous injection of CXCL1 (20 ng/kg/day) for 2 weeks (5 days per week) in 2-month-old male C57BL/6J mice. The shorter duration of this model (2 weeks) compared to the chronic MPTP model (5 weeks) offers a more efficient approach for investigating PD pathophysiology. Moreover, as

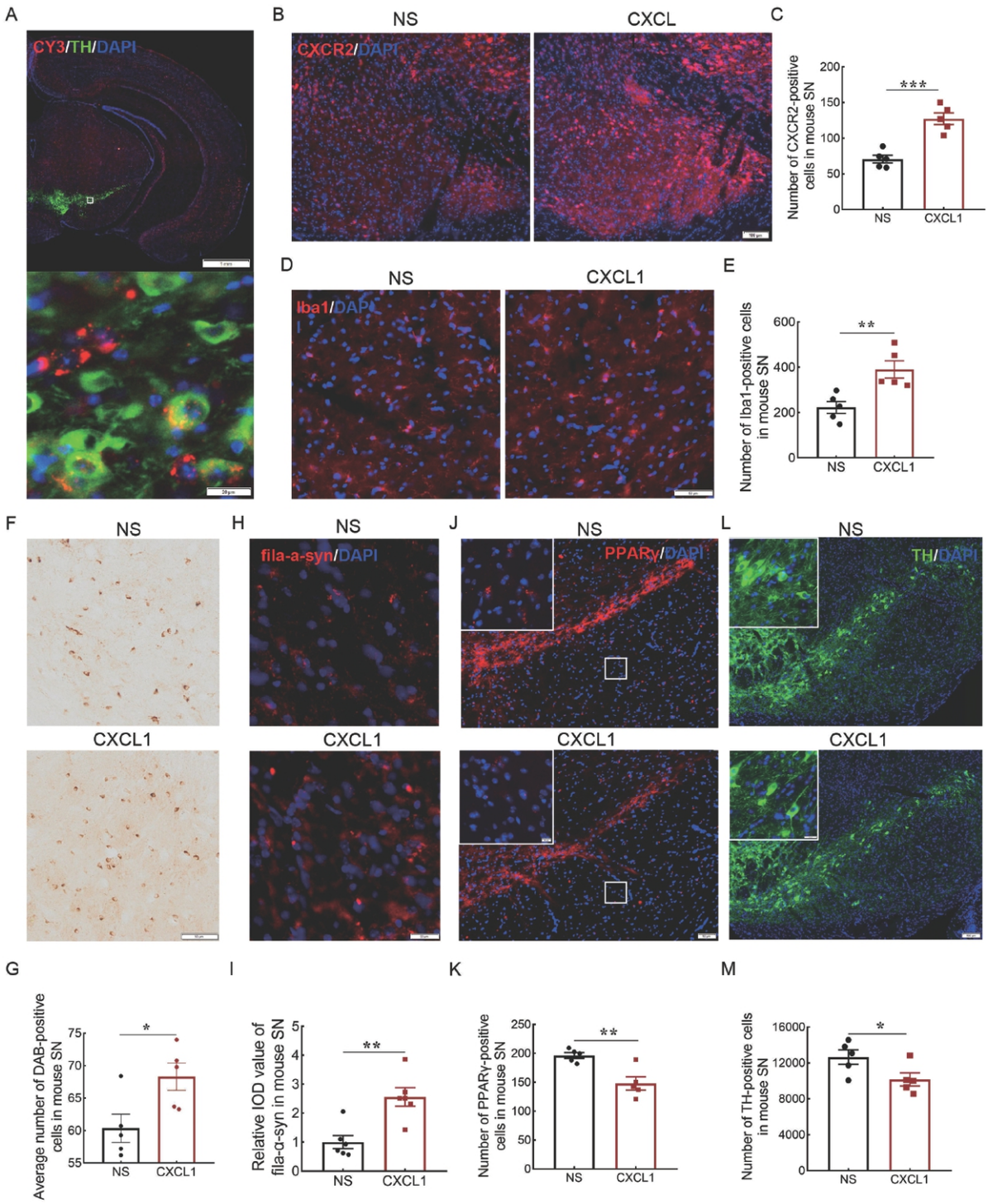


Figure 4 CXCL1 induces microglial activation, iron deposition, α-synuclein aggregation, PPAR inhibition, and dopaminergic neuronal loss across the blood-brain barrier

A: Fluorescent imaging of CY3 (red) and TH through immunofluorescence staining (green) of the SN of 2-month-old C57BL/6J male mice following intravenous CY3-CXCL1 administration (20 ng/kg/day for 5 days) (Scale bar: 1 mm, 20 μm). B, C: Immunohistochemical staining of CXCR2 in the SN of mice treated with intravenous CXCL1 for 2 weeks (Scale bar: 100 μm). D, E: Immunohistochemical staining of Iba1 in the SN (Scale bar: 50 μm). F, G: Perls'-DAB staining of iron in the SN (Scale bar: 50 μm). H, I: Immunohistochemical staining of fila-α-syn in the SN (Scale bar: 20 μm). J, K: Immunohistochemical staining of PPARγ in the SN (Scale bars: 50 μm, 10 μm). L, M: Immunohistochemical staining of TH in the SN (Scale bars: 100 μm, 20 μm). n=5, *: P<0.05; **: P<0.01; ***: P<0.001, student's t-test. Data are presented as mean±SEM.

a model driven by an inflammatory cytokine, this approach holds significant potential for exploring the role of inflammation in PD.

During the evaluation of this novel mouse model, several unexpected results emerged. Despite the loss of 19.7% of dopaminergic neurons, no significant alterations in DA metabolism were observed. The slight decrease in DA content suggests that the remaining 80.3% of surviving dopaminergic neurons may compensate for the functional deficits caused by neuronal loss. It is possible that extending the duration of

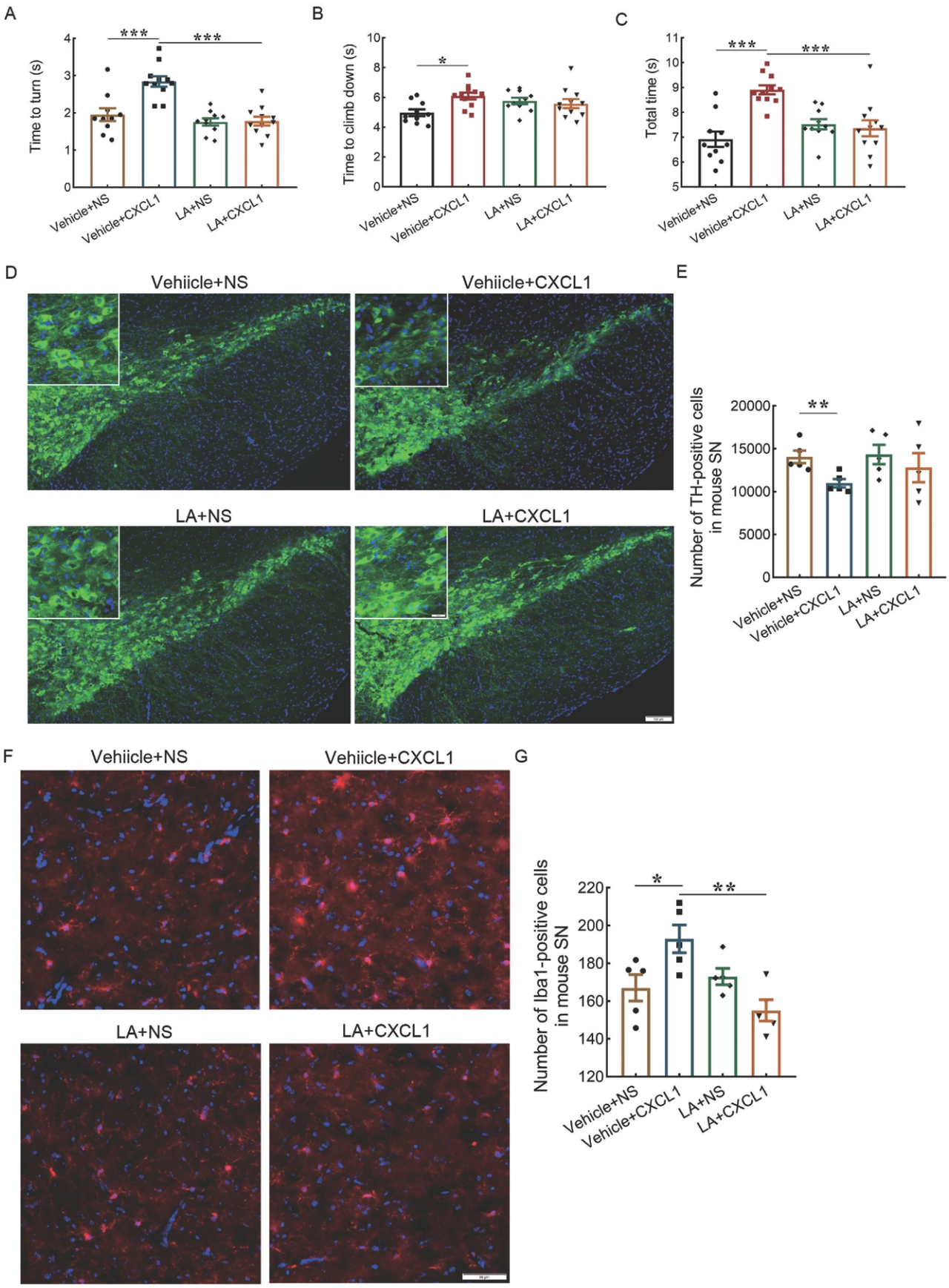


Figure 5 Linoleic acid (LA) inhibits movement disorder, neuroinflammation, and dopaminergic neuronal loss induced by CXCL1

A–C: Motor behavior assessment using the pole test in CXCL1-induced mice pre-treated with LA. D–G: Immunohistochemical staining of TH (D, E, scale bars: 100 μm, 20 μm) and Iba1 (F, G, scale bar: 50 μm)-positive cells in the SN (n=5). *: P<0.05; **: P<0.01; ***: P<0.001, one-way ANOVA with Newman-Keuls multiple-comparison test. Data are presented as mean±SEM.

CXCL1 administration may reveal more pronounced changes in DA metabolism.

To elucidate the molecular mechanisms underlying neuronal damage caused by elevated serum CXCL1, we determined whether peripheral CXCL1 can cross the BBB and directly affect the brain. As studies have indicated that CXCL1 activates the CXCR2 receptor at concentrations as low as 1 nmol/L (~9 ng/mL) and the CXCR1 receptor at approximately 100 nmol/L (~900 ng/mL) (Edman et al., 2008). In our CXCL1-induced mouse model, the serum and SN levels of CXCL1 were well below the threshold for CXCR1 activation, suggesting that central pathology may be mediated through CXCR2 activation.

To confirm whether CXCL1 crosses the BBB, a CY3-labeled CXCL1 fluorophore was injected intravenously into the blood of mice for tracing. Notably, CY3-CXCL1 was observed in the brains of treated mice, with no evidence of BBB dysfunction. Additionally, CXCR2 expression levels were up-regulated in the brain, further suggesting that CXCL1 can enter the brain from circulation and activate the CXCR2 receptor. Interestingly, although CY3-CXCL1 and up-regulated CXCR2 were detected diffusely across the brain, significant pathological changes were restricted to the SN. This region-specific damage may reflect the inherent vulnerability of the SN based on the role of microglia.

The SN pars compacta is distinguished by its exceptionally high density of microglia, which is 4–5 times greater than in other brain regions (Kim et al., 2000; Masuda et al., 2019). This microglial abundance is believed to contribute significantly to the vulnerability of dopaminergic neurons within the SN. Although only a small amount of CXCL1 entered the brain in our intravenous mouse model, it may still strongly activate microglia in the SN. The indispensable role of microglia activation in PD pathogenesis has been demonstrated in studies where microglia have been depleted using PLX5622, an inhibitor of colony-stimulating factor 1 receptor (CSF1R) (Ma et al., 2024). Collectively, these findings highlight the interplay between peripheral and central inflammation in driving neurodegeneration and suggest that CXCL1 may serve as a pivotal mediator in this process.

Our previous study demonstrated that CXCL1 exerts its effects by inhibiting the PPAR signaling pathway, with this inhibition primarily occurring in microglia (Ma et al., 2024). Considering the well-documented protective effects of the PPAR signaling pathway in regulating inflammation and lipid metabolism (Peiseler et al., 2022; Titus et al., 2024), the neuroprotective action of the PPAR ligand linoleic acid in chronic MPTP-treated mice likely arises through PPAR activation and its anti-inflammatory properties. In this study, linoleic acid, a PPAR-γ activator, effectively mitigated key pathological features of PD, including iron deposition, p-α-syn aggregation, dopaminergic neuronal loss, and DA metabolism disturbances, accompanied by suppression of microglial and astrocytic activation. Furthermore, mice that received intravenous injections of CXCL1 exhibited movement disorders, microglial activation, and dopaminergic neuronal loss, closely resembling the pathological and behavioral changes observed in MPTP-treated mice. Notably, these effects were mitigated by linoleic acid administration. Previous studies have shown that the PPAR-β/δ agonist GW0742 reduces CXCL1 production (Chehaibi et al., 2017), while the PPAR-γ activator Sirt1 similarly decreases CXCL1 expression (Wang et al., 2019a). Furthermore, studies in mice fed a high-fat diet have revealed that ethanol attenuates hepatic PPAR-γ activation while up-regulating hepatic CXCL1 expression (Wang et al., 2017). These findings suggest a potential feedback loop in which CXCL1-induced inhibition of the PPAR pathway exacerbates CXCL1 release, forming a self-reinforcing cycle of inflammation. Additional evidence supports this hypothesis. Notably, the PPAR-γ agonist pioglitazone reduces microglial proliferation and NF-κB activation in the SN in the 6-OHDA model of PD (Machado et al., 2019). Inhibition of NF-κB can up-regulate PPAR-γ and reduce CXCL1 levels (Qian et al., 2021; Venkataraman et al., 2021), while NF-κB pathway activation can induce CXCL1 secretion (Chung et al., 2018). Based on these observations, we hypothesize that CXCL1 activates NF-κB in microglia via its receptor CXCR2, subsequently inducing CXCL1 secretion through PPAR pathway inhibition, although the specific molecular mechanisms require further exploration (Figure 6).

Although several questions remain unanswered, our preliminary findings suggest that intravenous injection of CXCL1 establishes a novel and promising mouse model for studying PD pathogenesis and inflammation-driven neurodegeneration.

SUPPLEMENTARY DATA

Supplementary data to this article can be found online.

COMPETING INTERESTS

The authors declare that they have no competing interests.

AUTHORS' CONTRIBUTIONS

X.Z.M. and G.R.J. performed most experiments and composed the first draft. M.Y.L., S.H.Z., and Z.X.W. performed part of the experiments. N.S. guided the experiments and polished and finalized the article. Y.J.L. guided and performed experiments. J.X.X. conceived and directed the project. All authors read and approved the final version of the manuscript.

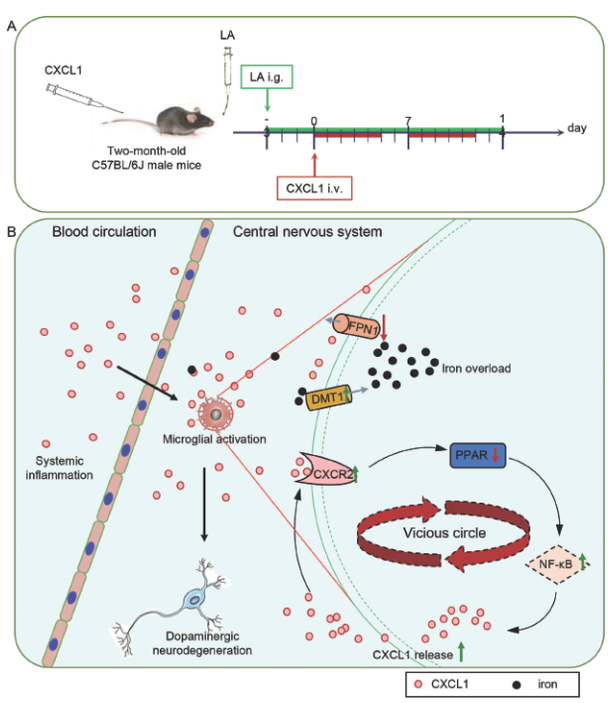


Figure 6 Graphical abstract

A: Flow chart of CXCL1-induced mice with pre-administered linoleic acid. B: Mechanistic diagram.

REFERENCES

Calvani R, Picca A, Landi G, et al. 2020. A novel multi-marker discovery approach identifies new serum biomarkers for Parkinson's disease in older people: an EXosomes in PArkiNson Disease (EXPAND) ancillary study. *Geroscience*, **42**(5): 1323–1334.

Chehaibi K, Le Maire L, Bradoni S, et al. 2017. Effect of PPAR-β/δ agonist GW0742 treatment in the acute phase response and blood-brain barrier permeability following brain injury. *Translational Research*, **182**: 27–48.

Chia SJ, Tan EK, Chao YX. 2020. Historical Perspective: Models of Parkinson's Disease. *International Journal of Molecular Sciences*, **21**(7): 2464.

Chung L, Thiele Orberg E, Geis AL, et al. 2018. Bacteroides fragilis Toxin Coordinates a Pro-carcinogenic Inflammatory Cascade via Targeting of Colonic Epithelial Cells. *Cell Host & Microbe*, **23**(2): 203–214.

Edman LC, Mira H, Erices A, et al. 2008. α-chemokines regulate proliferation, neurogenesis, and dopaminergic differentiation of ventral midbrain precursors and neurospheres. *Stem Cells*, **26**(7): 1891–1900.

Harms AS, Ferreira SA, Romero-Ramos M. 2021. Periphery and brain, innate and adaptive immunity in Parkinson's disease. *Acta Neuropathologica*, **141**(4): 527–545.

Horsager J, Andersen KB, Knudsen K, et al. 2020. Brain-first versus body-first Parkinson's disease: a multimodal imaging case-control study. *Brain*, **143**(10): 3077–3088.

Kim WG, Mohney RP, Wilson B, et al. 2000. Regional difference in susceptibility to lipopolysaccharide-induced neurotoxicity in the rat brain: role of microglia. *Journal of Neuroscience*, **20**(16): 6309–6316.

Ma XZ, Chen LL, Qu L, et al. 2024. Gut microbiota-induced CXCL1 elevation triggers early neuroinflammation in the substantia nigra of Parkinsonian mice. *Acta Pharmacologica Sinica*, **45**(1): 52–65.

Machado MMF, Bassani TB, Cóppola-Segovia V, et al. 2019. PPAR-γ agonist pioglitazone reduces microglial proliferation and NF-κB activation in the substantia nigra in the 6-hydroxydopamine model of Parkinson's disease. *Pharmacological Reports*, **71**(4): 556–564.

Masuda T, Sankowski R, Staszewski O, et al. 2019. Spatial and temporal heterogeneity of mouse and human microglia at single-cell resolution. *Nature*, **566**(7744): 388–392.

Michael BD, Bricio-Moreno L, Sorensen EW, et al. 2020. Astrocyte- and Neuron-Derived CXCL1 Drives Neutrophil Transmigration and Blood-Brain Barrier Permeability in Viral Encephalitis. *Cell Reports*, **32**(11): 108150.

Peiseler M, Schwabe R, Hampe J, et al. 2022. Immune mechanisms linking metabolic injury to inflammation and fibrosis in fatty liver disease - novel insights into cellular communication circuits. *Journal of Hepatology*, **77**(4): 1136–1160.

Qian LL, Li JZ, Sun XM, et al. 2021. Safinamide prevents lipopolysaccharide (LPS)-induced inflammation in macrophages by suppressing TLR4/NF-κB signaling. *International Immunopharmacology*, **96**: 107712.

Qin L, Wu X, Block ML, et al. 2007. Systemic LPS causes chronic neuroinflammation and progressive neurodegeneration. *Glia*, **55**(5): 453–462.

Titus C, Hoque MT, Bendayan R. 2024. PPAR agonists for the treatment of neuroinflammatory diseases. *Trends in Pharmacological Sciences*, **45**(1): 9–23.

Venkataraman B, Almarzooqi S, Raj V, et al. 2021. Thymoquinone, a Dietary Bioactive Compound, Exerts Anti-Inflammatory Effects in Colitis by Stimulating Expression of the Colonic Epithelial PPAR-γ Transcription Factor. *Nutrients*, **13**(4): 1343.

Wang J, Chen G, Lu L, et al. 2019a. Sirt1 inhibits gouty arthritis via activating PPARγ. *Clinical Rheumatology*, **38**(11): 3235–3242.

Wang W, Xu MJ, Cai Y, et al. 2017. Inflammation is independent of steatosis in a murine model of steatohepatitis. *Hepatology*, **66**(1): 108–123.

Wang Z, Zeng YN, Yang P, et al. 2019b. Axonal iron transport in the brain modulates anxiety-related behaviors. *Nature Chemical Biology*, **15**(12): 1214–1222.

Wijeyekoon RS, Moore SF, Farrell K, et al. 2020. Cerebrospinal Fluid Cytokines and Neurodegeneration-Associated Proteins in Parkinson's Disease. *Movement Disorders*, **35**(6): 1062–1066.

Williams GP, Schonhoff AM, Sette A, et al. 2022. Central and Peripheral Inflammation: Connecting the Immune Responses of Parkinson's Disease. *Journal of Parkinson's Disease*, **12**(s1): S129–S136.

Zheng et al. *Zool. Res.* 2025, 46(1): 236–248
https://doi.org/10.24272/j.issn.2095-8137.2024.256
https://cstr.cn/32248.14.zr.2024.256

ZR | Zoological Research

Article Open Access

Functional evolution of thyrotropin-releasing hormone neuropeptides: Insights from an echinoderm

Yingqiu Zheng[1,2], Huachen Liu[1], Xin Dang[2], Juan Diego Gaitán-Espitia[2,*], Muyan Chen[1,*]

[1] *The Key Laboratory of Mariculture*, *Ministry of Education*, *Ocean University of China*, *Qingdao*, *Shandong* 266003, *China*

[2] *The Swire Institute of Marine Science and School of Biological Sciences*, *The University of Hong Kong*, *Hong Kong SAR* 999077, *China*

ABSTRACT

Feeding behavior is regulated by a complex network of endogenous neuropeptides. In chordates, this role is suggested to be under the control of diverse factors including thyrotropin-releasing hormone (TRH). However, whether this regulatory activity of TRH is functionally conserved in non-chordate metazoans, and to what extent this process is underpinned by interactions of TRH with other neuropeptides such as cholecystokinin (CCK, known as a satiety signal), remain unclear. This study investigated the TRH signaling system in the echinoderm *Apostichopus japonicus*. Bioinformatic analyses and ligand-binding assays identified a functional TRH receptor (AjTRHR) that activated signaling via the MAPK/ERK1/2 pathways. Experimental administration of TRH significantly reduced feeding activity, while up-regulating CCK expression. RNA interference (RNAi) experiments confirmed that both CCK and TRH are essential components of satiety signaling, working synergistically to mediate feeding inhibition. Evolutionary analysis of TRH-type peptides revealed greater conservation of the short isoform of TRH compared to the long isoform, probably driven by strong selection acting on the functional redundancy. These findings provide compelling evidence of a TRH-mediated signaling system in non-chordate deuterostomes, expanding our understanding of neuropeptide-regulated feeding mechanisms in marine invertebrates.

Keywords: Thyrotropin-releasing hormone (TRH); Feeding behavior; Cholecystokinin (CCK); Evolution; Echinoderm; Satiety signals

INTRODUCTION

Feeding is a pivotal behavior in animal growth, development, reproduction, energetic homeostasis, and immune function. This intricate process is governed by complex neural circuits (Guo et al., 2021; Pool & Scott, 2014) that coordinate appetite and satiety signals through the actions of neuropeptides (Root et al., 2011). These signaling molecules, fundamental components of the neuroendocrine system, play critical roles in regulating diverse physiological and behavioral processes in animals (Burbach, 2011). Notably, neuropeptides, such as thyrotropin-releasing hormone (TRH), have been widely implicated as key regulators of feeding behavior (Al-Arabi & Andrews, 2006; Puga et al., 2016; Schuhler et al., 2007; Schwartz et al., 2013; Steward et al., 2003). Most of our current knowledge regarding the functional role of TRH in feeding regulation is derived from vertebrate studies. In rodents, such as rats and squirrels, TRH administration has been shown to suppress feeding motivation and inhibit feeding behavior (Al-Arabi & Andrews, 2006; Frare et al., 2021; Puga et al., 2016; Schuhler et al., 2007; Schwartz et al., 2013; Steward et al., 2003). However, the extent to which these effects are conserved across other taxa, particularly in relation to the evolutionary history of TRH signaling, remains unclear. Given the estimated 560-million-year evolutionary trajectory of this neuropeptide signaling pathway, its functional role in diverse chordate lineages and beyond is still not fully understood. This uncertainty is further compounded by the identification of TRH-type neuropeptides in various invertebrate metazoans, including mollusks (fulicins) (Ohta et al., 1991) and annelids/arthropods/nematodes/priapulids (EFLGamides) (Bauknecht & Jékely, 2015; Conzelmann et al., 2013; Van Sinay et al., 2017; Veenstra & Šimo, 2020; Zandawala et al., 2024), and in non-vertebrate deuterostomes (TRH) (Chen et al., 2019; Jékely, 2013; Rowe & Elphick, 2012; Semmens et al., 2016; Zandawala et al., 2017). Despite this broad taxonomic distribution, the functional roles of TRH-like neuropeptides in feeding regulation within these invertebrate groups remain largely uncharacterized.

Echinoderms, as deuterostome invertebrates, share a close evolutionary relationship with chordates, forming a sister group alongside hemichordates. This phylogenetic position, combined with ecological traits shared with marine protostomes (e.g., mollusks, annelids, and arthropods), such as feeding strategies, external fertilization, and larval

This is an open-access article distributed under the terms of the Creative Commons Attribution Non-Commercial License (http://creativecommons.org/licenses/by-nc/4.0/), which permits unrestricted non-commercial use, distribution, and reproduction in any medium, provided the original work is properly cited.

Copyright ©2025 Editorial Office of Zoological Research, Kunming Institute of Zoology, Chinese Academy of Sciences

Received: 01 October 2024; Accepted: 08 November 2024; Online: 09 November 2024

Foundation items: This work was supported by the National Natural Science Foundation of China (42276103)

*Corresponding authors, E-mail: jdgaitan@hku.hk; chenmuyan@ouc.edu.cn

development, provides an interesting opportunity to study and compare the evolutionary and functional conservationism of TRH and other neuropeptides in the regulation of feeding behavior. TRH-type neuropeptides have been identified across diverse echinoderm classes, including sea urchins (e.g., *Strongylocentrotus purpuratus*) (Rowe & Elphick, 2012), starfish (e.g., *Asterias rubens* and *Acanthaster planci*) (Semmens et al., 2016; Smith et al., 2017), ophiuroids (e.g., *Ophionotus victoriae*, *Amphiura filiformis*, and *Ophiopsila aranea*) (Zandawala et al., 2017), and sea cucumbers (e.g., *Apostichopus japonicus*, *Holothuria scabra*, *Holothuria glaberrima*, and *Holothuria leucospilota*) (Chen et al., 2019; Chieu et al., 2019; Rowe et al., 2014; Suwansa-Ard et al., 2018). Empirical evidence suggests that TRH-type neuropeptides in echinoderms are implicated in critical processes, including gonadal development in adults and feeding, attachment, and metamorphosis of larvae (Chaiyamoon et al., 2020; Mayorova et al., 2016; Zheng et al., 2022). Previous studies have uncovered key insights into the role of TRH-type neuropeptides in sea cucumbers, particularly their involvement in the up-regulation of the TRH-type precursor *AjTRHP* during aestivation, a physiological state during which feeding is suspended (Zhao et al., 2014). Recent single-cell RNA sequencing in *A. japonicus* also identified a neuronal population with markedly elevated *AjTRHP* expression, with TRH predicted to function as the central regulatory gene within this neuronal network governing feeding behavior (Zheng et al., 2024). Despite these advances, the precise mechanisms through which TRH regulates feeding cessation in sea cucumbers, and its potential parallels with vertebrate deuterostomes, remain unresolved, raising questions about the functional and evolutionary conservation of TRH-mediated feeding regulation (Zuckerkandl & Pauling, 1965).

To address these questions, the present study employed an integrated approach combining cellular, biochemical, and molecular methodologies to reconstruct the structure and dynamics of the TRH signaling pathway in *A. japonicus*. Furthermore, interactions between TRH and other neuropeptides potentially involved in satiety signaling, such as cholecystokinin (CCK), were explored. Notably, our study revealed the function of the TRH signaling system in feeding regulation within a non-chordate deuterostome, offering new insights into the neuroendocrine mechanisms underlying feeding regulation in marine invertebrates.

MATERIALS AND METHODS

Ethical approval

All applicable international, national, and/or institutional guidelines for the care and use of animals were strictly followed. All methods were carried out in accordance with the ARRIVE guidelines (https://arriveguidelines.org) for animal experiments. All animal care and use procedures were approved by the Institutional Animal Care and Use Committee of Ocean University of China (Permit No.: 20141201) and performed according to the Chinese Guidelines for the Care and Use of Laboratory Animals (GB/T 35892-2018).

Animals

Experimental animals were obtained from the Shandong Oriental Ocean Sea Cucumber Breeding Farm (Weihai, China) and transferred to the aquarium facilities at Ocean University of China. Laboratory culture conditions utilized filtered and ultraviolet (UV)-sterilized seawater sourced from the Qingdao coastal region, maintained at a temperature of 18–20°C, salinity of 32 ppt, and 12:12 h light/dark cycle. Following acclimation for one week, tissues including the circumoral nerve ring (CNR), intestine, longitudinal muscle, and gonads (male/female) were collected from six adults (106±3.82 g). Samples were snap-frozen in liquid nitrogen and stored at −80°C for reverse transcription and quantitative real-time PCR (RT-qPCR) analysis. The CNR and intestinal tissues were also fixed in 4% paraformaldehyde (PFA) in 0.1 mol/L phosphate-buffered saline (PBS) (G-CLONE, China) for *in situ* hybridization (ISH).

For injection experiments targeting AjTRH1 and AjTRH7, 180 sub-adult sea cucumbers (30±5.8 g) were randomly divided into six groups (30 individuals per group). Animals in each group were then transferred to five fiber-glass tanks (six individuals per tank). Samples for qPCR analysis of *AjTRHP* expression in the CNR and intestine were obtained from one individual per tank. For RNA interference (RNAi) experiments, 30 sea cucumbers (30±3.01 g) were randomly assigned to three groups (six individuals per group). During the experimental period, sea cucumbers were fed *ad libitum* each morning with a diet comprising a mixture of artificial commercial food and sea mud (1:3 ratio). The artificial food, purchased from the Shandong Oriental Ocean Sea Cucumber Breeding Farm (Weihai, China), included a blend of kelp, scallop skirt, brown alga (*Sargassum thunbergii*), gulfweed, *Ulva*, and yeast. Each tank was provided with 40–50 g of the diet daily, and uneaten food and feces were removed before the subsequent feeding to maintain optimal water quality.

Sequence analyses of *TRHP* and TRH-like peptides

The full-length cDNA sequence of *AjTRHP* was reported in our previous work (Zheng et al., 2022). Gene structure was predicted based on the *A. japonicus* reference genome (China National GeneBank DataBase (CNGBdb) under BioProject accession No. CNP0002776), and conserved domains were analyzed using the Simple Modular Architecture Research Tool (SMART). Synteny analysis was conducted by identifying the chromosomal locations of *TRHP* in the genomes of *Apostichopus japonicus*, *Asterias rubens*, and *S. purpuratus*, using publicly available data from NCBI (https://www.ncbi.nlm.nih.gov/). The three-dimensional (3D) structure of AjTRHP protein was predicted using the Robetta online platform (https://robetta.bakerlab.org/). Sequence alignments of mature TRH-type peptides from *A. japonicus* and other bilaterians (GenBank IDs, Supplementary Table S1) were performed using ClustalW in MEGA7 (v.7170509) with default parameters.

RNA extraction and RT-qPCR

Total RNA was extracted from tissues, including the CNR, intestine, longitudinal muscle, and gonads (male/female), using TRIzol reagent (Takara, Japan). RNA quality and integrity were determined using a NanoDrop 2000 spectrophotometer (Thermo Fisher Scientific, USA) and 1% agarose gel electrophoresis (OD260/280=1.9–2.1, c> 30 ng/μL, 28S/18S≥1.0). Relative gene expression levels were quantified using TB Green® Premix Ex Taq™ (Tli RnaseH Plus) (Takara, Japan) on a StepOnePlus Real-Time PCR System (ABI, USA). All reactions were conducted in triplicate. *β*-actin and *β*-tubulin were used as reference genes for normalization, and relative expression levels were analyzed using the $2^{-\Delta\Delta CT}$ method (significance threshold alpha=0.05),

as described previously (Zheng et al., 2022). Results are presented as mean±standard error of the mean (SEM) (n=6). The specific primers for *AjTRHP* amplification are given in Supplementary Table S2.

Identification, molecular cloning, and phylogenetic analysis of candidate *A. japonicus TRH* receptor (*AjTRHR*)

TRHR from the sea urchin *S. purpuratus* (GenBank accession No. XM_011684235.1) was used as a reference to identify candidate TRH-type neuropeptide receptors in the *A. japonicus* chromosome-level genome and CNR transcriptome data (GenBank accession No. GHCH00000000). Among the identified sequences, the top-scoring transcript (GenBank accession No. PIK53909.1) was designated as the candidate *A. japonicus TRH* receptor (*AjTRHR*). Full-length cDNA sequences of *AjTRHR* were then cloned using a SMARTer® RACE 5′/3′ Kit (Clontech, Japan) with specific primers (Supplementary Table S2) following the manufacturer's instructions.

A three-dimensional (3D) model of the AjTRHR protein was modeled using SWISS-MODEL (https://swissmodel.expasy.org/), while its transmembrane domain (TMD) was predicted using Protter (http://wlab.ethz.ch/protter/start/). To explore the evolutionary relationships between AjTRHR and TRHR-like protein in other species, a phylogenetic analysis was performed using the maximum-likelihood (ML) method implemented in MEGA7 (v.7170509) using default parameters. After trimming the leading and trailing sequence ends, the General Reversible Chloroplast+Frequency model (cpREV+G+I+F) was selected as the optimal substitution model. The analysis included 1 000 bootstrap replicates to infer a robust consensus tree. Receptors for gonadotropin-releasing hormone (GnRH)-like proteins, known to be closely related to TRH, were also included in this analysis (Suwansa-Ard et al., 2018). Kisspeptin receptor (KissR)-like sequence was selected as the outgroup for phylogenetic analysis. GenBank IDs of all sequences are listed in Supplementary Table S1. The alignment sequence file (Supplementary File 1) and Newick tree file (Supplementary File 2) are provided in the Supplementary Materials.

Ligands and plasmids

AjTRH1 (pQYFA, the short peptide isoform), AjTRH7 (pQLPGSPWKFWE, the long peptide isoform) along with their reverse sequences (AFYQ and EWFKWPSGPLQ), were synthesized by GL Biochem (Shanghai) Ltd. (China). The open reading frame (ORF) sequences of AjTRHR were subcloned into the pcDNA 3.1(+) and pEGFP-N1 vectors (Biofeng, China) to generate endo-free plasmids for transfection, as described previously (Li et al., 2022). Primer sequences used for cloning are provided in Supplementary Table S2.

Cell culture, transfection, and functional characterization of AjTRHR

Ligand binding assays, including intracellular calcium measurements and receptor localization and translocation assay were performed to confirm the ligand activity of AjTRH1 and AjTRH7 for AjTRHR. Human embryonic kidney (HEK293T) cells were purchased from ATCC (USA) and cultured in Dulbecco's Modified Eagle Medium (DMEM, HyClone, USA) supplemented with 10% fetal bovine serum (FBS) (Biological Industries, Israel) at 37°C in a 5% CO_2-humidified atmosphere. The HEK293T cells were plated on 6-well plates (Corning, USA) and transfected with AjTRHR plasmids using Lipofectamine 2000 Reagent (Invitrogen, USA) at approximately 70% confluence according to the manufacturer's instructions.

Intracellular calcium flux was measured using the fluorescent Ca^{2+} indicator Fura-2/AM and SRE-Luc reporter assays (Li et al., 2010). Briefly, HEK293T cells expressing AjTRHR-pcDNA 3.1(+) were incubated with 3 μmol/L Fura-2/AM (Thermo Fisher Scientific, USA) for 30 min and stimulated with AjTRH1/AjTRH7 at indicated concentrations (10^{-9}–10^{-5} mol/L). Calcium flux was detected using a Synergy H1 Hybrid Multi-Mode Reader (Biotek, USA). Receptor localization and translocation assays were conducted as described in previous research (Wang et al., 2020). HEK293T cells expressing AjTRHR-pEGFP-N1 were seeded on glass coverslips in 6-well plates and stimulated with 1 μmol/L AjTRH1/AjTRH7 for 30 min. The cells were fixed with 4% PFA in PBS at room temperature for 10 min, incubated with 4′,6-diamidino-2-phenylindole (DAPI, Beyotime, China) for 5 min, and visualized using an Olympus BX53F fluorescence microscope system (Japan). All ligand-binding experiments were repeated independently at least three times. Negative control groups included cells transfected with empty pcDNA3.1 (+) or pEGFP-N1 vectors or stimulated with reverse peptide sequences.

cAMP and ERK1/2 phosphorylation assays

HEK293T cells co-transfected with AjTRHR/pcDNA 3.1(+) and pCRE-Luc were used for cAMP-response element (CRE)-Luciferase (Luc) reporter gene assays. Cells were seeded into 12-well cell culture plates and incubated with AjTRH1/AjTRH7 (10^{-9}–10^{-5} mol/L) for 4 h at 37°C. Luciferase activity was detected using a Firefly Luciferase Reporter Gene Assay Kit (MKBio, China) following the manufacturer's instructions. The cAMP assay was performed as described previously (Wang et al., 2017). Briefly, gradient-diluted AjTRH1/AjTRH7 (10^{-9}–10^{-5} mol/L) was used to treat AjTRHR-pcDNA3.1 (+) or pcDNA3.1 (+) transfected cells for 30 min. After treatment, the cells were washed twice with PBS, lysed, and collected. Intracellular cAMP levels were quantified using a cAMP Assay Kit (R&D Systems, USA) following the manufacturer's protocols. All data were processed and imaged using GraphPad Prism v.9.4 (GraphPad Software, USA).

Phosphorylated ERK1/2 (pERK1/2) activity was measured as described in previous research (Wang et al., 2020). Briefly, cells expressing AjTRHR-pcDNA 3.1(+) were treated with AjTRH7 (10^{-6} mol/L) for varying durations (0, 5, 15, 30, 45, and 60 min) at 37°C. After treatment, cells were lysed, and total protein concentrations were determined using an Enhanced BCA Protein Assay Kit (Beyotime, China). Protein samples were separated using 10% sodium dodecyl-sulfate polyacrylamide gel electrophoresis (SDS-PAGE) and transferred onto polyvinylidene fluoride (PVDF) membranes. Immunoblotting was performed using the primary antibodies rabbit anti-pERK1/2 (1:2 000, Cell Signaling Technology, USA) and rabbit anti-tERK1/2 (1:1 000, Cell Signaling Technology, USA). A goat anti-rabbit IgG secondary antibody (1:2 000, Absin, China) was used for detection. Immunoreactive bands were visualized using an enhanced chemiluminescent reagent (Beyotime, China) and quantified using ImageJ. Negative controls included cells transfected with empty vectors.

Localization of *AjTRHP* and *AjTRHR* transcripts using ISH

ISH experiments were performed to localize the transcripts of

AjTRHP and *AjTRHR*, following established protocols (Li et al., 2022). Specific *AjTRHP* and *AjTRHR* antisense and sense digoxygenin (DIG)-labeled RNA probes were synthesized using a DIG RNA Labelling Kit (Roche, Switzerland). The primer sequences used for probe generation are listed in Supplementary Table S2. Tissues from *A. japonicus* were fixed in 4% PFA prepared in 0.1 mol/L PBS for 12 h at 4°C. Following fixation, tissues were embedded in paraffin, sectioned, and processed through dewaxing, permeabilization, and proteinase K digestion. After prehybridization and probe hybridization, the sections were stained using a DIG Nucleic Acid Detection Kit (Roche, Switzerland) and visualized using an Olympus bright field light microscope (Japan).

Effects of AjTRH1 and AjTRH7 on *A. japonicus* through *in vivo* experiments

To investigate the physiological roles of AjTRH1 and AjTRH7 in *A. japonicus*, *in vivo* pharmacological experiments were performed via AjTRH1/AjTRH7 injection into the coelom. Based on previous studies of neuropeptide effects in *A. japonicus* and the reported activity of TRH peptides in other species, optimal injection concentrations were set to 0.5 mg/mL or 0.05 mg/mL (Wang et al., 2020). AjTRH1 and AjTRH7 were dissolved in sterile seawater to a final concentration of 0.5 mg/mL or 0.05 mg/mL and administered via the oral cavity directly into the coelom every two days. A total of 180 sea cucumbers were randomly divided into six defined groups: high-concentration AjTRH1/AjTRH7 (0.5 mg/mL) injection groups (HTG), low-concentration AjTRH1/AjTRH7 (0.05 mg/mL) injection groups (LTG), and two seawater injection groups (NC). Each injection volume was set at 0.1% (v/w) and administered once every two days at noon. Sea cucumbers were maintained under identical feeding conditions throughout an over 25-day experimental period. Uneaten food was collected daily, dried, and weighed to monitor feed intake. The body weight of each individual was measured at the beginning and end of the experiment. Following the treatment period, fresh CNR and intestinal tissues were dissected and frozen in liquid nitrogen. The weight gain rate (WGR) and feed intake rate (FI) of 30 individuals per treatment were calculated as described previously (Liu et al., 2014).

Knockdown of *AjTRHP* expression *in vivo* using small interfering RNA (siRNA)

Knockdown experiments targeting *AjTRHP* were performed *in vivo* as described previously (Huang et al., 2021). Two specific siRNA sequences targeting *AjTRHP* (siRNA_*AjTRHP*) were designed and synthesized by GenePharma (China), along with a negative control (siRNA_NC), which was confirmed not to target any annotated genes in the *A. japonicus* transcriptome (Supplementary Table S2). To enhance stability, the siRNA sequences were modified with 2'-O-methylation. Sea cucumbers that received no treatment were used as an additional blank negative control (NC) to eliminate any injection effects. These siRNAs were dissolved in diethyl pyrocarbonate (DEPC)-treated seawater to a final concentration of 20 μmol/L. Working solutions were prepared by mixing 20 μL of siRNA, 20 μL of Lipo6000™ transfection reagent (Beyotime, China), and 60 μL of RNAase-free seawater. Each group consisted of 10 sea cucumbers (approximately 30 g), which were injected with 0.1% (v/m) of the working solution, forming both experimental and control groups. Twenty-four hours after injection, CNR tissues were collected to evaluate the knockdown efficiency of the two siRNA_*AjTRHP* using qPCR. The siRNA_*AjTRHP* with superior performance (knockdown rate>50%) was selected for further experiments. For subsequent treatments, siRNAs were injected into the coelom via the tentacles every 24 h over a five-day period. Following the treatment phase, CNR and intestinal tissues from six individuals were dissected and frozen in liquid nitrogen and analyzed for the relative expression of *AjCCKP1* (GenBank accession No. MH636358).

Statistical analysis

Statistical analyses for qPCR experiments were conducted using one-way analysis of variance (ANOVA) with Tukey *post-hoc* tests in SPSS v.27 (SPSS, USA). For the culture experiments, linear mixed models were applied to account for tank effects as random factors, with significance assessed through Tukey *post-hoc* tests conducted in R v.4.4.0.

RESULTS

Sequence and synteny analysis of *AjTRHP* and AjTRH precursor protein

The sequences of AjTRH precursors are shown in Figure 1A. Gene structure analysis revealed that the TRH precursor proteins in sea cucumbers, starfish, and sea urchins were all encoded by two exons and one intron, with intron phases primarily annotated as "0" or "1" (Figure 1B). A conserved TRH superfamily domain was predicted across these three groups (Supplementary Figure S1). The genomic context of *AjTRHP* was assessed in the reference genome, revealing neighboring genes such as TBC1 domain family member 22B isoform X1 (*TBC1D22B*), TPR repeat-containing protein DDB_G0287407-like (*TPRCP*), calcium-dependent secretion activator 1 (*CADPS1*), putative conserved oligomeric Golgi complex subunit 5 (*COGCS5*), two copies of putative sodium- and chloride-dependent GABA transporter 2 (*GAT-2*), and putative cytochrome P450 2J6 (*CYP2J6*) (Figure 1C). The location of neighboring ortholog genes was also examined in other clades of echinoderms, using *A. rubens* (GenBank accession number: GCA_902459465.3) and *S. purpuratus* (GenBank accession number: GCA_000002235.4). Results showed that these synteny blocks were also located around the *TRHP* gene (Figure 1C), indicating a conserved synteny encompassing the TRH region during echinoderm evolution.

The molecular weight of the AjTRHP protein was predicted to be 52.54 kDa (Figure 1D; 3D-model). C-terminal amide modification emerged as a conserved feature among bilaterians, except for the long-isoform peptides of the echinoderm *S. purpuratus*. Notably, N-terminal modifications were conserved only within the deuterostomian clade. Long isoforms of the TRH/TRH-type peptides were only identified in protostomes (TRH-type peptides exceeding six amino acids) and Ambulacraria (TRH peptides exceeding four amino acids). However, TRH signaling components have not been identified in crinoid species to date (Figure 2).

***In silico* identification of AjTRH receptors**

The putative *A. japonicus* TRH receptor gene (*AjTRHR*) was identified based on *in silico* analysis of genomic and transcriptomic data. After cDNA cloning, the full-length cDNA of candidate *AjTRHR* (GenBank accession number: WLK66377.1) was obtained and characterized, spanning 1 823 bp with an ORF of 1 110 bp. Structural analysis using

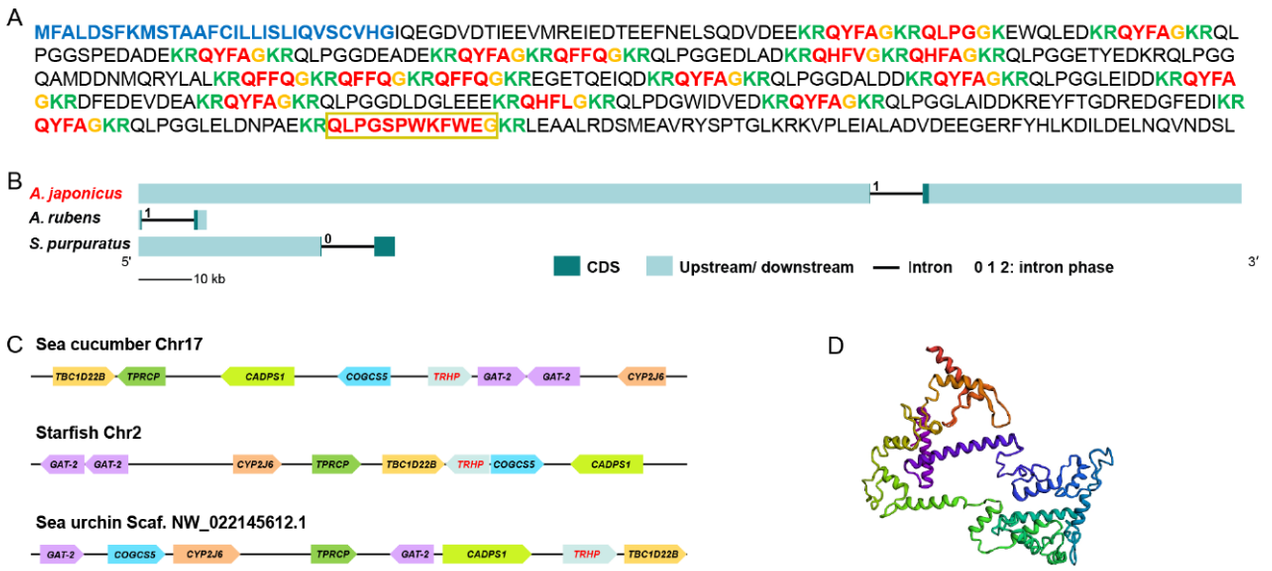


Figure 1 Sequence and synteny analysis of *TRHP* and TRH precursor protein

A: *Apostichopus japonicus* TRH precursor proteins. Blue, predicted signal peptides; Red, putative TRH peptides; Orange, putative C-terminal glycine (G) residues for amidation; green, putative monobasic/dibasic cleavage sites. Peptides confirmed by mass spectrometry are labeled with yellow boxes. B: Gene structure of echinoderm *TRHP*. C: Synteny analysis of *TRHP* in echinoderms including *A. japonicus*, *Asterias rubens* (GenBank accession No. GCA_902459465.3), and *Strongylocentrotus purpuratus* (GenBank accession No. GCA_000002235.4). D: 3D-model of AjTRHP protein. Gene abbreviations: TBC1 domain family member 22B isoform X1 (*TBC1D22B*), TPR repeat-containing protein DDB_G0287407-like (*TPRCP*), calcium-dependent secretion activator 1 (*CADPS1*), putative conserved oligomeric Golgi complex subunit 5 (*COGCS5*), two copies putative sodium- and chloride-dependent GABA transporter *2* (*GAT-2*) and putative cytochrome P450 2J6 (*CYP2J6*).

the Protter program revealed the presence of seven TMDs with an extracellular N-terminus, a cytoplasmic C-terminus, and typical glycosylation modifications (Supplementary Figure S2A). The 3D structural model of the candidate receptor is displayed in Supplementary Figure S2B. Phylogenetic analysis indicated that three receptor families were well grouped into three clades, with TRHR exhibiting a closer phylogenetic relationship with KissR than GnRHR. Within the TRHR clade, the candidate AjTRHR clustered with its counterpart in *S. purpuratus* and subsequently clustered with the ophiuroid species *O. victoriae*. These echinoderm TRHRs formed a sister group to TRHRs from other deuterostomes, which were clearly distinct from the protostomian clade (Figure 3).

AjTRH7 activates AjTRHR via the ERK1/2 phosphorylation pathway

As shown in Figure 4A–C, increasing concentrations of synthesized AjTRH7 (10^{-9}–10^{-5} mol/L) triggered intracellular Ca^{2+} mobilization (Figure 4A) and cAMP accumulation. The CRE-Luc reporter gene assay demonstrated that AjTRH7 activated AjTRHR (GenBank ID: OQ943938) signaling via the cAMP-PKA pathway (Figure 4B, C). Fluorescent cell staining revealed that AjTRHR expression was predominantly localized at the cell membrane (Figure 4D). An agonist-mediated receptor internalization assay, conducted in HEK293T cell expressing AjTRHR-pEGFP-N1, showed significant receptor internalization following stimulation with AjTRH7 for 30 min (Figure 4D). Results also indicated that p-ERK1/2, normalized to total ERK1/2 (t-ERK1/2), was gradually up-regulated, peaking 15 min after treatment with AjTRH7 and subsequently returning to baseline levels. Notably, p-ERK1/2 activity was markedly increased at 15 and 30 min following AjTRH7 stimulation (Figure 4E; $F_{(5,10)}$=5.563, P<0.05), confirming that AjTRHR is activated by AjTRH7 via the ERK1/2 phosphorylation pathway within the MAPK signaling cascade. Control experiments using the empty pcDNA 3.1(+) vector showed no significant responses (Figure 4E). Similarly, tests with reverse peptide sequences (EWFKWPSGPLQ) yielded no observable responses (Supplementary Figure S3B, C).

Expression and localization of *AjTRHP* and *AjTRHR* transcripts

The relative expression levels of *AjTRHP* in different tissues were examined by qPCR, revealing that *AjTRHP* was mainly expressed in CNR tissue (Supplementary Figure S4A). Furthermore, ISH analysis provided a detailed localization profile of *AjTRHP*, as shown in Supplementary Figure S4B–H. Positive signals were observed at the margins and within the connective tissue linking the radial nerve cord (RNC) and CNR (Supplementary Figure S4B, C). Additionally, *AjTRHP*-positive staining was identified in the connective tissues of the intestine (Supplementary Figure S4D–F).

The localization of *AjTRHR* transcripts was consistent with that of *AjTRHP*. The ISH results demonstrated that *AjTRHR* was primarily expressed in the RNC of the nervous system (Supplementary Figure S5A–C). Positive signals were also detected in the connective tissues of the intestine but not in the intestinal lumen (Supplementary Figure S5D–G). Negative control experiments using sense probes confirmed the specificity of the observed staining patterns (Supplementary Figure S4G, H; Supplementary Figure S5H, I). Notably, as reported in our previous study on *A. japonicus* (Li et al., 2022), the simple columnar epithelium of the intestine was prone to non-specific staining with sense probes.

Long-isoform AjTRH peptide (AjTRH7) induces feeding inhibition and body mass reduction

To explore the physiological role of TRH-type peptides in *A. japonicus*, experimental animals were exposed to AjTRH7 at

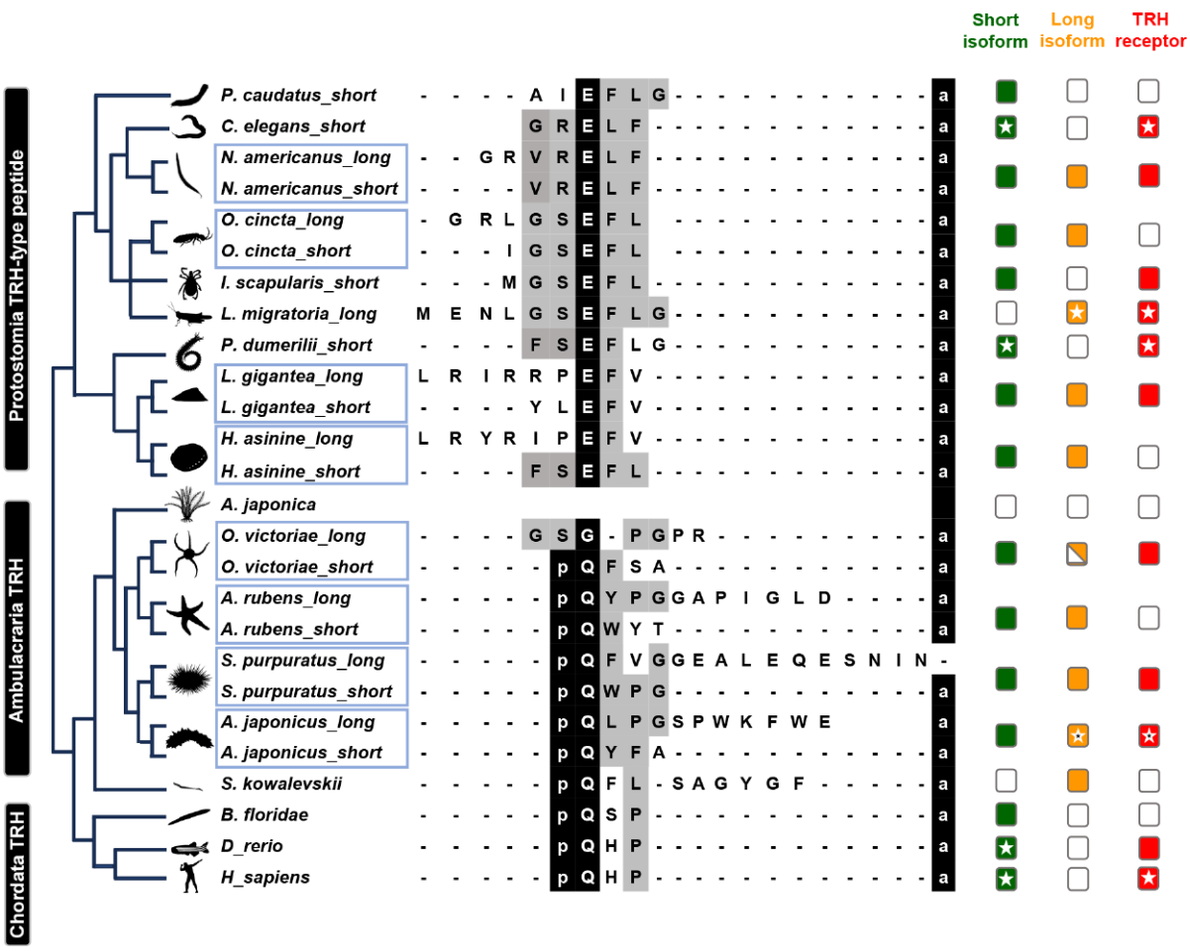


Figure 2 Evolution of TRH-type neuropeptide signaling system in bilaterians

Green box: Short isoform TRH/TRH-type peptide; Orange box: Long isoform TRH/TRH-type peptides; Red box: TRH/TRH-type receptor; Empty box: Not identified and/or absent; Half box: Long TRH peptide only identified in one precursor; asterisk: Functionally characterized. Blue box: Species with both short and long isoforms. GenBank IDs of all sequences are given in Supplementary Table S1. Organism silhouettes were downloaded from PhyloPic (www.phylopic.org).

two concentrations (0.5 mg/mL and 0.05 mg/mL). Injections were administered through the mouth into the coelom every two days over a one-month period. Ninety individuals were randomly divided into three groups: seawater injection group (NC), low-concentration AjTRH7 injection group (LTG), and high-concentration injection group (HTG), as displayed in Figure 5A. Results demonstrated significant effects of AjTRH7 on the WGR ($F_{(2,8)}$=5.248, P<0.05) and FI ($F_{(2,8)}$=18.509, P<0.05) of sea cucumbers. Sea cucumbers in the LTG and HTG groups exhibited significantly lower WGR compared to those in the NC group (P<0.05) (Figure 5B). Interestingly, AjTRH7 exhibited a stronger inhibitory effect in the LTG group than in the HTG group. Similarly, FI was significantly reduced in both the LTG and HTG groups compared to the NC group (Figure 5C).

Short-isoform AjTRH peptide (AjTRH1) binds to AjTRHR and inhibits food intake

The short-isoform peptide AjTRH1 also binds to AjTRHR, the receptor targeted by AjTRH7, leading to cAMP accumulation (Figure 6A). However, unlike AjTRH7, no Ca^{2+} mobilization was observed after AjTRH1 stimulation (Supplementary Figure S6). Control experiments with peptides containing reversed sequences (AFYQ) also showed no responses (Supplementary Figure S3A). Pharmacological experiments revealed that low-concentration (0.05 mg/mL) AjTRH1 (LTG) significantly inhibited FI ($F_{(2,8)}$=65.748, P<0.05) and reduced WGR ($F_{(2,8)}$=21.666, P<0.05). In contrast, high-concentration (0.5 mg/mL) AjTRH1 (HTG) did not produce significant differences in WGR or FI compared to the NC group (Figure 6B, C).

Gain- and loss-of-function studies reveal interaction between AjTRH and CCK

Results demonstrated significant differences in *AjCCKP1* expression among the three groups under AjTRH7 treatment in the CNR ($F_{(2,10)}$=6.852, P<0.05) and intestine ($F_{(2,10)}$= 8.091, P<0.05). Expression levels of *AjCCKP1* were significantly up-regulated in the CNR of the HTG group and in the intestines of the LTG group (Figure 7A, B). To further investigate this interaction, specific siRNA targeting *AjTRHP* (siRNA_*AjTRHP*) was applied to knockdown its expression (Figure 7C–E), resulting in a 55% reduction compared to the NC group (Figure 7C). Following five days of siRNA transfection (daily injections), the expression of *AjCCKP1* mRNA was significantly inhibited in the CNR ($F_{(2,10)}$=16.875, P<0.05) and intestine ($F_{(2,10)}$=10.744, P<0.05) (Figure 7D, E).

DISCUSSION

Food intake is tightly regulated by the integration of internal and external environmental signals processed through neural

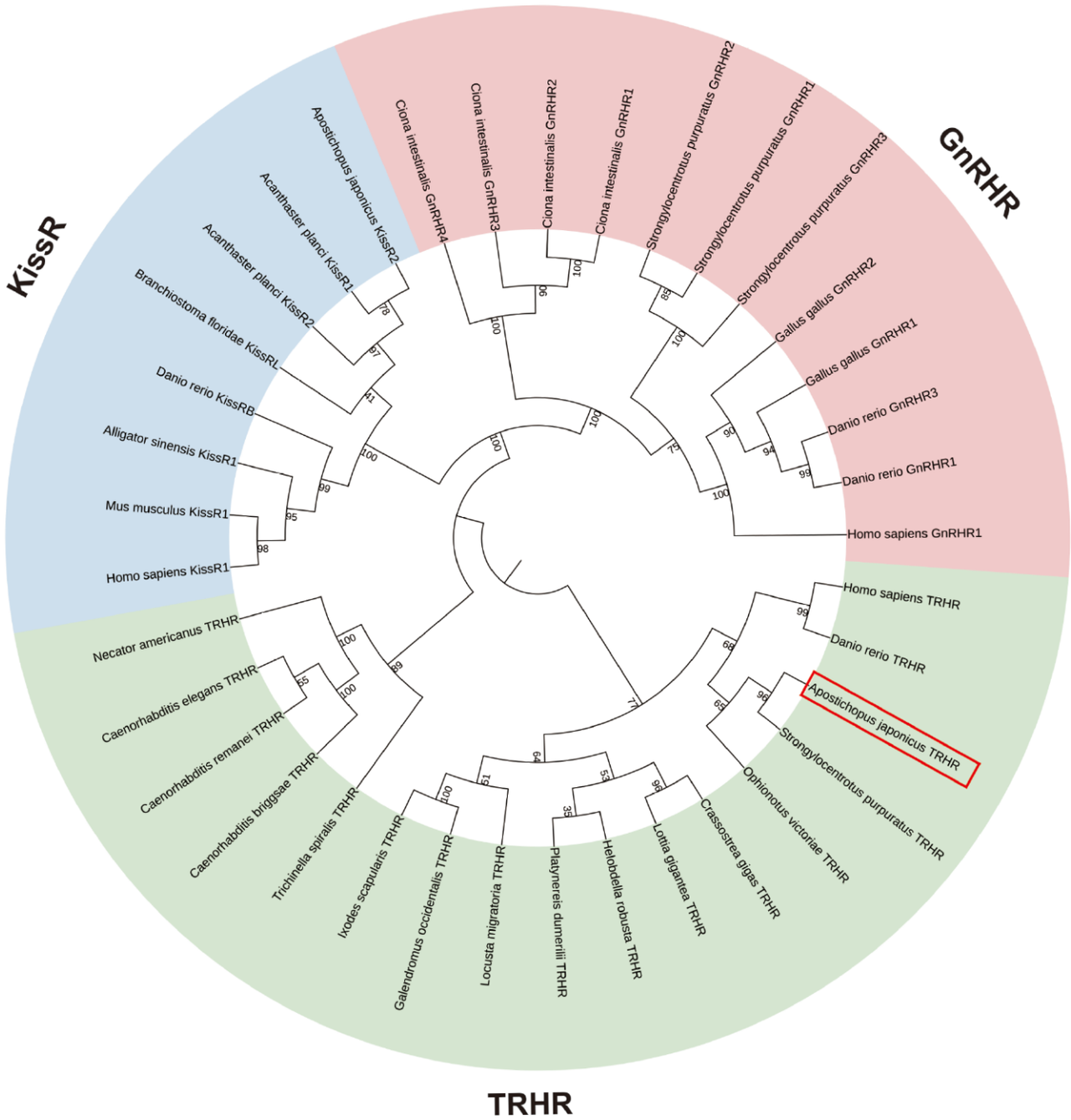


Figure 3 Identification and phylogenetic tree of TRHRs in bilaterians using maximum-likelihood (ML) analysis based on General Reversible Chloroplast+Frequency model, with KissRs and GnRHRs used as outgroups

Bootstrap consensus tree was inferred from 1 000 replicates.

circuits (Pool & Scott, 2014). In mammals, TRH signaling has been shown to play a critical role in feeding behavior by interacting with the satiety peptide CCK (Akieda-Asai et al., 2014; Wang et al., 2022). However, whether this interaction represents an evolutionarily conserved mechanism underlying feeding regulation in non-vertebrate animals has remained largely unexplored. This study provides the first evidence of functional responses elicited by a TRH-like peptide acting through a TRHR-like receptor in an invertebrate deuterostome, specifically the sea cucumber *A. japonicus*. Our findings elucidated the physiological role of TRH-like signaling in feeding and its interaction with the satiety peptide CCK, underscoring the conserved nature of this mechanism across evolutionary lineages.

Functional TRH signaling system is mediated by the ERK/MAPK intracellular pathway

AjTRH signaling, like most neuropeptide systems, is mediated through G protein-coupled receptors (GPCRs) known as TRHRs. In vertebrates, TRHRs are well-classified as Class A peptide GPCRs, typically signaling through $G_{q/11}$ proteins but also capable of activating other G protein subtypes under certain conditions (Ji et al., 2022; Trubacova et al., 2022). For example, activated TRHR couples to Gq to trigger the phosphatidylinositol (IP3)-calcium-protein kinase C (PKC) pathway (Xu et al., 2022), which subsequently activates the Ca^{2+}/CAMK (calmodulin-dependent protein kinase) and MAPK cascades (Cui et al., 1994; Trubacova et al., 2022). TRH-mediated signaling demonstrates diverse functional outcomes

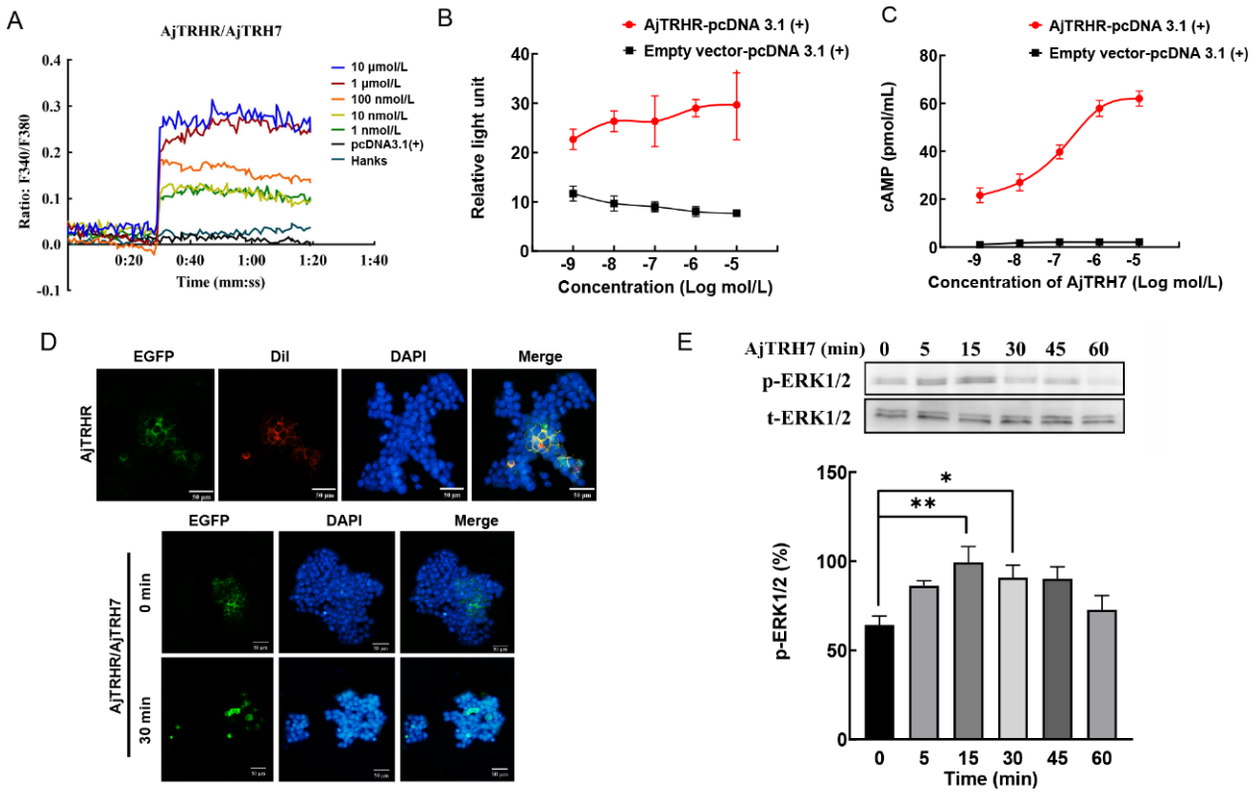


Figure 4 AjTRH7/AjTRHR cellular pathway identification

A: Ca^{2+} mobilization-mediated activity in HEK293T cells expressing AjTRHR (GenBank ID: OQ943938) in response to AjTRH7 (10^{-9}–10^{-5} mol/L), determined using Fura-2/AM. B: CRE-driven luciferase activities in AjTRHR-expressing HEK293T cells. C: cAMP content in HEK293T cells expressing AjTRHR in response to AjTRH7 (10^{-9}–10^{-5} mol/L), determined using a cAMP assay kit. D: Localization and internalization of *AjTRHR* after treatment with AjTRH7 (10^{-6} mol/L), DAPI (blue) was applied to stain the cell nucleus and DiI (red) was used to stain the cell membrane. E: ERK1/2 phosphorylation compared to total ERK1/2 after HEK293T cells were challenged with AjTRH7 (10^{-6} mol/L) for 0, 5, 15, 30, 45, and 60 min. Empty pcDNA 3.1(+) vector treated with AjTRH7 (10^{-5} mol/L) was used as a negative control. Values from six repetitions were determined and expressed as mean±SEM (n=6). Significant difference: *: P<0.05; **: P<0.01.

across species. For instance, TRH transiently induces intercellular Ca^{2+} influx in rat vagal nodose ganglion neurons, a response shorter in duration compared to other neuropeptides such as CCK-8, 5-HT, and ATP (Mamedova et al., 2022). In the frog species *Rana ridibunda*, TRHR activation mobilizes intracellular Ca^{2+} stores via Phospholipase C (PLC) activity (Galas et al., 1998). Similarly, TRH treatment in mice has been shown to induce significant changes in endoplasmic reticulum (ER) Ca^{2+} levels ([Ca^{2+}]ER) in the pituitary gland (Rojo-Ruiz et al., 2021). Furthermore, ERK/MAPK pathway activity has been reported to regulate TRHR expression in Sprague-Dawley rats, increasing under pathway activation and decreasing with its inhibition (Liu et al., 2015). In this study, we identified a functional TRH receptor (AjTRHR) in the sea cucumber *A. japonicus*, marking the first experimental demonstration of TRHR activity in non-chordate deuterostomes. Using bioinformatics and ligand-binding assays, we confirmed that synthetic AjTRH7 acts as an agonist for AjTRHR, functioning via a cAMP/PKA-ERK/MAPK cascade and possibly via Ca^{2+}-dependent pathway. AjTRH1, the short-isoform peptide, also activates AjTRHR by increasing cAMP levels, though it does not induce significant Ca^{2+} influx. Neuropeptide signaling systems are inherently complex, often involving multiple GPCR subtypes that linked to multiple signaling cascades. A single receptor can exhibit functional versatility, as different ligands binding to the same receptor may activate distinct G protein subtypes within the same cell (Mendel et al., 2020; Møller et al., 2003). The functional diversity is influenced by receptor structural polymorphism and variation in ligand-binding sites (Changeux, 2010; Wong et al., 2000), suggestingthat AjTRH1 and AjTRH7 may engage distinct binding domains on AjTRHR. Furthermore, it is plausible that additional, yet unidentified, receptors may mediate the activity of AjTRH peptides, contributing to the observed complexity of this signaling system.

TRH as a regulator of feeding cessation in aestivating sea cucumbers

Interestingly, relative expression of *AjTRHP* in the intestine of *A. japonicus* has been shown to increase significantly during the deep stages of aestivation, a state characterized by metabolic arrest and feeding cessation (Zhao et al., 2014). These observations, combined with findings from the current study, suggest a functional role for TRH in feeding inhibition during sea cucumber aestivation. This role aligns with findings in hibernating mammals, where endogenous TRH plays a crucial role in hypothermic states by reducing food intake and elevating body temperature, as observed in hamsters (Tamura et al., 2005). Similarly, increased TRH mRNA expression and activation of TRH neurons have been documented in torpor thirteen-lined ground squirrels (*Ictidomys tridecemlineatus*) and Arctic ground squirrel (*Urocitellus parryii*), respectively (Frare et al., 2021; Schwartz et al., 2013). Therefore, we speculate that TRH may play a broader role in seasonal

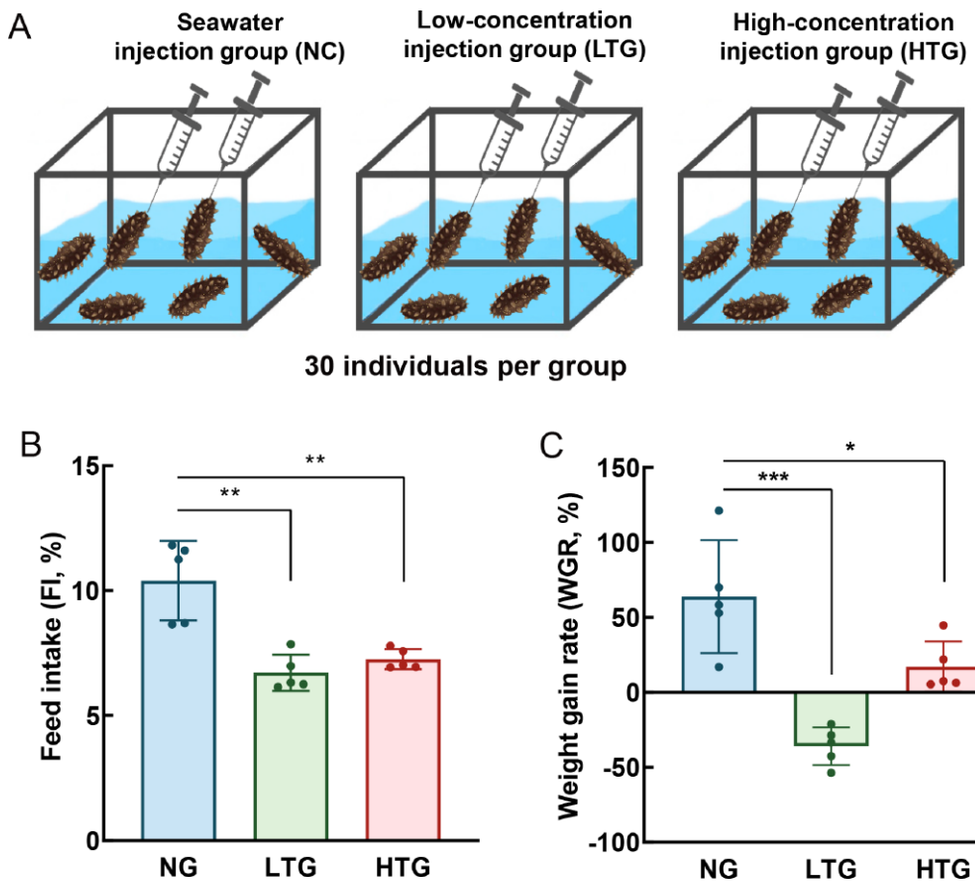


Figure 5 ***In vivo*** **pharmacological analysis of roles of AjTRH7 in feeding inhibition in** ***A. japonicus***

A: Groups subjected to pharmacological tests. B: Feed intake rate (FI) under AjTRH7 treatment in sea cucumbers in three groups (six individuals per tank and five tanks for each group). C: Weight gain rate (WGR). Values from six repetitions were determined and expressed as mean±SEM. *: $P<0.05$; **: $P<0.01$; ns: Not significant.

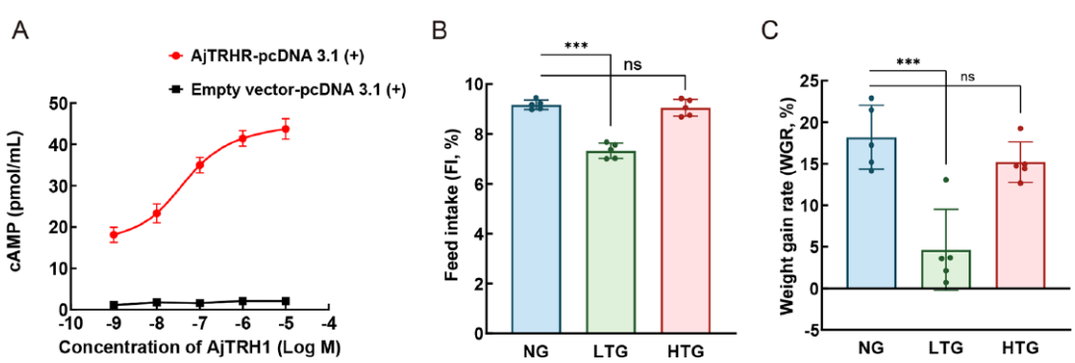


Figure 6 Identification of AjTRH1 receptor and ***in vivo*** **pharmacological analysis of AjTRH1 in feeding behavior**

A: cAMP content in HEK293T cells expressing AjTRHR in response to AjTRH1 (10^{-9}–10^{-5} mol/L). B: Feed intake rate (FI) under AjTRH1 treatment in sea cucumbers in three groups (six individuals per tank and five tanks for each group). C: Weight gain rate (WGR). Values from six repetitions were determined and expressed as mean±SEM. *: $P<0.05$; **: $P<0.01$; ***: $P<0.001$; ns: Not significant.

animal dormancy, such as aestivation, hibernation, and torpor, particularly in the regulation of feeding behavior during metabolic arrest. However, further research is needed to clarify the role of TRH signaling in these processes, providing deeper insights into its mechanisms and advancing research on metabolic arrest in animals.

TRH enhances CCK expression to amplify food intake inhibition

In vivo pharmacological experiments demonstrated that TRH-type neuropeptides significantly suppressed food intake, ultimately leading to body mass reduction in *A. japonicus*. Interestingly, this inhibitory effect was more pronounced at a lower concentration (0.05 mg/mL) compared to a higher concentration (0.5 mg/mL), possibly due to negative feedback mechanisms regulating endogenous TRH secretion.

In mammals, the interaction between TRH and CCK has been shown to modulate satiety signals, effectively reducing food consumption (Akieda-Asai et al., 2014; Wang et al., 2022). Similarly, in the echinoderm *A. rubens*, SK/CCK-type peptides have been implicated in suppressing the onset of feeding (Tinoco et al., 2021). To explore whether this TRH-CCK interaction is conserved in invertebrates, we explored its

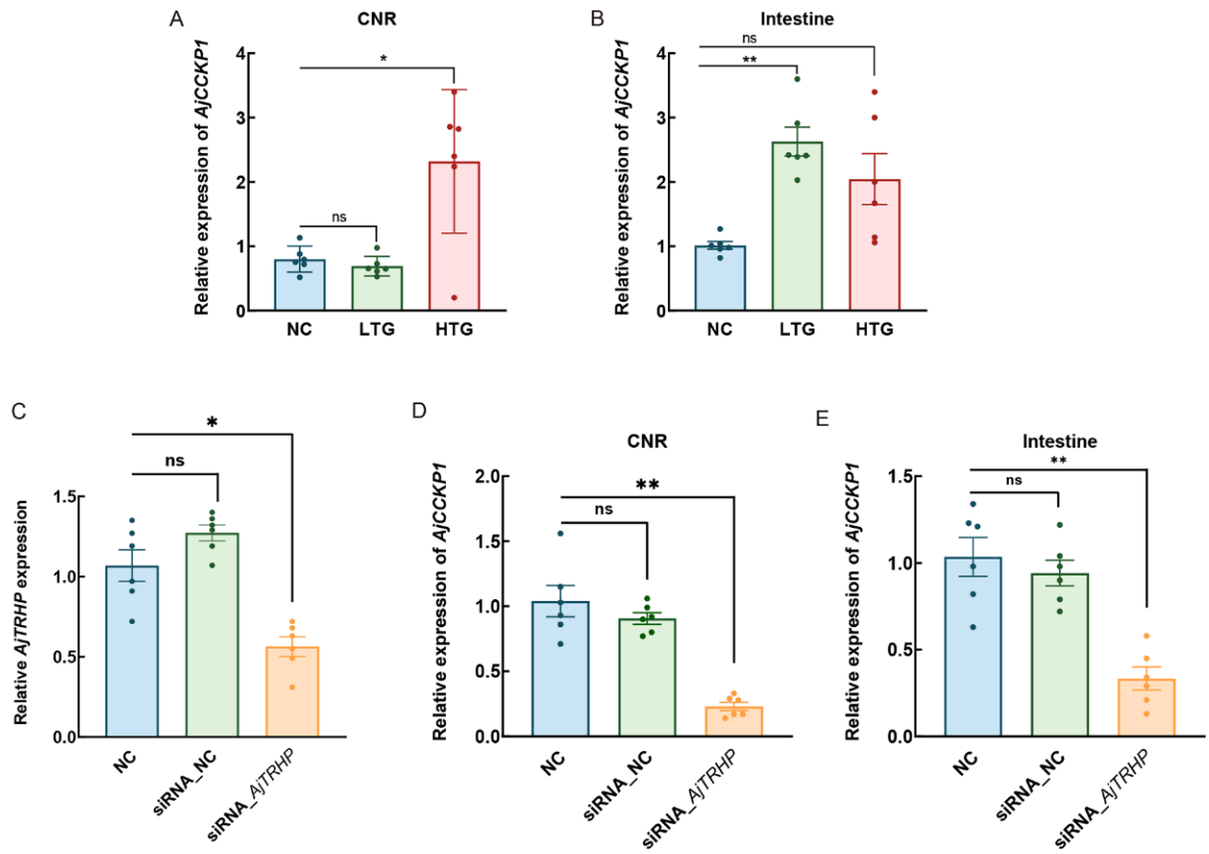


Figure 7 Analysis of relationship between *AjTRHP* and AjCCKP1 under AjTRH stimulation and *AjTRHP* knockdown

A: Relative *AjCCKP1* expression in response to AjTRH7 injection in circumoral nerve ring (CNR). B: Relative *AjCCKP1* expression in response to AjTRH7 injection in intestine. C: Knockdown effect of siRNA_*AjTRHP*. D: Relative *AjCCKP1* expression after siRNA_*AjTRHP* transfection in CNR. E: Relative *AjCCKP1* expression after siRNA_*AjTRHP* transfection in the intestine. *: P<0.05; **: P<0.01; ns: Not significant.

role in feeding regulation in *A. japonicus*. Experimental evidence showed that AjCCK1.2 significantly inhibited feeding in sea cucumbers (unpublished data). Notably, the relative expression of *AjCCKP1* closely mirrored the expression patterns of AjTRH7, increasing with AjTRH7 overexpression and decreasing following *AjTRHP* knockdown. These findings suggest that TRH interacts with appetite-regulating peptides such as CCK to inhibit feeding behavior in *A. japonicus* (Figure 8A). Additionally, the expression and localization patterns of *AjTRHP* in the nervous system and intestine further supported its pivotal role in feeding regulation in sea cucumbers.

Feeding behaviors are hypothesized to be under complex control of regulatory networks involving the synergistic actions of multiple neuropeptides (Gotoh et al., 2013; Guo et al., 2021; Loh et al., 2017; Matson et al., 2000; Nässel & Wu, 2022; Peters et al., 2006; Zels et al., 2015). In mammals, TRH is widely classified as an anorectic factor. For instance, prolonged TRH administration has been shown to elevate resting metabolic rates and suppress food intake, leading to reduced body weight in obese rats (Al-Arabi & Andrews, 2006). Central administration of TRH has similarly been found to decrease food intake in Sprague-Dawley rats and Siberian hamsters (*Phodopus sungorus*) (Choi et al., 2002; Schuhler et al., 2007; Steward et al., 2003). The regulation of feeding behavior in mammals is mediated by both central and peripheral mechanisms. Central regulation involves TRH production in second-order neurons located in the paraventricular nucleus (PVN) of the hypothalamus, while peripheral regulation integrates signals from CCK and other factors that communicate with the brain to modulate central responses, thus regulating feeding behavior (Valassi et al., 2008). Recent structural analyses of TRHR have revealed striking similarities to the CCK A receptor (CCKAR) (Ji et al., 2022), providing a molecular basis for the interaction between TRH and CCK signaling pathways. In this study, we demonstrated that TRH stimulates the release of the satiety peptide CCK, reducing food intake via satiety signaling. This finding underscores the conserved role of TRH-CCK interactions in regulating feeding behavior. However, in echinoderms, the integrated regulatory networks and neuronal circuits controlling feeding behavior remain largely unknown, limiting our understanding of the function and evolution of feeding-related peptidergic signals in these animals. Further research is essential to elucidate the mechanisms underlying the interactions between TRH, CCK, and other feeding-related peptides. Such studies will provide critical insights into the molecular pathways governing feeding behavior, particularly in marine invertebrates, and expand our understanding of the evolutionary dynamics of neuropeptide signaling in animals.

Functional evolution hypothesis of TRH-type peptides

The sequence of TRH (tripeptide pQHP-NH_2) is fully conserved across vertebrates, indicating strong evolutionary pressure to maintain its structure and physiological functions. However, in invertebrate deuterostomes, such as echinoderms, two distinct types of TRH peptides have been identified: short and long isoforms (Figure 8B). The short peptides (tetrapeptide) are considered orthologs of vertebrate

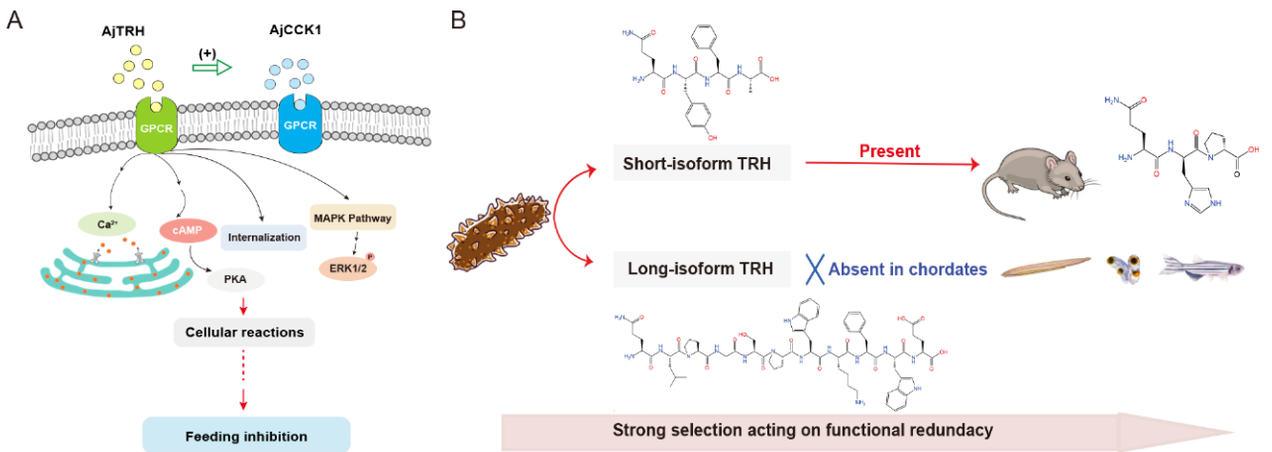


Figure 8 Schematic of physiological activity simulation

A: Diagram of thyrotropin-releasing hormone (TRH). B: Cholecystokinin (CCK) involvement in feeding inhibition and evolutionary hypothesis of TRH neuropeptides. (+), promoting the process. Abbreviations: GPCR, G protein-coupled receptor; P, phosphorylation; PKA, protein kinase A.

TRH (Van Sinay et al., 2017). In contrast, the long peptides exhibit unique structural and functional characteristics, suggesting a distinct evolutionary trajectory in which they were retained specifically in Ambulacraria. Our functional experiments demonstrated that both short (AjTRH1) and long isoforms (AjTRH7) inhibited food intake in sea cucumbers, indicating functional conservation of the short isoform with vertebrate TRH. Interestingly, in protostomes, EFLGa has been identified as the ligand for the TRH receptor ortholog in *Platynereis*, sharing some similarity with the TRH ortholog in the sea urchin *Strongylocentrotus purpuratus*. This finding suggests an evolutionary relationship between EFLGa and deuterostome TRH (Bauknecht & Jékely, 2015; Rowe & Elphick, 2012). Based on these similarities, we classified these peptides collectively as “TRH-type”. TRH-type neuropeptides have been identified in other protostomes (Van Sinay et al., 2017; Veenstra & Šimo, 2020; Zandawala et al., 2024), including *Necator americanus*, *Orchesella cincta*, *Lottia gigantea*, and *Haliotis asinina*, which contain both short and long isoforms. The absence of long isoforms in vertebratesmay reflect natural selection acting on functional redundancy between long and short isoforms. Alternatively, the long isoform may have arisen independently in the ambulacrarian ancestor, suggesting a more parsimonious evolutionary scenario. From a phylogenetic perspective, the functional redundancy of the two isoforms is plausible, as both can independently regulate feeding behavior. However, variations in the strength of their inhibitory effects have been observed, with the long isoform functioning through two pathways, while the short isoform acts via the cAMP pathway. These differences may arise from distinct signaling pathways or species-specific ecological contexts, although there is overlap in the way both isoforms function. Further research is required to determine whether organisms with only the short isoform exhibit lower feeding inhibition compared to those with the long isoform, or whether this variation is context-dependent, influenced by ecological or evolutionary pressures. Expanding studies across additional species will be critical to refine our understanding of the evolutionary history of TRH signaling and its functional adaptations.

CONCLUSIONS

This study advances our understanding of the function and signaling pathways of ancestral TRH-type neuropeptides, shedding light on their evolutionary and physiological significance. Our findings demonstrate that intercellular Ca^{2+} mobilization, receptor internalization, and cAMP accumulation are induced when TRH binds to its functional receptor, AjTRHR, which operates via the ERK1/2 phosphorylation pathway within the MAPK cascade. Furthermore, TRH signaling suppresses feeding activity by interacting with CCK-type neuropeptide-mediated satiety signals, a mechanism likely conserved in aestivating *A. japonicus*. The observed functional redundancy of TRH peptides suggests that the loss of long-isoform TRH in chordates reflects evolutionary trade-offs driven by natural selection. Differences in signaling mechanisms between long and short isoforms suggest potential context-dependent or nuanced roles that warrant further exploration. Future studies examining TRH signaling across diverse species will be crucial to confirm the proposed evolutionary history of TRH signaling. This work offers novel insights into the evolutionary history of TRH signaling and highlights the cooperative interactions of peptidergic pathways in regulating feeding behavior in marine invertebrates.

SUPPLEMENTARY DATA

Supplementary data to this article can be found online.

COMPETING INTERESTS

The authors declare that they have no competing interests.

AUTHORS’ CONTRIBUTIONS

Conceptualization: M.C.; Methodology: Y.Z., M.C., and J.D.G.-E.; Data curation: Y.Z., H.L., and X.D.; Investigation: Y.Z., H.L., and X.D.; Writing–original draft: Y.Z.; Formal analysis: M.C. and J.D.G.-E.; Writing–review and editing: M.C. and J.D.G.-E.; Supervision: M.C.; Funding acquisition: M.C. All authors read and approved the final version of the manuscript.

REFERENCES

Akieda-Asai S, Poleni PE, Date Y. 2014. Coinjection of CCK and leptin reduces food intake via increased CART/TRH and reduced AMPK phosphorylation in the hypothalamus. *American Journal of Physiology-Endocrinology and Metabolism*, **306**(11): E1284–E1291.

Al-Arabi A, Andrews JF. 2006. The effect of TRH and norepinephrine on the triglyceride droplets (TGD) in brown adipose tissue in warm acclimated rats. *Biomedical Sciences Instrumentation*, **42**: 507–512.

Bauknecht P, Jékely G. 2015. Large-scale combinatorial deorphanization of *Platynereis* neuropeptide GPCRs. *Cell Reports*, **12**(4): 684–693.

Burbach JPH. 2011. What are neuropeptides?. *In*: Merighi A. Neuropeptides. New York: Humana Press, 1–36.

Chaiyamoon A, Tinikul R, Nontunha N, et al. 2020. Characterization of TRH/GnRH-like peptides in the sea cucumber, *Holothuria scabra*, and their effects on oocyte maturation. *Aquaculture*, **518**: 734814.

Changeux JP. 2010. Allosteric receptors: from electric organ to cognition. *Annual Review of Pharmacology and Toxicology*, **50**: 1–38.

Chen MY, Talarovicova A, Zheng YQ, et al. 2019. Neuropeptide precursors and neuropeptides in the sea cucumber *Apostichopus japonicus*: a genomic, transcriptomic and proteomic analysis. *Scientific Reports*, **9**(1): 8829.

Chieu HD, Suwansa-Ard S, Wang TF, et al. 2019. Identification of neuropeptides in the sea cucumber *Holothuria leucospilota*. *General and Comparative Endocrinology*, **283**: 113229.

Choi YH, Hartzell D, Azain MJ, et al. 2002. TRH decreases food intake and increases water intake and body temperature in rats. *Physiology & Behavior*, **77**(1): 1–4.

Conzelmann M, Williams EA, Krug K, et al. 2013. The neuropeptide complement of the marine annelid *Platynereis dumerilii*. *BMC Genomics*, **14**: 906.

Cui ZJ, Gorelick FS, Dannies PS. 1994. Calcium/calmodulin-dependent protein kinase-II activation in rat pituitary cells in the presence of thyrotropin-releasing hormone and dopamine. *Endocrinology*, **134**(5): 2245–2250.

Frare C, Williams CT, Drew KL. 2021. Thermoregulation in hibernating mammals: the role of the “thyroid hormones system”. *Molecular and Cellular Endocrinology*, **519**: 111054.

Galas L, Lamacz M, Garnier M, et al. 1998. Involvement of extracellular and intracellular calcium sources in TRH-induced *α*-MSH secretion from frog melanotrope cells. *Molecular and Cellular Endocrinology*, **138**(1-2): 25–39.

Gotoh K, Masaki T, Chiba S, et al. 2013. Nesfatin‐1, corticotropin‐releasing hormone, thyrotropin‐releasing hormone, and neuronal histamine interact in the hypothalamus to regulate feeding behavior. *Journal of Neurochemistry*, **124**(1): 90–99.

Guo D, Zhang YJ, Zhang S, et al. 2021. Cholecystokinin-like peptide mediates satiety by inhibiting sugar attraction. *PLoS Genetics*, **17**(8): e1009724.

Huang BW, Lv ZM, Li YN, et al. 2021. Identification and functional characterization of natural resistance-associated macrophage protein 2 from sea cucumber *Apostichopus japonicus*. *Developmental & Comparative Immunology*, **114**: 103835.

Jékely G. 2013. Global view of the evolution and diversity of metazoan neuropeptide signaling. *Proceedings of the National Academy of Sciences of the United States of America*, **110**(21): 8702–8707.

Ji SY, Dong YJ, Chen LN, et al. 2022. Molecular basis for the activation of thyrotropin-releasing hormone receptor. *Cell Discovery*, **8**(1): 116.

Li CY, Zheng YQ, Cong X, et al. 2022. Molecular and functional characterization of the luqin-type neuropeptide signaling system in the sea cucumber *Apostichopus japonicus*. *Peptides*, **155**: 170839.

Li G, Shi Y, Huang HS, et al. 2010. Internalization of the human nicotinic acid receptor GPR109A is regulated by G_i, GRK2, and arrestin3. *Journal of Biological Chemistry*, **285**(29): 22605–22618.

Liu CJ, Li LB, Ha M, et al. 2015. The PI3K/Akt and ERK pathways elevate thyroid hormone receptor β1 and TRH receptor to decrease thyroid hormones after exposure to PCB153 and *p, p′*-DDE. *Chemosphere*, **118**: 229–238.

Liu YZ, He G, Wang QC, et al. 2014. Hydroxyproline supplementation on the performances of high plant protein source based diets in turbot (*Scophthalmus maximus* L.). *Aquaculture*, **433**: 476–480.

Loh K, Zhang L, Brandon A, et al. 2017. Insulin controls food intake and energy balance via NPY neurons. *Molecular Metabolism*, **6**(6): 574–584.

Mamedova E, Dmytriyeva O, Rekling JC. 2022. Thyrotropin-releasing hormone induces Ca^{2+} increase in a subset of vagal nodose ganglion neurons. *Neuropeptides*, **94**: 102261.

Matson CA, Reid DF, Cannon TA, et al. 2000. Cholecystokinin and leptin act synergistically to reduce body weight. *American Journal of Physiology-Regulatory, Integrative and Comparative Physiology*, **278**(4): R882–R890.

Mayorova TD, Tian S, Cai WG, et al. 2016. Localization of neuropeptide gene expression in larvae of an echinoderm, the starfish *Asterias rubens*. *Frontiers in Neuroscience*, **10**: 553.

Mendel HC, Kaas Q, Muttenthaler M. 2020. Neuropeptide signalling systems–An underexplored target for venom drug discovery. *Biochemical Pharmacology*, **181**: 114129.

Møller LN, Stidsen CE, Hartmann B, et al. 2003. Somatostatin receptors. *Biochimica et Biophysica Acta (BBA)-Biomembranes*, **1616**(1): 1–84.

Nässel DR, Wu SF. 2022. Cholecystokinin/sulfakinin peptide signaling: conserved roles at the intersection between feeding, mating and aggression. *Cellular and Molecular Life Sciences*, **79**(3): 188.

Ohta N, Kubota I, Takao T, et al. 1991. Fulicin, a novel neuropeptide containing a D-amino acid residue isolated from the ganglia of Achatina fulica. *Biochemical and Biophysical Research Communications*, **178**(2): 486–493.

Peters JH, Simasko SM, Ritter RC. 2006. Modulation of vagal afferent excitation and reduction of food intake by leptin and cholecystokinin. *Physiology & Behavior*, **89**(4): 477–485.

Pool AH, Scott K. 2014. Feeding regulation in *Drosophila*. *Current Opinion in Neurobiology*, **29**: 57–63.

Puga L, Alcántara-Alonso V, Coffeen U, et al. 2016. TRH injected into the nucleus accumbens shell releases dopamine and reduces feeding motivation in rats. *Behavioural Brain Research*, **306**: 128–136.

Rojo-Ruiz J, Navas-Navarro P, Nuñez L, et al. 2021. Imaging of endoplasmic reticulum Ca^{2+} in the intact pituitary gland of transgenic mice expressing a low affinity Ca^{2+} indicator. *Frontiers in Endocrinology*, **11**: 615777.

Root CM, Ko KI, Jafari A, et al. 2011. Presynaptic facilitation by neuropeptide signaling mediates odor-driven food search. *Cell*, **145**(1): 133–144.

Rowe ML, Achhala S, Elphick MR. 2014. Neuropeptides and polypeptide hormones in echinoderms: new insights from analysis of the transcriptome of the sea cucumber *Apostichopus japonicus*. *General and Comparative Endocrinology*, **197**: 43–55.

Rowe ML, Elphick MR. 2012. The neuropeptide transcriptome of a model echinoderm, the sea urchin *Strongylocentrotus purpuratus*. *General and Comparative Endocrinology*, **179**(3): 331–344.

Schuhler S, Warner A, Finney N, et al. 2007. Thyrotrophin‐releasing hormone decreases feeding and increases body temperature, activity and oxygen consumption in Siberian hamsters. *Journal of Neuroendocrinology*, **19**(4): 239–249.

Schwartz C, Hampton M, Andrews MT. 2013. Seasonal and regional differences in gene expression in the brain of a hibernating mammal. *PLoS One*, **8**(3): e58427.

Semmens DC, Mirabeau O, Moghul I, et al. 2016. Transcriptomic identification of starfish neuropeptide precursors yields new insights into neuropeptide evolution. *Open Biology*, **6**(2): 150224.

Smith MK, Wang TF, Suwansa-Ard S, et al. 2017. The neuropeptidome of the Crown-of-Thorns Starfish, *Acanthaster planci*. *Journal of Proteomics*, **165**: 61–68.

Steward CA, Horan TL, Schuhler S, et al. 2003. Central administration of thyrotropin releasing hormone (TRH) and related peptides inhibits feeding behavior in the Siberian hamster. *Neuroreport*, **14**(5): 687–691.

Suwansa-Ard S, Chaiyamoon A, Talarovicova A, et al. 2018. Transcriptomic discovery and comparative analysis of neuropeptide precursors in sea cucumbers (Holothuroidea). *Peptides*, **99**: 231–240.

Tamura Y, Shintani M, Nakamura A, et al. 2005. Phase-specific central regulatory systems of hibernation in Syrian hamsters. *Brain research*, **1045**(1–2): 88–96.

Tinoco AB, Barreiro-Iglesias A, Guerra LAY, et al. 2021. Ancient role of sulfakinin/cholecystokinin-type signalling in inhibitory regulation of feeding processes revealed in an echinoderm. *eLife*, **10**: e65667.

Trubacova R, Drastichova Z, Novotny J. 2022. Biochemical and physiological insights into TRH receptor-mediated signaling. *Frontiers in Cell and Developmental Biology*, **10**: 981452.

Valassi E, Scacchi M, Cavagnini F. 2008. Neuroendocrine control of food intake. *Nutrition, Metabolism and Cardiovascular Diseases*, **18**(2): 158–168.

Van Sinay E, Mirabeau O, Depuydt G, et al. 2017. Evolutionarily conserved TRH neuropeptide pathway regulates growth in *Caenorhabditis elegans*. *Proceedings of the National Academy of Sciences of the United States of America*, **114**(20): E4065–E4074.

Veenstra JA, Šimo L. 2020. The TRH-ortholog EFLamide in the migratory locust. *Insect Biochemistry and Molecular Biology*, **116**: 103281.

Wang TM, Cao Z, Shen ZF, et al. 2020. Existence and functions of a kisspeptin neuropeptide signaling system in a non-chordate deuterostome species. *eLife*, **9**: e53370.

Wang TM, Yang Z, Zhou NM, et al. 2017. Identification and functional characterisation of 5-HT4 receptor in sea cucumber *Apostichopus japonicus* (Selenka). *Scientific Reports*, **7**(1): 40247.

Wang YT, Xu WX, Zhang JM, et al. 2022. Effects of glycyrrhizin (GL) supplementation on survival, growth performance, expression of feeding-related genes, activities of digestive enzymes, antioxidant capacity, and expression of inflammatory factors in large yellow croaker (*Larimichthys crocea*) larvae. *Aquaculture Nutrition*, **2022**: 5508120.

Wong AHC, Buckle CE, Van Tol HH. 2000. Polymorphisms in dopamine receptors: what do they tell us?. *European Journal of Pharmacology*, **410**(2–3): 183–203.

Xu Y W, Cai H M, You C Z, et al. 2022. Structural insights into ligand binding and activation of the human thyrotropin-releasing hormone receptor. *Cell Research*, **32**(9): 855–857.

Zandawala M, Amir MB, Shin J, et al. 2024. Proteome-wide neuropeptide identification using NeuroPeptide-HMMer (NP-HMMer). *General and Comparative Endocrinology*, **357**: 114597.

Zandawala M, Moghul I, Yañez Guerra LA, et al. 2017. Discovery of novel representatives of bilaterian neuropeptide families and reconstruction of neuropeptide precursor evolution in ophiuroid echinoderms. *Open Biology*, **7**(9): 170129.

Zels S, Dillen S, Crabbé K, et al. 2015. Sulfakinin is an important regulator of digestive processes in the migratory locust, *Locusta migratoria*. *Insect Biochemistry and Molecular Biology*, **61**: 8–16.

Zhao Y, Yang HS, Storey KB, et al. 2014. RNA-seq dependent transcriptional analysis unveils gene expression profile in the intestine of sea cucumber *Apostichopus japonicus* during aestivation. *Comparative Biochemistry and Physiology Part D: Genomics and Proteomics*, **10**: 30–43.

Zheng YQ, Cong X, Liu HC, et al. 2022. Nervous system development and neuropeptides characterization in embryo and larva: insights from a non-chordate deuterostome, the sea cucumber *Apostichopus japonicus*. *Biology*, **11**(10): 1538.

Zheng YQ, Cong X, Liu HC, et al. 2024. Neuronal cell populations in circumoral nerve ring of sea cucumber *Apostichopus japonicus*: ultrastructure and transcriptional profile. *Comparative Biochemistry and Physiology Part D: Genomics and Proteomics*, **52**: 101263.

Zuckerkandl E, Pauling L. 1965. Evolutionary divergence and convergence in proteins. *In* Bryson V, Vogel HJ. Evolving Genes and Proteins. New York: Academic Press, 97–166.

Zheng et al. *Zool. Res.* 2025, 46(1): 249−260
https://doi.org/10.24272/j.issn.2095-8137.2024.195
https://cstr.cn/32248.14.zr.2024.195

ZR | Zoological Research

Review Open Access

Advances and applications of genome-edited animal models for severe combined immunodeficiency

Xiao Zheng[1,#], Chun-Hui Huang[2,3,#], Sen Yan[2,3,4,*], Ming-Deng Rong[1,*]

[1] *Stomatological Hospital*, *School of Stomatology*, *Southern Medical University*, *Guangzhou*, *Guangdong* 510280, *China*

[2] *Guangdong Key Laboratory of Non-Human Primate Models*, *Guangdong-Hongkong-Macau Institute of CNS Regeneration*, *Jinan University*, *Guangzhou*, *Guangdong* 510632, *China*

[3] *School of medicine*, *Jinan University*, *Guangzhou*, *Guangdong* 510632, *China*

[4] *Department of Neurology*, *Guangzhou Red Cross Hospital*, *Faculty of Medical Science*, *Jinan University*, *Guangzhou*, *Guangdong* 510220, *China*

ABSTRACT

Severe combined immunodeficiency disease (SCID), characterized by profound immune system dysfunction, can lead to life-threatening infections and death. Animal models play a pivotal role in elucidating biological processes and advancing therapeutic strategies. Recent advances in gene-editing technologies, including zinc-finger nucleases (ZFNs), transcription activator-like effector nucleases (TALENs), CRISPR/Cas9, and base editing, have significantly enhanced the generation of SCID models. These models have not only deepened our understanding of disease pathophysiology but have also driven progress in cancer therapy, stem cell transplantation, organ transplantation, and infectious disease management. This review provides a comprehensive overview of current SCID models generated using novel gene-editing approaches, highlighting their potential applications in translational medicine and their role in advancing biomedical research.

Keywords: Gene-editing technology; Animal model; Translational biomedicine; Severe combined immunodeficiency disease

INTRODUCTION

Severe combined immunodeficiency disease (SCID) is a hereditary disease marked by profound immune system dysfunction (Cirillo et al., 2015). The estimated prevalence of SCID ranges from 1 to 2 in 100 000 live births (Zhang et al., 2023). Early clinical manifestations typically include recurrent and severe infections, dysplasia, pneumonia, otitis media, skin infections, and disseminated Bacillus Calmette-Guerin infection. A hallmark feature of SCID is the absence of T lymphocytes in the peripheral blood and lymphoid tissues (Chien et al., 2015). SCID can be broadly classified into two subtypes: those with or without B lymphocytes. Approximately 23%–30% of SCID patients have detectable levels of natural killer (NK) cells but no B and T lymphocytes. The absence of functional T, B, and NK cells severely compromises immune responses, necessitating robust animal models to investigate disease mechanisms and therapeutic approaches (Kim et al., 2021).

Immunodeficient animal models, which either harbor congenital genetic mutations or exhibit immune deficiencies induced through biotechnological methods, serve as indispensable tools in biomedical research. These models are widely applied in oncology, stem cell therapy, immune system, and infectious disease studies (Kim et al., 2021). The emergence of genome-editing technologies, including zinc finger nucleases (ZFN), transcription activator-like effector nucleases (TALEN), and clustered regularly interspaced short palindromic repeats associated with protein-9 nuclease (CRISPR/Cas9), has revolutionized the development of SCID animal models by providing precise and efficient tools for targeted genetic modification (Wang & Doudna, 2023; Wood et al., 2011). Several SCID animal models have been developed using mice (*Mus musculus*), rats (*Rattus*), and pigs (*Sus scrofa*) (Boettcher et al., 2020; He et al., 2019; Mombaerts et al., 1992; Suzuki et al., 2012). Humanized derivatives of these models, which incorporate human immune components, have gained popularity in both academic and

This is an open-access article distributed under the terms of the Creative Commons Attribution Non-Commercial License (http://creativecommons.org/licenses/by-nc/4.0/), which permits unrestricted non-commercial use, distribution, and reproduction in any medium, provided the original work is properly cited.

Copyright ©2025 Editorial Office of Zoological Research, Kunming Institute of Zoology, Chinese Academy of Sciences

Received: 25 September 2024; Accepted: 29 October 2024; Online: 30 October 2024

Foundation items: This work was supported by the Postdoctoral Fellowship Program of CPSF (GZC20231064), China Postdoctoral Science Foundation (2024M761345), Guangzhou Basic and Applied Basic Research Foundation (2024A04J6615), Scientific Research Project of Southern Medical University Stomatological Hospital (PY2023004), National Key Research and Development Program of China (2021YFA0805300) and National Natural Science Foundation of China (82171244, 32470564)

#Authors contributed equally to this work

*Corresponding authors, E-mail: 231yansen@163.com; rmdeng@smu.edu.cn

commercial settings. Despite these advancements, the selection of appropriate SCID models for specific research applications remains a complex and critical challenge.

This review presents a comprehensive analysis of the development and application of SCID animal models generated using advanced gene-editing technologies based on DNA nucleases. It examines the characteristics of SCID models created using different gene-editing approaches and explores their potential future applications as experimental models. Overall, the generation of SCID animal models represents a critical resource for advancing disease research.

PATHOLOGICAL AND IMMUNOLOGICAL CHARACTERISTICS OF SCID MODEL

SCID is characterized by a range of clinical features, including persistent diarrhea, persistent oral thrush, recurrent, severe, or opportunistic infections, lymphadenopathy, hepatosplenomegaly, erythrodermic rash (Omenn's syndrome), and lymphopenia (Rivers & Gaspar, 2015). A key pathological hallmark of SCID, according to the 2022 diagnostic and classification criteria, is the significant reduction or absence of autologous T cells. Genetic analyses have identified pathogenic variants of SCID-associated genes in 93% of patients, with seven genes (*IL2RG*, *RAG1*, *ADA*, *IL7R*, *DCLRE1C*, *JAK3*, and *RAG2*) accounting for 89% of typical SCID cases. Additionally, three genotypes (*RAG1*, *ADA*, and *RMRP*) are implicated in 57% of leakage or atypical SCID cases (Dvorak et al., 2023). The underlying pathogenesis of SCID involves various genetic defects that disrupt critical immune functions (Table 1), including anomalies in cytokine signaling (*IL2RG*, *JAK3*, and *IL7RA*), defects in V(D)J recombination, T cell receptor (TCR) assembly (*RAG1/RAG2*, *DCLRE1C*, *NHEJ1*, *LIG4*, and *PRKDC*), impaired survival of hematopoietic precursors (*AK2*), accumulation of toxic metabolites (*ADA*), abnormalities in TCR signaling (*CD45*, *CD3D*, *CD3Z*, *CD3δ*, *CD3ε*, and *CORO1A*), and thymic abnormalities (*FOXN1*) (Kumrah et al., 2020).

NOVEL GENOME-EDITING TECHNIQUES FOR GENERATING SCID ANIMAL MODELS

Gene-editing technologies have revolutionized the development of gene therapies by enabling precise modifications of DNA sequences and gene functions, facilitating the treatment of various diseases (Gaj et al., 2016). Various gene-modified animal models, including transgenic, gene knockout (KO), and gene insertion models, have been constructed using genetic manipulation methods, such as lentiviral vectors, transposons, embryonic stem cells, and targeted nucleases (Doyle et al., 2012). However, the application of traditional approaches to establish gene-edited large animal models remains underexplored (Volobueva et al., 2019). This gap highlights the critical importance of employing gene-editing technologies to generate SCID animal models (Figure 1).

DNA nuclease-based gene-editing techniques, such as ZFN, TALEN, CRISPR/Cas9, base editing, and prime editing, represent the forefront of genomic engineering (Newby & Liu, 2021). These technologies continue to advance, offering increased efficiency, reduced costs, and an ever-expanding range of applications. While base and prime editing operate through distinct mechanisms, the other three technologies rely on the repair of DNA double-strand breaks (DSBs) via homologous recombination or non-homologous end-joining (Zhou et al., 2022). The following sections review SCID models constructed using specific gene-editing techniques (Table 2).

SCID models constructed using ZFN

Before the emergence of ZFN technology, targeted genetic engineering was highly challenging in both animal models and human tissue culture systems (Palpant & Dudzinski, 2013). In 2010, researchers reported the first successful ZFN-based construction of an X-linked SCID rat model via *IL2RG* gene knockout (Mashimo et al., 2010). These rats exhibited abnormal thymus and spleen development, significantly reduced lymphocyte populations, and susceptibility to human tumor cell xenotransplantation, leading to tumor formation. Subsequent advancements included the generation of *RAG1*-KO rats, which displayed a near-complete absence of lymphocytes in the spleens and lymph nodes, and the simultaneous knockout of *PRKDC* and *IL2RG*, resulting in FSG rats with an immunodeficient phenotype.

ZFN technology has also demonstrated versatility in large animal models. Notably, Yang et al. (2011) successfully knocked out *PPARG* in pigs using ZFN, although the resulting phenotypes were not described. Similarly, Watanabe et al.

Table 1 SCID-related genes and their phenotypic changes

Pathogenesis	Gene name	Phenotypic changes
Thymic abnormalities	*FOXN1*	No hair, no thymus Lymphocyte reduction
Cytokine signaling anomalies	*IL2RG* *JAK3* *IL7RA*	Lack of T and NK cells, dysfunction of B lymphocytes
V(D)J recombination and T-cell receptor defects	*RAG1/RAG2* *DCLRE1C* *NHEJ1* *LIG4* *PRKDC*	T and B cell deficiency
Defective survival of hematopoietic precursors	*AK2*	T, B, and NK cell deficiency
Toxic metabolite accumulation	*ADA*	T, B, and NK cell deficiency
TCR abnormalities	*CD45* *CD3* *CORO1A*	T cell deficiency
Others	*B2M* *PRF1*	T and NK cell deficiency

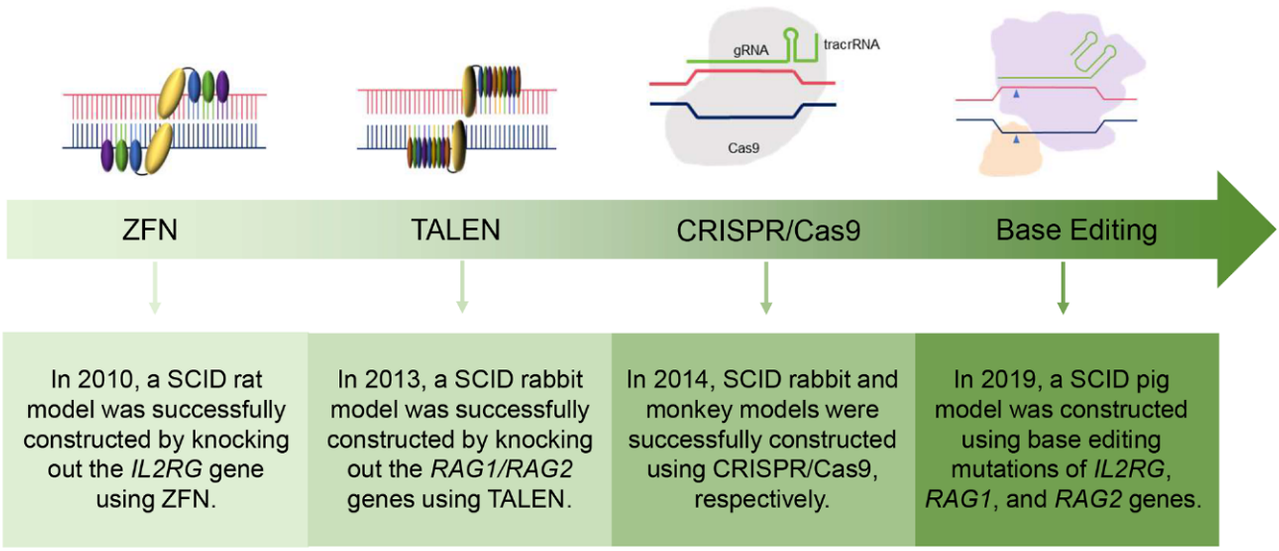


Figure 1 SCID animal models generated based on different DNA gene-editing techniques

Table 2 SCID animal models generated using different gene-editing techniques

Gene-editing technology	Species	Targeted genes	References
ZFNs	Rat (*Rattus*)	*IL2RG*	Mashimo et al., 2010
	Rat (*Rattus*)	*RAG1*	Zschemisch et al., 2012
	Rat (*Rattus*)	*PPARG*, *IL2RG*	Mashimo et al., 2012
	Pig (*Sus scrofa*)	*PPARG*	Yang et al., 2011
	Pig (*Sus scrofa*)	*IL2RG*	Watanabe et al., 2013
	Monkey (*Callithrix jacchus*)	*IL2RG*	Sato et al., 2016
TALENs	Mouse (*Mus musculus*)	*IL2RG*	Xiao et al., 2015
	Rat (*Rattus*)	*IL2RG*	Ménoret et al., 2018
	Rat (*Rattus*)	*RAG2*	Liu et al., 2015; Noto et al., 2018
	Rabbit (*Oryctolagus cuniculus*)	*RAG1/ RAG2*	Song et al., 2013
	Pig (*Sus scrofa*)	*RAG2*	Lee et al., 2014
	Pig (*Sus scrofa*)	*RAG1/ RAG2*	Huang et al., 2014
	Monkey (*Callithrix jacchus*)	*IL2RG*	Sato et al., 2016
CRISPR/Cas9	Mouse (*Mus musculus*)	*FOXN1*	Wei et al., 2017
	Rat (*Rattus*)	*IL2RG*, *RAG2*	Miyasaka et al., 2022
	Rabbit (*Oryctolagus cuniculus*)	*RAG1*, *RAG2*, *IL2RG*	Yan et al., 2014
	Rabbit (*Oryctolagus cuniculus*)	*FOXN1*	Song et al., 2021
	Rabbit (*Oryctolagus cuniculus*)	*FOXN1*, *RAG1*, *RAG2*, *IL2RG*, *PRKDC*	Song et al., 2017, 2018
	Rabbit (*Oryctolagus cuniculus*)	*IL2RG*	Hashikawa et al., 2020
	Pig (*Sus scrofa*)	*IL2RG*	Kang et al., 2016; Ren et al., 2020
	Pig (*Sus scrofa*)	*DCLRE1C*, *IL2RG*	Boettcher et al., 2020
	Monkey (*Macaca fascicularis*)	*PPARG*, *IL2RG*	Niu et al., 2014
Base Editor	Pig (*Sus scrofa*)	*IL2RG*, *RAG1*, *RAG2*	Xie et al., 2019
	Monkey (*Macaca fascicularis*)	*IL2RG*, *RAG1*	Zheng et al., 2023

(2013) established *IL2RG*-KO pigs, characterized by a complete absence of thymus, T cells, and NK cells, closely resembling the immunological profile of patients with X-linked SCID. Sato et al. (2016) generated a marmoset model with SCID by efficiently editing the *IL2RG* gene to produce an immunodeficiency phenotype, providing insights into thymocyte development in primates and novel therapeutics for human X-linked SCID. However, despite its relatively high editing efficiency, ZFN technology has several limitations that constrain its broader application, such as off-target effects, potential for carcinogenesis, and cumbersome operation.

SCID models constructed using TALEN

TALEN technology offers several advantages over ZFN, including easier design and construction and the ability to target any genomic site with high precision and efficiency. TALEN technology was first employed in 2013 to generate an immunodeficient rabbit model via *RAG1* and *RAG2* knockout (Song et al., 2013). Since then, TALEN has been utilized across a wide range of applications, from creating genetically modified crops and livestock to developing experimental models in diverse organisms. TALEN became the first genome-editing tool to achieve clinical success, curing relapsed refractory CD19-positive acute lymphoblastic leukemia, and further demonstrated its versatility with the commercialization of the first genome-edited crop (Becker & Boch, 2021; Menz et al., 2020; Qasim et al., 2017).

TALEN has played a pivotal role in constructing SCID

mouse models with distinct immunodeficiency phenotypes based on *IL2RG* gene editing. For example, Xiao et al. (2015) utilized these models to validate ANGPTL7 as a regulator of human hematopoietic stem and progenitor cell expansion and regeneration. Ménoret et al. (2018) generated *IL2RG*-deficient rats using TALEN, which exhibited more severe immunodeficiencies compared to *RAG1*-deficient rats, characterized by the partial loss of T, B, and NK cells. When these *IL2RG*-deficient rats were crossed with *RAG1*-deficient rats, the resulting offspring displayed severe immunosuppression, with undetectable levels of T, B, and NK cells (Ménoret et al., 2018). Previous studies have also developed *RAG2*-KO rats using TALEN technology, which demonstrated a deficiency in mature T and B cells, along with a compensatory increase in NK cells, making them highly susceptible to infections such as cowpox virus and xenotransplantation of human tumor cells (Liu et al., 2015; Noto et al., 2018). Song et al. (2013) successfully obtained *RAG*-KO rabbits via microinjection of TALEN mRNA into embryos, resulting in underdeveloped lymphoid organs, early obstruction of T and B cell development, and obstacles in V(D)J recombination.

TALEN technology has further been employed in large animal models. For example, Huang et al. (2014) developed *RAG*-KO pigs, which exhibited immune organ hypoplasia, an inability to undergo V(D)J rearrangement, and a loss of mature B and T cells. By targeting the *RAG2* gene in pigs using TALEN, Lee et al. (2014) produced an SCID model lacking both T and B cells, with subsequent injection of human-induced pluripotent cells inducing teratoma formation that recapitulated various human tissues. Furthermore, Sato et al. (2016) developed an immunodeficient marmoset model using both ZFN and TALEN vectors with distinct DSB activities, which improved editing efficiency and reduced the risk of chimerism but also posed challenges due to its technical complexity.

SCID models constructed using CRISPR/Cas9

CRISPR/Cas9 has become a widely used gene-editing approach due to its high efficiency, single-guide RNA (sgRNA) design, high specificity, and low off-target effects (Hochheiser et al., 2018). Using this approach, Wei et al. (2017) generated a novel nude NOD/SCID/*IL2rg*$^{-/-}$ (NSIN) mouse strain by knocking out *Foxn1* in NOD/SCID/*IL2rg*$^{-/-}$ (NSI) mice. The absence of B, T, and NK cells in these mice impaired T cell reconstruction and thymus regeneration ability following allogeneic bone marrow nucleated cell transplantation while enhancing engraftment of leukemia and solid tumor cells. Similarly, Miyasaka et al. (2022) used CRISPR/Cas9 to successfully edit *IL2RG* and *RAG2* in rats, generating SRG models that lacked mature T, B, and circulating NK cells. Yan et al. (2014) also applied this technology to simultaneously knockout *RAG1*, *RAG2*, and *IL2RG* in rabbits, although the production of live immunodeficient animals was not reported. Subsequent efforts have successfully produced immunodeficient rabbits with mutations in *FOXN1*, *RAG1*, *RAG2*, *IL2RG*, and *PRKDC*, which demonstrated reproductive transmission and yielded F1 generation offspring (Song et al., 2017, 2018). Notably, X-SCID rabbits generated by targeting *IL2RG* alone showed T and B cell loss, thymic hypoplasia, and improved outcomes in allogeneic skin tissue transplantation (Hashikawa et al., 2020). With CRISPR/Cas9 tools, Song et al. (2021) edited *FOXN1* in rabbits, producing hairless, thymus-free animals with severe immunodeficiency, suitable for human stem cell xenotransplantation.

CRISPR/Cas9 has also shown remarkable utility in large animal models. Notably, Boettcher et al. (2020) performed site-specific CRISPR/Cas9 mutations in *IL2RG* from pigs with an *ART*$^{-/-}$ genetic background, generating T^{-}B^{-}NK^{-}SCID pigs lacking T, B, and NK cells in their peripheral blood and lymphoid tissues. Similarly, *IL2RG*-KO pigs generated using CRISPR/Cas9 technology have been shown to exhibit a SCID phenotype (Kang et al., 2016) and support the growth of human melanoma-derived tumors (Ren et al., 2020). Niu et al. (2014) employed CRISPR/Cas9 technology to precisely target the *PPAR-γ* and *RAG1* genes in crab-eating monkeys. Ongoing efforts to optimize CRISPR/Cas9 for SCID model development include the use of engineered Cas9 variants and the identification of immune orthogonal orthologs to minimize adverse events and improve editing outcomes (Uddin et al., 2020).

SCID models constructed using base editing

Base editing systems, including cytosine base editors (CBE), adenine base editors (ABEs), and guanine editors, enable precise genetic modifications without causing DNA DSBs, thereby avoiding activation of the DNA double-strand repair mechanisms. Xie et al. (2019) first used base editing to mutate *IL2RG*, *RAG1*, and *RAG2* in pigs, generating an immunodeficient model that exhibited severe infections and high mortality. Similarly, Zheng et al. (2023) employed the CBE4max system to inactivate *IL2RG* and *RAG1* in monkeys, establishing an immunodeficient model characterized by lymphopenia, lymphoid organ atrophy, and a lack of mature T cells. These base-edited monkeys supported the engraftment and growth of human breast cancer cells, leading to tumor formation.

Although base editing has shown promise, challenges remain regarding off-target effects associated with CRISPR/Cas9-based systems, including base and prime editing technologies. These limitations continue to hinder the therapeutic and clinical translation of CRISPR/Cas9-based systems for treating diseases. Furthermore, the use of gene-editing technology to generate SCID animal models requires ongoing refinement to enhance their precision and applicability.

COMPARISON OF GENE-EDITING TECHNIQUES AND SPECIES IN GENERATING SCID MODELS

Comparison of gene-editing technologies

ZFN technology, despite being one of the earliest genome-editing tools, faces significant challenges due to off-target effects and associated cytotoxicity (Carroll, 2011). Furthermore, the immune responses triggered by the microinjection of mRNA encoding ZFNs, along with inefficiencies in the process and the generation of mutant chimeras during SCID model construction, significantly limit the applicability of this technology (Li et al., 2014; Mashimo, 2014). Additional factors such as strain variability, species differences, chromatin structure, and technical manipulation also impact its efficiency in genetic modification.

In contrast, TALEN technology employs a DNA binding module that recognizes single nucleotides (Tsai et al., 2022), offering greater precision and ease in targeting specific genomic loci. TALEN was the first gene-editing tool that could

be designed and constructed relatively easily for precise genome editing. However, cytotoxicity and off-target effects remain concerns, and the extensive molecular cloning and sequencing required for constructing SCID models using TALEN present certain limitations in terms of technical manipulation and model construction cycle.

CRISPR/Cas9 has gained prominence due to its simplicity, requiring only the design and synthesis of gRNAs targeting specific genes (Bhatia et al., 2023). However, its reliance on DSBs introduces risks, such as DNA damage (Haapaniemi et al., 2018), chromosomal fragmentation and instability (Wang et al., 2019), off-target effects (Zhang et al., 2015b), and immunogenicity associated with Cas9 nucleases (Crudele & Chamberlain, 2018; Mehta & Merkel, 2020). Thus, when constructing SCID models with CRISPR/Cas9, considerations extend beyond gene-editing efficiency to include the evaluation of pathological phenotypes, immunological changes, off-target effects, and cytotoxicity.

Base editing has the advantages of programmability and flexibility, overcoming the limitations of traditional Cas9 nuclease gene editing (Porto et al., 2020). Optimized base editing techniques allow precise targeting of immunodeficiency genes, improving gene-editing efficiency. However, comprehensive safety evaluations remain essential to address potential off-target effects. Advances in sequencing technologies and bioinformatics analysis are critical for achieving the precision needed to assess and mitigate these risks (Blattner et al., 2020).

Prime editing, although still in its infancy, represents a promising development in gene editing. It has been successfully applied in cell lines, post-mitotic neurons, mice, organoids, and plants (Gao et al., 2021; Schene et al., 2020; Xu et al., 2020). Despite these advances, prime editing faces many obstacles, including off-target effects, delivery selection, and immunogenicity. Notably, SCID models generated using prime editing have not yet been reported.

SCID models generated using these technologies have successfully replicated the phenotypes of immunodeficiency diseases. As gene-editing methods continue to advance, improvements in efficiency, ease of operation, and safety will also occur. While CRISPR/Cas9 technology is currently the most widely used due to its versatility, the appropriate gene-editing technology should be selected according to the target organism and specific gene to be edited. Simultaneously, the exploration and development of alternative methods like base and prime editing should not be overlooked. To address possible off-target effects, robust evaluations are required, including quantification of input DNA, unbiased bioinformatics analysis, traceable validation methods, and sensitivity assessments. In addition, while comparing different gene-editing techniques for SCID model construction, the appropriateness of the technical conditions during operation and possible differences between species should be considered.

Comparisons across species

Recent advancements in gene-editing techniques have enabled the development of a diverse range of SCID animal models, encompassing both large and small species. These models are widely used in biomedicine, each offering unique advantages, with a primary focus on mice, rats, rabbits, pigs, and non-human primates (NHPs).

SCID mice: Small immunodeficient animal models, particularly mice, are extensively utilized due to their short reproductive cycles, high fertility rates, ease of husbandry, and well-characterized genomes. The availability of mature gene modification technologies further enhances their applicability. Common SCID mouse models include SCID, NOD/SCID, NOD-SCID-Il2rgnull, NRG, and BRG mice (Shultz et al., 1995, 2007). The development of humanized mouse models, achieved through homozygous mutations in *PRKDC*-SCID or defects in *RAG1/RAG2*, has facilitated the effective implantation of human immune system components and xenografts. These humanized mouse models represent innovative platforms for human tumor immunology research, enabling study of the interaction between human tumors and the immune system and evaluation of immunotherapy efficacy (Cogels et al., 2021).

Despite significant advances in the translational potential of humanized mice in clinical oncology, no mouse model can fully replicate all aspects of human biology (Chuprin et al., 2023). Additionally, some SCID mice develop immune leakage as they age, although the underlying molecular mechanisms remain unclear. Consequently, there is an urgent need to develop immunodeficient models that more closely resemble human physiology to address the limitations of existing systems and improve translational research outcomes.

SCID rats: Before the advent of gene-editing technology, progress in developing immunodeficient rat models was slow. The emergence of these technologies has facilitated the generation of many immunodeficient rat strains, providing a valuable complement to mouse models. Existing immunodeficient rat strains include X-SCID (*IL2RG*), RAG1-KO (*RAG1*), SDR (*RAG2*), SCID (*PRKDC*), FSG (*PRKDC*, *IL2RG*), NSGL (*PRKDC*, *IL2RG*, *hSIRPα*), SD-RG (*RAG1*, *RAG2*, *IL2RG*), and SRG (*RAG2*, *IL2RG*) (Liu et al., 2015; Mashimo et al., 2010, 2012; Ménoret et al., 2020; Noto et al., 2020; Yang et al., 2018; Zschemisch et al., 2012).

SCID rats offer several advantages over mouse models. Notably, they support the engraftment of a broader range of human cells and tissues and have a longer lifespan, enabling extended studies. Their larger size facilitates surgical procedures and allows the collection of more experimental samples, addressing several shortcomings of mice. In addition, rats have been widely used in pharmacology and toxicology experiments, enhancing their utility in translational studies.

However, SCID rats have certain limitations. For instance, human $CD34^+$ hematopoietic stem cells cannot be successfully transplanted into FSG rats, hindering their use in developing humanized immune systems. Furthermore, *PRKDC*-KO rats exhibit growth inhibition (Mashimo et al., 2012), which may affect experimental outcomes and limit their application.

SCID rabbits: Genome-edited rabbit models hold significant promise for advancing our understanding of disease mechanisms and facilitating the development of novel gene therapies (Hornyik et al., 2022). Rabbits possess a unique immune system that makes them valuable for immunological and microbiological studies. Their extensive B cell repertoire enables the production of a diverse array of antibodies, and their affinity optimization mechanisms are more effective than those of rodents (Weber et al., 2017), making them particularly useful for antibody production studies. Additionally, rabbits are highly sensitive to a range of viruses and pathogenic bacteria, making SCID rabbit models well-suited for studying human

microbial infections and their associated diseases.

SCID pigs: Minipigs, widely used as non-rodent large laboratory animals in biomedical research, possess gastrointestinal, digestive, renal, and immune systems similar to humans, making them valuable models for studying human diseases. In addition, minipigs offer practical advantages over NHPs, including easier handling, husbandry, sampling, and drug administration. They are also free from zoonotic diseases commonly associated with NHPs and pose fewer ethical and conservation concerns. The availability of sexually mature animals and ease of transportation further enhance their utility.

Miniature pigs are widely used in biomedicine, not only as an ideal model for human diseases but also for organ xenotransplantation, cardiovascular research, and neurological studies. Compared with small animal models, pigs exhibit higher sequence similarity with human heterologous receptors, allowing for more accurate predictions of pharmacological and pharmacokinetic responses. Using advanced gene-editing techniques, researchers have developed various immunodeficient pig models, which are increasingly recognized as indispensable tools in translational and preclinical research.

Non-human primates SCID models: The availability of complete genome sequences has significantly advanced our understanding of biological processes at the molecular level. This has fueled the development of SCID models in NHPs, which provide critical insights from a molecular and developmental biology perspective (Nakamura et al., 2021). Although NHP-SCID models are promising, they face certain limitations, such as higher early infection mortality. This challenge necessitates anti-infection measures to ensure animal survival for meaningful studies. In addition, the problem of chimerism in NHP-SCID models presents a significant barrier to their use in pathophysiological studies.

In summary, SCID models derived from different species exhibit distinct disease phenotypes due to variations in anatomical, physiological, and genetic characteristics. While humanized mouse models are the most widely used for studying the human immune system, large-animal models, such as pigs and NHPs, more closely replicate human biological systems (Li & Lai, 2024; Rahman et al., 2023; Zhao et al., 2019), offering higher translational relevance. However, small animal models offer advantages such as shorter reproduction cycles and lower costs, characteristics that somewhat limit the widespread use of large animals. In addition, large-animal models are constrained by higher ethical and logistical considerations, including societal acceptance and regulatory restrictions. The optimal approach involves the joint use of different species to address specific research goals. Selecting the appropriate species for SCID model development should be guided by the experimental design, research objectives, and practical considerations such as cost and ethical implications.

SCID ANIMAL MODEL APPLICATIONS

The continuous development of targeted gene-editing techniques has transformed the generation of SCID animal models, expanding their applications in tumor xenotransplantation, immunology, stem cell therapy, and infectious disease treatment. These models provide invaluable insights into SCID-related diseases and facilitate translational biomedical research (Figure 2).

Tumor xenotransplantation

SCID animal models are essential for studying tumor growth, metastasis, and recurrence, as well as for evaluating antitumor drug screening. Cell-derived xenograft models, created by implanting tumor cell lines subcutaneously, intravenously, or *in situ* into immunodeficient or humanized animals, enable the study of subcutaneous or *in situ* tumor growth (Tsumura et al., 2020). While traditional *in vitro* cell lines lack the complexity of primary tumor microenvironments, patient-derived xenograft (PDX) models have addressed this limitation by transferring tumor tissues from patients into immunodeficient animals, paving the way for personalized therapeutic strategies (Yin et al., 2021). For example, *IL2RG*-deficient rats can serve as hosts for human ovarian cancer xenografts, with X-SCID rats developing tumors within 14 days of cell injection (Mashimo et al., 2010). Similarly, SCID mice subcutaneously inoculated with human medulloblastoma cells have provided insights into the protective effects of human protein analogs against TMZ-induced apoptosis in male germ cells (Jia et al., 2019). Non-small cell lung cancer models have also been developed by implanting *in vitro* tumor cells into SCID mice, enabling researchers to evaluate disease outcomes (Anderson et al., 2003). In addition, SCID mice have been used to construct skin xenograft models, facilitating the study of long-term ultraviolet irradiation effects (Hachiya et al., 2009).

The continuous optimization of SCID models and the anatomical limitations of small-animal systems have driven the development of SCID models in larger species, such as rabbits, pigs, and monkeys, using advanced gene-editing techniques and enabling comprehensive evaluation through tumor xenografts. For example, the breast cancer cell line MDA-MB-231 was successfully transplanted into a CRISPR/Cas9-generated immunodeficient monkey model (Zheng et al., 2023). Similarly, *FOXN1*-KO naked rabbits generated using CRISPR/Cas9-mediated editing have been applied for teratoma detection, tissue engineering, and vascular transplantation, while NOD/SCID/*IL2rg*$^{-/-}$ mice have facilitated *in vivo* monitoring and imaging of solid tumors (Wei et al., 2017). Moreover, *IL2RG*$^{-/Y}$ pigs created with CRISPR/Cas9 support human tumorigenesis, forming teratomas representing various human tissues when injected with human-induced pluripotent stem cells (Lee et al., 2014). Therefore, SCID models have significantly advanced our understanding of tumorigenesis and the complex interactions between tumors and host environments.

Immunotherapy

The successful transplantation of human tumors and active human immune cells into SCID mice has been a cornerstone for the development and use of humanized mouse models to evaluate cancer therapy efficacy (Bankert et al., 2001). The clinical success of immunotherapy has spurred interest from academic researchers, as well as biotechnology and pharmaceutical industries, in its potential role in cancer treatment. However, given the high cost of clinical development and the risk of inflammatory toxicity, robust model systems are essential for preclinical research. These systems include transplantable tumor models, transgenic or gene knockout tumor-generating models, and humanized mouse models inoculated with human tumor xenografts (Dranoff, 2011). Selecting the most appropriate animal models is critical for conducting systematic preclinical cancer

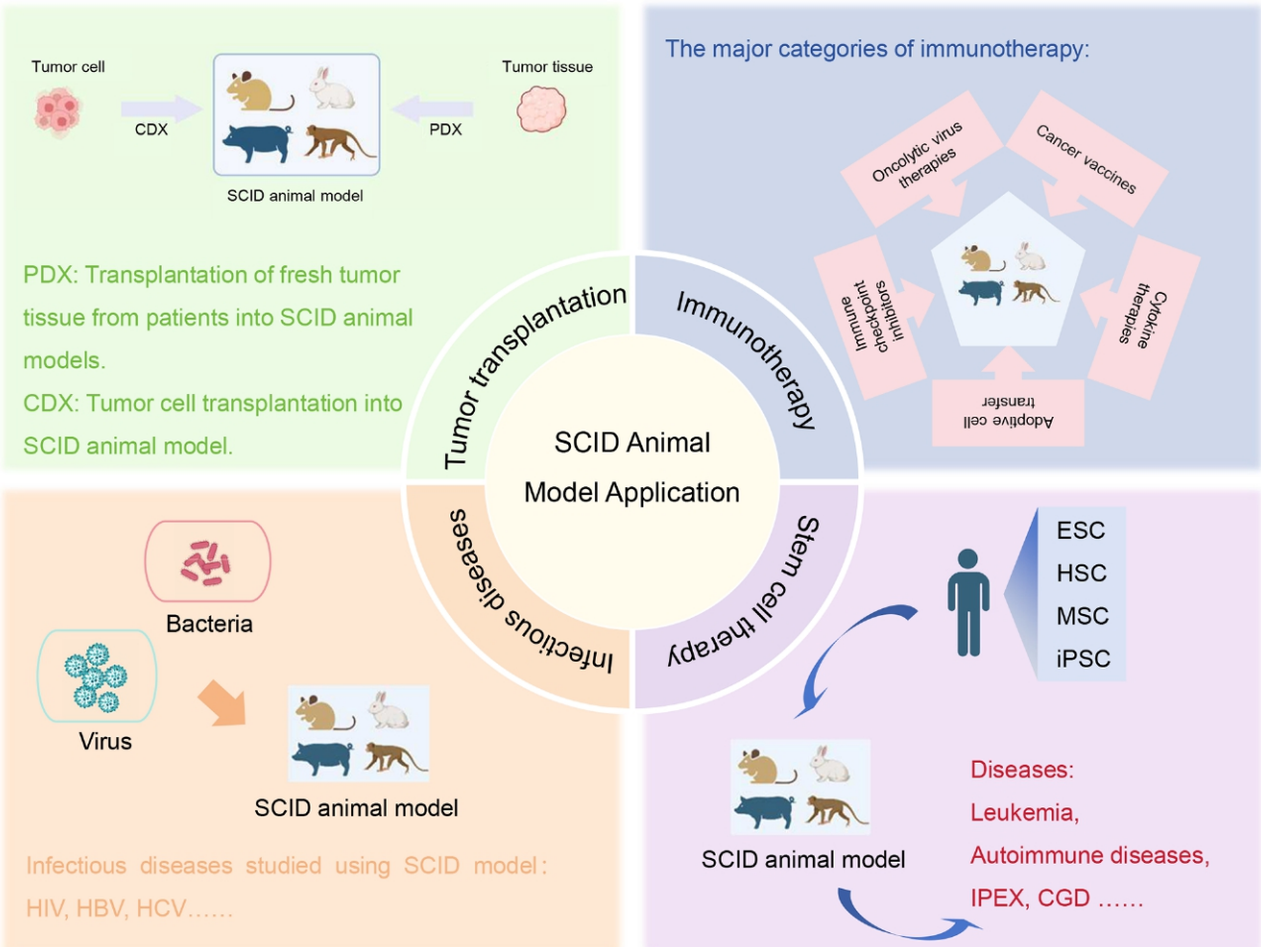


Figure 2 SCID animal model applications

Created using BioRender.com. CDX: Cell line-derived xenograft. PDX: Patient-derived xenografts. IPEX: Immune dysregulation, polyendocrinopathy, enteropathy, X-linked. CGD: X-linked chronic granulomatous disease.

immunotherapy studies.

Currently, cancer immunotherapies encompass oncolytic viral therapies, cancer vaccines, cytokine therapies, adoptive cell transplantation, and immune checkpoint inhibitors, all of which have shown promise in clinical practice (Zhang & Zhang, 2020). SCID models have been instrumental in advancing basic and translational research in these areas. For example, preclinical studies using NSG mice carrying human tumors and treated with specific antibodies against human CD47 have demonstrated effective tumor cell phagocytosis and elimination, reinforcing CD47 as an effective target for cancer treatment (Willingham et al., 2012). Similarly, the efficacy of CAR-T cell therapy for leukemia has been evaluated using NSG mice engineered with T cells expressing CD33-specific antigen receptors (Kenderian et al., 2015). In addition, humanized peripheral blood mononuclear cell (PBMC)-transfected MHC class I/II-deficient NOG mice have proven valuable for assessing human immune responses (Yaguchi et al., 2018), providing a platform for testing cancer immunotherapy drugs (Morillon et al., 2020). Therefore, the generation of novel humanized SCID animal models with reconstructed immune systems represents a significant advancement in preclinical immunotherapy research, allowing for comprehensive assessment of potential risks, such as cytokine storms and localized effects of CAR-T cells on tissues.

Stem cell therapy

SCID models, characterized by their immunodeficient status, are ideal for studying stem cell therapy as they can receive human cell transplants without triggering the immune system. For example, NOD/SCID and NOD-SCID-IL2Rγnull (NSG) mouse models are commonly used to determine the multispectral implantation potential and safety of candidate classes of hematopoietic stem cells (HSCs) from different sources. These models also serve as platforms for evaluating gene-edited HSCs as potential therapies for human immunodeficiency virus (HIV) (Holt et al., 2010; Li et al., 2013; Lux et al., 2019; Watanabe et al., 2007). Similarly, SCID rats have been used in preclinical studies involving human-induced pluripotent stem cell-derived neural precursor cell transplantation to model neonatal hypoxic-ischemic brain injury (Beldick et al., 2018). X-SCID rats further demonstrate their utility in stem cell research by tolerating transplants of human dopaminergic neurons derived from artificial blood stem cells without initiating an immune response, enabling evaluation of human dopaminergic neuronal function *in vivo* and providing a theoretical basis for stem cell therapies targeting neurological diseases (Samata et al., 2015).

Beyond rodents, SCID models in larger species have expanded the scope of stem cell research. In X-SCID dogs, $CD34^+$ bone marrow cells have been shown to re-establish normal B and T cell function (Bauer et al., 2013). SCID pig

models have also been instrumental in advancing stem cell research, ranging from HSC transplantation to regenerative medicine (Boettcher et al., 2019). Humanized SCID models are particularly valuable for studying rare genetic immune system disorders, such as immune dysregulation, polyendocrinopathy, enteropathy, X-linked syndrome (IPEX) (Goettel et al., 2015), inflammatory bowel disease (Goettel et al., 2019), and X-linked chronic granulomatous disease (CGD) (Naumann et al., 2007). These models enable preclinical evaluation of HSC-based gene therapies or *in situ* gene correction studies, offering a safer alternative to direct patient trials. Overall, humanized SCID animal models provide a critical platform for preclinical studies of stem cell gene therapies and *in situ* gene correction, while reducing risks to patients.

Infectious diseases

Animal models are invaluable for testing the efficacy and safety of experimental vaccines and therapies prior to human studies (Sarkar & Heise, 2019). The heightened sensitivity of SCID animals to environmental bacteria and viruses makes them ideal for studying microbial infections and host-pathogen interactions. For example, the development of a humanized mouse model based on TK-NOG has advanced research into hepatitis B virus (HBV) and hepatitis C virus (HCV) infections (Kosaka et al., 2013). Likewise, SCID rats have been utilized to monitor and manage symbiotic multi-tumor viruses through T cell monitoring strategies (Besch-Williford et al., 2017; Rigatti et al., 2016; Tanaka et al., 2018). X-linked SCID dogs have been developed to analyze the progression of metastatic squamous cell carcinoma (SCC) during advanced oncoviral infection (Goldschmidt et al., 2006). SCID pigs have also been used to study the replication dynamics of porcine reproductive and respiratory syndrome virus (Chen et al., 2015). Furthermore, SCID rats have been used to explore the role of host immunity in regulating the carrying capacity of *Hymenolepis diminuta* within the intestinal tract (Ohno et al., 2018), with antibiotic interventions found to be useful for managing *Campylobacter bovis*-associated clinical disease (Pires et al., 2023). Additionally, SCID mouse models engrafted with human lung tissue have been used to investigate SARS-CoV-2 infection (Fu et al., 2021).

While SCID models are useful for infectious disease research, their inability to fully replicate the complexity of the human immune response limits their utility in studying emerging infectious diseases. The prevention and control of infectious diseases require multifaceted approaches, and SCID models should be complemented with other research systems to gain insights into complex disease mechanisms and immune interactions.

SUMMARY AND FUTURE PERSPECTIVES

The continuous emergence of novel SCID models has driven advancements in biomedical research. This review systematically examined SCID animal models, including mice, rats, rabbits, pigs, and monkeys, constructed using CRISPR/Cas9 and other gene-editing technologies, highlighting their potential applications and contributions.

CRISPR-based genome editing technologies include CRISPR/Cas9, CRISPR-Cas12a, base editing, prime editing, transcriptional regulation, and RNA editing, which provide targeted and precise genome modification capabilities (Pacesa et al., 2024). Compared to the more complex and off-target effects of ZFN and TALEN, CRISPR offers a simpler yet highly versatile platform. However, limitations persist, particularly regarding editing activity, specificity, and delivery. Despite these challenges, the refinement of CRISPR-based technologies has significantly advanced SCID model development and disease research.

Currently, HSC transplantation remains the primary treatment for patients with SCID. Recent progress in CRISPR genome editing has shifted from preclinical studies based on cellular and animal models to human clinical trials. Therefore, the use of gene correction strategies has brought SCID gene therapy closer to reality (Iancu et al., 2023), consisting of the extraction of leukocytes from the bone marrow of an affected child, the correction of genetic defects via gene editing, and the reinfusion of modified cells into the patient. These developments emphasize the expanding utility of SCID models in both therapeutic innovation and fundamental disease research.

Species-specific differences further underscore the importance of selecting appropriate animal models for SCID research. For instance, in the development of STING agonist-based anticancer drugs, DMXAA and CMA demonstrated robust antitumor activity in preclinical mouse and rat models but failed in clinical trials due to their inability to effectively activate human STING (Cavlar et al., 2013; Zhang et al., 2015a).

These findings highlight the critical need for models that closely mimic human genetic and immunological responses. Large SCID animal models have become indispensable for translational research due to their genetic, anatomical, physiological, and phylogenetic similarities to humans. Microinjection and somatic cell nuclear transfer (SCNT) are the main methods for preparing gene-edited animal models (Matoba & Zhang, 2018; Shakweer et al., 2023). Microinjection, commonly used for small animal models such as mice, rats, and rabbits, presents challenges, such as chimeric outcomes and the inability to genotype animals until after birth, making it less cost-effective for large animal models. In contrast, SCNT permits genotype identification of nuclear donor cell clones before birth, thereby reducing costs and increasing efficiency. This method has been successfully employed in generating gene-edited pigs, although it requires a high level of technical expertise.

Pigs have emerged as highly suitable animal models for studying human SCID (Iqbal et al., 2019). In addition to their application in SCID research, pigs have garnered significant attention in organ transplantation and clinical applications. Recent breakthroughs include successful pig-to-human transplants of the heart (Griffith et al., 2022; Mohiuddin et al., 2023), kidney (Stone, 2023), and liver (Mallapaty, 2024). Notably, the first living pig kidney transplantation was performed at Massachusetts General Hospital in 2024, with the patient demonstrating positive recovery (Mallapaty & Kozlov, 2024).

Given their phylogenetic relationship with humans, NHPs provide another critical platform for SCID research, with gene-editing technologies, such as CRISPR/Cas9 editing and single nucleotide editing, significantly advancing the development of SCID monkey models. Researchers have successfully produced homozygous NHP models, incorporating reproductive techniques and F1 generation semen to establish immunodeficient monkeys within a reasonable timeframe. Furthermore, the ability to generate monkey embryos and

offspring with specific gene mutations or insertions with high efficiency has expanded the scope of NHP-based studies (Lu et al., 2022; Qiu et al., 2019). Innovative techniques, such as xenotransplantation of testicular tissue, have accelerated sperm maturation, thereby shortening cycle time and improving the utility of NHPs for both basic and biomedical research (Liu et al., 2016; Yao et al., 2018). Additionally, SCNT-based methods have proven invaluable for constructing genetically modified NHP models (Liu et al., 2018, 2019), including SCID monkeys. Despite the remarkable progress in SCID animal model development, the effectiveness of genome editing in such models must be further validated to ensure reproducibility and reliability. Additionally, the ethical concerns, high costs, and supply issues associated with large animal models should be addressed to ensure broader application.

Although SCID models have become an indispensable tool in biomedical research, their continued refinement is essential to better simulate human diseases and evaluate treatments. Enhancements, such as targeting multiple immunodeficiency-related genes, could further amplify the immunodeficiency phenotype, improving model fidelity for translational studies. Large-animal SCID models hold particular promise for future stem cell therapies, regenerative medicine, transplantation studies, infectious diseases, immunology, and cancer therapy. Nevertheless, challenges persist, including limited model availability, high costs, the need for standardized protocols, ethical concerns, improving the accuracy of disease representation, and optimizing gene-editing and humanization techniques for SCID models.

CONCLUSIONS

SCID animal models have become invaluable tools for advancing our understanding of hematopoietic and immune system regulation, offering insights into the cellular and molecular mechanisms underlying various human diseases, with unique applications in virology, regenerative medicine, hematology, cancer, immunology, and immunodeficiency. Compared to traditional models, SCID animal models generated by gene editing more accurately replicate the complex phenotypes associated with immunodeficiency and provide a robust platform for studying disease pathophysiology and translational biomedicine.

COMPETING INTERESTS

The authors declare that they have no competing interests.

AUTHORS' CONTRIBUTIONS

X.Z. wrote the original draft. C.H.H., S.Y., and M.D.R. revised the manuscript. All authors read and approved the final version of the manuscript.

REFERENCES

Anderson TM, Hess SD, Egilmez NK, et al. 2003. Comparison of human lung cancer/SCID mouse tumor xenografts and cell culture growth with patient clinical outcomes. *Journal of Cancer Research and Clinical Oncology*, **129**(10): 565–568.

Bankert RB, Egilmez NK, Hess SD. 2001. Human-SCID mouse chimeric models for the evaluation of anti-cancer therapies. *Trends in Immunology*, **22**(7): 386–393.

Bauer TR, Tuschong LM, Calvo KR, et al. 2013. Long-term follow-up of foamy viral vector-mediated gene therapy for canine leukocyte adhesion deficiency. *Molecular Therapy*, **21**(5): 964–972.

Becker S, Boch J. 2021. TALE and TALEN genome editing technologies. *Gene and Genome Editing*, **2**: 100007.

Beldick SR, Hong J, Altamentova S, et al. 2018. Severe-combined immunodeficient rats can be used to generate a model of perinatal hypoxic-ischemic brain injury to facilitate studies of engrafted human neural stem cells. *PLoS One*, **13**(11): e0208105.

Besch-Williford C, Pesavento P, Hamilton S, et al. 2017. A naturally transmitted epitheliotropic polyomavirus pathogenic in immunodeficient rats: characterization, transmission, and preliminary epidemiologic studies. *Toxicologic Pathology*, **45**(5): 593–603.

Bhatia S, Pooja, Yadav SK. 2023. CRISPR-Cas for genome editing: classification, mechanism, designing and applications. *International Journal of Biological Macromolecules*, **238**: 124054.

Blattner G, Cavazza A, Thrasher AJ, et al. 2020. Gene editing and genotoxicity: targeting the off-targets. *Frontiers in Genome Editing*, **2**: 613252.

Boettcher AN, Cunnick JE, Powell EJ, et al. 2019. Porcine signal regulatory protein alpha binds to human CD47 to inhibit phagocytosis: implications for human hematopoietic stem cell transplantation into severe combined immunodeficient pigs. *Xenotransplantation*, **26**(2): e12466.

Boettcher AN, Li YS, Ahrens AP, et al. 2020. Novel engraftment and T cell differentiation of human hematopoietic cells in ART$^{-/-}$ IL2RG$^{-/Y}$ SCID Pigs. *Frontiers in Immunology*, **11**: 100.

Carroll D. 2011. Genome engineering with zinc-finger nucleases. *Genetics*, **188**(4): 773–782.

Cavlar T, Deimling T, Ablasser A, et al. 2013. Species-specific detection of the antiviral small-molecule compound CMA by STING. *The EMBO Journal*, **32**(10): 1440–1450.

Chen NH, Dekkers JCM, Ewen CL, et al. 2015. Porcine reproductive and respiratory syndrome virus replication and quasispecies evolution in pigs that lack adaptive immunity. *Virus Research*, **195**: 246–249.

Chien YH, Chiang SC, Chang KL, et al. 2015. Incidence of severe combined immunodeficiency through newborn screening in a Chinese population. *Journal of the Formosan Medical Association*, **114**(1): 12–16.

Chuprin J, Buettner H, Seedhom MO, et al. 2023. Humanized mouse models for immuno-oncology research. *Nature Reviews Clinical Oncology*, **20**(3): 192–206.

Cirillo E, Giardino G, Gallo V, et al. 2015. Severe combined immunodeficiency--an update. *Annals of the New York Academy of Sciences*, **1356**(1): 90–106.

Cogels MM, Rouas R, Ghanem GE, et al. 2021. Humanized mice as a valuable pre-clinical model for cancer immunotherapy research. *Frontiers in Oncology*, **11**: 784947.

Crudele JM, Chamberlain JS. 2018. Cas9 immunity creates challenges for CRISPR gene editing therapies. *Nature Communications*, **9**(1): 3497.

Doyle A, Mcgarry MP, Lee NA, et al. 2012. The construction of transgenic and gene knockout/knockin mouse models of human disease. *Transgenic Research*, **21**(2): 327–349.

Dranoff G. 2011. Experimental mouse tumour models: what can be learnt about human cancer immunology?. *Nature Reviews Immunology*, **12**(1): 61–66.

Dvorak CC, Haddad E, Heimall J, et al. 2023. The diagnosis of severe combined immunodeficiency: Implementation of the PIDTC 2022 Definitions. *Journal of Allergy and Clinical Immunology*, **151**(2): 547–555. e5.

Fu WK, Wang W, Yuan LZ, et al. 2021. A SCID mouse-human lung xenograft model of SARS-CoV-2 infection. *Theranostics*, **11**(13): 6607–6615.

Gaj T, Sirk SJ, Shui SL, et al. 2016. Genome-editing technologies: principles and applications. *Cold Spring Harbor Perspectives in Biology*, **8**(12): a023754.

Gao P, Lyu Q, Ghanam AR, et al. 2021. Prime editing in mice reveals the

essentiality of a single base in driving tissue-specific gene expression. *Genome Biology*, **22**(1): 83.

Goettel JA, Biswas S, Lexmond WS, et al. 2015. Fatal autoimmunity in mice reconstituted with human hematopoietic stem cells encoding defective FOXP3. *Blood*, **125**(25): 3886–3895.

Goettel JA, Kotlarz D, Emani R, et al. 2019. Low-dose interleukin-2 ameliorates colitis in a preclinical humanized mouse model. *Cellular and Molecular Gastroenterology and Hepatology*, **8**(2): 193–195.

Goldschmidt MH, Kennedy JS, Kennedy DR, et al. 2006. Severe papillomavirus infection progressing to metastatic squamous cell carcinoma in bone marrow-transplanted X-linked SCID dogs. *Journal of Virology* **80**(13): 6621–6628.

Griffith BP, Goerlich CE, Singh AK, et al. 2022. Genetically modified porcine-to-human cardiac xenotransplantation. *New England Journal of Medicine*, **387**(1): 35–44.

Haapaniemi E, Botla S, Persson J, et al. 2018. CRISPR-Cas9 genome editing induces a p53-mediated DNA damage response. *Nature Medicine*, **24**(7): 927–930.

Hachiya A, Sriwiriyanont P, Fujimura T, et al. 2009. Mechanistic effects of long-term ultraviolet B irradiation induce epidermal and dermal changes in human skin xenografts. *The American Journal of Pathology* **174**(2): 401–413.

Hashikawa Y, Hayashi R, Tajima M, et al. 2020. Generation of knockout rabbits with X-linked severe combined immunodeficiency (X-SCID) using CRISPR/Cas9. *Scientific Reports*, **10**(1): 9957.

He D, Zhang JH, Wu WW, et al. 2019. A novel immunodeficient rat model supports human lung cancer xenografts. *FASEB Journal* **33**(1): 140–150.

Hochheiser K, Kueh AJ, Gebhardt T, et al. 2018. CRISPR/Cas9: a tool for immunological research. *European Journal of Immunology*, **48**(4): 576–583.

Holt N, Wang JB, Kim K, et al. 2010. Human hematopoietic stem/progenitor cells modified by zinc-finger nucleases targeted to *CCR5* control HIV-1 *in vivo*. *Nature Biotechnology* **28**(8): 839–847.

Hornyik T, Rieder M, Castiglione A, et al. 2022. Transgenic rabbit models for cardiac disease research. *British Journal of Pharmacology*, **179**(5): 938–957.

Huang J, Guo XG, Fan NN, et al. 2014. RAG1/2 knockout pigs with severe combined immunodeficiency. *The Journal of Immunology*, **193**(3): 1496–1503.

Iancu O, Allen D, Knop O, et al. 2023. Multiplex HDR for disease and correction modeling of SCID by CRISPR genome editing in human HSPCs. *Molecular Therapy-Nucleic Acids*, **31**: 105–121.

Iqbal MA, Hong K, Kim JH, et al. 2019. Severe combined immunodeficiency pig as an emerging animal model for human diseases and regenerative medicines. *BMB Reports*, **52**(11): 625–634.

Jia Y, Lue Y, Swerdloff RS, et al. 2019. The humanin analogue (HNG) prevents temozolomide-induced male germ cell apoptosis and other adverse effects in severe combined immuno-deficiency (SCID) mice bearing human medulloblastoma. *Experimental and Molecular Pathology*, **109**: 42–50.

Kang JT, Cho B, Ryu J, et al. 2016. Biallelic modification of *IL2RG* leads to severe combined immunodeficiency in pigs. *Reproductive Biology and Endocrinology*, **14**(1): 74.

Kenderian SS, Ruella M, Shestova O, et al. 2015. CD33-specific chimeric antigen receptor T cells exhibit potent preclinical activity against human acute myeloid leukemia. *Leukemia*, **29**(8): 1637–1647.

Kim YY, Yun JW, Kim JS, et al. 2021. Comparison of genetically engineered immunodeficient animal models for nonclinical testing of stem cell therapies. *Pharmaceutics*, **13**(2): 130.

Kosaka K, Hiraga N, Imamura M, et al. 2013. A novel TK-NOG based humanized mouse model for the study of HBV and HCV infections. *Biochemical and Biophysical Research Communications*, **441**(1): 230–235.

Kumrah R, Vignesh P, Patra P, et al. 2020. Genetics of severe combined immunodeficiency. *Genes & Diseases*, **7**(1): 52–61.

Lee K, Kwon DN, Ezashi T, et al. 2014. Engraftment of human iPS cells and allogeneic porcine cells into pigs with inactivated *RAG2* and accompanying severe combined immunodeficiency. *Proceedings of the National Academy of Sciences of the United States of America*, **111**(20): 7260–7265.

Li HL, Nakano T, Hotta A. 2014. Genetic correction using engineered nucleases for gene therapy applications. *Development, Growth & Differentiation*, **56**(1): 63–77.

Li LJ, Krymskaya L, Wang JB, et al. 2013. Genomic editing of the HIV-1 coreceptor CCR5 in adult hematopoietic stem and progenitor cells using zinc finger nucleases. *Molecular Therapy*, **21**(6): 1259–1269.

Li XJ, Lai LX. 2024. A booming field of large animal model research. *Zoological Research*, **45**(2): 311–313.

Liu Q, Fan CF, Zhou SY, et al. 2015. Bioluminescent imaging of vaccinia virus infection in immunocompetent and immunodeficient rats as a model for human smallpox. *Scientific Reports*, **5**: 11397.

Liu Z, Cai YJ, Liao ZD, et al. 2019. Cloning of a gene-edited macaque monkey by somatic cell nuclear transfer. *National Science Review*, **6**(1): 101–108.

Liu Z, Cai YJ, Wang Y, et al. 2018. Cloning of macaque monkeys by somatic cell nuclear transfer. *Cell*, **172**(4): 881–887. e7.

Liu Z, Nie YH, Zhang CC, et al. 2016. Generation of macaques with sperm derived from juvenile monkey testicular xenografts. *Cell Research*, **26**(1): 139–142.

Lu ZY, He ST, Jiang J, et al. 2022. Base-edited cynomolgus monkeys mimic core symptoms of STXBP1 encephalopathy. *Molecular Therapy*, **30**(6): 2163–2175.

Lux CT, Pattabhi S, Berger M, et al. 2019. TALEN-Mediated Gene Editing of HBG in Human Hematopoietic Stem Cells Leads to Therapeutic Fetal Hemoglobin Induction. *Molecular Therapy-Methods & Clinical Development*, **12**: 175–183.

Mallapaty S. 2024. First pig liver transplanted into a person lasts for 10 days. *Nature*, **627**(8005): 710–711.

Mallapaty S, Kozlov M. 2024. First pig kidney transplant in a person: what it means for the future. *Nature*, **628**(8006): 13–14.

Mashimo T. 2014. Gene targeting technologies in rats: zinc finger nucleases, transcription activator-like effector nucleases, and clustered regularly interspaced short palindromic repeats. *Development, Growth & Differentiation*, **56**(1): 46–52.

Mashimo T, Takizawa A, Kobayashi J, et al. 2012. Generation and characterization of severe combined immunodeficiency rats. *Cell Reports* **2**(3): 685–694.

Mashimo T, Takizawa A, Voigt B, et al. 2010. Generation of knockout rats with X-linked severe combined immunodeficiency (X-SCID) using zinc-finger nucleases. *PLoS One*, **5**(1): e8870.

Matoba S, Zhang Y. 2018. Somatic cell nuclear transfer reprogramming: mechanisms and applications. *Cell Stem Cell*, **23**(4): 471–485.

Mehta A, Merkel OM. 2020. Immunogenicity of Cas9 protein. *Journal of Pharmaceutical Sciences*, **109**(1): 62–67.

Ménoret S, Ouisse LH, Tesson L, et al. 2018. Generation of immunodeficient rats with *Rag1* and *Il2rg* gene deletions and human tissue grafting models. *Transplantation*, **102**(8): 1271–1278.

Ménoret S, Ouisse LH, Tesson L, et al. 2020. In vivo analysis of human immune responses in immunodeficient rats. *Transplantation*, **104**(4): 715–723.

Menz J, Modrzejewski D, Hartung F, et al. 2020. Genome edited crops touch the market: a view on the global development and regulatory environment. *Frontiers in Plant Science*, **11**: 586027.

Miyasaka Y, Wang JX, Hattori K, et al. 2022. A high-quality severe combined immunodeficiency (SCID) rat bioresource. *PLoS One*, **17**(8):

e0272950.

Mohiuddin MM, Singh AK, Scobie L, et al. 2023. Graft dysfunction in compassionate use of genetically engineered pig-to-human cardiac xenotransplantation: a case report. *The Lancet*, **402**(10399): 397–410.

Mombaerts P, Iacomini J, Johnson R S, et al. 1992. RAG-1-deficient mice have no mature B and T lymphocytes. *Cell*, **68**(5): 869–877.

Morillon YM, Sabzevari A, Schlom J, et al. 2020. The development of next-generation PBMC humanized mice for preclinical investigation of cancer immunotherapeutic agents. *Anticancer Research*, **40**(10): 5329–5341.

Nakamura T, Fujiwara K, Saitou M, et al. 2021. Non-human primates as a model for human development. *Stem Cell Reports*, **16**(5): 1093–1103.

Naumann N, De Ravin SS, Choi U, et al. 2007. Simian immunodeficiency virus lentivector corrects human X-linked chronic granulomatous disease in the NOD/SCID mouse xenograft. *Gene Therapy*, **14**(21): 1513–1524.

Newby GA, Liu DR. 2021. *In vivo* somatic cell base editing and prime editing. *Molecular Therapy*, **29**(11): 3107–3124.

Niu YY, Shen B, Cui YQ, et al. 2014. Generation of gene-modified cynomolgus monkey via Cas9/RNA-mediated gene targeting in one-cell embryos. *Cell*, **156**(4): 836–843.

Noto FK, Adjan-Steffey V, Tong M, et al. 2018. Sprague dawley *Rag2*-null rats created from engineered spermatogonial stem cells are immunodeficient and permissive to human xenografts. *Molecular Cancer Therapeutics*, **17**(11): 2481–2489.

Noto FK, Sangodkar J, Adedeji BT, et al. 2020. The SRG rat, a sprague-dawley Rag2/Il2rg double-knockout validated for human tumor oncology studies. *PLoS One*, **15**(10): e0240169.

Ohno T, Kai T, Miyasaka Y, et al. 2018. Intestinal immunity suppresses carrying capacity of rats for the model tapeworm, Hymenolepis diminuta. *Parasitology International*, **67**(4): 357–361.

Pacesa M, Pelea O, Jinek M. 2024. Past, present, and future of CRISPR genome editing technologies. *Cell*, **187**(5): 1076–1100.

Palpant NJ, Dudzinski D. 2013. Zinc finger nucleases: looking toward translation. *Gene Therapy*, **20**(2): 121–127.

Pires EM, Pugazhenthi U, Fink MK, et al. 2023. Antibiotic treatment of *Corynebacterium bovis*-associated clinical disease in NSG mice. *Comparative Medicine*, **73**(6): 461–465.

Porto EM, Komor AC, Slaymaker IM, et al. 2020. Base editing: advances and therapeutic opportunities. *Nature Reviews Drug Discovery*, **19**(12): 839–859.

Qasim W, Zhan H, Samarasinghe S, et al. 2017. Molecular remission of infant B-ALL after infusion of universal TALEN gene-edited CAR T cells. *Science Translational Medicine*, **9**(374): eaaj2013.

Qiu PY, Jiang J, Liu Z, et al. 2019. BMAL1 knockout macaque monkeys display reduced sleep and psychiatric disorders. *National Science Review*, **6**(1): 87–100.

Rahman A, Li YH, Chan TK, et al. 2023. Large animal models of cardiac ischemia-reperfusion injury: Where are we now?. *Zoological Research*, **44**(3): 591–603.

Ren JL, Yu DW, Fu R, et al. 2020. *IL2RG*-deficient minipigs generated via CRISPR/Cas9 technology support the growth of human melanoma-derived tumours. *Cell Proliferation*, **53**(10): e12863.

Rigatti LH, Toptan T, Newsome JT, et al. 2016. Identification and characterization of novel rat polyomavirus 2 in a colony of X-SCID rats by P-PIT assay. *mSphere*, **1**(6): e00334–16.

Rivers L, Gaspar HB. 2015. Severe combined immunodeficiency: recent developments and guidance on clinical management. *Archives of Disease in Childhood*, **100**(7): 667–672.

Samata B, Kikuchi T, Miyawaki Y, et al. 2015. X-linked severe combined immunodeficiency (X-SCID) rats for xeno-transplantation and behavioral evaluation. *Journal of Neuroscience Methods*, **243**: 68–77.

Sarkar S, Heise MT. 2019. Mouse models as resources for studying infectious diseases. *Clinical Therapeutics*, **41**(10): 1912–1922.

Sato K, Oiwa R, Kumita W, et al. 2016. Generation of a nonhuman primate model of severe combined immunodeficiency using highly efficient genome editing. *Cell Stem Cell*, **19**(1): 127–138.

Schene IF, Joore IP, Oka R, et al. 2020. Prime editing for functional repair in patient-derived disease models. *Nature Communications*, **11**(1): 5352.

Shakweer WME, Krivoruchko AY, Dessouki SM, et al. 2023. A review of transgenic animal techniques and their applications. *Journal of Genetic Engineering and Biotechnology*, **21**(1): 55.

Shultz LD, Ishikawa F, Greiner DL. 2007. Humanized mice in translational biomedical research. *Nature Reviews Immunology* **7**(2): 118–130.

Shultz LD, Schweitzer PA, Christianson SW, et al. 1995. Multiple defects in innate and adaptive immunologic function in NOD/LtSz-scid mice. *The Journal of Immunology*, **154**(1): 180–191.

Song J, Hoenerhoff M, Yang DS, et al. 2021. Development of the nude rabbit model. *Stem Cell Reports*, **16**(3): 656–665.

Song J, Wang GS, Hoenerhoff MJ, et al. 2018. Bacterial and *Pneumocystis* infections in the lungs of gene-knockout rabbits with severe combined immunodeficiency. *Frontiers in Immunology*, **9**: 429.

Song J, Yang DS, Ruan JX, et al. 2017. Production of immunodeficient rabbits by multiplex embryo transfer and multiplex gene targeting. *Scientific Reports*, **7**(1): 12202.

Song J, Zhong J, Guo XG, et al. 2013. Generation of *RAG*1- and 2-deficient rabbits by embryo microinjection of TALENs. *Cell Research*, **23**(8): 1059–1062.

Stone L. 2023. Kidney xenotransplantation. *Nature Reviews Urology*, **20**(11): 641.

Suzuki S, Iwamoto M, Saito Y, et al. 2012. *Il2rg* gene-targeted severe combined immunodeficiency pigs. *Cell Stem Cell*, **10**(6): 753–758.

Tanaka M, Kuramochi M, Nakanishi S, et al. 2018. Rat polyomavirus 2 infection in a colony of X-linked severe combined immunodeficiency rats in Japan. *Journal of Veterinary Medical Science*, **80**(9): 1400–1406.

Tsai HC, Pietrobon V, Peng MY, et al. 2022. Current strategies employed in the manipulation of gene expression for clinical purposes. *Journal of Translational Medicine*, **20**(1): 535.

Tsumura R, Koga Y, Hamada A, et al. 2020. Report of the use of patient‐derived xenograft models in the development of anticancer drugs in Japan. *Cancer Science*, **111**(9): 3386–3394.

Uddin F, Rudin CM, Sen T. 2020. CRISPR gene therapy: applications, limitations, and implications for the future. *Frontiers in Oncology*, **10**: 1387.

Volobueva AS, Orekhov AN, Deykin AV. 2019. An update on the tools for creating transgenic animal models of human diseases - focus on atherosclerosis. *Brazilian Journal of Medical and Biological Research*, **52**(5): e8108.

Wang HF, Nakamura M, Abbott TR, et al. 2019. CRISPR-mediated live imaging of genome editing and transcription. *Science*, **365**(6459): 1301–1305.

Wang JY, Doudna JA. 2023. CRISPR technology: a decade of genome editing is only the beginning. *Science*, **379**(6629): eadd8643.

Watanabe M, Nakano K, Matsunari H, et al. 2013. Generation of interleukin-2 receptor gamma gene knockout pigs from somatic cells genetically modified by zinc finger nuclease-encoding mRNA. *PLoS One*, **8**(10): e76478.

Watanabe S, Ohta S, Yajima M, et al. 2007. Humanized NOD/SCID/IL2Rgamma(null) mice transplanted with hematopoietic stem cells under nonmyeloablative conditions show prolonged life spans and allow detailed analysis of human immunodeficiency virus type 1 pathogenesis. *Journal of Virology* **81**(23): 13259–13264.

Weber J, Peng HY, Rader C. 2017. From rabbit antibody repertoires to rabbit monoclonal antibodies. *Experimental & Molecular Medicine*, **49**(3): e305.

Wei XR, Lai YX, Li BH, et al. 2017. CRISPR/Cas9-mediated deletion of *Foxn1* in NOD/SCID/IL2rg$^{-/-}$ mice results in severe immunodeficiency. *Scientific Reports*, **7**(1): 7720.

Willingham SB, Volkmer JP, Gentles AJ, et al. 2012. The CD47-signal regulatory protein alpha (SIRPa) interaction is a therapeutic target for human solid tumors. *Proceedings of the National Academy of Sciences of the United States of America*, **109**(17): 6662–6667.

Wood AJ, Lo TW, Zeitler B, et al. 2011. Targeted genome editing across species using ZFNs and TALENs. *Science*, **333**(6040): 307–307.

Xiao YR, Jiang ZW, Li Y, et al. 2015. ANGPTL7 regulates the expansion and repopulation of human hematopoietic stem and progenitor cells. *Haematologica*, **100**(5): 585–594.

Xie JK, Ge WK, Li N, et al. 2019. Efficient base editing for multiple genes and loci in pigs using base editors. *Nature Communications*, **10**(1): 2852.

Xu RF, Li J, Liu XS, et al. 2020. Development of plant prime-editing systems for precise genome editing. *Plant Communications*, **1**(3): 100043.

Yaguchi T, Kobayashi A, Inozume T, et al. 2018. Human PBMC-transferred murine MHC class I/II-deficient NOG mice enable long-term evaluation of human immune responses. *Cellular & Molecular Immunology*, **15**(11): 953–962.

Yan QM, Zhang QJ, Yang HQ, et al. 2014. Generation of multi-gene knockout rabbits using the Cas9/gRNA system. *Cell Regeneration*, **3**(1): 12.

Yang DS, Yang HQ, Li W, et al. 2011. Generation of PPARγ mono-allelic knockout pigs via zinc-finger nucleases and nuclear transfer cloning. *Cell Research*, **21**(6): 979–982.

Yang XL, Zhou JL, He JJ, et al. 2018. An immune system-modified rat model for human stem cell transplantation research. *Stem Cell Reports*, **11**(2): 514–521.

Yao X, Liu Z, Wang X, et al. 2018. Generation of knock-in cynomolgus monkey via CRISPR/Cas9 editing. *Cell Research*, **28**(3): 379–382.

Yin ZY, Maswikiti EP, Liu Q, et al. 2021. Current research developments of patient-derived tumour xenograft models (review). *Experimental and Therapeutic Medicine*, **22**(5): 1206.

Zhang H, Han MJ, Tao JL, et al. 2015a. Rat and human STINGs profile similarly towards anticancer/antiviral compounds. *Scientific Reports*, **5**: 18035.

Zhang XH, Tee LY, Wang XG, et al. 2015b. Off-target effects in CRISPR/Cas9-mediated genome engineering. *Molecular Therapy-Nucleic Acids*, **4**: e264.

Zhang XP, Kang XY, Yang MY, et al. 2023. A variant of *RAG1* gene identified in severe combined immunodeficiency: a case report. *BMC Pediatrics*, **23**(1): 56.

Zhang YY, Zhang ZM. 2020. The history and advances in cancer immunotherapy: understanding the characteristics of tumor-infiltrating immune cells and their therapeutic implications. *Cellular & Molecular Immunology*, **17**(8): 807–821.

Zhao JG, Lai LX, Ji WZ, et al. 2019. Genome editing in large animals: current status and future prospects. *National Science Review*, **6**(3): 402–420.

Zheng X, Huang CH, Lin YQ, et al. 2023. Generation of inactivated IL2RG and RAG1 monkeys with severe combined immunodeficiency using base editing. *Signal Transduction and Targeted Therapy*, **8**(1): 327.

Zhou WL, Yang JR, Zhang YL, et al. 2022. Current landscape of gene-editing technology in biomedicine: applications, advantages, challenges, and perspectives. *Medcomm*, **3**(3): e155.

Zschemisch NH, Glage S, Wedekind D, et al. 2012. Zinc-finger nuclease mediated disruption of *Rag1* in the LEW/Ztm rat. *BMC Immunology*, **13**: 60.

Zoological Research Editorial Board (2025)

EDITOR-IN-CHIEF:

Yong-Gang Yao — Kunming Institute of Zoology, CAS, China

ASSOCIATE EDITORS-IN-CHIEF:

Wai-Yee Chan — The Chinese University of Hong Kong, China
Xue-Long Jiang — Kunming Institute of Zoology, CAS, China
Yong-Tang Zheng — Kunming Institute of Zoology, CAS, China

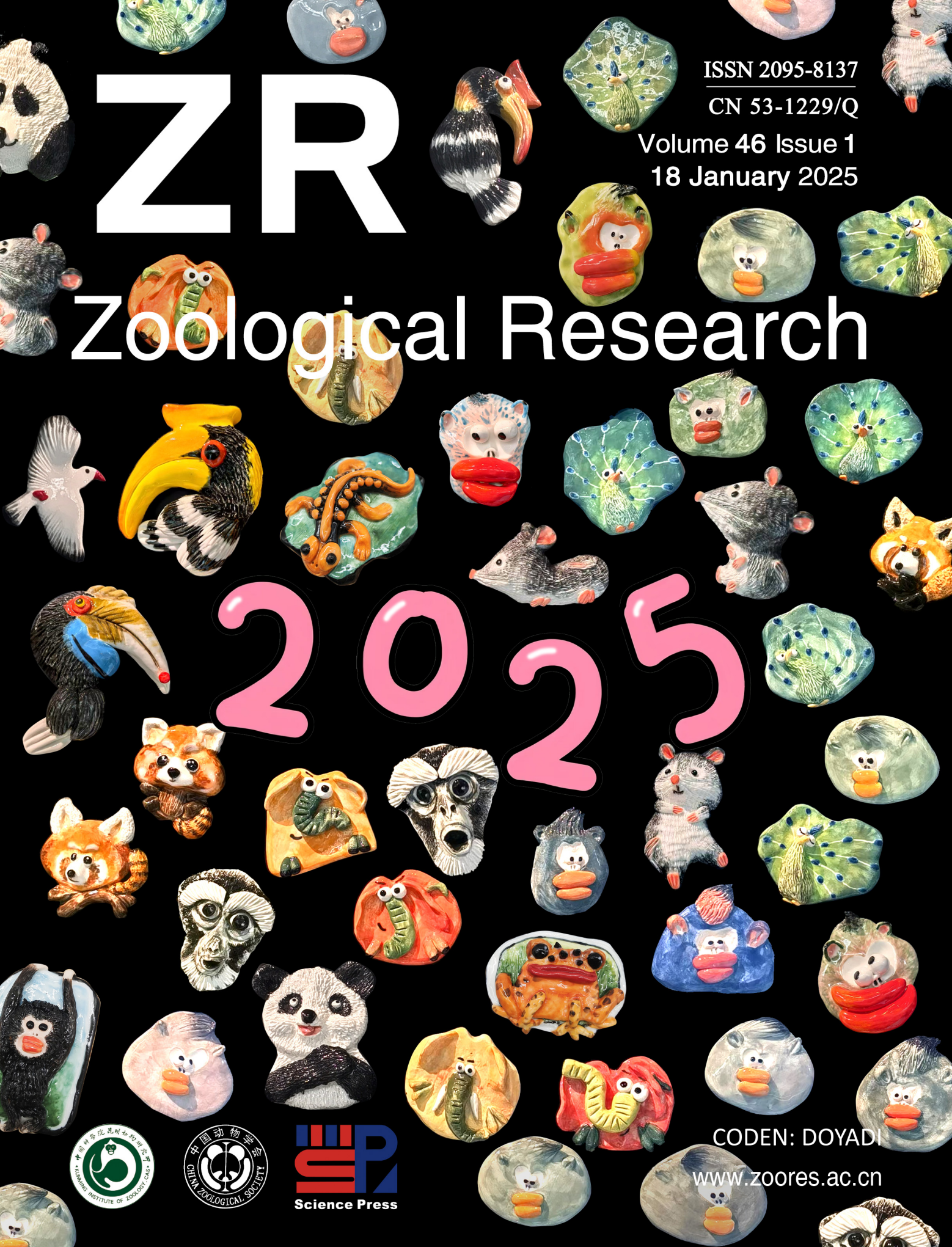
ASSOCIATE EDITORS:

Jiong Chen — Ningbo University, China
Peng-Fei Fan — Sun Yat-sen University, China
David Irwin — University of Toronto, Canada
Jia-Tang Li — Chengdu Institute of Biology, CAS, China
Shu-Qiang Li — Institute of Zoology, CAS, China

MEMBERS:

Amir Ardeshir — University of California, Davis, USA
Yong-Li Bao — Northeast Normal University, China
Yu-Hai Bi — Institute of Microbiology, CAS, China
Chao Bian — Shenzhen University, China
Jean Philippe Boubli — University of Salford, UK
Wen-Jun Bu — Nankai University, China
Kevin L. Campbell — University of Manitoba, Canada
Gang Cao — Huazhong Agricultural University, China
Colin Chapman — McGill University, Canada
Ce-Shi Chen — Kunming Medical University, China
Jia-Yu Chen — Tongji University, China
Liang-Biao Chen — Shanghai Ocean University, China
Luo-Nan Chen — Center for Excellence in Molecular Cell Science, CAS, China
Xiang-Jun Chen — Zhejiang University, China
Xue-Xin Chen — Zhejiang University, China
Yong-Chang Chen — Kunming University of Science and Technology, China
Dao-Jun Cheng — Southwest University, China
Ying Cheng — Yunnan University, China
Sandra Chiu — University of Science and Technology of China, China
Yu-Peng Cun — Chongqing Medical University, China
Ji Dai — Shenzhen Institute of Advanced Technology, CAS, China
Zhi-Fang Dong — Chongqing Medical University, China
Jiu-Lin Du — Center for Excellence in Brain Science and Intelligence Technology, CAS, China
Li-Na Du — Guangxi Normal University, China
Zhen-Yu Du — East China Normal University, China
Miguel Angel Esteban — BGI-Shenzhen & Guangzhou Institutes of Biomedicine and Health, CAS, China
Guang-Yi Fan — BGI-Shenzhen, China
He Zhi Fang — Cancer Hospital, Chinese Academy of Medical Sciences and Peking Union Medical College, China
Ji-Feng Fei — Southern Medical University, China
Ze-Xia Gao — Huazhong Agricultural University, China
Chu-Tian Ge — Zhejiang Wanli University, China
De-Yan Ge — Institute of Zoology, CAS, China
Shao-Yu Ge — SUNY at Stony Brook, USA
Cyril C. Grueter — The University of Western Australia, Australia
Jian-Fang Gui — Institute of Hydrobiology, CAS, China
Chang-Jun Guo — Sun Yat-sen University, China
Xian-Guang Guo — Chengdu Institute of Biology, CAS, China
Hong-Xuan He — Institute of Zoology, CAS, China
Shun-Ping He — Institute of Hydrobiology, CAS, China
Yong-Han He — Kunming Institute of Zoology, CAS, China
David Hillis — University of Texas at Austin, USA
Chun-Hui Hou — Kunming Institute of Zoology, CAS, China
Ji Hu — ShanghaiTech University, China
Zhong-Hua Hu — Xiangya Hospital, Central South University, China
Xiao-Xiang Hu — China Agricultural University, China
Jin-Lian Hua — Northwest A&F University, China
Lu-Sheng Huang — Jiangxi Agricultural University, China
You-Hua Huang — South China Agricultural University, China
Andrew Hutchins — Southern University of Science and Technology, China
William R. Jeffery — University of Maryland, USA
Xiang Ji — Wenzhou University, China
Jian-Ping Jiang — Chengdu Institute of Biology, CAS, China
Yu Jiang — Northwest A&F University, China
Le Kang — Hebei University, China
Yun Hak Kim — Pusan National University, Republic of Korea
Esther N. Kioko — National Museums of Kenya, Kenya
Randall C. Kyes — University of Washington, USA
Liang-Xue Lai — Guangzhou Institutes of Biomedicine and Health, CAS, China
Ren Lai — Kunming Institute of Zoology, CAS, China
Xiao-Jian Lai — Jimei University, China
Tian-Ming Lan — Northeast Forestry University, China
Kai Lei — Westlake University, China
Peng Lei — Sichuan University, China
Cheng-Hua Li — Ningbo University, China
Da-Li Li — East China Normal University, China
Dai-Qin Li — National University of Singapore, Singapore
Di-Yan Li — Chengdu University, China
Dong-Ming Li — Hebei Normal University, China
Gang Li — Shaanxi Normal University, China
Guo-Gang Li — Qinghai Normal University, China
Hai-Peng Li — Shanghai Institute of Nutrition and Health, CAS, China
Hong Li — Nanjing Normal University, China
Jin-Song Li — Center for Excellence in Molecular Cell Science, CAS, China
Jing Li — Sichuan University, China
Lei Li — Shenzhen Institute of Advanced Technology, CAS, China
Ming Li — Institute of Zoology, CAS, China
Ming Li — Kunming Institute of Zoology, CAS, China
Ming Li — University of Nebraska-Lincoln, USA
Ming-Zhou Li — Sichuan Agricultural University, China
Wei Li — Guangzhou Medical University, China
Wei-Dong Li — Shanghai Jiao Tong University, China
Xiao-Jiang Li — Jinan University, China
Xue-Ling Li — Inner Mongolia University, China
Xue-Yan Li — Kunming Institute of Zoology, CAS, China
Zhan-Jun Li — Jilin University, China
Wei Liang — Hainan Normal University, China
Qiang Lin — South China Sea Institute of Oceanology, CAS, China
Wei-Qiang Lin — Zhejiang University, China
Bing Liu — Fifth Medical Center of Chinese PLA General Hospital, China
Chun-Yu Liu — Shanghai Jiao Tong University, China
Ci-Rong Liu — Center for Excellence in Brain Science and Intelligence Technology, CAS, China
Huan-Zhang Liu — Institute of Hydrobiology, CAS, China
Jian-Hua Liu — South China Agricultural University, China
Lei Liu — Ningbo University, China
Sheng Liu — Sun Yat-sen University, China

Xing-Yue Liu	China Agricultural University, China
Zhen Liu	Institute of Neuroscience, CAS, China
Zhen Liu	Kunming Institute of Zoology, CAS, China
Jia-Hong Lu	University of Macau, China
Li Lu	Kunming Institute of Zoology, CAS, China
Anders Pape Møller	Université Paris-Saclay, France
Li Ma	Kunming Institute of Zoology, CAS, China
Ya-Fei Mao	Shanghai Jiao Tong University, China
Zi-Ning Meng	Sun Yat-sen University, China
Changjong Moon	Chonnam National University, Republic of Korea
Masaharu Motokawa	Kyoto University Museum, Japan
Yong-Gang Nie	Institute of Zoology, CAS, China
Sang-Bing Ong	The Chinese University of Hong Kong, China
Hong-Bo Pan	Shanghai Ocean University, China
Hyun Park	Korea University, Republic of Korea
Julian Kerbis Peterhans	Roosevelt University, USA
Nikolay A. Poyarkov, jr.	Lomonosov Moscow State University, Russia
Xiao-Guang Qi	Northwest University, China
Jian-Wen Qiu	Hong Kong Baptist University, China
Qiang Qiu	Northwestern Polytechnical University, China
Jing Qu	Institute of Zoology, CAS, China
Ming-Qiang Rong	Hunan Normal University, China
Christian Roos	Leibniz-Institute for Primate Research, Germany
Chang-Wei Shao	Yellow Sea Fisheries Research Institute, CAFS, China
De-Li Shi	Sorbonne University, France
Qing-Hua Shi	University of Science and Technology of China, China
Qiong Shi	Shenzhen University, China
Wei-Feng Shi	Shanghai Jiao Tong University, China
Xing-Feng Si	East China Normal University, China
Ning Song	Qingdao University, China
Bing Su	Kunming Institute of Zoology, CAS, China
Jian-Guo Su	Huazhong Agricultural University, China
Qiang Sun	Center for Excellence in Brain Science and Intelligence Technology, CAS, China
Yong-Hua Sun	Institute of Hydrobiology, CAS, China
Yu-Hua Sun	Institute of Hydrobiology, CAS, China
Chatmongkon Suwannapoom	University of Phayao, Thailand
Yi-Gang Tong	Beijing University of Chemical Technology, China
Christoph W. Turck	Max Planck Institute of Psychiatry, Germany
Guo-Hao Wang	National Institutes of Health, USA
Ding Wang	Institute of Hydrobiology, CAS, China
Kai Wang	Kunming Institute of Zoology, CAS, China
Kun Wang	Northwestern Polytechnical University, China
Ming-Shan Wang	Kunming Institute of Zoology, CAS, China
Wen Wang	Northwestern Polytechnical University, China
Xiao-Hui Wang	Changchun Institute of Applied Chemistry, CAS, China
Xiao-Qun Wang	Beijing Normal University, China
Yan-Jiang Wang	Third Military Medical University, China
Ying-Yong Wang	Sun Yat-sen University, China
Bin Wei	Shanghai University, China
Fu-Wen Wei	Jiangxi Agricultural University, China
Dong-Dong Wu	Kunming Institute of Zoology, CAS, China
Jun-Hong Xia	Sun Yat-sen University, China
Hui Xiang	South China Normal University, China
Zuo-Fu Xiang	Central South University of Forestry & Technology, China
Shi-Jun Xiao	Jilin Agricultural University, China
Xiao Xiao	Fudan University, China
Can Xie	Zhejiang University, China
Song-Guang Xie	Hainan University, China
Yu-Yun Xing	Jiangxi Agricultural University, China
Fu-Qiang Xu	Shenzhen Institute of Advanced Technology, CAS, China
Luo-Hao Xu	Southwest University, China
Shi-Qing Xu	Soochow University, China
Qing-Pi Yan	Jimei University, China
Sen Yan	Jinan University, China
Da-Hai Yang	East China University Of Science and Technology, China
Guang Yang	Nanjing Normal University, China
Jia-Long Yang	East China Normal University, China
Lian-Dong Yang	Institute of Hydrobiology, CAS, China
Shi-Hua Yang	South China Agricultural University, China
Wei-Li Yang	Jinan University, China
Xin-Wang Yang	Kunming Medical University, China
Xing-Lou Yang	Kunming Institute of Zoology, CAS, China
Yun-Peng Yang	Yangzhou University, China
Zhi-Yuan Yao	Shenyang Normal University, China
Bing Ye	University of Michigan, USA
Wen-Hua Yu	Guangzhou University, China
Ti-Fei Yuan	Shanghai Mental Health Center, China
Vitaliy Zablotskyy	Institute of Physics of the Academy of Sciences, the Czech Republic
Jian-Xiong Zeng	Shanghai Jiao Tong University, China
Bao-Wei Zhang	Anhui University, China
Bo Zhang	Southern Ocean Science and Engineering Guangdong Laboratory-Zhanjiang, China
Chi-Yu Zhang	Shanghai Public Health Clinical Center, Fudan University, China
Guo-Jie Zhang	Zhejiang University, China
Jing-Song Zhang	Naval Medical University, China
Shi-Chang Zhang	Hubei University, China
Xin Zhang	Hefei Institutes of Physical Science, CAS, China
Ya-Ping Zhang	Kunming Institute of Zoology, CAS, China
Yan Zhang	Peking University, China
Yun Zhang	Nanjing Drum Tower Hospital, Nanjing University, China
Yun-Wu Zhang	Xiamen University, China
Zhi Zhang	University of Science and Technology of China, China
Zhi-Jun Zhang	Southeast University, China
Bo Zhao	Kunming Institute of Zoology, CAS, China
Hua-Bin Zhao	Wuhan University, China
Hui Zhao	The Chinese University of Hong Kong, China
Jian-Guo Zhao	Institute of Zoology, CAS, China
Qian-Jun Zhao	Institute of Animal Science, CAAS, China
Tian Zhao	Southwest University, China
Wen-Ming Zhao	Beijing Institute of Genomics, CAS, China
Ya-Hui Zhao	Institute of Zoology, CAS, China
Ping Zheng	Fudan University, China
Gui-Sheng Zhong	ShanghaiTech University, China
Jiang Zhou	Guizhou Normal University, China
Peng Zhou	Guangzhou National Laboratory, China
Qi Zhou	Zhejiang University, China
Wu Zhou	The University of Mississippi, USA
Xin Zhou	China Agricultural University, China
Xu-Ming Zhou	Institute of Zoology, CAS, China
Yang Zhou	Huazhong Agricultural University, China
Xian-Jun Zhu	Sichuan Provincial People's Hospital, China
Kang Zou	Nanjing Agricultural University, China



ISSN 2095-8137
CN 53-1229/Q
Volume 46 Issue 1
18 January 2025

KUNMING INSTITUTE OF ZOOLOGY, CAS
CHINA ZOOLOGICAL SOCIETY
Science Press

CODEN: DOYADI
www.zoores.ac.cn

ZOOLOGICAL RESEARCH
动物学研究
Bimonthly, Since 1980
Volume 46 Issue 1, 18 January, 2025

中国最具国际影响力期刊
中国科技核心期刊
中国百强报刊

Editor-in-Chief: Yong-Gang Yao

Executive Editor-in-Chief: Xue-Long Jiang

Editors: Su-Qing Liu Long Nie Rong-Fu Wang

Edited by Editorial Office of Zoological Research

(Kunming Institute of Zoology, Chinese Academy of Sciences, 17 Longxin Road, Kunming, Yunnan, Post Code: 650201 Tel: +86 871 65199026 E-mail: zoores@mail.kiz.ac.cn)

Sponsored by Kunming Institute of Zoology, Chinese Academy of Sciences; China Zoological Society

Supervised by Chinese Academy of Sciences

Published by Editorial Office of Zoological Research, Kunming Institute of Zoology, Chinese Academy of Sciences©

Printed by Kunming Xiaosong Plate Making & Printing Co, Ltd

Domestic distribution by Yunnan Post and all local post offices in China

International distribution by China International Book Trading Corporation (Guoji Shudian) P.O.BOX 399, Beijing 100044, China

Overseas Code: BM358

Domestic Postal Issue No.: 64-20

Price: 25.0 USD/150.0 CNY

ISSN 2095-8137

CN 53-1229/Q

ISSN 2095-8137